eman ta zabal zazu

Universidad del País Vasco
Euskal Herriko Unibertsitatea

Electronic Technology Department
Teknologia Elektronikoa Saila
Departamento de Tecnología Electrónica

Double Smart Energy Harvesting System for self-powered Industrial IoT

Submitted for the degree of Doctor of Philosophy in the UPV/EHU by

Borja Pozo Larrocha

Directed by:
Dr. Jose Ignacio Garate Añibarro
Dr. Susana Ferreiro del Rio

Bilbao, 2018

Supported by:

And with the collaboration of:

Aita, Ama eta Leire
hau zuentzat da

We are nothing in the vastness of the universe,
let us do things to be it.

Borja Pozo Larrocha

Eskerrak /Agradecimientos /Acknowledgement/Anerkennungsbrief

Preface

Future factories would be based on the Industry 4.0 paradigm. Industrial Internet of Things (IIoT) represent a part of the solution in this field. As autonomous systems, powering challenges could be solved using energy harvesting technology. The present thesis work combines two alternatives of energy input and management on a single architecture. A mini-reactor and an indoor photovoltaic cell as energy harvesters and a double power manager with AC/DC and DC/DC converters controlled by a low power single controller. Furthermore, the aforementioned energy management is improved with artificial intelligence techniques, which allows a smart and optimal energy management. Besides, the harvested energy is going to be stored in a low power supercapacitor. The work concludes with the integration of these solutions making IIoT self-powered devices.

Resumen

1. Introducción

1.1 Paradigma de la Industria 4.0 e Internet de las Cosas Industriales (IIoT)

Hoy en día el término Industria 4.0 se está convirtiendo en un término extendido para describir la cuarta revolución industrial. Esta busca una total interconectividad de todas las actividades de producción a través de la digitalización. Las consecuencias de la cuarta revolución industrial no son meramente tecnológicas. La integración de las tecnologías de producción y las TICs, en forma de sistemas de producción ciberfísicos, está cambiando la forma en que la industria aporta "valor añadido". Las fábricas de la Industria 4.0 requieren sistemas sensóricos o IIoT para facilitar el procesamiento de la información.

Los sensores con inteligencia embebida o IIoT, que pueden comunicarse con un control central y están integrados dentro de los sistemas de gestión de la empresa, constituyen un cambio en la arquitectura del sistema en el proceso de automatización y control. Hoy en día, las máquinas son capaces de medir parámetros como el tiempo de uso, el consumo de energía, la eficiencia, los niveles de fluidos y otras características operativas, sin embargo, esta información es sólo sobre la máquina. Los dispositivos IIoT están destinados a proporcionar mejoras cuantificables en la economía de producción a través de la recolección remota de datos con post-procesamiento; mejorando la programación, el uso y el mantenimiento.

Una red IIoT está constituida por sensores autónomos distribuidos espacialmente con el objetivo de monitorizar las condiciones físicas o ambientales, tales como temperatura, sonido, vibración, presión, movimiento o contaminantes, para posteriormente transmitir cooperativamente sus datos a través de la red a una ubicación principal. Las redes son a menudo bidireccionales, ello también permite controlar la actividad de los sensores

1.2. Los sistemas de IIoT se enfrentan al reto de ser autónomos y autosuficientes energéticamente

Transformar las fábricas actuales en plantas inteligentes de la Industria 4.0 requerirá grandes cantidades de dispositivos y sensores IIoT. Sin embargo, la instalación de más IIoT aumenta la demanda de energía. Por lo tanto, uno de los requisitos para los dispositivos IIoT es que deben tener un consumo de energía reducido.

Las comunicaciones inalámbricas permiten una reducción progresiva del número de comunicaciones por cable; sin embargo, los dispositivos electrónicos deben alimentarse a través de cables de red. Debido a los desafíos que implica el objetivo de sistemas inalámbricos completos, tales como: puntos de medición de acceso difícil y gastos de despliegue, la instalación de cables no siempre es factible. Hoy en día la solución más común para alimentar los dispositivos IIoT son los dispositivos de almacenamiento de energía, i.e., baterías.

Aunque los fabricantes de baterías han mejorado considerablemente la vida útil de las mismas, a medida que cambian las condiciones ambientales, tales como la temperatura, la humedad o los picos de carga, se reducen la vida útil de las mismas. Una fábrica grande requerirá cientos o miles de dispositivos sensores inalámbricos, estos

sistemas pueden tener baterías, las cuales requieren un mantenimiento periódico; por lo tanto, miles de horas de trabajo se sumarían a los gastos de las baterías. Estos hechos constituyen un desafío para implementar la filosofía de los IIoT. Además, las baterías agotadas producen residuos que deben ser reciclados.

La recolección de energía es una alternativa para superar los retos técnicos antes mencionados. Los sistemas de captación de energía utilizan las fuentes de energía disponibles en los entornos industriales, como las vibraciones mecánicas, los gradientes de temperatura, la luz natural o artificial, los altos niveles de ruido o las tuberías con fluido de aire o agua, las cuales podrían utilizarse para alimentar los sistemas IIoT.

1.3. La recolección de energía como solución para la Industria 4.0

La tecnología de recolección de energía desarrolla e investiga sistemas para recolectar energía del entorno y utilizar esta energía para alimentar diferentes sistemas inalámbricos tales como dispositivos electrónicos de sensorización y sus respectivas comunicaciones. Sus principales objetivos son eliminar el cable de alimentación y eliminar o reducir la dependencia en las baterías, y aumentar o mantener la vida útil de los sistemas autónomos de IIoT.

Resumiendo, los principales objetivos de la tecnología de recolección de energía son:

- Retirar la última conexión física, el cable de alimentación.
- Eliminar o reducir la dependencia de las baterías.
- Aumentar la vida útil de los dispositivos IIoT/WSN.
- Mantener la misma funcionalidad que el sistema con batería y/o aumentar la funcionalidad.
- Fácil instalación.
- Bajo coste.

1.4. Solución propuesta

El trabajo presentado, se ha desarrollado en cuatro líneas de investigación diferentes, y se centra en la mejora del conocimiento, el suministro de energía y los sistemas de gestión para IIoT dentro del paradigma de la Industria 4.0.

La primera línea investigación propone un recolector del flujo de viento. En la industria, varios procesos de fabricación utilizan tuberías con fluidos. El recolector del flujo de viento podría proporcionar energía, por ejemplo, para dos casos. Por un lado, medir los diferentes parámetros necesarios para implementar una fábrica inteligente. Por otro lado, conocer la cantidad de fluido que pasa por una tubería y realizar una gestión eficiente del mismo, convirtiendo las fábricas del futuro en fábricas verdes.

Por lo general, la recolección de energía utiliza un solo recolector con su sistema de gestión y almacenamiento. Existen condiciones de operación en las que la energía disponible de una sola fuente no es suficiente, por lo que en el presente trabajo se investigan los requisitos de un sistema que combina dos fuentes de energía diferentes: un recolector eólico y una fuente solar comercial. La selección de los recolectores no es aleatoria, la arquitectura de la fuente de alimentación integra dos tipos diferentes de convertidores, AC/DC y DC/DC, para recolectores de flujo eólico y fotovoltaico respectivamente.

Como la energía debe ser almacenada dado que el sistema de consumo no hace uso constantemente de la energía recolectada, i.e., la recolección y el consumo no ocurren en el mismo período. Por lo tanto, conocer su comportamiento y poder modelar cambios en los niveles de almacenamiento con diferentes cargas de consumo, evita la colocación de elementos de almacenamiento adicionales cuando no son necesarios, disminuyendo costes y reduciendo el impacto ambiental. La solución propuesta resultado de la investigación realizada, constituye en una herramienta de simulación compuesta por nuevos algoritmos para modelar y predecir el comportamiento de los supercondensadores en distintas condiciones de operación.

Las técnicas de Inteligencia Artificial (IA) como la minería de datos se están convirtiendo en una práctica común en las centrales eléctricas, para mejorar su rendimiento y eficiencia. El presente trabajo aplica las mismas técnicas para los sistemas de baja energía, es decir, transferir las técnicas y la tecnología de los macrosistemas a los microsistemas. La IA contribuye a predecir la disponibilidad de energía en el medio, ayudando así a la gestión energética a procesar mejor la energía entrante.

2. Recolector de viento o mini-turbina

La presente contribución pertenece al campo de los recolectores de energía eólica para redes de sensores inalámbricos. Este recolector de energía podrá proporcionar suficiente energía a un nodo de acceso remoto en ambientes ventosos.

El funcionamiento de la turbina se basa en el movimiento rotativo del rotor para crear un campo magnético variable. Los rodamientos de la turbina, situados en la periferia del eje, permiten el libre movimiento rotativo del rotor. Cuando comienza el movimiento, los anillos magnéticos crean un campo magnético variable. El campo magnético generado es variable debido a que los anillos magnéticos tienen, en su parte periférica, los imanes del generador. Estos imanes describen un movimiento circular que forman parte del rotor que es girado por el flujo de un fluido que fluye a través de la mini-turbina. La existencia de un campo electromagnético variable induce una corriente eléctrica en las bobinas dispuestas en el estator, i.e., en el circuito impreso.

2.1 Prueba de concepto

El proceso comenzó con el diseño mecánico y simulaciones estructurales y magnéticas. Durante el diseño de las partes mecánicas de ultra-precisión del sistema, se tuvo en cuenta la complejidad de las diferentes piezas con pequeñas tolerancias y altos riesgos para la integración posterior. Las simulaciones magnéticas se utilizaron para estudiar la densidad de flujo magnético (B) en la superficie de la PCB y la fuerza electromotriz inducida en las bobinas. Paralelamente, el cálculo estructural involucrado en la verificación del diseño de la turbina se completó para continuar con la siguiente tarea, rediseñando partes del sistema. Posteriormente, se diseñó el primer prototipo del generador teniendo en cuenta los requisitos mecánicos y magnéticos establecidos por las tareas previas. Previamente a la fabricación del generador, el sistema eléctrico fue modelado matemáticamente para simular y analizar las frecuencias críticas de las bobinas y los niveles de potencia de las señales de salida. Después de este proceso y comprobado que todos los resultados obtenidos eran satisfactorios se realizó la fabricación de piezas mecánicas y eléctricas. A continuación, tuvo lugar la integración de componentes físicos (micromecánica-PCB), así como la integración de ensamblajes de procesos

interrelacionados para diversos módulos (efecto flujo, movimiento, generación de energía, etc.). Finalmente, se realizaron pruebas para verificar la hipótesis establecida.

2.2. Mejora de la prueba de concepto

La mini-turbina con generador monofásico constituye la prueba de concepto. Sin embargo, después de desarrollar la idea se introdujeron algunas mejoras en el sistema para lograr un prototipo útil. La arquitectura del generador trifásico constituye una mejora en comparación con el generador monofásico. Después de diseñar y verificar el comportamiento del nuevo generador, las partes mecánicas más importantes fueron fabricadas con un proceso de fabricación más complejo. Además, esta nueva elaboración se realizó con mejores materiales. Para verificar y validar el nuevo prototipo, se diseñó y fabricó un banco de pruebas.

Posteriormente, se realizaron los test correspondientes con los dos tipos de generadores. Los resultados más representativos se presentan en los siguientes puntos:

- El generador trifásico genera una potencia máxima de salida de 333 mW.
- El generador monofásico genera una potencia máxima de salida de 182 μW.
- La máxima velocidad angular alcanzada es de 40000 rpm.

3. Doble gestor y almacenamiento de baja potencia

En este capítulo se desarrolló un doble gestor de potencia para los recolectores eólico y fotovoltaico. Dispone de fuentes de alimentación DC y AC con sus correspondientes convertidores, DC/DC y AC/DC respectivamente. La energía recolectada por ambas fuentes se combina y se entrega a la carga a través de un supercondensador, que es usado como dispositivo de almacenamiento.

Estableciendo el requisito de no insertar más dispositivos (como otro paso de conversión o gestión) en el doble gestor de energía y mantener la eficiencia del sistema, el nivel de voltaje en el punto de almacenamiento debe ser de 3 V como mínimo y 5 V como máximo. Este requisito debe cumplirse en todas las condiciones ambientales. Además, no se utilizará el punto de máxima potencia de salida si no se cumple el requisito establecido.

3.1 Sistema DC

El sistema de DC se compone de un recolector fotovoltaico, un convertidor DC/DC y el dispositivo de almacenamiento compartido con el sistema de AC.

3.1.1 Modelo de la celda fotovoltaica

El modelo equivalente de la célula fotovoltaica desarrollado en el presente trabajo se basó en investigaciones anteriores. El modelo depende de la radiación solar G y de la temperatura del aire T_a. Para realizar una simulación con el modelo es necesario introducir los parámetros del panel solar suministrados en la hoja de datos del fabricante.

Los resultados mostraron que las celdas producen más energía a temperaturas más altas para el mismo nivel de irradiancia. También que la irradiancia tiene más efecto en

la producción de energía que la temperatura. Se obtuvo que la celda genera 22.333 mW con 0.1 soles a 5 ºC y 306.812mW con 1 sol a 60 ºC.

3.1.2 Convertidor DC/DC

A continuación, se empleó un convertidor DC/DC con topología elevadora, controlándolo mediante la técnica de Modulación de Ancho de Pulso (PWM).

El principal reto que presentó el diseño de este convertidor es que debía gestionar bajos niveles de potencia y tensión, lo que limitaba el rendimiento y la disponibilidad de semiconductores. La selección del valor de la bobina, el MOSFET y los diodos se realizaron con herramientas de simulación que probaban el rendimiento del convertidor en condiciones extremas.

La modelización antes mencionada se analiza, ajusta y busca la máxima eficiencia del convertidor en diferentes condiciones ambientales y niveles de potencia de entrada.

Los resultados mostraron que la eficiencia era siempre superior al 92 %. El mayor rendimiento era del 94,03 % y se obtuvo con 0,5 soles a 15 ºC. El rendimiento más bajo era del 92,30 % y se consiguió con 0,75 soles a 40 ºC. Los resultados corroboraron que el convertidor funcionaba correctamente en modo elevador para todas las condiciones ambientales.

3.2 Sistema AC

El sistema AC incluye el recolector de flujo de viento, el convertidor AC/DC y el dispositivo de almacenamiento compartido con el sistema DC.

3.2.1 Modelo de la mini-turbina/reactor

Después de algunas pruebas, los principios físicos de operación de la mini-turbina no estaban totalmente claros.

Se calcularon los valores teóricos y la potencia generada para verificar cuál era el principio de funcionamiento en concordancia con los resultados obtenidos en el capítulo III. Los resultados teóricos y medidos corroboraron la diferencia de modo de operación del recolector dependiendo del área de aplicación (espacio abierto o tubería).

Finalmente se descubrió que si el recolector se instalaba dentro de un tubo ventoso, la energía cinética absoluta recolectada era 0 y la potencia recolectada sería sólo la energía potencial. Por el principio de Bernoulli y considerando que el aire es incompresible, las velocidades del viento deben ser las mismas en ambos lados de la tubería, $v_1=v_2$. Además, debido al teorema del principio de energía, P_1 debe ser mayor que P_2, $P_1>P_2$, y por consiguiente $\Delta P=P_1-P_2$.

Por lo tanto, la energía recolectada correspondía a la energía potencial del viento, y no a la energía cinética, **terminológicamente no es una mini-turbina, es un mini-reactor.** Y el ambiente correcto o apropiado para trabajar para este recolector es dentro de una tubería.

A continuación, se desarrolló el modelo electromecánico equivalente del mini-reactor utilizando los valores de potencia de entrada y comportamiento del sistema. La energía eólica y la conversión de esta en energía mecánica y posteriormente en eléctrica se modela a través de ecuaciones matemáticas, fuentes controladas por voltaje y corriente y componentes pasivos.

3.2.2 Convertidor AC/DC

En la literatura, hay tres técnicas principales de conversión AC/DC: rectificación directa de señales AC a DC, rectificación AC más conversión DC/DC y conversión AC/DC directa. La primera alternativa sólo rectifica la señal de entrada, proporcionando un nivel bajo de señal debido a las pérdidas en el rectificador. En la segunda alternativa, la señal es primero rectificada y posteriormente transformada en el nivel de DC deseado con un convertidor DC/DC, usualmente un convertidor elevador. Si se compara con otras alternativas, el número de pasos que requiere esta alternativa reduce su eficiencia. La tercera y última alternativa fue la elegida en la presente investigación, la conversión AC/DC.

Consecuentemente, se implementó el convertidor AC/DC seleccionando la arquitectura adecuada para el caso de uso de este trabajo.

En esta tarea se simularon cinco arquitecturas con el objetivo de obtener la máxima potencia de salida con las menores pérdidas posibles o la máxima eficiencia en la carga resistiva en modo DC. Las arquitecturas utilizadas fueron: puente de diodos, duplicador de tensión, Side-diode, Split N y Split NP.

Todas las arquitecturas fueron analizadas en dos condiciones extremas, 3 y 10 m/s. Además, se realizaron cinco simulaciones de barrido diferentes para cada condición y arquitectura.

El puente de diodos y el duplicador de tensión no alcanzaron el valor mínimo de tensión de los requisitos definidos, por lo que estas dos arquitecturas fueron directamente rechazadas. Por lo tanto, la selección se realizó entre las otras tres arquitecturas restantes. Y en base a los resultados obtenidos, Split NP fue seleccionado como convertidor de AC/DC del sistema AC del doble gestor de energía.

3.3 Supercondensador

El primer paso para seleccionar un supercondensador es dimensionar la capacitancia y el factor de forma para la aplicación objetivo, lo que requiere una caracterización completa del patrón de consumo de energía de la aplicación objetivo. Esta información y un modelo de supercondensador suficientemente preciso permiten determinar el valor de capacitancia requerido para diferentes condiciones.

3.3.1 Test experimentales

El modelo matemático fue verificado a través de varias pruebas experimentales. Los resultados obtenidos se utilizaron posteriormente para los procesos de formación y verificación de los algoritmos de aprendizaje automático. Las pruebas también proporcionaron el perfil de corriente de carga para el modelo matemático.

Con este conjunto de variables se implementó, para cada supercondensador, 15 pruebas de carga y 21 de descarga. Además, se construyó una placa de evaluación y cada una de las condiciones de prueba se reprodujo en una cámara climática.

3.3.2 Modelo matemático

La estructura física, las reacciones químicas y la distribución de la corriente dentro del condensador se pueden modelar a través de expresiones matemáticas.

El modelo matemático desarrollado se basa en ecuaciones integro-diferenciales. El estado del arte de los modelos electro-matemáticos implementa sólo uno o dos parámetros, lo que produce un modelo limitado. El presente trabajo aumenta el número de parámetros (ciclo de vida de la capacitancia, tensión, tiempo, temperatura, humedad, ESR y resistencia a las fugas) para caracterizar el comportamiento del supercondensador y los integra en un único modelo.

Las ecuaciones antes mencionadas requirieron un post-procesamiento para obtener sus coeficientes y definir las curvas equivalentes de condensador. El modelo matemático completo se implementó en MATLAB®. Para simular las condiciones de funcionamiento deseadas, las variables y el perfil de corriente de carga, es decir, un archivo de datos, deben introducirse manualmente en las ecuaciones.

La validación de los resultados fue realizada mediante las técnicas estadísticas RMSE, MAE, MSE y MAPE.

4. Técnicas de aprendizaje automático y minería de datos para sistemas de recolección de energía

4.1 Selección de células fotovoltaicas mediante análisis de datos

En este apartado se consideró una metodología para realizar una correcta selección de un recolector según el caso de uso, teniendo en cuenta el tamaño, la tecnología, la potencia generada, etc.

4.1.1 Selección con análisis de medición

La tarea para la selección de los módulos solares se basó en una búsqueda avanzada entre los fabricantes y distribuidores de células solares. Además, las celdas seleccionadas debían poder operar en el caso de uso de este trabajo.

Seis pruebas en condiciones de baja irradiancia y una con efecto solar en invierno fueron realizadas con los tres módulos fotovoltaicos seleccionados.

Considerando esta evaluación inicial, basada en los resultados de la experimentación, parecía que el IXYS10 podría ser el mejor candidato para ser seleccionado. Sin embargo, IXYS08 parecía ser más eficiente. Por lo tanto, se realizaron pruebas estadísticas para identificar si existía una diferencia estadística significativa entre el comportamiento de cada célula o si podrían ser causadas simplemente por efectos de aleatoriedad.

4.1.2 Selección con algoritmos de análisis de datos

Empleando los algoritmos ANOVA y HSD de Tukey, se establecieron dos objetivos para el desarrollo de la tarea:

1. Seleccionar la célula solar más adecuada en términos de eficiencia.
2. Evaluar la utilidad de este tipo de técnicas estadísticas para la selección del sistema más adecuado entre un conjunto de sistemas con diferentes características y beneficios.

Finalmente, como conclusión tras aplicar ANOVA y la prueba HSD de Tukey, parecía que existían diferencias significativas entre los valores obtenidos con las tres células solares. IXYS08 y IXYS10 tenían una mayor capacidad para recolectar energía bajo las mismas condiciones de trabajo que la célula solar AM1816. Basado en las pruebas estadísticas, IXYS10 sería el mejor candidato para utilizar. Sin embargo, contrastando estos resultados con los criterios, parecía que la capacidad de recolección de energía para la célula solar IXYS10 era mayor porque tiene más número de bancos; y teniendo en cuenta esta premisa, IXS08 sería mejor en términos de eficiencia.

4.2 Mejora de la precisión del modelo de supercondensadores con técnicas de aprendizaje automático

Se aplicaron técnicas de aprendizaje automático para evaluar la precisión y estabilidad de este tipo de algoritmos con el fin de predecir las curvas y comparar los resultados de ambos tipos de modelización: modelización matemática/teórica y modelización de aprendizaje automático. Se aplicaron cuatro algoritmos de aprendizaje automático:

- W-M5P
- NeuralNet
- W-MultilayerPerceptron
- Lineal SVM

4.2.1 Primera aproximación: Modelado de la curva de carga

En cuanto a la precisión y desviación del modelo, a partir de esta evaluación inicial se pudo considerar que Neural Net y W-M5P podían ser las mejores opciones; principalmente el algoritmo Neural Net, cuya precisión era la mayor y uno de los algoritmos con menor grado de desviación, y también el W-M5P, que no fue descartado de nuestra selección porque su precisión seguía siendo mayor que el resto a pesar de su medida de desviación.

4.2.2 Segunda aproximación: Modelado de la curva de descarga

Como en el caso de los datos de carga, los algoritmos W-M5P y NeuralNet proporcionaron el mejor rendimiento, se decidió minimizar el número de análisis, aplicando sólo estos dos algoritmos con los datos de descarga.

4.2.3 Conclusiones de las aproximaciones

Una vez realizado el análisis, se pudo concluir que algunos de los algoritmos de aprendizaje automático proporcionan la capacidad de predecir las curvas de carga y descarga, así como el modelo matemático.

En general, los modelos de aprendizaje automático tienen un mejor rendimiento en comparación con los modelos matemáticos y proporcionan una precisión mejorada.

4.3 Estrategia de gestión de potencia predictiva

En esta sección se explican dos casos de uso diferentes, el sistema DC y el sistema AC. El objetivo de este trabajo fue evaluar su precisión y extender esta evaluación a varios algoritmos predictivos. Por lo tanto, se buscaron varios algoritmos de series de tiempo con el objetivo de predecir la energía recolectada de los sistemas de DC y AC:

- exponential smoothing
- exponentially weighted moving-average (EWMA)
- linear regression
- support vector regression (SVR)
- auto-regressive integrated moving average (ARIMA)

4.3.1 Sistema DC

Los datos utilizados para este trabajo se obtuvieron a partir de la potencia del sistema de DC (célula solar y convertidor DC/DC). Se modelaron diferentes perfiles de producción de energía bajo tres condiciones de iluminación diferentes: luminancia constante, luminancia variable y luminancia y temperatura variables.

Para los experimentos se construyeron dos series de tiempo con los perfiles de energía: una para entrenar los algoritmos y otra para probarlos.

El conjunto de entrenamiento se utilizó para estimar coeficientes en LR, SVR y ARIMA. Para SVR y ARIMA, el kit de entrenamiento también se utilizó para ajustar sus hiperparámetros. Para ETS, el conjunto de entrenamiento se utilizó para seleccionar un valor para el coeficiente alfa. En el caso de EWMA, el conjunto de capacitación se utilizó para la inicialización.

Además de esto, se agregó ruido aleatorio de una distribución uniforme a los datos. El ruido se utiliza para simular pequeñas variaciones en las condiciones de recolección de energía. El nivel de ruido era de ±10 mW, o aproximadamente ±8% del valor máximo de la serie. Y finalmente, se llevaron a cabo los siguientes grupos de experimentos:

- Datos limpios
- Datos de entrenamiento ruidosos
- Datos ruidosos

En todos los casos, los cinco algoritmos (ETS, EWMA, LR, SVR y ARIMA) fueron probados en la tarea de predecir el siguiente valor (1 minuto después) de la energía recolectada.

De los resultados se obtuvo que el error para EWMA es mayor que para los otros algoritmos, debido a que la predicción de EWMA se basa en días anteriores. Y los algoritmos LR y ARIMA son los que mejor comportamiento ofrecen.

4.3.2 Sistema AC

Los datos del sistema AC (mini-reactor y convertidor AC/DC) fueron simulados en condiciones experimentales de potencia, velocidad y presión. En este sentido, se modelaron diferentes perfiles de producción de energía bajo tres condiciones ambientales diferentes: Indistinto, invierno y verano.

Utilizando el mismo procedimiento descrito en la sección anterior y bajo variabilidad de vientos pequeños y medianos, se han obtenido los resultados correspondientes. Sin embargo, en estos experimentos el nivel de ruido utilizado fue de ±20 mW, de nuevo ±8% del valor máximo de la serie.

Se observó que la variabilidad del viento tiene un efecto notable en el rendimiento de los modelos. Por lo tanto, la condición de gran variabilidad del viento fue también probada.

Considerando los resultados y teniendo en cuenta la complejidad de los algoritmos, LR y ARIMA fueron otra vez los que mejor comportamiento demostraron.

5. Conclusiones

El presente trabajo de investigación propone e implementa un mini-reactor para recolectar energía de los fluidos en entornos industriales. Los resultados de las pruebas muestran que el sistema desarrollado proporciona una eficiencia del 20% y entrega a la carga una potencia entre 15 y 333 mW para presiones de aire en tuberías de 20 a 163 mbar, respectivamente.

Para analizar la viabilidad de un gestor dual de potencia en sistemas de recolección, se han utilizado dos tipos de recolectores de referencia en este trabajo, uno DC (panel solar) y otro AC, el mini-reactor. El proceso para obtener los datos para diseñar y escalar la potencia y eficiencia de los convertidores AC/DC y DC/DC, requiere modelar los recolectores. Así, esta investigación introduce un modelo estructural y eléctrico de la celda solar y un nuevo modelo electromecánico del mini-reactor. Los resultados de las pruebas presentadas muestran que el sistema de DC basado en células solares proporciona más energía durante largos períodos, debido a la disponibilidad periódica de la luz. Por otra parte, el mini-reactor y su convertidor AC/DC suministran más energía a la carga, pero durante períodos cortos. El objetivo de los futuros desarrollos es lograr un sistema universal de gestión de la energía para n-número de fuentes de energía.

El modelo matemático y el algoritmo de inteligencia artificial desarrollados en el presente trabajo están dedicados a las aplicaciones de recolectores de energía para redes inalámbricas de sensores de baja potencia. Esta tarea, constituye una mejora del estado del arte en los modelos electro-matemáticos de supercondensadores para aplicaciones de baja potencia ya que utiliza sus parámetros más característicos. Además, los resultados de simulación y las pruebas muestran que proporciona la misma precisión que los modelos electroquímicos y mayor precisión que los modelos matemáticos más avanzados. La mejora del modelo electro-matemático con algoritmos de aprendizaje automático requiere menos

datos experimentales que los modelos electroquímicos para lograr la misma precisión. Además, el algoritmo de aprendizaje automático no requiere ningún parámetro electroquímico para implementar el modelo.

Los recientes esfuerzos de investigación en nuevas tecnologías y técnicas para la recolección de energía muestran que esta es una tecnología prometedora para mejorar la huella energética de los dispositivos electrónicos. Sin embargo, los sistemas de energía ambiental, como las células solares, luchan contra sus fluctuaciones y su dependencia de factores ambientales y externos. Así, la energía recolectada no es ni constante ni continua. El presente trabajo evalúa si los métodos y algoritmos predictivos, tomados del campo de la inteligencia artificial y de la analítica avanzada, constituyen la solución para superar los retos técnicos de la gestión de potencia. El trabajo propuesto se basa en la posibilidad de predecir tanto la disponibilidad de energía como los requisitos de consumo de energía. Y gracias a ello, el sistema de gestión de la energía podría tomar decisiones en situaciones críticas y abordar tareas relacionadas con el uso y la distribución de la energía disponible en una red de sistemas IIoT. Sin embargo, los resultados obtenidos en este trabajo muestran que no todos los algoritmos testeados son adecuados para los sistemas IIoT, por lo que se requiere más investigación en algoritmos, recolectores y aplicaciones de recolección de energía. Uno de los campos de investigación pertinentes debería ser el consumo de energía y la eficiencia energética de los algoritmos.

Resumiendo, la investigación presentada en esta tesis demuestra que los sistemas de recolección de energía son una alternativa factible para reducir o eliminar la dependencia de las baterías de los dispositivos IIoT, contribuyendo así al paradigma de la Industria 4.0 y a su despliegue efectivo.

Index

I. Introduction 1

1. Introduction and motivation 3

1.1 Industry 4.0 paradigm and Industrial Internet of Things (IIoT) 3

1.2 IIoT systems challenges to become autonomous and energy self-sufficiency 7

1.3 Energy Harvesting as a solution for Industry 4.0 10

1.4 Double smart energy harvesting system for self-powered industrial IoT 14

1.5 Memory structure 18

II. Principles of energy harvesting, low power management and storage 23

2. Energy harvesters' technologies 25

2.1 Photovoltaic harvester's technology and devices 25

2.2 Kinetic harvester's technology and devices 28

2.2.1 Piezoelectric transduction 29

2.2.2 Electromagnetic transduction 31

2.2.3 Electrostatic transduction 33

2.2.4 Pyroelectric transduction 35

2.3 Thermoelectric harvester's technology and devices 38

2.4 Magnetic harvester's technology and devices 40

2.5 RF harvester's technology and devices 42

2.6 Dynamic fluid energy harvesting 44

2.6.1 Wind harvester's technology and devices 44

2.6.2 Water flow harvester's technology and devices 46

2.7 Acoustic noise harvester's technology and devices 47

3. Low power management 49

3.1.1 Low power principles 49

3.1.2 Low power management principles 52

3.2 Power conditioning reference analog circuits 54

3.2.1 Buck converter 55

3.2.2 Boost converter 55

3.2.3 Buck-Boost converter and 56

3.2.4 AC–DC rectifier 56
3.2.5 Regulators 57
3.3 Examples of low power managers for different energy harvesters 58
3.3.1 Power management for solar harvesters 58
3.3.2 Power management for kinetic harvesters 58
3.3.3 Power management for thermoelectric harvesters 61
3.3.4 Power management for magnetic harvesters 61
3.3.5 Power management for RF harvesters 62
3.3.6 Power management for wind and water harvesters 63
3.3.7 Power management for acoustic harvesters 63
3.3.8 Hybrid power source devices 64
3.3.9 Present commercial digital power management 64
4. Low energy storage devices 65
4.1 Supercapacitors 67
4.1.1 Electric double-layer capacitor 68
4.2 Rechargeable batteries 70
4.2.1 Lithium-ion batteries 71
5. Machine learning and data mining techniques for energy harvesting systems 74
5.1 Data science principles 74
5.2 Data science state of art for energy harvesting systems 76
5.2.1 Data Mining examples 76
5.2.2 Machine Learning examples 76
5.2.3 Predictive Modelling examples 77
6. WSN systems 78
6.1 WSN theoretical principles 78
6.2 WSN nodes hardware 81
6.2.1 Sensing unit 81
6.2.2 Processing unit 82
6.2.3 Transceiver unit 82

III. Mini wind turbine harvester 85
7. Mini-turbine 87
7.1 System principles 87
7.1.1 System objective and hypothesis 87
7.1.2 System operation description 87
7.1.3 Development methodology 88
7.2 Proof of concept 90
7.2.1 Ultra-precision mechanical design of proof of concept 90
7.2.2 Magnetic simulation 93
7.2.3 Mechanic structural behaviour calculations 103
7.2.4 Monophasic electrical generator design and simulation 104
7.2.5 Electrical monophasic generator manufacture 108
7.2.6 Mechanical manufacture and assembly process 111
7.2.7 Test and results 114
7.3 Improvement of proof of concept 116
7.3.1 Three-phase electric generator design and simulation 116
7.3.2 Electrical manufacture 119
7.3.3 Mechanical manufacture 121
7.3.4 Test-bench 123
7.3.5 Laboratory tests set-ups 126
7.3.6 Test Results 127
7.4 Target application 134
7.4.1 Industry 134
7.4.2 Railway 135
IV. Double low power management and storage 137
8. DC input system 139
8.1 Photovoltaic electro-physical model 139
8.1.1 Theoretical principles of photovoltaic model 139
8.1.2 Photovoltaic module model 143
8.1.3 Tests set-up for model verification and validation 146

8.1.4 Comparison between model and test results 148
8.1 DC/DC converter 150
8.1.1 Context, objective and development methodology 150
8.1.2 Boost architecture definition 151
8.1.3 Simulations and results of the converter 156
9. AC input system 159
9.1 Mini-turbine/reactor electro-mechanical model 160
9.1.1 Theoretical principles of mini turbine/reactor operation 160
9.1.2 Tests for model construction 168
9.1.3 Mini-reactor model construction 173
9.1.4 Comparison between model and test results 176
9.2 AC/DC converter 178
9.2.1 Context, objective and development methodology 178
9.2.2 Diode and MOSFET selection for AC/DC converter 180
9.2.3 Used architectures, their operation principles, simulations and results 183
9.2.4 Summarize of results and circuit selection 207
10. Supercapacitor 209
10.1 Principles of supercapacitor model 209
10.2 Experimental test 210
10.2.1 Test definition 210
10.2.2 Evaluation-board design and build 211
10.2.3 Tests results 212
10.3 Electro-mathematical model 214
10.3.1 Equations 214
10.3.2 Model architecture and development 216
10.3.3 Results 217
10.4 Results of supercapacitor models 221
10.5 Application example of supercapacitor model 224
V. Machine learning techniques for energy harvesting systems 227
11. Photovoltaic cell selection by data analysis 229

11.1 Measurement process 229
11.1.1 Solar cell selection 229
11.1.2 Test description 230
11.1.3 Measurement results 231
11.2 Cell selection with data analysis algorithms 234
11.2.1 ANOVA 234
11.2.2 Tukey's HSD test 235
11.2.3 Results 236
12. Supercapacitor model accuracy improvement with machine learning techniques 241
12.1 Objective and Experimental setup 241
12.2 Machine learning algorithms 242
12.3 Evaluation method 243
12.4 Experimental Results 243
12.4.1 First approach: Charging curve modelling 243
12.4.2 Second approach: Discharge curve modelling 245
12.4.3 Approaches conclusions 247
12.5 Validation of machine learning and mathematical modelling 247
13. Predictive power management strategy 249
13.1 Use case definition 250
13.2 Research and development of the algorithms 250
13.3 DC system 252
13.3.1 Data acquisition and consumption profile definition 252
13.3.2 Evaluation procedure 255
13.3.3 Experimental results 256
13.4 AC system 259
13.4.1 Data acquisition and consumption profile definition 259
13.4.2 Evaluation procedure 263
13.4.3 Experimental results 263
13.5 Energy management strategy 268

VI. Conclusions and future work 269

14. Conclusions 271

14.1 General conclusions 271

14.2 Mini-reactor conclusions 271

14.3 Double low power management conclusions 272

14.4 Supercapacitor modelling with mathematical and machine learning techniques 273

14.5 Data mining and machine learning techniques for energy harvesting systems conclusions 274

15. Future works and opened research lines 275

15.1 Future works 275

15.1.1 PCB development 275

15.1.2 Controls implementation in the microcontroller 277

15.1.3 Extend the application of predictive algorithms 277

15.1.4 Mini-reactor application and extend to fluid ambient fields 278

15.2 Opened research lines 278

15.2.1 Multi-harvester universal power manager at energy harvesting systems 279

15.2.2 Machine learning and data mining in energy harvesting systems 279

VII. References 281

VIII. Appendix 293

16. Appendix 294

16.1 Mini-reactor 294

16.1.1 Magnetic simulations 294

16.1.2 Electrical generators theoretical calculus 297

16.1.3 Test-bench mechanical designs 302

16.1.4 Results graphics 303

16.2 DC input system 310

16.2.1 Photovoltaic harvester model vs test result interpolation and plot functions 310

16.2.2 Photovoltaic module model + DC/DC converter schematic 312

16.2.3 DC/DC converter behaviour signals 313

16.3 AC input system 315
16.3.1 Power coefficients comparison 315
16.3.2 Micro-reactor model + AC/DC converter circuits 316
16.3.3 AC/DC converters behaviour signals 321
16.4 Supercapacitor 329
16.4.1 Schematic evaluation board 329
16.4.2 Test to validate supercapacitor models 330
16.4.3 Electro-mathematical model code 333

I.
Introduction

The chapter aims to define and establish the motivation and the scope of this doctoral thesis project, as well as to identify its contribution and potential regarding the development of a fully functional smart double energy harvesting system under the paradigm of Industry 4.0 and Industrial Internet of Things (IIoT) devices.

To this end, this chapter is divided into four sections:

- Section 1.1 Industry 4.0 paradigm and Industrial Internet of Things (IIoT)
- Section 1.2 IIoT systems challenges to become autonomous and energy self-sufficiency
- Section 1.3 Energy Harvesting as a solution for Industry 4.0
- Section 1.4 Double smart energy harvesting system for self-powered industrial IoT
- Section 1.5 Memory structure

Firstly, Section 1.1 provides an overview of the current industrial transformation; the so-called the fourth industrial revolution 'Industry 4.0', which is supported by the convergence of technological components to achieve smart industry goals regarding new technologies and innovation.

Industrial Internet of Things (IIoT) is one of the priority group of technologies for the definition and the development of the 'Industry 4.0' paradigm. It is a subcategory of the term of Internet of Thing (IoT), which aims to increase the efficiency and improve the health and safety, focused primarily on industrial applications. Section 1.2 reviews the concept of IIoT, emphasising the challenges to be addressed by researchers related to energy consumption and management. One of the main problems lies with the reduction of the energy consumption and its management. Nowadays, both, batteries and mains powered are being used in spite of the short life of batteries and the technical impossibility to connect a long power supply wire.

A proposed solution, called Energy Harvesting (EH), emerged around 2006 [1] to address some of these challenges. It constitutes a way to get the energy from the ambient and power the IIoT device. This concept is explained in Section 1.3. and introduces the new generation of Energy Harvesting for Wireless Sensor Networks within the paradigm of 'Industry 4.0'.

Section 1.4 defines the scope and objectives of this thesis project, highlighting its main contributions and results regarding Energy Harvesting systems focused on its use as IIoT technology.

Finally, Section 1.5. provides the description of the structure and the content of the memory.

1. Introduction and motivation

1.1 Industry 4.0 paradigm and Industrial Internet of Things (IIoT)

Nowadays Industry 4.0 is becoming more popular as the term to describe the fourth industrial revolution, which aims for complete interconnectivity of the all production activities through digitization [2]. According to the impulses of this movement, the first industrial revolution emerged at the end of the eighteenth century along with the introduction of mechanical equipment powered by steam engines in the manufacturing industry. The second industrial revolution was initiated at the beginning of the twentieth century, well-supported in electricity and characterized by the mass production of goods, it was based on an increased division of labour. The third industrial revolution, which began in the early 1970s and reaches to present day, uses electronics and information technology to increase the automation of manufacturing processes. The fourth revolution is an "a priori" announcement of something that is being searched [3].

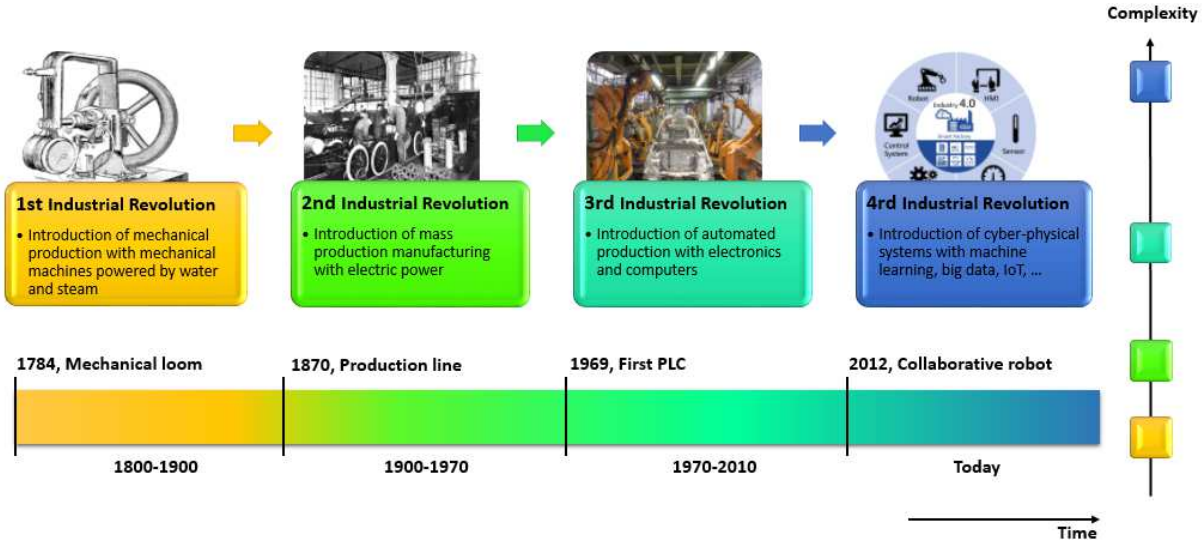

Figure 1-1: Industrial revolutions timeline.

The fourth industrial revolution consequences are not merely technological [4]. The integration of production technologies and ICT, in the form of cyber-physical production systems, is changing the way in which the industry brings "added value". Industry 4.0 factories achieve this objective adding interoperability, information transparency, technical assistance and decentralized decision-making, which is obtained through capabilities of interoperability, connectivity, and communication between machines, devices, sensors and people. In addition, it requires information transparency to create a virtual copy of the physical world through sensor data to ease the information processing.

Therefore, future smart factories must be more efficient, intelligent and connected [5]. The application of these technologies is an ongoing discussion of the industry 4.0 paradigm [6]-[8].

In this context, reference companies in automation processes and manufacturing equipment, such as Siemens, Bosch, General Electric, ABB, Schneider Electric, Honeywell, etc. are ensuring that all the research efforts reach to make new machines with fully digital technology [9], where listed technologies are the most important supporters of this revolution.

In 2015, Siemens (Munich, Germany) presented MindSphere®, their Industry 4.0 platform, offering the online monitoring and analysis of globally distributed machine tools, industrial robots, or industrial equipment such as compressors and pumps. Additionally, again in 2015 General Electric (Fairfield, CT, USA) launched Predix® an operating system of the Industrial Internet for connecting industrial equipment, analysing data, and delivering real-time insights [10], and where smart and connected devices play a crucial role in the Predix system architecture: data and information gathering.

Other, manufacturers like Bosch (Stuttgart, Germany) are not only focusing on the higher levels of the digitalization of industry [9], but also they are shifting to generate novel sensor technologies that meet the expectations of self-powered, integrability, connectivity, intelligence, flexibility and indeed cost [11][12]. Some of the latest examples of this paradigm shift in the Bosch sensor portfolio are found in the APAS®, a bunch of intelligent systems for man-machine collaboration, including fully sensorized and connected robots and workplaces.

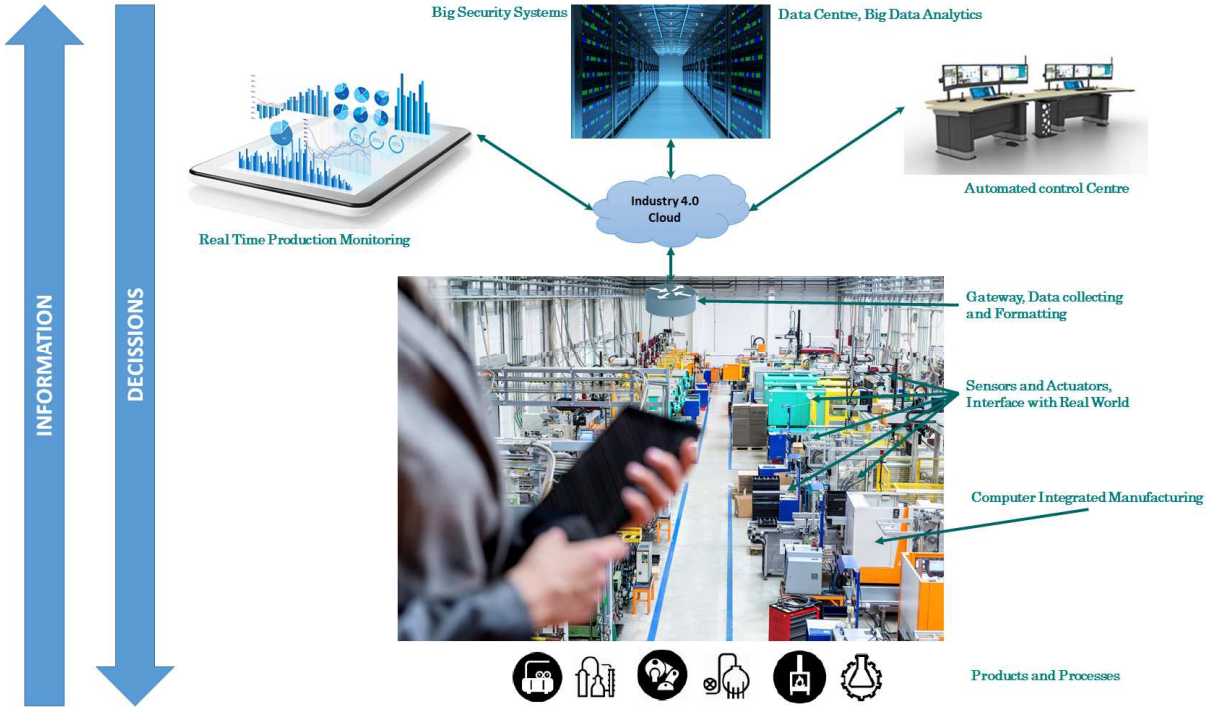

Figure 1-2: Overview of Industry 4.0 paradigm.

Smart sensors with embedded intelligence that can communicate for control and are integrated within the enterprise business systems constitute a change of system architecture in automation and control process. For this, Industry 4.0 draws a future of factories where thousands of end-points coexist, creating smart monitoring end-points, help to make strategic decisions and changing operational functions. Nowadays, machines measure parameters as usage, energy consumption, efficiency, fluid levels and other operational characteristics. Nevertheless, this information is only about the machine. Industrial Internet of Things (IIoT) devices are aimed to provide measurable improvements in production economics through remote data harvesting with post-processing; scheduling improvement, usage, and maintenance.

Also, if IIoT devices are installed in manufactured products and follow the same process as described above, specifications data, configuration, authenticity, usage, wear, and maintenance are an example of the added value to the product. This would provide

information to facilitate lifecycle management, such as equipment assembly, configuration, maintenance, safety, and compatibility. To make able the implementation of previously mentioned requirements, it would be necessary to measure many physical parameters. Then, achieve the information, process and give the final user the necessary information to make the best decision.

The application of IIoT [13] is part of an ongoing discussion throughout the industry 4.0 paradigm [14] [15]. Smart sensors with embedded intelligence that can communicate for control and integrate with enterprise business systems represent an obvious system architecture change of automation and control process.

The Internet of Things (IIoT is the industrial implementation term of IoT) is considered the next step, and challenge, for the Internet engineering community, users of technology, companies, and society. Nowadays, information in media, orient to their economic potential. For example, Forbes published "Between 2015 to 2020, BCG predicts revenue from all layers of the IoT technology stack will attain a least a 20% Compound Annual Growth Rate (CAGR). B2B customers are the most focused on services, IoT analytics, and applications, making these two areas of the technology stack the fastest growing. By 2020, these two layers will have captured 60% of the growth from IoT. Each of these two top two layers is predicted to generate €60B ($64.1B) reversible by 2020" [17]. In Business Insider was published, "The enterprise sector will account for 39% of the roughly 23 billion active IoT devices we expect by the year 2019. We believe it will be the largest of the three main IoT markets including enterprise, home, and government. Spending on enterprise IoT products and services will reach $255 billion globally by 2019, up from $46.2 billion this year, according to our estimates. This represents a 5-year CAGR of 40%" [18]. The International Organization for Standardization (ISO) published, "Technology consulting firm Gartner, Inc. projects that 6.4 billion connected things will be in use worldwide this year, up 30 % from last year. Moreover, this number is expected to grow by more than three times to nearly 21 billion by the year 2020" [19]. However, the Washington Post published, "By 2025, says McKinsey, the potential economic impact of having sensors and actuators connected by networks to computing systems (McKinsey's definition of the Internet of Things) could be more than $11 trillion annually" [20]. Instead of this notice, they mentioned that the society is under-hyping the IoT. Figure 1-3 [21] shows the market of IoT devices.

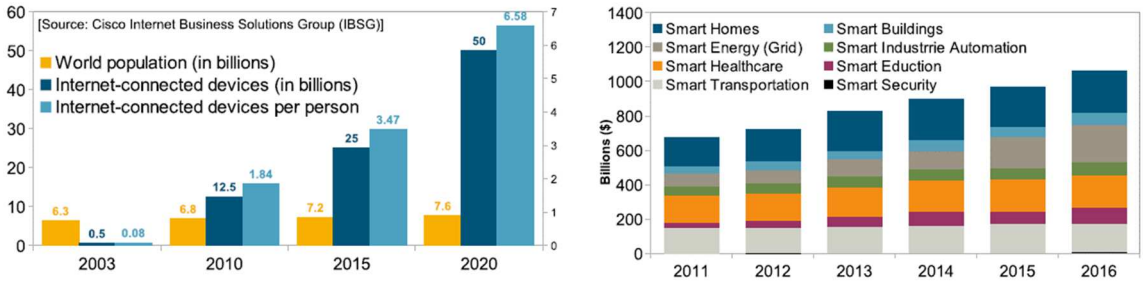

Figure 1-3: a) Growth in the Internet Connected Devices/objects by 2020, b) Smart product sale by the market in last years.

As a conclusion, the deployment of IoT devices is growing exponentially, sold and new applications are also increasing. However, the society perhaps may not be awaiting progress at the same pall of the technology, and this economic expectation may not be accomplished.

IIoT will make business more efficient, a claim that is backed up by some early evidence [22]. The digitization of machines, vehicles, and other elements of the physical world is a powerful idea. Even at this early stage, the IIoT is starting to have a real impact by changing how goods are made and distributed and how products are serviced and

refined. However, capturing the full potential of IIoT applications will require innovation in technologies and business models, as well as investment in new capabilities and talent. With policy actions to encourage interoperability, ensure security, and protect privacy and property rights, the IIoT can begin to reach its full potential especially if leaders truly embrace data-driven decision making.

Actual systems called wireless sensor network (WSN) include communication capabilities, information and control processing and sensors monitoring. IIoT devices, next generation of WSN, should include the following requirements:

- Energy self-sufficiency and energy harvesting
- Autonomous sensor interaction
- Sensor verification
- Plug and Play
- Virtual description supporting continuous engineering
- Traceability and compliance
- Self-calibration
- Self-diagnosis
- Standardized communication
- Maintenance and operating functions
- Sensor data access rights control
- Standards compatible

Once defined the IIoT requirements, its architecture and the network of an IIoT device is going to be introduced.

An IIoT network consists of spatially distributed autonomous sensors with the objective of monitoring physical or environmental conditions, such as temperature, sound, vibration, pressure, motion or pollutants and to cooperatively pass their data through the network to the main location. The networks are often bidirectional, also enabling to control the activity of the sensors [23]. The standard architecture of an IIoT is divided into three sections [24]. The first one includes the sensor system with the processor and the radio to transmit/receive the information. This system also has an energy storage device to power the equipment.

The second part of IIoT is the network created to connect several installed sensors with the central area node and transmit information to process it [25]. This central node also controls different parameters of sensor devices and maintain the communication with the cloud. The operation mode is a gateway, i.e., a communication bridge between different sensor devices and cloud.

The third section is composed of the cloud, the central system and the central control room [26]. The cloud is an online infrastructure, often located on Internet, which enable ubiquitous access to shared point to configure resources or provide any data. Then the central processor system saves all information in a database and is processed with big data techniques (another technology that has born from smart society/industry paradigm). From the central control room, all relevant information is checked; consequently, appropriate decisions are made. The described system block diagram is shown in figure 1-4.

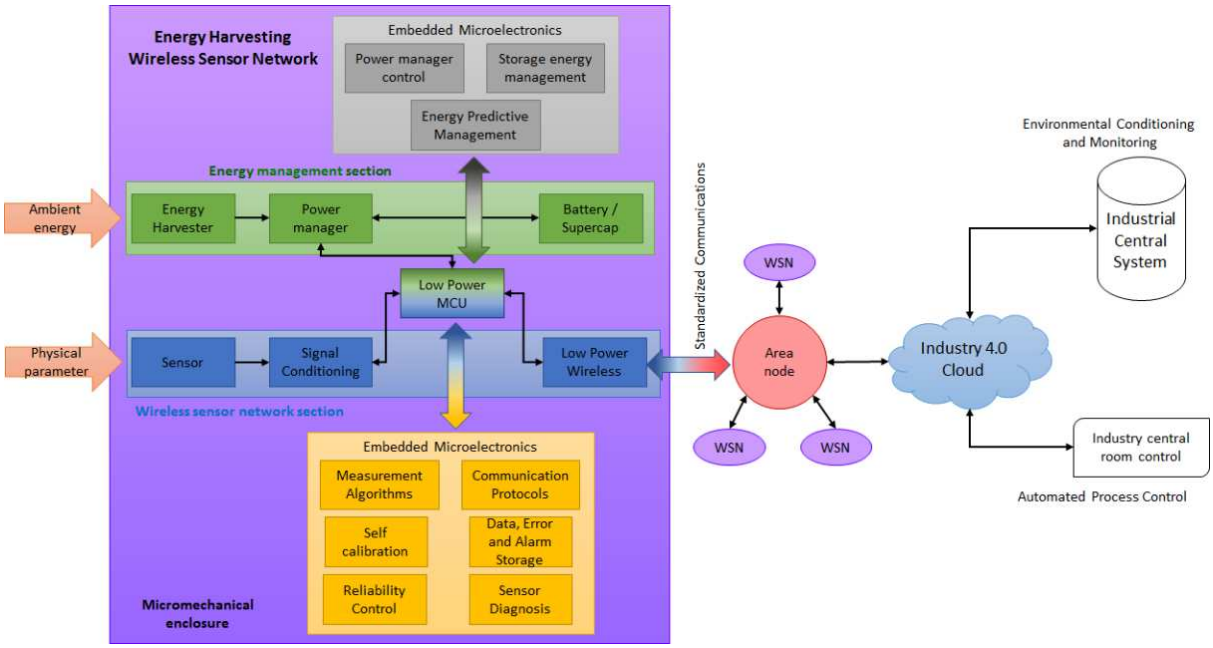

Figure 1-4: Block diagram of an IIoT system compound by Wireless Sensor Network and Energy Harvesting systems and connected to a local net and then to the Industry 4.0 cloud via standardized interfaces.

The core requirements for an IIoT are summarized below:

- **Very Low Power design and operation** to achieve a real self-power behaviour, near to the perpetual operation.
- **Scalability and support for Large Networks** (up to hundreds/thousands of nodes) that allow monitoring entirely building scenarios.
- **Limited cost for the nodes,** allowing affordable deployments even for large-scale buildings.
- **Standardized interfaces** to allow the coexistence and cooperating with existing systems.

1.2 IIoT systems challenges to become autonomous and energy self-sufficiency

Transform actual factories in smart plants industry 4.0 would require large quantities of IIoT devices and sensors. However, installing more IIoT increases the energy demand. Therefore, one of the requirements for IIoT devices is low power consumption [27][28].

To solve the aforementioned issues several universities, research centers, and enterprises are improving the efficiency of the technologies involved in all the process. In the communication field, there are research lines to reduce the energy consumption based on protocols and radio technology [29]. Low power wireless nets are designed with low bit rate, secure and with low quantity of energy consumption. Big communications enterprises as LORA, Sig-Fox, Bluetooth, Zigbee, Enocean offer low power protocols. Improve the microcontroller's efficiency is another strategy available. Reference companies, such as Texas Instrument [30], NXP [31] and Silicon Labs [32] are working on this line, in fact, over the last year, they have released a new brand of low power microcontrollers.

This comes from the refinement of silicon architecture microcontrollers and reducing energy leakages [33]. Besides, different work modes could be used, such as normal operation, run without memory, run without some peripherals, run without all peripherals, standby, sleep and stop [34]. Therefore, flexibility in microcontroller's

operation mode gives them availability to reduce the consumption, allowing the installation of this devices in low power system and giving the benefits which, this entails.

Wireless communications allow a progressive reduction of the number of wired communications; however, electronic devices have to be powered through mains wires. Due to the challenges that involve the full wireless goal, such as difficult access measure points and deploy expenses, install wires is not always feasible. Two different ways could solve this issue. Putting an electric wire until the IIoT device or placing an energy storage device, like a battery.

One of the problems of power supply wires is the price of the copper. It has been increasing for several years until now [35]. Despite during 2015 and 2016, the price went down, now is increasing and it cost near 7000 $ per ton [36].

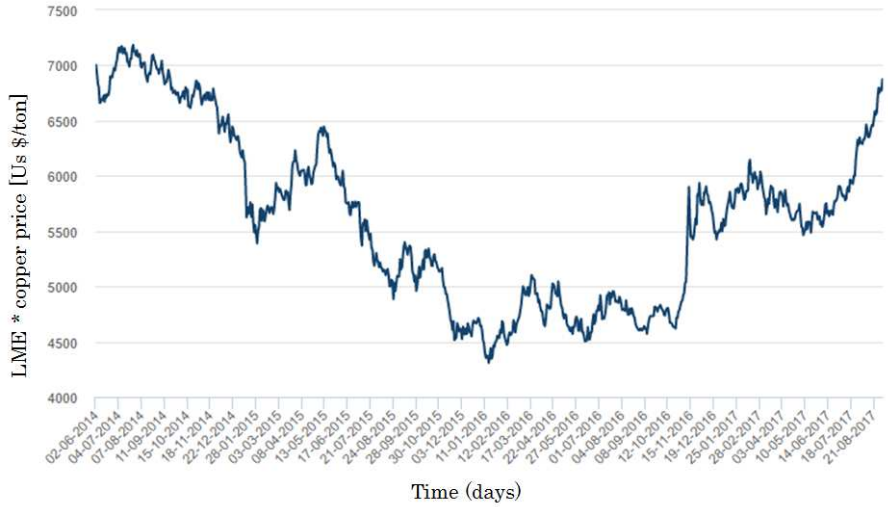

Figure 1-5: Cooper price timeline at London Metal Exchange (LME) during last 3 years.

For example, 1 km copper wire with 1,5 millimetre of diameter has 1583 kg of weight, and its price now is of 11081 $. The same wire but 100 km has 158300 kg of weight and 1108100 $ cost. Translating this into practical cases: Porsche 911 car has 3 km wire, Eurocopter EC135 22 km and Airbus A380 530 km [37]. Consequently, due to the cooper high costs, its use must be reduced to the minimum as possible.

Over the world, due to its high price, the copper wire stealing is a common problem [38]. Another obstacle occurs if the system is installed in countrysides, i.e., nature, cities underground, etc., animals like rats and finally brake the wires that consequently must be replaced increasing the investments.

In addition, when thousands of sensor systems with electric power supply wires must be installed in a big factory; the length of copper wire will be so large and with high costs. Consequently, it is not a feasible solution. Furthermore, sometimes it is not possible to install a wire, as the example of figure 1.6.

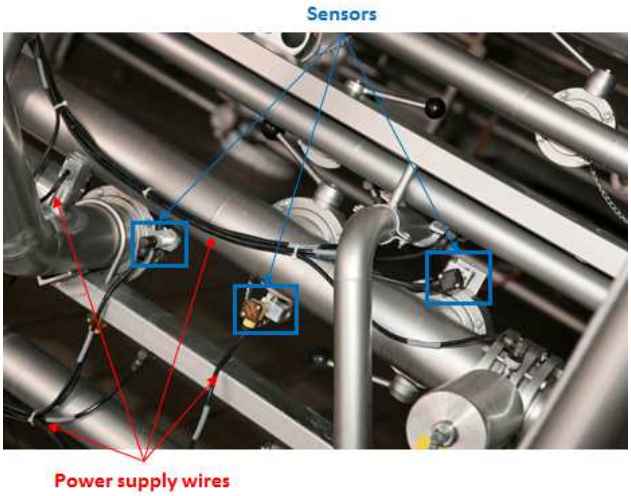

Figure 1-6: Installed sensor system with electric power supply wires.

Nowadays the most common solution to power IIoT devices are energy storage devices. Battery manufacturers have significantly improved battery life [39], there are batteries that claim to last, theoretically, 10 years, nonetheless, changing ambient conditions as temperature, moisture or charge peaks reduce lifetime. A big factory will require hundreds or thousands wireless sensor devices; these systems may have batteries, which require periodical maintenance; therefore, thousands of work hours would be added to the batteries expenses. These facts constitute a challenge to implement the philosophy of IIoT. Moreover, exhausted batteries produce wastes that need recycling [40]. Batteries are composed of a great variety of metals and chemicals composites. Some of these chemicals, such as nickel and cadmium, are extremely toxic and cause damages to the environment, animals, and humans. They may cause water and ground pollution, killing wildlife. E.g., battery hazard components can accumulate in fishes, which diminish their numbers and makes them inappropriate for human consumption.

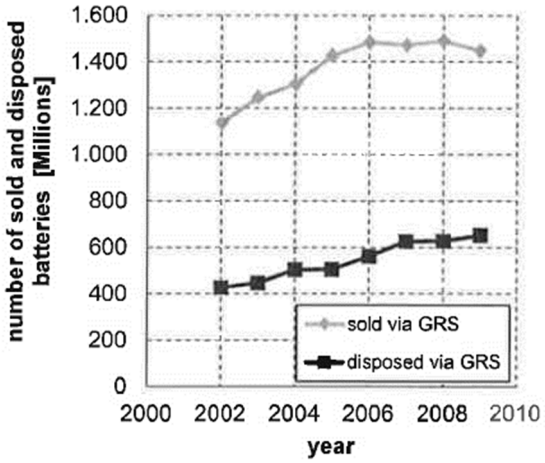

Figure 1-7: Battery produced quantity vs. recycled quantity.

These days, two types of batteries are used, primary batteries and secondary batteries or rechargeable batteries. Primary batteries convert automatically chemical energy into electrical energy until they are emptied. This kind of battery cannot be recharged and are thrown away after their use, increasing the environmental problems.

Energy self-sufficiency is one of the most significant problems at IIoT devices, and proposed solutions with power wires or batteries are not appropriate or useful. Energy harvesting is an alternative to overcome the aforementioned technical challenges [41][42]. Energy harvesting systems use the energy sources available on industrial

environments, such as, mechanical vibration, temperature gradients, natural or artificial light, high levels of noise, pipes with air or water fluid and more, which could be used to power IIoT systems.

1.3 Energy Harvesting as a solution for Industry 4.0

Energy harvesting technology develops and research's on systems to harvests energy from the environment and use this energy to power wireless systems such as electronic sensing devices and communications [43][44]. Its main objectives are to remove the mains power supply wire, eliminate or reduce dependence on batteries and increase or maintain the lifetime of IIoT autonomous systems.

Energy harvesting is becoming one of the most popular technologies, which helps to approach the worldwide problem of energy. As has been underlined, energy harvesting is a technology which captures energy from different ambient sources. Then this energy is managed and stored to be used for any IIoT device. Of course, the main aim of energy harvesting is not to produce power at large scale but to save reduced quantity of energy in a storage device and use in a day-to-day industrial process. Taking into account usual operation mode of energy harvesting system which harvests during the peak time slots of energy availability, storage devices are required to meet the demand and supply in specified periods.

Summarizing, main objectives of energy harvesting technology are:

- Remove the last physical connection, the power supply wire.
- Eliminate or reduce reliance on batteries.
- Increase the lifetime of IIoT/WSN.
- Maintain the same functionality, as a system with a battery or/and increase the functionality.
- Easy installation.
- Low cost.

Energy harvesting systems are composed of three main elements [45]: A harvester, a low power management, and a low power storage system. The operation process starts with the harvest of energy from the environment via harvester device. Then the power management converts incoming energy to be usable for the next step; this change must be the most efficient as possible. Finally, the storage system stores the harvested energy and power the use case device when it is necessary to achieve correct operation.

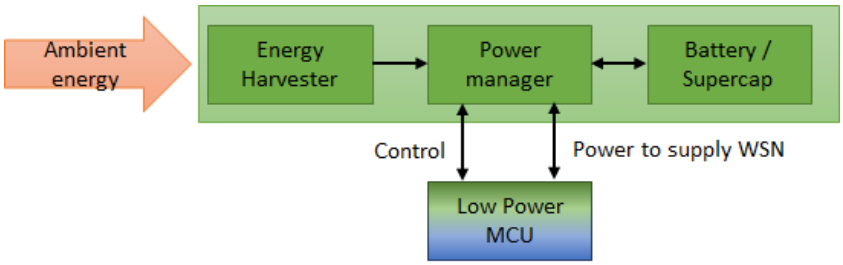

Figure 1-8: Reference energy harvesting system block diagram.

Harvester devices convert/harvest ambient energy into electrical energy with physical/chemical principles; harvesting technology is chosen depending on the environment where the IoT system is going to work. Each harvester technology type has his physical/chemical operation mode and generated electric power depends on harvesting technology. Nevertheless, with a bigger size or more harvester in serial or parallel more

power can be harvested with the same technology. Also produced power depends on application field. For example, kinetic harvesters achieve more energy in industrial applications than with human, due to the vibration source is bigger. Figure 1-9 shows different types of harvesters [46-56], which are extensively exposed in chapter 2 section 1.

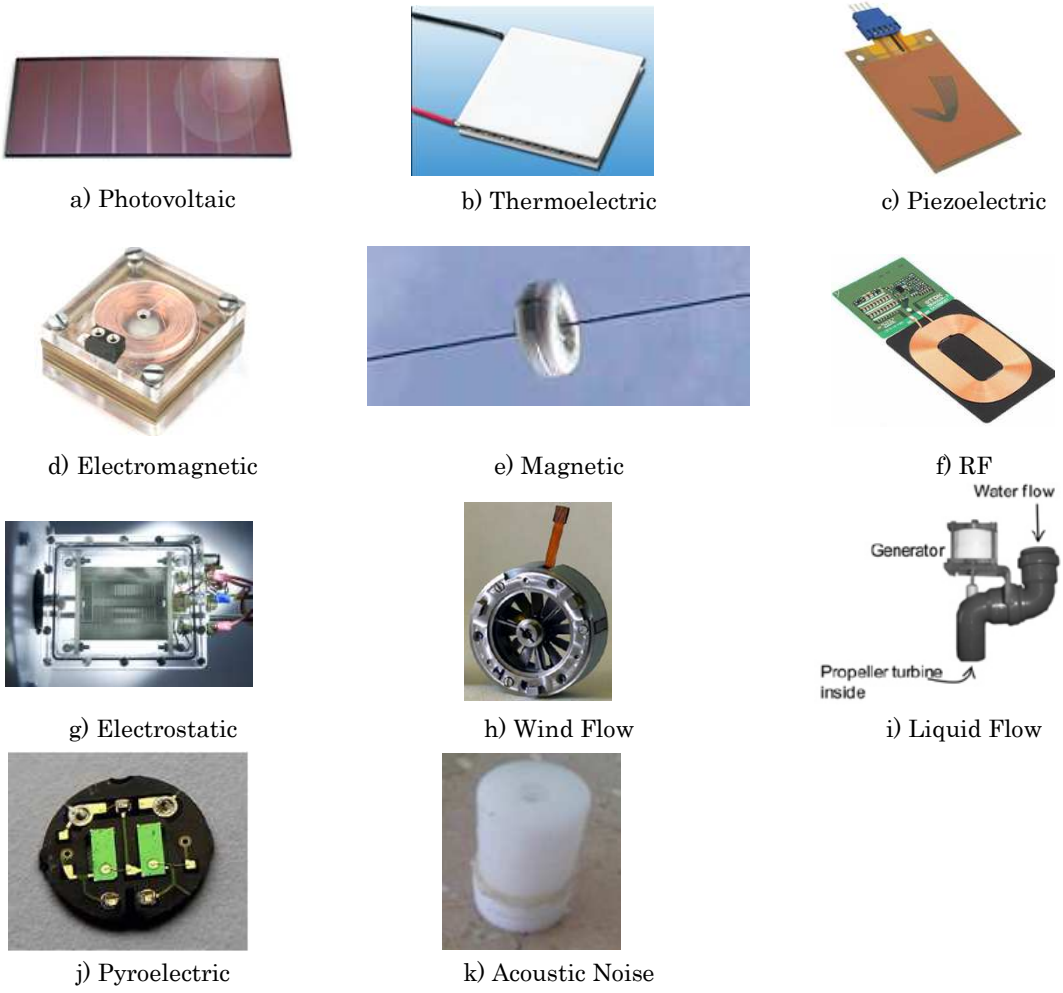

a) Photovoltaic b) Thermoelectric c) Piezoelectric

d) Electromagnetic e) Magnetic f) RF

g) Electrostatic h) Wind Flow i) Liquid Flow

j) Pyroelectric k) Acoustic Noise

Figure 1-9: Different technology harvester examples.

Matures technologies like photovoltaic [57], thermoelectric [58], piezoelectric [59] and RF [60] have already commercial devices at market produced by different companies. These technologies were introduced some years ago in common devices; for example, a solar cell in calculators or RF cards for transport ticket. Now, after several improvements, same philosophy has been reconverted to power IIoT devices. Moreover, listed harvesters at the start of the paragraph are the most used in devices with energy harvesting. Other harvester technologies are no currently available in the market; they are only prototypes under research by universities and research institutes.

After harvest ambient energy and convert it into electrical power, low power manager has to adequate the input electrical signal to a usable mode. So, the power manager has the following objectives:

1. Supply energy to storage device/s.
2. Voltage level transformation to the required one with DC/DC converter.
3. Signal type conversion from AC to DC (if the harvester produces alternate signal).
4. Maintain high-efficiency conversion.
5. Quiescent power consumption of few μW.

6. Achieve an optimal impedance match between harvester, storage device, and load.

As a final remark, it should be bear in mind that a low power manager has the dependence on harvester, storage device and load.

With the increasing utilization of renewable energy harvesting devices, a new generation of storage devices have emerged [61][62]. Low Energy Storage systems provide peak energy demand by using energy generated and stored during periods of lower demand. Any energy harvesting system will not directly power the WSN nodes because the peak current is drawn operation may go beyond what is achievable using the harvester alone. The use of rechargeable batteries charged with harvested energy is an alternative to the problem of the wastes primary batteries produces [63]. In addition, energy storage devices operation mode is complex, and several parameters must be considered, such as high charge/discharge efficiency, peaks current, small size and weight, peak power requirement, extended operation of lifetime, low leakage and low self-discharge levels, variable with temperature, humidity, life-cycles, charge power and capacity.

From a few years to now, energy harvesting is increasing exponentially, and nowadays, "ad-hoc" harvesters or commercial devices are being introduced in the market. Furthermore, the sales increase of these energy harvesting devices have let to open new commercial lines by several electronic devices manufacturers [64]-[66]. These companies offer evaluation boards with different energy inputs and energy managers for developers. In addition, power management chips and regulators for different low energy levels directly for use are offered. The positive side of these commercial devices is that useful energy harvesting components are available at an affordable price and in a short period. This option saves part of the development costs, and the remaining task is only the application. On the other hand, energy harvesting systems should be designed oriented to the application. However, the devices on sale operate in a wider range but usually inefficiently. Therefore, if enough input power is available to carry out all activities by the IIoT device, this solution is correct. In conclusion, the electronic elements of commercial energy conversion or management are only for harvesters with mature technology, i.e., solar, thermoelectric, vibrations and RF. If the harvester is from other technology, system design, and implementation must be done ad-hoc.

In addition, several market studies have been done about future of energy harvesting technology. Two examples of the energy harvesting systems market forecast are presented in next lines. In [67] according to a new market research report: “The overall energy harvesting system market is expected to be valued at USD 645.8 million by 2023, growing at a CAGR of 10.62% between 2017 and 2023. The growing demand for safe, power-efficient, and durable systems that require minimum or no maintenance and extensive implementation of IoT devices in automation and energy harvesting technology in building and home automation are expected to generate a higher demand for energy harvesting systems. The key restraining factors for the growth of the energy harvesting system market are limitations of remotely installed networking modules and higher initial cost associated with energy harvesting systems curtails the market growth in developing countries.” On a second study [68] is predicted that: “the global energy harvesting market has been projected to grow at the CAGR of 19.6% during 2016-2022. Globally energy harvesting market generated a revenue of more than $268.6 million in 2015, and now it has been expected to reach $974.4 million by 2022. The factors driving the market are increasing demand for a safe and durable power source, wide implementation of IoT for building automation and increasing green environment initiatives by the governments". Thus, apparently, the market of this technology is consolidated and growing up. However,

the future of energy harvesting is dependent on future investments and the consolidation of the market.

In the industry, many applications use photovoltaic, kinetic, thermoelectric and RF harvesting. E.g., "low-power-consumption boost converter with maximum power tracking algorithm for indoor photovoltaic energy harvesting has been developed for industrial uses [69] that improves the harvesting and the management efficiency. This research work [70] presents an example of electromagnetic harvesting. It proposes the condition monitoring of an industrial centrifugal pump with a system that is powered by the vibration energy of the own pump. E.g. [71], describes the thermoelectric harvesting for industrial application, where low-temperature cooling water waste heat is used as energy source. Industrial water working below 90 ºC, as a hot source, and fresh water about 15 ºC, as a cold sink. E.g., RF harvesting within IIoT devices [72] that manage the information of industrial vehicles status. This system combines ultra-low power consumption and RF energy harvesting to enable active safety function in industrial vehicles. The paper claims that the installation extends the battery lifetime.

An example of industry 4.0 IIoT device with energy harvesting systems applied to a refinery could be an energy autonomous, wireless solution capable of sensing fluids in many points of interest of a refinery with real-time monitoring in compliance with the ATEX directive.

This example represents a paradigm of digital disruption in the energy sector. The benefits become clear when considering the use of large energy infrastructures such as refineries, where there are a large number of points of interest in which it is attractive to know the state of fluids. Currently, monitoring these points of interest is carried out through periodic samples that are sent to laboratories for analysis or employing high-cost isolated sensors.

The example is to have in the future real micro-laboratories of fluids distributed in the thousands of points of interest of the plant with a pseudo-perpetual life. Integrating three different technologies, low-cost photonic sensors, energy harvesting, and wireless communications, these systems will be fully self-contained and relatively easy to install. Respecting IIoT concept, these systems will be interconnected with a central control station for their monitoring in real time.

The innovative nature of the example lies in the development of an autonomous, low-cost solution for monitoring physical and chemical parameters of fluids (degradation rate, particle detection and presence of water). The idea is not only focused on transferring the ability to obtain important measurements in real time, in multiple points of interest, but also on providing a solution to control the installation, configuration, and maintenance of these sensors. So, their deployment is compatible both in human effort and unit cost with a number of units close to thousands. This approach represents the concept of Industry 4.0 and IIoT; installing, configuring and disposing of the sensor with close to zero maintenance thanks to its ability to self-supply using ambient energy.

Figure 1-10: Examples of IIoT application in a refinery industry.

In addition, these sensors will include energy harvesting systems, which allow these sensors to provide a pseudo-perpetual autonomy without the need for external power supply or battery replacement.

Finally, to enable real-time and centralized access to information on all these sensors from the control centre, the sensors will be equipped with a wireless communications system compatible with the WIFI networks currently present in the refineries.

1.4 Double smart energy harvesting system for self-powered industrial IoT

As has been described, small quantities of energy are needed to power IIoT devices in the development of the future smart industry. The presented solutions as power supply wires or batteries are not a feasible, sustainable and environmentally solutions. Batteries replacement and the problem they cause to the environment could be solved harvesting energy from the environment. Moreover, the use of wires is no possible in several situations, and the use of copper make it not a viable solution in short to medium term because of its price. Consequently, energy harvesting has been presented as a new and viable solution.

The work presented in this PhD focuses on the improvement of knowledge, energy supply, and management systems for IIoT at industry 4.0 paradigm, through four different lines of research.

The first research proposes a wind flow harvester. Several industrial manufacturing processes use fluid pipes for heating systems, gaseous or fluid distribution. The wind flow harvester could provide energy for example for two cases. On the one hand, to measure different parameters needed to implement it within an intelligent factory. On the other hand, to know the amount of fluid that goes through a pipe and makes efficient management on it, making the factories of the future in green factories.

Usually, energy harvesting uses a single harvester with its management and storage system. There are operation conditions where the energy available from a single source is not enough, thus the present work analyses the requirements for a system that combines two different sources of energy, a wind harvester with a commercial solar source. The selection of harvesters is not random, the power supply architecture integrates two different types of converters, AC/DC and DC/DC, for wind flow and photovoltaic harvesters respectively.

Then, the energy must be stored due to principal reasons. The consumer system does not always need the energy harvested. And the harvesting and consumption do not happen at the same period. Knowing their behavior, a user could simulate storage levels change, avoiding the placement of extra storage elements, decreasing costs and environmental damages. Therefore, the proposed solution is based on a simulation tool,

which is made by some algorithms for supercapacitors behavior simulation. In addition, the tool would provide information about the available energy, charged, discharged with different losses, can be used.

Artificial Intelligence (AI) techniques such as data mining or big data are becoming common practice in power plants, to improve their performance and efficiency. The present work applies the same techniques for low energy systems, i.e., transfer macro-systems techniques and technology into micro-systems. AI also could contribute to predicting energy availability in the environment, thus helping the energy management processing better the incoming energy. E.g., if the income energy and operating profile of the consuming system are known, it would be possible to manage the available energy and guarantee the essential task within systems were always attend or fulfilled.

Table 1-1 identifies the elements, main contributions, and benefits presented in the thesis project:

KEY ELEMENTS			CONTRIBUTIONS	BENEFITS
Contributions of Energy Harvesting Technology advances to the field of Industry 4.0	***Harvester***	Wind harvesting	▪ Small (diameter=32 mm) wind turbine design and manufacturing ▪ Monophasic and three-phase generators ▪ Test bench design and manufacturing to validate the small wind turbine ▪ Mini-reactor concept introduction	New type of harvester (patent pending) Maximize and extend the life of the energy and provide it even when some sources are not available Potential use in novel applications (i.e. in a factory small pipes with fluid flow)
	Double power manager	Multi power manager Photovoltaic + DC/DC Turbine + AC/DC	▪ Harvested energy from multiple sources (Dual-source: solar and wind) ▪ Mixture of commercial and non-commercial harvester devices ▪ Different conversions AC/DC and DC/DC ▪ Control algorithm implementation for the small wind turbine. ▪ Design and control validation by means of specifications.	Maximize and extend the life of the energy and provide it even when some sources are not available The combination of devices provides flexibility to increasing WSN tasks or active time Novel control design and implementation
	Energy Storage	Supercapacitor Electro-mathematical model	▪ Tool to simulate supercapacitor behaviour of charge and discharge at different conditions ▪ Electro-mathematical model taking account life cycle, voltage, time, temperature, moisture, Equivalent Series Resistance (ESR) and leakage resistance parameters	Model all types of supercapacitors for low power applications and any type of environment conditions Machine learning model increases the accuracy of the electro-mathematical model
		Machine learning model	▪ Use Artificial Neuronal Networks (ANN) in the modelling of low power storage devices.	
	Machine learning and data mining techniques	Low energy prediction Commercial harvester selection	▪ Data analytics and machine learning algorithms to provide accurate estimations of future energy availability ▪ Algorithms to be applied easily also for the prediction of future energy consumption ▪ Data mining techniques to select the proper harvester for the use case	Better understanding about the capacity and way to generate energy and its short-term future availability Improvement of the energy demand management through the WSN Avoid errors in the selection of a commercial harvester

Table 1-1: Contributions and benefits of this thesis.

The different researches that involve the contributions of these thesis to the field of science/technological knowledge are integrated into one system to verify and validate their goodness, as shown in figure 1-11. Moreover, they have as purpose to be able to use separately or together in any energy harvesting system.

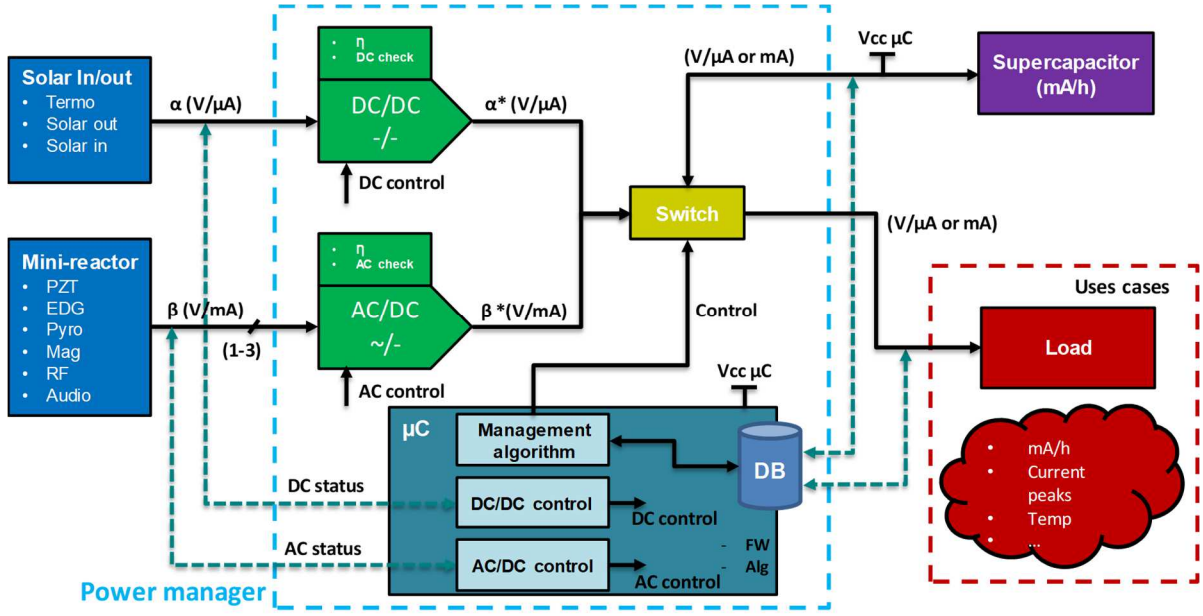

Figure 1-11: System block diagram.

The mini wind harvester provides energy from a fluid flow. The term mini refers to the small size of the turbine, 32 mm of section. In fact, the harvester has such a small size because its interference in the flow of the duct where it is installed is intended to be as small as possible. The harvester can be installed in factory small pipes with fluid flow. As the pipes are a place of limited and difficult access, the device solves the problem of the its power supply, due to the fact that there is no need to change the battery, making the system perpetual or quasi-perpetual, as it is a self-powered device. Also, if the application aims to measure the fluid consumption could be obtained with any extra measurement sensor.

[73]-[76] Double power manager involves the AC/DC and DC/DC converters integrated into one system with each control management integrated into a low power microcontroller. Two different input sources provide more energy to enable IIoT system performing more tasks or extending the lifetime. In one hand, was decided to use a commercial solar cell as a harvester and in the other hand an own made harvester, the mini-reactor. This proves the possibility of mixing commercial and non-commercial devices with the flexibility that this option provides. In addition, each of the two converters use different technologies, i.e., one has an alternating signal as input and the other a continuous signal, thus covers the two processing fields in energy management described above. Finally, control algorithms have been developed theoretically with the aim to implement in future in a low energy microcontroller, which belongs to the new commercial line of very low power processors.

When supercapacitor model for energy harvester references were consulted [77]-[82], it was observed that there was no mathematical-electronic model to simulate with the required operation of supercapacitors with all the variables that affect them in charging and discharging. To verify the goodness of the mathematical model several tests were done with different environmental and electric conditions. Once these actions were carried out, further researches were done with machine learning techniques to improve

the mathematical model accuracy. The mathematical model is more generic, i.e., it is valid for all types of supercapacitor and with different environment variables, but it is not as precise as the machine learning model. On the other hand, the machine learning model is more specific, since it has learned from the tests carried out but by performing other tests, it would also obtain the modelling for those conditions, on the other hand, it is no longer as direct as the mathematical model.

The predictive strategy determines the optimal management of low power energy harvested by the solar panel processed by the DC/DC converter, the harvester energy by the micro-reactor processed by the AC/DC converter and storage in the energy collection system called supercapacitor. This contribution employs Artificial Intelligence (A.I.) techniques, advanced statistics, and data analysis, allowing an estimation in future the amount of energy that would be stored in the supercapacitor. Initially, specific methods identified in the literature and used in other works have been tested [83]-[86]. These methods have been evaluated and compared with other types of techniques from the A. I. field before establishing the most reliable predictive model. By predicting the amount of energy available in the near future and the particular consumption profile of the network of systems under study, the most appropriate strategy has been determined for the correct and optimal management of the energy generated available, being able to make decisions about when and in which systems to use this energy. Another use of data mining techniques has been to select commercial devices in base their characteristics and energy production, such as photovoltaic cells.

1.5 Memory structure

The present chapter contextualizes the present Ph.D. work inside the Industry 4.0 paradigm, IIoT world and the necessity of low power consumption and management. The technology used/needed to solve the problem is energy harvesting.

Chapter 2: Principles of energy harvesting, low power management, and storage. Reviews the state of the art regarding technology and application environment. It is divided into three parts, hardware, firmware, and system.

Hardware part has three subdivisions which involves harvesters, power managers, and low energy storage devices. The section starts with energy harvesters; their physical and/or chemical operation mode, mature of state of the art, efficiency, equivalent electric circuit and application examples are described. Then, low power managers work principles and an example of a power manager for each harvester, describing the architecture and work operation is given. The final part contains the low energy storage state of the art. The same procedure used with harvesters has been applied to put in contact with this technology and existing devices. Principles and existing devices are presented.

Firmware section describes predictive analytics applied to energy harvesting systems are advanced. An overview of data mining, machine learning, and predictive modelling technologies is done. The section is complete with some related work with predictive analytics with low energy management systems.

System section research about IIoT systems with energy harvesting. Usually used systems for IIoT are WSN, so a small description is given about their typical architecture and work operation. Some real uses cases of energy harvesting IIoT system are shown.

Chapter 3: Wind mini-turbine harvester. This chapter describes and presents the process realized to create a new wind flow energy harvester. System objectives, hypothesis

defined, operation principle and used methodology is introduced to the lecturer in the first part of the chapter.

The second section involves the development of the proof of concept. The realized mechanical designs, magnetic and mechanic simulations, first electrical design and manufacture process. Finally, test and results are shown.

Satisfactory results were obtained with the proof of concept. However, some errors were detected in the system and it was improved. Thus, a new mechanic was manufactured with a more efficient generator. Furthermore, a test-bench was implemented to verify the operation of the new turbine. In addition, the last section contains achieved test results. Finally, some applications examples are described shortly.

Chapter 4: Bi low power management and storage. This chapter presents the research and development of the double power management and storage device.

The first section contains the work related to the DC system. A photovoltaic physical-electrical model has been developed of the selected cell and tested in different application environments with the shape of DC input signal. Then, the steps for the development of a high-efficiency DC/DC converter are presented.

The second section contains the work related to the AC system. Mini-turbine electro-mechanical model has been developed and tested with different wind velocities and electrical loads. Then, the steps and the selection for the development of an AC/DC converter are presented.

The chapter end section develops a supercapacitor mathematical model. In addition, did it test with specific test bench and in several conditions and the obtained result are exposed. The last subsection provides an example of an implementation case of the model.

Chapter 5: Machine learning and data mining techniques for energy harvesting systems. Machine learning and data mining techniques applied to improve energy harvesting systems are presented in this chapter.

Manufacturers data-sheets do not always provide the necessary information to make a correct selection of a commercial harvester. Photovoltaic cell selection by data mining after measuring energy production in different scenarios and conditions is presented in this chapter.

Supercapacitor model accuracy improvement with artificial neuronal network was the second step to complete the objective of this chapter. Taking as reference develop supercapacitor mathematical model in chapter 4, the try and achieve processes for model accuracy improvement is presented.

The task of predictive power management strategy was started with the achievement of energy input/generation data. This information was needed for algorithms development; algorithms learn from this data and then work to improve the management of the available energy. In next step, data pre-processing methodology and development to have all data correctly to work with them is related. Finally, used algorithms and resulting predictive values accuracy is shown.

Finally, the three different tasks implemented in this chapter, the aim of verifying the utilization of named techniques for energy harvesting systems is validated.

Chapter 6: Conclusions and future work. The last chapter is about the conclusions and future work. At the same time, it indicates the lines of investigation that this thesis leaves open for future research and development.

Figure 1-12 shows the main memory structure:

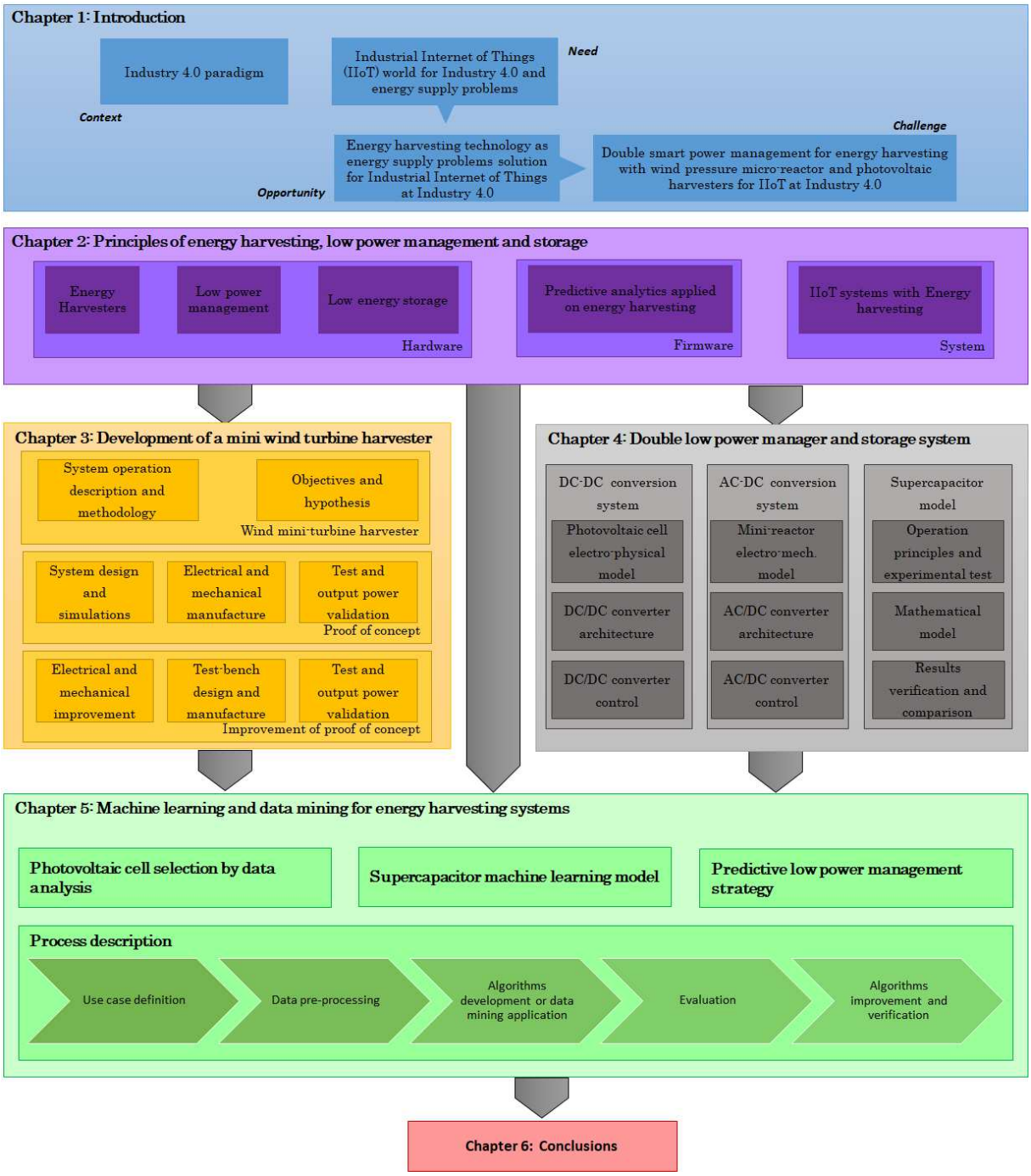

Figure 1-12: Thesis Outline.

The relevant notable scientific, technological and industrial advances of this thesis are listed in next table, together with the chapters and publications in which they are addressed.

Table 1-2: Communications, publications, and patents generated.

Science, Technology and Industrial advances of this thesis	Chapter	Publication	Comments
Double smart power management with wind mini-reactor and photovoltaic cell energy harvester for Industry 4.0 IIoT devices	[1]-[3]-[4]-[5]-[6]	SPIE conference commercial + scientific sensing; SPIE digital library	Paper + oral presentation; Orlando, Florida, USA
Energy Harvesting Wireless Sensor Networks	[2]	UPV/EHU I doctoral conferences	Poster + oral presentation; Finalist as best doctoral works on engineering of EHU/UPV
Advanced Materials in Energy Harvesting and Storage in IK4-TEKNIKER	[2]	European Materials Research Society 2018 Spring	Oral presentation, Strasbourg, France
Mini-turbine	[3]	Patent Mini-turbine	PCT under second evaluation
Supercapacitor Electro-Mathematical and Machine Leaning Modelling for Low Power Applications	[4]-[5]	Electronics MDPI journal	Paper, Q1, SJR 0.46; Journal cover page of the month, April 2018, Vol. 7, Iss. 4
Machine Learning techniques for Energy Harvesting	[5]	Journal	*Under writing process

II.
Principles of energy harvesting, low power management and storage

In this chapter the state of art of energy harvesting systems and elements which compose are shown. Existing harvesters and storage technologies and low power management techniques are included in the following pages of this chapter. In addition, state of the art of machine learning techniques, data mining which are used inside in this work are also included in this chapter. Finally, the composition of IoT/WSN devices is included in the last part of this chapter.

Furthermore, this chapter has been divided into five sub-chapters:

- Chapter 2 Energy harvesters' technologies
- Chapter 3 Low power management
- Chapter 4 Low energy storage devices
- Chapter 5 Machine learning techniques and data mining for energy harvesting systems
- Chapter 6 WSN systems

Chapter 2 harvesting technologies are described through their operation principles, equivalent circuits, state of technology, different families, and examples.

Chapter 3 low power and low power management principles are exposed at the start of this chapter. Then, reference power condition topologies are presented to use as the base for final part of the chapter. The last section of the chapter shows different harvesters' power manager examples.

Chapter 4 presents low energy storage devices and principles. Supercapacitor and rechargeable batteries technologies basics, state and differences between them are described.

Chapter 5 introduces data science principles, such as data mining, machine learning, artificial neuronal networks and predictive modelling. Then, through examples, these technologies applied to energy harvesting systems are shown.

Chapter 6 involves the description of how IoT/WSN systems work, their networks topologies and their hardware architecture.

2. Energy harvesters' technologies

Nowadays, several energy harvesters' technologies have been developed [87]-[90]. Table 2-1 summarizes state of the art in harvester technologies showing their characteristic parameters, operation mode, power density, system efficiency, technology development status and generated signal type.

Table 2-1: Actual energy harvesters' technologies characteristics summarize [91-96].

Harvester	Physical/Chemical operation mode	Power density	Efficiency (%)	Mature/ emerging
Photovoltaic	Photovoltaic effect	Outdoors: 15 mW/cm^2 Indoors: 10-100 µW/cm^2	Until 40	Mature
Piezoelectric	Piezoelectric effect	330 µW/cm^3 shoes insert	Until 30	Mature
Electromagnetic	Faraday's law	Human: 4 µW/cm^3 @ kHz Industrial: 306 µW/cm^3 @ kHz	Until 67	Mature
Electrostatic	Vibration-dependent capacitors	50 to 100 µW/cm^3	9.5-23.6	Emerging
Pyroelectric	Olsen cycle	3.5 µW/cm^3 at the temperature rate of 85 °C/s @ 0.11 Hz	1-3.5	Emerging
Thermoelectric	Seebeck effect	Human: 100 µW/cm^3 Industrial: 100 mW/cm^3	10-15	Mature
Magnetic	Ampere, Maxwell, and Faraday laws	1.8 mW/cm^3 with 400 A at 4 cm from conductor	0.1325	Emerging
RF	Ubiquitous radio transmitters	GSM: 0.1 µW/cm^2 WiFi: 0.01 µW/cm^2	50-70	Mature
Wind and Water	Faraday's law	1.16 mW/cm^3 at the speed of 5 m/s 4.91 µW/cm^3 at the speed of 3 l/s	0.61-17.6 1.7-29.5	Emerging in small scale
Acoustic	Helmotz effect	1.436 mW/cm^2 at 123 dB	0.012	Emerging

2.1 Photovoltaic harvester's technology and devices

Photovoltaic harvesters [97]-[99] generate electrical power converting sunlight or artificial light into electricity using the photovoltaic principle. The solar panel is a modular device, which is composed of n cell in parallel and series. Thus, it can be scaled to desired size or power generation. So, harvested energy is proportional to the surface area of the module. Photovoltaic cells operate with sunlight as well as artificial light. Nevertheless, they are dependent on weather conditions or switch on periods.

Efficiency limits photovoltaic harvesters' electric energy generation. Moreover, this efficiency is wholly related with materials which compose the cell. Actual photovoltaic cells are separated into four categories based on their composition: multijunction, crystalline silicon, thin-films and emerging. The comparison between various solar cells technologies is shown in table 2-2 and figure 2-3: [100]:

Table 2-2: Comparison of various solar cells types.

Classification	Efficiency	Advantage	Disadvantage
		Silicon solar cells	
Monocrystalline	15–24%	High conversion efficiency and reliability	High cost, Large silicon consumption Complex production process
Polysilicon	15–20.4%	No efficiency recession can be fabricated on substrates Lower cost than monocrystalline	Large silicon consumption Cost complex production process
		Multijunction solar cells	
CdS	Up to 16%	Low cost Easiness of mass production	Toxic cadmium
CdTe	28%	High light absorption rate High conversion efficiency Stable performance	Limited natural tellurium reserves High cost Toxic cadmium
GaAs	Up to 30%	High light absorption coefficient High Conversion efficiency Strong resistant of temperature	High cost
CIGS	Up to 20%	Low cost Good weak light performance Wide applicability of substrate Adjustable optical band gap	Rare materials

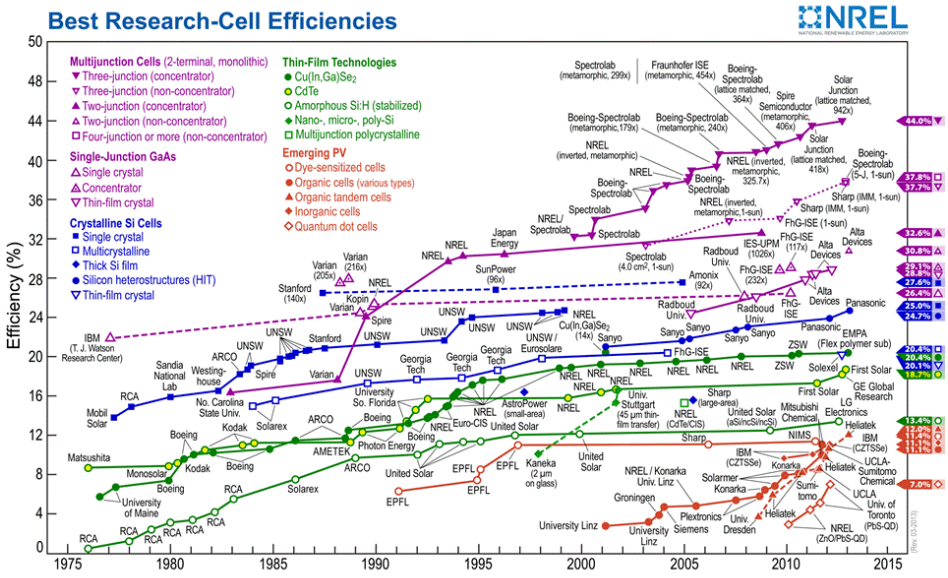

Figure 2-1: Cell efficiencies research state.

A solar cell is an unbiased diode that is exposed to light, and free electron-hole pairs are created during this process. The minority carriers diffuse to the depletion region where they experience the built-in filed which sweeps them to the opposite side of the junction. Under open circuit conditions, the separation of carriers leads to the build-up of the open-circuit voltage (V_{oc}) across the junction. If a resistance-free current path connects the n and p regions, the short circuit current will flow, I_{sc}, to balance the flow of minority carriers across the junction. Thus, when a load is connected to the cell, the generated power can be harvested.

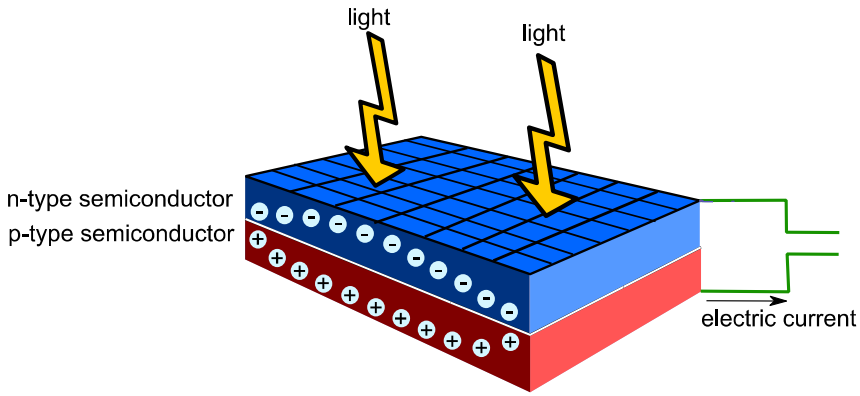

Figure 2-2: Photovoltaic harvester.

When electrical contacts are connected to the p-n junction, and a voltage is applied, the cell exhibits a rectifying behaviour. The current passing through the cell shows the ideal diode equation:

$$I = I_{ph} - I_d, \qquad I_d = I_0\left(e^{qV/kT} - 1\right) \tag{2-1}$$

, where k_B is the Boltzmann constant, T is the absolute temperature, q is the electron charge and V is the voltage at the terminals of the cell. I_0 is the current generated by the cell in dark light condition. The photogenerated current I_{ph} is the photon flux incident on the cell and depends on the light wavelength, quantum efficiency or spectral response. In the ideal case, the short-circuit current must be equal to the photogenerated current. Thus, equation 2-2 gives the open circuit voltage V_{oc}:

$$V_{oc} = \frac{k_B T}{q} ln\left(1 + \frac{I_{ph}}{I_0}\right) \tag{2-2}$$

Finally, photovoltaic cell energy conversion efficiency is the ratio of the maximum electrical power obtained from the incident light power. Is given equation 2-3 and is dependent on short-circuit current I_{sc}:

$$\eta = \frac{P_p}{P_i} = \frac{V_p I_p}{P_i} = \frac{f I_{sc} V_{oc}}{P_i} \tag{2-3}$$

Figure 2-4 shows an equivalent circuit for an ideal solar cell, which is represented by a current source connected in parallel with a rectifying diode, series (R_s) and parallel (or shunt, R_p) resistances. The current source produces I_L, which is equivalent to the current generated at the cell when light effect in it. Then, the diode through I_d current flows is the modelling of the internal cell architecture. Series resistance performs the internal resistance of the cell material and parallel the equivalent resistance between cells connections inside a photovoltaic module. Figure 2-3 shows the equivalent circuit:

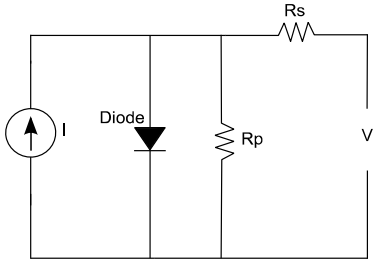

Figure 2-3: Photovoltaic harvester equivalent circuit.

Photovoltaic devices used for energy harvesting activity work for outdoor as well as indoor operations. The intensity of light in indoors is much lower than in outdoors.

Basically, due to sun generated power intensity is much higher than generated by artificial light sources such as an incandescent light bulb, fluorescent tube or halogen lamp. Thus, is important to consider the cell spectral properties to achieve the maximum power as possible. The spectral characteristics determine the operation range of each light type. Consequently, photovoltaic cell would be more efficient for determinate wavelength of the range depending on the material which is made. Figure 2-4 shows the spectral operation range of different type of lights [101]:

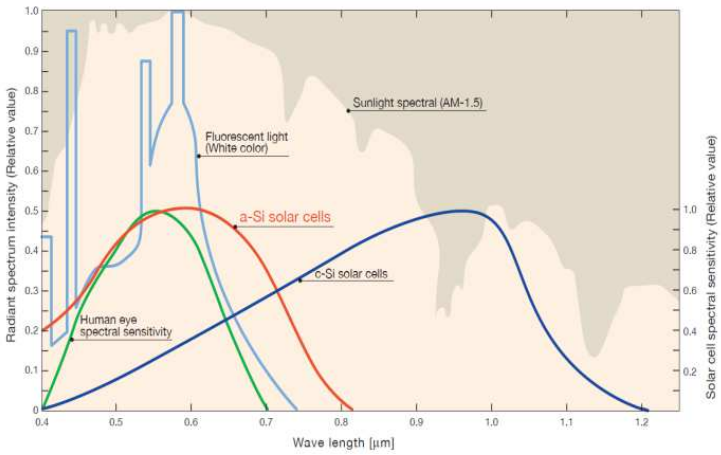

Figure 2-4: Relative Spectra of Sunlight and Artificial Light from Incandescent Bulbs and from Fluorescent Lamps.

2.2 Kinetic harvester's technology and devices

These devices convert mechanical energy into electrical energy through electromechanical transducers. The most common transduction mechanisms are piezoelectric conversion and electromagnetic.

Most of the kinetic energy harvesters harvest power in the range of tens to hundreds of microwatts and resonance frequencies of these systems are typically tens or hundreds of Hertz.

Overall, the energy to be harvested mechanically is limited by the moving sources. Kinetic harvesters are sensitive to driving frequencies; they can provide peak power only in a narrow band. Tuneable designs have been demonstrated, but these require a technician to set the frequency of the device manually. Table 2-3 [102] lists a brief comparison of available power from various techniques.

Table 2-3: Comparison of various vibrational-harvesting technologies.

	Piezoelectric devices	Electromagnetic devices	Electrostatic devices
Advantage	-high output voltages -high capacitances -no need to control	-high output currents -long lifetime -robustness	-high output voltages -low-cost systems -coupling coefficient easily adjustable -high coupling coefficients -size reduction increases capacitances
Disadvanta	-expensive materials -coupling coefficient linked to material properties	-low output voltages - expensive material -low efficiency in low frequencies and small sizes	-low capacitances -high impact of parasitic capacitances -no direct mechanical-to-electrical conversion for electret-free converters

2.2.1 Piezoelectric transduction

Piezoelectric energy harvesters [103]-[105] are based on bending mechanical elements, i.e., beams or membranes, as they allow resonance at a frequency ranging from tens to hundreds of Hz.

Vibration of a rigid body can be caused by several factors such as unbalanced mass in a system, tear and wear materials and can occur in almost all dynamical systems. The characteristic behaviour is unique to each system and can be simply described by two parameters: damping constant and natural frequency. Most commonly, a single degree of freedom lumped spring-mass system is utilized to study the dynamic characteristics of a vibrating body associated with energy harvesting.

The general principle of a resonant inertial vibration harvester can be understood through the lumped model. The governing equation of motion for the system can be obtained from energy balance equation of D' Alembert's principle. Which is given by differential equation 2-4:

$$m\frac{d^2z}{dt^2} + D_v\frac{dz}{dt} + kz + F = -m\frac{d^2Z}{dt^2} \tag{2-4}$$

Since energy is extracted from relative movement between the mass and the inertial frame, the following equations apply. The standard steady-state solution for the displacement of the mass is given by:

$$z(t) = \frac{\omega^2}{\sqrt{\left(\frac{k}{m} - \omega^2\right)^2 + \left(\frac{c_t\omega}{m}\right)^2}} Y\,sin(\omega t - \phi), \qquad \phi = tan^{-1}\left(\frac{c_t\omega}{(k - \omega^2 m)}\right) \tag{2-5}$$

The maximum energy is extracted when the excitation frequency is equal to that of the natural frequency of the system, ω_n, given by:

$$\omega_n = \sqrt{\frac{k}{m}} \tag{2-6}$$

The maximum power generated therefore occurs when the device is driven at its natural frequency, ω_n and hence the output power is given by the following equation:

$$P_{max} = \frac{mY^2\omega_n^3}{4\zeta_T} \tag{2-7}$$

In addition, it should be considered the effect of the applied frequency, the magnitude of the excitation vibrations and the maximum displacement mass. If the input acceleration is high enough, then increased damping will result in a broader bandwidth response and hence result in a generator that is less sensitive to variations in excitation frequency, which might be caused by changes in temperature or other environmental parameters or may vary over time. Excessive device amplitude can also lead to nonlinear behaviour and introduce difficulties in keeping the generator operating at resonance. Both the frequency of the generator and the level of damping should be designed to match specific application requirements in order to maximize the power output. And this power is proportional to the mass, which should be maximized subject to any given size constraints. The vibration spectra should be studied before designing the generator to identify the most appropriate frequency of operation within the design constraints of generator size and maximum permissible displacement. Figure 2-5 shows the piezoelectric harvester movement example.

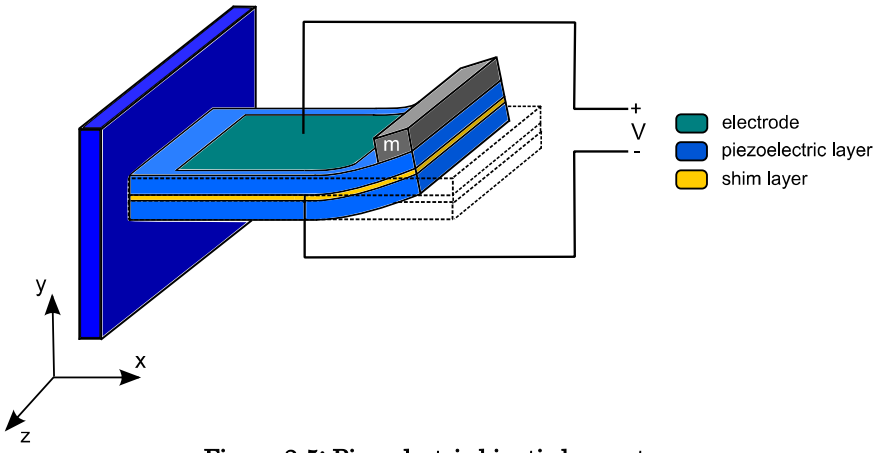

Figure 2-5: Piezoelectric kinetic harvester.

Piezoelectric contains dipoles, which cause the material to become electrically polarized when subjected to mechanical force. The degree of polarization is proportional to the applied strain. Conversely, an applied electric field causes the dipoles to rotate, which results in the material deforming. The piezoelectric effect is found in single crystal materials (quartz), ceramics (lead zirconite titanate PZT), thin-film materials (sputtered zinc oxide), screen printable thick films based upon piezoceramic powders and polymer materials (polyvinylidene fluoride PVDF). Such materials have anisotropic piezoelectric behavior.

Piezoelectric materials are represented by two subscript constants, as shown in table 2-4. For example, the three direction refers to piezoelectric materials that have been polarized along their thickness (i.e., having electrodes on the top and the bottom surfaces). If a mechanical strain is applied in the same direction, the constants are denoted with the subscript 33, e.g., d_{33}. If the strain is applied perpendicular to the direction of the polarization, the constant is denoted with the subscript 31, e.g., d_{31}.

Table 2-4: Coefficients of common piezoelectric materials.

Property	Quartz	PZT-5H	PZT-5A	$BaTiO_3$	PVDF
Material type	Single crystal	Piezoceramic	Piezoceramic	Piezoceramic	Polymer
d_{33} (10^{12} C/N)	-2.3 (d_{11})	593	374	149	-33
d_{31} (10^{12} C/N)	-0.93 (d_{12})	-274	-171	78	23
g_{33} (10^3 Vm/N)	-58	19.7	24.8	14.1	330
g_{31} (10^3 Vm/N)	-	-9.1	-11.4	5	216
k_{33}	0.07	0.75	0.71	0.48	0.15
k_{31}	-	0.39	0.31	0.21	0.12
Relative permittivity($\varepsilon/\varepsilon_0$)	4.4	3400	1700	1700	12
Curie temperature(C)	573	195	365	120	~150

In most of the scenarios, piezoelectric harvesters operate in the lateral 31 mode. Due to the piezoelectric element is often bonded to the surface of a mechanical spring element that converts vertical displacements into a lateral strain across the piezoelectric element. Some designs operate in the compressive 33 mode, and these have the advantage of exploiting the 33 constants, which are typically higher than the 31 equivalents. Compressive strains, however, are typically much lower than the lateral strains occurring when the piezoelectric is bonded onto a flexing structure.

Figure 2-6 shows an equivalent circuit for the quartz crystal resonator. This circuit is valid when the resonator vibrates in the thickness shear mode close to the fundamental resonance frequency. The components are related to the properties of the quartz.

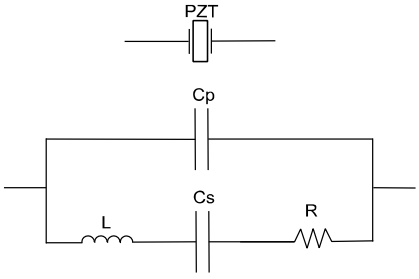

Figure 2-6: Quartz piezoelectric harvester equivalent circuit.

, where R_1 represents the losses in energy due to the viscous damping of the oscillation in the surrounding media, C_0 is related to the capacitance of the electrodes deposited on the surfaces of the crystal disc, C_1 is related to the elasticity of the crystal (oscillation energy stored in the crystal) and L corresponds to the inertial component of the oscillation.

2.2.2 Electromagnetic transduction

Electromagnetic harvesters [106]-[108] are based in an electromotive force induced by a varying magnetic flux through a conductive coil according to Faraday's law. The magnetic flux (B) source is obtained with a permanent magnet. The motion of the seismic mass attached to either the coil or magnet induces the variation of magnetic flux necessary to generate a current in the coil.

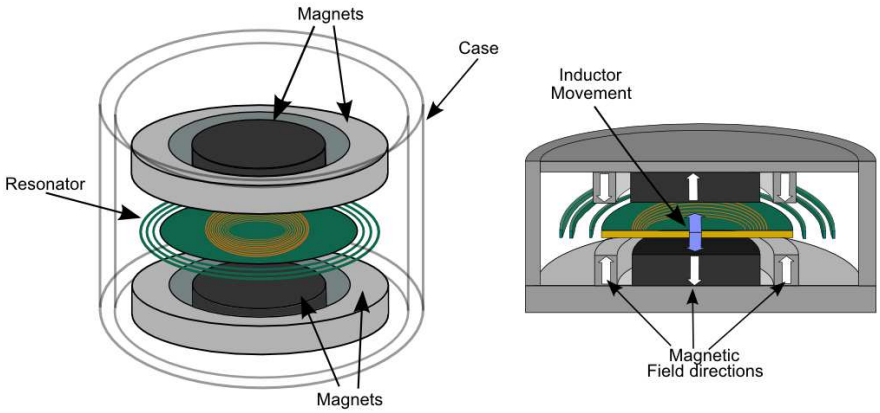

Figure 2-7: Magnetic kinetic harvester.

When an electric conductor is moved through a magnetic field, an electromotive force (emf) is induced between the ends of the conductor. The voltage induced in the conductor (V) is proportional to frequency of the magnetic flux linkage (Φ) of the circuit. The generator is a multiturn coil (N), and permanent magnets create the magnetic field.

$$V = -\frac{d\emptyset}{dt} \rightarrow V = -N\frac{d\emptyset}{dt} \tag{2-8}$$

There are two possible cases:

1. Linear vibration
2. Time-varying magnetic field, B.

In the first case, a relative motion between the coil and the magnet in the x-direction, the voltage induced in the coil can be expressed as the product of a flux linkage

gradient and the velocity of movement, left equation 2-9. In the second case, where the flux density is uniform over the area, A, of the coil, the induced voltage is dependent of the angle (α) between the coil area and the direction of the flux density, right equation 2-9.

$$V = -N\frac{d\emptyset}{dx}\frac{dx}{dt} \qquad V = -NA\frac{dB}{dt}\sin\alpha \tag{2-9}$$

Power is extracted from the generator by connecting the coil to a load resistance, R_L. The resulting current in the coil creates its magnetic field, which opposes the field giving rise to it. This opposition results in an electromagnetic force, F_{em} that opposes the generator motion, which transfers mechanical energy into electrical energy. F_{em} is proportional to the current and the velocity. It is expressed as equation 2-10:

$$F_{em} = D_{em}\frac{dx}{dt}, \qquad D_{em} = \frac{1}{R_L + R_c + j\omega L_c}\left(\frac{d\Phi}{dx}\right)^2 \tag{2-10}$$

, where D_{em} is the electromagnetic damping and is multiplied with velocity. Therefore, for the maximum electrical power output, the generator design must maximize D_{em} and velocity.

Maximizing D_{em} requires the flux linkage gradient to be maximized and the coil impedance to be minimized. The flux linkage gradient is a function of the coil impedance to be minimized. The flux linkage gradient is a function of the strength of the magnets, their arrangement concerning the coil and the direction of movement and the area and number of turn for the coil.

The magnetic field strength is governed by the type of magnetic material used. Permanent magnets are made from ferromagnetic materials. The magnetizing force is H, and figure merit is the maximum energy product, BH_{MAX}, which can be determined for a material's magnetic hysteresis loop. Finally, another consideration is the Curie temperature, which is the maximum operating temperature that the material can with withstand before becoming demagnetized. Properties of some common magnetic materials are summarized in table 2-5:

Table 2-5: Properties of some common magnetic material.

Material	$(BH)_{MAX}$ (kJ/m³)	Flux Density (mT)	Max. Work. Temp. (C)	Curie Temp. (C)	Density (kg/m³)
Ceramic	26	100	250	460	4980
Alnico	42	130	550	860	7200
SmCo (2:17)	208	350	300	750	8400
NdFeB(N38H)	306	450	120	320	7470

Conductor materials characteristics used by the generator are given in table 2-6:

Table 2-6: Conductor materials resistivity and conductive properties.

Material	ρ (Ω·m) at 20 °C	σ (S/m) at 20 °C	Material	ρ (Ω·m) at 20 °C	σ (S/m) at 20 °C
Silver	1.59×10^{-8}	6.30×10^{7}	Tungsten	5.60×10^{-8}	1.79×10^{7}
Copper	1.68×10^{-8}	5.96×10^{7}	Zinc	5.90×10^{-8}	1.69×10^{7}
Annealed copper	1.72×10^{-8}	5.80×10^{7}	Nickel	6.99×10^{-8}	1.43×10^{7}
Gold	2.44×10^{-8}	4.10×10^{7}	Lithium	9.28×10^{-8}	1.08×10^{7}
Aluminium	2.65×10^{-8}	3.77×10^{7}	Iron	9.71×10^{-8}	1.00×10^{7}
Calcium	3.36×10^{-8}	2.98×10^{7}	Tungsten	5.60×10^{-8}	1.79×10^{7}

Figure 2-8 represents the equivalent circuit model for vibration driven harvester using electromagnetic damping.

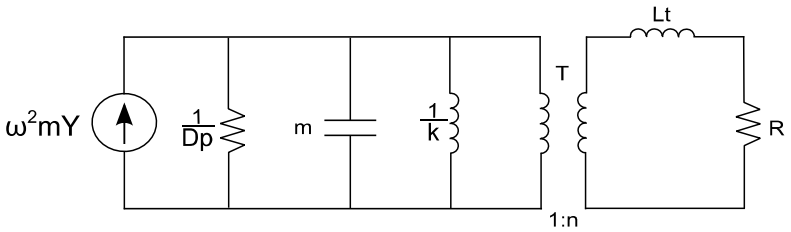

Figure 2-8: Equivalent circuit of electromagnetic force harvester.

, where the part of the circuit connected to the primary side of the transformer models is the mechanical representation. The current source represents the movement energy, the capacitor represents the mass, the inductor represents the spring and the resistor represents the parasitic damping. The elements connected to the secondary of the transformer represent the electrical part. The inductor represents the self-inductance of the coil in the electromagnetic device.

2.2.3 Electrostatic transduction

Electrostatic harvesters [109]-[111] consist of a variable capacitor whose two plates are electrically isolated from each other by air, a vacuum, or an insulator. The external mechanical vibrations cause the gap between the plates to vary and hence the capacitance changes. To harvest energy, the plates must be charged, and the mechanical vibrations work against the electrostatic forces present in the device. So, for a linear load circuitry, the motion of the movable electrode can generate an electrical power only if a voltage V biases the capacitor.

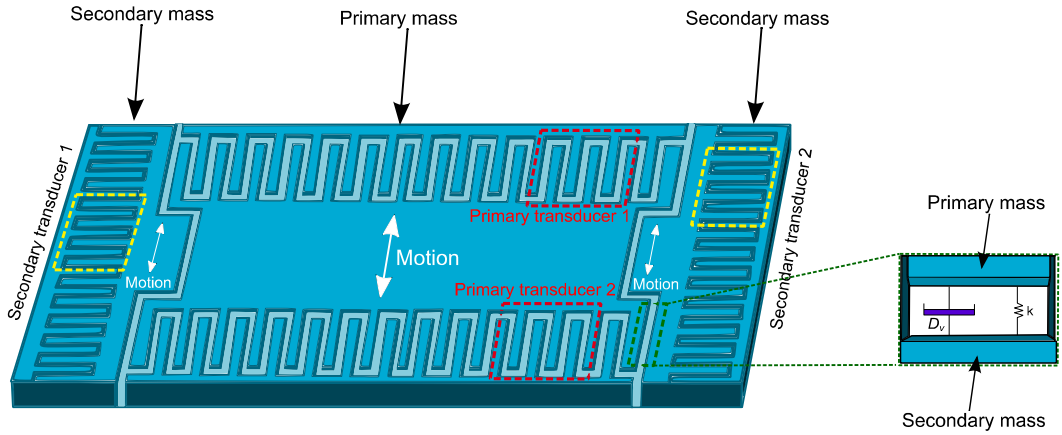

Figure 2-9: Electrostatic kinetic harvester.

The fundamental equations for this work mode are equation 2-11 and 2-12:

$$C = \frac{Q}{V} = \varepsilon \frac{A}{d} \rightarrow V = \frac{Qd}{\varepsilon_0 A} \tag{2-11}$$

$$E = 0.5QV = 0.5CV^2 = 0.5\,Q^2/C \tag{2-12}$$

, where C is the capacitance (F), V is the voltage (V), Q is the charge (C), A is the area of the plates (m^2), d is the gap between plates (m), ε is the permittivity of the material between the plates (Fm^{-1}), ε_0 is the permittivity of free space and E is the stored energy (J).

Electrostatic generators can be either voltage or charge constrained. Voltage constrained devices have a constant voltage applied to the plates and therefore the charge stored on the plates varies with changing capacitance. This typically involves an operating cycle that starts with the capacitance being at a maximum value (C_{max}). At this stage, the capacitor is charged up to a specified voltage (V_{max}) from a reservoir while the capacitance remains constant. The voltage is held constant while the plates move apart until the capacitance is minimized (C_{min}). The excess charge flows back to the reservoir as the plates move apart and the net energy gained is given by equation 2-13:

$$E = \frac{1}{2}(C_{max} - C_{min})V_{max}^2 \tag{2-13}$$

Charge-constrained devices use a constant charge on the capacitive plates, and therefore the voltage will vary with changing capacitance. The plates are initially charged when the variable capacitance is at a maximum. As the capacitor plates separate, the capacitance decreases until C_{min}. Since the amount of charge is fixed, the voltage across the plates increases. The initial charge is returned to the reservoir controlled by the system electronics, and the initial charge is returned to the reservoir at the end of the cycle. Alternatively, a fixed charge can be obtained using electrets materials, such as Teflon or Praylene. In either case, the mechanical work against the electrostatic forces is converted into electrical energy. The net energy gained in this case is given by equation 2-14:

$$E = \frac{1}{2}(C_{max} - C_{min})V_{max}V_{start} \tag{2-14}$$

In both cases, Vmax must be carefully chosen to be compatible with the associated electronics and its associated fabrication technology. These two approaches have different strengths and weaknesses.

The electrostatic generator can be broadly classified into three types:

1. Out of plane, gap varying, voltage constrained.
2. In a plane, overlap varying, charge constrained.
3. In a plane, the gap is varying.

Table 2-7: Electrostatic force variation for the three configurations.

Structure	Charge constrained	Voltage constrained
Out of plane gap varying	F_e constant	$F_e \sim 1/x$
In-plane overlap varying	$F_e \sim 1/x^2$	F_e constant
In-plane gap varying	$F_e \sim x$	$F_e \sim 1/x^2$

Compared with other vibration energy harvesting methods, the electrostatic energy harvesters have many advantages such as high Q, wide tuning range, low noise, small size and low quality.

Figure 2-10 represents the equivalent circuit model for vibration driven harvester using electrostatic damping.

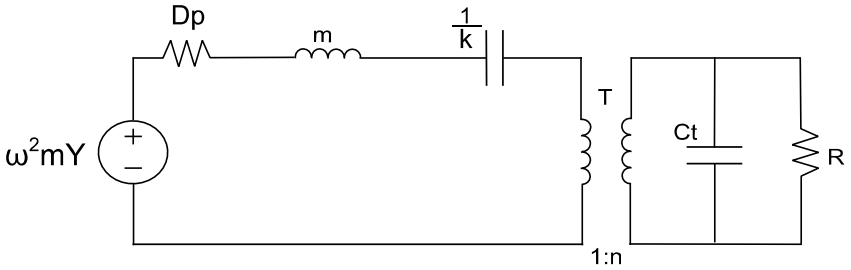

Figure 2-10: Equivalent circuit of electrostatic force harvester.

, where the part of the circuit connected to the primary side of the transformer models the mechanical behaviour of the harvester. The voltage source represents the vibration source, the capacitor, represents the mass, the inductor, represents the spring and the resistor represents the parasitic damping. The terminals on the secondary of the transformer represent the electrical part or generator. The capacitor represents the terminal capacitance of either the piezoelectric material or the moving capacitor in the electrostatic device.

2.2.4 Pyroelectric transduction

The pyroelectric harvester [112]-[114] converts a temperature change into electric current or voltage. It is similar to the piezoelectric effect, with another type of ferroelectric behaviour. Pyroelectricity requires time-varying inputs and suffers from small power outputs in energy harvesting applications due to its low operating frequencies. However, one key advantage of pyroelectrics over thermoelectric is that many pyroelectric materials are stable up to 1200 ºC or higher, enabling energy harvesting from high-temperature sources and thus increasing thermodynamic efficiency.

Pyroelectric materials are materials whose spontaneous polarization P presents strong temperature dependence due to their crystallographic structure. These materials have a spontaneous polarization defined as the average electric dipole moment per unit volume in the absence of an applied electric field. A subclass of pyroelectric materials known as ferroelectric materials can switch the direction and magnitude of the spontaneous polarization by reversing the applied coercive electric field. However, the converse is not true that the unipolar hysteresis curves between electric displacement D and electric field E exhibited by ferroelectric materials at two different temperatures T_{cold} and T_{hot}. The curves travel in a counter-clockwise direction upon isothermal cycling of the electric field applied across the sample. When a ferroelectric material is heated above its Curie temperature T_{Curie}, it undergoes a phase transition from ferroelectric to paraelectric. Then, the spontaneous polarization vanishes. The electric displacement D of the material at temperature Tand electric field E is defined as in equation 2-15:

$$D(E,T) = \varepsilon_0 \epsilon_r(T) E + P_s(T) \tag{2-15}$$

, where ε_o is the vacuum permittivity, $\varepsilon_r(T)$ is the relative permittivity of the material, E is the applied electric field, and $P_s(T)$ the saturation polarization.

In next points and in figure 2-11, pyroelectric harvester operation basics are shown:

a. Pyroelectric free charges (represented as positive and minus circles) are attracted to the material due to its spontaneous polarization.
b. Electrodes are connected to an ammeter at a constant temperature. The spontaneous polarization is constant, and no current is flowing.

c. The harvester is being heated. The spontaneous polarization is reduced through a reduction in the dipole moment. The result is that the quantity of bound charges at the electrodes decreases, and the subsequent redistribution of charges results in current flowing through the external circuit.
d. The harvester is being cooled. The spontaneous polarization is increased, and the current sign is reversed.

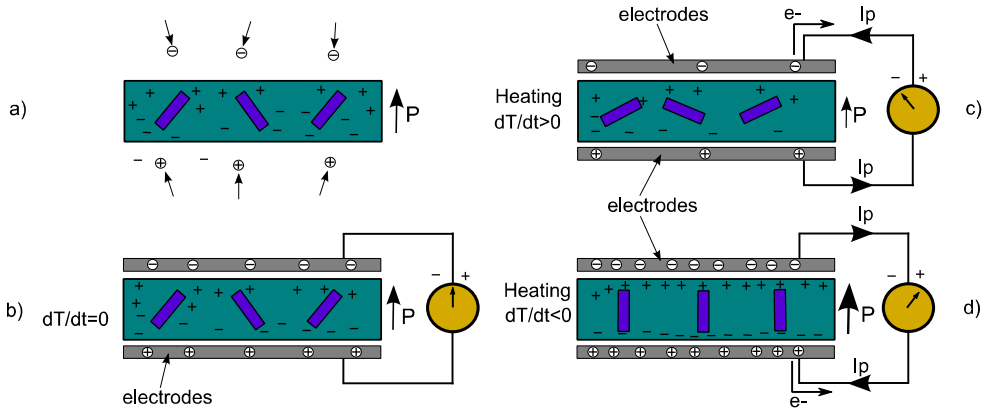

Figure 2-11: A pyroelectric material used as the dielectric in a capacitor.

Equation 2-16 shows the pyroelectric current I_p produced during the cycle:

$$I_p = A_f \frac{dP_s}{dt} = A_f p \frac{dT}{dt} \tag{2-16}$$

, where A_f is the surface area of the pyroelectric thin film capacitor, P_S is the pyroelectric thin film polarization, T is the pyroelectric capacitor temperature, and p is the pyroelectric coefficient. The net output power N_p from the pyroelectric capacitor is given by equation 2-17:

$$N_p = V_{appl} I_p = V_{appl} A_f p \frac{dT}{dt} \tag{2-17}$$

, where V_{appl} is the externally applied voltage across the pyroelectric capacitor. The cumulative pyroelectric conversion output work W_{out} from the cycle over the area is as follows:

$$W_{out} = \oint V_{appl}\, dq = \int N_p\, dt = \int V_{appl} A_f p \frac{dT}{dt} \tag{2-18}$$

Figure 2-12 shows a pyroelectric harvester with the bimorph cantilevered structure. The down pyroelectric layer has a large coefficient of thermal expansion (TCE) while the thicker lower metal layer is composed of a low CTE metal, such as Ti. The upper thin metal layer is thick (typically 10-50 nm) that it forms a continuous metal film over the P(VDF-TrFE) dielectric layer, but not so thick that it contributes to the bimorph bending of the cantilever. The bimorph metal and P(VDF-TrFE) layers are typically 2-10 μm thick.

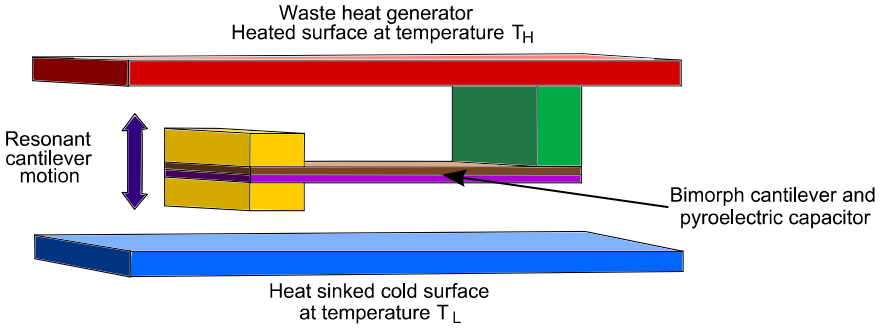

Figure 2-12: Pyroelectric harvester.

The cantilever structure initially heats through the anchor, causing the cantilever to bend towards the lower cold heat sunk surface. On contacting the cold surface, the structure rapidly loses heat and bends towards the hot upper surface. On contacting the upper surface, it then rapidly heats and bends from the upper surface and again makes contact with the lower surface. This process is repeated indefinitely. Good thermal contact with the hot and cold surfaces is key to transfer substantial amounts of thermal energy to the pyroelectric capacitor on the cantilever. Heat transfer is enabled by small stiction forces between the cantilever proof masses and the hot and cold surfaces, which will counteract the bimorph mechanical force pulling the cantilever structure away from the surfaces once contact has been made and the temperature increased or decreased in the structure. Hence the faster the temperature can be cycled back and forth across the device, the more efficient the energy conversion process is and the higher the amount of electrical energy generated. Also, the amount of current and electrical energy generated by this circuit is dependent on the magnitude of the pyroelectric coefficient p, the size of the capacitor (plate area A, and very importantly, on the rate of change in the temperature across the pyroelectric capacitor. Cantilever surface contact time can also be controlled by alternately applying an electric potential between the proof masses and the adjacent surface. The equivalent electric representation of the harvester is shown in figure 2-13:

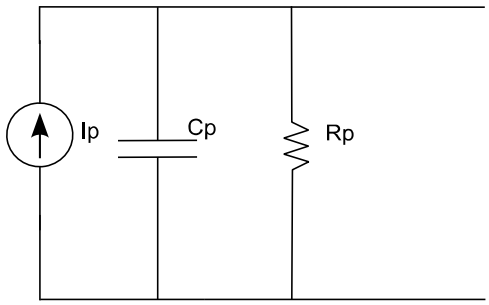

Figure 2-13: Pyroelectric harvester equivalent circuit.

The useful work is thermodynamically limited by the Carnot efficiency, given by equation 2-19:

$$\eta_{Carnot} = 1 - \frac{T_L}{T_h} \tag{2-19}$$

, where T_H is the temperature of the heat source and T_L is the temperature of the heat sink. Thermal energy gradient power generators convert heat (Q_{in}) into electrical energy (W_{out}) with efficiency:

$$\eta = \frac{W_{out}}{Q_{in}} = \frac{W_E - W_P}{C_v \Delta T + Q_{Int} + Q_{Leak}} \tag{2-20}$$

, where W_E is the generated electrical energy, W_P is the energy lost in the temperature cycle, C_v is the heat capacity of the pyroelectric device, Q_{Int} are the intrinsic heat losses in the thermal cycle, and Q_{Leak} is the heat leakages between the hot and cold sources.

The actual energy conversion efficiency for any thermal energy recovery device depends on the temperature difference between the hot and cold sources. For temperature differences in the range 10-20 ºC, maximum overall efficiencies are in the range of 3-7%. With higher temperature differences in the range 100-300 ºC, efficiencies are in the range of 20- 40%.

2.3 Thermoelectric harvester's technology and devices

Thermoelectric harvesters [115]-[117] are used in environments that naturally contain temperature gradients. This harvester technology converts thermal energy into electric energy based in Seebeck effect. The temperature difference provides the potential for efficient energy conversion, while heat flow provides the power. Even with large heat flow, however, the extractable power is typically low due to low Carnot and material efficiencies. The best thermoelectric materials are heavily doped semiconductors.

Thermoelectric harvesters are solid-state devices with no moving parts. They are silent, reliable and scalable and easily installed, so suitable for energy harvesting application.

The thermoelectric effects arise because charge carriers in metals and semiconductors are free to move much like gas molecules while carrying charge as well as heat. When a temperature gradient is applied to a material, the mobile charge carriers at the hot end preferentially diffuse to the cold end. The build-up of charge carriers results in a net charge (negative for electrons, e^- and positive for holes, h^+) at the cold end, producing voltage. Equilibrium is reached between the chemical potential for diffusion and the electrostatic repulsion due to the accumulation of charge. This property is known as the Seebeck effect and is the basis of thermoelectric power generation. Figure 2-14 shows operation mode of a thermoelectric harvester:

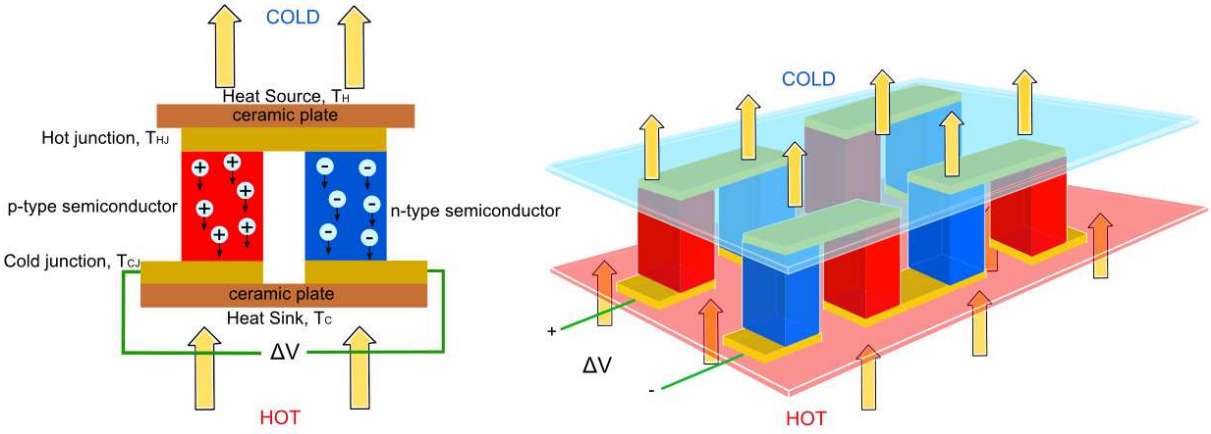

Figure 2-14: Thermoelectric harvester.

A thermoelectric generator utilizes heat flow across a temperature gradient to power an electric load through the external circuit. The temperature difference provides the voltage ($V=\alpha\Delta T$) from the Seebeck effect, while the heat flow drives the electrical current, which therefore determines the power output. The thermoelectric figure of merit of the materials (zT) depends on the Seebeck coefficient (α), absolute temperature (T), electrical resistivity (ρ) and thermal conductivity (κ) of the material:

$$zT = \frac{\alpha^2 T}{\rho k} \tag{2-21}$$

To obtain a practical output voltage and power at low temperature difference, many thermocouples can be arranged electrically in series and thermally in parallel, forming the thermoelectric device. Equations 2-22, 2-23 and 2-24 express the Seebeck voltage V_G, the current I_L and the load resistance R_L of a thermoelectric device with N number of thermocouples:

$$V_G = \Delta V_{pn} = N\alpha_{pn}(\Delta T_{TEG}) = N\alpha_{pn}(T_h - T_c) \tag{2-22}$$

$$I_L = \frac{V_G}{R_{in} + R_L} = \frac{N\alpha_{pn}(T_h - T_c)}{R_{in} + R_L} \tag{2-23}$$

$$R_{in} = \frac{N2\rho h}{A_{leg}} \tag{2-24}$$

The maximum efficiency of a thermoelectric device is determined by its figure of merit (zT), which is an average of the component materials zT values. The energy conversion efficiency is limited by the Carnot factor, which is expressed as in equation 2-25:

$$\eta_{Carnot} = \frac{\Delta T}{T_h} \tag{2-25}$$

Where $\Delta T = T_h - T_c$ is the temperature difference across the thermoelectric. And equation 2-26 shows the dependency of generated electric power (P) on convert's heat (Q) and system efficiency (η).

$$P = \eta Q \tag{2-26}$$

While the exact thermoelectric materials efficiency is complex, the constant properties approximation leads to the equation 2-27 for efficiency:

$$\eta = \frac{\Delta T}{T_h} \frac{\sqrt{1 + ZT} - 1}{\sqrt{1 + ZT + T_c/T_h}} \tag{2-27}$$

The efficiency of an actual thermoelectric device its about 90% of this value due to losses from electrical interconnects, thermal electrical contact resistances and other thermal losses.

An equivalent circuit model of the thermoelectric energy harvester is shown in figure 2-15. The temperature difference, ΔT_{TEG}, across the junctions of the TEG is lower than the temperature gradient, $\Delta T = T_H - T_C$, that is externally imposed across the thermal energy harvester. This is because of the thermal contacts and thermal grease resistances residing in the cold and hot sides of the thermal energy harvester, i.e., $R_{con}(H)$, $R_{con}(C)$ and $R_g(H)$, $R_g(C)$, respectively. To minimize this negative effect, the thermal resistance, RTEG, of the TEG is made as high as possible and/or conversely, the rest of the thermal resistance of the thermal energy harvester is designed to be as small as possible.

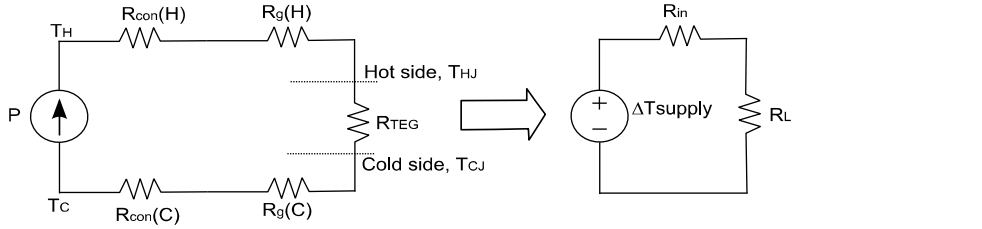

Figure 2-15: A typical thermal circuit in a thermoelectric energy harvesting device.

From this thermal circuit, the temperature difference across the thermoelectric is given by equation 2-28:

$$P = \Delta T_{supply} \frac{R_L}{R_{in} + R_L} \tag{2-28}$$

And the heat flow through the circuit is given by equation 2-29:

$$Q = \frac{\Delta T_{supply}}{R_{in} + R_L} \tag{2-29}$$

Combining these two equations with the linear relationship between efficiency and ΔT_{TE} gives the electric power value:

$$P = \eta_1 {\Delta T_{supply}}^2 \frac{R_L}{(R_{in} + R_L)^2} = N^2 {\alpha_{pn}}^2 {\Delta T_{supply}}^2 \frac{R_L}{(R_{in} + R_L)^2} \tag{2-30}$$

As shown in equation 2-30, the higher number of thermocouples, the larger temperature difference between the hot and cold junctions, together with higher absolute Seebeck coefficient, and lower internal resistance are desirable to generate higher output power.

2.4 Magnetic harvester's technology and devices

Magnetic harvesters [118]-[120] operate under Faraday's law of induction. When the harvester is placed near a magnetic field, an induced electromotive force is generated in an inductor; this principle is electromagnetic induction. The electricity is generated when a changing magnetic field influences the harvesting device. Furthermore, the harvester is composed of a ferromagnetic material and an inductor.

The most common source of magnetic field is a conductor carrying electrical current. Thus, a typical application is to wrap the harvester around an electric power line, due to the high-power source and high magnetic variability. Nevertheless, achieve power from electric power-lines noise is also possible. Power lines in the magnetic fields are considered harmful noise. However, they are necessary for our society. Thus, another source but less efficient is detected for magnetic harvesters.

The flow of electric charge has an associated magnetic field. Moreover, ferromagnetic materials are ideal materials for this harvester technology. These materials have the propriety to attract a magnet and transfer electromagnetic energy to electric energy. Some common ferromagnetic materials are iron, nickel, cobalt, alnico and an alloy of aluminium-nickel-cobalt. Ferromagnetic materials are classified under relative permeability parameter. The permeability ratio of material concerning a vacuum at the same magnetic field strength defines the relative permeability of a material. In addition, the relative permeability factor increases the magnetic field across the material. Table 2-8 shows relative permeability of different ferromagnetic materials.

Table 2-8: Relative permeabilities of conventional ferromagnetic materials.

Material	Relative Permeability (μr)	Material	Relative Permeability (μr)
Cobalt	250	Permalloy	100000
Nickel	600	Fe_3O_4 (Magnetite)	100
Iron	6000	Ferrites	5000
Supermalloy	107	Mumetal	100000
Steel	100	Permendur	5000
Silicon iron	7000	-	-

Another consideration in the implementation process of magnetic energy harvester are coil properties. The number of coil turns and the resistance are the parameters that determine the voltage and availably power generated by the harvester. The number of turns depends on the geometry of the coil, the diameter of the wire and the density with

which the coil wire has been wound. The insulated circular wire does not fill completely the volume of the coil with conductive material and the percentage of copper inside a coil receives its fill factor. The area of the wire can be related to the total cross-sectional area of the coil, A_{coil}, assuming a certain copper fill factor, $A_{wire} = A_{coil} / N$. The copper fill factor depends on the tightness and the shape of the winding, and the variations in the thickness of the insulation. Described harvester is shown in figure 2-16:

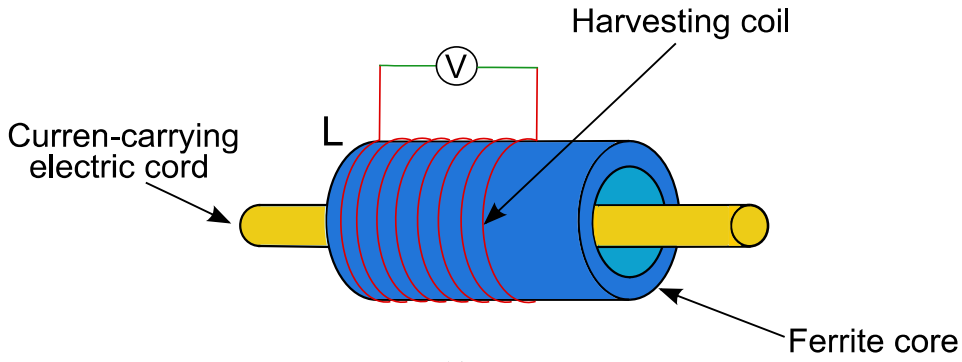

Figure 2-16: Magnetic harvester.

The calculations to obtain harvester produced voltage, coil inductance value and power are based on Faraday's equations. The produced open circuit voltage on an N turn coil placed in a D diameter and l length cylindrical core with μ_r relative permeability is given by equation 2-31:

$$V_{oc} = 2\pi f \mu_{eff} N \pi \left(\frac{D}{2}\right)^2 B \tag{2-31}$$

, where B is the magnetic flux density (in air) parallel to the coil axis and f is his frequency. μ_{eff} is the effective relative permeability, which inside $1 < \mu_{eff} < \mu_r$ range. Then coil self-inductance is obtained by equation 2-32:

$$L_s = \frac{\left[\pi \mu_0 \mu_{eff} N \pi \left(\frac{D}{2}\right)^2 N^2\right]}{\left[l + 0.9\left(\frac{D}{2}\right)\right]} \tag{2-32}$$

As in all harvesters' technologies, maximum output power is obtained when impedance matching is produced. If the coil open circuit voltage V_{oc} under some defined conditions is optimally obtained, the output voltage V_{out} will be the half of V_{oc}.

$$V_{out} = 0.5 V_{oc} = \pi f \mu_{eff} N \pi \left(\frac{D}{2}\right)^2 B \tag{2-33}$$

Finally, output power per unit volume in W/m^{-3} is represented as in equation 2-34:

$$P_{out}/Vol = \frac{\pi^2 DN}{4\rho l} \mu_{eff}{}^2 (fB)^2 \tag{2-34}$$

, where ρ is the resistance per unit length of the wire.

The electric circuit representation of described equations is shown in figure 2-17. When there is current flow in the core conductor, an electric field proportional to the current is generated. By the principle of induction, a current proportional to the electrical field, scaled by the transformer ratio and is induced in the secondary coil. Besides, ferromagnetic material resistance could be added to secondary coil to make a more precise model. Finally, resistance represents the internal resistance of the inductor.

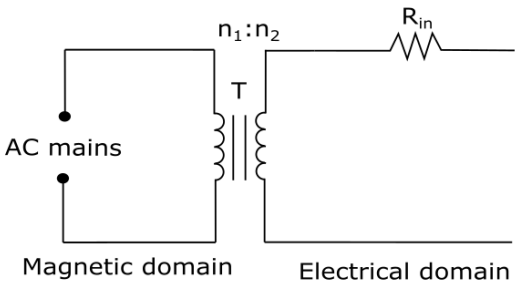

Figure 2-17: Equivalent circuit of the harvesting coil with ideal matching.

Transformer ratio will change regarding the distance between core and conductor line. Also, if the magnitude of the primary current is reduced or the distance of the inductance from the conductor increases, the maximum energy harvested by the harvester decreases exponentially. Therefore, it becomes impossible to convert the magnetic field energy into electrical energy due to the low efficiency.

Example of harvested power [119] are shown in table 2-9:

Table 2-9: Comparison of different coil modules.

Harvester	Power density (μW/cm³)		Harvester	Power density (μW/cm³)	
	21.2 μT	200 μT		21.2 μT	200 μT
Coil 1	0.81	71	Coil 3	0.08	7.6
Coil 2	1.47	130	Coil 4	0.21	18

The magnetic field harvesting could be used for electric lines monitoring because current carrying conductors become an ideal source for energy harvesting. For example, self-powered smart metering at medium voltage electric lines to measure the energy direction change and each phase current.

2.5 RF harvester's technology and devices

Radio Frequency of RF harvesters [121]-[123] achieves electric energy from wireless microwave power. Usual sources for this kind of harvesting are located in cities or populates areas. The background RF radiation, emitted by broadcast transmitters, cell phone towers, and Wi-Fi nets or low power wireless networks, serve as energy harvesting source.

In this context, radio frequency waves include frequencies from 3 kHz to 300 GHz. The harvested power depends on the incident power density, the distance between the transmitter and receiver, power conversion efficiency and harvester antenna size. Thus, the intercepted power is directly proportional to the size of the antenna aperture.

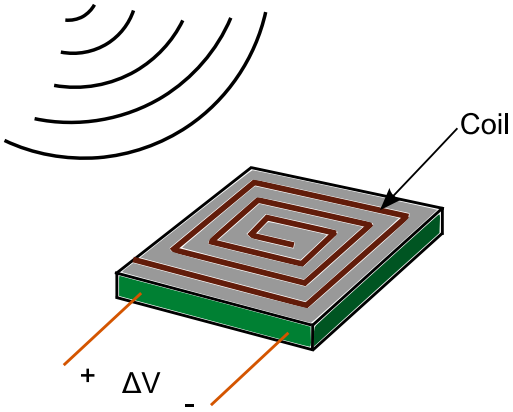

Figure 2-18: RF harvester.

A coil and a separator compose RF harvesters. The coil is made of conductive materials (table 2-6) and the separator by nonconductive materials, to avoid short-circuit situations and maintain the coil integrity.

RF radiation is quantified regarding electric field strength (V/m). In the far-field region, the electric field strength is converted into incident power density using equation 2-42:

$$S = \frac{E^2}{Z_0} \tag{2-35}$$

, where S is the incident power density (W/m^2) and Z_0 is the free space characteristic impedance. The incident power density is also dependent on the distance between the source and the receivers. However, the power density is also dependent on direction.

For a system with two antennae, the received power P_R as a function of the transmitted power P_T is given by equation 2-36:

$$P_R = P_T \frac{G_T G_R \lambda^2}{(4\pi)^2 r^2} \tag{2-36}$$

, where G_T is the gain of the transmission antenna and G_R the gain of the receive antenna, λ is the signal wavelength, and r is the distance between the two antennas. Equation 2-41 is valid only for the antennas operating in the far-field region. The far-field region r_{ff} is related to antenna physical dimensions and the signal wavelength.

$$r_{ff} = \frac{2D^2}{\lambda} \tag{2-37}$$

RF harvester device is usually composed by the harvester circuit and an integrated rectifier. Thus, the equivalent circuit is made by these two elements. An example rectifier circuit consists of a single Schottky diode. The Schottky diode makes a dynamic switching in the GHz range. Figure 2-19 shows the equivalent circuit:

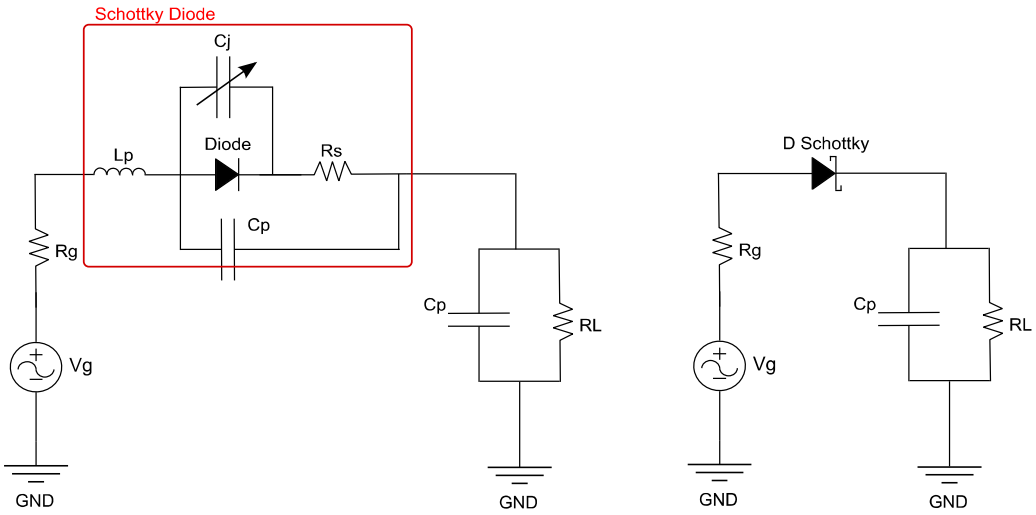

Figure 2-19: The equivalent circuit of a loaded rectifier.

At table 2-10 [121] could be seen some different RF energy harvesting experiments and the numerical result obtained on them. The table shows that the energy harvesting rate dependency on the source power and distance. The energy harvested is around some μW, with this energy only could operate on ultra-low power devices.

Table 2-10: RF energy harvesting experimental data.

Source	Source power (W)	Frequency (MHz)	Distance (m)	Power harvested rate (µW)
Isotropic RF trans.	4	902-928	15	5.5 µW
Isotropic RF trans.	1.78	868	25	2.3 µW
Isotropic RF trans.	1.78	868	27	2 µW
TX91501 power trans.	3	915	5	189 µW
TX91501 power trans.	3	915	11	1 µW
KING-TV tower	960000	674-680	4100	60 µW

2.6 Dynamic fluid energy harvesting

Dynamic fluid energy includes wind [124]-[126] and flowing water power [127][128]. Two methods can harvest the kinetic energy of the fluid. Mechanical parts such as mini-turbine systems generate the electricity. The idea is to use large-scale generator technology principles in small-scale generators.

In this case, both harvester technologies could have the same equivalent electromechanical circuit model [129]. And it can be built analysing the system, as shown in figure 2-20:

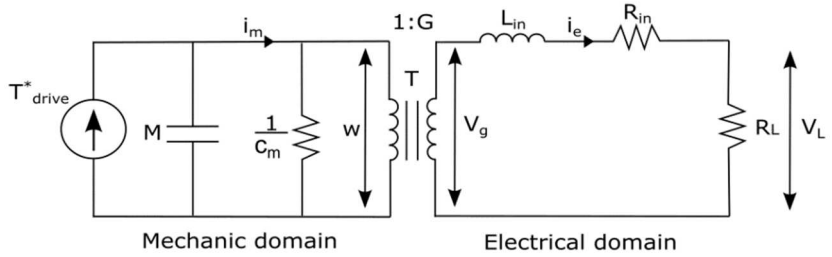

Figure 2-20: Micro wind harvester equivalent circuit schematic.

, where T*drive is the fluid flow power, M the mass of the rotational parts, c_m the coefficient of frictional torque, G the electromechanical conversion coefficient, ω the mechanical angular velocity, Vg the generated voltage at the coils, Li_n generator coils inductance and R_{in} coils internal resistance.

2.6.1 Wind harvester's technology and devices

The wind flow harvester is composed of a mechanical and an electrical part. The system converts wind energy into mechanical energy, then in electromagnetic and finally into electrical energy. The electromagnetic wind generators are reliable and have small mechanical damping and magnets suitable to operate at low wind velocities.

When the airflow passes through the system structure, the airflow force pushes the blades and rotate the pivoting axis. Magnets which are joined to blades generate a variable magnetic flux with the movement. The magnetic field is harvest by generator inductors which give as a result of electric energy.

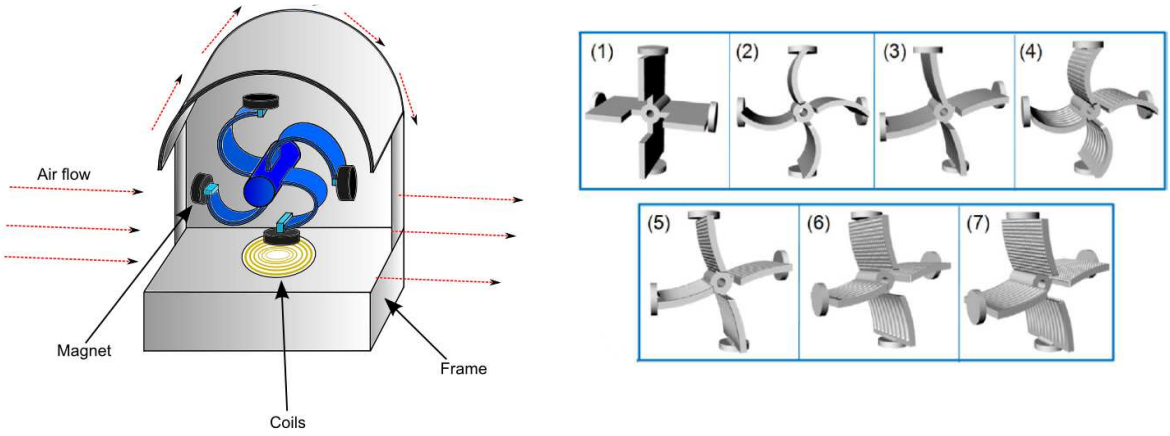

a) Micro wind harvester. b) Wind harvester possible blades topologies.

Figure 2-21: Micro wind harvester.

As the MHAWT starts to work under the wind condition, the rotor will rotate, capturing and transforming the kinetic energy of the incoming wind into mechanical energy. By the aerodynamic equation of [130], the available kinetic power from the airflow is:

$$P_{wind} = \frac{\rho * A * v^3}{2} \tag{2-38}$$

However, the transformation of wind power into rotational power by the turbine rotor is a complex aerodynamic phenomenon [131]-[133]. Ideally, the power extracted from the ambient wind (P_{aero}) is expressed as in equation 2-39:

$$P_{aero} = \frac{C_p(\lambda, \theta) * \rho * A * v^3}{2} \tag{2-39}$$

, where C_p is the power coefficient or the aerodynamic efficiency of the rotor, which is a nonlinear function of the pitch angle θ of the turbine blades and tip speed ratio λ. This final parameter is expressed as in equation 2-40:

$$\lambda = \frac{\omega * r}{v} \tag{2-40}$$

, where ω is the angular velocity and r the radius of the rotor. The power coefficient $C_p(\lambda, \theta)$ for different small wind turbines were examined, and the approximation equations were proposed by [134]-[136].

$$C_p(\lambda, \theta) = C_1 \left[\left(\frac{C_2}{\lambda_i}\right) - c_3\theta - c_4\theta^{c_5} - c_6\right] e^{\left(-\frac{c_7}{\lambda_i}\right)} \tag{2-41}$$

$$\lambda_i = \frac{1}{\left[\frac{1}{(\lambda + c_8\theta)}\right] - \left[\frac{c_9}{(\theta^3 + 1)}\right]} \tag{2-42}$$

In addition, the aerodynamic profiles of turbine blades have a significant influence on the rotating efficiency. The blades affect directly to the system torque force, which influences to the output power level. The number of blades also affects the performance of the energy harvester. System maximum efficiency and out power are also depending on impedance matching between the load, the torque force, and the wind flow.

Finally, table 2-11 shows achieved results with several wind flow harvesters.

Table 2-11: Results of different wind harvesters.

Ref.	Type	Wind velocity (m/s)	Generated power (mW)
[137]	Electrostatic	10	4.761
[124]	Turbine-Electromagnetic	10	4.3
[125]	Electromagnetic	5	13.5
[126]	Electromagnetic	7	70

2.6.2 Water flow harvester's technology and devices

The main difference between water flow and wind flow harvesters is the source where they achieve energy. The operation principles of physics change from aerodynamics to hydraulics.

The flowing water contains kinetic energy due to the water pressure fluctuation. This kind of harvesters convert hydraulic kinetic energy into electrical energy by a mechanic and electromagnetic conversions.

Water flow environments offer a high potential for energy harvesting. However, small-scale water harvesters are not easy to find or develop due to their mechanical complexity. Figure 2-22 shows the generator design of harvester, which are immensely used at large scale generator but difficult to implement in low scale harvesters.

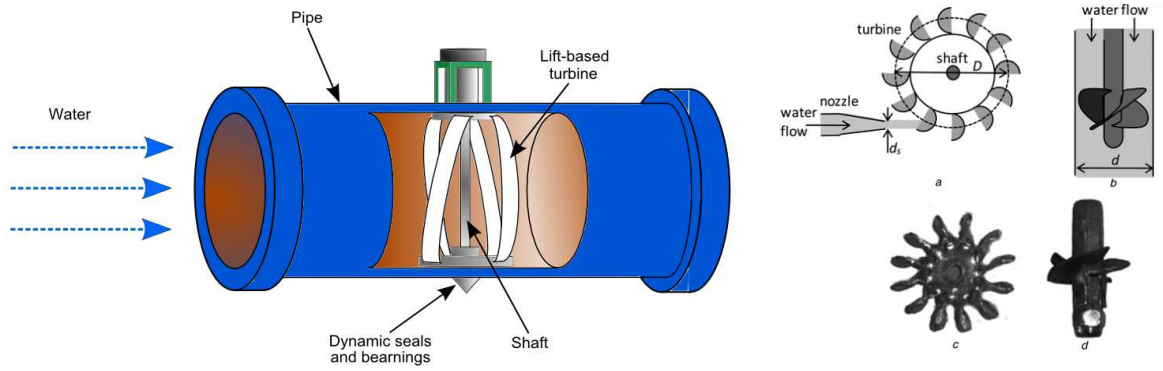

a) Example of water flows energy harvester. b) Usual generators design.

Figure 2-22: Water flow harvester.

In large-scale water flow, energy generation systems Pelton and propeller turbines are usually used. Pelton turbines are more efficient for high heads and low-water flows; however, propeller turbines are more efficient for low heads. Therefore, the available power is proportional to the product of the flow rate with the head and equation 2-43 shows the available power of a hydraulic system

$$P_T = \rho g Q H \tag{2-43}$$

, where ρ is the water density, g is the gravity acceleration, Q is the flow rate, and H is the effective height. Thus, the theoretical velocity is:

$$v_1 = \sqrt{2gH} \tag{2-44}$$

The flow rate is given by equation 2-45:

$$Q = A v_1 = \frac{\pi d_s^2}{4} v_1 \tag{2-45}$$

, where A is the cross-sectional area, d_s is the diameter and $v_1/2$ is the maximum peripheral speed.

In [127] example of water flow harvester is presented considering the requirement of reduced dimensions of energy harvesting application. The rotor is a permanent magnetic ring with a diameter of 20 mm and a height of 5 mm. In addition, a three-phase generator is located at the stator with nine coils with a maximum diameter of 5 mm. Finally, they test several types of turbines with different water flow velocities. Table 2-12 shows the results achieved.

Table 2-12: Hydro system turbines results examples.

Turbine	P (mW)	V (m/s)	A (cm^3)	η (%)	P/V (mV/cm^3)
Pelton 2.2 mm	42	1	76	22.6	0.55
	287	3		26.5	3.78
	663	5		29.5	8.72
Pelton 3.2 mm	92	1	76	24.5	1.21
	500	3		26.5	6.58
	1125	5		28.4	14.80
Small Pelton	4.4	1	7	1.7	0.63
	194	3		14.1	27.71
	491	5		17.0	70.14
Three-bladed propeller	118	0.5	135	5.0	0.87
	340	1		5.5	2.52
	592	1.5		5.5	4.39
Four-bladed propeller	105	0.5	135	4.4	0.78
	265	1		4.3	1.96
	462	2		4.3	3.42

The water flow energy harvesters could be used to monitor the water quality and hydraulic state of water distribution systems or rivers, etc.

2.7 Acoustic noise harvester's technology and devices

Energy harvesting through sound is quite new technology at energy harvesting world [138]-[140]. Noise is one of the most significant pollution sources at cities and can be used as a source to generate energy and power low power electric devices. Table 2-13 shows [138] several sources of acoustic noise and their intensity.

Table 2-13: Example of harvested power with different sound sources.

Sound Source	Sound Intensity (dB)	P (μW)
Mess Kitchen	60	1.476
Child Shouting	76	4.600
Mechanical	88	7.280
Group of people	90	10.540
Motorbike	92	14.040
Tractor	102	23.000
Car horn	109	35.960
Truck horn	128	98.700

Air and material permittivity are the parameters which affect the propagation of electromagnetic waves. However, in acoustic waves case, systems are dependable of mass density ρ and the bulk modulus B of a medium. The refractive index of the medium for acoustic waves is given by equation 2-46:

$$n = v_0\sqrt{\frac{\rho}{B}} \tag{2-46}$$

, where v_0 is the speed of sound in the air. And the effective modulus of the system B_{eff} is calculated with equation 2-47:

$$B_{eff} = B_o\left(1 - \frac{F\omega_0^2}{\omega^2 - \omega_0^2}\right)^{-1} \tag{2-47}$$

, where B_0 is the bulk modulus. The system frequency of the acoustic harvester is dependent of the structural factor, the resonance frequency, neck area, neck length, and the volume of the cell or acoustic tube. Equation 2-48 represent the equation to calculate the resonance frequency of the system:

$$\omega_1 = \omega_0\sqrt{1+F} = v_0\sqrt{\frac{S_h}{l'\Omega_h}}\sqrt{1+\frac{\Omega_h}{\Omega}} \tag{2-48}$$

When the acoustic signal comes, and pressure varies, the membrane diaphragm moves in response to the changing force in the air. When the membrane starts moving, the magnet is also moved producing a variable electromagnetic field. The system inductors convert the electromagnetic field into electric energy, and a small voltage is produced in a connected load. In figure 2-23 acoustic harvester architecture is shown:

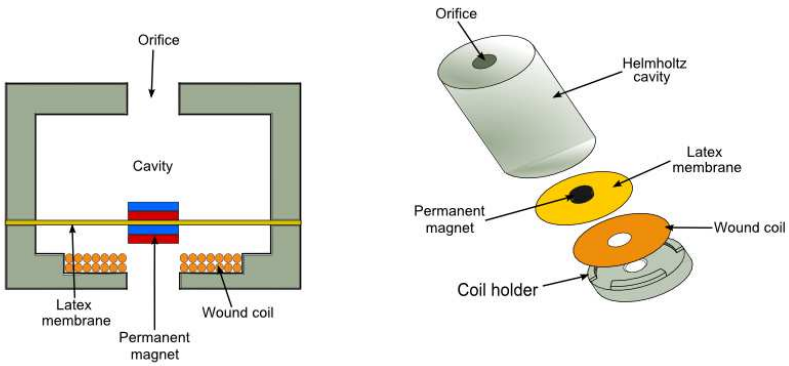

Figure 2-23: Acoustic noise harvester.

This harvester mechanic design is composed by the acoustic signal insertion orifice and the system cavity. Then, the generator consists in a hard-core magnet inserter in a thin elastic material membrane. Under the elastic membrane, the generator inductor is placed. Thus, a Helmholtz Resonator.

Due to the low power of usual acoustic signals, the harvester construction must consider the availability of a suitable movement also with low-pressure variations. Another consideration is the frequency change during the system operation due to the noise level change, producing variations in the vibration and decreasing system efficiency.

The equivalent circuit for acoustic harvester is shown in figure 2-24:

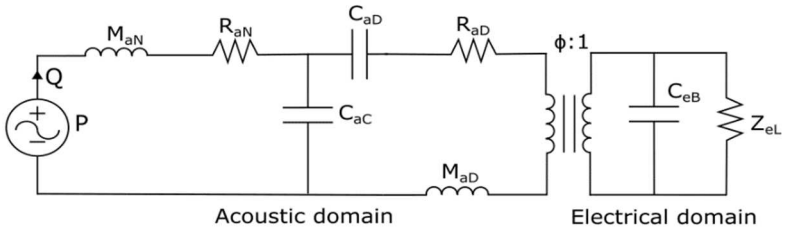

Figure 2-24: Equivalent circuit of an acoustic harvester.

The equivalent circuit is divided in the acoustic and electric domains. At first side, mass M_{aN}, damper R_{aN} acoustic cavity C_{ac}, lumped mass M_{aD}, compliance C_{aD} and radiation resistance values are located, basically mechanical parameters. The union between acoustic and electric domain or energy transfer is represented with a transformer, which has a transduction ratio of Φ. At second side, electrical blocked capacitance C_{eB} and dielectric loss resistance Z_{eL} are represented. An electric load has to be connected in parallel to get electric energy.

Finally, differences of acoustic harvesting with piezoelectric and electrodynamic technologies are exposed in table 2-14 [139]:

Table 2-14: Comparison of the developed acoustic energy harvesters.

Type	Device dimensions (mm)				SPL (dB)	F (kHz)	R (Ω)	P (μW)
	Neck		Cavity					
	Diameter	Height	Diameter	Height				
Piezoelectric	2.39	3.18	6.35	16.1	149	13.57	1000	$6x10^{-6}$
Piezoelectric	2.39	3.18	6.35	16.1	100	24	550	$11x10^{-6}$
Piezoelectric	2.42	3.16	6.34	16.4	161	2.64	20000	$30x10^{3}$
Piezoelectric	0.1	0.18	1.2	1.02	100	3.5	1000	$1.69x10^{-3}$
Electrodynamic	2.5	4	6.5	16	125	0.143	66	1503.4

3. Low power management

3.1.1 Low power principles

Low-power electronics are identified in a power range from a few milliwatts to most 1 W [141]. Figure 3-1 shows the state of art of low power [142].

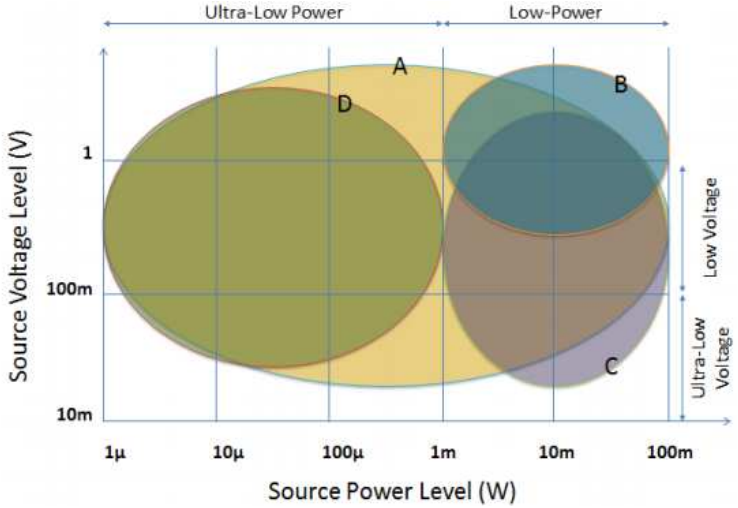

Figure 3-1: state of the art of low voltage and low power converters.

The low power concepts are applied in systems with the following characteristics:

1. Systems that need to be portable and run on a battery or other power source, with a long service life or long time between recharges.
2. Systems that operate harvesting relatively small amounts of energy from their environment. The system is miniaturized, and the source supplies less energy, being the power limitation higher.
3. Systems that measure some physical/chemical value and transmit the information to central systems to process the data obtained.

And low power systems design task requires to follow the next guidelines [143]:

- Standard circuits and devices for the most part
- Standard protocols
- Saving in system and module architecture
- Savings in algorithms and coding
- Saving in choice and use of protocols

Design efforts in low energy management are increasing due to the need to design low energy consumption systems, as well as to improve performance and costs. In the field where the energy available is considerably lower, the management task is further complicated due to a shortage of energy resources.

So, energy management is becoming an increasing issue in almost design categories, such as energy reduction by function, lower energy consumption and higher performance of the electronic infrastructure.

Then, energy management is based in system information, which is represented by the states of variables at the physical system. To save energy, the amount of information that is going to be processed must be reduced. Thus, the low-power design requires a broad knowledge of devices, circuits, and systems.

Low power electronics have several applications fields, such as medical, consumer electronics, home automation and many more (table 3-1).

Table 3-1: Examples of applications of low power electronics.

Applications of low power electronics			
Industry	**Bioelectronics**	**Home automation**	**Aerospace systems**
Metering	Portable medical	Acces control	Space remote devices
Monitoring	Implantable devices	Light control	Avionics
SHM	Intelligent medicine	Climate control	SHM
		Electrical appliance	

In the next lines some application examples of table 3-1 are introduced, such as biomedical, transport, Industry 4.0, structural health monitoring for smart cities and aerospace are exposed:

Biomedical:

- Glucose monitoring smart contact for people with diabetes (figure 3-2a). An antenna thinner than a human hair receives RF energy to harvest. The system also incorporates a miniaturised glucose sensor [144].

- Perpetual peacemaker: A piezoelectric device harvest electrical energy from heart motion (figure 3-2b). So, this could eradicate the replacement of the pacemaker battery [145].

Transport:

- Damage monitoring system for train rail axle bearings (figure 3-2c). A vibration induction device harvests energy from train generated low-frequency vibrations [146].

Industry 4.0:

- Devices to build smart factories. EHWSN are an essential component of industrial interconnectedness and harvest ambient power sources that replace batteries and minimize operational maintenance and costs [147].

Structural health monitoring for smart cities:

- Monitoring the degradation of a suspension highway (figure 3-2d). A vibration-based SHM algorithm is used to detect the structural performance degradation of a suspension highway and system necessary energy is harvested by wind or solar [148].

Aerospace:

- Low power management to squeeze available energy. Improve low power management with EH strategies to apply on satellites and planetary rovers' sensors. A possibility of harvesting energy from solar cells or thermo-electric generator (temperature gradient between space and satellite) [149].

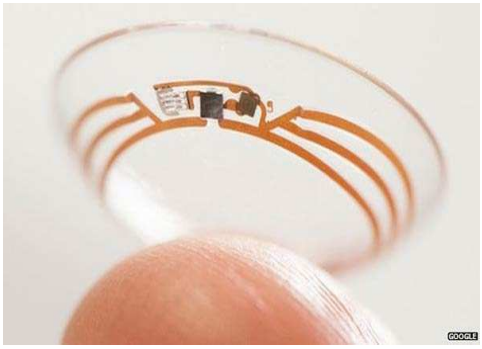

a) Glucose monitoring smart contact for people with diabetes.

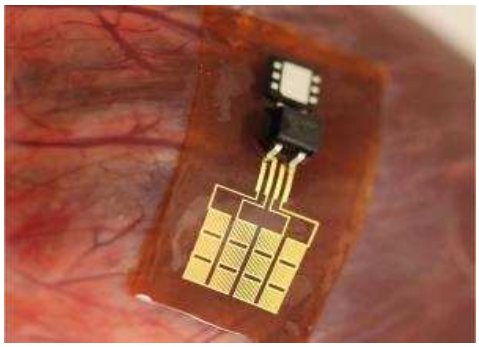

b) Perpetual pacemaker.

c) Structural health monitoring of a bridge.

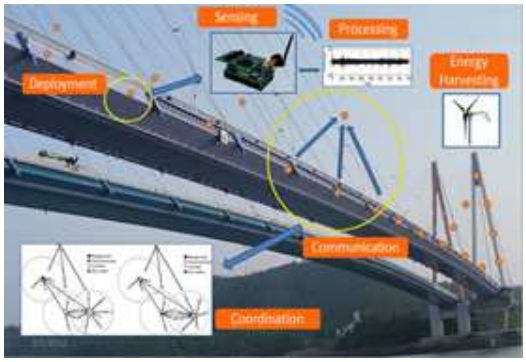

d) Rail axle bearings damage monitoring.

Figure 3-2: Low power application examples.

3.1.2 Low power management principles

Low power management convert harvested energy in usable energy with the maximum efficiency possible for the system load. Could be a step-down linear regulator converter and no/yes resonant step-up converter. An energy harvesting low power manager depends on the harvester, storage device, and load.

The low power management device has the next tasks:

- Voltage level transformation
- Signal type conversion
- Supply energy to the system
- High efficiency ($\eta > 80$ %, if it is possible)
- Maximum a few μW of power consumption, as less as possible
- Active control of harvester and storage device
- Optimal impedance match between harvester, storage device, and load

Power management systems acts as a buffer between the sources, loads, and energy storage elements. Single integrated circuits can rectify and regulate the input voltage to produce the desired output voltage and to shunt excess energy not to exceed this voltage level. They control the distribution of power to their outputs and connected storage elements to maximize performance and ensure sufficient power is available when loads require it. Figure 3-2 shows described operation [150]:

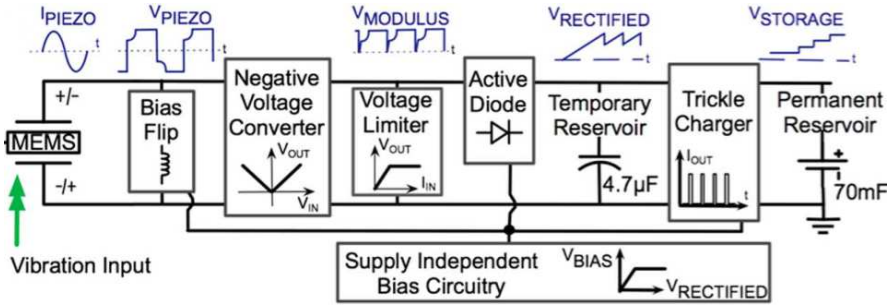

Figure 3-3: Overview of a power management circuit.

The output of an energy harvester cannot be directly applied to circuits because of variations in its power and voltage over time, thus, a power management circuit is required. This power management unit should be able to handle little feeding power and be able to adapt its input to the energy harvester and its output to the load. It should also be self-starting. Is easier to build an efficient power management system working in mW range than in 100 μW range because of the energy available to turn on.

If the power generated is of the order of mW, is easier to build than at 100.

As is explained in upcoming section 3.2.1, there are several architectures or circuits which have the purpose of suit the electric signal module of the harvested energy electric signal.

There are many low power management architectures, but they depend on harvester type. The recommended technique is to use an exclusive power management circuit for each technique. Some harvesters produce alternate current (AC) for that cases AC/DC converter is needed. Other harvesters produce direct current (DC), for which cases a DC/DC converter is needed. This division is represented in table 3-2.

Table 3-2: Power management architecture topology for each harvester technology.

Harvester	Converter type	Rectify	Converter	V_{in} vs. V_{out}	Input	Output
Photovoltaic	DC/DC	No	Buck-Boost	$V_{in}>V_{out}$ or $V_{in}\leq V_{out}$	Voltage	Voltage and Current
Piezoelectric Electromagnetic Electrostatic Pyroelectric	AC/DC	Yes	Buck-Boost	$V_{in}\leq V_{out}$	Current	
Thermoelectric	DC/DC	No	Boost	$V_{in}\leq V_{out}$	Voltage	
Magnetic	AC/DC	Yes	Boost	$V_{in}\leq V_{out}$	Current	
RF			Boost	$V_{in}\leq V_{out}$		
Wind			Buck-Boost	$V_{in}>V_{out}$ or $V_{in}\leq V_{out}$		
Water			Buck-Boost	$V_{in}>V_{out}$ or $V_{in}\leq V_{out}$		
Acoustic			Boost	$V_{in}\leq V_{out}$		

After selecting the power manager architecture, the control of the convert could be implemented. There are several management techniques which make able the energy conversion. Simple converters conversion efficiency is not so good as in complex techniques that effectively reach high values. There are several parameters to decide which type of conversion used; efficiency, input energy signals complexity and the aim to develop a new control technique. For example, the simplest is to make a discrete power manager with a simple PWM [151]. In this case, discrete MOSFETs are usually employed to drive the input signal. These types of converters vary their output current in response to load changes. A pulse width modulation (PWM) controls the power switch output power by varying ON and OFF times. Another example is an integrated energy harvesting low power converter/charger management solution with an Integrated Circuit (IC) [152]. These devices are specifically designed to acquire efficiently and manage the microwatts (μW) to milliwatts (mW). The last example consists in Bio-inspired control strategies [153]: Implementation of smart management algorithms for low energy systems with self-learning, self-adaptive, prediction, machine learning, evolutionary algorithms or neuronal dynamics techniques.

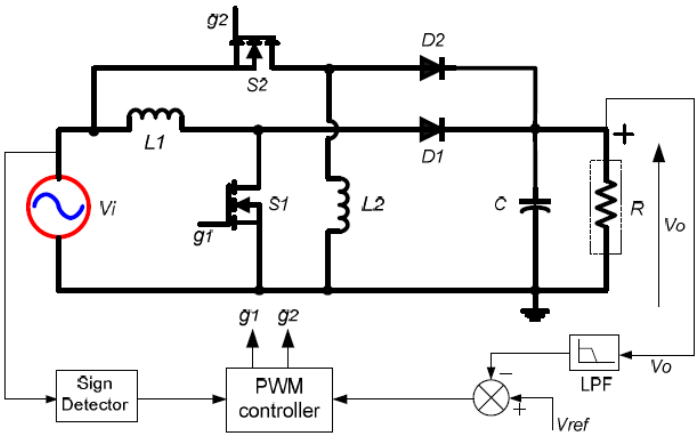

a) PWM based control.

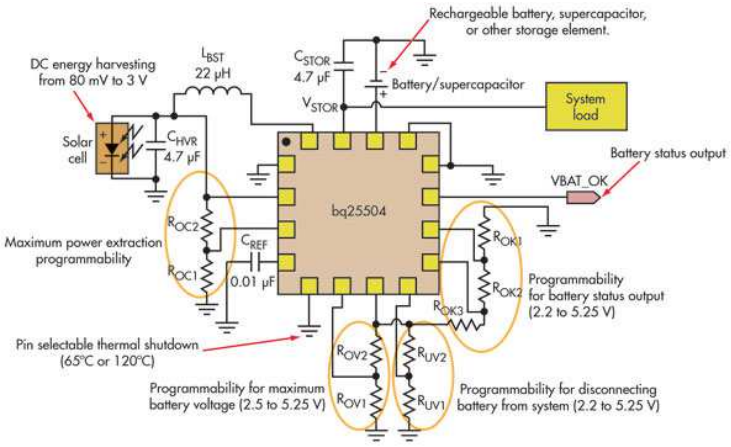

b) Management with an integrated circuit.

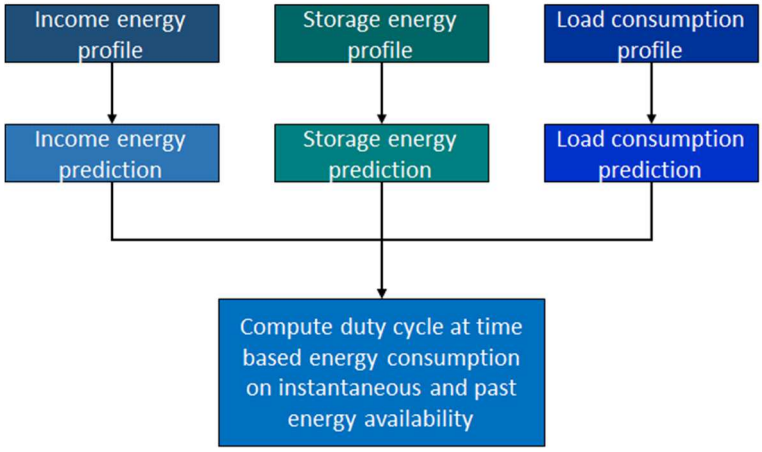

c) Management with artificial intelligence techniques.

Figure 3-4: Examples of different power management techniques.

3.2 Power conditioning reference analog circuits

Power conditioning refers to adapt the power delivered by the harvester to the needs of load or storage device. Analog circuit power conditioning [154] is mainly achieved through the use of voltage converters and/or regulators. In addition, their power waste should be less than the power gain. Whenever the load or some of its parts is in sleep mode, the corresponding voltage regulator should be disabled or set into shutdown mode to save power. Regardless, it must be assured that the MCU (or the circuit that controls the power conditioning stage) never loses its power supply otherwise, the circuit will not be able to restart.

In converter and regulator systems, efficiency (η) is defined as the ratio of power output ($P_{OUT} = V_{OUT}/I_{OUT}$) to power input ($P_{IN} = V_{IN}/I_{IN}$), where V and I are the voltage and current.

$$\eta = \frac{P_{out}}{P_{in}} = \frac{V_{out} I_{out}}{V_{in} I_{in}} \tag{3-1}$$

The inductor current (i_L) defines two different modes of DC/DC converters operation. Continuous conduction mode CCM, in which the inductor current is always greater than zero. Discontinuous Conduction Mode DCM, when the inductor current is zero during a portion of the switching period.

3.2.1 Buck converter

This topology decreases the voltage level of the input source Vs, i.e., step-down. It consists of a controlled switch S, diode D, filter inductor L, filter capacitor C, and load resistance R. Figure 3-5 shows buck converter architecture and internal waveforms.

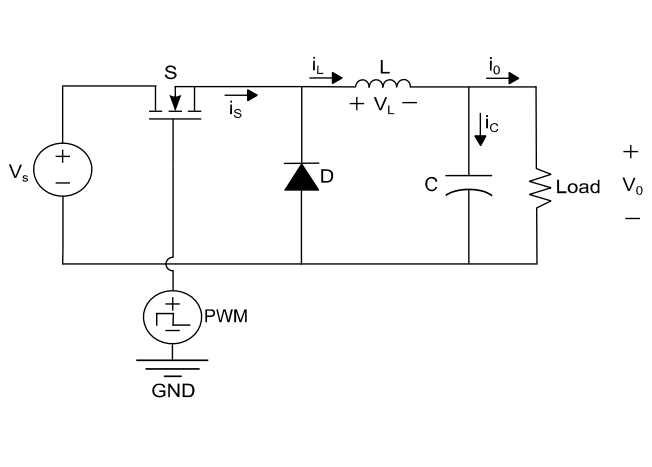

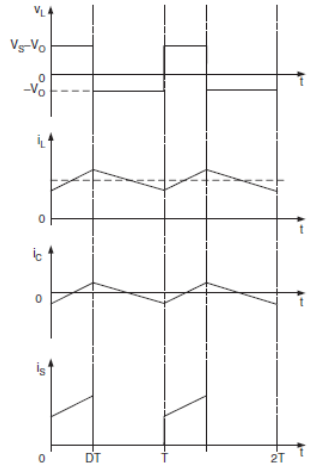

a) Architecture. b) Waveforms.

Figure 3-5: Buck converter architecture and waveforms.

With the switch on and the diode off, the inductor current increases. When the switch is turned off, the inductor current flows to the load. In this situation, the average increase of the current reduces the voltage. The output voltage level is set adjusting the duty-cycle. Equation 3-2 gives the boost converter transfer function 3-2:

$$M = \frac{V_o}{V_s} = D \tag{3-2}$$

3.2.2 Boost converter

This topology increases the voltage level of the input source Vs, i.e., step-down. It is made of the same components as the buck converter, but with a different distribution. Figure 3-6 shows boost converter architecture and internal waveforms.

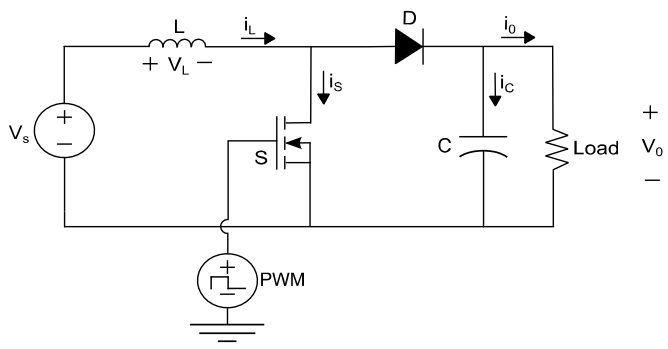

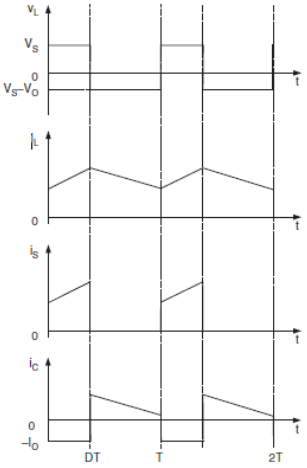

a) Architecture. b) Waveforms.

Figure 3-6: Boost converter architecture and waveforms.

The input voltage in series with the inductor acts as a current source. The energy stored in the inductor increase when the switch is closed. When the switch is opened, inductor current flows to the load. In this situation, the voltage across the load increase.

Furthermore, the output voltage level is varied by adjusting the duty-cycle. Equation 3-3 gives the boost converter transfer function 3-3:

$$M = \frac{V_o}{V_s} = \frac{1}{1 - D} \tag{3-3}$$

The current supplied to the output RC circuit is discontinuous. Thus, a higher value of the capacitor is required in boost topology in comparison with buck topology.

3.2.3 Buck-Boost converter and

This topology increases and decreases the voltage level of the input source V_S, i.e., step-up/ down. It is made of the same components as the buck and boost converters, but with a different arrangement. Figure 3-7 shows buck-boost converter architecture and internal waveforms.

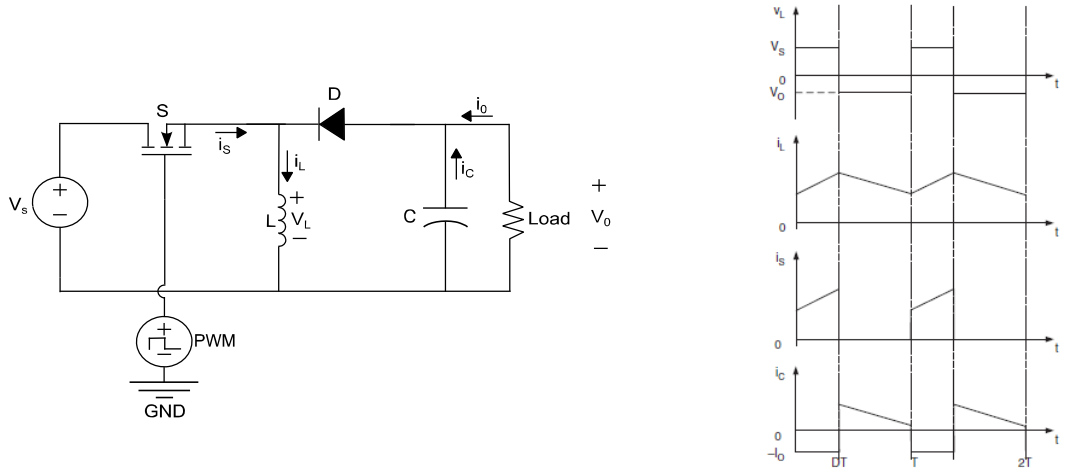

a) Architecture. b) Waveforms.

Figure 3-7: Buck-Boost converter.

With the switch on and the diode off, the inductor current increases. When the switch is turned off, the inductor current flows through the path provided by the diode. However, the output voltage V_O is negative to the ground. Voltage level could be either higher or smaller (equal at D = 0.5) than the input voltage, as a step-up/down. Moreover, the transfer function of the buck-boost converter is given by equation 3-4:

$$M = \frac{V_o}{V_s} = -\frac{D}{1 - D} \tag{3-4}$$

3.2.4 AC–DC rectifier

When the input signal is AC type, a full-wave rectification is needed, which could be achieved without transformers employment. So, the circuit is composed of four diodes in single-phase, a capacitor and a resistive load. This circuit configuration is known as D-bridge [155]. Figure 3-8 shows the circuit topology and wave rectification operation.

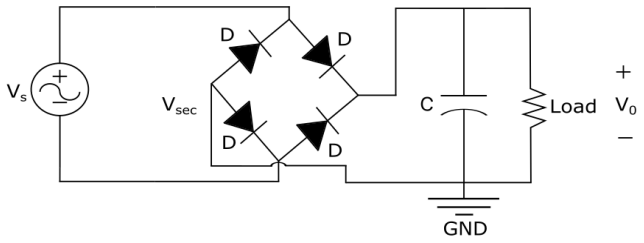

a) Architecture.

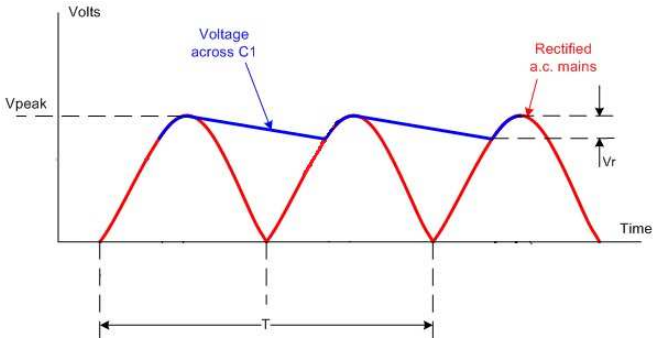

b) Waveforms.

Figure 3-8: AC-DC full wave rectifier (D-bridge) architecture and waveform.

The diode bridge makes half-wave rectification. Diodes D_1 and D_2 conduct when the input signal is in the positive half and diodes D_3 and D_4 with the negative one. The capacitor makes the second half wave rectification. The full-wave rectified voltage is achieved when the voltage is applied across the load. The output voltage ripple should be minimize using smaller values at filter components.

3.2.5 Regulators

Regulators are systems which adapt the voltage level of the power source to the internal electronics voltage level [156][157].

Energy Harvesting Wireless Sensor Networks systems are conditioned by specific characteristics of functionality that involve variable consumption patterns. These characteristics have implications for supply systems that affect their performance. Consequently, the design must be done correctly to avoid any supply problem.

An example of voltage regulator architecture is shown in the block diagram of figure 3-9. This system consists of a linear or switched converter with fixed current limit and a high-value capacitor.

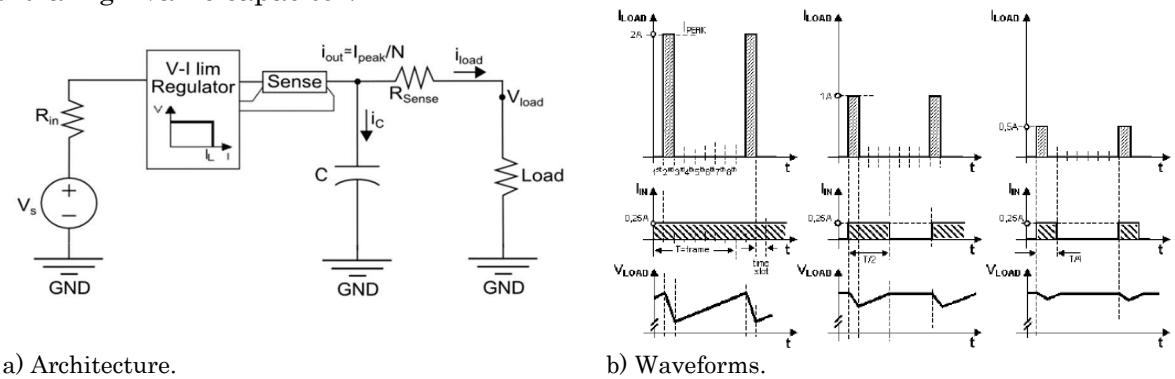

a) Architecture. b) Waveforms.

Figure 3-9: Example of an energy supply and storage system with an intermediate regulator.

Figure 3-9 shows that the voltage regulator limits the input current and, at the same time, produced the desired voltage level. In this example, the current through the input I_{in} would remain near the maximum average consumption value. Consequently, the regulator would be able to provide the system with the maximum power that the charge could consume maintaining the desired voltage level. Resistor, R_{sense}, is used to measure the current charge or the capacitor discharge and to limit the maximum current of the converter. After that, the capacitor function is to store the energy required during the discontinuous charge.

3.3 Examples of low power managers for different energy harvesters

3.3.1 Power management for solar harvesters

The example of a power manager for solar harvester is a modified buck-boost converter circuit with additional isolation and metrology circuitry [158], as shown in figure 3-10.

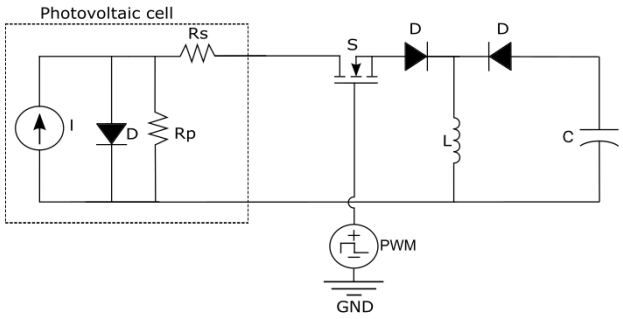

Figure 3-10: Power manager for the photovoltaic harvester.

This circuit acts to maintain a constant voltage across its input terminals to keep the photovoltaic module at a voltage set by the user. The photovoltaic module is maintained at the selected voltage to keep its operation range in indoor MPP voltage. In this case, the converter operation range is set between 100-1000 lux, usual indoor light levels.

3.3.2 Power management for kinetic harvesters

The magnitude of the signal generated by the kinetic harvesters, lead to a non-constant control. Thus, a flexible circuit is necessary to operate when the mechanical excitation changes.

Rectification, filtering, and voltage regulation are the minimum requirements to make the convert the kinetic energy harvester AC signal to a useable one. In addition, to maximize the usable power is required to optimize the management through some additional implementations, such as synchronous rectifiers, switched-mode converters, peak power trackers and tuning techniques.

3.3.2.1 Power management for piezoelectric harvesters

A power manager for piezoelectric harvester is presented in next example [159], which and is composed of diode bridge rectifier and a flyback-type DC-DC converter. Figure 3-11 shows the described architecture.

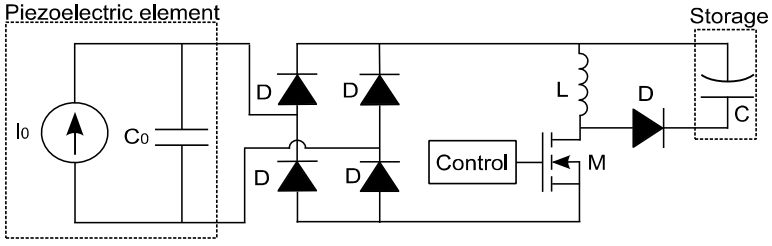

Figure 3-11: SECE device buck-boost architecture for piezoelectric harvester power management.

This circuit uses the Synchronous Electric Charge Extraction (SECE) technique. The voltage is determined by a control circuit that detects maximum and zero levels of

rectified voltage. When the rectified voltage reaches a maximum, MOSFET is put into ON state. Also, piezoelectric harvester energy is transferred to converter inductor. When all the energy has been extracted from the harvester, and zero level voltage is detected at rectifier, the MOSFET is set at off state. This operation is repeated periodically to allow the current flow from harvester to inductor and then from the inductor to the storage capacitor.

Finally, remark that the optimal duty cycle of the converter (to achieve desirable voltage level) depends on the circuit inductance, switching frequency, piezoelectric capacitance and piezoelectric mechanical frequency.

3.3.2.2 Power management for electromagnetic harvesters

The general requirements for interfacing an electromagnetic harvester are the next ones:

- Rectification.
- Voltage step-up capability.
- Emulating a resistive load for the impedance match or impedance control.

Not always controlled converters are needed to manage income signal. Alternatively, Villard and Dickson multiplier can be used to rectify and boost the voltage from the transducer [160]. Figure 3-12 shows multiple stages put into cascade, produces a higher step-up. These techniques do not assure impedance matching.

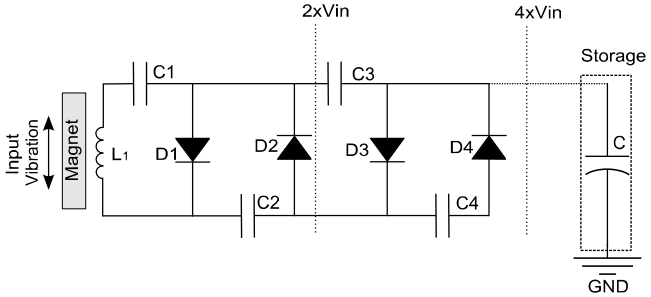

Figure 3-12: Power manager for electromagnetic harvester, using a Villard voltage multiplier for voltage up conversion.

A half cycle is processed by one part of the circuit and the other half cycle by the other part of the circuit. The negative half-signal peak charges C_1 capacitor through the D_1 diode. When the positive half-signal starts the potential storage at C_1 is added and charges C_2 capacitor through the D_2 diode. Consequently, the input voltage level is doubled. If an additional stage of two diodes and two capacitors are added to the circuit, the output voltage will increase by twice the input voltage level.

3.3.2.3 Power management for electrostatic harvesters

The requirements for the interface circuit to operate an electrostatic harvester are:

- Pre-charge the electrodes while they are at their maximum capacitance.
- Keep the electrodes connected to a constant voltage source, or open circuit during electrode separation, depending on the chosen mode of generator operation.

The example of power manager for electrostatic harvester [52] is shown in figure 3-13:

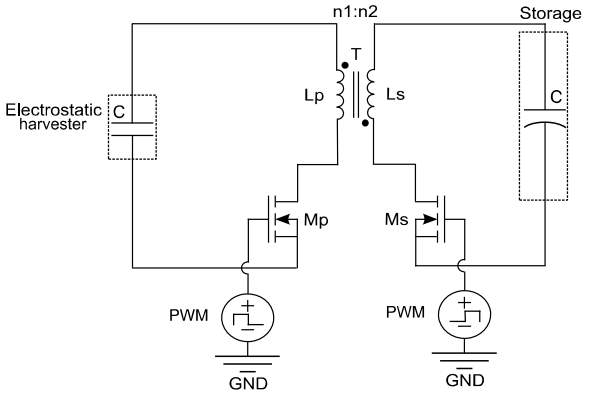

a) Schematic.

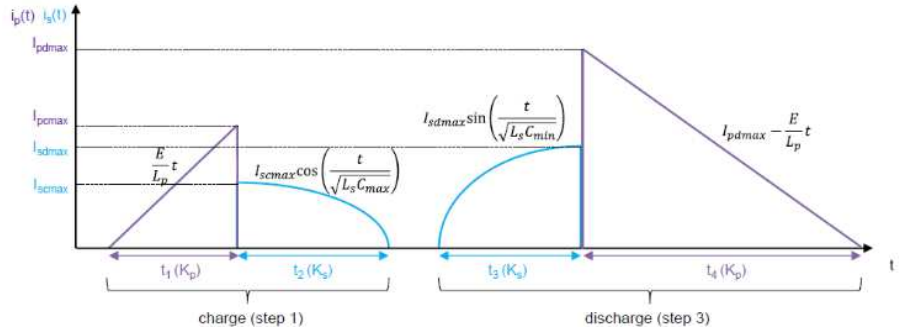

b) Operation mode.

Figure 3-13: Bidirectional flyback converter for power management of electrostatic harvester.

Figure 3-13 bidirectional flyback converter has three operation stages. In the first step, when the capacitor is charging, M_p is closed for a time t_1, because energy has to be sent to the harvester to polarize it, is transferred from the supply source to the inductance L_p that charges the magnetic core T. Then, when M_p is open, and M_s is close until inductor current I_s becomes equal to 0. This operation corresponds to the time needed to transfer the energy stored in the magnetic core T to the capacitor of the energy harvester C. In the second step, is produced the mechanical-to-electrical conversion. This conversion is achieved when M_p and M_s are open and let the energy harvester in open circuit condition, allowing a free varying of the voltage across C. In the third step the capacitor is discharged. M_s is closed for the t_2 time, to transfer the energy stored in the capacitor C to the magnetic core T through L_s. Then, M_s is open, and M_p is closed until inductor current I_p becomes equal to 0, which corresponds with the time where the energy stored in the magnetic core T is transfer to the storage element.

3.3.2.4 Power management for pyroelectric harvesters

A quasi-isothermal cycle, as is explained in section 2.2.4, is very inefficient and produces a low quantity of power. Presented pyroelectric harvester power manager example uses Ericson thermal energy cycle to extract electrical energy from the thermal gradient method, which achieves better efficiencies [161].

The cycle starts with the pyroelectric harvester at low temperature, and the ferroelectric capacitor charged. As the temperature increases constant voltage is applied at the harvester and accumulated charge at harvester capacitor is forced to flow into the converter. The converter is a diode bridge rectifier and stores energy in the capacitor. Then, the applied voltage at the harvester is reduced, and the temperature at the pyroelectric harvester decreases. Consequently, another current flow (with opposite sign) is produced into the external circuit, as shown in figure 3-14:

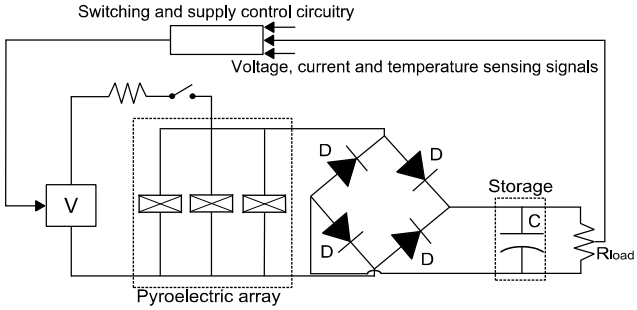

Figure 3-14: The electrical circuit that generates electrical power from an array of pyroelectric capacitors.

Described work cycle allows working in an extended range of temperatures while applying alternating voltages on the harvesters. This operation principle is known as a dynamic control technique.

3.3.3 Power management for thermoelectric harvesters

A power manager for thermoelectric harvester example [162] uses a commercial DC/DC boost converter (LTC3108), see figure 3-15. The power management system includes two super-capacitors: the first (C_1) one is connected to the TEG. This supercapacitor accumulates energy from the TEG and drives the following DC/DC converter. The second one is placed after the DC/DC converter and saves the power from the converter to drive it to the load.

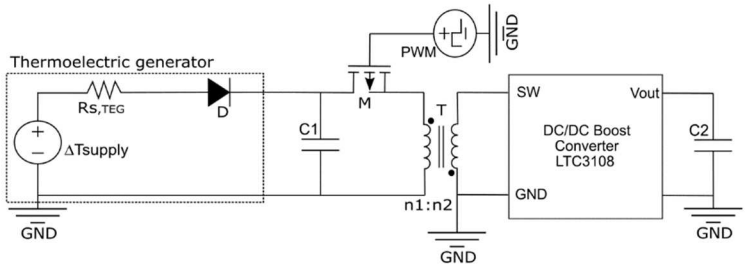

Figure 3-15: Power manager for thermoelectric harvester with two supercapacitors and a commercial DC/DC boost converter.

The control strategy is composed of two charging steps, C_1 charging and C_2 charging. In C_1 charging procedure, the switch S_1 is turned off, where charging time depends on TEGs internal resistance. For C_2 charging procedure, S_1 is turned on to charge C_2 with C_1 charge, where charging time depends on discharge + convert + charge time.

3.3.4 Power management for magnetic harvesters

The power manager for magnetic harvesters' example uses a bi-directional switch connected in a common source configuration [163]. The switches are pulsed together without floating gate circuit because the circuit ground is familiar with the MOSFETs source path. Also, harvester leakage inductance and transformer are used as a transfer element, not requiring an external inductor. This description is represented in figure 3-16 schematic.

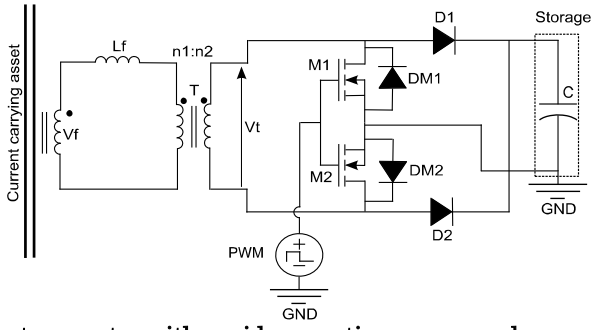

Figure 3-16: AC-DC boost converter with a wide operating range used as power management for the magnetic harvester.

This converter works in boost operation, using the AC input signal as the reference. The complete operating mode is described in table 3-3:

Table 3-3: AC-DC boost converter with an operating mode.

Mode	Switch status	Primary side	Secondary side
Mode 1: $0<\omega t<\pi$	D=1 SW1 and SW2 ON	Current comes out of the dot of the flux concentrator and goes into the dot of the step-up transformer	Current comes out of the dot and flows through SW1 and SW2. Leading to short-circuit of the transformer secondary and hence charging of the transformer leakage inductance.
	D=0 SW1 and SW2 OFF	Same as above	Current comes out of the dot and flows through D1, output load and the body diode of SW2. This leads to transfer of energy stored in the leakage inductance to the load.
Mode 2: $\pi<\omega t<2\pi$	D=1 SW1 and SW2 ON	Current goes into the dot of the flux concentrator and comes out of the dot of the step-up transformer	Current goes into the dot and flows through SW2 and SW1. Leading to short circuit of the transformer secondary and hence charging of the transformer leakage inductance.
	D=0 SW1 and SW2 OFF	Same as above	Current goes into the dot and flows through D2, output load and the body diode of SW1. This leads to transfer of energy stored in the leakage inductance to the load.

3.3.5 Power management for RF harvesters

RF harvester power manager example is based on impedance matching methodology to transfer the energy from the harvester to the load [164]. Furthermore, DCM mode is used because allows a static impedance matching by separating the input from the output.

Figure 3-17 shows the flyback topology used as converter architecture, which should match the antenna's input impedance to maximize the power transfer.

Furthermore, when the converter works in DCM condition, the input impedance control can regard the output load conditions independently. Moreover, since the antenna impedance is constant over a wide range of input power, open loop control is possible. In addition, the converter output voltage level depends only on the output load.

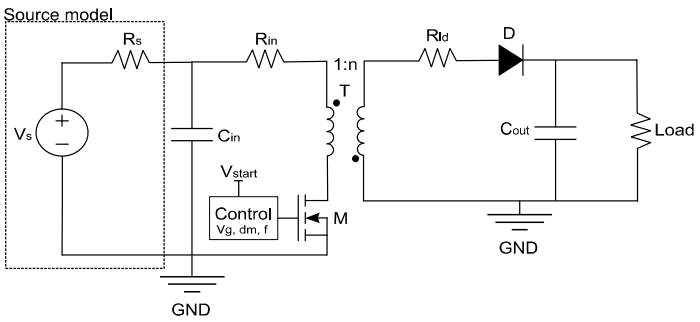

Figure 3-17: RF harvester power manager with flyback converter topology.

Also, described impedance matching technique does not need a "sophisticated" control circuit. Open-Loop control is applied using an oscillator circuit which sets the optimal frequency and the duty-cycle values.

3.3.6 Power management for wind and water harvesters

The example of a power manager for wind and water harvesters is a diode bridge as a rectifier and buck-boost DC-DC converter [165], as shown in figure 3-18. Is going to be explained further in chapter IV-9.

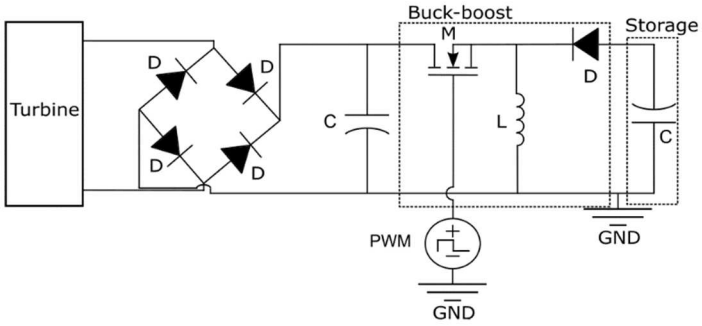

Figure 3-18: Power manager for wind and water harvester with rectifier and buck-boost converter topology.

The produced signal is rectified and stepped up or down depending on the rectified voltage level. When input level signal is higher than the minimum level defined, the buck-boost converter is turned on, and the supercapacitor is charged. The converter switch is with a PWM signal, and the circuit operates in DCM mode. Besides, the control runs under a MPTT algorithm.

3.3.7 Power management for acoustic harvesters

The example of a power manager for acoustic harvesters is a diode bridge as rectifier and flyback converter [166], see figure 3-19.

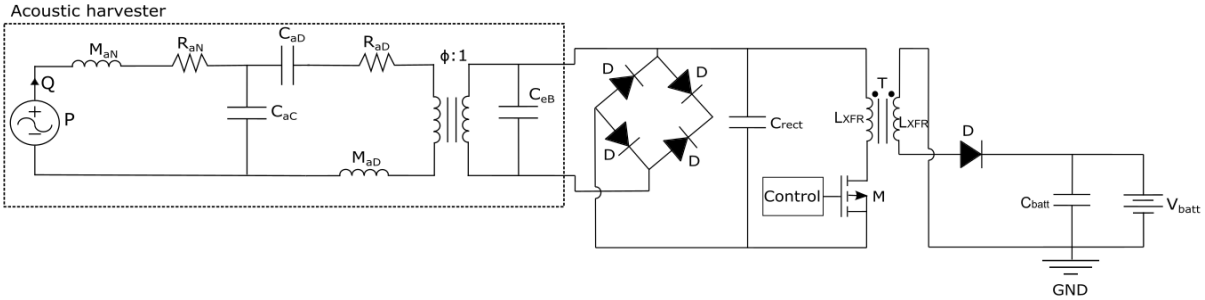

Figure 3-19: Acoustic harvester power management with diode bridge rectifier and flyback converter.

The flyback converter achieves the optimal loading condition for the rectifier. With optimal loading condition, maximum power is transferred to the load. Thus, the converter is placed between the harvester and load to decouple and provide the optimal resistance.

This converter works in DCM mode, where the transformer works as the inductance of the flyback transformer. Maximum output power is achieved by varying the duty-cycle.

3.3.8 Hybrid power source devices

The example of a hybrid power manager circuit is composed of two different harvesters (solar and thermoelectric) and a single power manager [167]. Figure 3-20 shows the two harvesters connected to the boost converter and finally to the storage element.

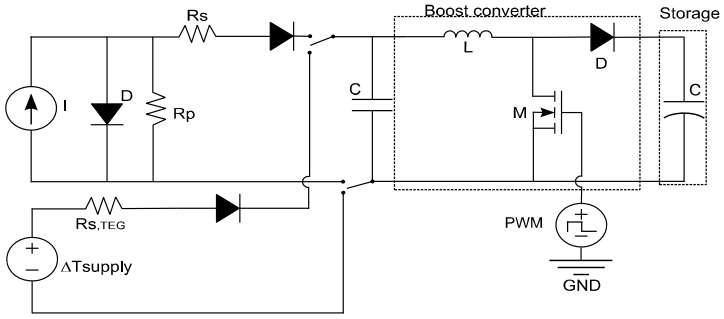

Figure 3-20: Solar and/or thermoelectric harvesters power management with a boost converter.

The operation of the boost converter is based on the fixed voltage reference approach. The MPPT voltage reference signal is compared with the feedback voltage signal, from the output of the energy harvester, which is also the input of the boost converter with voltage reference MPPT control. The resultant voltage error signal is fed into a proportional-integral controller to generate a low-frequency PWM signal and control the boost converter correctly.

3.3.9 Present commercial digital power management

Nowadays, different companies have developed digital devices to make able the low power management. Ultra-low power microcontrollers and digital power-battery management devices are an example.

On the one hand, low power µCs are typically used in WSN to process the digital data and to obtain the measured quantity from a digital code. In addition, microcontroller units enable measurement of DC voltages, frequency or period, control of converters and regulators, including functionalities of battery protection.

These devices have several power modes:

- Sleep. All the modules are disabled except for a low-power timer to wake up the µC and save energy.
- Stand-by. Some of the modules are measuring a parameter and waiting for the signal to change the system state to active.
- Active. The system is working under the defined requirements (always under low power condition).

Table 3-3 shows some parameters of the present commercial µCs [168]-[170]:

Table 3-4: Technical specifications of three low power commercial µcontroller units.

Model	Vin (V)	$I_{\mu C, sleep}$ (µA/MHz)	$I_{\mu C,active}$ (µA/MHz)	Wake up time from sleep (µs)	Wake up time from reset (µs)
msp430fr5969	1.8 to 3.6	65	100	6 µs	250 µs
EFM32GG990	1.98 to 3.8	80	219	-	-
STM32L051x6	1.65 to 3.6	37	139	5 µs	50 µs

On the other hand, there are digital low power management solutions, which fulfil the digital control for low power applications. These devices are specifically designed to acquire and manage power generated from different harvesters, from µW to mW. The have an integrated MPPT control, DC converters (boost, buck-boost, …) and storage elements such as rechargeable Li-Ion batteries, thin film batteries, and supercapacitors. Table 3-4 shows some present commercial MCUs [171][172]:

Table 3-5: Technical specifications of two low power commercial managements units.

Model	$V_{in\text{-}start\ up}$	MPPT	P_{in_cold}	I_{in_peak}	I_{bat_leak}
bq25504 EVM	330 mV	78 %	10 µW	200 mA	1 nA
ADP5090	380 mV	80 %	16 µW	100 mA	15 nA

4. Low energy storage devices

Energy harvesting systems do not power directly IIoT devices. Energy harvesting storage devices work under demand, using harvested power during periods of lower demand.

Selecting the right energy storage for a specific IIoT application depends on a variety of factors, such as peak power requirement, the cycle-life, storage capacity, size, and cost. Nowadays, two main technologies are used for low energy storage: supercapacitors [173] and rechargeable batteries [174].

These two technologies are based on electrochemistry, which involves electric charges moving between the electrodes and the electrolyte. Thus, an electrochemical cell (the storage device based on electrochemistry) is a device which generates energy from a chemical reaction or allows chemical reactions when electrical energy is introduced. Figure 4-1 shows the different families of electrochemical cells.

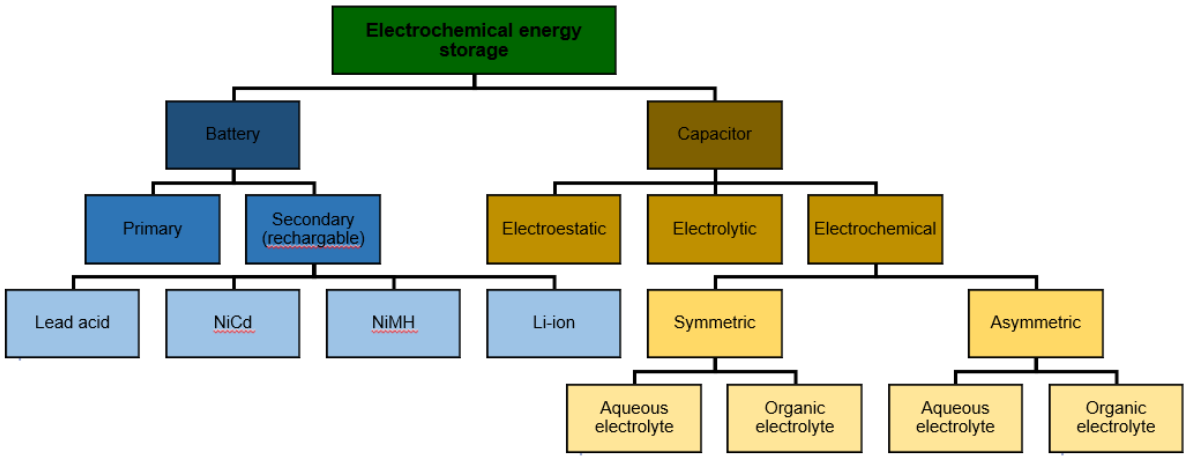

Figure 4-1: Electrochemical energy storage devices.

Energy and power densities are main parameters in the selection of a storage type device. On the one hand, the energy density is the energy that can be extracted from a storage cell per unit volume (Wh/l). It depends on the amount of active material inside the cell. On the other hand, power density is the power that can be extracted from a storage cell per unit volume (Wh/l). In this case, it depends on the internal impedance (current collector area and electrolyte conductivity).

So, based on their physical/chemical properties supercapacitors have higher power density than batteries. However, energy density has the opposite behaviour in these two elements, as figure 4-2 shows [175]. Consequently, batteries are better for long period of "constant" input of power and supercapacitor for peaks of power.

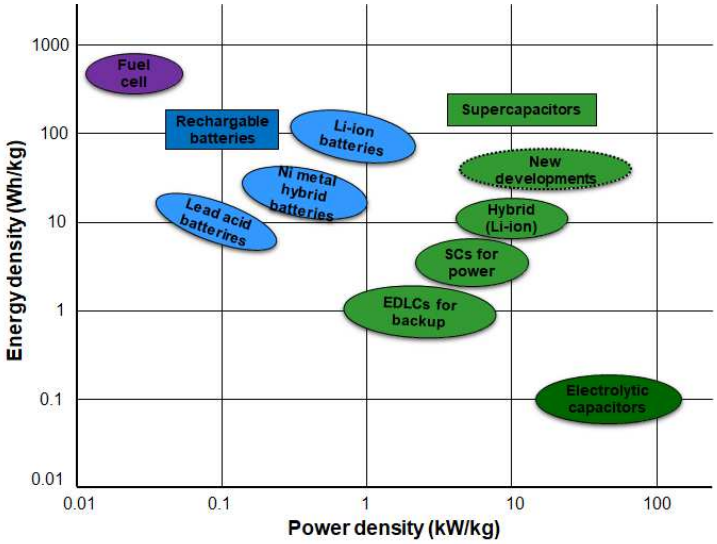

Figure 4-2: Energy density vs. power density for energy storage devices.

Energy storage devices [176] operation mode is complex, and several parameters must be considered, such as, high charge/discharge efficiency, good acceptance of different level of currents, small size and weight, peak power requirement, extended operation of lifetime, low leakage and low self-discharge levels, variable with temperature, humidity, life-cycles, charge power and capacity.

Energy storage devices essential parameters:

- Capacity (C): is the total electrical charge that can be accepted by the device at fully charged state under specific discharge conditions (discharge rate, end voltage, and temperature).
- Voltage level (V): Is the parameter that identifies the charge level of the device or depending on the situation the discharge level of the device. The voltage level depends on the internal impedance and temperature.
- Self-discharge: Self-discharge or leakage current are the loses produced (due to the chemical reactions) at the device in steady state. Leakage current is higher when the temperature increases.
- Temperature Effects: The rate of chemical reactions increases with increasing temperature, under Arrhenius rule, double rate every 10 °C. This behaviour produces the lifetime reduction and higher leakage.
- Depth of Discharge and State of Charge (only batteries): Depth of discharge (DOD) indicates how much charge has been extracted or state of charge (SOC) how much charge remains.

In table 4-1 listed parameters for supercapacitors and Li-ion batteries are shown:

Table 4-1: Characteristics of low energy storage supercapacitor and Li-ion battery.

Type	Supercapacitor	Li-ion battery
Physical/Chemical operation mode	Electrostatic charges on opposite surfaces. Electrode-Electrolyte ions	A reversible insertion/ extraction of lithium ions into/from a host matrix
Capacity	Units of μAh-hundreds of mAh (unit of mF-hundreds of F)	Units of mAh-miles of Ah
Energy density (mWh/cm3)	1-10	150-400 (depending on material)
Series resistance	Units of mΩ to tens of Ω	75-500 mΩ
Leakage	Units of tens of μA	1-5 per month
Maximum voltage (V/cell)	5.4	2.4-4.2 (depending on material)
Temperature range (°C)	-20 to 70	-20 to 60
Number of cycles	1.000.000	100.000
Ageing (10 years at RT and nominal voltage)	15% to 30% C loss, 40% ESR increase	40 % worse operation after 10.000 cycles

Finally, table 4-2 shows existing energy harvesting storage devices advantages and disadvantages:

Table 4-2: Energy storage devices advantages and disadvantages.

Energy storage comparisons		
Conventional batteries	Supercapacitors	Thin film batteries
+High discharge current	+Peak power delivery	+High discharge current
+High energy density	+Long life	+High energy density
+Inexpensive	+Inexpensive	+Near zero leakage
-Limited life	+Form factor	+Long life / Permanent
-Replacement labour cost	-High leakage	+Form factor
-Unsafe, polluting	-Low energy density	+ Safe / Eco-friendly
-Form factor	-High temp degradation	+Broader temp range

4.1 Supercapacitors

Supercapacitors are commonly used in EHWSN to store harvested energy. They are attractive because they have higher power density than batteries, do not require special charging circuitry, and have a long operational lifetime. To minimize or optimize the power consumption, supercapacitors on energy harvesting systems must act as a primary storage device with a battery backup whenever it is necessary [177]. The benefits of using supercapacitors are many, like extended battery life, less electromagnetic interferences and better operation of analogic electronics. They are explained at length in the literature [178][179].

There are two types of supercapacitors depending on the storage mechanism, Electrochemical Double Layer Capacitors (EDLCs) and pseudo-capacitors. The first type, EDLCs the ions are accumulated at the electrode/electrolyte interface with a pure electrostatic attraction. The electrodes are usually made of activated carbon. The second type, pseudo-capacitors, electrons under Faradic reactions are transferred to or from the valence bands of the redox cathode or anode reagent using conducting polymers or metal oxides. Figure 4-3 shows the different families of supercapacitors [180].

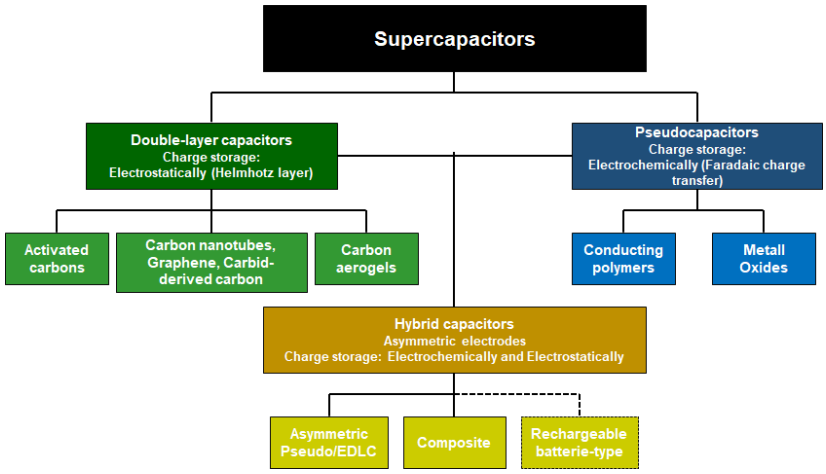

Figure 4-3: Hierarchical classification of supercapacitor types.

4.1.1 Electric double-layer capacitor

Electric double-layer capacitors (EDLCs) or supercapacitors are electrochemical capacitors that have high energy density and capacitance in comparison with another type of capacitors. Furthermore, conventional EDLCs are essentially DC devices.

Supercapacitors store energy on opposite surfaces of the double layer in the form of electrostatic charges, which is formed between of the electrodes and the electrolyte ions. Supercapacitors have tens of thousands of cycle-life, are not affected by deep discharges and are fasters than batteries due to electric charges move between solid-state materials and no through chemical reactions.

The capacitance value is proportional to the surface of plates and dielectric constant of the substance, and inversely proportional to the plate separation. Furthermore, the capacitance of an EDLC is also dependent on the characteristics of the electrode material, which is usually nanoporous. Nowadays, electric double-layer capacitors storage density is trying to be improved using different nanoporous materials as [181]-[184]:

- Activated charcoal
- Carbon nanotubes
- Carbon aerogel
- Graphene

When supercapacitors are full of charge, they stop accepting the charge. However, the recombination effect starts inside the device [185]. However, there is no danger of overcharge or 'memory effect' as in batteries and does not require a full-charge detection circuit.

Thus, the parameters which affect supercapacitor behaviour under operation and the initial capacitance are life cycle, voltage, time, temperature, moisture, Equivalent Series Resistance (ESR) and leakage resistance.

Analysing supercapacitors work principles, the solvated ions in the electrolyte are attracted to the electrode surface by an equal opposite charge in the nanoporous electrode. In addition, the two layers are conductive in isolation condition. However, the physics at the interface in contact do not allow significant current flow between the layers. These two-layer or parallel regions of charge give the name of double layer to this technology devices. Figure 4-4 shows EDLC physical composition.

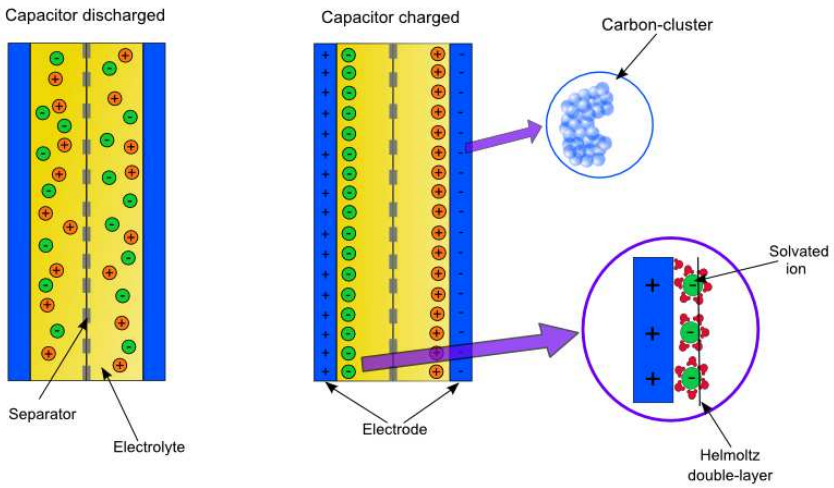

Figure 4-4: EDLC physical composition and internal work mode.

The arrangement of ions and solvent on the electrolyte side of the double layer can be assigned to three layers.

1. The first layer consists of solvent molecules as well as specifically adsorbed species (ions or molecules) and the plane formed by the loci of the charge centers of the specifically adsorbed ions is referred to as inner Helmholtz plane (IHP).
2. The second layer is based on the arrangement of fully solvated ions attracted to the electrode surface. Due to the solvation shell, the charge center loci of these ions have a more considerable distance to the surface then the IHP, and thus, it is called the outer Helmholtz plane (OHP).
3. The third layer is based on a region connecting the OHP with the bulk electrolyte. In this region, there is still a high concentration of ions attracted to the electrode surface leading to an imbalance in charge. In case of low electrolyte concentrations, this third region is still contributing to the charge of the double layer and thus, is defined as the diffuse layer.

The capacitors charge state equation is directly proportional to potential, equation 4-1 gives capacitor geometry and used materials:

$$Q = \rho_s A = DA = \frac{\varepsilon UA}{d}; \overset{\Delta}{\rightarrow} C = \frac{Q}{U} = \frac{\varepsilon A}{d} = \frac{(\varepsilon_0 + \varepsilon_0 \chi)A}{d} = \frac{\varepsilon_0 \varepsilon_r A}{d} \qquad (4\text{-}1)$$

, where capacitance (F/V) is obtained with the surface current density at the conducting plate area (C/m^2). Then, from electromagnetic laws of Maxwell's, the divergence of electric flux, D, is the source of the electric field. Moreover, for any dielectric medium, the constitutive relation plus dielectric polarization define the total electric flux. Where dielectric material susceptibility, χ, is a measure of the material contribution to total permittivity, ε, and ε_0 is the permittivity of free space. What this means is that for a given potential, U, across the parallel plate capacitor having charge separation distance, d, an electric field, will be set up that in turn elicits a total electric flux, D.

As with harvesters or other storage devices, supercapacitors could be represented by an equivalent electric circuit. From state of the art, several examples have been provided. For example ideal capacitor and simplified models of Figure 2a,b do not suffice for supercapacitor characterization [186]. Thus, as with standard capacitors like tantalum or electrolytic [187], it could use an equivalent electrical model of distributed components, Figure 2c, based on the physic morphology of the supercapacitor [188][189].

The electrical model represented in Figure 2c uses a distributed capacitance architecture in which each capacitance branch has a capacitance equation that emulates a particular physical behaviour. The coefficients of these equations are obtained empirically. The dynamic characteristic of supercapacitor and its nonlinear leakage current behaviour limit the advantages of this model. Some studies have tried to improve this model with more complex and elaborate RC nets [190].

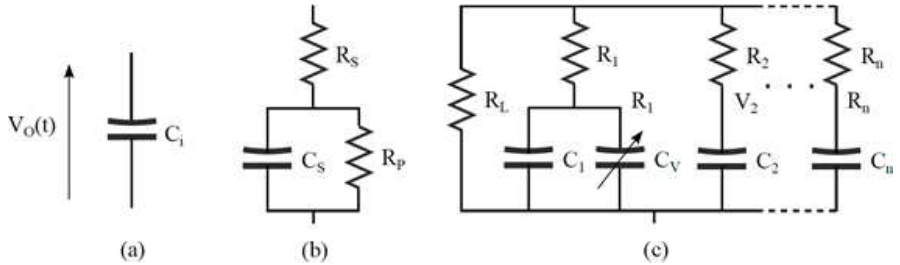

Figure 4-5: Circuit-based supercapacitor models: (a) an ideal capacitor. (b) A simplified model including a series and parallel resistance. (c) RC ladder circuit with a voltage-dependent capacitance in its first branch, which may be extended to n branches.

The process to fabricate a cylindrical supercapacitor is based on following steps.

1. The collectors (blue layer at figure 4-6a) which would act as a bridge between the electrode material and the external terminals are coated with an electrode material.
2. The electrodes are kept apart by an ion-permeable membrane, known as the separator (green layer at figure 4-6a). This construction is rolled into a cylindrical shape and inserted in an aluminium can.
3. The cell is impregnated with an ionic conductor, i.e., liquid electrolyte. This ionic conductor enters through the carbon electrodes (grey layer at figure 4-6a) pores and makes (across the separator) the connection between the electrodes.
4. The housing is hermetically sealed to avoid leaks and maintain a correct operation during the life-cycle.

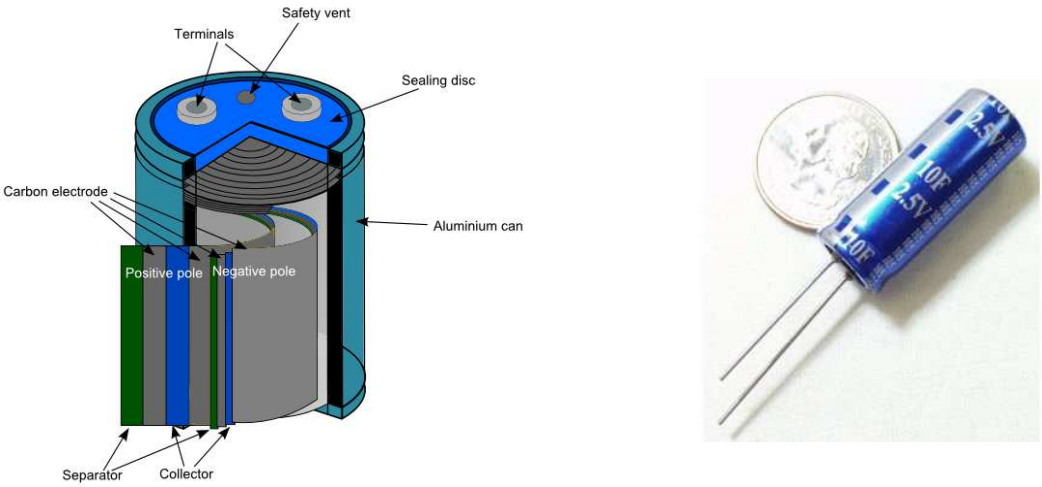

a) Description view. b) Real view.

Figure 4-6: EDLC cylindrical commercial example.

4.2 Rechargeable batteries

The main difference between primary batteries and secondary batteries (rechargeable) is that second one can be electrically recharged. Thus, it could be used in energy harvesting applications.

Rechargeable batteries have lower energy density than primary batteries because require designs to facilitate the recharge process and maximize their life-cycle [191]. Nevertheless, rechargeable batteries have higher energy density than supercapacitors. Rechargeable batteries have low leakage currents, avoiding a self-discharge state (no totally but yes for long periods of time). Besides, the lifetime of rechargeable batteries is given by the amount of charge-discharge cycles under a correct performance. The end-of-life criteria is defined by the time required for the battery to reach 80% of its original capacity.

As in supercapacitors, operation basics and life-cycle are affected by several conditions, such as operation temperature, DOD, charge and discharge current peaks, the used charge control method and exposition to overcharge and over-discharge [192].

4.2.1 Lithium-ion batteries

Lithium-ion batteries involve a reversible insertion/extraction of lithium ions into/ from a host matrix during the discharge/charge process [193] as shown in figure 4-7.

The lithium-ion battery is composed of a negative electrode (anode) and a positive electrode (cathode) which act as a host for the lithium ions (Li^+). Lithium ions move from the anode to the cathode during discharge and are inserted in the crystallographic structure of the cathode, in this situation electric current is produced. The ions reverse direction during charging, due to the electric current inserted in the battery. Figure 4-7 shows this operation mode.

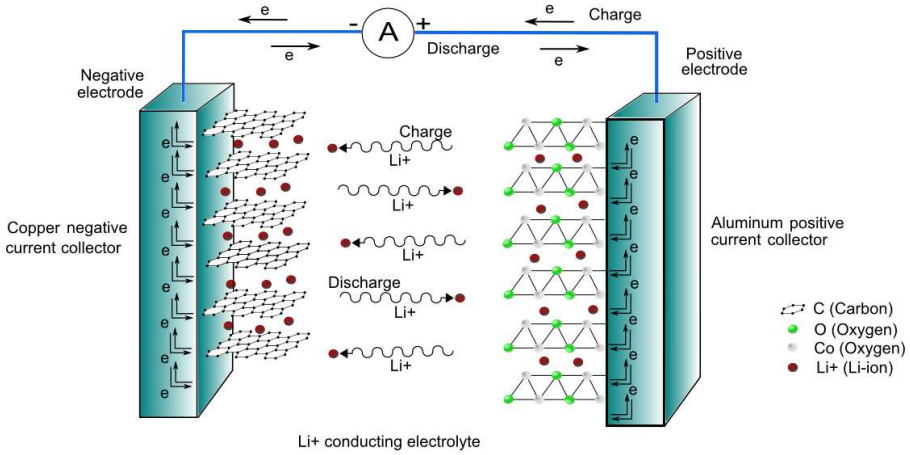

Figure 4-7: Li-ion battery physical composition and internal work mode.

There is a separator between anode and cathode has the function of preventing direct contact between both layers and stop charge or discharge processes impeding the transport of ions. The separator is composed of pores, which allow the transfer of lithium ions by diffusion during charge and discharge. Separator thickness, porosity, permeability, toughness, and resistance to penetration vary considerably depending on desired cell properties. Polyethylene, polypropylene, or composite polyethylene/ polypropylene porous films are examples of elements used as separators. These films are in the range of 10 and 40 µm.

Figure 4-8 [194] shows how the voltage changes in a low current charge and discharge process when different materials are used in same technology batteries.

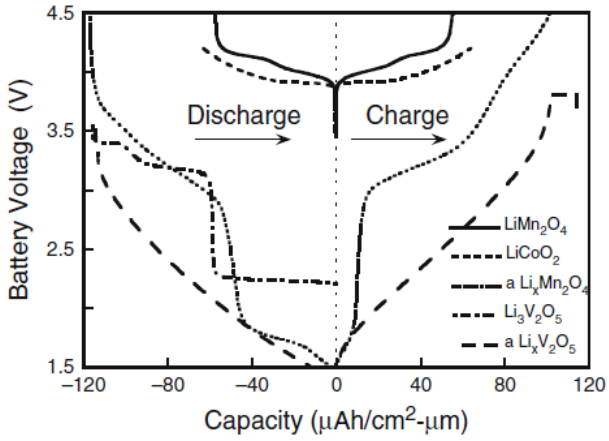

Figure 4-8: Battery voltage for a low-current discharge and charge cycle with five different batteries.

Taking as an example the lithium-ion cells which use graphite and layered $LiCoO_2$ as the lithium anode and cathode materials, the reaction process of a rechargeable battery is described. First step is to make electrolyte, taking a lithium-containing salt (for example, $LiPF_6$) and dissolving in a mixture of aprotic solvents like ethylene carbonate (EC) and diethyl carbonate (DEC). Then, during the charging process, the lithium ions are extracted from the layered $LiCoO_2$ cathode, flow through the electrolyte, and get inserted into the layers of the graphite anode, while the electrons flow through the external circuit from the $LiCoO_2$ cathode to the graphite anode to maintain charge balance. During the charging process, an oxidation reaction occurs (Co^{3+} to Co^{4+}) at the cathode and a reduction reaction at the anode. At discharge process, the reverse reactions occur at the anode and cathode with the flow of lithium ions in the opposite direction. The chemical reaction which occurs during the described process are shown in next lines.

The positive electrode half-reaction is given by:

$$LiCoO_2 \leftrightarrows Li_{1-x}CoO_2 + xLi^+ + xe^- \tag{4-2}$$

, and the negative electrode half-reaction is given by:

$$Li^+ + xe^- + xC_6 \leftrightarrows xLiC_6 \tag{4-3}$$

At initial charging (which takes place during battery manufacturing) lithium ions move from the lithium compound of the cathode to the carbon material of the anode, as in equation 4-4:

$$LiCoO_2 + C_6 \rightarrow Li_{1-x}CoO_2 + Li_xC_6 \tag{4-4}$$

Equation 4-5 represents the charge/discharge reactions (lithium ions go from the anode to the cathode or vice versa).

$$Li_{1-x}CoO_2 + Li_xC \leftrightarrows Li_{1-x+dx}CoO_2 + Li_{x-dx}C_6 \tag{4-5}$$

, where the arrow which marks left/right direction, is the charge/discharge process reaction. Finally, the reaction has a limit, battery cycle-life. Over-discharge supersaturates lithium cobalt oxide, producing lithium oxide and consequently an irreversible reaction, which is given by equation 4-6:

$$Li^+ + e^- + LiCoO_2 \rightarrow LiO_2 + CoO \tag{4-6}$$

Finally, the open circuit voltage V_{oc} of the Li-ion cell is given by the equation 4-7:

$$V_{oc} = \frac{\mu_{Li(c)} - \mu_{Li(a)}}{F} \quad (4\text{-}7)$$

, where F is the Faraday constant. The cathode should have a low-lithium chemical potential ($\mu Li_{(c)}$), and the anode should have a high-lithium chemical potential ($\mu Li_{(a)}$) to maximize the cell voltage (V). Implying the transition metal ion in the lithium insertion compound should have a high oxidation state to serve as a cathode and a low oxidation state to serve as an anode.

Li-ion rechargeable batteries work in a voltage range, which is specified by cell chemistry. For example, if the full discharge of SOC is 3.0 V and full charge of SOC is 4.2 V, then, the nominal voltage can be 3.6 V. The battery will always work in that ranges, and discharge below 3 V can cause degradation of the electrode and, if the situation is repeated, a cell failure.

Self-discharge effect is increased at batteries with temperature and DOC. The battery is faster fully-charged at higher ambient temperature, but the capacity is decreased. In addition, batteries need a control step for the fully-charged state. If this situation is not under control, the lithium-ion rechargeable battery could lose until 10% of its capacity in three months, due to the exothermic degradation of the electrodes.

Thus, a cylindrical cell is built by stacking alternating layers of electrodes following the next steps:

1. Batteries must be manufactured in a rigorously controlled environment.
2. The separator separates alternating layers of anode and cathode, i.e., the porous film.
3. Then, an organic solvent electrolyte allows the lithium ion transport.
4. Electrode stacks or rolls can be inserted into hard cases that are sealed with gaskets, laser-welded hard cases, or enclosed in foil pouches with heat-sealed seams. The cases are made of aluminium or steel.
5. Another process in construction is the elimination of all water in the device. Then, the assembly must be done in dry and low humidity conditions.
6. The last step is the process of the initial charging and verifies the correct operation of the device.

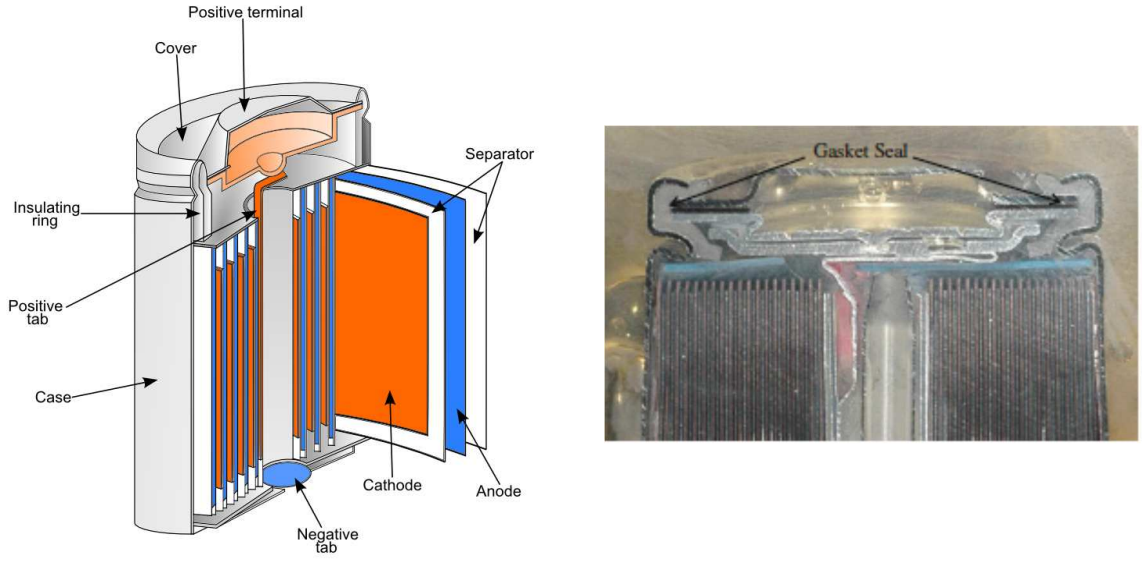

a) Battery architecture. b) Real battery profile.

Figure 4-9: Lithium-ion battery commercial example.

Lithium-ion batteries require a high level of safety. Due to the ionic state inside the battery at over normal operating ranges. Maybe producing in the worst case, a flaming situation.

5. Machine learning and data mining techniques for energy harvesting systems

5.1 Data science principles

Data science is an interdisciplinary field of data processing scientific methods. Data science encompass data mining, machine learning, artificial intelligence, and statistic. Thus, it represents the concept to unify data techniques under a single science. The main techniques are introduced in next lines.

Data Mining is the science which acquires and makes smart managing of application data (usually from different information sources) and finally search patterns and trends [195]. The main objective is to give useful information from income data. To complete the objective, consistent patterns and relationships between variables techniques are applied [196]. Data mining application range goes from data analysis to system behaviour optimization. Figure 5-1 shows the relationship between different techniques of data mining worlds.

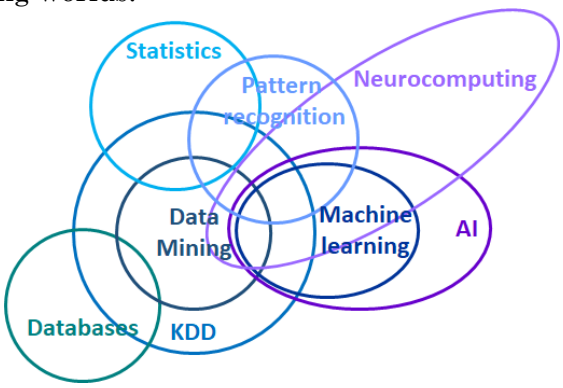

Figure 5-1: Data mining Veen diagram.

Machine learning as defined in [197] is a subfield of artificial intelligence closely related to data mining. It aims to develop algorithms that allow the machines to learn from data, i.e., to create programs able to induce models that improve their performance with the incoming data flow over time. It mixes mathematical elements with statistics and computational sciences such as classification trees, induction rules, neural networks, Bayesian networks, regression algorithms, supported vector machines or clustering [198]. Figure 5-2 shows the process to apply machine learning modelling.

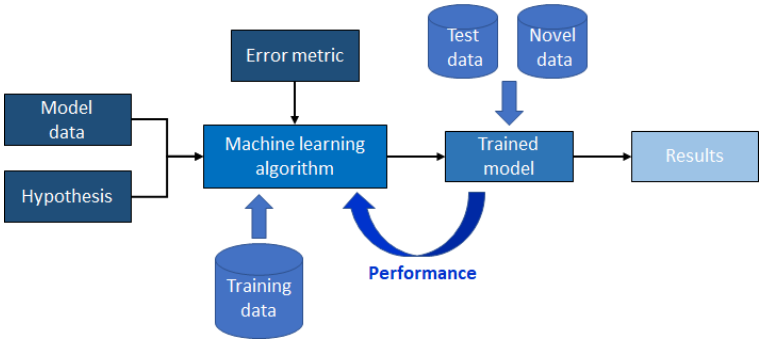

Figure 5-2: Machine learning modelling process block diagram.

Artificial Neural Network (ANN) is a mathematical, computational model, which processes the information like biological neural systems such as the brain [199]. It consists of a group of interconnected artificial neurons, which solves problems working in unison and processing information employing a connectionist approach to computation. An ANN is an adaptive system that changes its structure based on information that flows through the neural network over the learning or training phase. The aforementioned phase involves adjusting the existing synaptic connections between neurons, thus, updating the network architecture and the connection weights. ANN is one of the most widespread learning algorithms used within machine learning to model complex nonlinear relationships between inputs and outputs and find patterns in data. Its increasing popularity is due to its seemingly low dependence on any domain-specific knowledge and the availability of efficient learning algorithms, computational power, ability to model any given function, convergence speed and statistics. For this reason, ANN has been successfully applied to a broad spectrum of data-intensive applications.

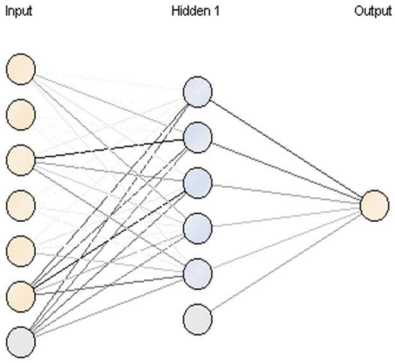

Figure 5-3: Example of a neural net architecture.

Predictive modelling has the objective to build a model which predicts future values of the desired system or use case [200], as shown in figure 5-4. This process needs data acquisition in real time and past situations, data analysis application and training process must give a prediction algorithm or model as results. The model representation consists of a set of attributes, operators, and constants in a structured way. Another goal of predictive modelling is to minimize the difference between the predicted and real values. Predictive modelling must minimize the difference or error between real and predicted values. Predictive analytics encompasses statistical techniques, such as predictive modelling, machine learning, and data mining, help to analyse.

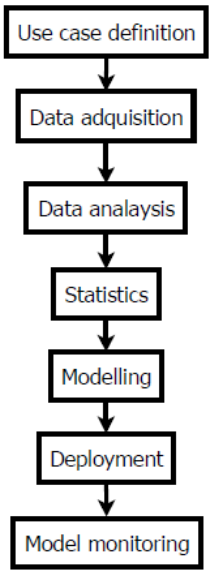

Figure 5-4: Flux diagram of predictive analytics process.

These techniques have been applied in the development of this work, specifically in chapter V.

5.2 Data science state of art for energy harvesting systems

5.2.1 Data Mining examples

Nowadays, there is not too much work developed using data mining techniques for energy harvesting. However, the use of these techniques to save power at WSN devices or in their communications is more usual.

Following this line of research, at [201] a data mining technique for sensor collaboration and energy consumption reduction work is presented. This paper describes a data mining approach to situation-aware sensor actuation in WSN. To validate their work, three approaches were made with WSN:

1. Sensor collaboration with pre-set parameters.
2. Sensor collaboration using data mining technologies.
3. Without sensor collaboration.
4. It is demonstrated that the environment-aware collaboration reduces the data transmission rate over the networks between other net sensors and the central node.

In a second work [202], efficient management of available energy is proposed. To complete this task, the authors analyse the modulation type and the energy model of the net. With the final porpoise of finding the best energy efficiency and maintain the best Quality of Service (QoS). The metrics used under data mining techniques in performance evaluation are energy consumption, throughput, average jitter, end to end delay and signal received. Finally, after process the data, achieved results give that each modulation is better than other depending the parameter analysed.

Table 5-1 [203] shows the state of art other works which use data mining techniques for WSNs, along with the applied techniques and obtained benefits.

Table 5-1: Data mining techniques for WSNs state of art.

Paper number	Techniques	Benefits in WSNs
1	Distributed algorithm	Energy conservation
2	Spectral Classification	Energy save and increase the lifetime
3	Data Relay clustering Algorithm	Network performance with minimum energy consumption
4	Co-locating services	Communication energy cost is reduced
5	Means clustering algorithm	Power consumption is reduced

5.2.2 Machine Learning examples

In literature, some examples use machine learning models to characterize some parameters of capacitor and energy storage devices. Work in [204] develops an algorithm for automotive applications that has one-layer feed-forward ANN. This ANN is trained using a back-propagation algorithm that takes into account temperature, chemistry, and life cycle. The work presented in [205] implements a current impedance test using machine learning. This test set-up presents an equivalent circuit base on the theory of

electrochemical impedance spectroscopy that defines a first-phase linear model. In a second step, a multi-layer of Artificial Neuronal Network (ANN) establishes relationships among non-linear parameters of the capacitances and resistances. The aforementioned ANN is trained with experimental data banks using a back-propagation algorithm. Combining ANN and the equivalent circuit, the author, can create an online nonlinear dynamic model. The research of [206] models a hybrid energy storage system for a Toyota Rav4EV with a stochastic nonlinear predictive control. Power demand is modelled as a Markov chain that had been trained with real-world driving cycles and simulation results given with a model in the loop.

In the research work of this thesis supercapacitor modelling with machine learning techniques is going to be developed. Table 5-2 provides the state of art supercapacitor models using machine learning techniques. The error figures of table 5-1 must be used with care because the reference models have specific target applications and operating conditions, and the research models are devoted for low power electronic systems and generic conditions of temperature, humidity, capacitance, load and charge and discharge time. Thus, some deviations are expected.

Table 5-2: Comparison between supercapacitor modelling with ML techniques.

Model Type	Ref. Numb.	Statistical Error	Ref. Result
M.L. → ANN	[206]	MSE	0.089
M.L. → Kalman Filtering	[207]	MAE	0.50
		RMSE	0.63

5.2.3 Predictive Modelling examples

Energy availability is the key parameter in the research of energy harvesting technology. Practical use of energy harvesting technologies needs to deal with the variability of the energy sources, which change the amount and the period of the harvested energy. In case of predictable, non-controllable power sources, energy prediction methods can be used to forecast the source availability and estimate the expected income energy. This prediction tasks may help to make a decision and allowing the system to make critical decisions about the utilization of the stored energy.

For example, prediction techniques are used in the field of energy management by energetic companies. If prediction techniques are used, energy storage and distribution losses are decreased, consequently increasing system efficiency [208]. In referenced work, analyse wind energy and weather data. Then, applying statistical regression technique obtain a model which gives. As a result of the correlation between wind energy and wind direction on different dates. Thus, after they know that east and west sides of the harvesters have higher intensities of wind and maximum available energy is produced during December and January. Therefore, knowing this kind of works, several works have changed the point of view of technology transferring macro systems solutions to microsystems.

As has been remarked, energy harvesting wireless sensors will have better efficiency if income energy information is predicted. Moreover, giving to the power manager the amount of energy that can be harvested in the future. However, this prediction suffers errors, which cause a degrade in the prediction model performance and consequently in the system. To solve this problem in [209] have developed a fundamental framework to manage the predicted energy efficiently. They derive theoretically a set of Budget Assigning Principles (BAPs) to maximize the amount of harvested energy, which

can be utilized by a sensor when a non-correct operation happens in an energy storage device. The performance of this work is verified via theoretical analysis and computer simulations using real data from an energy harvesting system.

In another study [210], a reinforcement learning-based throughput on demand (ToD) for dynamic power management is proposed. The idea is to give a perpetual operation and satisfying the ToD requirements to an actual energy harvesting wireless sensor node. With the objective to achieve the demanded throughput, the system monitories environmental conditions and adjusts power manager operational duty cycle under criteria of energy neutrality. Then observation-adjustment interactions are evaluated, and reinforcement learning process is completed. After some interaction, the system can be adjusted autonomously. The results give an improvement of 10.7 % for the most stringent ToD requirement. However, the prediction algorithm is implemented in an output computer and no inside an integrated power manager. Nevertheless, is a first step in the development of prediction algorithms for energy harvesting systems.

6. WSN systems

6.1 WSN theoretical principles

A Wireless Sensor Network (WSN) consists of spatially distributed autonomous sensors with the objective of monitoring physical or environmental conditions, such as temperature, sound, vibration, pressure, motion or pollutants and to cooperatively pass their data through the network to the main destination [211]. This destination, called Base Station, works as a Gateway between the sensors and the end user and it can be accessed locally or remotely.

Wireless Sensor Networks are formed by nodes, whose density can range from few to several hundred or even thousand, where each node is connected to another or several ones. Each such sensor network node has the following parts: a microcontroller, a radio transceiver with an internal antenna or connection to an external antenna, an electronic circuit for interfacing with the sensors and an energy source, usually a battery and/or an embedded form of energy harvesting. Size and cost constraints on sensor nodes result in corresponding constraints on resources such as energy, memory, computational speed and communications bandwidth.

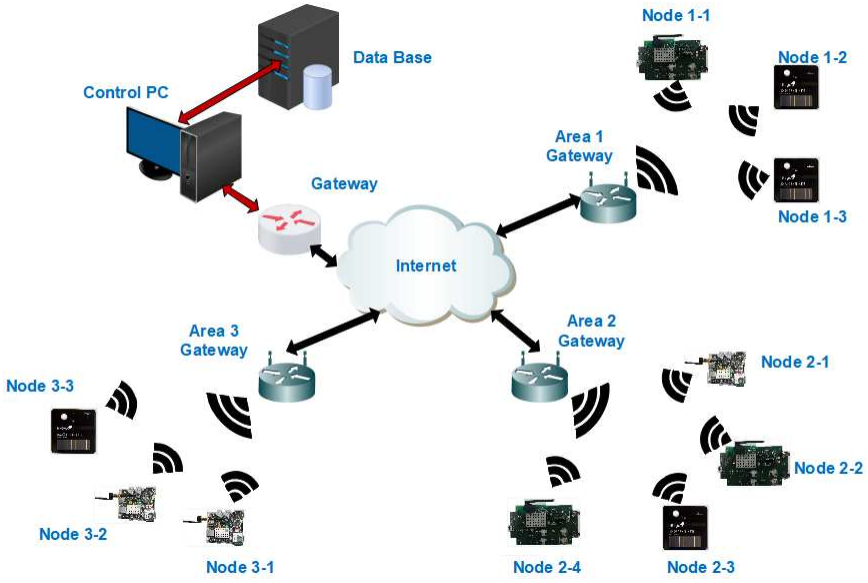

Figure 6-1: Example of a typical WSN.

A WSN design has to take into account the next properties:

- Low Power Consumption
- Self-configurability
- Scalability
- Low Node Cost
- Adaptability
- Reliability
- Fault Tolerance
- QoS Support
- Communication Channel Utilization
- Security

In WSNs, some network topologies are used to coordinate the base station, end nodes, and other routers. Router nodes are similar to end nodes, with the difference that they are only used to pass measurement data from other nodes.

The basic topology and most common is the star, in which each node maintains a single path of direct communication with the base station. This topology is simple but restricts the distance that the network can reach.

The range could be increased with a cluster or tree topology. Where in each node maintains a single direct communication path to the base station, but with the possibility to use other nodes to route its data to that path. However, this topology has a drawback. If the router node fails, all nodes that depend on that router lose their communication paths to the base station.

Mesh network topology solves this issue through redundant communication paths that increases system reliability. In a mesh network, nodes maintain multiple communication paths with the base station, so if the router node fails, the network automatically routes data through a different path. Mesh topology, although very reliable, suffers from increased network latency as data must make multiple jumps before reaching the base station.

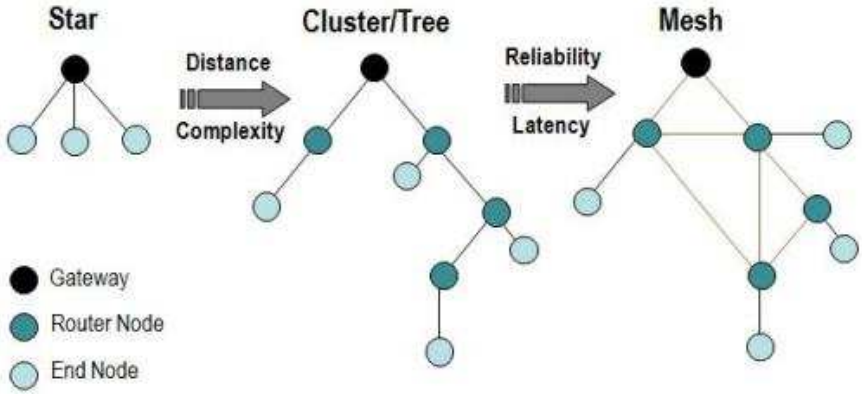

Figure 6-2: Networking topologies.

Actions over a shared channel are coordinated through a medium access control (MAC) protocol coordinates. The most commonly used solutions are contention-based. One general contention-based strategy is for a node which has a message to transmit to test the channel to see if it is busy, if not busy then it transmits, else if busy it waits and tries again later. After colliding, nodes wait random amounts of time trying to avoid re-colliding. If two or more nodes transmit at the same time, there is a collision and all the nodes colliding try again later. Many wireless MAC protocols also have a dozen mode

where nodes not involved with sending or receiving a packet in a given timeframe go into sleep mode to save energy.

In general, most MAC protocols optimize the arbitrary communication patterns and workloads. However, a wireless sensor network has more dedicated requirements that include a local unit-or broadcast. Traffic is generally from nodes to one, or a few skinks have a periodic or rare communication and must consider energy consumption as a significant factor. An effective MAC protocol for wireless sensor networks must consume little power, avoid collisions, be implemented with small code size and memory requirements, be efficient for a single application, and be tolerant to changing radio frequency and networking conditions.

Figure 6-3 shows different examples of present wireless sensor networks.

a) Hit2gap H2020 EU project was sensing node with energy harvesting system.

b) Zonesec FP7 EU project sensing node.

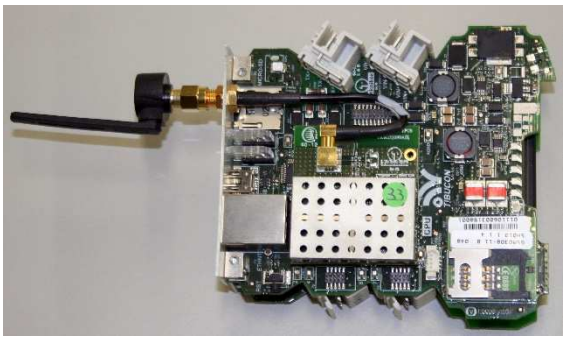

c) WSN gateway Evacuate FP7 EU project.

d) WSN gateway for I2V (infrastructure to a vehicle) industrial project.

Figure 6-3: Examples of wireless sensor networks nodes and gateways.

To extend battery life, a WSN node is periodically turned on to acquire and transmit data and then turned off to conserve power. The WSN radio must transmit a signal efficiently and allow the system to shut down with minimal power consumption. The processor must also be able to switch itself on and off efficiently. Trends in microprocessor technology for WSNs include reducing power consumption and maintaining or increasing processor speed.

Table 6-1 shows some examples of WSN applications:

Table 6-1: WSN applications examples.

Environmental monitoring	Structural health monitoring	Smart cities and houses	Healthcare applications
Air pollution	Buildings	Smart roads	Behaviour monitoring
Forest fire detection	Transports	Smart lighting	Medical monitoring
Natural disaster prevention	Transported items quality conditions	Smart parking	Sports activity monitoring
Radiation levels measurement	Engines	Smart home	
Electromagnetic levels measurement	Industrial machine	Remote metering	
Water quality	Machine-tool	Noise urban maps	
Agriculture quality enhancing			
Water leakages			
Animal and item location			

6.2 WSN nodes hardware

This section identifies the different components of a sensor node which consume the energy harvested. A WSN contains many power active elements. So, the sensor node is usually constituted of the following (figure 6-4) hardware components [212]:

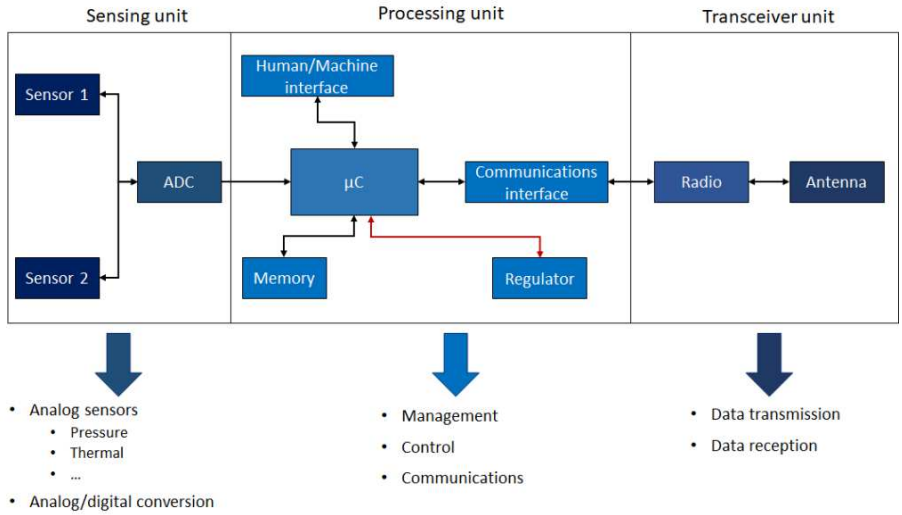

Figure 6-4: Typical contents of a WSN block in EHWSN.

6.2.1 Sensing unit

Sensor nodes may have one or several sensor devices. The sensing unit is composed of elements which measure physical parameter quantities such as temperature, pressure, sound, wind velocity, etc. and converts the measurement in an analog electrical signal.

The electrical signal generated by the sensors must be passed through an Analog to Digital Converter (ADC). The ADC converts the analog electric signal into a digital electrical signal. The digital signal is subsequently encoded with a binary code.

6.2.2 Processing unit

This unit is at least composed of memory, human/machine interface connection, voltage regulator and a micro. Use case requirements must drive the choice of the different components to achieve the best trade-off between cost and expected performance levels. Microcontrollers programmed way, and use will impact significantly on the power consumption. Many parameters must be considered, such as programming language, the number of calls to memory, the complexity of operations, cryptography, etc.

6.2.3 Transceiver unit

The functionality of both transmitter and receiver are combined into a single device known as a transceiver.

WSN often use Industrial, Scientific and Medical (ISM) band, which gives free radio, spectrum allocation and global availability. Radio frequency-based communication is the common implemented technology. However, in some cases, optical (laser) and infrared have been used as communication. Lasers require less energy but need line-of-sight for communication and are sensitive to atmospheric conditions. Infrared is limited in its broadcasting capacity.

Table 6-2 shows some low power wireless protocols characteristics [213]-[221]:

Protocol	LoraWAN	Sig-Fox	Weightless-N	Weightless-P	Ingenu	WAVIoT	NB-IOT	Thread	Zigbee	Z-wave	BLE	Enocean
Type	LPWAN							Short-range				
Frequency range	Sub-GHz	868 MHz	Sub-GHz	Sub-GHz	2.4 GHz	868 MHz	868 MHz	2.4 GHz	868 MHz y 2.4 GHz	868 MHz	2.4 GHz	868 MHz
Modulation	CSS	BPSK	DBPSK	FDMA/TDMA	DSSS	DBPSK	OFDM	DSSS	BPSK OQPSK	GFSK	GFSK	ASK
Bandwidth	125 kHz	100 Hz	200 Hz	12.5 kHz	1 MHz	100 Hz	180 kHz	83 Hz	2 MHz	300-400 KHz	0.5-2 MHz	280 kHz
Typical range	Rural: 22 Km Urban: 3-15 Km	Rural: 30-50 Km Urban: 3-10 Km	5 Km	2 Km	15 Km	Rural: 50 Km Urban: 16 Km	35 km	20-30 m	10-20 m	30 m	100 m	30-300 m
Typical data rate	0.2-100 kbps	100 bps	300-100 kbps	0.2-100 kbps	0-8 kbps	10-100 bps	62.5 kbps	250 kbps	250 kbps	40 kps	2 MB/s	125 kbps
Package Size	Defined by user	12 bytes	-	-	6 bytes to 10 Kbytes	-	-	-	-	-	245 bytes	14 bytes
Net	LAN	LAN	LAN	LAN	LAN	LAN	LAN	LAN	LAN	LAN	LAN	LAN
Type	Star & Star on Star	Star	Star	Star	Star/tree	Mesh	Mesh	Mesh	Mesh, Star, Tree	Mesh	Scatternet, Mesh	Mesh
Network Size	Uplink:>1M Downlink:<100k	1 M	Unlimited	Unlimited	384k by sector	2 M	55000	250	65535	232	8	2^{32}
Max. # Messages/day	Unlimited	140 messages/day	-	-	-	-	-	-	Unlimited	Unlimited	Unlimited	-
Max. output power	20 dBm	20 dBm	17 dBm	17 dBm	-	30 dBm	20/23 dBm	-	-	2.5 dBm	-	6 dBm
Link Budget	154 dB	151 dB	-	172 dB	-	164 dB	164 dB	-	-	-	-	-
Latency	2 s	500 ms	-	-	-	-	1.6-10 s	-	-	6 ms	2 ms	1 s
Immunity interference	Very high	Baja	-	-	-	-	-	-	-	-	-	-
Coexistence	Yes	No	-	-	-	-	-	-	-	-	-	-
Security	Fully addressed	Partially addressed	Fully addressed	Fully addressed	Fully addressed	Bidirectional encryption	-	Yes	-	Yes	-	-
Downlink	Yes	Yes	No	Yes	Yes	-	-	Yes	-	-	-	-
Encryption	AES-128 E2E	AES-128	As GSM	As GSM	-	XTEA 256 bit key	-	AES, public key	128 AES	-	128 AES with counter mode CBC-MAC	Rolling code and 128 AES
ISM Band	Yes	Yes	Yes	Yes	Yes	-	-	Yes	-	Yes	Yes	-
Two-way link	Yes	Yes	Time-division duplex	Time-division duplex	No	-	Half-duplex	Yes	-	-	-	Yes
Mobility/location	Yes	Limited mobility, no location	-	-	-	-	Yes	-	-	-	Yes	-
Protocol ownership	Partially proprietary	Proprietary	Standard	Standard	Proprietary	Standard	Standard (3-GPP)	Standard	Standard	Standard	Proprietary	Standard
Power Tx	419 mW	147 mW	-	-	-	-	792 mW	-	75.9 mW	-	97.2 mW	-
Power Rx	44.06 mW	39 mW	-	-	-	-	72 mW	-	62.7 mW	-	90 mW	-
Power Sleep	4.32 µW	4.34 µW	-	-	-	-	14.4 µW	-	2.97 µW	-	3.24 µW	-
Energy Harvesting	Yes	Yes	-	-	-	-	Yes	Yes	Yes	Yes	Yes	Yes

Table 6-2: LPWAN different technologies and their characteristics.

III.
Mini wind turbine harvester

IV.
Double low power management and storage

In this chapter, a double power manager for the wind and photovoltaic harvesters are developed. Figure IV-1 shows the block diagram of the system. It has a DC and an AC power source with their corresponding converters, DC-DC and AC-DC respectively. The energy harvested from both sources is combined and delivered to the load through a supercapacitor, as a support storage device [231].

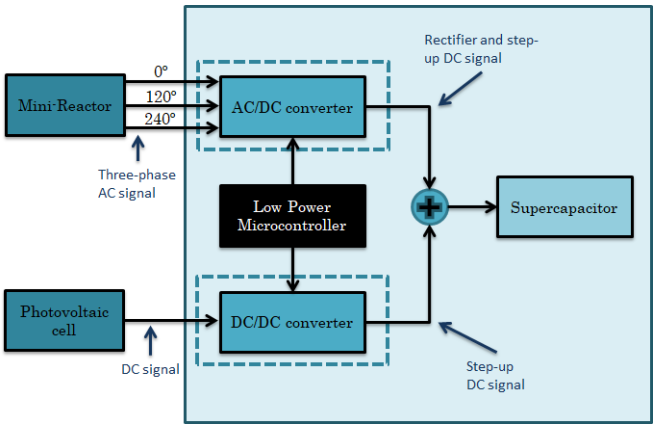

Figure IV-17-64: Union of both harvester's systems in a single system.

The requirement to avoid inserting more devices (as another step of conversion or management) at the double power manager and maintain the system efficiency, the voltage level at storage point must be 3 V as minimum and 5 V as the maximum. Furthermore, even not using the maximum output power point if doesn't fulfil the voltage range. This requirement must be filed at all ambient conditions.

This chapter includes the implementation of harvesting DC system, AC system and energy storage device, and this chapter has been divided into three sub-chapters:

- Chapter 8 DC input system
- Chapter 9 AC input system
- Chapter 10 Supercapacitor

Chapter 8 is focused on developments, simulations, and verifications of the DC system inside the double power manager. The first section corresponds to the construction of an electro-physical model of the photovoltaic harvester. The second section deals with the selection of the appropriate DC/DC architecture and its construction. Then, the selected architecture is simulated under different ambient conditions to find the best operation point.

Chapter 9 presents the developments, simulations, and verifications of the AC system inside the double power manager. The first section corresponds to the construction of an electro-mechanical model of the wind harvester. In the second section is selected suitable AC/DC architecture among different topologies. Finally, best efficiencies are searched in different input energy ranges.

Chapter 10 proposes a new model of supercapacitor to analyse the charge and discharge behaviour of a supercapacitor with an accuracy equivalent to that of the electromechanical models. The techniques used to reach the objective has been based on electro-mathematical equations algorithms. Besides, this model could provide information of the supercapacitors for EHWSN systems without using complex electrochemical models.

8. DC input system

The DC system is made of a photovoltaic harvester, a DC/DC converter and the storage device shared with AC system. In this system, the energy has several steps of conversion. On a first step, the light power is harvested and converted to electrical power with an efficiency $\eta_{photovoltaic\_cell}$. Then, the level of the harvested DC signal is adequate to an appropriate level for his storage. This step is made with a DC/DC converter, again with a quantity of efficiency, $\eta_{converter}$. Finally, the capacitor storages the energy.

Equation 8-1 calculate the described process mathematically, which is a multiplication between system conversion efficiencies and input light power.

$$P_4 = \eta_{tot} * P_1 = \left(\eta_{photovoltaic\_cell} * \eta_{converter}\right) * P_1 = (\eta_1 * \eta_2) * P_1 \quad (8\text{-}1)$$

The figure 8-1 shows the DC system block diagram and energy conversions with respective efficiencies:

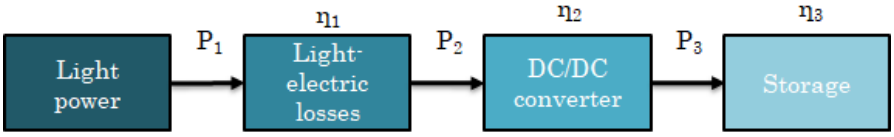

Figure 8-1: Block diagram of complete DC system of the double power manager.

This part of the work has named DC system because harvester produces electrical energy in a DC signal. Only photovoltaic and thermoelectric harvesters produce energy as DC signal, others work at AC regime.

8.1 Photovoltaic electro-physical model

The objective of this section is to implement an equivalent electro-physical model of the photovoltaic cell. This model is going to predict the electrical operation of a selected photovoltaic generator under different operating conditions, such as irradiance (mW/mm^2) and temperature (^{o}C).

The used information in the model construction is:

1. Parameters of cells in standard conditions and TONC (data-sheet)
2. The incident solar radiation and the ambient temperature

Existing mathematical models are implemented in mathematical software's, as MATLAB© [232][233]. However, in this case, is needed to study the behaviour in the time-domain. Furthermore, it is also necessary to study the interaction between the photovoltaic module and the converter connected directly to the solar cell.

8.1.1 Theoretical principles of photovoltaic model

8.1.1.1 Theoretical equations for the model

The construction of an equivalent model of a photovoltaic cell was based on the work of [234][235] references.

The photovoltaic harvester is based on a five-parameters equation described in chapter 2 section 1, whose respective expression is the next one:

$$I = I_{ph} - I_0\left(e^{\frac{q(V+IR_s)}{nkt_c}} - 1\right) - \frac{V + IR_s}{R_{sh}} \quad (8\text{-}2)$$

, where I_{ph} is the light generated current, I_o is the dark saturation current due to recombination, q (is the electron charge, R_s is a series resistance, n is the ideal factor, k is the Boltzmann constant, T_c is the cell temperature, and R_{sh} is a shunt resistance. The five unknown parameters are I_{ph}, I_o, n, R_s, R_{sh}.

This model is a function of the solar radiance G and the air temperature T_a. The equation 8-2could be used to measure the value of the parameters I_{ph}, I_o, n, R_s, R_{sh} under the real-time ambient conditions. However, manufacturers do not usually provide these parameters in their cells data-sheets. As short-circuit current (I_{sc}), open-circuit voltage (V_{oc}), voltage and current in MPP (V_{mpp} and I_{mpp}), rated peak power (P_n), temperature coefficient for the short circuit current (α_{Isc}) and temperature coefficient for the open circuit voltage (α_{Voc}). Usually, data-sheet parameters are given in Nominal Operating Condition Temperature (NOCT). The NOCT is directly related with ambient (T_a) and cell (T_c)temperatures with the next equation:

$$T_c = T_a + \frac{G}{G^*}(NOCT - T_2) \quad (8\text{-}3)$$

The datasheet contains information about the number of connected in series cells and the number of parallel branches in the photovoltaic module. Therefore, characteristic currents and voltages of a photovoltaic cell are calculated through:

$$V_{cell} = \frac{V_{module}}{N_s} \quad (8\text{-}4)$$

, where N_s is the number of cells connected in series. Then, the current through each cell is calculated with:

$$I_{cell} = \frac{I_{module}}{N_p} \quad (8\text{-}5)$$

, where N_p is the number of cells groups connected in parallel. Moreover, the current generated by light is directly proportional to the solar irradiance, expressed as:

$$I_{ph} = G_{pu}[I_{sc}^0 + \alpha_{sc}(T_c - 25)] \quad (8\text{-}6)$$

, where G_{pu} = G/1000 is the relative solar irradiance, I^o_{sc} is the short circuit current, and α_{sc} is the current-temperature coefficient. All these parameters are at STC. T_c-25 is the mismatch between the cell temperature and the STC cell temperature. The structure of equation 8-5 is approximately valid also for the I_{mpp}:

$$I_{mpp} = G_{pu}\left[I_{mpp}^0 + \alpha_{sc}(T_c - 25)\right] \quad (8\text{-}7)$$

The equation 8-7 states that the current in maximum power point depends on the solar irradiance and the module temperature. From equation 8-1, the dark saturation current I_o depends on the cell temperature, whereas the series resistance Rs depends on the ambient conditions. Dark saturation current has two characteristic values for V = 0 and V = V_{oc}, i.e., in short- and open-circuit condition. For these extreme values, dark

saturation current ranges go from zero to I_o, because the exponential term ranges from 1 to 0. This term can be represented as:

$$\beta e^{\left(V+\alpha V_{oc}\Delta T-V_{oc}^{0}\right)} \tag{8-8}$$

, equalling the exponential term to 0, the open circuit voltage equation is obtained:

$$V_{oc} = V_{oc}^{0} - \alpha_{oc}\Delta T \tag{8-9}$$

Moreover, the following mathematical relation is approximately also valid for V_{mpp} achievement:

$$V_{mpp} = V_{mpp}^{0} - \alpha_{oc}\Delta T \tag{8-10}$$

Last terms of equation 8-2 refer to R_s and R_{sh} resistors. These resistors do not represent a real item within the cell, even though they correspond to a dissipation phenomenon within the photovoltaic module. For this aim, firstly the equations describing the values of the resistances are proposed and inserted into the general I-V equation, then the characteristic parameters are derived.

R_{sh} is related to the slope of the I-V curve in the short-circuit condition; thus, it could be calculated as:

$$R_{sh} = \frac{V_{mpp}^{0} - \alpha V_{oc}\Delta T}{G_{pu}\left(\frac{I_{sc}^{0} - I_{mpp}^{0}}{2}\right)} = \frac{V_{sh}}{I_{sh}} \tag{8-11}$$

Then, R_s is related to the slope of the I-V curve in the open circuit condition, and expressed as:

$$R_s = \frac{\frac{\left(V_{oc}^{0} - V_{mpp}^{0}\right)}{4}}{G_{pu}\left(I_{mpp}^{0} - \alpha I_{sc}\Delta T\right)} = \frac{V_s}{I_s} \tag{8-12}$$

The resultant electrical equivalent circuit is shown in figure 8-2. The figure represents the electrical circuit of a single photovoltaic cell.

The circuit is composed of a main circuit and two sub-circuits to modify R_{sh} and R_s values when changing the ambient condition.

The main circuit has the current source, a diode, the effect of open circuit state represented with two opposite voltage sources and cell dissipate phenomena equivalent resistors. The current generated by the light source (equation 8-5) is represented by two current sources and a resistor in shunt, which is irradiance dependent. Effects of temperature are inserted with two opposite voltage sources in series.

The two sub-circuits represent the real-time resistors calculation. Equations 8-10 and 8-11 have been translated to circuit representation to obtain the resistors values.

The photovoltaic model is completed with manufacturer data-sheet and the calculated parameters.

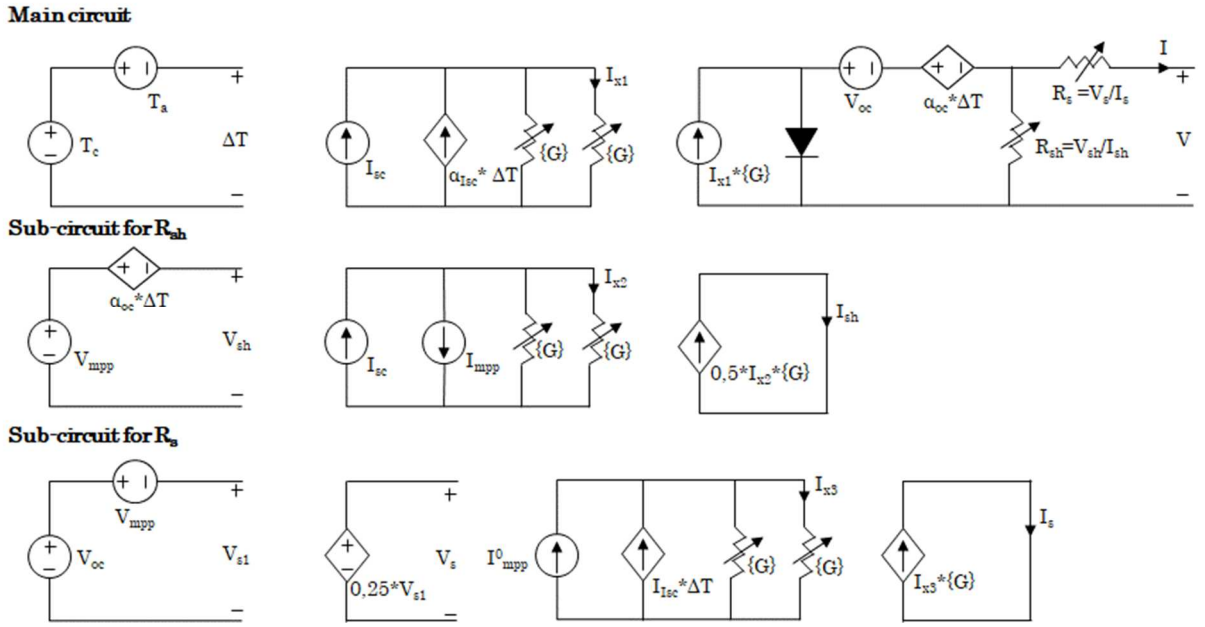

Figure 8-2: Single cell equivalent electrical model.

8.1.1.2 Used photovoltaic cell characteristics

The solar harvester devised for this research uses the solar module SLMD481H08 manufactured by IXOLARTM. Chapter 11 section 1 describes the methodology and process to select this module between several options.

The selected monocrystalline module has a width of 88.8 mm and a height of 54.7 mm. Each individual cell has 20 x 12 mm^2 = 2 x 1.2 cm^2 = 2.4 cm^2. The whole module has 16 cells distributed in two branches connected in parallel each one made of 8 cells. The cell has a nominal efficiency of 22%. It also has the broad photonic response over a wide range of wavelengths. Thus, it is suitable for both indoor and outdoor applications. Figure 8-3 shows used module architecture and dimensions.

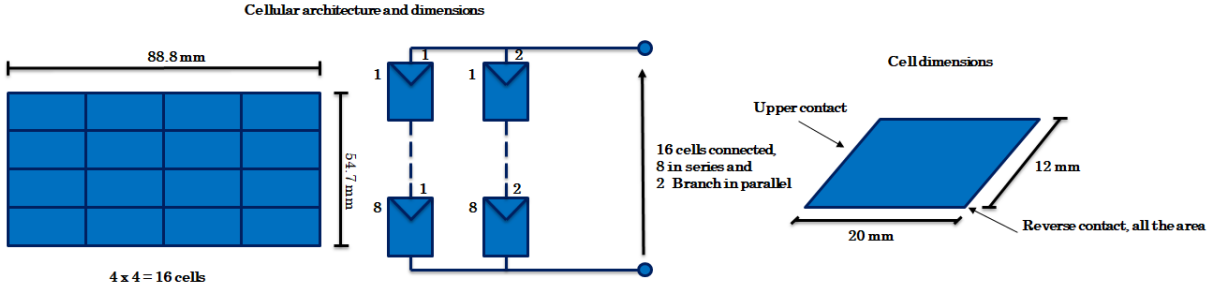

Figure 8-3: Used cellular architecture and dimensions.

Electrical characteristics of the selected solar module provided by manufacturer are presented in table 8-1:

Table 8-1: SLMD481H10 solar module electrical characteristics.

Symbol	Cell parameter	Value
V_{oc}	Open circuit voltage	5.04 V
I_{sc}	Shor circuit current	200 mA
V_{mpp}	Voltage at max. power point	4 V
I_{mpp}	Current at max. power point	178 mA
P_{mpp}	Maximum peak power	712 mW
FF	Fill factor	> 70 %

η	Solar cell efficiency	22 %
$\Delta V_{oc}/\Delta T$	Open circuit voltage temp. coefficient	-2.1 mV/K
$\Delta J_{sc}/\Delta T$	Short circuit current temp. coefficient	0.12 mA/(cm²K)

Some of these values could be used directly in the implementation of the model. However, other values must be calculated. The first step is to go to cell level and use module data-sheet data/graphics, which allows to define the relationship between open circuit and maximum voltages and short circuit and maximum currents:

$$\frac{V_m}{V_{oc}} = \frac{4\ V}{5.04\ V} = 0.7936 \quad \rightarrow \quad \frac{I_m}{I_{sc}} = \frac{178\ mA}{200\ mA} = 0.89$$

Then, each cell V_{oc}, V_m, I_{sc} and I_m values are needed to be obtained for model construction:

$$V_{oc\_cell} \approx 0.63\ V \rightarrow\ V_{m\_cell} = \frac{V_m}{V_{oc}} *\ V_{oc\_cell}\ = 0.7936 * 0.63\ V = 0.5\ V$$

$$J_{sc} \approx 42\ {}^{mA}/_{cm^2} \rightarrow\ I_{sc\_cell} = J_{sc} * A = 42\ {}^{mA}/_{cm^2} * 2.4\ cm^2 = 100.8\ mA$$

$$I_{m\_cell} = \frac{I_m}{I_{sc}} * I_{sc\_cell} = 0.89 * 100.8\ mA = 89.712\ mA$$

Verification concludes with the validation of provided efficiency (η) and Fill Factor (FF) by the manufacturer.

$$FF = \frac{Max\ power\ from\ real\ module}{Max\ porwer\ from\ ideal\ module} = \frac{V_m I_m}{V_{oc} I_{sc}} = \frac{712\ mW}{1008\ mW} = 0.7063 \rightarrow 70.63\ \%$$

$$\eta = \frac{{}^{P_m}/_{A}}{P_{incident}} * 100 = \frac{{}^{(0.5\ V * 89.712\ mA)}/_{2.4\ cm^2}}{100\ mW/cm^2} * 100 = 18.69\ \%$$

Obtained Fill Factor is consistent with data provided by manufacturer; however, efficiency is 3.31 points lower.

8.1.2 Photovoltaic module model

8.1.2.1 Complete model construction

In order to build the photovoltaic module model is to connect main circuit cells (8.1.1.1 section) with the configuration of selected module (8.1.1.2 section). The unconnected point at the main circuit represents the output of the cell, and other parts are just configuration of external parameters or variables. So, this part is taken and repeated as many times as cells quantity has the solar module, 16 in this case. Then, cells are connected as selected photovoltaic module architecture, 8 cells in series per 2 branches in parallel. Finally, an electric load is connected in parallel with 2 branches and the model construction is completed. The described procedure is based on Kirchhoff's law, and the result is shown in figure 8-4.

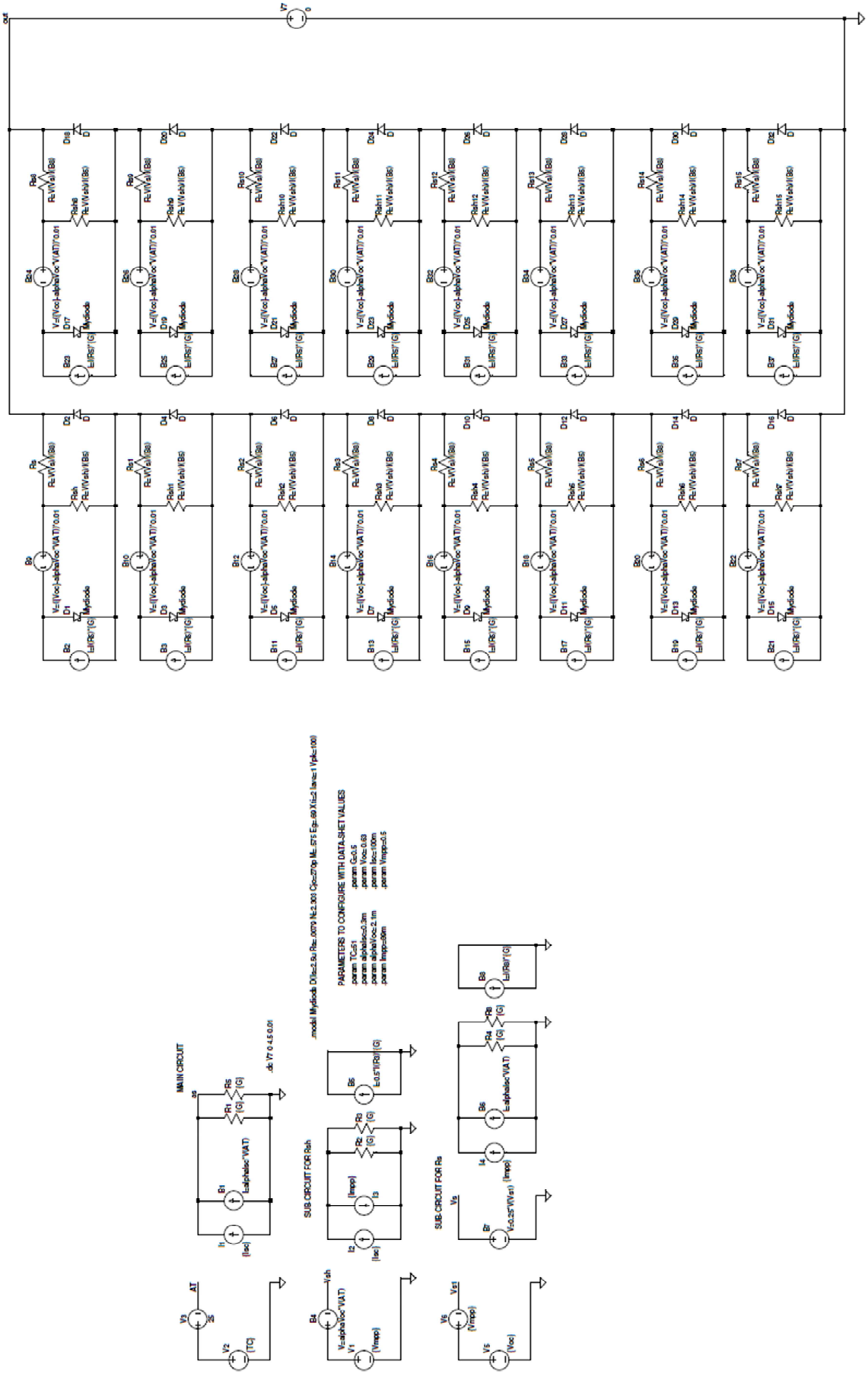

Figure 8-4: Schematic of photovoltaic physical-electric model.

8.1.2.2 Model simulation results

The simulations allow to verify the output V-I-P curves and values. These simulations have been done at six different ambient conditions, basically with the aim to demonstrate that the model response changes with temperature and irradiance changes.

Figure 8-5a, which shows parametric simulation results, irradiance is left fixed and the temperature is changed. In figure 8-5b temperature is left fixed and irradiance is changed.

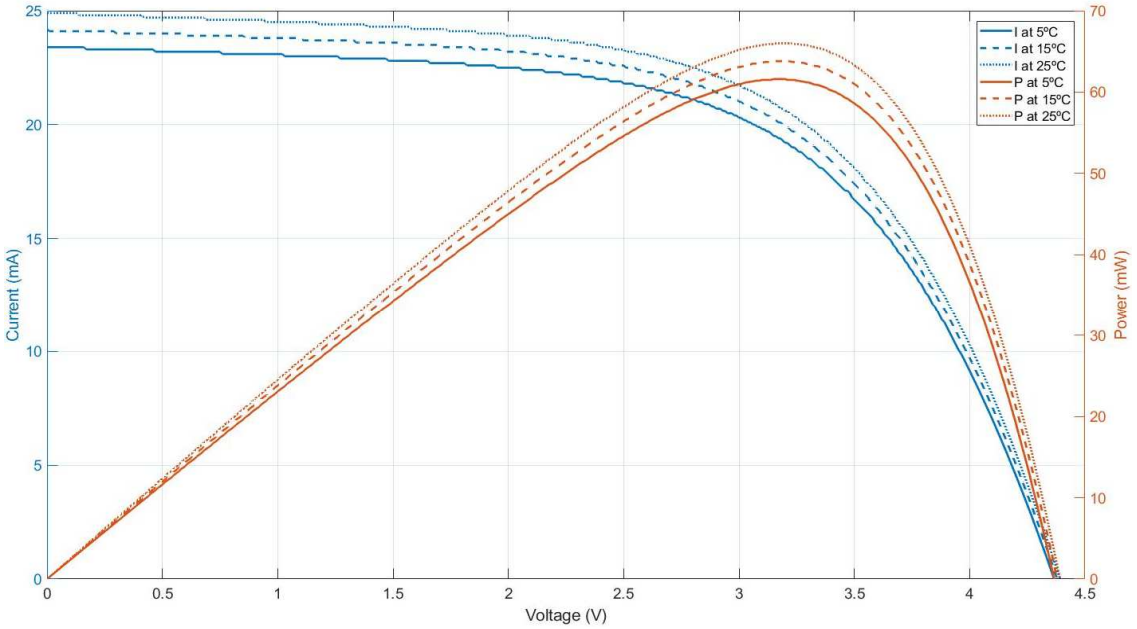

a) 0.25 suns of irradiance at 5, 15 and 25 ºC.

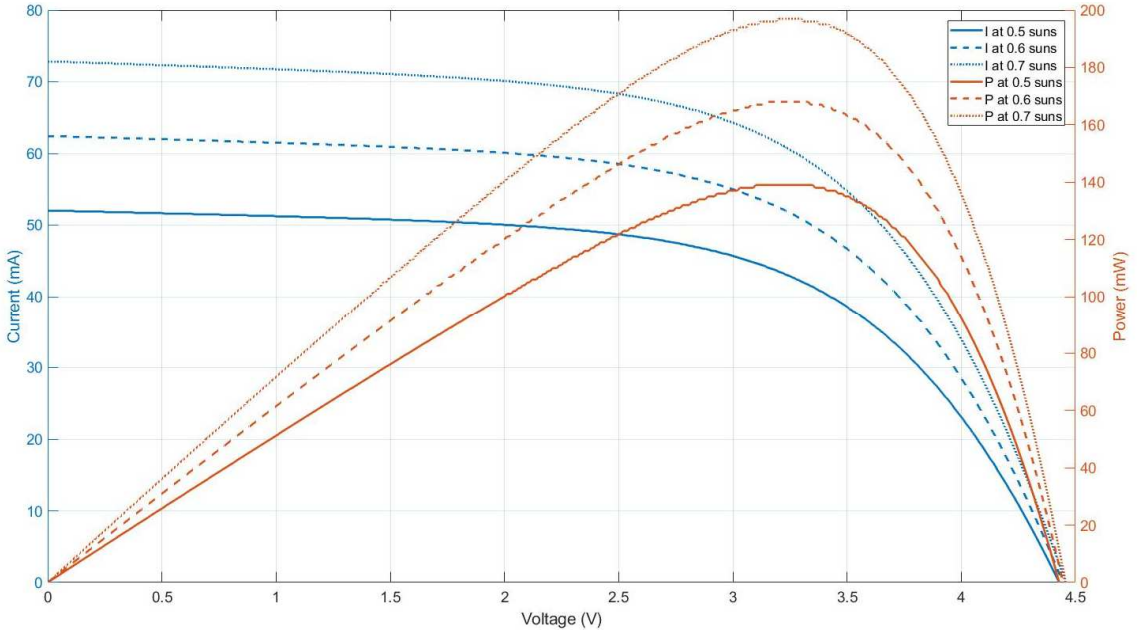

b) 40 ºC temperature of irradiance at 0.5, 0.6 and 0.7 suns.

Figure 8-5: Simulated V-I curves with the photovoltaic electro-physical model.

The results show that with more irradiance power, output electric power/current are higher and vice versa. The same behaviour occurs with temperature, so the basics principles of solar cell operation are achieved correctly.

With the V-I-P curves of the photovoltaic cell, the next step the power generation of the module in different ambient conditions (irradiance and temperature) is obtained. The aforementioned simulations provide the maximum out power for the selected ambient conditions. Table 8-2 and figure 8-6 show achieved results:

Table 8-2: Maximum voltage, current and power obtained with simulation under different operation conditions.

G (suns)	T (°C)	R_{load} (Ω)	V_{out} (V)	I_{out} (mA)	P_{out} (mW)
0.1	5	380	2.913	7.666	22.333
0.1	25	360	2.937	8.157	23.956
0.25	10	160	3.167	19.792	62.675
0.25	30	155	3.224	20.803	67.077
0.5	15	80	3.204	40.044	128.281
0.5	45	75	3.258	43.437	141.511
0.75	20	55	3.324	60.439	200.908
0.75	40	50	3.275	65.502	214.525
1	22	40	3.304	82.606	272.948
1	60	35	3.277	93.627	306.812

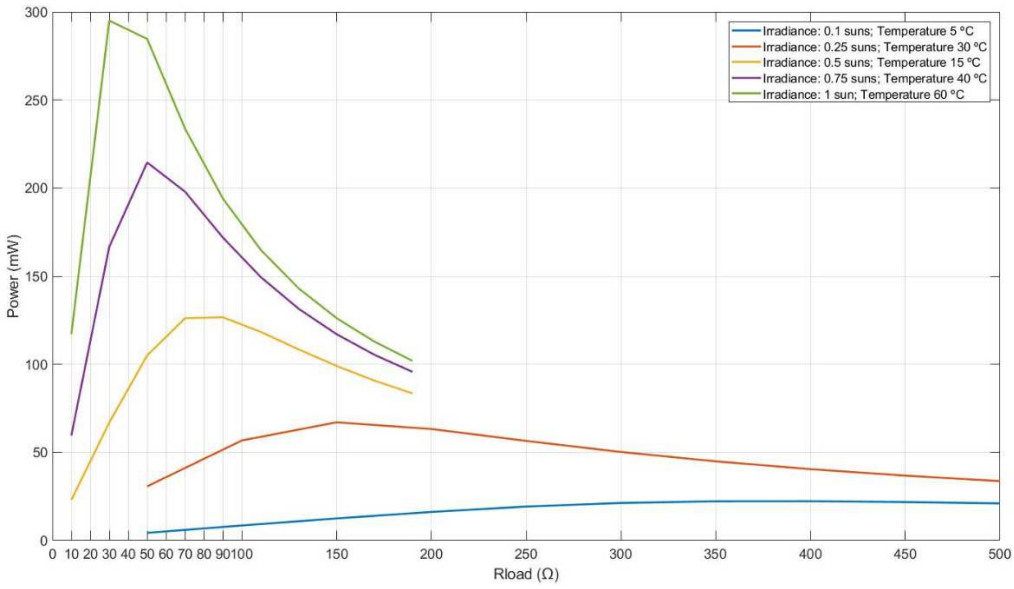

Figure 8-6: Simulated power curves with load sweep for 0.1, 0.25, 0.5, 0.75 and 1 sun irradiance at different temperatures.

Table 8-2 and figure 8-6 results show that the cells produce more power at higher temperatures for the same irradiance level. Also, irradiance has more effect on power production than temperature, e.g., 0.25 suns and 10 °C against 0.1 suns 25 °C. The cell generates power generation range goes from 22.333 mW with 0.1 suns at 5 °C to 306.812mW with 1 sun at 60 °C.

8.1.3 Tests set-up for model verification and validation

To verify and validate the accuracy of the photovoltaic electro-physical model solar test have been employed a sun luminaire. The test set-up has the following elements:

- Solar module
- Temperature measurement system
- Temperature sensor PT-100

- Data Logger
- Electronic load
- PC
- Black box
- Sun luminaire

Figure 8-9 shows the block diagram of test set-up:

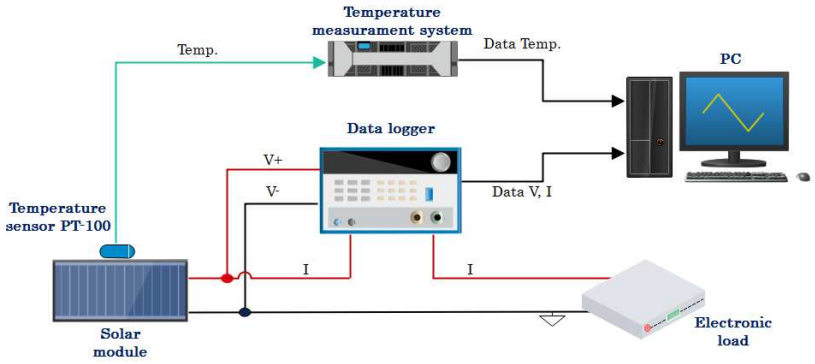

Figure 8-7: Photovoltaic cell test set-up block diagram.

This test has been done with a sun luminaire, a controlled source of light. This solar light had the restriction to produce a maximum of 0.5 suns. In addition, a black box has been used to avoid any interference of irradiance on the test and maintain the light seal. Furthermore, the black colour is selected because it does not absorb and diffract light and all effect of light is centralized in the solar cell.

The test procedure has been the following one:

1. Locate the solar module inside the black box and the under the luminaire.
2. Connect an electronic load, for the sweep measurement.
3. Connect the data logger to measure and register the voltage and current produced by the solar cell.
4. Insert the PT-100 sensor into the box. The temperature was measured near the solar module, saving data with a 1-minute period.
5. During the tests procedures: Registered data of temperature, voltage and current were visualized for real-time verification and saved for future processing.

Figure 8-8 shows described and mounted elements:

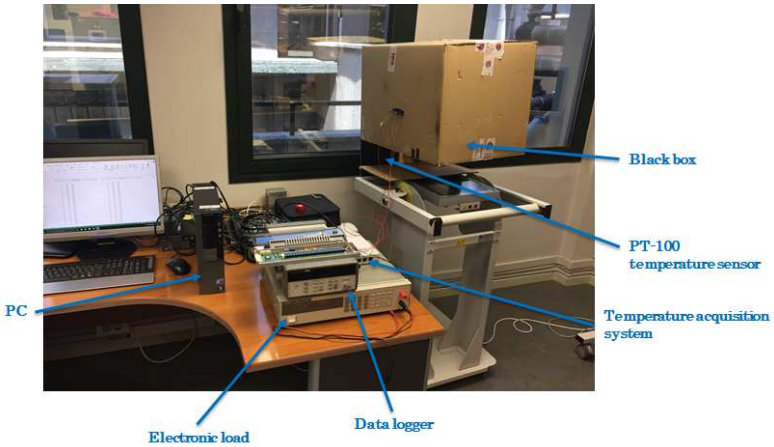

Figure 8-8: Photovoltaic cell test set-up.

Three tests under different irradiance and temperature conditions were developed to verify the model. The realized test conditions are the next ones:

1. Solar irradiance 0.25 suns and 46 ºC temperature.
2. Solar irradiance 0.5 suns and 65 ºC temperature.
3. Solar irradiance 0.5 suns and 51 ºC temperature.

8.1.4 Comparison between model and test results

In this section deviation and error between simulations and measured results are calculated.

The aforementioned three tests are compared with electro-physical model simulations. In next figures (8-9/10/11), the blue traces are the simulation results and the orange traces are the values measured during the test.

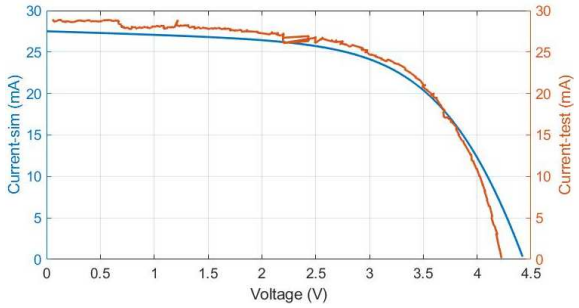

a) Simulated vs. measured current.

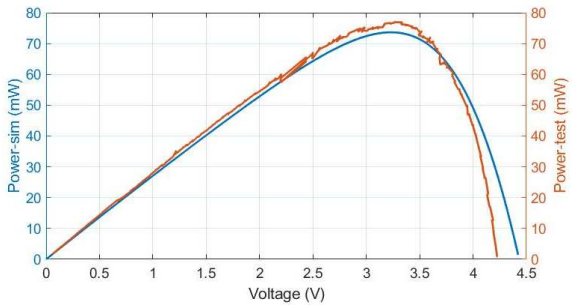

b) Simulated vs. tested power.

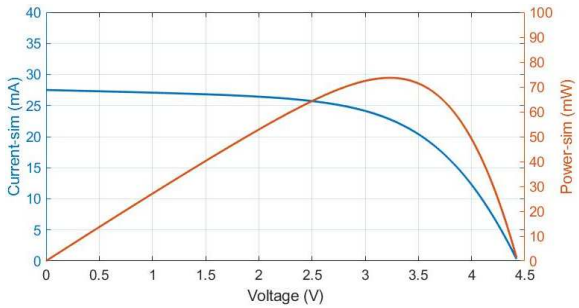

c) Simulated V-I-P curve.

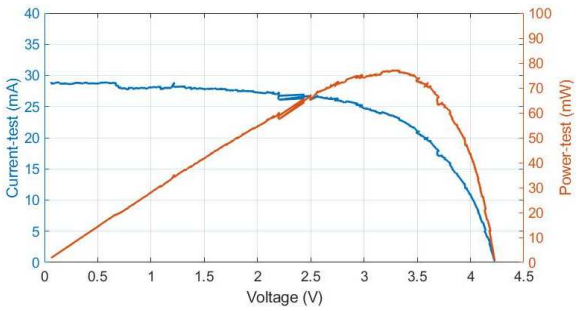

d) Tested V-I-P curve.

Figure 8-9: Test vs. simulation photovoltaic module results with 0.25 suns irradiance and 46 ºC temperature.

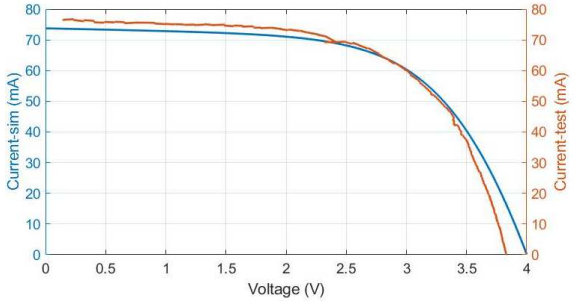

a) Simulated vs. measured current.

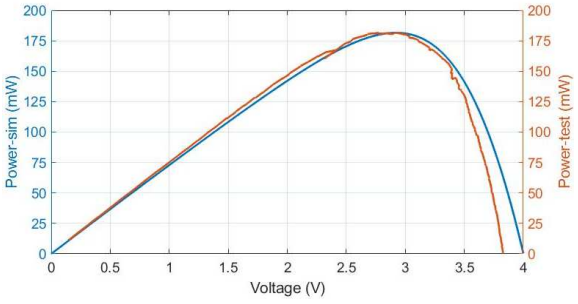

b) Simulated vs. tested power.

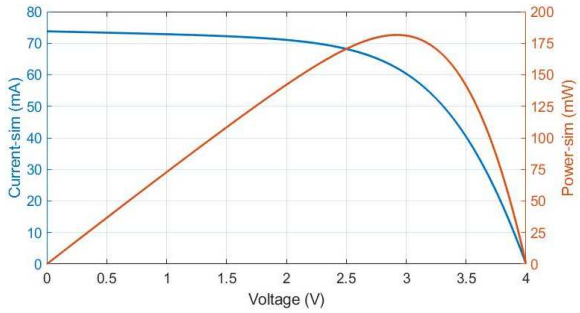

c) Simulated V-I-P curve.

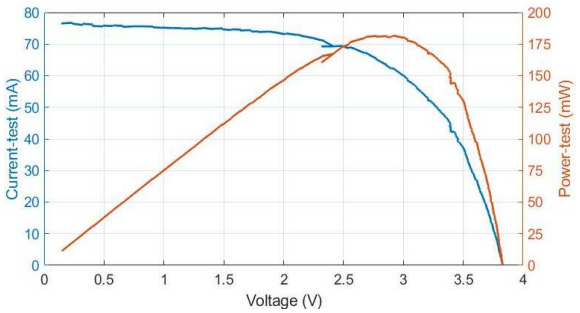

d) Tested V-I-P curve.

Figure 8-10: Test vs. simulation photovoltaic module results with 0.5 suns irradiance and 65 °C temperature.

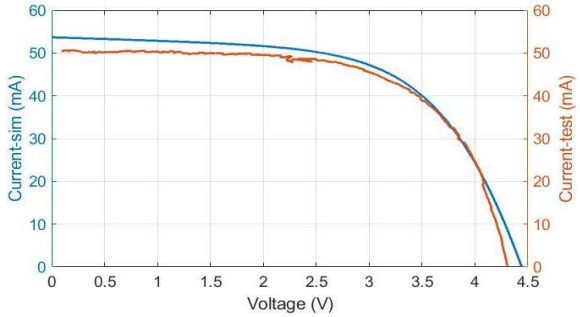

a) Simulated vs. measured current.

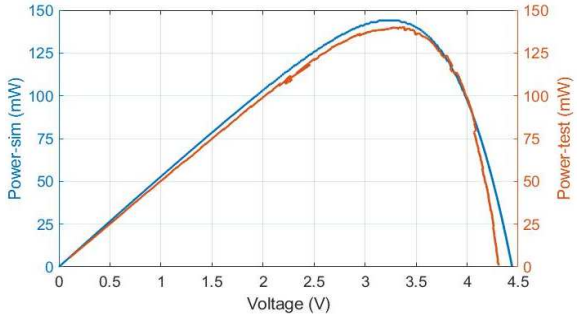

b) Simulated vs. tested power.

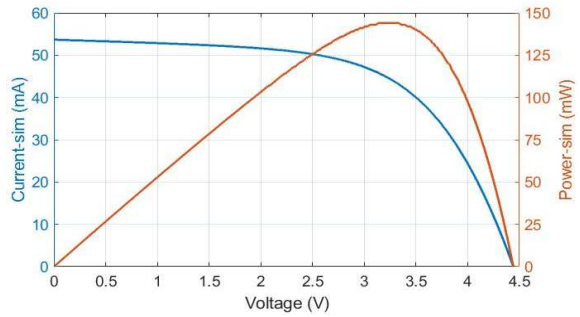

c) Simulated V-I-P curve.

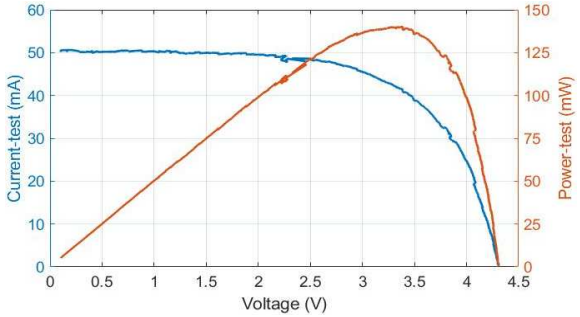

d) Tested V-I-P curve.

Figure 8-11: Test vs. simulation photovoltaic module results with 0.5 suns irradiance and 51 °C temperature.

At figure 8-9 case, short circuit current has 27 mA value, and maximum power point track or MPPT is 75 mW and is produced around 3.4 voltage level. At figure 8-10 case, short circuit current has 78 mA value, and maximum power point track or MPPT is 180 mW and is produced around 2.9 voltage level. At figure 8-11case, short circuit current has 52 mA value, and maximum power point track or MPPT is 148 mW and is produced around 3.3 voltage level.

The results confirm that photovoltaic cells operation principles are fulfilled.

- When temperature and/or irradiance grow up, generated current/power also increase.
- Current and power achieve 0 level at the same point of voltage.
- At short circuit condition, the current has the maximum level.

To verify the model, the deviation between model values and measured data has been determined. Due to the difference of points quantity between model curves and measured curves, an interpolation was realized to be able to make the comparison. This interpolation introduces an error; consequently, the visualized deviation is higher than real.

Table 8-3: Comparison between simulation and test results values at different ambient conditions.

Ambient conditions		Mean Standard Deviation			Total average	
G (suns)	Temp (ºC)	I (mA)	P (mW)	Average per test	I (mA)	P (mW)
0.25	46	1.760	5.056	3.408		
0.5	51	2.960	6.953	4.956	3.781	10.087
0.5	65	6.625	18.254	12.439		
		Mean Percent Deviation				
		I (%)	P (%)	Average per test	I (%)	P (%)
0.25	46	3.148	3.009	3.078		
0.5	51	4.539	4.425	4.482	3.334	3.305
0.5	65	2.316	2.395	2.355		

The worst deviation is 4.539 % of current in G=0.5 suns and T=51 ºC, being the average of all test deviation a 3.3 %. The lower deviation in current, as well as, in power, is produced in G=0.5 suns and T= 65 ºC test. Thus, could be said that temperature parameter introduces more error than irradiance parameter.

The results confirm that the model could be used in the DC/DC converter construction.

8.1 DC/DC converter

8.1.1 Context, objective and development methodology

The DC/DC converter is included in the power manager between the harvester and the storage device. The system block diagram is shown in figure 8-12:

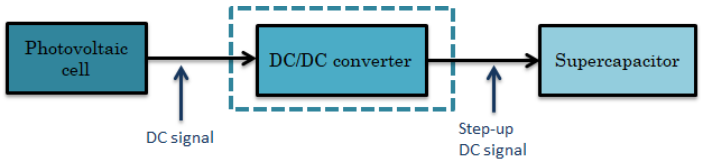

Figure 8-12: DC complete system with the harvester (photovoltaic cell), power management (DC/DC converter) and the storage device (supercapacitor).

The main objective of this subsection is to research, built, simulate and verify the development of a **DC/DC converter** for the mini-photovoltaic cell for all voltage and frequency ranges with more than a 80 % of efficiency.

The DC/DC converter requirements are:

- Impedance matching.
- Step up the voltage received from harvesting.
- Maintain operation functionality and efficiency with sun irradiance as well as with artificial light irradiance.

The best DC/DC converter must be implemented following the next methodology:

1. Select the appropriate architecture for the use case of this work.
2. Converter operation power range has been defined with harvester output values at different ambient conditions.
3. Considering the low power levels in energy harvesting applications, appropriate diode and MOSFET are selected under their viability to work in these conditions.

4. The coil value and switching frequency for MOSFET control must be defined. Due to the input range is extensive, depend on ambient condition switching frequency would be different for each case, i.e., shift control.
5. Use sweep simulations to search maximum output power and system efficiencies.

Figure 8-13 shows described methodology in a flux diagram:

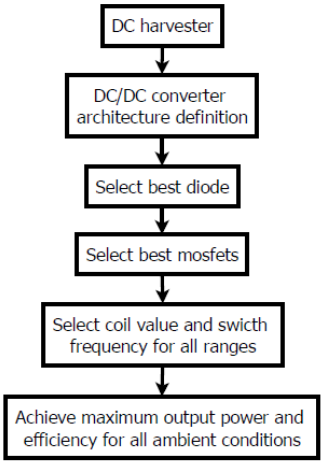

Figure 8-13: Flux diagram of steps used in this task.

8.1.2 Boost architecture definition

The architecture employed in the DC-DC converter is the boost topology showed in figure 8-14. The main challenge that presents the design of this converted is that it must manage low power levels and voltage, which limits the performance and availability of the semiconductors.

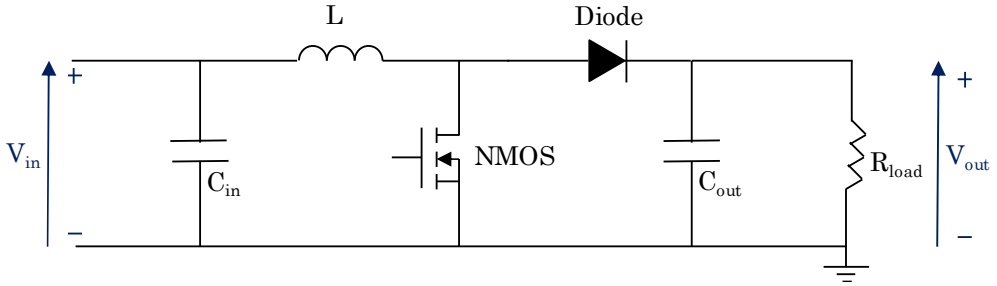

Figure 8-14: DC-DC boost architecture for photovoltaic module converter.

Boost control techniques would be based on the change of the duty cycle value. This element controls the steady-state output concerning the input voltage. This operation mode has been described in section 3-2.

The control technique used in this converter is the Pulse Width Modulation (PWM). Pulse-width modulation uses a rectangular pulse wave whose pulse width is modulated resulting in the variation of the average value of the waveform.

The last step before starting the selection of converter devices is to make the connection between the converter and photovoltaic module models. The connection is made between output point of solar module and input point of DC/DC boost converter circuit.

The DC/DC converter construction starts with the selection of coil value, MOSFET, and diode appropriate devices. To make this selection two different work ambient conditions have been used:

1. Minimum → G=0.1 suns and Temperature = 5 ºC
2. Maximum → G=1 sun and Temperature = 60 ºC

The selection of coil value, MOSFET and diode devices is made with simulation tools testing the performance of the converter in extreme conditions, i.e., 0.1 at 5 ºC and 1 sun at 60 ºC.

The first step involves the MOSFET selection, and different conditions were set in the circuit simulation to accomplish it.

In first case, with minimum ambient conditions, switching frequency was 50 kHz, duty-cycle 0.15, coil inductance 270 µH, R_{load} = 400 Ω and the commercial diode model MBR0520L. Then, several commercial MOSFETs were selected to test in base their appropriate characteristics for the present use case, such as Si1555DL_N, Si8416DB, SiA436DJ, Si1553CDLN, Si8466EDB, Si3900DV. Moreover, finally, simulated with their appropriate spice model. In table 8-4 and figure 8-15 achieved results with detailed conditions are shown:

Table 8-4: Comparative results between different MOSFETs at 0.1 suns and 5 ºC temperature ambient conditions.

MOSFET	Pcontrol (µW)	Rds (mΩ)	Qg (nC)	Vin (Vp)	Vout (V)	Iout (mA)	Pout (mW)	Pin (mW)	η (%)
Si1555DL_N	61.252	0.63	0.8	2.221	2.674	6.686	17.884	19.438	91.94
Si8416DB	1197.9	21	17	2.185	2.655	6.639	17.618	19.183	90.64
SiA436DJ	1189.1	8.7	15	2.182	2.653	6.633	17.603	19.159	90.69
Si1553CDLN	26.717	0.55	0.578	2.256	2.69	6.726	18.096	19.679	91.93
Si8466EDB	592.41	6.8	0.05	2.246	2.685	6.714	18.032	19.608	91.37
Si3900DV	156.68	130	2.1	2.261	2.694	6.735	18.144	19.711	91.89

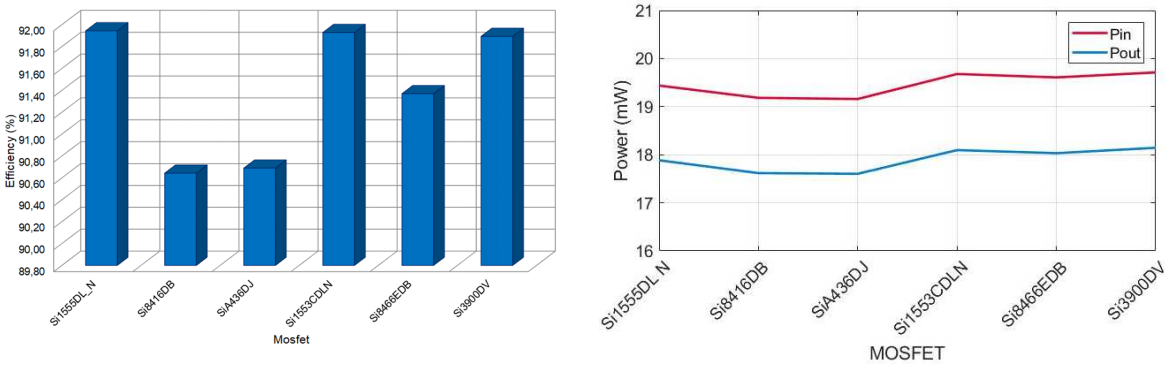

a) Efficiency. b) Input/output power.

Figure 8-15: Comparisons results between MOSFETs at 0.1 suns and 5 ºC temperature ambient conditions.

At second case for MOSFET selection, with maximum ambient conditions, switching frequency was 20 kHz, duty-cycle 0.16, R_{load} = 50 Ω and maintaining coil value and diode. Table 8-5 and figure 8-16 details the test condition and show the results obtained.

Table 8-5: Comparative results between different MOSFETs at 1 sun and 60 ºC temperature ambient conditions.

MOSFET	Pcontrol (µW)	Rds (mΩ)	Qg (nC)	Vin (Vp)	Vout (V)	Iout (mA)	Pout (mW)	Pin (mW)	η (%)
Si1555DL_N	28.181	0.63	0.8	3.424	3.772	75.45	284.64	305.836	93.04
Si8416DB	487.35	21	17	3.416	3.778	75.568	285.532	305.964	92.83
SiA436DJ	476.33	8.7	15	3.415	3.778	75.57	285.548	305.984	92.84

Si1553CDLN	11.603	0.55	0.578	3.432	3.768	75.364	283.989	305.708	92.88
Si8466EDB	242.1	6.8	0.05	3.418	3.778	75.569	285.537	305.935	93.09
Si3900DV	64.318	130	2.1	3.421	3.777	75.548	285.382	305.884	93.23

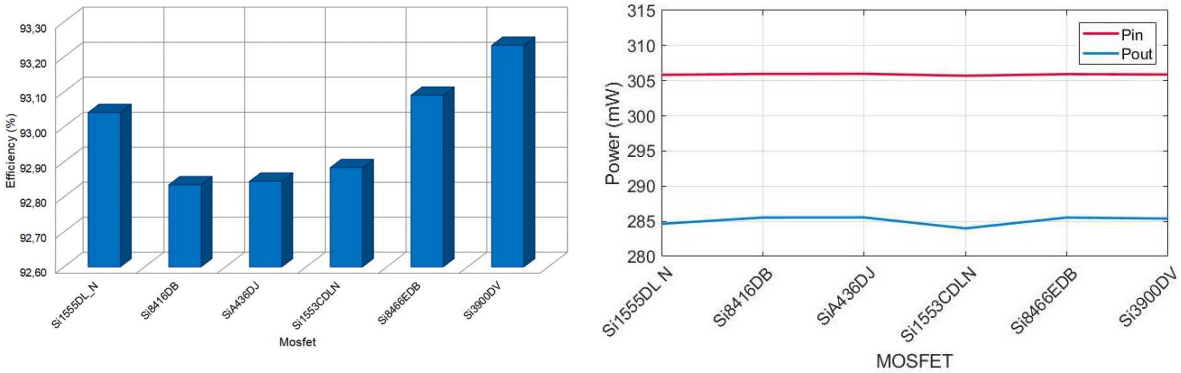

a) Efficiency. b) Input/output power.

Figure 8-16: Comparisons results between MOSFETs at 1 sun and 60 ºC temperature ambient conditions.

Efficiencies in both conditions are higher than 90 % with all MOSFETs. Moreover, in low light and temperature ambient reach until 91 % and in high conditions until 93 %. Si1555DL_N and Si3900DV present the best efficiency regarding the rest of devices. However, Si1555DL_N and Si1553CDLN have the less consumption at both work operation modes. For exposed reasons, Si1555DL_N MOSFET has been selected to be the MOSFET at the DC/DC boost converter. However, Si3900DV also is appropriate to use.

The second step involves the diode selection. Employing same procedure used in MOSFET selection, same minimum circuit values were adopted. So, several commercial diodes were selected in base their characteristics for the present use case, such as MBR0520L, BAT15-03W, 1PS79SB31, NSR20F30NXT5G, NSR0320MW2T1G, NSVR351SDSA3, STPS20L15G. So finally, simulated with their appropriate spice model. In table 8-6 and figure 8-19 achieved results with detailed conditions are shown:

Table 8-6: Comparative results between different diodes at 0.1 suns and 5 ºC temperature ambient conditions.

Diode	Vin (Vp)	Vout (V)	Iout (mA)	Pout (mW)	Pin (mW)	η (%)
MBR0520L	2.221	2.674	6.686	17.884	19.438	92.01
BAT15-03W	2.332	2.636	6.591	17.378	20.177	86.13
1PS79SB31	2.253	2.675	6.687	17.89	19.692	90.85
NSR20F30NXT5G	2.268	2.688	6.72	18.066	19.759	91.43
NSR0320MW2T1G	2.238	2.676	6.69	17.907	19.55	91.60
NSVR351SDSA3	2.273	2.669	6.673	17.815	19.79	90.02
STPS20L15G	2.089	2.614	6.536	17.092	18.485	92.46

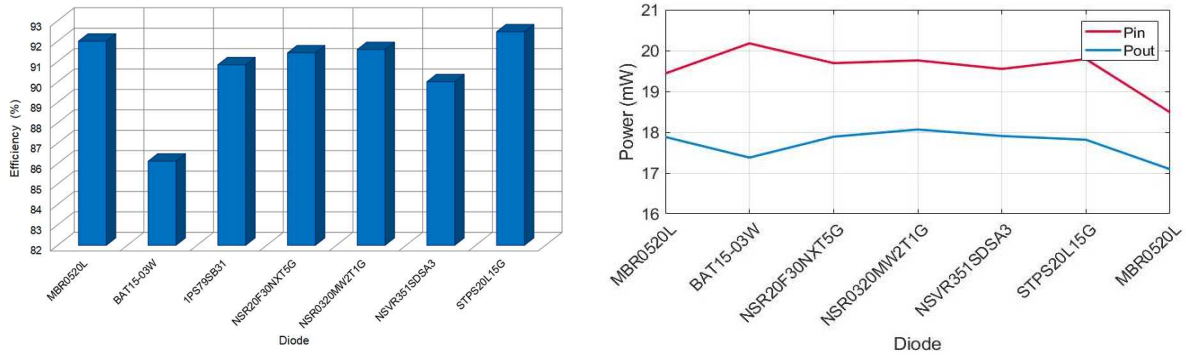

a) Efficiency. b) Input/output power.

Figure 8-17: Comparisons results between diodes at 0.1 suns and 5 ºC temperature ambient conditions.

Then, in the second case of diode selection, table 8-5 and figure 8-18 show achieved results with the maximum ambient condition:

Table 8-7: Comparative results between different diodes at 1 sun and 60 ºC temperature ambient conditions.

Diode	Vin (Vp)	Vout (V)	Iout (mA)	Pout (mW)	Pin (mW)	η (%)
MBR0520L	3.221	3.761	75.229	282.974	304.822	92.83
BAT15-03W	3.456	3.502	70.046	245.324	305.18	80.39
1PS79SB31	3.254	3.731	74.635	278.525	305.531	91.16
NSR20F30NXT5G	3.226	3.756	75.129	282.222	304.939	92.55
NSR0320MW2T1G	3.236	3.748	74.97	281.028	305.166	92.09
NSVR351SDSA3	3.31	3.675	73.502	270.134	306.289	88.20
STPS20L15G	3.134	3.805	76.108	289.623	302.117	95.86

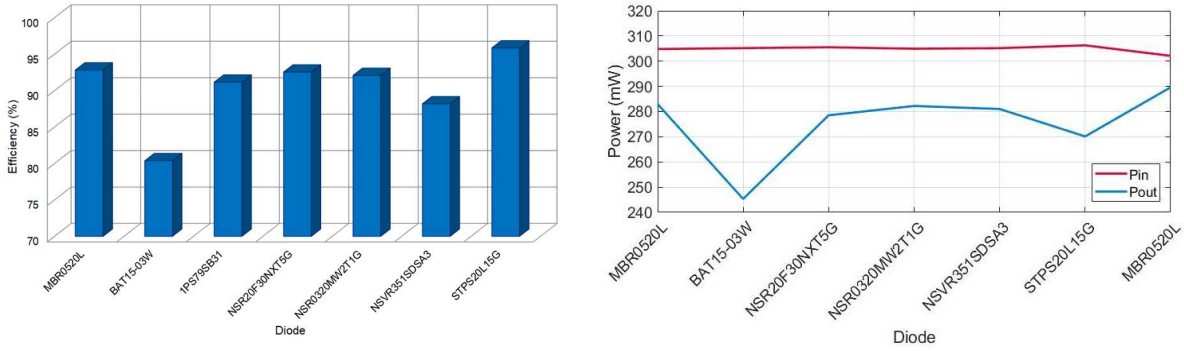

a) Efficiency. b) Input/output power.

Figure 8-18: Efficiency and input/output power comparisons between diodes at 1 sun and 60 ºC temperature ambient conditions.

Efficiencies in this case at both conditions are higher than 90 % except with BAT15-03W diode. Moreover, in low light and temperature ambient reach until 92 % and in high conditions until 95 %. STPS20L15G and MBR0520L present the best efficiency regarding the rest of diodes. However, with STPS20L15G converter efficiency is 0.4 % higher at worst conditions and 3 % better in best ambient conditions. Due to exposed reasons, the STPS20L15G diode has been selected to be the diode of DC/DC boost converter. However, after having simulation problems with STPS20L15G, MBR0520L is going to be used for simulations and STPS20L15G in the future hardware implementation.

The third step has the aim to obtain coil value and switching frequency, setting some conditions at the circuit simulation as in other both cases. In this first case, with minimum ambient conditions, duty-cycle 0.2, R_{load} = 2 kΩ and the selected diode and. In table 8-8 and figure 8-19 achieved results with detailed conditions are shown:

Table 8-8: Comparative results between different coils and frequencies at 0.1 suns and 5 ºC temperature ambient conditions.

L (µH)	T (µs)	fsw (kHz)	Vin (Vp)	Vout (V)	Iout (mA)	Pout (mW)	Pin (mW)	Pcontrol (µW)	η_total (%)
100	10	100	2.377	5.872	2.936	17.249	20.458	137.85	84.18
	20	50	1.611	5.168	2.584	13.354	14.614	62.802	91.32
	30	33.3	1.094	4.282	2.141	9.171	10.06	38.516	91.12
	40	25	0.938	4.03	2.015	8.124	8.659	29.024	93.79
	50	20	0.768	3.6	1.8	6.482	7.113	24.891	91.10
200	10	100	3.278	6.266	3.133	19.635	20.743	133.97	94.52
	20	50	2.386	6.192	3.096	19.175	20.512	60.406	93.42

	30	33.3	1.86	5.628	2.814	15.841	16.68	41.029	94.93
	40	25	1.604	5.19	2.595	13.471	14.549	30.029	92.56
	50	20	1.298	4.667	2.333	10.891	11.882	24.737	91.63
	10	100	3.334	6.221	3.11	19.351	20.168	124.32	95.82
	20	50	3.076	6.518	3.259	21.245	22.034	66.122	96.35
300	30	33.3	2.604	6.448	3.224	20.794	21.639	44.911	96.05
	40	25	2.12	6.021	3.011	18.127	18.712	34.287	96.84
	50	20	1.894	5.628	2.814	15.841	16.96	26.132	93.38

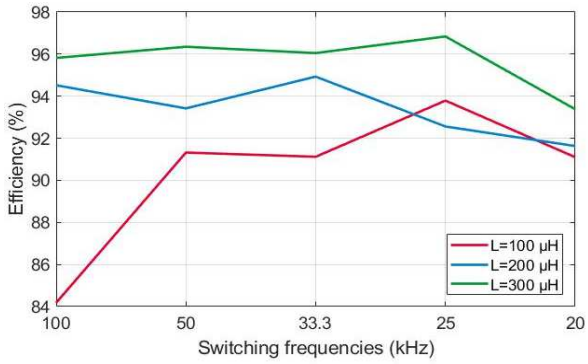

a) Efficiency vs. switching frequency.

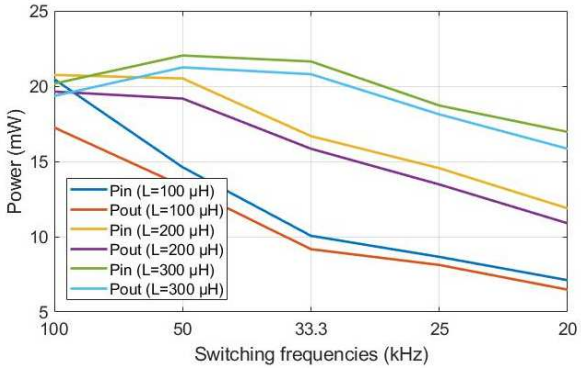

b) power input/output vs. switching frequency.

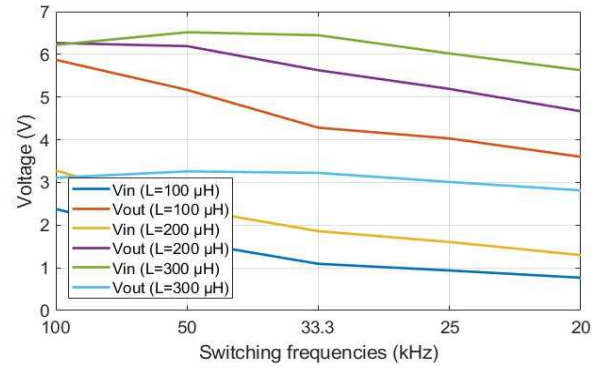

c) Voltage input/output vs. switching frequency

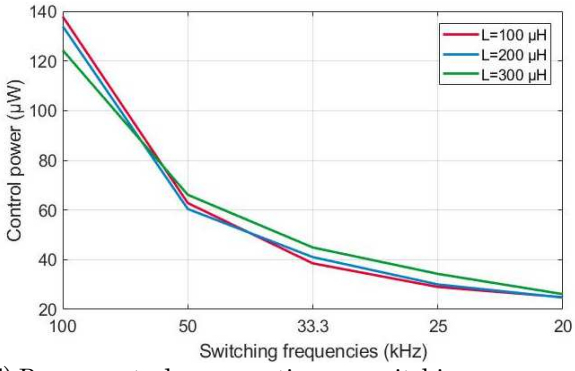

d) Power control consumption vs. switching frequency.

Figure 8-19: Comparative results between different coils and frequencies at 0.1 suns and 5 °C temperature ambient conditions.

In the second case, simulations have been realized with 1 sun and 60 °C temperature ambient conditions. Table 8-9 and figure 8-20 show achieved results:

Table 8-9: Comparative results between different coils and frequencies at 1 sun and 60 °C temperature ambient conditions.

L (µH)	T (µs)	fsw (kHz)	Vin (Vp)	Vout (V)	Iout (mA)	Pout (mW)	Pin (mW)	Pcontrol (µW)	η_total (%)
	10	100	4.1	6.408	32.04	205.319	217.159	144.07	94.40
	20	50	3.785	7.228	36.143	261.27	276.827	76.571	94.30
100	30	33.3	3.48	7.546	37.724	284.631	304.52	52.631	93.42
	40	25	3.263	7.512	37.561	282.178	305.686	33.705	92.28
	50	20	2.765	7.2	35.977	258.887	280.732	28.683	92.19
	10	100	4.207	5.848	29.242	171.023	178.726	143.69	95.55
200	20	50	4.127	6.327	31.639	200.212	209.853	73.559	95.33
	30	33.3	3.988	6.805	34.018	231.554	243.55	48.988	95.03

	40	25	3.89	7.208	36.04	259.786	277.011	36.973	93.74
	50	20	3.74	7.303	36.487	266.706	286.158	29.011	93.17
	10	100	4.207	5.848	29.24	171.023	179.139	143.8	95.33
	20	50	4.218	5.813	29.067	168.984	176.696	71.312	95.56
300	30	33.3	4.136	6.322	31.617	199.987	212.42	48.61	94.10
	40	25	4.009	6.678	33.391	223.001	238.667	37.604	93.40
	50	20	3.992	6.904	34.52	238.333	256.205	28.677	93.00

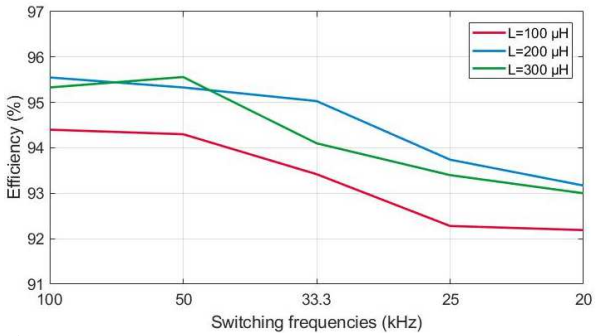

a) Efficiency vs. switching frequency.

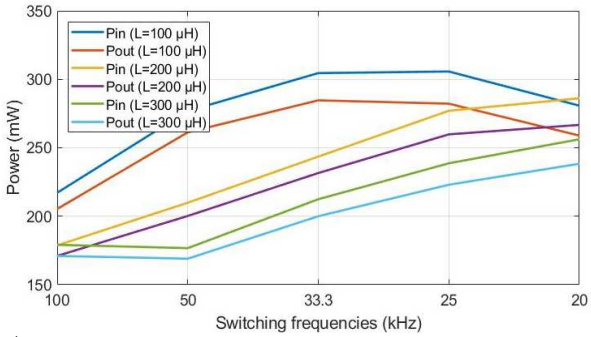

b) power input/output vs. switching frequency.

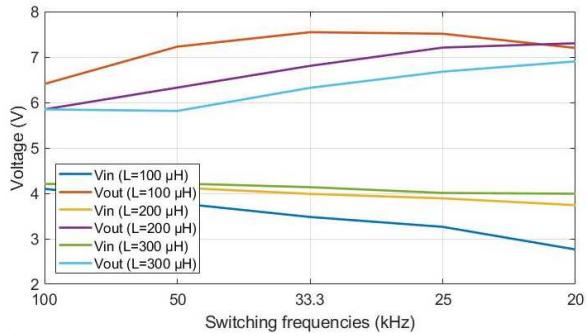

c) Voltage input/output vs. switching frequency.

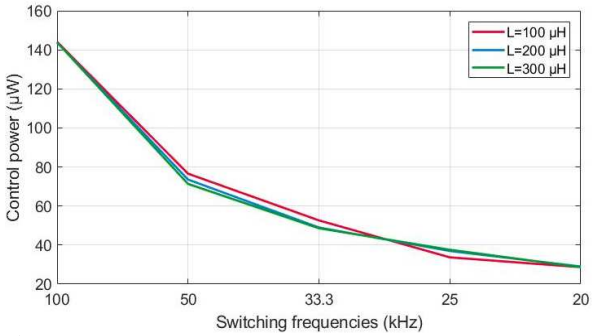

d) Power control consumption vs. switching frequency.

Figure 8-20: Comparative results between different coils and frequencies at 1 sun and 60 °C temperature ambient conditions.

The simulation results give that the suitable value for the coil is 200 µH. With 0.1 suns and 5 °C temperature condition best coil value is 100 µH and with 1 sun and 60 °C temperature best coil is 300 µH. However, each value in opposite condition is the worst one; consequently, 200 µH is an intermediate value which gives stability.

Selection of switching frequency depends on input condition. For low input power, the switching frequency which has the best behaviour is 100 kHz. Moreover, for high input power, the switching frequency which has the best behaviour is 20 kHz. Thus, a value close to these frequencies would be used at the corresponding condition of irradiance and temperature. It could be observed, control frequency switching must be dynamic, depending on ambient conditions or input ranges. Finally, appropriate duty-cycle and resistive load for each case would be searched in next section.

8.1.3 Simulations and results of the converter

After making components selection and establish operation modes of control, several simulations have been realized to analyse, adjust and search the maximum efficiency of the converter at different ambient conditions and input power levels.

Table 8-10 and figure 8-22 shows maximum output values obtained in simulations:

Table 8-10: Converter sweep maximum results with different irradiance and temperature.

Ambient conditions		DC/DC operation conditions			Output values				
G (suns)	T (ºC)	f_{sw} (kHz)	R_{load} (Ω)	D	V_{in} (V)	V_{out} (V)	P_{in} (mW)	P_{out} (mW)	η (%)
0.1	5	150	500	0.2	2.858	3.856	22.633	21.247	93.88
0.25	30	86	400	0.3	3.043	4.958	65.51	61.476	93.84
0.5	15	66	150	0.3	3.141	4.283	130.061	122.292	94.03
0.75	40	45	100	0.3	3.074	4.42	210.78	195.57	92.78
1	60	25	50	0.2	3.206	3.76	304.45	283.18	93.45

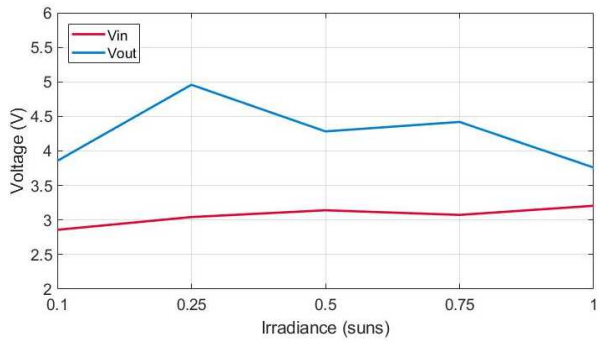

a) Input/output voltage.

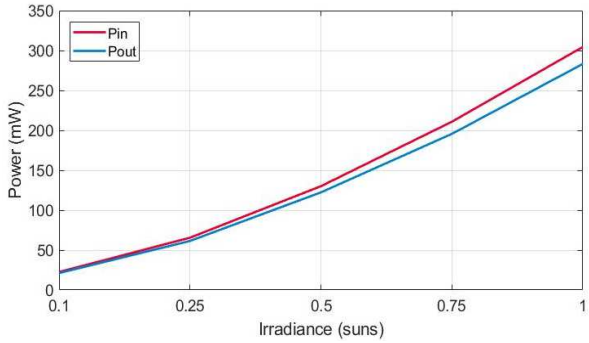

b) Input/output power.

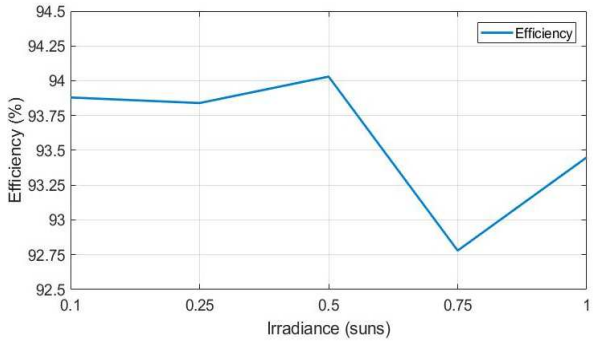

c) Efficiency.

Figure 8-21: Converter sweep maximum results with different irradiance and temperature.

The table 8-10 and figure 8-21c shows that the efficiency is always higher than 92 %. The highest efficiency is 94.03 % and is obtained with 0.5 at 15 ºC. The lowest efficiency is 92.30 % and is achieved with 0.75 at 40 ºC. Figure 8-21b shows that the power increases linearly with irradiance. When the input irradiance power is higher, the difference between input and output power increases. In addition, the output voltage is always inside the range limits, 3.7 V as minimum and to 4.9 V as the maximum (figure 8-21a).

All exposed maximum values were obtained after a load and duty-cycle sweep in selected five ambient condition ranges. Figure 8-22 shows obtained sweep results:

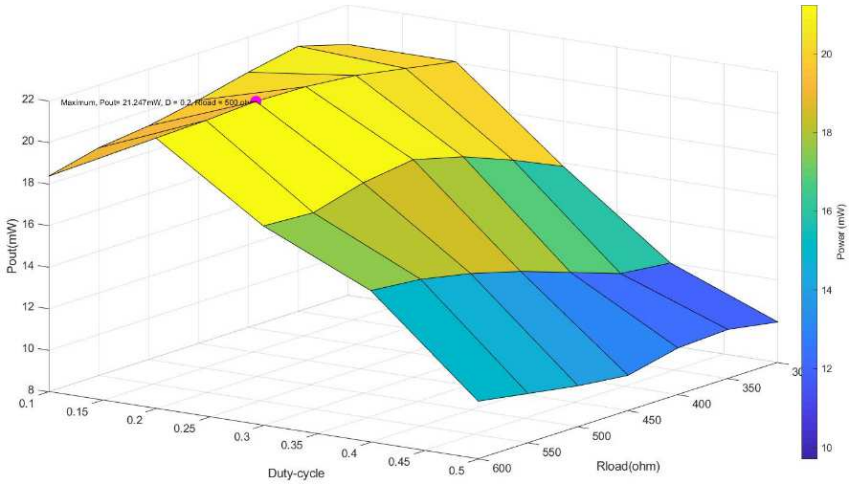

a) 0.1 suns irradiance, 5 ºC and 150 kHz switching frequency.

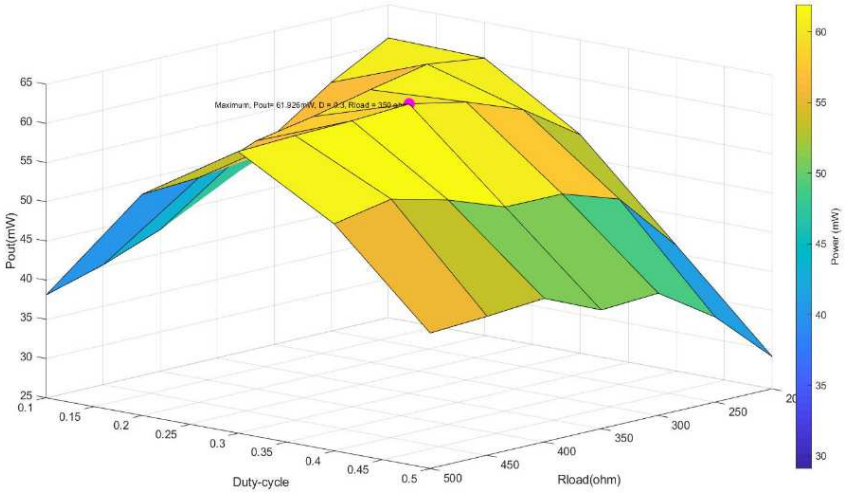

b) 0.25 suns irradiance, 30 ºC and 86 kHz switching frequency.

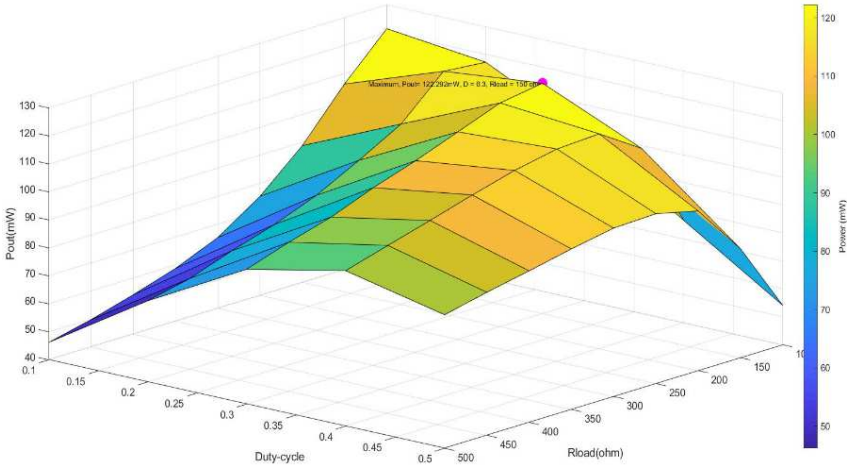

c) 0.5 suns irradiance, 15 ºC and 66 kHz switching frequency.

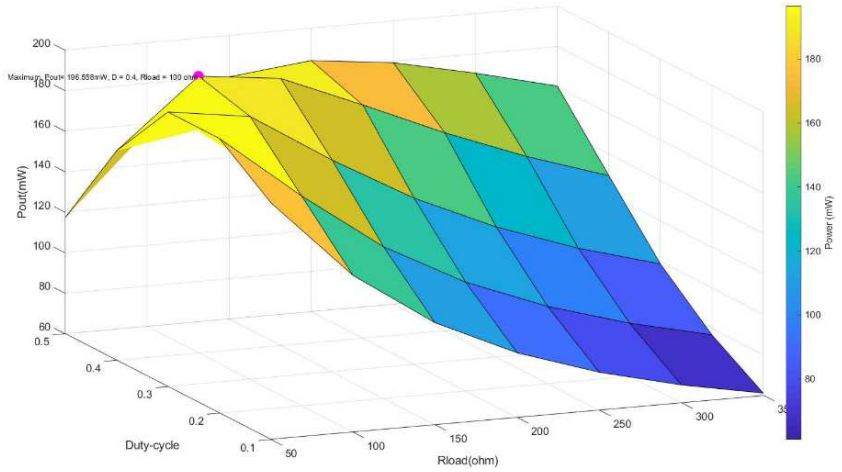

d) 0.75 suns irradiance, 40 ºC and 45 kHz switching frequency.

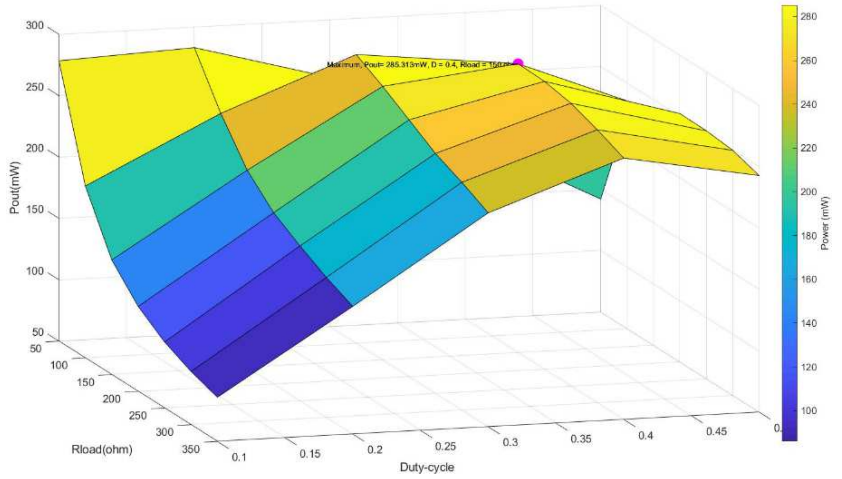

e) 1 sun irradiance, 60 ºC and 25 kHz switching frequency.

Figure 8-22: DC-DC output values dependent on different input and configuration conditions.

In the first case (figure 8-22a), the highest output power is 21.247 mW and is obtained with 0.2 duty-cycle and 500 Ω resistive load. In the second case (figure 8-22b), the highest output power is 61.476 mW and is obtained with 0.3 duty-cycle and 400 Ω resistive load. In the third case (figure 8-22c), the highest output power is 122.292 mW and is obtained with 0.3 duty-cycle and 150 Ω resistive load. In fourth case (figure 8-22d), the highest output power is 195.57 mW and is obtained with 0.3 duty-cycle and 100 Ω resistive load. In fifth case (figure 8-22e), the highest output power is 283.18 mW and is obtained with 0.2 duty-cycle and 50 Ω resistive load.

The results corroborate that converter works appropriately in boost mode for all ambient conditions.

Remark that, MOSFETs, diodes and coils operation signals are shown in appendix 16.2.3.

9. AC input system

The AC system includes the wind flow harvester, the AC/DC converter and the storage device shared with DC system. This system converts the wind potential energy into to mechanical energy, then to electromagnetic and afterward into the electrical one. First, the wind pressure power is harvested and converted to mechanical power with an efficiency $\eta_{mechanic}$. Next, mechanic power is converted to electric energy through the

generated electromagnetic field, with an efficiency of $\eta_{electric}$. Then, the necessity to convert and adequate the level of the harvested AC signal to a DC signal an appropriate level for his storage is made with an AC/DC converter, again with a quantity of efficiency, $\eta_{converter}$. Finally, the energy is stored at the capacitor.

Equation 9-1 calculate the described process mathematically, which is a multiplication between system conversion efficiencies and input wind power.

$$P_4 = \eta_{tot} * P_1 = \left(\eta_{mechanic} * \eta_{electric} * \eta_{converter}\right) * P_1 = \left(\eta_1 * \eta_2 * \eta_3\right) * P_1 \quad (9\text{-}1)$$

The figure 9-1 shows the AC system block diagram and energy conversions with respective efficiencies:

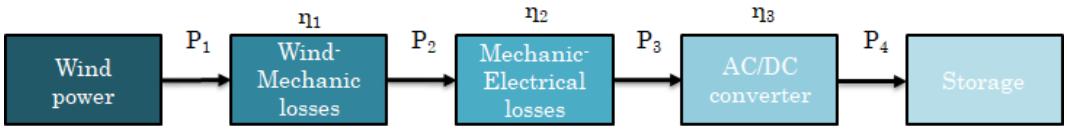

Figure 9-1: Block diagram of complete AC system of the double power manager.

9.1 Mini-turbine/reactor electro-mechanical model

From [129], the construction of an equivalent model of the turbine cell has started. The referenced work proposes a single phase electro-mechanical model of a miniature horizontal axis wind turbine or MHAWT. The implementation consists of the conversion of physical parameters and system behaviour in an electronic model to be able to simulate.

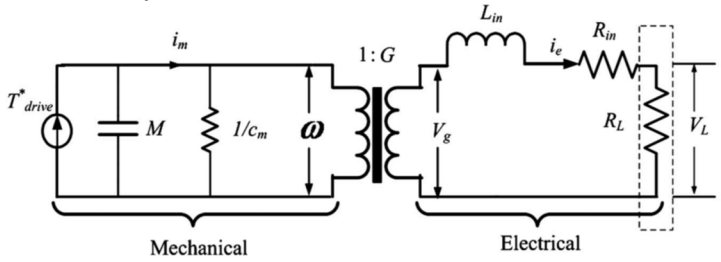

Figure 9-2: Reference horizontal turbine electro-mechanical model.

Instead of using a voltage generator as harvester output at simulation circuit, an equivalent electro-mechanical model has been implemented. This realistic model would give higher accuracy to AC/DC converter simulations.

9.1.1 Theoretical principles of mini turbine/reactor operation

T^*_{drive} of figure 9-2 represents the wind power value. At this point, after some tests, the physical operation principles of the turbine were not clear. With same wind flow velocity, when the turbine was inserted inside the same diameter pipe, higher output power level was observed in comparison with open space. From [236][237] was discovered that the main reason is the type of energy harvested. At open space location, the turbine harvest air kinetic energy, i.e., wind velocity. However, in a pipe, the turbine harvests air potential energy, i.e., wind pressure inside the pipe. Figure 9-3 shows described situation.

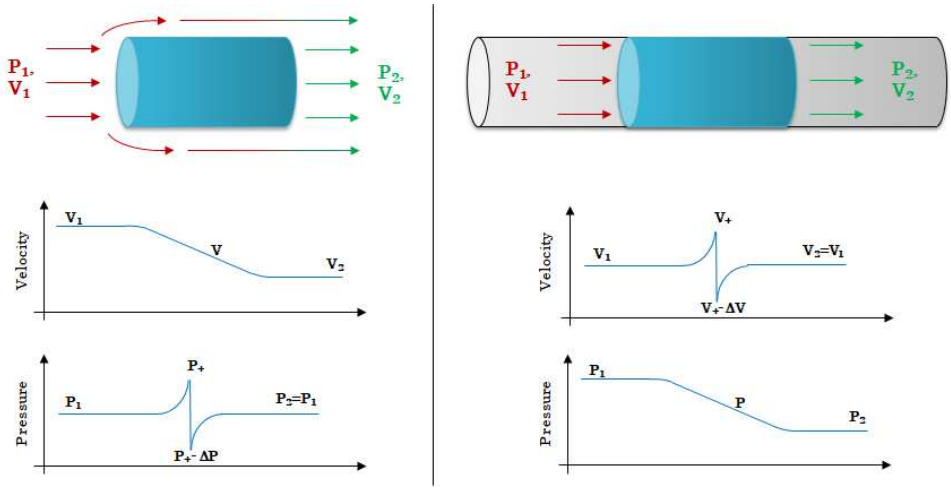

Figure 9-3: Open space operation principle versus test-bench operation principle.

In both cases, can see how happens the law of conservation of energy. On the left case, one side potential energy cancels the other side one and harvested energy comes from wind kinetic energy. On the right situation, the same behaviour happens but kinetic energy is cancelled and harvested energy comer from wind potential energy. Described behaviour is expressed as in equation 9-2:

$$E_{potential1} + E_{kinetic1} = E_{potential2} + E_{kinetic2} - E_{harvested} \tag{9-2}$$

In one hand, if the turbine is installed in a windy open space, absolute potential energy is 0, and the harvested power will be only the kinetic one, as equation 9-3. Where $P_1=P_2$ of potential energy. Besides, because of energy principle theorem, v_1 must be bigger than v_2, $v_1>v_2$, and consequently $\Delta v=v_1-v_2$.

$$E_{harvested} = \frac{1}{2}\rho(v_2^2 - v_1^2) \tag{9-3}$$

When the turbine starts to work under the wind condition, the rotor will rotate, harvest and convert the kinetic energy of the wind into mechanical energy. Wind kinetic power, by the aerodynamic equation of [130], is given by equation 9-4. However, the transformation of wind power into rotational power by the turbine rotor is a complex aerodynamic phenomenon described in [131] [132] [133]. Ideally, the power extracted from the ambient wind (P_{aero}) could be expressed as:

$$P_{wind} = \frac{1}{2}\rho v_1^3 A \rightarrow P_{aero} = \frac{1}{2}\rho v_1^3 A C_p(\lambda, \theta) \tag{9-4}$$

, where ρ is air density, v_1 is air velocity, A turbine area, and C_p Betz's law coefficient. This power coefficient or the aerodynamic efficiency of the rotor, which is a nonlinear function of the pitch angle θ of the turbine blades and tip speed ratio λ. θ is the angle of the blade element concerning the plane of rotation and λ is quotient between the tangential speed of the rotor blade tips and the incoming wind speed, expressed as:

$$\lambda = \frac{\omega * r}{v} \tag{9-5}$$

, where ω is the angular velocity (rad/s) and r the radius of the rotor. The power coefficient, $C_p(\lambda, \theta)$ Betz power coefficient equation is shown as in 9-6:

$$C_p(\lambda, \theta) = C_1\left[\left(\frac{c_2}{\lambda_i}\right) - c_3\theta - c_4\theta^{c_5} - c_6\right]e^{\left(-\frac{c_7}{\lambda_i}\right)} \tag{9-6}$$

, where λ_i is obtained with:

$$\lambda_i = \frac{1}{\left[\frac{1}{(\lambda + c_8\theta)}\right] - \left[\frac{c_9}{(\theta^3 + 1)}\right]} \tag{9-7}$$

Then, theoretical values and generated power have been calculated to verify if the operation principle is in concordance with obtained results in chapter 3. In addition, some dimensional and mechanic characteristics where measured and table 9-1 shows each element value.

Table 9-1: Micro-reactor dimensional-mechanic characteristics.

System values	
ρ	1.225
A_turbine	0.00045
r_turbine	0.016
r_rotor	0.00355
length_blades	0.01476
θ	34.45
weight	0.0032
length_swept	0.024
A_small_pipe	3.31E-05
A_big_pipe	0.000829

[134][135][136] propose Betz power coefficients for big turbines. However, in works [129][131] with small wind turbines Betz power coefficients are different. Hypothetically, second coefficients are adequate for this work. However, both coefficient pack were verified for this system with mathematical calculations. Analysing results could be say that coefficients for mini-turbines were more adequate (see appendix 16.3.1).

Table 9-2: Used Betz power coefficients for mathematical calculation of operation parameters.

C_p coefficient	c1	c2	c3	c4	c5	c6	c7	c8	c9
CSMWT	0.6	160	0.93	0	0	9.3	9.8	0.037	0

Before showing achieved results, the way to obtain angular velocity parameter in rad/s is explained. To make the conversion from w (rpm) to w (rad/s) must multiply rpm value with 0,1047. This value has an explanation, if N is defined as the number of revolutions per minute and N/60 are revolutions performed in one second. Then, one revolution is equal to 2π radians. Finally, the conversion is made with 2πN/60, which is equivalent to 0,1047N.

The parameter wind flow is obtained by multiplying turbine area with flow velocity. And finally, for P_{wind}, P_{aero}, $C_p(\lambda,\theta)$, λ_i and λ parameters calculation has been done with described equations 9-4, 9-5, 9-6 and 9-7 respectively. Table 9-3 and figure 9-4 show achieved results.

Table 9-3: Wind and mechanical calculated values at open space condition.

w (rpm)	w (rad/s)	Velocity (m/s)	P_{wind} (mW)	P_{aero} (mW)	$C_p(\lambda.\theta)$	λ_i	λ	Q (m^3/s)
9495	997	3	13.719	3.622	0.264	2.454	1.180	0.002
14271	1498	4	32.518	9.104	0.280	2.605	1.330	0.003
19344	2031	5	63.513	18.147	0.286	2.717	1.442	0.004
24057	2526	6	109.750	31.443	0.286	2.769	1.495	0.005
26180	2749	7	174.279	49.484	0.284	2.669	1.394	0.006
30666	3219	8	260.148	74.230	0.285	2.704	1.429	0.007
35995	3779	9	370.405	106.114	0.286	2.765	1.491	0.007
39616	4159	10	508.101	145.507	0.286	2.751	1.477	0.008

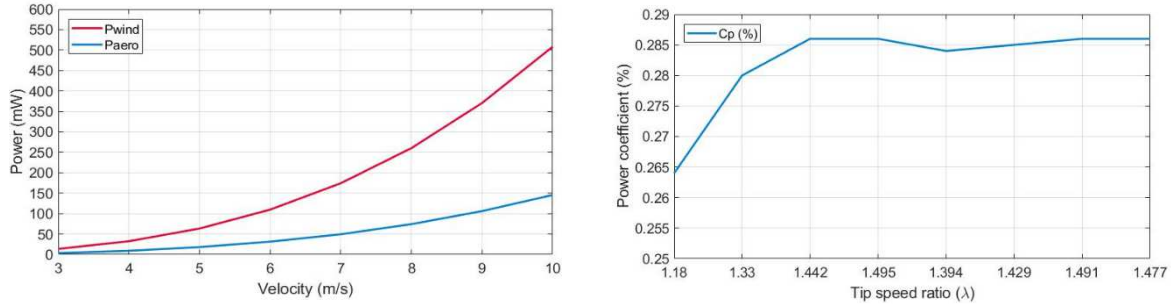

a) The power difference between P_{wind} and P_{aero} at different wind velocities.

b) Aerodynamic efficiency at same ranges.

Figure 9-4: Open space system values.

For this case, the mechanical design seems to be incorrect for this purpose. P_{wind} and P_{aero} are sometimes lower than achieved results with test exposed in chapter 3. Moreover, the electrical efficiency is going to be near 0 as could be seen in table 9-3. Instead, these results were decided to continue with the calculation [129] of harvested electric power to claim this theory was not valid to apply in this system.

After turbine captures the wind kinetic energy, the rotor rotates at a specific angular velocity under the drive torque.

$$T_{drive} = \frac{P_{aero}}{\omega} = \frac{\rho v_1^3 A C_p(\lambda,\theta)}{2\omega} \tag{9-8}$$

The drive torque is proportional to the cubic of the wind velocity, power coefficient and inversely proportional to the angular velocity of the rotor. Moreover, when the turbine rotates in a low tip speed ratio, the ratio of C_p=ω mostly remained constant. Therefore, the drive torque (T_{drive}) is expressed as in 9-9 and could be treated as a constant if the ambient wind speed remains constant. For this system, T_{drive} achieved values are shown in table 9-4 and figure 9-5.

Table 9-4: Numerical values of the torque vs. angular velocity.

Angular Velocity (rad/s)	Tdrive (mW/rad/s)
997	0.0036
1498.51	0.0061
2031.14	0.0089
2526	0.0124
2749	0.0180
3219.99	0.0231
3779.50	0.0281
4159.75	0.0350

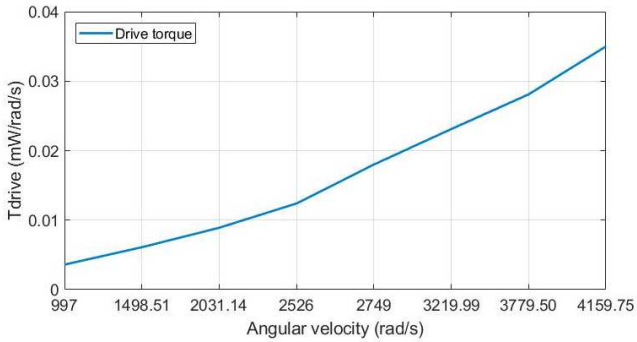

Figure 9-5: Torque vs angular velocity.

The electro-mechanical coefficient, G (Volt/rad/s), is obtained with a linear relationship between the generated voltage, v (m/s), and the angular velocity, ω (rad/s):

$$G = \frac{v}{\omega} \tag{9-9}$$

Electro-mechanical coefficient results for different air velocities (3-10 m/s) are exposed in table 9-4 and figure 9-6:

Table 9-5: Numerical values of the electro-mechanical coefficient for different air velocities.

Velocity (m/s)	Voltage (V)	w (rad/s)	G (Volt/rad/s)
3	2.05	997	0.00205
4	3.02	1498.51	0.00202
5	4.17	2031.14	0.00205
6	5.32	2526	0.00211
7	5.98	2749	0.00218
8	6.66	3219.99	0.00207
9	7.57	3779.50	0.00200
10	8.38	4159.75	0.00202

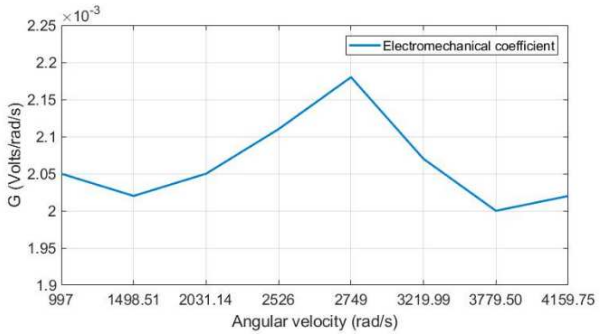

Figure 9-6: Electro-mechanical coefficient for different air velocities.

Then, harvested power is calculated at load with equation 9-10:

$$P_{e\_load} = \frac{G^2 \omega^2 R_L}{(R_L + R_{in})^2} \tag{9-10}$$

Harvested power results for different loads (1-36 Ω) and air velocities (3-10 m/s) are exposed in table 9-6 and figure 9-7:

Table 9-6: Calculated harvester power values for different loads and air velocities.

Pe_load (mW)													
Velocity (m/s)	1 Ω	4 Ω	7 Ω	10 Ω	13 Ω	16 Ω	19 Ω	22 Ω	25 Ω	28 Ω	31 Ω	34 Ω	36 Ω
3	0.029	0.074	0.090	0.095	0.095	0.092	0.088	0.085	0.081	0.077	0.074	0.070	0.068
4	0.063	0.163	0.198	0.207	0.206	0.201	0.193	0.185	0.176	0.168	0.161	0.153	0.149
5	0.121	0.309	0.376	0.394	0.392	0.382	0.367	0.351	0.335	0.320	0.305	0.292	0.283
6	0.196	0.503	0.611	0.641	0.638	0.621	0.597	0.571	0.545	0.520	0.497	0.475	0.461
7	0.248	0.636	0.773	0.811	0.807	0.785	0.755	0.723	0.690	0.658	0.629	0.600	0.583
8	0.308	0.789	0.959	1.006	1.002	0.974	0.937	0.897	0.856	0.817	0.780	0.745	0.723
9	0.398	1.018	1.237	1.299	1.293	1.257	1.209	1.157	1.105	1.054	1.007	0.962	0.933
10	0.488	1.250	1.519	1.594	1.587	1.543	1.484	1.420	1.356	1.294	1.235	1.180	1.146

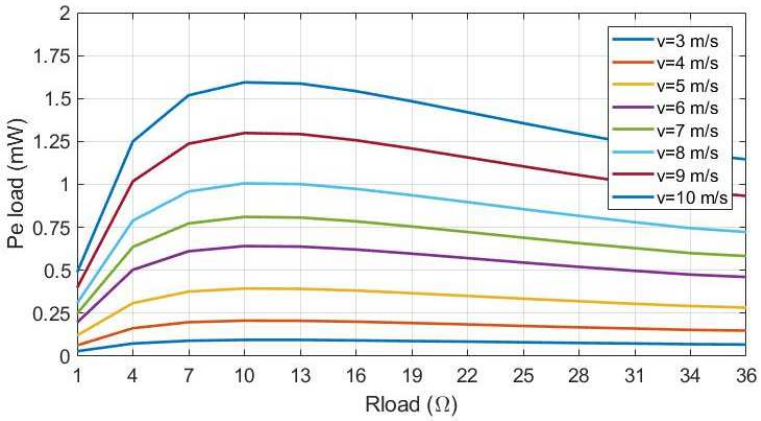

Figure 9-7: Calculated harvester power values for different loads and air velocities.

Finally, electric losses dependent on internal resistance (R_{in}) are given by equation 9-11:

$$P_{e\_load} = \frac{G^2 \omega^2 R_{in}}{(R_L + R_{in})^2} \tag{9-11}$$

Electric power losses results for 1-36 Ω and 3-10 m/s ranges are shown in table 9-7 and figure 9-8:

Table 9-7: Calculated harvester electric losses values for different loads and air velocities.

Pe_loss (mW)													
Velocity (m/s)	1 Ω	4 Ω	7 Ω	10 Ω	13 Ω	16 Ω	19 Ω	22 Ω	25 Ω	28 Ω	31 Ω	34 Ω	36 Ω
3	0.320	0.205	0.142	0.104	0.080	0.063	0.051	0.042	0.036	0.030	0.026	0.023	0.021
4	0.698	0.447	0.310	0.228	0.175	0.138	0.112	0.092	0.092	0.06	0.057	0.050	0.046
5	1.328	0.850	0.590	0.434	0.332	0.262	0.212	0.176	0.176	0.126	0.108	0.094	0.087
6	2.160	1.382	0.960	0.705	0.540	0.427	0.346	0.286	0.240	0.204	0.176	0.154	0.141
7	2.732	1.748	1.214	0.892	0.683	0.540	0.437	0.361	0.304	0.259	0.223	0.194	0.178
8	3.390	2.170	1.507	1.107	0.848	0.670	0.542	0.448	0.377	0.321	0.277	0.241	0.221
9	4.375	2.800	1.945	1.429	1.094	0.864	0.700	0.579	0.486	0.414	0.357	0.311	0.285
10	5.370	3.437	2.387	1.754	1.343	1.1	0.859	0.710	0.597	0.508	0.438	0.382	0.350

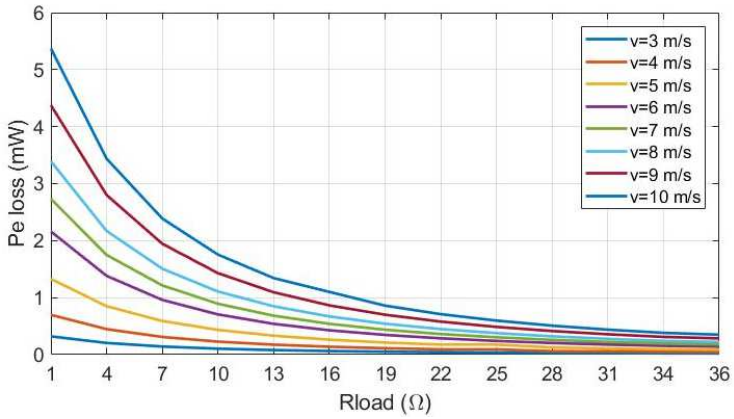

Figure 9-8: Calculated harvester electric losses for different loads and air velocities.

Analysing mathematical results is observed that incorrect conditions are produced. $P_{wind} < P_{electric}$ and $P_{aero} < P_{electric}$, these behaviours are entirely impossible because they do not fulfil the law of conservation of energy. To corroborate mathematical results and avoid a possibility of error in calculations, four tests were done at open space condition.

An experiment was carried out in open space ambient to verify described basics. A fan with controllable wind velocity levels, an anemometer to measure the wind velocity, the mini-turbine to analyse and the oscilloscope to measure generated signals and energy levels were used for open space tests, as could be seen in figure 9-9.

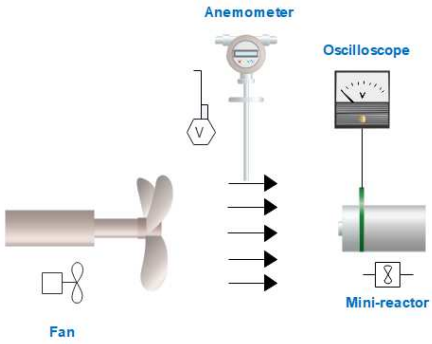

Figure 9-9: Test set-up diagram to measure wind power at open space for turbine model.

For test were carried out:

- Wind velocity → 3 m/s and 4 m/s
- Resistive load → 36 Ω and 1e6 Ω

Table 9-8 and figure 9-10 show obtained values with tests. These results are similar to calculated values with the mathematical equation of described operation principle.

Table 9-8: Open space test to verify turbine operation mode.

	V = 3 m/s		V = 4 m/s	
R_{load} (Ω)	36	1e6	36	1e6
Voltage (V_{pp})	0.06	0.152	0.116	0.28
$P_{electric}$ (mW)	0.037	8.66e-6	0.14	2.95e-5
P_{wind} (mW)	13.718		32.518	
P_{aero} (mW)	0.389	0.473	1.019	1.295
λ	0.043	0.088	0.066	0.124
$C_p(\lambda.\theta)$	0.028	0.034	0.031	0.039
Efficiency (%)	0.269	6.31e-6	0.43	9.07e-5

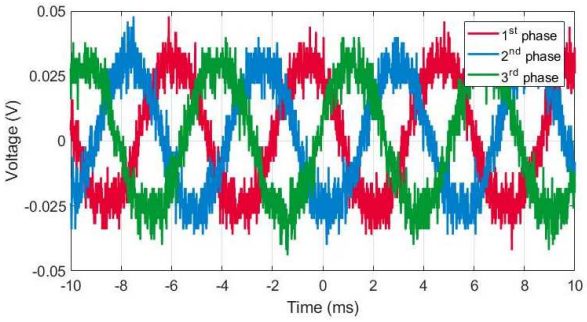

a) 3 m/s air velocity at open space for 36 Ω load.

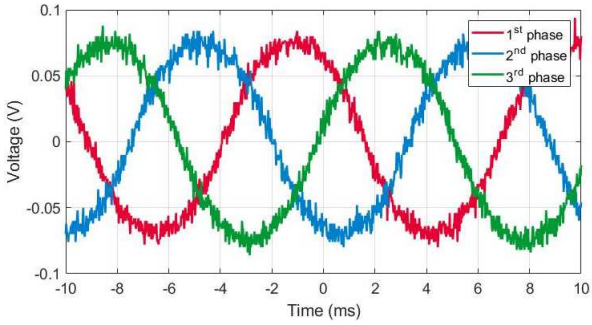

b) 3 m/s air velocity at open space for 1e6 Ω load.

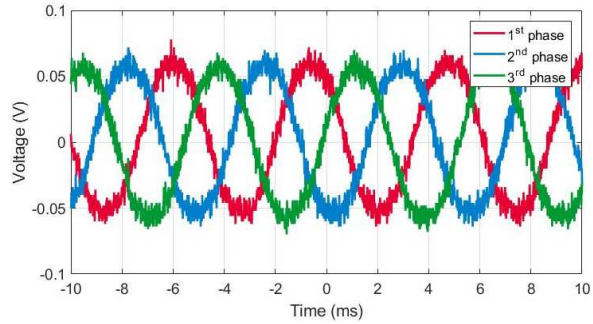

c) 4 m/s air velocity at open space for 36 Ω load.

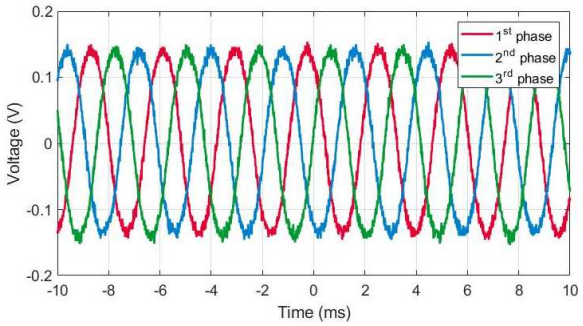

d) 4 m/s air velocity at open space for 1e6 Ω load.

Figure 9-10: Measured signals of the turbine.

Achieved results are in concordance with calculating results. **Consequently, the conclusion which has been obtained with calculated and achieved results is the equation (9-4), and it is not useful to calculate wind power in a pipe**. The main reason is that the environment it is different, and pressures parameter must be considered to achieve the correct value of wind power through the turbine.

Thus, if the turbine is installed inside a windy pipe, absolute kinetic energy is 0, and the harvested power will be only the potential energy, as equation 9-8. By Bernoulli's principle and considering that the air is incompressible, wind velocities must be same in both sides of the pipe, $v_1=v_2$. In addition, due to energy principle theorem, P_1 must be bigger than P_2, $P_1>P_2$, and consequently $\Delta P=P_1-P_2$.

$$E_{harvested} = E_{potential1} - E_{potential2} \tag{9-12}$$

Next hydraulic equation gives potential wind power:

$$P_{wind} = \gamma Q H \tag{9-13}$$

, where γ is air specific weight, Q is the flow quantity across the pipe (A*v), and H is the dynamic pressure difference between both sides. Electric power is achieved form wind potential power including mechanical power loses and calculated as in 9-10 equation:

$$P_{electric} = \Delta P_{wind} - P_{mechanic\_losses} \tag{9-14}$$

So harvested energy corresponds to the potential energy of wind, no kinetic energy. In addition, mechanical efficiency is achieved by subtracting air power with electrical power. Moreover, no application of Betz's numbers or law is produced as in wind turbines. This law is only for turbines that harvest energy from wind velocity, i.e., from kinetic energy. From exposed reasons, which this system harvest energy from available pressure and no from wind velocity, **terminologically it is not a mini-turbine it is a mini-reactor**.

Moreover, the correct or appropriate environment to work for this harvester is inside a pipe or in a piping area.

9.1.2 Tests for model construction

With the aim to build the equivalent electro-mechanical model of the mini-reactor and verify that the harvested energy is potential, two tests were done. A first test to achieve the wind flow power parameter and a second for system damping value. In next two sub-sections, these tests are described.

9.1.2.1 Achievement of wind power

Wind flow equivalent electric power must be obtained to be used as the input value in the electro-mechanical model of the mini-reactor. Thus, some new measurement must be done with the prototype at the test-bench. Despite, the developed test-bench must be modified to be able to obtain wind power value for each wind pressure/velocity. The test-bench has been updated for this activity with next elements:

- Air pump
- Gate valve
- Control valve with gauge
- Connection pipe
- Two pitot tube
- Anemometer
- Oscilloscope
- Test-bench
- Micro-turbine

An air pump with gate valve provides the air flow, which pressure control valve controls its insertion. The pitot tubes measure the pressure value before and after the mini-reactor and the anemometer measures the air velocity. Measurements and data are collected with the oscilloscope for postprocessing. The set-up diagram with described elements is shown in figure 9-11:

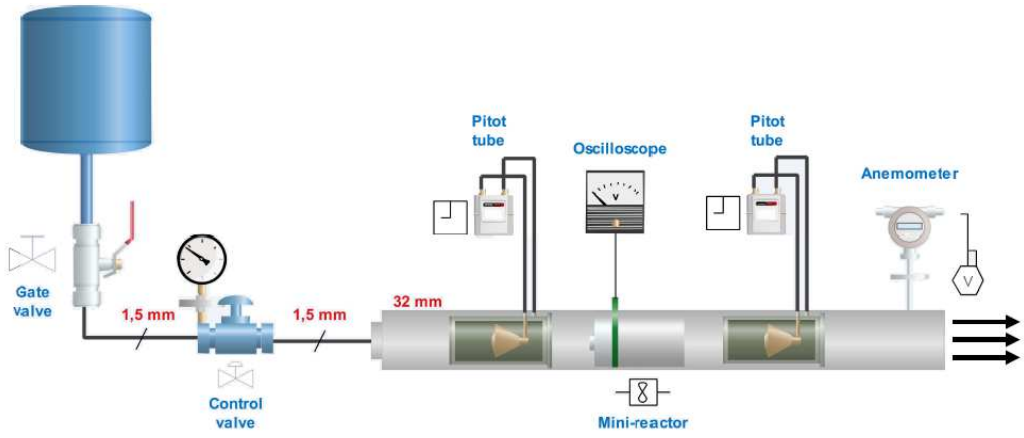

Figure 9-11: Test set-up diagram to measure wind power for the micro-reactor model.

For installing the new measurement devices, some changes have been done in the test-bench. Three new holes were manufactured, one just before the mini-turbine, another just after the mini-turbine (for pitot tubes) and the third one near the pipe end to measure the air velocity with the anemometer.

After that, the measurement devices were installed, and the tests to achieve the pressure level for different wind velocities were realized. Finally, obtained pressure values are shown in table 9-9. In addition, equivalent wind power for each level is calculated and put it in the same table.

Table 9-9: Obtained wind power values at different wind flow ranges.

γ (g/cm³)	A (cm²)	v (cm/s)	Q (cm³/s)	H (mbar)	Wind power (mW)
0.0013	8.04	300	2412	20	62.712
0.0013	8.04	400	3216	36	150.509
0.0013	8.04	500	4020	52	271.752
0.0013	8.04	600	4824	91	570.679
0.0013	8.04	700	5628	112	819.437
0.0013	8.04	800	6432	142	1187.347
0.0013	8.04	900	7236	144	1354.579
0.0013	8.04	1000	8040	163	1703.676

Unless the harvested energy corresponds to pressure energy, several graphics and data are expressed as a function of the air flow velocity and not as a function of the pressure because in m/s the scale is linear. A linear scale of velocity between 3-10 m/s than a non-linear scale of pressure between 62-1703 mbar is easier to interpret. However, table 9-9 could be used as the reference to make the conversion.

After achieving wind power for each flow velocity, in next pages reactor efficiencies, powers and losses are presented for same loads used through this work. Losses and efficiencies help to know the behaviour of different system parts.

Firstly, table 9-11 and figure 9-12 show results with impedance matching load, 27 Ω. These values gave the maximum efficiency and produced electrical power, thus, lowest mechanical losses.

Table 9-10: Generated electric power, mechanical losses, and system efficiency values from 3 m/s to 10 m/s with 27 Ω load.

Wind power (mW)	Elec. Power (mW)	Mech. losses (mW)	Efficiency (%)
62.712	15.284	47.428	24.37
150.509	31.155	119.354	20.70
271.752	55.489	216.263	20.42
570.679	111.023	459.657	19.45
819.437	160.716	658.721	19.61
1187.347	239.686	947.661	20.19
1354.579	272.543	1082.036	20.12
1703.676	333.146	1370.530	19.55

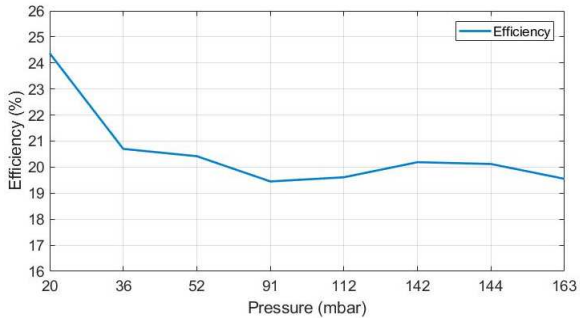

a) System efficiency

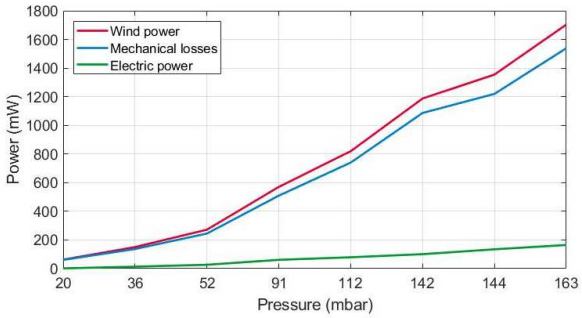

b) power differences/losses through different steps of micro-reactor.

Figure 9-12: Generated values with 27 Ω load.

Secondly, table 9-12 and figure 9-13 show results with 11 Ω load. In this case, due to the impedance mismatching mechanical losses increase and system efficiency starts to decrease.

Table 9-11: Generated electric power, mechanical losses, and system efficiency values from 3 m/s to 10 m/s with 11 Ω load.

Wind power (mW)	Elec. Power (mW)	Mech. losses (mW)	Efficiency (%)
62.712	7.770	54.942	12.39
150.509	12.543	137.966	8.33
271.752	16.933	254.819	6.23
570.679	89.150	481.529	15.62
819.437	129.939	689.497	15.86
1187.347	182.704	1004.643	15.39
1354.579	246.128	1108.451	18.17
1703.676	313.920	1389.756	18.43

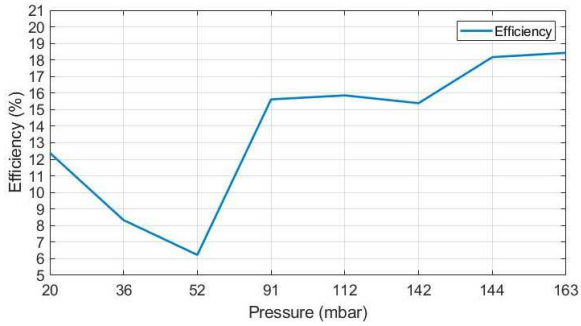

a) System efficiency

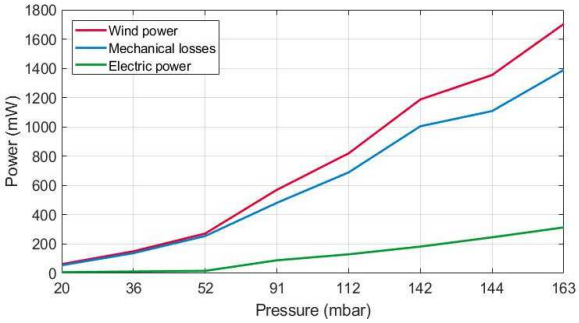

b) power differences/losses through different steps of micro-reactor.

Figure 9-13: Generated values with 11 Ω load.

Thirdly, table 9-13 and figure 9-14 show results 100 Ω load. In this case, there is a higher impedance mismatching, and mechanical losses increase more than in before case. System efficiency does not reach the 11 %.

Table 9-12: Generated electric power, mechanical losses, and system efficiency values from 3 m/s to 10 m/s with 100 Ω load.

Wind power (mW)	Elec. Power (mW)	Mech. losses (mW)	Efficiency (%)
62.712	1.872	60.840	2.98
150.509	13.639	136.870	9.06
271.752	26.907	244.845	9.90

570.679	61.339	509.340	10.75
819.437	79.250	740.187	9.67
1187.347	100.866	1086.481	8.50
1354.579	134.793	1219.786	9.95
1703.676	164.983	1538.693	9.68

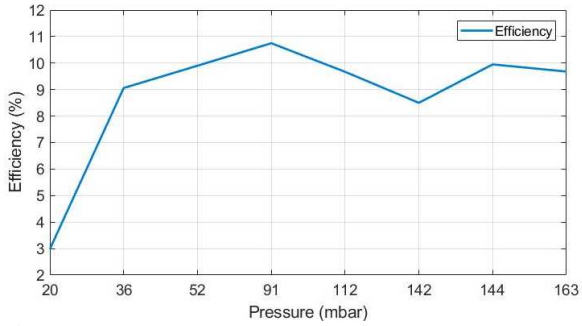

a) System efficiency

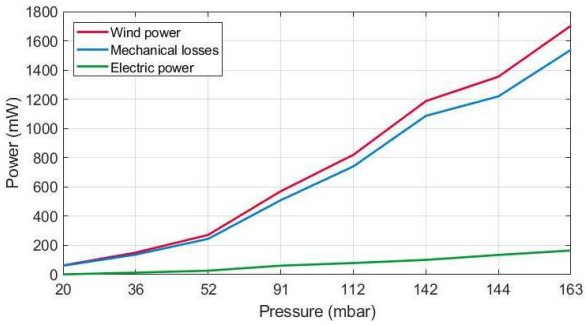

b) power differences/losses through different steps of micro-reactor.

Figure 9-14: Generated values with 100 Ω load.

Finally, table 9-14 and figure 9-15 show results with 1 MΩ load or equivalent to open circuit condition. Efficiency reaches 2.57 %, and mechanical losses are practically equivalent to wind power.

Table 9-13: Generated electric power, mechanical losses, and system efficiency values from 3 m/s to 10 m/s with 1000 Ω load.

Wind power (mW)	Elec. Power (mW)	Mech. losses (mW)	Efficiency (%)
62.712	1.613	61.099	2.57
150.509	3.446	147.063	2.29
271.752	6.721	265.031	2.47
570.679	11.036	559.644	1.93
819.437	13.684	805.753	1.67
1187.347	16.799	1170.549	1.41
1354.579	21.210	1333.369	1.57
1703.676	26.863	1676.813	1.58

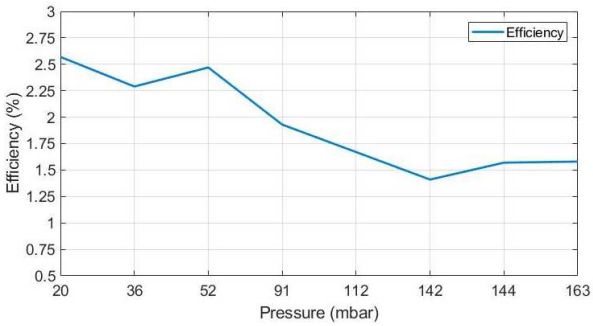

a) System efficiency

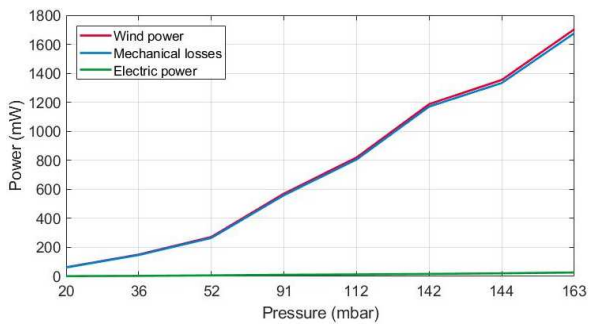

b) power differences/losses through different steps of micro-reactor.

Figure 9-15: Generated values with 1000 Ω load.

Electric impedance matching is correlated with the generated power. In one hand, if impedance matching is the adequate, maximum electrical efficiency is achieved, and mechanical losses decrease dramatically. The system efficiency with impedance matching is approximately 20 %. In the other hand, if impedance mismatching is produced, electric

efficiency is close to 0, and mechanical losses are next to wind power. This effect has been seen when 27 Ω or 1 MΩ are connected to the mini-reactor.

9.1.2.2 Achievement of damping value

Damping effect constitutes a mechanical element at the electro-mathematical model. This behaviour is represented in the model by resistance with the value of:

$$R_{damping} = \frac{1}{c_m} \tag{9-15}$$

, where c_m is the damping coefficient. The aerodynamic damping can be determined using non-linear time domain equation. However, the damping δ (aerodynamic plus structural damping) can also be calculated from the logarithmic decrement, as follows:

$$\delta = \frac{1}{n} log\left(\frac{x_{n-p}}{x_n}\right) \tag{9-16}$$

This relation is only meaningful for underdamped systems because the logarithmic decrement is defined as the natural log of the ratio of any two successive amplitudes, and only underdamped systems exhibit oscillation. This system belongs to this group, consequently defined equation 9-16 could be used for damping coefficient calculation.

A method to derive the aerodynamic damping ratio is to analyse the decay of the free vibration of the tower top after a pulse loading. For that, the test to measure and save data of damper curve has proceeded. First, the mini-reactor has been put it in normal work operation. When the usual operation mode was achieved, the mini-reactor was dramatically braked, saving at the same time the voltage data at the output of the generator. Figure 9-16 shows the mentioned curve:

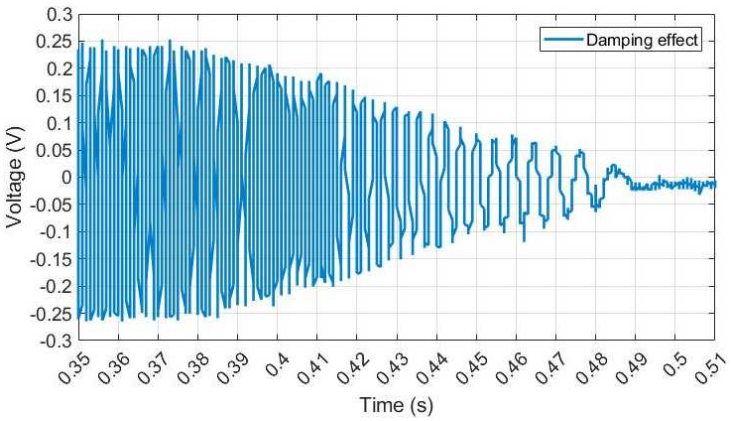

Figure 9-16: Damping ratio of mini-reactor.

Several points have been measured to improve accuracy and to avoid any incongruent/fail result. Three different points have been taken from measured damper curve besides the reference point x_0. x_2, x_6, and x_{10} points would the corroborate the similar value of damping coefficient. Finally, equation 9-16 has been applied, achieving as result values presented in table 9-14:

Table 9-14: Coefficient of frictional torque calculation values.

x_0	x_2	δ
0.169	0.153	0.0215
x_0	x_6	δ
0.169	0.129	0.0195

x_0	x_{10}	δ
0.169	0.0965	0.0243

Being 0.0215 an intermediate value, it has been selected to be used in the electro-mechanical model of the mini-reactor as the damping effect resistance.

From [129] and figure 9-17, the construction of an equivalent model of the turbine cell has started. The referenced work proposes a single phase electro-mechanical model of a miniature horizontal axis wind turbine or MHAWT. The implementation consists of the conversion of physical parameters and system behaviour in an electronic model to be able to simulate.

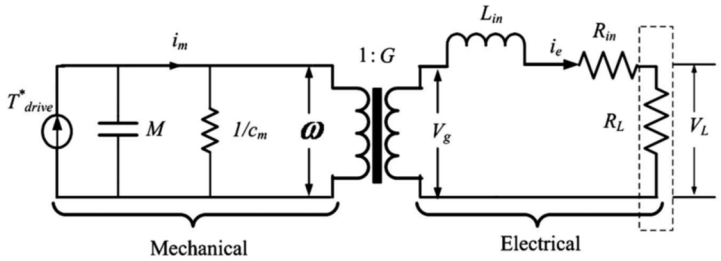

Figure 9-17: Reference horizontal turbine electro-mechanical model.

Instead of using a voltage generator as harvester output at simulation circuit, an equivalent electro-mechanical model has been implemented. This realistic model would give higher accuracy to AC/DC converter simulations.

9.1.3 Mini-reactor model construction

From reference model shown in figure 9-2, a new model has been developed for the mini-reactor. Figure 9-18 shows the mixed structural-electric model of the mini-reactor. The wind energy and the conversion of energy to mechanical and electrical is modelled through mathematical equations, voltage and controlled current sources and passive components.

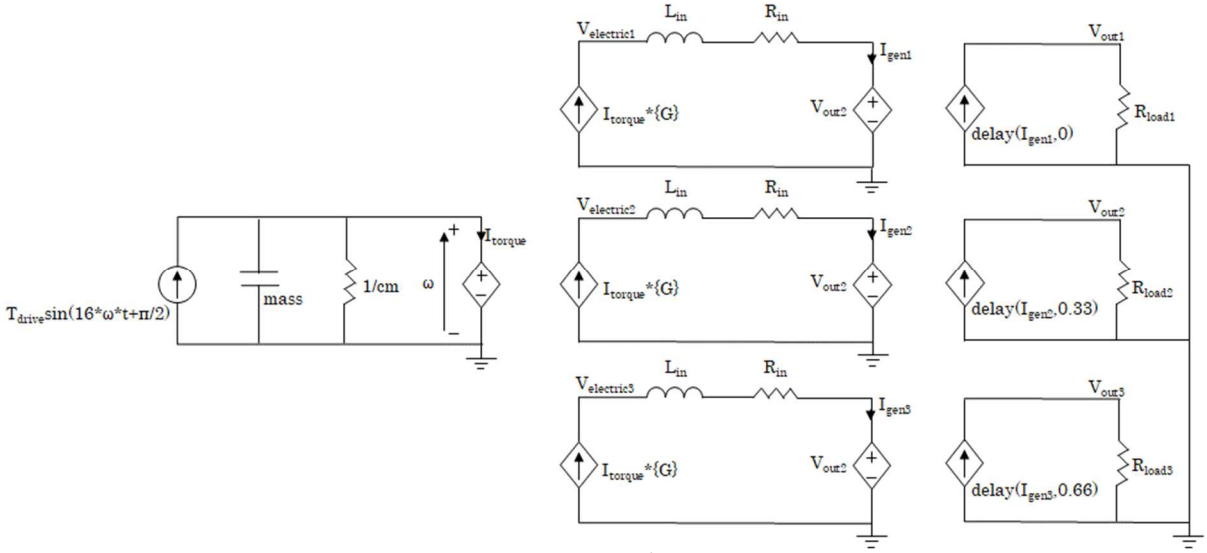

Figure 9-18: Final schematic of micro-turbine model.

The presented equivalent model is based on different equations and elements which represent an equivalence with work operation principles and electro-mechanical characteristics of the system shown in figure 9-17. In next lines, three parts which compound the circuit are described.

The first part involves the wind and mechanical parts. Wind power is characterized by the amplitude of the input sinusoidal current source. From equation 9-17 of [129] the drive torque (T^*_{drive}) is deduced as:

$$T^*_{drive} = M\dot{\omega} + \omega\left[\frac{c_m + G^2}{R_{in} + R_L}\right] \tag{9-17}$$

, where M is the mass of the mini-reactor and is represented with a capacitor due to capacitor basis. Nevertheless, when the flow has a constant pressure/velocity, the mini-reactors operates in a constant angular velocity condition. Consequently, the angular acceleration becomes zero. Therefore, equation 9-18 is rewritten as:

$$T^*_{drive} = \omega\left[\frac{c_m + G^2}{R_{in} + R_L}\right] \tag{9-18}$$

, where c_m is the described damping coefficient Damping effect and represented with a resistance. Then, G is the electro-mechanical coefficient.

The equivalence between wind power and harvested mechanical power is represented with equation 9-19:

$$P = V.I = \omega.Torque \tag{9-19}$$

This representation of angular velocity and torque of reactor is translated to the circuit as a voltage source and the current which pass through the source.

Angular velocity and torque have dependency such as wind power as with the resistive load of the system, which make leads to a complex relationship. However, the following conclusion could be made: the drive torque is directly proportional to the angular velocity under a constant resistive load condition.

Input sinusoidal signal is also dependable in angular velocity. Circuit angular velocity must be a constant and not a sinusoidal signal. Angular velocity conversion must be achieved for a correct calculation of input current signal. To solve this issue, the solution adopted has been to calculate in real time the root mean square value of angular velocity with equation 9-11.

$$\omega_{ef} = n * \sqrt{\frac{1}{t}\int_{t_0}^{t_0+t} (V(\omega(t)) * delay(V(\omega(t)), t))^2} \tag{9-20}$$

, where n is pole quantity on the mini-reactor and the parameters inside the root symbol the similar formula of a continuous function for a defined interval.

Next part of circuit involves the electric side. As described in chapter III the mini-reactor contains a three-phase electric generator. Thus, the electric part is triplicated. R_{in} and L_{in} are designed and manufactured coils induction value and the internal resistance at the PCB. The union between mechanical and electric parts or magnetic field losses are represented with the electro-mechanical coefficient, G.

In the present case, the effect of induction in the microgenerator is, and L_{in} in can be neglected in the calculation of output voltage. Consequently, the output voltage is written as:

$$V_{out} = \frac{G\omega R_L}{(R_{in} + R_L)} \tag{9-21}$$

and the current generated from the generator is expressed as:

$$i = \frac{G\omega R_L}{(R_{in} + R_L)} \tag{9-22}$$

Considering both equations and described elements, the relationship between mechanical and electrical part is done with a voltage and current source with the electromechanical coefficient, simulating a transformer operation. Maintaining effects on angular velocity from the resistive load.

The final part consists in an interpretation of phase-shift of the three-phase system. To achieve a 120º phase-shift per phase a delay element provided by the LTspice© simulation software has been used. The same architecture used in the conversion from mechanical to electric part has been utilized, i.e., a voltage source and current source but without any coefficient being the conversion 1 to 1, only applying the delay effect. The phase-shift updates continually, due to the connection with angular velocity RMS value:

$$I_{delay} = delay\left(I_{in}, \frac{0 \text{ V } 0.333 \text{ V } 0.666}{2.57 * \omega_{ef}}\right) \tag{9-23}$$

, where 0, 0.333 and 0.666 represent the phase-shift of 120º and 240º in unit value. To be able this normalized use of shift the 2.57 value is due to the three-phase electromechanical design of the micro-reactor.

Figures 9-19 and 9-20 summarized the performance of the system for three load conditions, 10 Ω, 60 Ω and 100 Ω, and two wind flow velocity conditions, 3 m/s, and 10 m/s. The load changes both the output voltage and the frequency. If the load remains constant and the wind flow changes the system behaves the same. Thus, decreasing the load or the wind flows leads reduce the output AC voltage amplitude and frequency.

In first simulations, flow velocity has been set as lowest one, i.e., 3 m/s.

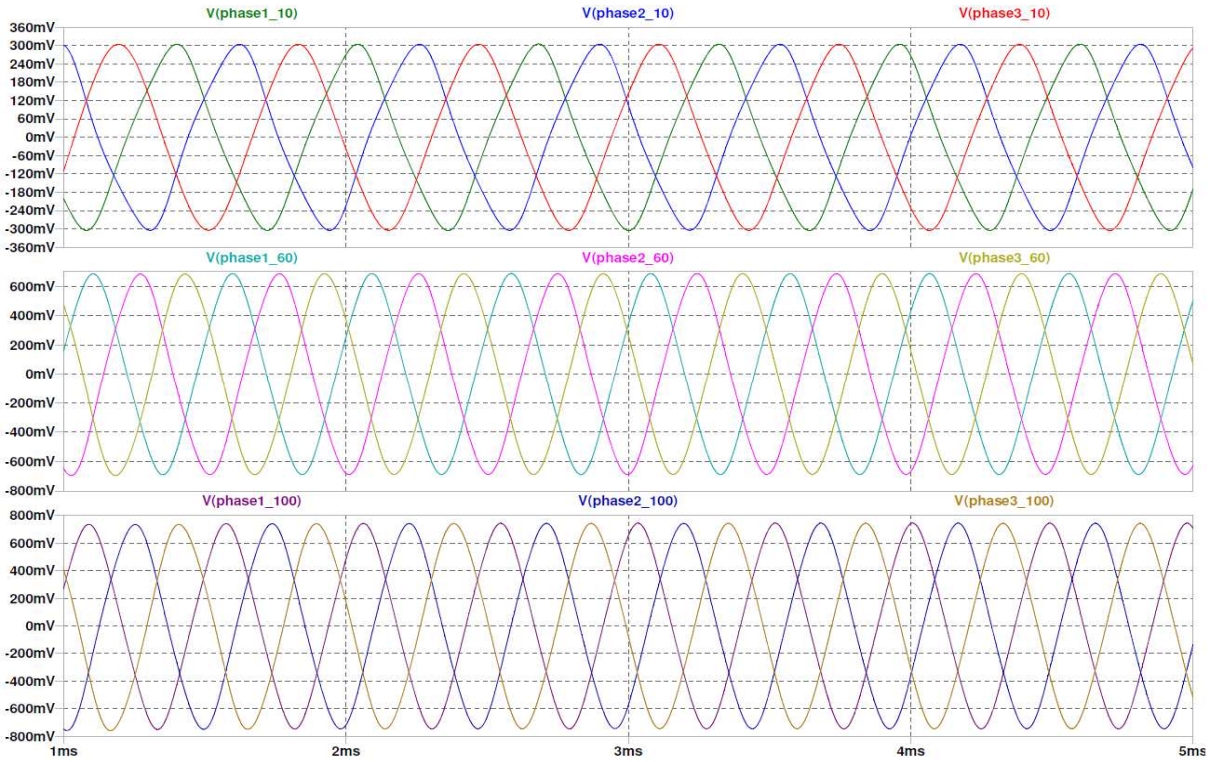

Figure 9-19: Model simulation results with 10 Ω, 60 Ω and 100 Ω loads at 3 m/s flow velocity.

In the second simulation, flow velocity has been set at 10 m/s, the highest one.

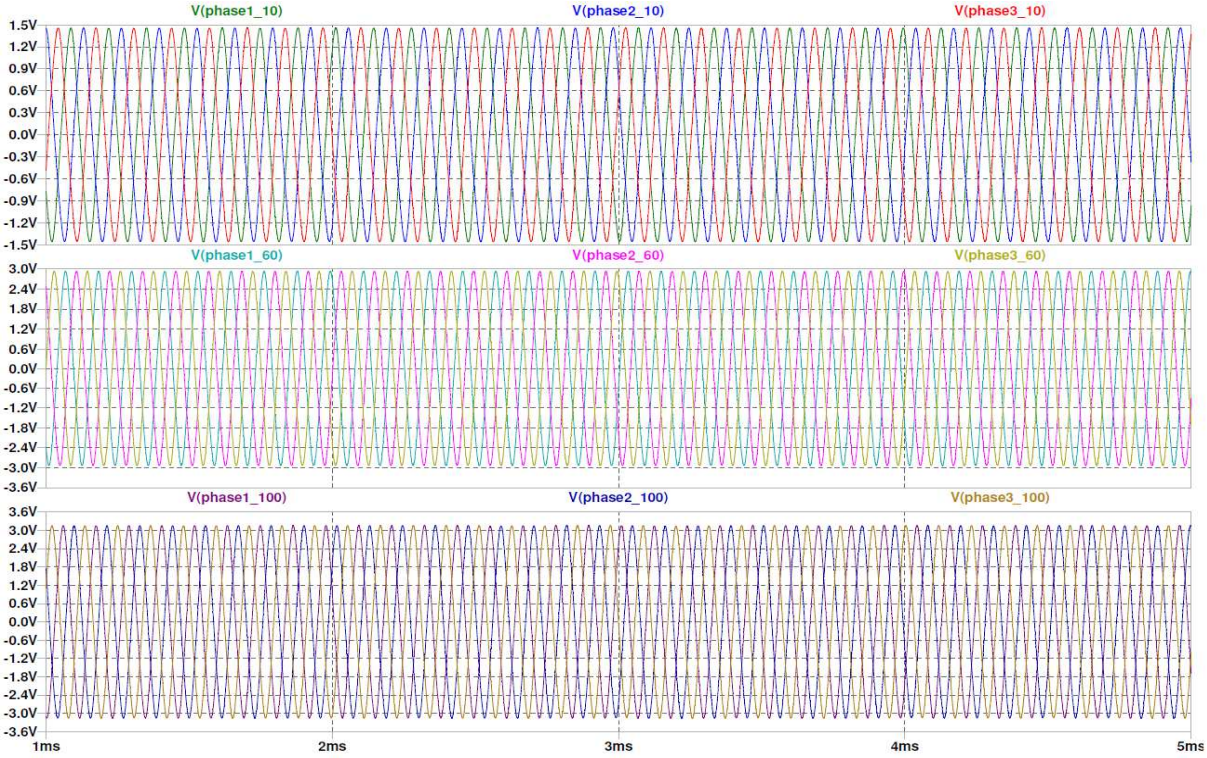

Figure 9-20: Model simulation results with 10 Ω, 60 Ω and 100 Ω loads at 10 m/s flow velocity.

9.1.4 Comparison between model and test results

The model verification is realized comparing simulations results with tests measured values. Simulation results are taken from previous section results and measured from chapter III. In addition, model accuracy is also evaluated in this section.

Three test conditions are compared. Lowest velocity/pressure value of wind flow, the maximum value of wind flow, and a range sweep with the impedance matching load. Voltage, power, and frequency of each system are shown, with their respective standard deviation.

In table 9-15, comparison results at minimum wind flow power condition are shown:

Table 9-15: Comparison between simulation and results values with minimum input flow value.

V_{min}						
R_{load} (ohm)	Results			Statistics		
	V_p (V)	P_{out} (mW)	f (kHz)	V_p	P_{out}	f
	Test			Standard deviation		
11	0.252	8.660	1.405	0.021	1.490	0.025
27	0.524	15.254	1.9	0.013	0.796	0.005
100	0.670	6.734	2.200	0.050	1.3	0.102
1000	1.021	1.564	2.532	0.117	0.328	0.105
	Simulation			Mean standard deviation		
11	0.281	10.767	1.369	0.050	0.919	0.059

27	0.543	16.381	1.899	
100	0.741	8.236	2.056	
1000	0.856	1.099	2.384	

Table 9-16 shows comparison results at maximum wind flow power condition:

Table 9-16: Comparison between simulation and results values with maximum input flow value.

V_{max}						
R_{load} (ohm)	Results			Statistics		
	V_p (V)	P_{out} (mW)	f (kHz)	V_p	P_{out}	f
	Test			Standard deviation		
11	1.551	328.037	7.664	0.024	10.058	0.013
27	2.388	316.808	8.372	0.042	11.399	0.279
100	3.148	148.649	8.715	0.208	18.716	0.208
1000	3.933	23.203	9.794	0.170	2.3	0.544
	Simulation			Mean standard deviation		
11	1.517	313.812	7.683	0.111	10.559	0.261
27	2.448	332.928	8.766			
100	2.854	122.180	9.009			
1000	4.173	26.121	10.564			

Table 9-17 shows the results of deviation at impedance matching condition. Furthermore, figure 9-21 shows the comparative relation of output peak to peak voltage, output power, and frequency.

Table 9-17: Results of standard deviation between model and test at load matching condition.

R_{load} = 27 Ω									
V (m/s)	Results						Statistics		
	Real			Model			Standard Deviation		
	V_p (V)	P_{out} (mW)	f (kHz)	V_p (V)	P_{out} (mW)	f (kHz)	V_p	P_{out}	f
3	0.525	15.28	1.9	0.543	16.381	1.899	0.013	0.775	0.005
4	0.745	31.16	2.569	0.729	29.525	2.548	0.012	1.153	0.015
5	0.998	55.49	3.452	0.977	53.029	3.425	0.015	1.739	0.019
6	1.413	111.02	5.047	1.437	114.721	5.5	0.017	2.615	0.013
7	1.702	160.72	6.093	1.732	166.657	6.075	0.021	4.201	0.013
8	2.085	239.69	7.311	2.079	240.125	7.301	0.005	0.310	0.007
9	2.207	272.54	7.794	2.224	274.788	7.809	0.012	1.587	0.011
10	2.451	333.15	8.766	2.469	338.665	8.65	0.013	3.902	0.080
							Mean Standard Deviation		
							0.013	2.035	0.020

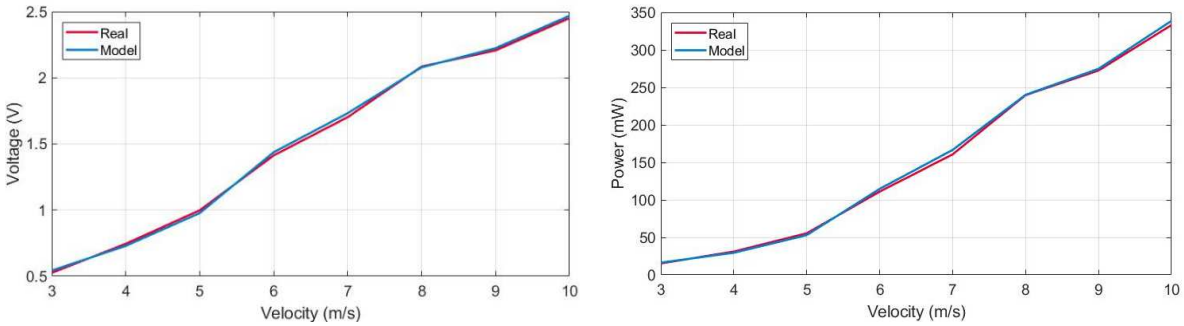

a) Voltage. b) Power.

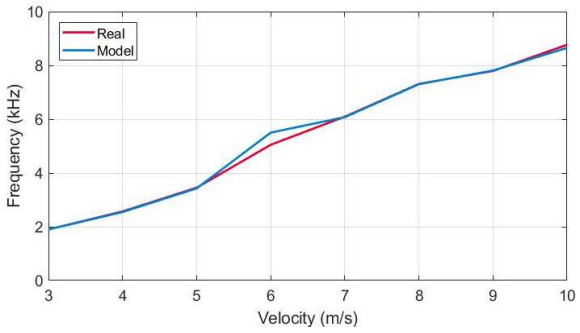

c) Frequency.

Figure 9-21: Model vs. real values comparison with 27 Ω resistive load.

From achieved results following conclusions are given:

- The deviation is higher when wind flow has more power.
- Voltage and frequency have a better response than power.
- The maximum deviation is 3.5 %.

Due to achieved results in statistical comparisons between model and tests, the model could be used as harvester simulator for AC/DC converter development. The deviation among both blocks is valid for this work.

9.2 AC/DC converter

9.2.1 Context, objective and development methodology

Wireless sensor networks electronics work in DC regime. Consequently, a converter which converses from AC regime to DC regime must be included when harvester works at AC regime.

In the literature, there are three main techniques of AC-DC conversion: direct rectification of AC signals into DC, AC rectification plus the DC/DC conversion and direct AC-DC conversion. The first alternative only rectifies the input signal, thus providing a low signal level due to losses in the rectifier. In the second one, the signal is rectified first into DC and, later, transformed into desired DC level with a DC-DC converter, usually, a boost converted that step up the voltage. If compared with other alternatives, the number of steps that this alternative requires reduce its efficiency. The last alternative is the one chosen in the present research, the AC-DC direct conversion.

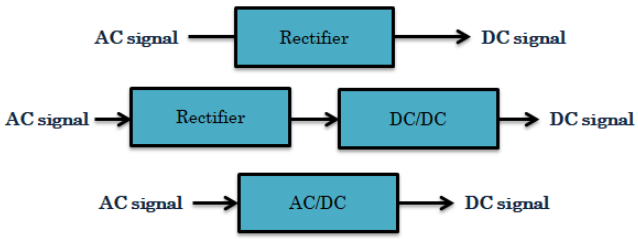

Systems	Complexity	Efficiency
Rectifier	Low	Low
Rectifier+ DC/DC	Medium	Medium
AC/DC	High	High

Figure 9-22: Comparisons between different types of rectification and conversion for an AC signal.

As could be seen in figure 9-22, complexity and efficiency are not equal in all topologies, where conversion efficiency and complexity go hand in hand.

Figure 9-23 shows the block diagram AC system and AC/DC converter integration in the system:

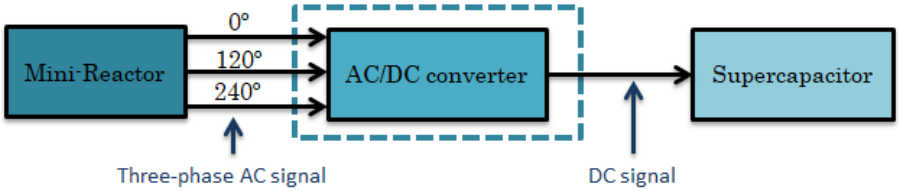

Figure 9-23: AC complete system with the harvester (mini-reactor), power management (AC/DC converter) and the storage device (supercapacitor).

The main objective of this subsection is:

Research, built, simulate and verify the feasibility of development and implementation of an **AC/DC converter** for the mini-reactor for all the input voltage and frequency ranges with more than a 50 % of efficiency.

However, input operation principles are given by the mini-reactor which gives some design requirements to the converter, such as:

- Low-value coil → only 2 µH.
- High input voltage for energy harvesting usual converters.
- 8 kHz range frequency input → Switching frequency changing.
- Beware of the reactive power of the generator.

These design requirements aim for a proper and efficient integration between the harvester and the converter.

The best AC/DC converter must be implemented by selecting the appropriate architecture for the use case of this work. Thus, operation power range has been defined with harvester output values at different ambient conditions. Then, considering the low power levels in energy harvesting applications, appropriate diode and MOSFET are selected under their viability to work in these conditions. After that, several architectures are simulated and switching frequency for MOSFET control is defined. Because input range is extensive, depend on ambient condition switching frequency would be different for each case, i.e., shift control. Finally, using sweep simulations maximum output power and system efficiencies would be searched for each architecture. Summarizing, a similar methodology used in the development of DC/DC converter but using the same procedure as many times as simulated architectures. Figure 9-24 shows described methodology in a flux diagram:

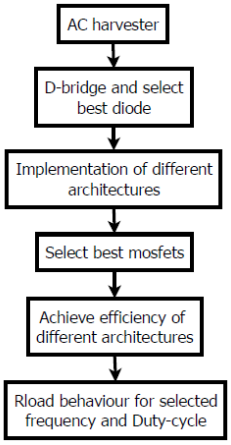

Figure 9-24: Flux diagram of steps used in this task.

Finally, remark that all topologies are going to be analysed in two extreme situations:

1- Minimum wind velocity condition 3 m/s, i.e., when available power as input is the minimum possible.
2- Maximum wind velocity condition 10 m/s, i.e., when available power as input is the maximum possible.

9.2.2 Diode and MOSFET selection for AC/DC converter

The diode selection is realized with the same procedure described in section 8.2.2. However, in this case, diode selection has been made with diode bridge architecture.

Several commercial diodes were selected in base their appropriate characteristics, being the same of used in the DC/DC converter, such as: MBR0520L, BAT15-03W, 1PS79SB31, NSR20F30NXT5G, NSR0320MW2T1G, NSVR351SDSA3, STPS20L15G. Then, using their appropriate spice model were simulated. In table 9-18 and figure 9-25 achieved results with minimum input condition are shown:

Table 9-18: Comparative results between different diode with 3 m/s wind velocity at D-bridge architecture.

Diode	R_{load} (Ω)	f_{in} (kHz)	V_{in} (Vp)	V_{out} (V)	I_{out} (mA)	P_{out} (mW)	P_{in} (mW)	η
MBR0520L	40	1.768	0.886	0.405	10.147	4.118	7.359	55.96
BAT15-03W	40	1.944	1.209	0.309	7.73	2.39	13.703	17.44
1PS79SB31	40	1.808	0.948	0.391	9.782	3.827	8.425	45.42
NSR20F30NXT5G	40	1.782	0.904	0.398	9.974	3.979	7.661	51.94
NSVR351SDSA3	40	1.847	1.019	0.374	9.353	3.499	9.734	35.94
STPS20L15G	30	1.546	0.584	0.394	13.154	5.191	12.789	40.59

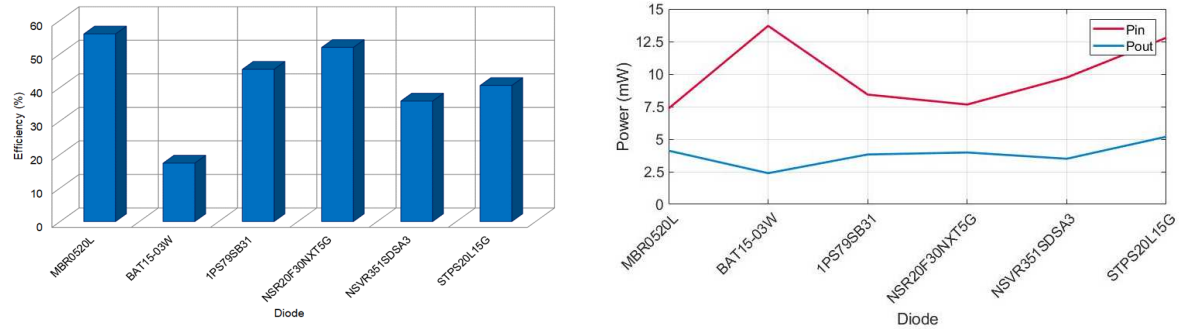

a) Efficiency. b) Input/output power.

Figure 9-25: Efficiency and input/output power comparisons between diodes with 3 m/s wind velocity at D-bridge.

Then, table 9-19 and figure 9-26 show achieved results with maximum input condition:

Table 9-19: Comparative results between different diode with 10 m/s wind velocity at D-bridge architecture.

Diode	R_{load} (Ω)	f_{in} (kHz)	V_{in} (Vp)	V_{out} (V)	I_{out} (mA)	P_{out} (mW)	P_{in} (mW)	η
MBR0520L	30	6.717	2.575	1.995	66.572	132.957	248.648	53.47
BAT15-03W	30	7.629	3.9	1.753	58.451	102.497	190.125	53.91
1PS79SB31	30	6.857	2.751	1.972	65.649	129.646	283.80	45.68
NSR20F30NXT5G	30	6.73	2.588	1.992	66.405	132.291	251.165	52.67
NSVR351SDSA3	30	7.106	3.1	1.915	63.961	122.73	360.375	34.06
STPS20L15G	30	6.497	2.321	2.047	68.261	139.789	202.014	69.20

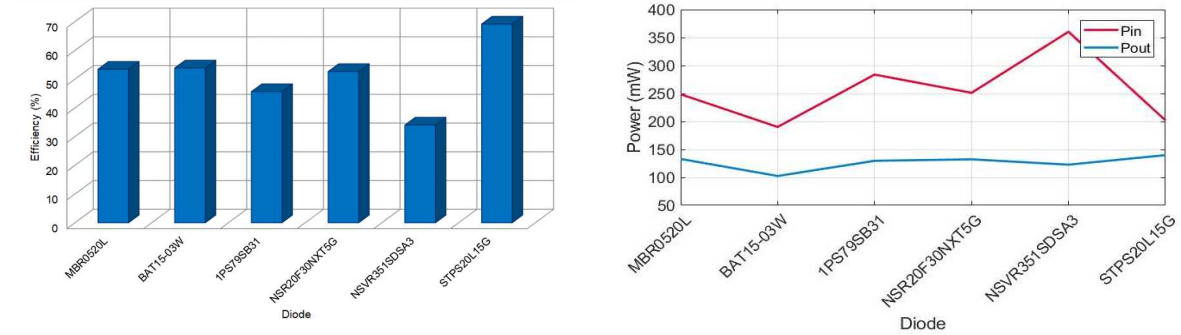

a) Efficiency. b) Input/output power.

Figure 9-26: Efficiency and input/output power comparisons between diodes with 3 m/s wind velocity at D-bridge architecture.

In low wind velocity condition efficiency reach until 55.96 % with MBR0520L and in high conditions until 69.20 % with STPS20L15G. However, at low condition STPS20L15G achieves 40.59 % efficiency. Thus, due to MBR0520L stability in both conditions, is the selected diode.

Also, the MOSFET selection is realized with the same procedure described in section 8.2.2. However, in this case, MOSFET selection has been made with Split N capacitor topology.

Before selecting the appropriate MOSFET, the restriction and the behaviour in converter topologies is presented. Converter topologies use a bidirectional switch for operation. Nevertheless, a single MOSFET with bidirectional conduction and blocking behaviour does not exist. A MOSFET channel is capable of conduction in both directions when it is sufficiently turned on. However, due to MOSFET body diode, reverse direction current cannot be blocked. A bidirectional switch is obtained by connecting the drain of an

n-MOSFET to the source of a n or p-MOSFET (dependent of topology). Consequently, the current in the opposite direction is blocked by respective MOSFET body diodes. Therefore, when the MOSFETs are turned on and off at the same time, they could block currents in both directions.

In the selection of MOSFETs, the following conditions have been considered at minimum input state: 500 kHz switching frequency, 0.05/0.1 duty-cycle, R_{load} = 80/90 Ω and the commercial diode model MBR0520L. Then several commercial MOSFETs were selected in base their appropriate characteristics for the present use case, such as Si1555DL_N, Si8466EDB, IRLU3802 and Si1553CDLN. And finally, simulated with their appropriate spice model. In table 9-20 and figure 9-27 achieved results with detailed conditions are shown:

Table 9-20: Comparative results between different MOSFETs with 3 m/s wind velocity.

MOSFET	V_{in} (Vp)	f_{in} (kHz)	R_{load} (Ω)	D	f_{sw} (kHz)	Q_g (nC)	R_{ds} (mΩ)	V_{out} (V)	I_{out} (mA)	P_{out} (mW)	$P_{contr.}$ (mW)	P_{out} (mW)	η
Si1555DL	1.025	1.9	80	0.05	500	0.8	0.63	0.677	8.469	5.73	0.523	5.20	44.05
Si1555DL	1.025	1.9	90	0.1	500	0.8	0.63	0.709	7.887	5.59	0.527	5.	42.83
Si8466EDB	1.025	1.9	80	0.05	500	6.8	0.05	0.683	8.538	5.83	6.79	-0.96	-8.12
Si8466EDB	1.025	1.9	90	0.1	500	6.8	0.05	0.719	7.997	5.74	7.313	-1.57	-13.30
IRLU3802	1.025	1.9	80	0.05	500	27	8.5	0.664	8.303	5.51	20.476	-14.96	-126.6
IRLU3802	1.025	1.9	80	0.1	500	27	8.5	0.657	8.224	5.40	20.4	-15	-126.9
Si1553CDLN	1.025	1.9	80	0.05	500	0.55	0.578	0.68	8.51	5.78	0.341	5.43	**46.01**
Si1553CDLN	1.025	1.9	90	0.1	500	0.55	0.578	0.715	7.945	5.68	0.350	5.33	45.09

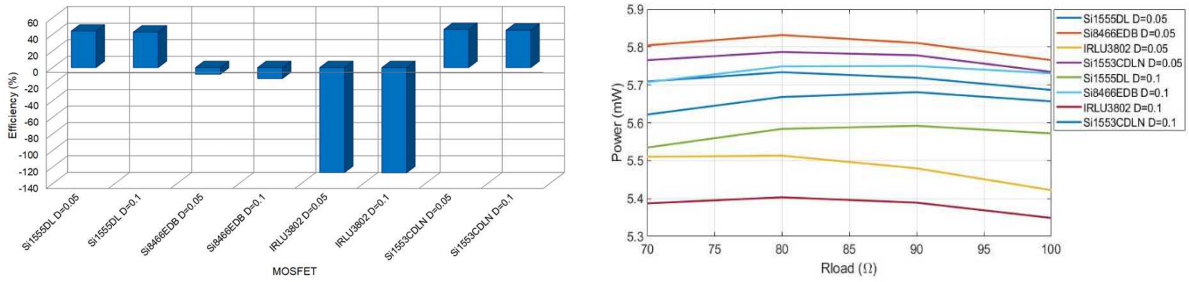

a) Efficiency. b) Input/output power.

Figure 9-27: Efficiency and input/output power comparisons between MOSFETs with 3 m/s wind velocity.

In the selection of MOSFETs at maximum input state, the following conditions have been considered: 1000 kHz switching frequency, R_{load} = 70/80 Ω and maintain duty-cycle values. In table 9-21 and figure 9-28 achieved results with detailed conditions are shown:

Table 9-21: Comparative results between different MOSFETs with 10 m/s wind velocity.

MOSFET	V_{in} (Vp)	f_{in} (kHz)	R_{load} (Ω)	D	f_{sw} (kHz)	Q_g (nC)	R_{ds} (mΩ)	V_{out} (V)	I_{out} (mA)	P_{out} (mW)	$P_{contr.}$ (mW)	P_{out} (mW)	η
Si1555DL	4.17	8.766	70	0.05	1000	0.8	0.63	3.252	46.471	151.12	1.027	150.09	77
Si1555DL	4.17	8.766	80	0.1	1000	0.8	0.63	3.451	43.147	148.90	1.1	147.83	75.90
Si8466EDB	4.17	8.766	70	0.05	1000	6.8	0.05	3.252	46.47	151.12	12.374	138.74	71.23
Si8466EDB	4.17	8.766	80	0.1	1000	6.8	0.05	3.451	43.146	148.89	14.505	134.38	69
IRLU3802	4.17	8.766	70	0.05	1000	27	8.5	3.2	45.724	146.31	36.684	109.62	56.28
IRLU3802	4.17	8.766	80	0.1	1000	27	8.5	3.398	42.486	144.36	37.422	1.93	54.90
Si1553CDLN	4.17	8.766	70	0.05	1000	0.55	0.578	3.264	46.638	152.22	0.519	151.70	**77.89**
Si1553CDLN	4.17	8.766	80	0.1	1000	0.55	0.578	3.471	43.389	150.60	0.57	150	77.033

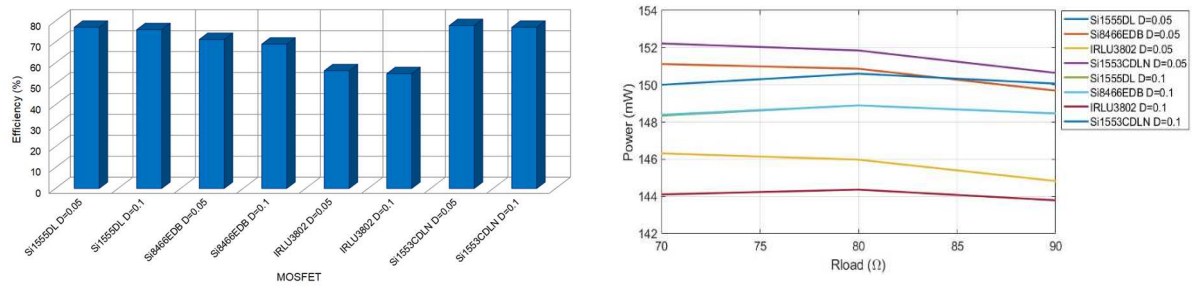

a) Efficiency. b) Input/output power.

Figure 9-28: Efficiency and input/output power comparisons between MOSFETs with 10 m/s velocity.

Efficiencies are dependent on wind flow velocity condition or input voltage/power level. In the first case, maximum efficiency is 46.01 % with Si1553CDLN MOSFET. Moreover, existing a negative efficiency due to the income power quantity and the consumption of Si8466EDB and IRLU3802. Otherwise, when the situation is the opposite, i.e., income power is the maximum, all efficiencies are positive on the range between 55 % and 78 %. Moreover, Si1553CDLN MOSFETs grants a 77.89 % of maximum efficiency to the converter. Si1553CDLN have the less consumption at both work operation mode, and converter achieves the maximum efficiency and power output. For apparent reasons, Si1553CDLN MOSFET has been selected to be the MOSFET at the AC/DC converter.

Coil operation behaviour must be taken into consideration. It is known that if the converter works in discontinuous conduction mode (DCM), the system has many advantages:

1. A constant duty cycle extracts constant power from the source, enabling a simple control
2. When the converter operates with a constant duty cycle has only one fundamental and switching harmonic frequency. Consequently, offering a resistive load to the mini-reactor.
3. DCM operation reduces switching losses which are essential in energy harvesting applications.

Next step is to evaluate some topologies/architectures to make the selection of the efficient one and which gives more power to the storage device.

9.2.3 Used architectures, their operation principles, simulations and results

The selection of an AC/DC architecture is aimed to obtain the maximum efficiency. Five architectures have been selected to get this goal. Two are rectifier or multiplier architectures based on diodes. The other three alternatives are AC/DC converter topologies which rectify and boost the input signal.

Requirements:

- Minimum valid voltage level must be 3 V.
- Maximum valid voltage level must be 5 V.
- The converter must maintain its performance within the whole range of voltage and generator operating conditions.

IIoT devices usually operate at 3 V. If this level is not reached, the voltage must be raised by a step-up device. In the opposite case, if the voltage level exceeds 5 V, the power storage system will be damaged, needing a decreasing of voltage with a step-down device.

For this case, these situations are not valid because an extra element is needed, consequently, not fulfilling the established requirements.

9.2.3.1 Three-phase Diode bridge rectifier

Three-phase diode bridge rectifier is going to be taken as reference for the other topologies/architectures analysed in this work. Figure 9-29 shows the architecture of three-phase diode bridge rectifier.

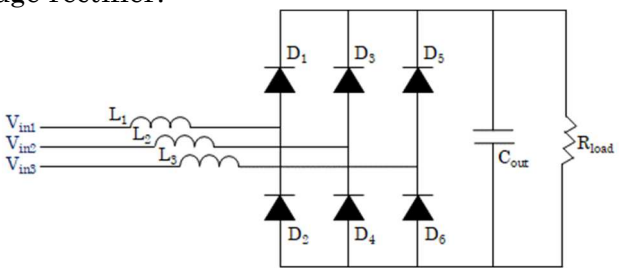

Figure 9-29: Three-phase diode bridge architecture.

The three-phase rectifier work as follows: D1 rectifies the positive half cycle signals1, D_3 and D_5 are the conducting diodes, rectifying the income positive half signal. The negative half cycle signals are rectified by D_2, D_4, and D_6 conducting diodes. Each diode pairs rectify their pertinent signal phase, e.g., D_1 and D_2 1st phase. The average DC output is improved using a capacitor between diodes and resistive load, C_{out}. At the same time, this capacitor reduces the ripple of the signal and acts as a storage device.

The simulation results with wind minimum velocity condition are shown in table 9-22 and figure 9-30:

Table 9-22: Diode bridge simulations sweep results with minimum input condition.

R_{load} (Ω)	V_{in} (V)	f_{in} (kHz)	V_{out} (V)	I_{out} (mA)	P_{out} (mW)	$\eta_{generator}$ (%)	$\eta_{converter}$ (%)	$\eta_{general}$ (%)
10	0.66	1.687	0.17	17.31	2.97	16.75	27.13	4.54
20	0.76	1.735	0.27	13.83	3.81	16.43	34.24	5.63
30	0.83	1.756	0.34	11.67	4.04	15.83	36.76	5.82
40	0.88	1.768	0.40	10	4.04	15.17	37.69	5.72
50	0.92	1.776	0.44	8.94	4	14.57	37.78	5.50
60	0.96	1.781	0.48	8.02	3.85	14.02	37.49	5.26
70	0.99	1.785	0.50	7.25	3.67	13.53	37	5.01
80	1.01	1.788	0.53	6.65	3.54	13.09	36.4	4.76
90	1.03	1.79	0.55	6.13	3.38	12.71	35.7	4.54
100	1.05	1.792	0.57	5.71	3.26	12.35	35.02	4.32

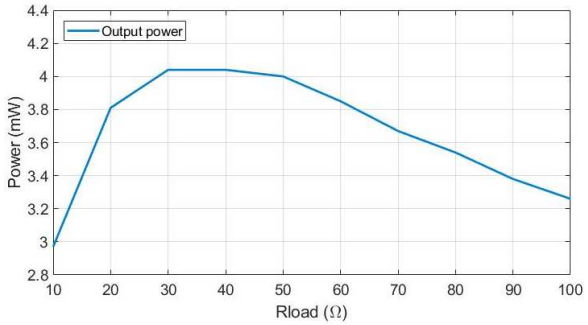

a) Output power.

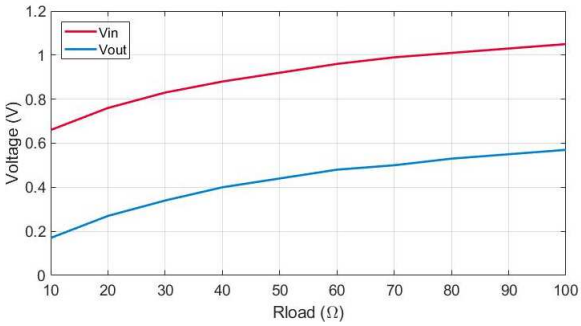

b) Output and input voltage.

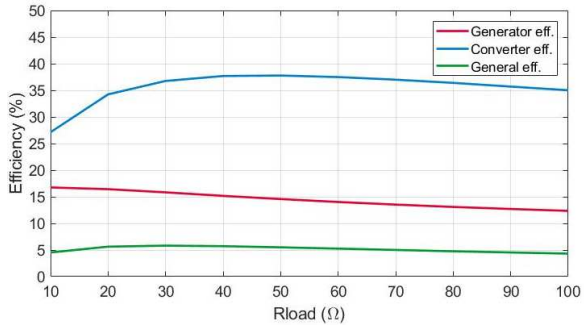

c) Generator, converter and complete system efficiencies.

Figure 9-30: Graphic results of sweep simulation with diode bridge topology at 3 m/s wind velocity.

The maximum output power is 4.04 mW, and it is achieved for resistive loads of 30 or 40 Ω. The maximum voltage level achieved is 0.57 Volts for 100 Ω load and 3.26 mW at the output. The required resistive load value to achieve 3 Volt level would be so big that the output power would be near zero, emulating an open circuit condition. Thus, this architecture is not valid.

Despite the fact that the topology is not valid, the simulations with 10 m/s wind velocity condition have been done for comparison between architecture. Table 9-23 and figure 9-31 show the aforementioned results:

Table 9-23: Diode bridge simulations sweep results with maximum input condition.

R_{load} (Ω)	V_{in} (V)	f_{in} (kHz)	V_{out} (V)	I_{out} (mA)	P_{out} (mW)	$\eta_{generator}$ (%)	$\eta_{converter}$ (%)	$\eta_{general}$ (%)
10	1.64	6.63	1.3	1.32	113.02	10.34	58.94	6.09
20	2.20	6.694	1.62	81.12	131.58	11.19	60.78	6.80
30	2.57	6.717	1.99	66.42	132.32	11.23	58.79	6.60
40	2.84	6.729	2.26	56.55	127.93	11.06	56.12	6.21
50	3.04	6.736	2.47	49.40	122.02	10.82	53.44	5.78
60	3.21	6.742	2.63	43.90	115.65	10.57	50.94	5.38
70	3.34	6.745	2.77	39.6	109.78	10.33	48.62	5.02
80	3.45	6.748	2.88	36.02	103.78	10.11	46.45	4.70
90	3.54	6.75	2.97	33.08	98.50	9.91	44.44	4.40
100	3.63	6.752	3.1	30.61	93.70	9.72	42.64	4.15

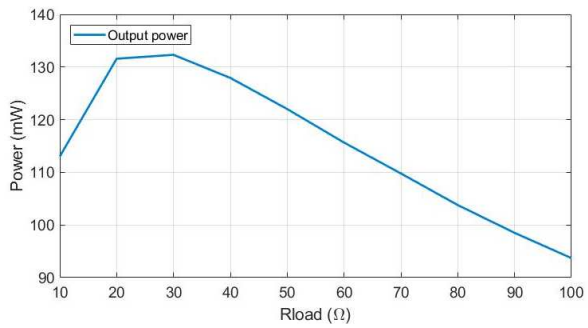

a) Output power.

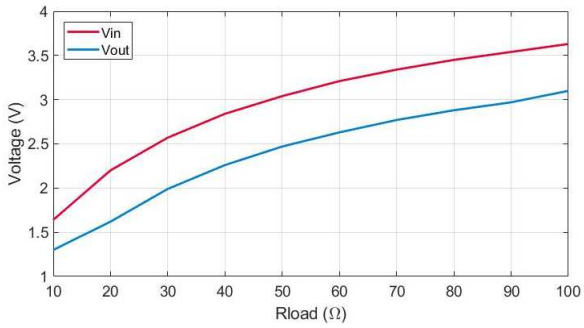

b) Output and input voltage.

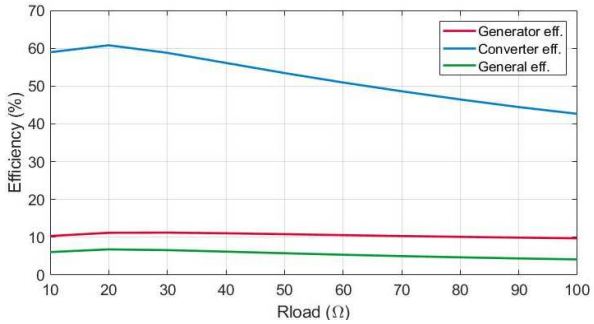

c) Generator, converter and complete system efficiencies.

Figure 9-31: Graphic results of sweep simulation with diode bridge topology at 10 m/s wind velocity.

3 Volt output level is only achieved for 100 Ω resistive load, obtaining 93.70 mW. Nevertheless, the maximum obtained power is 132.32 mW for 30 Ω load and 1.99 Volt signal.

Rectifier efficiencies are 38 % and 61 % for 3 m/s and 10 m/s wind velocities respectively. Complete system efficiency is around 5 % in both ambient conditions.

In both cases, the input voltage is lower than the output voltage. Diode bridge architecture only rectifies income signal and requires a second stage to step-up the voltage; consequently, it is not a flexible alternative.

9.2.3.2 Voltage doubler topology

The three-phase voltage doubler is the second architecture analysed in this work. A network of capacitors and diodes composes this topology. Figure 9-32 shows the architecture of three-phase voltage doubler.

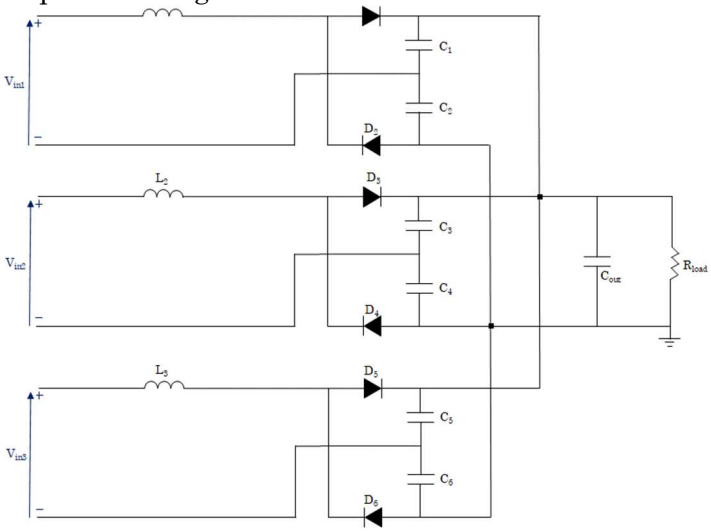

Figure 9-32: Voltage doubler three-phase circuit.

The voltage doubler operation mode is described in next points:

1. At the positive half: the potential of C_1, C_3, C_5 adds with the source, charging C_2, C_4, C_6 to double voltage through D_2, D_4, and D_6.
2. At the negative half: The C_2, C_4, C_6 capacitors are charged through diode D_1, D_3, and D_5.
3. In next positive half: the potential of C_2, C_4, C_6 rises to 2 x V. The output voltage would rise until 2 x V is reached.

4. In next negative half: the potential of C_1, C_3, C_5 would be dropped to 0 V allowing C_1, C_3, C_5 be charged through D_1, D_3, and D_5 to 2 x V.

To increase twice more times the peak of AC voltage at the output voltage, the additional stage must be inserted with two diodes and two capacitors.

Table 9-24 and figure 9-33 show simulation results with wind minimum velocity condition:

Table 9-24: Voltage doubler sweep simulations results with minimum input condition.

R_{load} (Ω)	V_{in} (V)	f_{in} (kHz)	V_{out} (V)	I_{out} (mA)	P_{out} (mW)	$\eta_{generator}$ (%)	$\eta_{converter}$ (%)	$\eta_{general}$ (%)
10	0.60	1.363	0.13	13.54	1.83	12.22	21.94	2.68
20	0.70	1.412	0.23	11.65	2.71	11.73	32.17	3.77
30	0.77	1.435	0.3	10.15	3.09	10.98	37.69	4.14
40	0.82	1.448	0.35	8.98	3.22	10.27	40.69	4.18
50	0.86	1.456	0.4	8.02	3.22	9.636	42.27	4.07
60	0.89	1.462	0.43	7.22	3.13	9.086	43.00	3.91
70	0.92	1.466	0.46	6.57	3.02	8.624	43.15	3.72
80	0.94	1.469	0.48	6.03	2.91	8.233	42.92	3.53
90	0.95	1.472	0.5	5.56	2.79	7.904	42.43	3.35
100	0.97	1.474	0.51	0.51	2.66	7.611	41.84	3.18

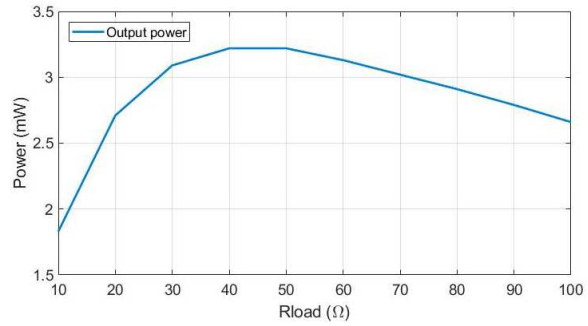

a) Output power.

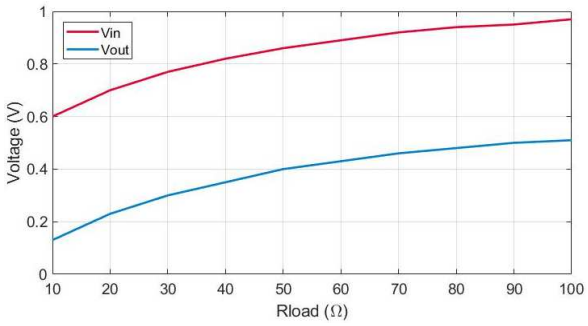

b) Output and input voltage.

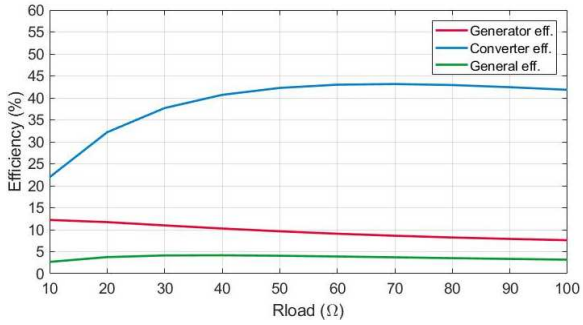

c) Generator, converter and complete system efficiencies.

Figure 9-33: Output power and voltage values with resistive sweep load at 3 m/s wind velocity.

The maximum output power is 3.22 mW, and it is achieved for resistive loads of 40 or 50 Ω. The maximum voltage level achieved is 0.51 Volts for 100 Ω load and 2.66 mW at the output. The same behaviour happened with the diode bridge architecture appears.

Although the topology is not valid, the simulations with 10 m/s wind velocity condition have been done for comparison between architecture. Table 9-25 and figure 9-34 show the aforementioned results:

Table 9-25: Voltage doubler simulations sweep results with maximum input condition.

R_{load} (Ω)	V_{in} (V)	f_{in} (kHz)	V_{out} (V)	I_{out} (mA)	P_{out} (mW)	$\eta_{generator}$ (%)	$\eta_{converter}$ (%)	$\eta_{general}$ (%)
10	1.45	4.823	0.88	88.98	79.17	6.43	67.79	4.36
20	2.04	4.911	1.48	74.31	110.45	8.19	71.68	5.87
30	2.44	4.944	1.89	63	119.07	8.82	70	6.17
40	2.71	4.961	2.17	54.25	117.74	8.88	67.74	6.02
50	2.91	4.971	2.37	47.47	112.71	8.66	65.69	5.69
60	3.06	4.978	2.52	42.09	106.29	8.37	63.70	5.33
70	3.17	4.983	2.64	37.75	99.8	8.02	62.05	4.98
80	3.27	4.988	2.73	34.19	93.56	7.70	60.35	4.65
90	3.34	4.991	2.81	31.24	87.87	7.38	58.89	4.35
100	3.40	4.992	2.87	28.75	82.68	7.11	57.40	4.08
110	3.45	4.995	2.92	26.61	77.93	6.84	56.11	3.84
120	3.5	4.996	2.97	24.78	73.70	6.6	54.87	3.62
130	3.54	4.998	3.01	23.17	69.84	6.38	53.68	3.42

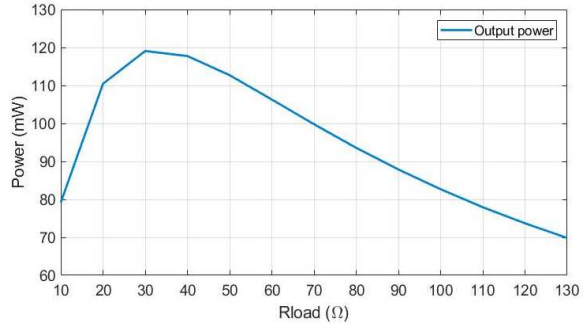

a) Output power.

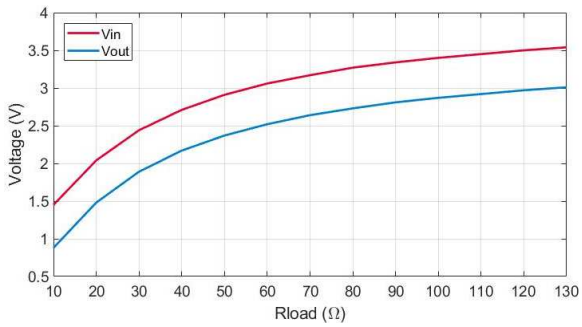

b) Output and input voltage.

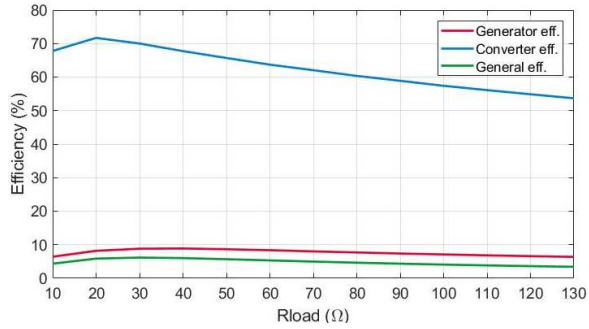

c) Generator, converter and complete system efficiencies.

Figure 9-34: Output power and voltage values with resistive sweep load at 10 m/s wind velocity.

3 Volt output level is reached for 130 Ω resistive load, obtaining 69.84mW. However, the maximum obtained power is 119.07 mW for 30 Ω load and 2.44 Volt signal.

Voltage doubler efficiencies are 42.27 % and 70 % for 3 m/s and 10 m/s wind velocities respectively. Complete system efficiency is around 4 % in both ambient conditions.

In both cases, the input voltage is lower than the output voltage. As in diode bridge, architecture voltage doubler only rectifies income signal due to the impedance mismatching. This architecture requires a second stage to step-up the voltage; consequently, it is not a flexible alternative.

9.2.3.3 Secondary side diode-based topology

The circuit schematic of the secondary side diode-based [238] converter is presented in figure 9-34. A single inductor for each phase (inside the mini-reactor harvester) is used for the boost operation. Two n-channel MOSFETs (selected in before section) per each phase, are connected in series. Due to their bidirectional capability, boost operation is realized in positive and negative half cycles of input AC signal voltage. The converter operates in DCM mode reducing MOSFET switching losses, and the rectifier diodes would have low recovery losses.

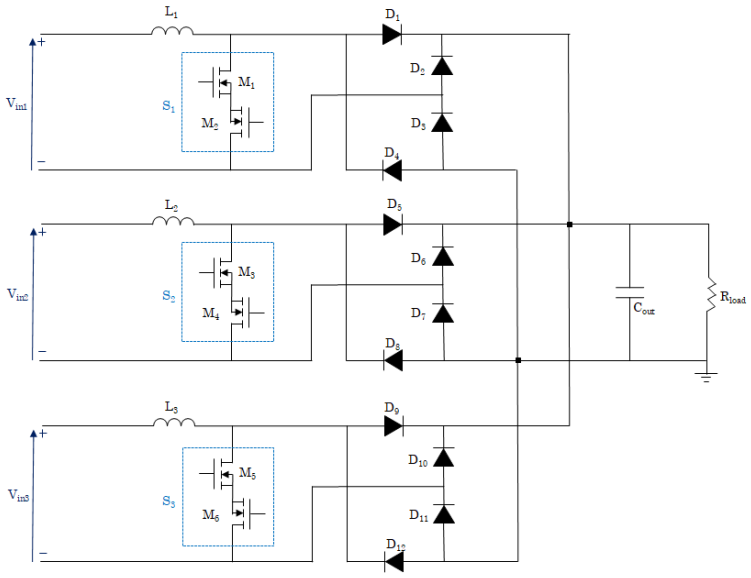

Figure 9-35: Secondary side diode three-phase circuit.

The converter has four operating modes. Mode I & II are for positive input voltage while Mode III & IV are for negative input voltage. The operation modes are dependents on input signals half cycles. There are two modes per each half cycle, so four modes in total. It must be noted, that the modes have an application delay of 120º and 240º equivalent in time respect the first phase part.

This converter has four operation modes and two cycles, positive and negative.

In the positive half cycle:

Mode I: MOSFETs (M_1, M_2, M_3, M_4, M_5 and M_6) are turned on thus inductor's currents (I_{L1}, I_{L2}, and I_{L3}) built up from zero.

Mode II: The MOSFETs are turned off. Hence, the inductor forward biases the diode, the diode, D_1, D_4, D_5, D_8, D_9 and D_{12} and charges the C_{out} capacitor. During this process, the stored energy in the inductors charges the output capacitor.

In the negative half cycle:

Mode III: In this mode, all the MOSFETs are turned on to increase inductor current in the opposite polarity of mode I, i.e., in a negative direction.

Mode IV: The MOSFETs are turned off. Now, the inductors forward bias the diodes, D_2, D_3, D_6, D_7, D_{10} and D_{11} charging the capacitor C_{out}. The charging currents have the reverse polarity of mode II.

Then, to make able the described modes the control of each phase is shown in figure 9-36:

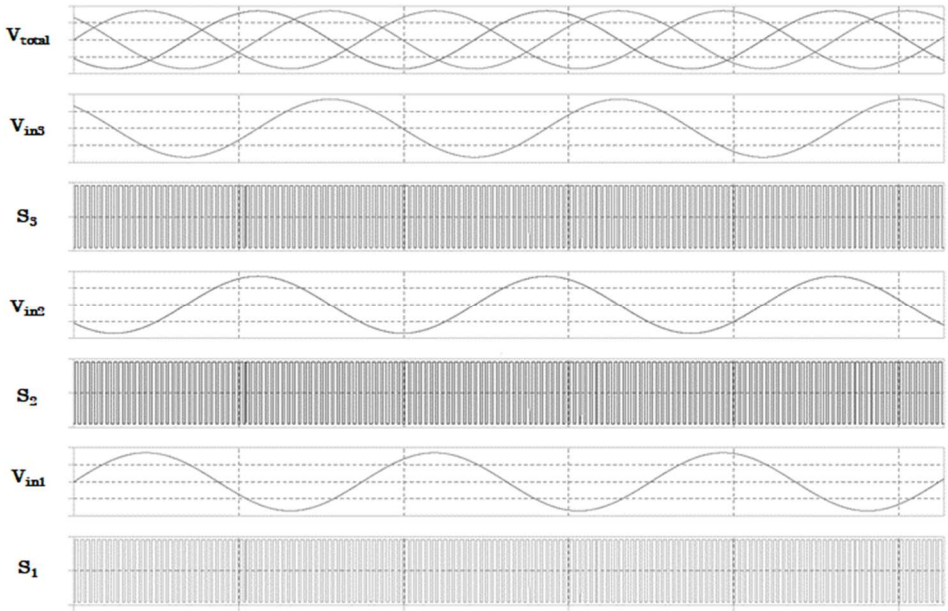

Figure 9-36: Control signals for Secondary side diode three-phase topology.

Each phase control S_1, S_2, and S_3 are always same as the signal, being a constant PWM. The process to obtain the best output power level is based on the change of duty-cycle and frequency.

To verify the architecture maximum output power and efficiency, simulations have been done changing values of different variables, such as switching frequency, duty-cycle, and resistive load.

Table 9-26 shows simulations results with minimum (3 m/s) wind velocity. Sweeps have been done between 100 and 2100 Ω resistive load, 0-1 and 0.9 duty-cycles, with 200 and 333 kHz switching frequencies.

Table 9-26: Side diode topology converter simulations best results with minimum input conditions.

Peak	V_{in} (V_{pp})	f_{in} (kHz)	R_{load} (Ω)	D	f_{sw} (kHz)	V_{out} (V)	I_{out} (mA)	P_{out} (mW)	$P_{control}$ (mW)	P_{out} (mW)
1st	0.72	2.6	300	0.4	200	1.63	5.45	8.93	1.23	7.7
2nd	0.4	2.4	1500	0.5	200	3.08	2.05	6.32	1.22	5.10
1st	0.76	2.254	300	0.4	333	1.38	4.62	6.4	2.04	4.36
2nd	0.41	2.04	1700	0.4	333	3.27	1.92	6.31	2.03	4.28

Table 9-26 1st peak notations means “short-circuit” and 2nd peak “load match”. In the first case, the converter works as a rectifier maintaining the voltage level with a small boost operation. In the second case, the converter rectifies and boosts the voltage level of the input signal. To respect the double power manager requirement of output voltage level between 3 and 5 Volts, the second peak is the appropriate one when wind velocity is 3 m/s input condition.

Maximum valid output power with side diode topology at 3 m/s wind velocity condition is 5.1 mW for 1500 Ω load and 3.08 V level signal. In addition, appoint that highest power levels happen when duty-cycle is between 0.4 and 0.5 and with 200 kHz switching frequency.

Control power consumption represents the 19 % of the total available power with 200 kHz switching. When switching frequency is set at 333 kHz, it rises to 33 %.

Figure 9-37 shows sweep results of a) output power, b) output voltage, c) generator efficiency, d) converter efficiency and e) complete system efficiency.

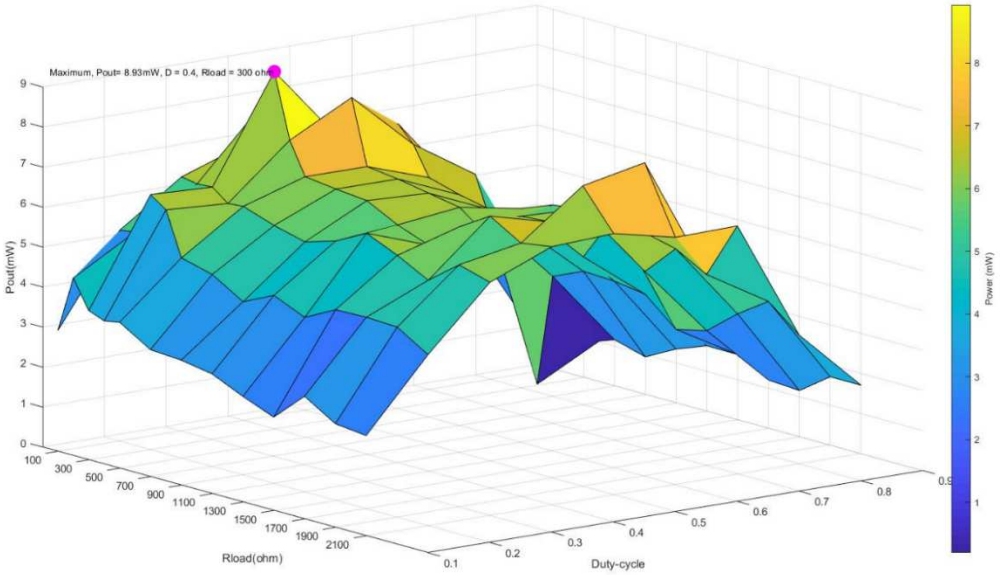

a) Output power sweep at resistive load.

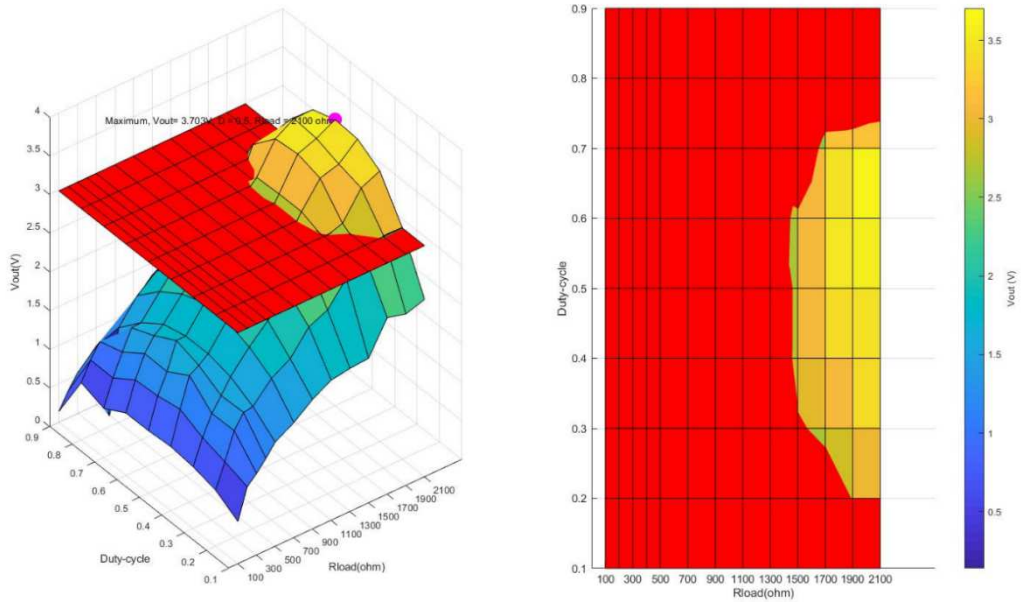

b) Output voltage sweep at resistive load; red plane of 3 Volt as minimum needed.

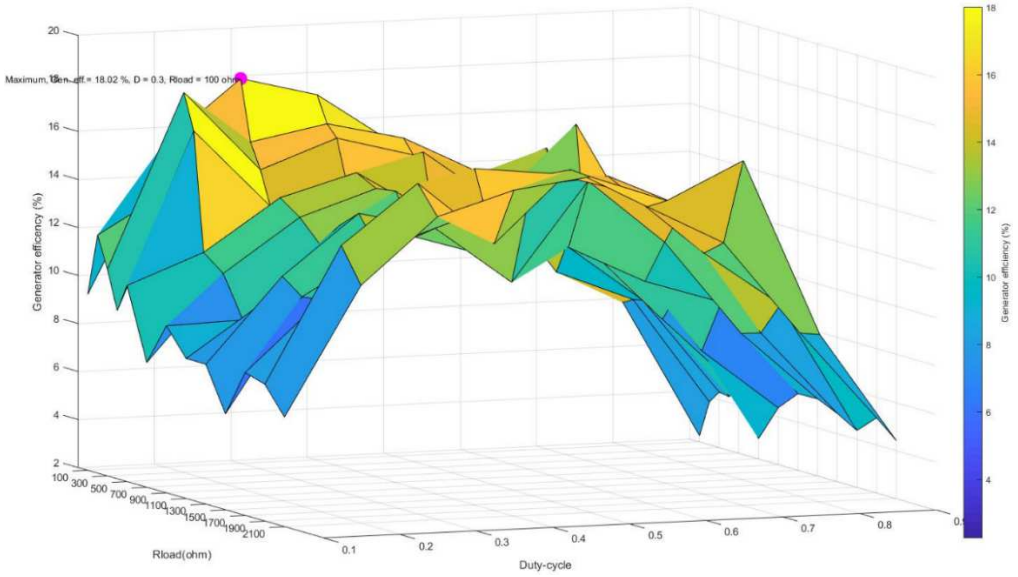

c) Generator efficiency sweep.

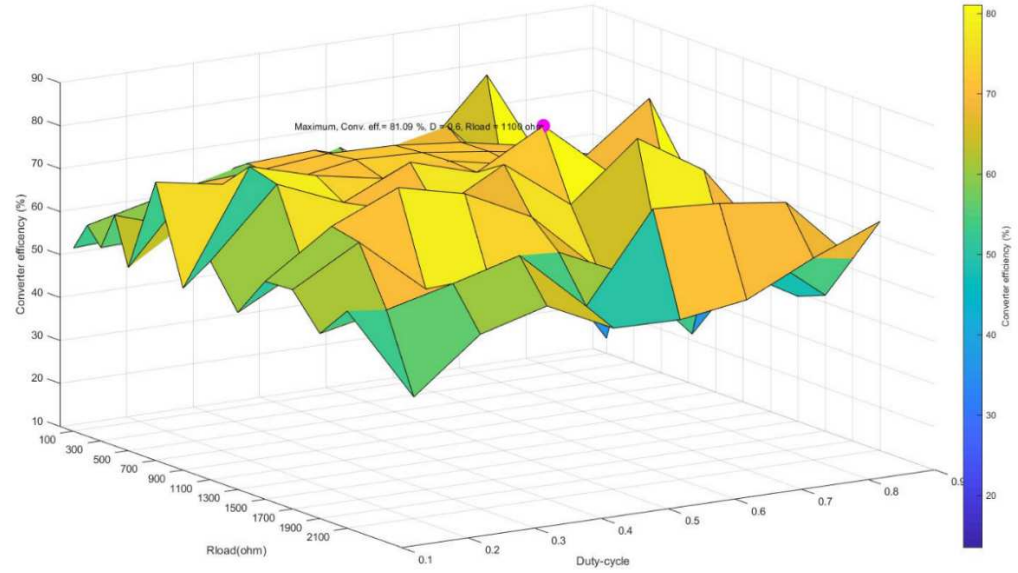

d) Side diode converter efficiency sweep.

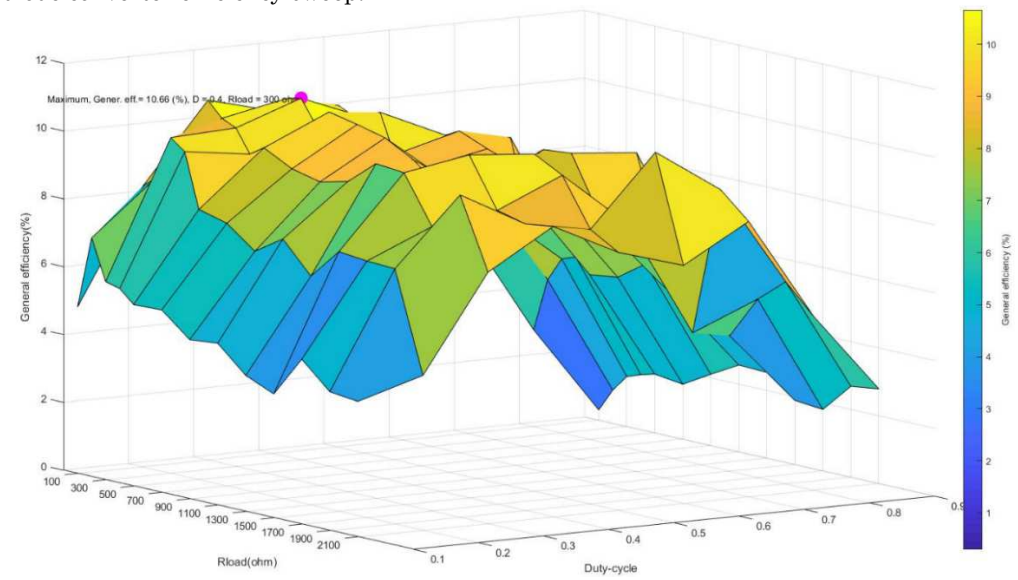

e) Complete system (generator + side diode converter) efficiency sweep.

Figure 9-37: Side-diode converter sweep with minimum wind condition.

Generator maximum efficiency is 18.06 % for 100 Ω load and 0.3 duty-cycle. Converter efficiencies are higher than 40 %, achieving maximum efficiency of 81.09 % with

a duty-cycle of 0.6 for 1100 Ω resistive load. Moreover, complete system maximum efficiency is 10.66 % for 300 Ω load and 0.4 duty-cycle.

Table 9-27 shows simulations results with maximum (10 m/s) wind velocity. Sweeps have been done between 100 and 2100 Ω resistive load, 0-1 and 0.9 duty-cycles, with 500 and 1000 kHz switching frequencies.

Table 9-27: Side diode topology converter simulations best results with maximum input conditions.

Peak	V_{in} (V_{pp})	f_{in} (kHz)	R_{load} (Ω)	D	f_{sw} (kHz)	V_{out} (V)	I_{out} (mA)	P_{out} (mW)	$P_{control}$ (mW)	P_{out} (mW)
1st	3.91	5.28	100	0.4	500	4.19	41.95	176.02	3.4	172.62
2nd	4.13	6.29	1700	0.5	500	15.27	8.98	137.3	3.46	133.84
1st	4.14	6.12	100	0.5	1000	4.22	42.206	178.13	6.79	171.34
2nd	4.19	6.78	800	0.5	1000	10.01	12.52	125.47	6.87	120.6

Respect the double power manager requirement of output voltage level between 3 and 5 Volts, the first peak is the appropriate one when wind velocity is 10 m/s input condition.

Maximum valid output power with side-diode topology at 10 m/s wind velocity condition is 172.62 mW for 100 Ω load and 4.19 V level signal. Besides, appoint that highest power levels happen when duty-cycle is between 0.4 and 0.5 and with 500 kHz switching frequency.

Control power consumption represents the 1.9 % of the total available power with 500 kHz switching. When switching frequency is set at 1000 kHz, it rises to 2.5 %.

Figure 9-38 shows sweep results of a) output power, b) output voltage, c) generator efficiency, d) converter efficiency and e) complete system efficiency.

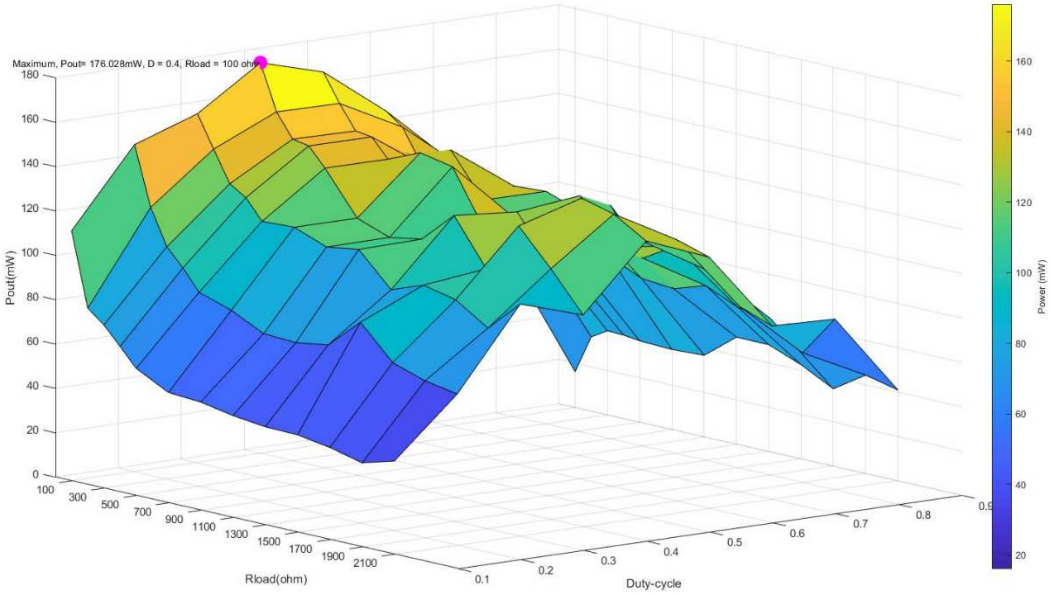

a) Output power sweep at resistive load.

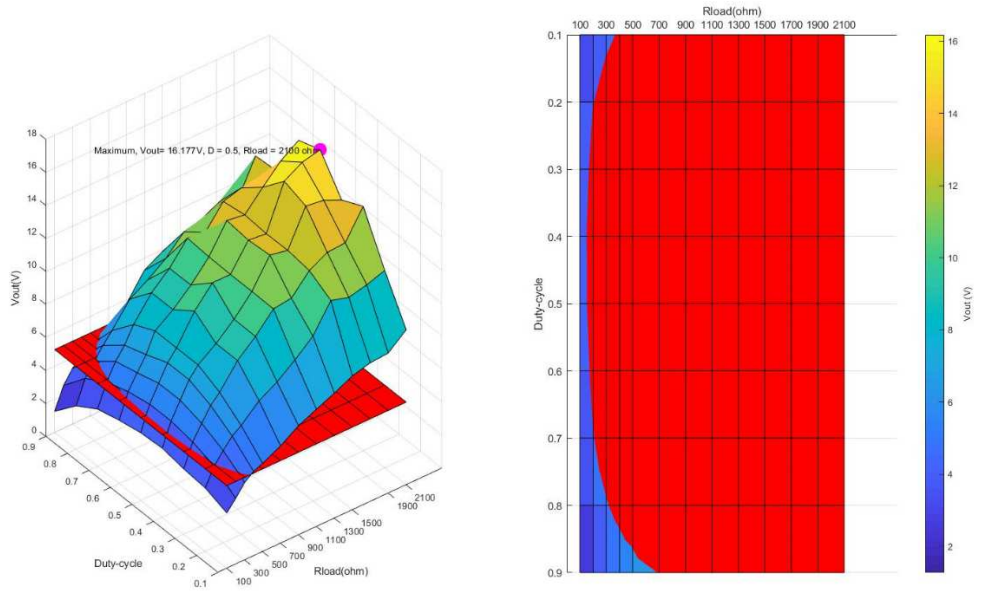

b) Output voltage sweep at resistive load; red plane of 3 Volt as minimum needed.

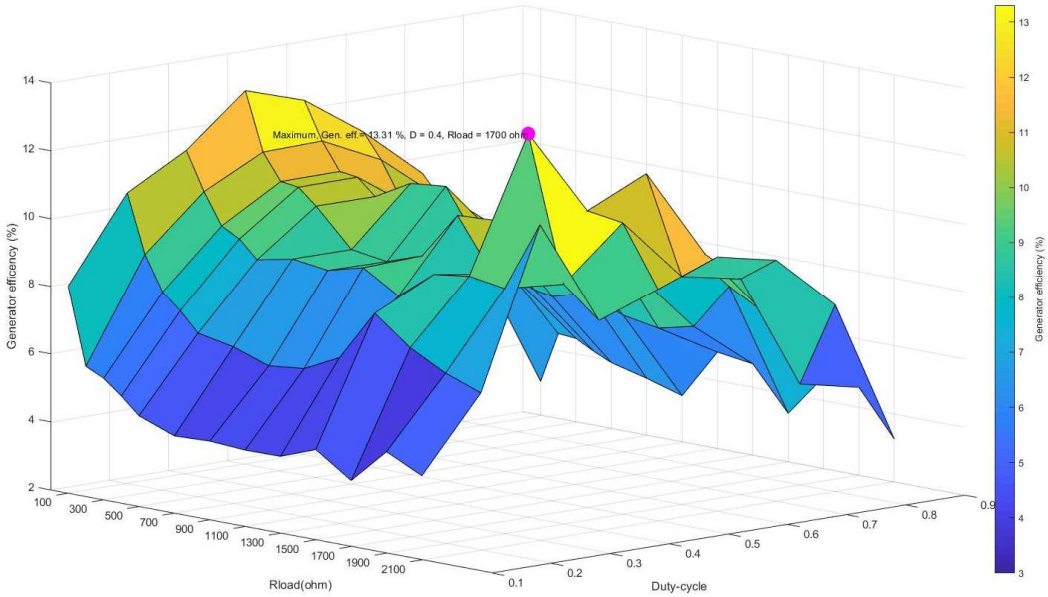

c) Generator efficiency sweep.

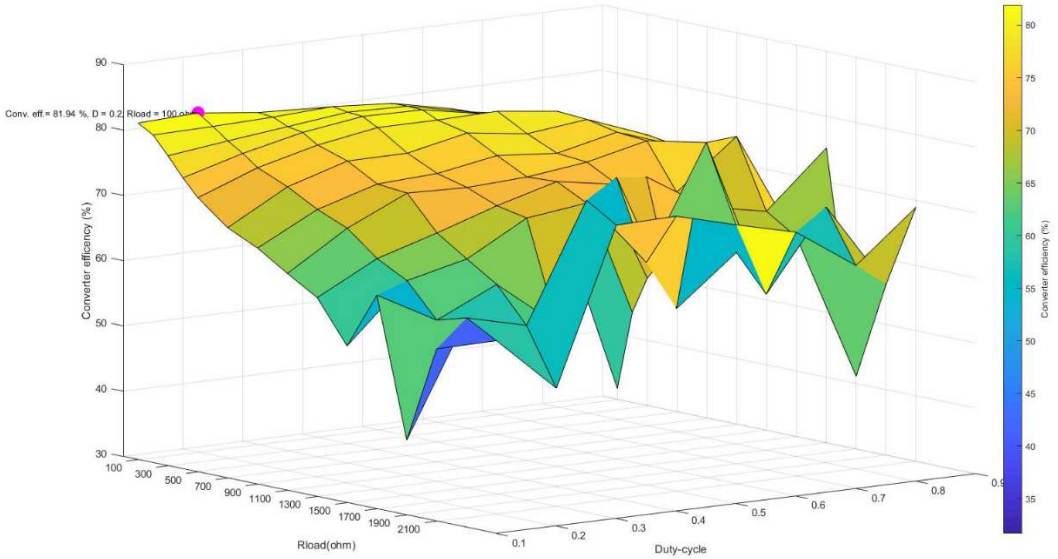

d) Side diode converter efficiency sweep.

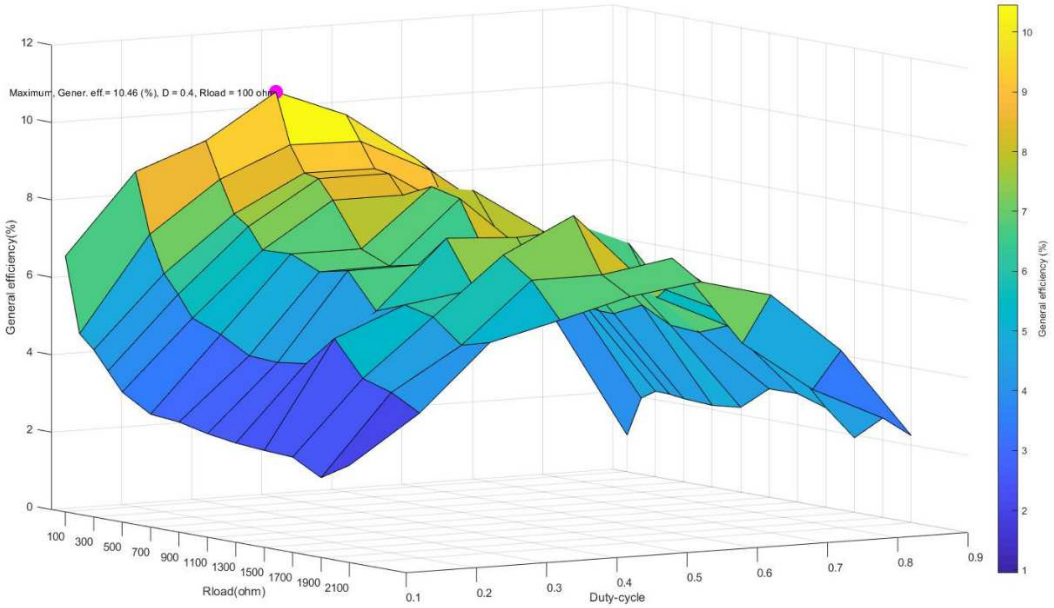

e) Complete system (generator + side diode converter) efficiency sweep.

Figure 9-38: Side diode sweeps with maximum wind condition.

Generator maximum efficiency is 13.31 % for 1700 Ω load and 0.4 duty-cycle. Converter achieves a maximum efficiency of 81.94 % with a duty-cycle of 0.2 for 100 Ω resistive load. Moreover, complete system maximum efficiency is 10.46 % for 100 Ω load and 0.4 duty-cycle.

9.2.3.4 Split capacitor topology

The split capacitor topology-based converter [239][240] is composed by sixth MOSFETs (M1, M2, M3, M4, M5, and M6). Which are connected as the same way as in side-diode topology and making able the bidirectional switching. The diodes (D1, D2, D3, D4, D5, and D6) provide rectifying path in each half cycle for each phase. Six capacitors (two per phase) with same capacitance value, are used for charge recycling and to replace the diodes D3, D4, D7, D8, D11 and D12 of the side diode topology. Diode forward voltage drop is avoided thanks to this, having fewer losses and improving system efficiency. The output capacitor saves the required DC voltage for the resistive load.

Inside this architecture type, two variations are going to be simulated and analysed:

9.2.3.4.1 Split topology with N-type MOSFETs

The denominated N-type Split topology is composed of six N-type MOSFETs (M_1, M_2, M_3, M_4, M_5 and M_6). This topology schematic is shown in figure 9-39:

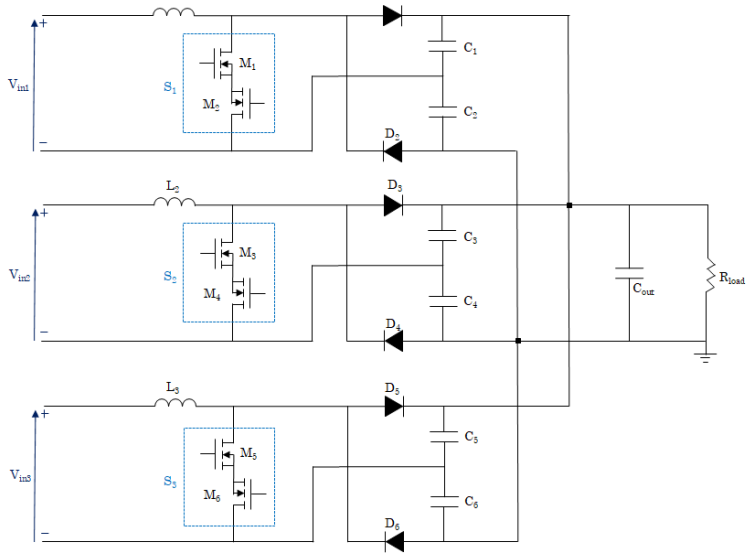

Figure 9-39: Split N capacitor three-phase circuit.

This converter has four operation modes and two cycles, positive and negative.

In the positive half cycle:

Mode I: MOSFETs (M_1, M_2, M_3, M_4, M_5 and M_6) are turned on thus inductor's currents (I_{L1}, I_{L2} and I_{L3}) built up from zero.

Mode II: The MOSFETs are turned off. Hence, the inductor forward biases the diode, D_1, D_3 and D_5 and charges the capacitors. The charging currents into C_1, C_3, and C_5 are positive and negative for C_{out} capacitor.

In the negative half cycle:

Mode III: In this mode, all the MOSFETs are turned on to increase inductor current in the opposite polarity of mode I, i.e., in the negative direction.

Mode IV: The MOSFETs are turned off. Now, the inductors forward bias the diodes, D_2, D_4 and D_6 charging the capacitors. The charging currents have the reverse polarity of mode II, negative for C_2, C_4, and C_6 and positive for C_{out}.

Substituting diodes by capacitors in the rectification part of the circuit, forward diode losses are reduced in this architecture compared with side-diode architecture.

Table 9-28 shows simulations results with minimum (3 m/s) wind velocity. Sweeps have been done between 100 and 1700 Ω resistive load, 0-1 and 0.9 duty-cycles, with 200 and 333 kHz switching frequencies.

Table 9-28: Split N capacitor topology converter simulations best results with minimum input conditions.

Peak	V_{in} (V_{pp})	f_{in} (kHz)	R_{load} (Ω)	D	f_{sw} (kHz)	V_{out} (V)	I_{out} (mA)	P_{out} (mW)	$P_{control}$ (mW)	P_{out} (mW)
1st	0.83	2.19	300	0.5	200	1.68	5.62	9.49	1.2	8.29
2nd	0.76	1.8	1500	0.4	200	2.70	1.80	4.88	1.2	2.66
1st	1.02	2.34	100	0.5	333	0.99	9.9	9.8	2	7.8
2nd	0.85	1.57	1300	0.5	333	3.20	2.46	7.88	2	5.88

Respect the double power manager requirement of output voltage level between 3 and 5 Volts, the second peak is the appropriate one when wind velocity is 3 m/s input condition.

Maximum valid output power with Split N topology at 3 m/s wind velocity condition is 5.88 mW for 1300 Ω load and 3.20 V level signal. In addition, appoint that highest power levels happen when duty-cycle is between 0.4 and 0.5 and with 500 kHz switching frequency.

Control power consumption represents the 12 % of the total available power with 200 kHz switching. When switching frequency is set at 333 kHz, it rises to 20 %.

Figure 9-40 shows sweep results of a) output power, b) output voltage, c) generator efficiency, d) converter efficiency and e) complete system efficiency.

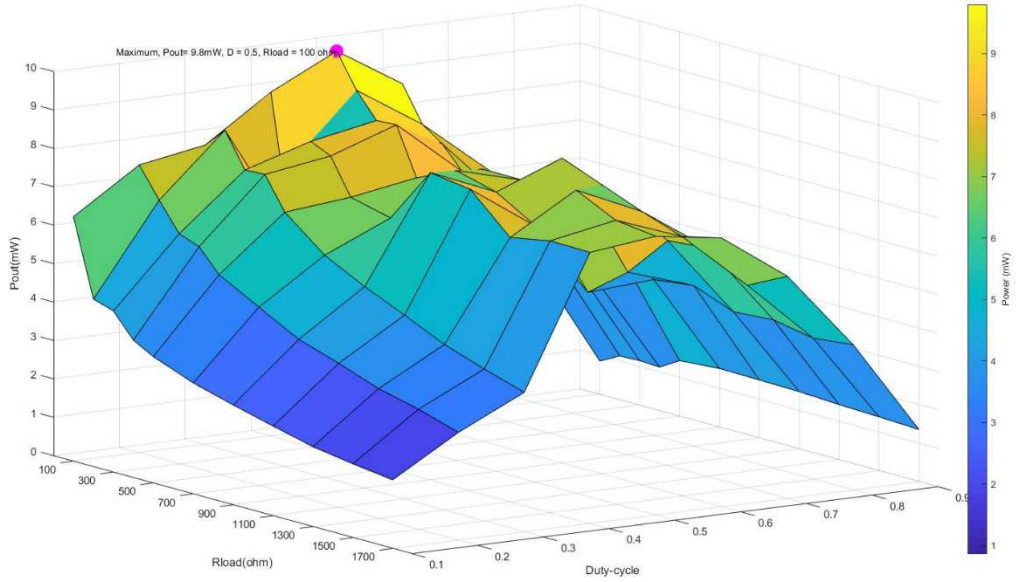

a) Output power sweep at resistive load.

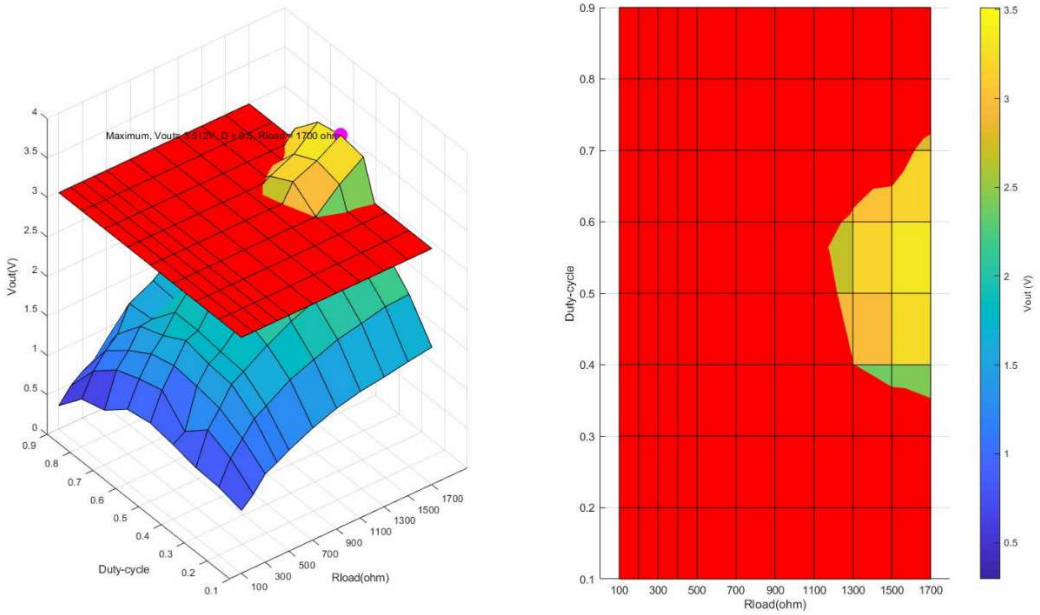

b) Output voltage sweep at resistive load; red plane of 3 Volt as minimum needed.

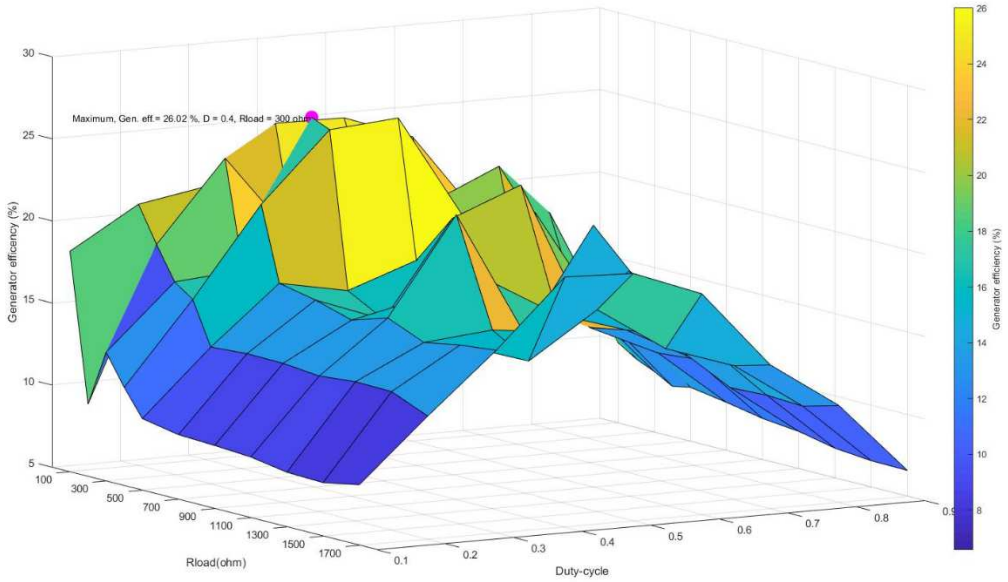

c) Generator efficiency sweep.

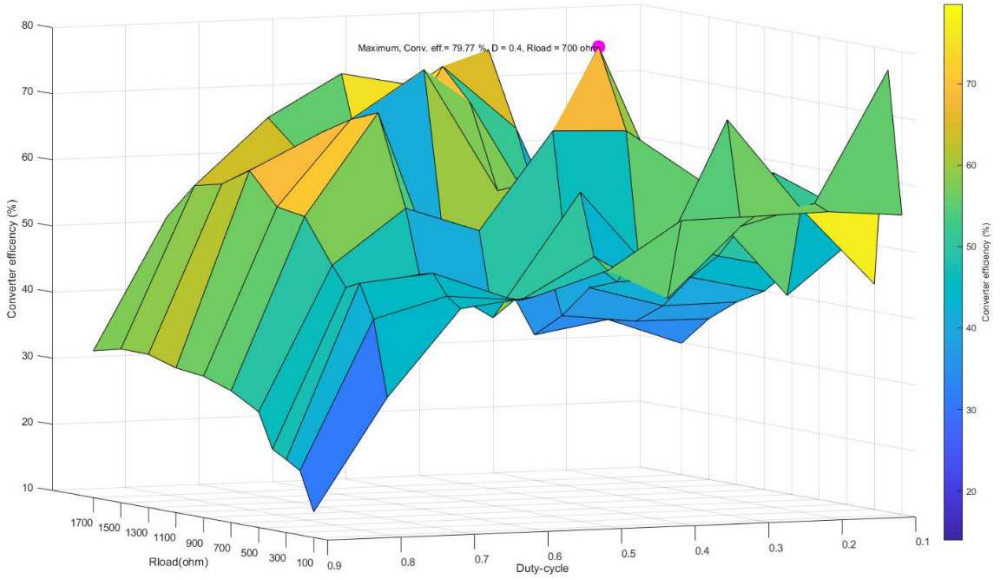

d) Side diode converter efficiency sweep.

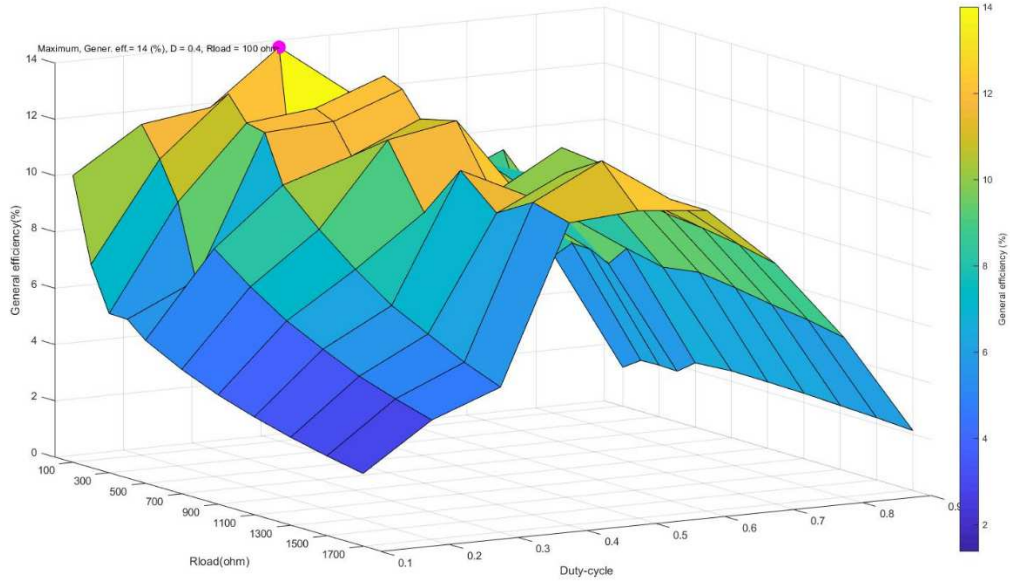

e) Complete system (generator + side diode converter) efficiency sweep.

Figure 9-40: Split N converter sweep with minimum wind condition.

Generator maximum efficiency is 26.02 % for 300 Ω load and 0.4 duty-cycle. Converter efficiencies are higher than 40 %, achieving maximum efficiency of 79.77 % with a duty-cycle of 0.4 for 700 Ω resistive load. And complete system maximum efficiency is 14 % for 100 Ω load and 0.4 duty-cycle.

Table 9-29 shows simulations results with maximum (10 m/s) wind velocity. Sweeps have been done between 100 and 2100 Ω resistive load, 0-1 and 0.9 duty-cycles, with 500 and 1000 kHz switching frequencies.

Table 9-29: Split N capacitor topology converter simulations best results with maximum input conditions.

Peak	V_{in} (V_{pp})	f_{in} (kHz)	R_{load} (Ω)	D	f_{sw} (kHz)	V_{out} (V)	I_{out} (mA)	P_{out} (mW)	$P_{control}$ (mW)	P_{out} (mW)
1st	4.09	6.42	100	0.4	500	4.26	42.63	181.77	3.29	178.48
2nd	3.27	6.78	1100	0.5	500	13.23	10.18	134.77	3.26	131.51
1st	3.66	7.33	100	0.3	1000	4.07	40.75	166.07	6.57	159.5
2nd	2.96	7.71	1400	0.5	1000	12.36	12.36	152.78	6.58	146.20

In this case, the first peak is the appropriate one when wind velocity is 10 m/s input condition.

Maximum valid output power with Split N topology at 10 m/s wind velocity condition is 178.48 mW for 100 Ω load and 4.26 V level signal. In this case, also the highest power levels happen when duty-cycle is between 0.4 and 0.5 and with 500 kHz switching frequency.

Control power consumption represents the 1.8 % of the total available power with 500 kHz switching. When switching frequency is set at 1000 kHz, it rises to 2.4 %.

Figure 9-41 shows sweep results of a) output power, b) output voltage, c) generator efficiency, d) converter efficiency and e) complete system efficiency.

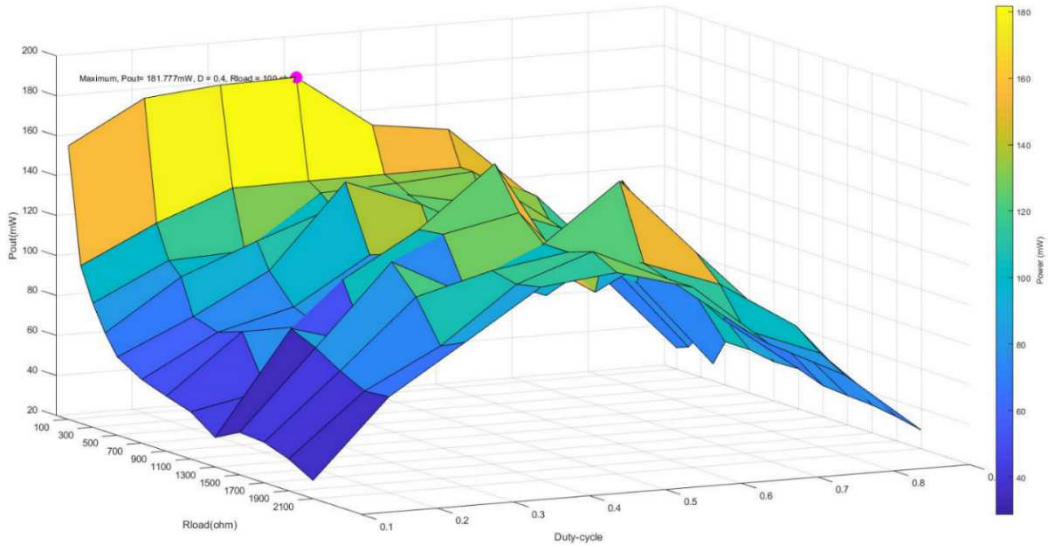

a) Output power sweep at resistive load.

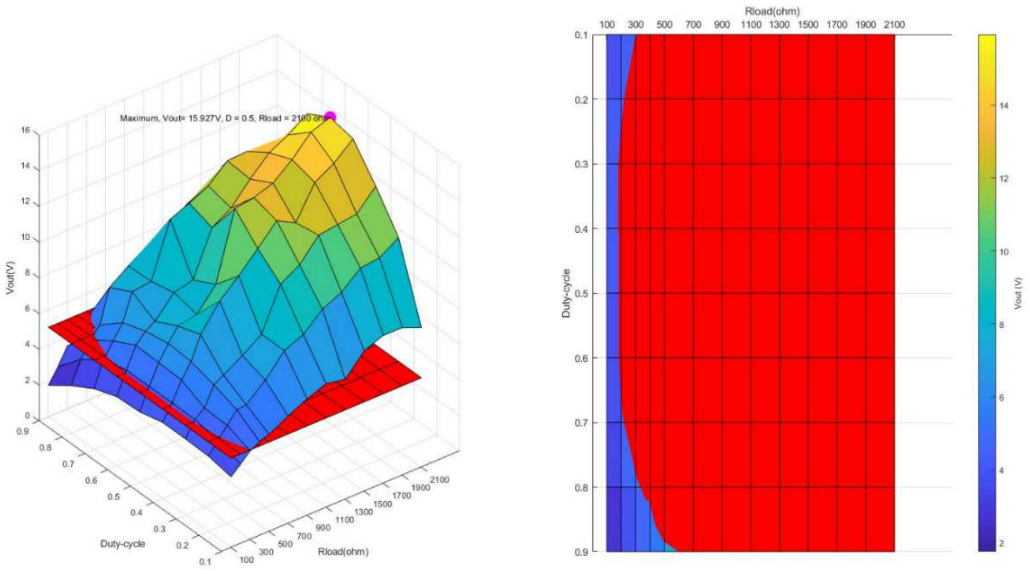

b) Output voltage sweep at resistive load; red plane of 3 Volt as minimum needed.

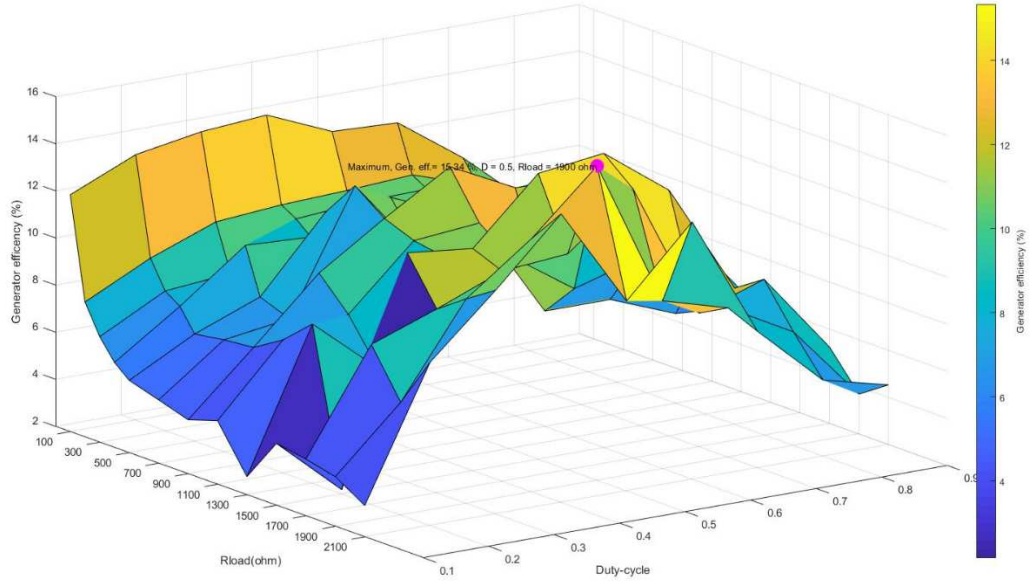

c) Generator efficiency sweep.

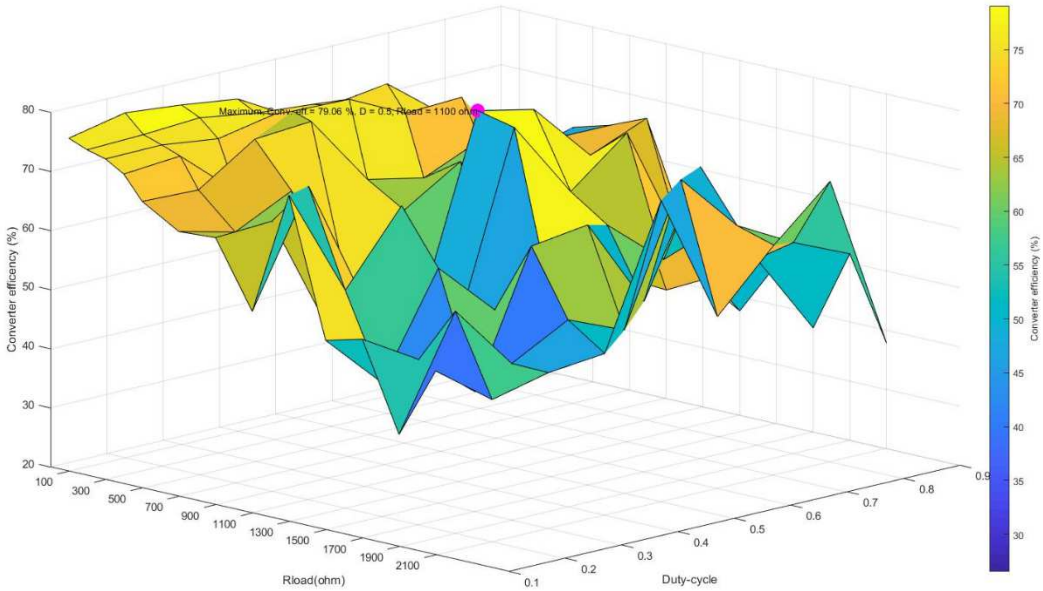

d) Side diode converter efficiency sweep.

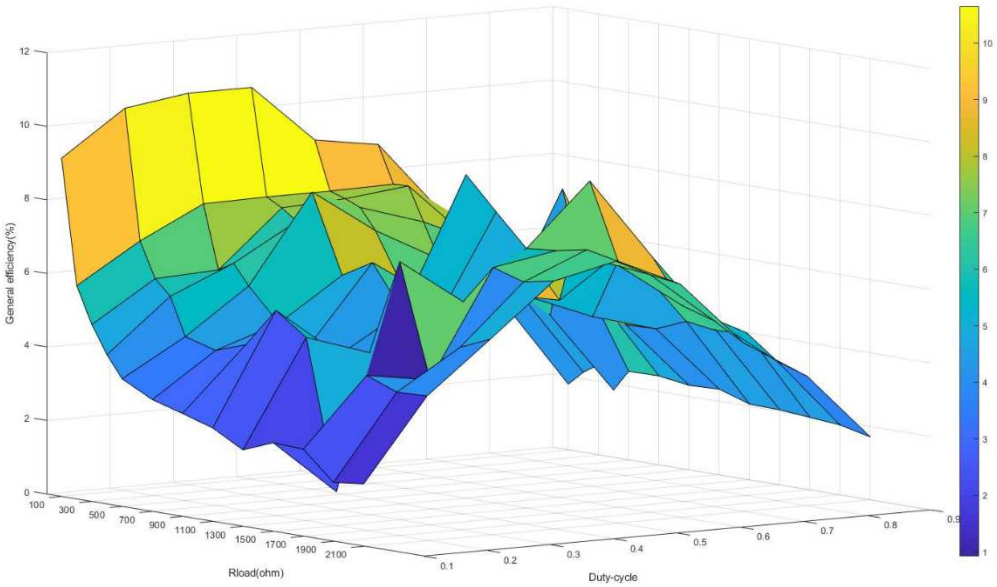

e) Complete system (generator + side diode converter) efficiency sweep.

Figure 9-41: Split N converter sweeps with maximum wind condition.

Generator maximum efficiency is 15.34 % for 1900 Ω load and 0.5 duty-cycle. Converter achieves a maximum efficiency of 79.06 % with a duty-cycle of 0.5 for 1100 Ω resistive load. And complete system maximum efficiency is 14 % for 100 Ω load and 0.4 duty-cycle.

9.2.3.4.2 Split topology with N and P-type MOSFETs

The denominated Split NP topology is composed by six MOSFETs, three P-type (M_1, M_3, and M_5) and other three N-type (M_2, M_4, and M_6). This topology schematic is shown in figure 9-42:

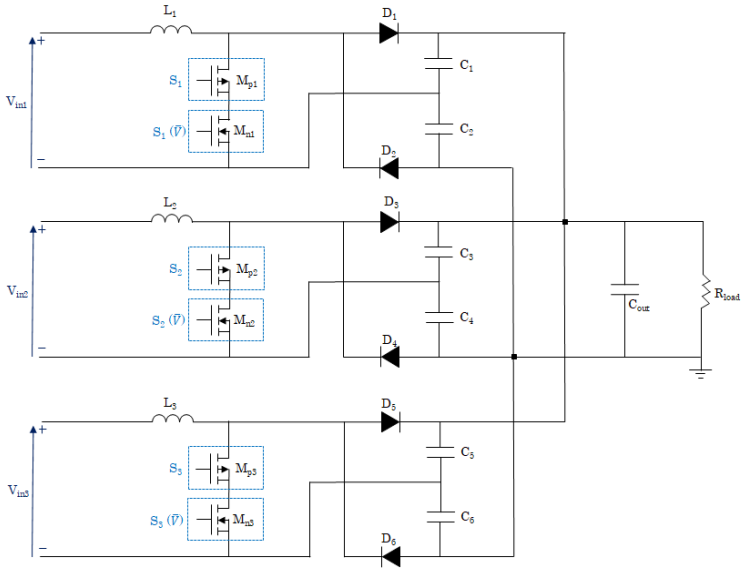

Figure 9-42: Split capacitor three-phase circuit with P and N MOSFETs, Split NP.

The control signals to work as a rectifier boost mode in three phases with six MOSFETs are shown in figure 9-43:

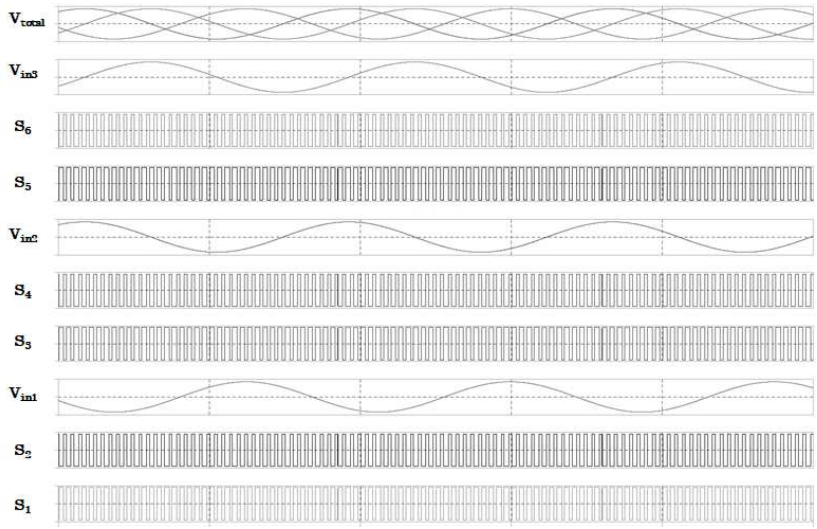

Figure 9-43: Control signals of split capacitor three-phase circuit with P and N MOSFETs.

Each phase has two different control signals. Due to the behaviour of P-type MOSFETs, which need negative level voltage signal in the source path.

Thus, S_1 and S_2, S_3 and S_4, S_5 and S_6 are going to be control signals for first, second and third phase respectively. S_2 is the neglected voltage value of S_1, i.e., $S_2=\overline{S_1}$. Also, the same effect at other phases control signals, $S_4=\overline{S_3}$ and $S_6=\overline{S_5}$.

Table 9-30 shows simulations results with minimum (3 m/s) wind velocity. Sweeps have been done between 100 and 1900 Ω resistive load, 0-1 and 0.9 duty-cycles, with 200 and 333 kHz switching frequencies.

Table 9-30: Split NP capacitor topology converter simulations best results with minimum input conditions.

Peak	V_{in} (V_{pp})	f_{in} (kHz)	R_{load} (Ω)	D	f_{sw} (kHz)	V_{out} (V)	I_{out} (mA)	P_{out} (mW)	$P_{control}$ (mW)	P_{out} (mW)
1st	0.96	1.92	100	0.5	200	1.02	1.21	10.43	1.96	8.47
2nd	0.686	2.12	1300	0.5	200	3.41	2.62	8.95	1.95	7
1st	0.969	2.41	100	0.5	333	0.92	9.28	8.61	3.32	5.29
2nd	0.689	2.42	1700	0.4	333	3.28	1.92	6.33	3.24	3.09

Respect the double power manager requirement of output voltage level between 3 and 5 Volts, the second peak is the appropriate one when wind velocity is 3 m/s input condition.

Maximum valid output power with Split NP topology at 3 m/s wind velocity condition is 8.95 mW for 1300 Ω load and 3.41 V level signal. In addition, appoint that highest power levels happen when duty-cycle is 0.5 and with 500 kHz switching frequency.

Control power consumption represents the 21 % of the total available power with 200 kHz switching. Reducing the output power from 8.95 mW to 7 mW.

Figure 9-44 shows sweep results of a) output power, b) output voltage, c) generator efficiency, d) converter efficiency and e) complete system efficiency.

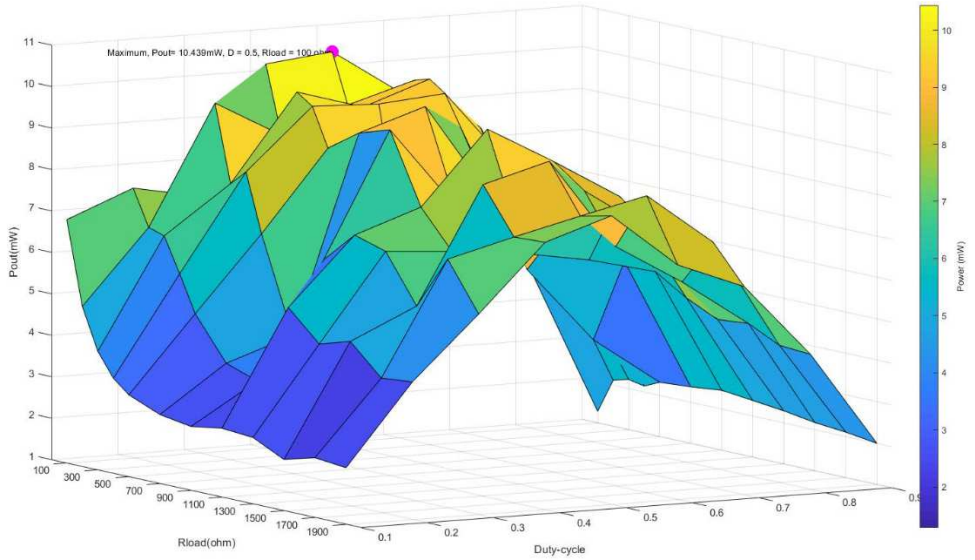

a) Output power sweep at resistive load.

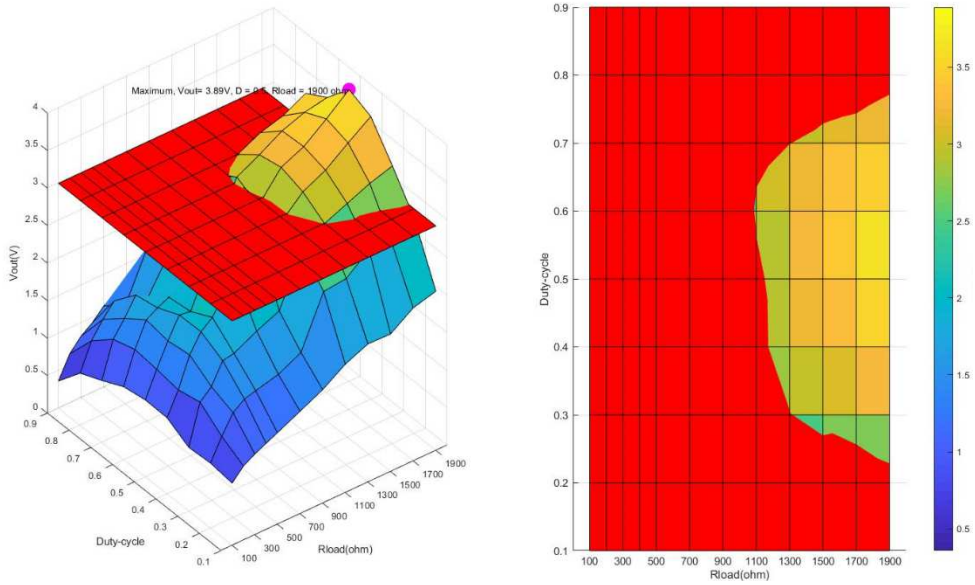

b) Output voltage sweep at resistive load; red plane of 3 Volt as minimum needed.

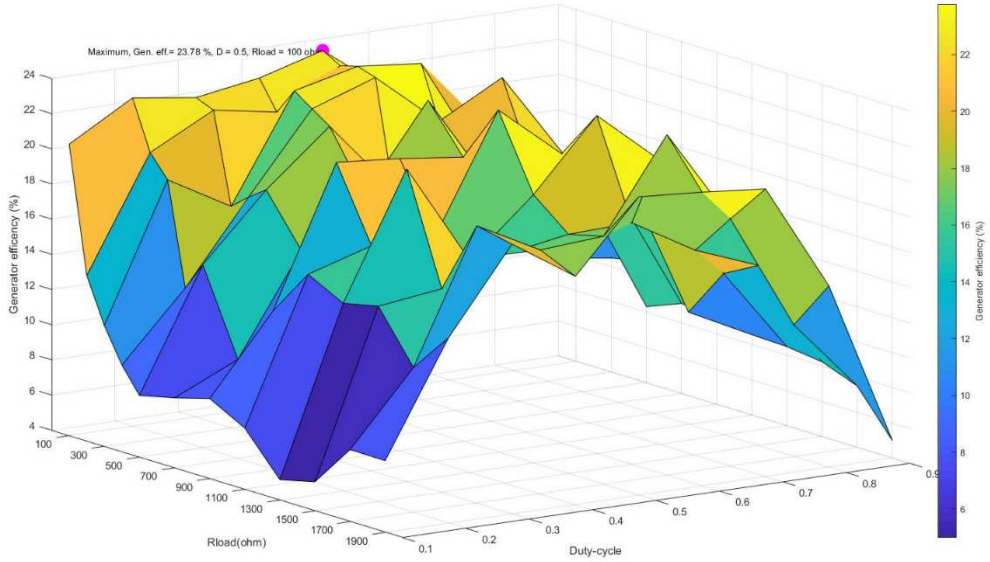

c) Generator efficiency sweep.

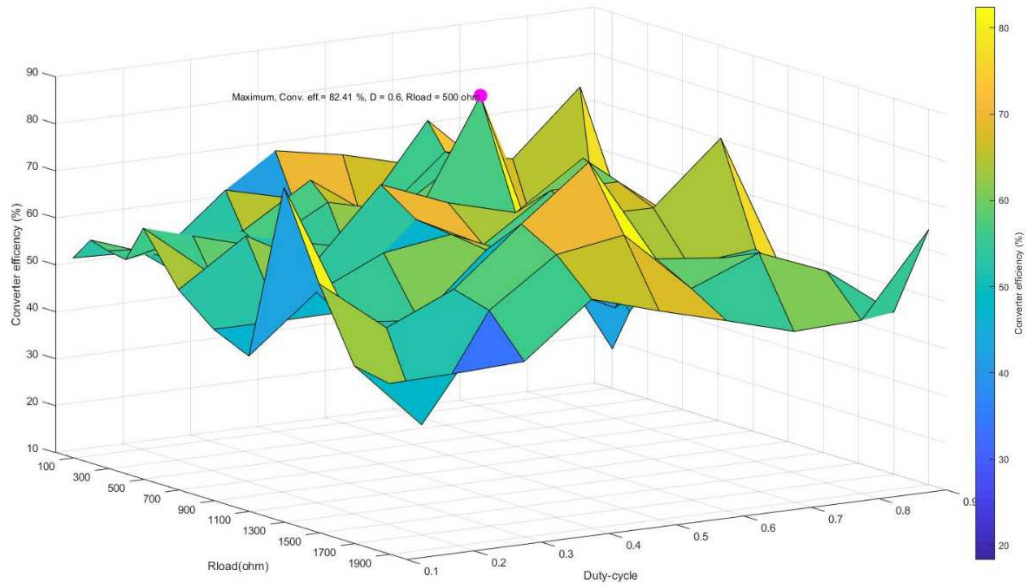

d) Side diode converter efficiency sweep.

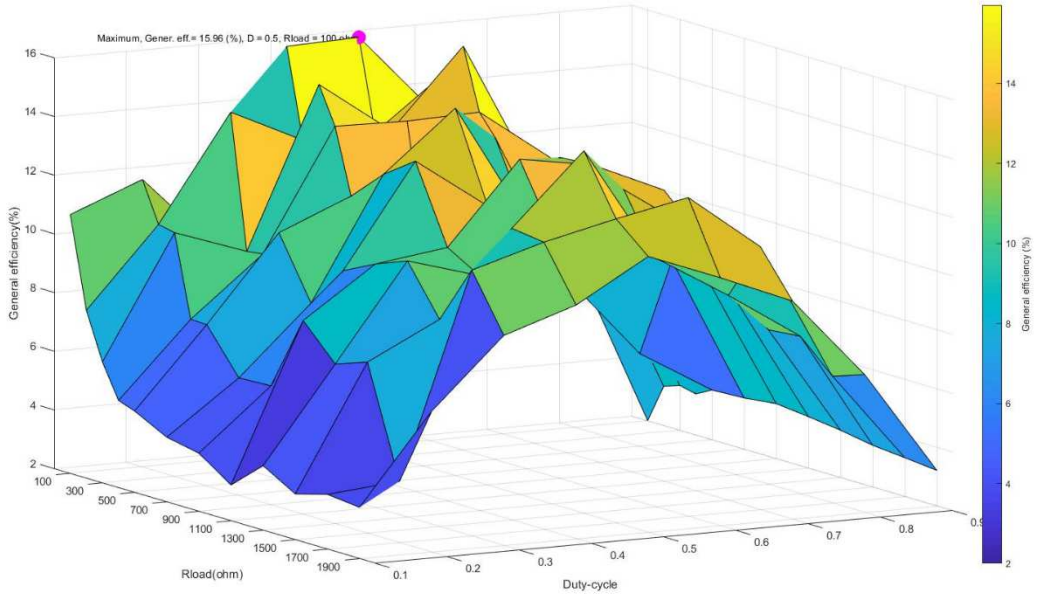

e) Complete system (generator + side diode converter) efficiency sweep.

Figure 9-44: Split NP converter sweeps with minimum wind condition.

Generator maximum efficiency is 23.78 % for 100 Ω load and 0.5 duty-cycle, being similar to 24 % achieved with 27 Ω load without any converter or rectifier, i.e., perfect impedance matching. Converter efficiencies are higher than 50 %, achieving maximum efficiency of 82.41 % with a duty-cycle of 0.6 for 500 Ω resistive load. And complete system maximum efficiency is 15.96 % for 100 Ω load and 0.5 duty-cycle.

Table 9-31 shows simulations results with maximum (10 m/s) wind velocity. Sweeps have been done between 100 and 2100 Ω resistive load, 0-1 and 0.9 duty-cycles, with 500 and 1000 kHz switching frequencies.

Table 9-31: Split NP capacitor topology converter simulations best results with maximum input conditions.

Peak	V_{in} (V_{pp})	f_{in} (kHz)	R_{load} (Ω)	D	f_{sw} (kHz)	V_{out} (V)	I_{out} (mA)	P_{out} (mW)	$P_{control}$ (mW)	P_{out} (mW)
1st	2.31	7.77	100	0.4	500	4.33	43.34	187.84	5.01	182.83
2nd	2.27	7.65	900	0.5	900	10.03	11.15	111.88	4.99	106.89
1st	3.25	8.49	100	0.3	1000	3.87	38.78	150.41	10.53	139.88

2nd	3.39	8.25	1600	0.4	1000	13.25	8.28	109.74	10.05	99.69

In this case, the first peak is the appropriate one when wind velocity is 10 m/s input condition.

Maximum valid output power with Split NP topology at 10 m/s wind velocity condition is 187.84 mW for 100 Ω load and 4.33 V level signal. In this case, also the highest power levels happen when duty-cycle is between 0.4 and 0.5 and with 500 kHz switching frequency.

Control power consumption represents the 2.5 % of the total available power with 500 kHz switching. When switching frequency is set at 1000 kHz, it rises to 10 %.

Figure 9-45 shows sweep results of a) output power, b) output voltage, c) generator efficiency, d) converter efficiency and e) complete system efficiency.

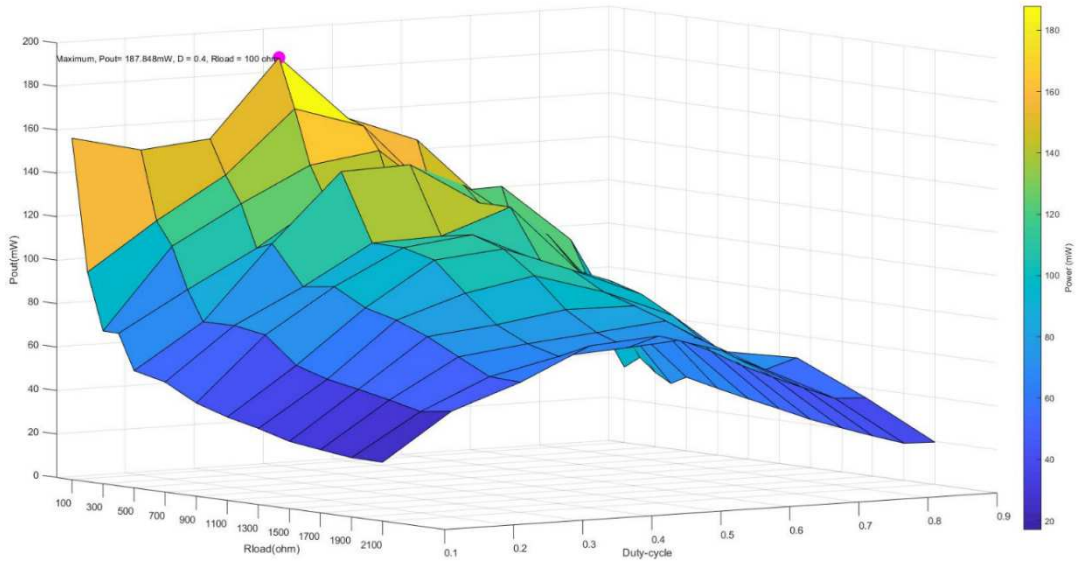

a) Output power sweep at resistive load.

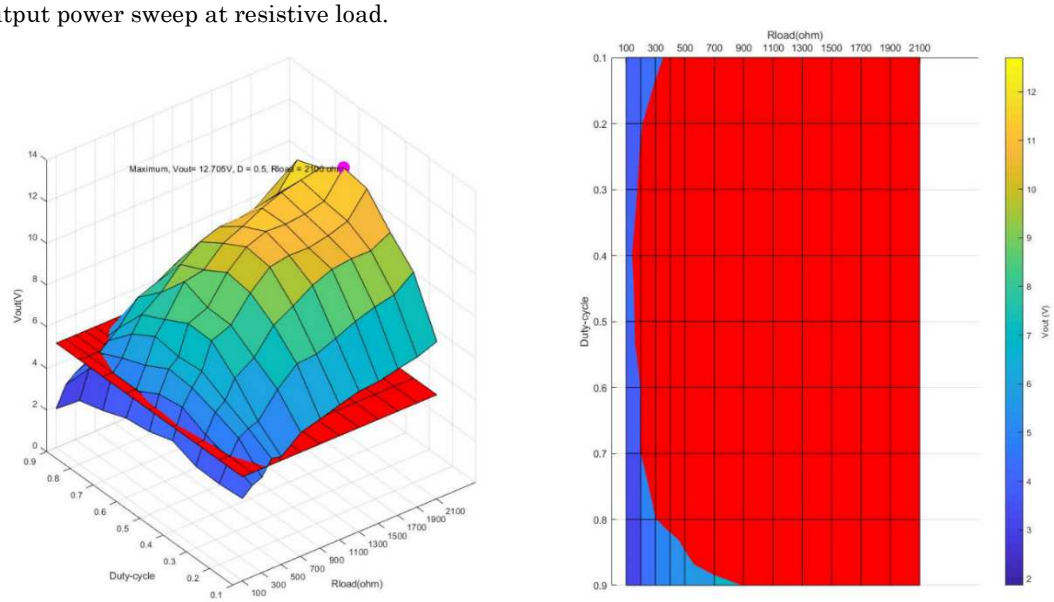

b) Output voltage sweep at resistive load; red plane of 3 Volt as minimum needed.

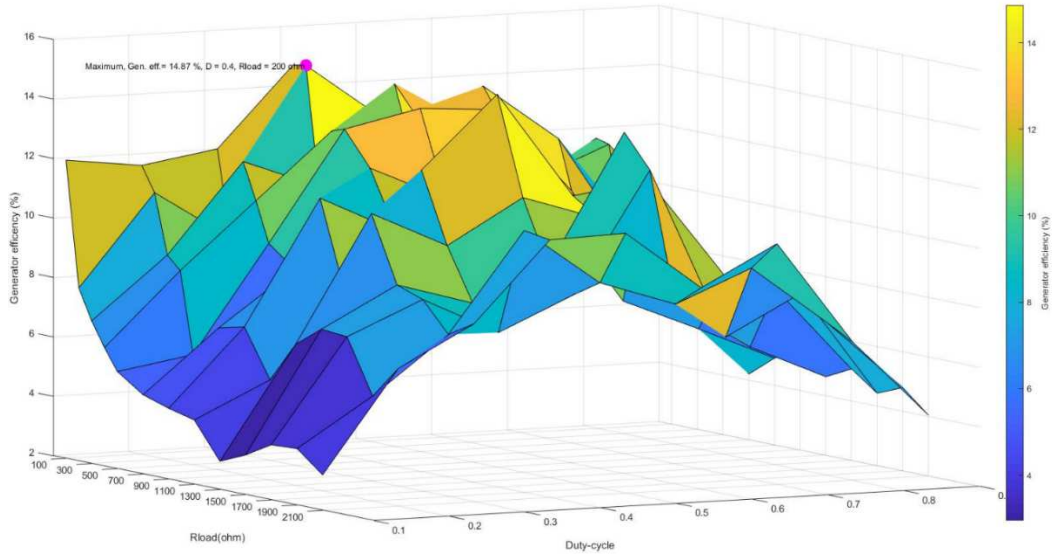

c) Generator efficiency sweep.

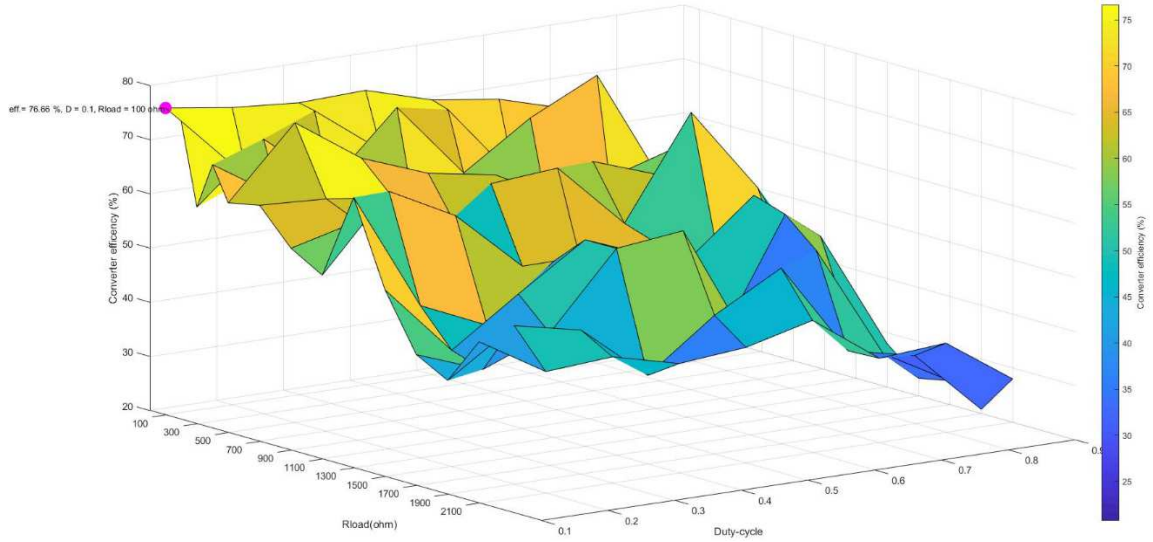

d) Side diode converter efficiency sweep.

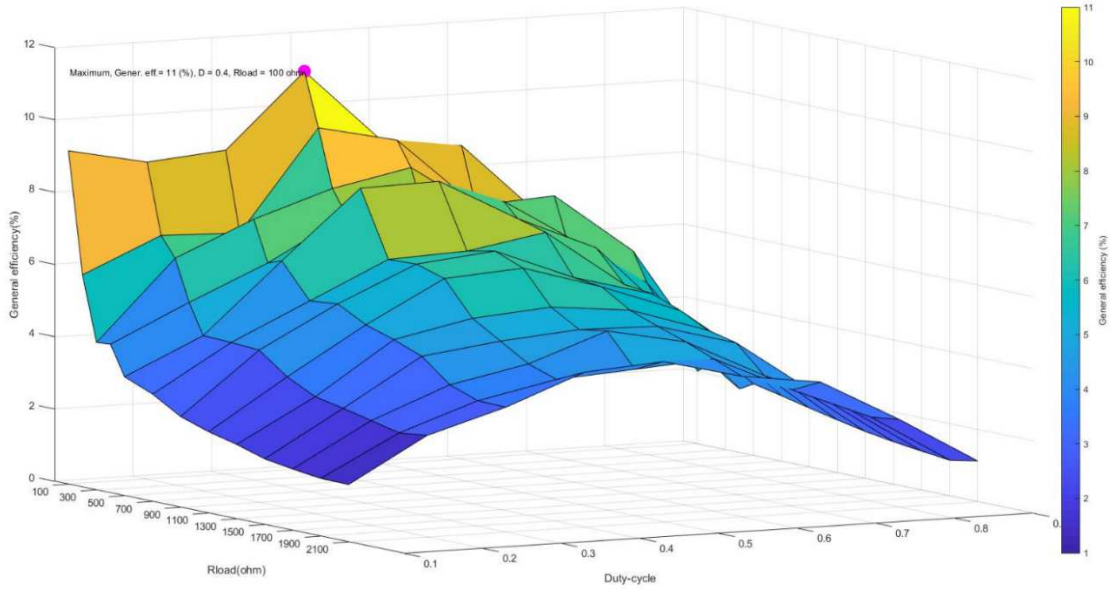

e) Complete system (generator + side diode converter) efficiency sweep.

Figure 9-45: Split NP converters sweep with maximum wind condition.

Generator maximum efficiency is 14.87 % for 200 Ω load and 0.4 duty-cycle. Converter achieves a maximum efficiency of 76.66 % with a duty-cycle of 0.1 for 100 Ω

resistive load. And complete system maximum efficiency is 11 % for 100 Ω load and 0.4 duty-cycle.

To conclude, analysing all generator efficiency sweeps, could be seen that output power value at the resistive load is directly related with system highest efficiency. In addition, general efficiency is more dependent on generator efficiency than converter efficiency, i.e., the generator has more weight in the system efficiency.

9.2.4 Summarize of results and circuit selection

All the converters simulations results achieved through this section are summarized in this section. Harvester efficiency is set 100 % in all cases. In addition, at the end of the sub-section selected architecture is presented, giving several reasons for this decision.

Table 9-32 and figure 9-46 show results achieved with simulations when wind velocity is minimum, 3 m/s.

Table 9-32: Converters best result with the minimum input value.

Architec.	V_{in} (V_{pp})	f_{in} (kHz)	R_{load} (Ω)	D	f_{sw} (kHz)	V_{out} (V)	I_{out} (mA)	P_{out} (mW)	$\eta_{generator}$ (%)	$\eta_{converter}$ (%)	$\eta_{general}$ (%)
Harvester	0.54	1.89	27	-	-	0.54	28.24	15.25	24.37	100	24.37
D-bridge	1.05	1.79	100	-	-	0.57	5.71	3.26	12.35	35.02	4.32
Volt. dou.	0.97	1.47	100	-	-	0.51	0.51	2.66	7.61	41.84	3.18
Side diode	0.4	2.4	1500	0.5	200	3.08	2.05	6.32	13.6	74.32	10.11
Split N	0.85	1.57	1300	0.5	333	3.20	2.46	7.88	15.37	75	11.53
Split NP	0.68	2.12	1500	0.5	200	3.41	2.62	8.95	17.61	81.52	14.36

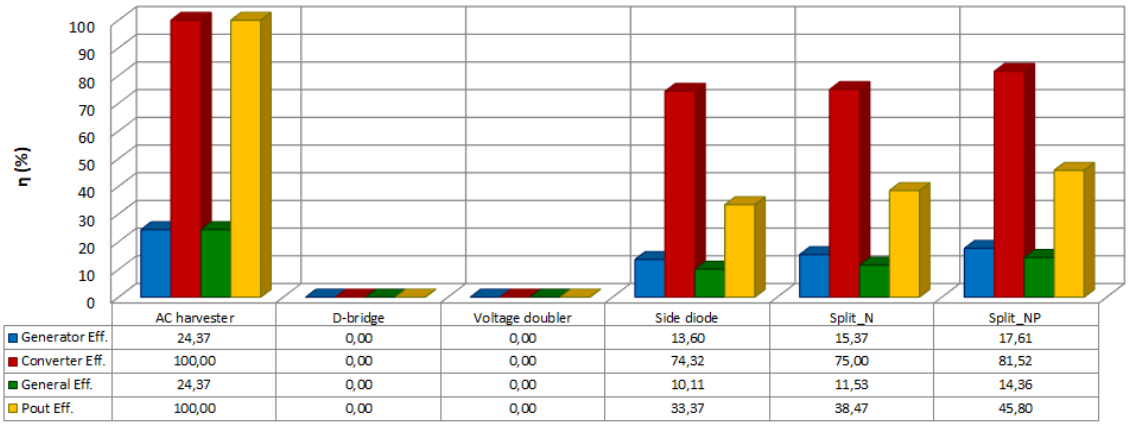

Figure 9-46: Generator, converter and complete system efficiencies with different topologies minimum input value.

Best efficiencies are obtained with Split NP architecture, being 17.61 % of the generator, 81.52 % of the converter, 14.36 % of the complete system and 45.80 % of output power respect the achieved with harvesters at impedance matching situation. Then, figure 9-47 shows the total power at the output point including the control consumption:

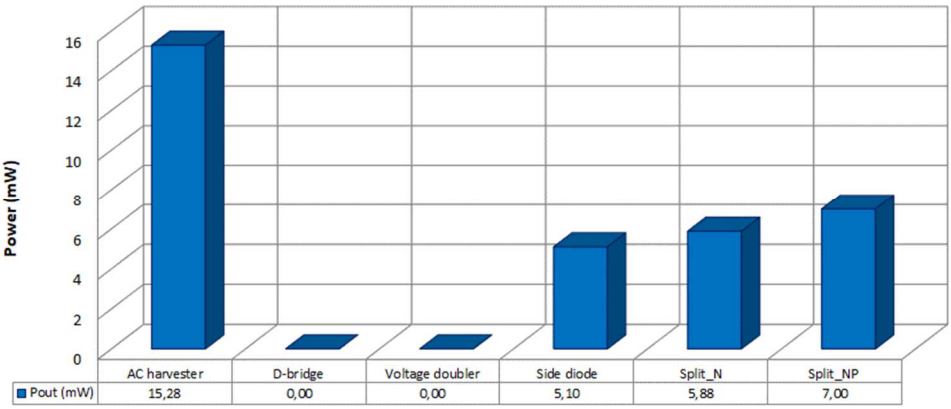

Figure 9-47: Different topology converters output maximum power with 3 m/s wind velocity.

Maximum available power is 7 mW and is obtained with Split NP topology. D-bridge and voltage doubler systems do not reach the minimum requirement of 3 Volt at output point; consequently, they are not valid.

Table 9-33 and figure 9-48 show results achieved with simulations when wind velocity is maximum, 10 m/s:

Table 9-33: Converters best result with the maximum input value.

Architec.	V_{in} (V_{pp})	f_{in} (kHz)	R_{load} (Ω)	D	f_{sw} (kHz)	V_{out} (V)	I_{out} (mA)	P_{out} (mW)	$\eta_{generator}$ (%)	$\eta_{converter}$ (%)	$\eta_{general}$ (%)
Harvester	2.44	8.76	27	-	-	2.44	136.4	332.9	19.55	100	19.55
D-bridge	3.63	6.75	100	-	-	3.1	30.6	93.7	9.72	42.64	4.15
Volt. dou.	3.54	4.99	130	-	-	3.01	23.1	69.8	6.38	53.68	3.42
Side diode	3.91	5.28	100	0.4	500	4.19	41.95	176.0	13.01	80.04	10.46
Split N	4.09	6.42	100	0.4	500	4.26	42.63	181.7	13.97	76.20	10.65
Split NP	2.31	7.77	100	0.4	500	4.33	43.34	187.8	14.8	74.33	11.00

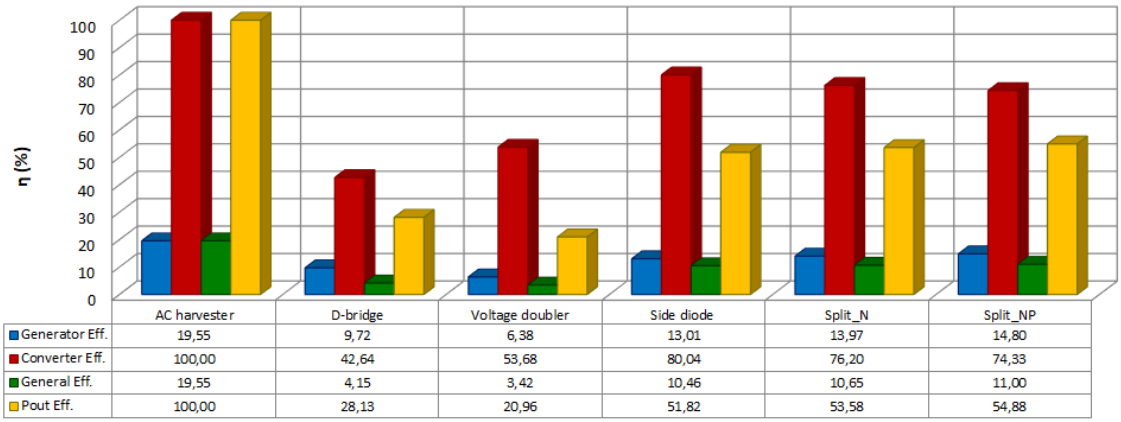

Figure 9-48: Generator, converter and complete system efficiencies with different topologies maximum input value.

In this case, best efficiencies are also obtained with Split NP architecture. Being 14.81 % of the generator, 74.33 % of the converter, 11 % of the complete system and 54.88 % of output power respect the achieved with harvesters at impedance matching situation. Split NP has not the best conversion efficiency, nevertheless, has the best matching with the generator. So as has been exposed, generator efficiency has more weight than converter efficiency for the final result. Then, figure 9-49 shows the total power at the output point including the control consumption:

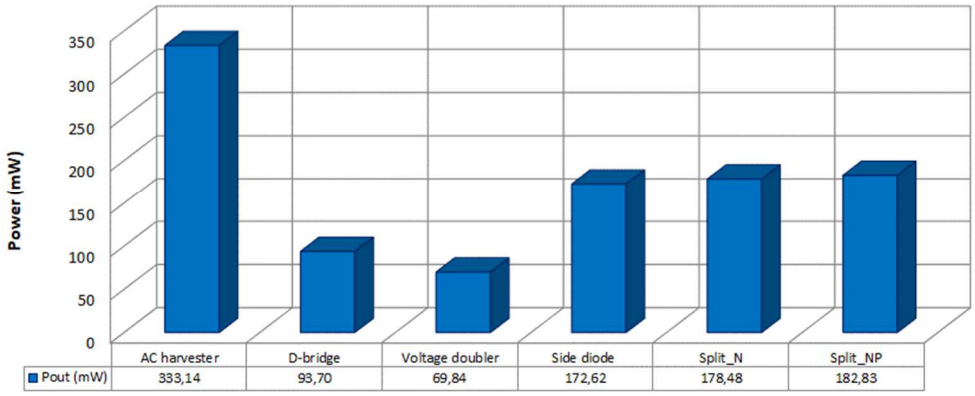

Figure 9-49: Different topology converters output maximum power with 10 m/s wind velocity.

Maximum available power is 182.83 mW and is obtained with Split NP topology. In this condition, D-bridge and voltage doubler systems reach the limit of 3 Voltage of minimum at output point. However, they not produce the highest level of output power with respective load.

Efficiencies are directly realted with wind flow velocity/pressure condition or input voltage/power level. Furthermore, the same effect occurs to the converters with the selection of MOSFETs. Due to the MOSFETs operations principles are the maximum responsible for the efficiency of the AC / DC converter.

Based on following reasons Split NP was selected as AC/DC converter of double power manager AC system:

- Adaptatively possibility
- Control less consumption
- More passive device quantity, thus less losses at system devices
- The highest efficient system with 3 m/s wind flow velocity condition as well as with 10 m/s wind flow velocity condition
- However, two types of control are needed.

10. Supercapacitor

Low power Energy Harvesting Wireless Sensor Nodes (EHWSN), whenever is feasible, uses supercapacitors to store energy instead of batteries due to their fast charging capability, low maintenance, and low environmental footprint.

So, the supercapacitor is set as low power storage element of the double low power system. The battery would be a better option for photovoltaic input system (constant energy input in long periods of time). However, due to the characteristic of AC input system behaviour (high power in short periods of time), the selected storage element has been the supercapacitor.

10.1 Principles of supercapacitor model

The supercapacitor is selected based on the capacitance needed and form factor for the target application, which requires to characterize the power consumption pattern of the target application. This information determines the size of the supercapacitor and whether if primary or secondary battery backup is needed. However, supercapacitors could not only be analysed based on its capacitance. Load current drain patterns, work cycle,

and temperature conditions change the characteristic of charge and discharge profiles [241]. The previous statement is especially true on energy harvesting applications because changes occur more often. Therefore, when the application must optimize the last drop of energy harvested, even in extreme conditions, simple model of supercapacitors are not enough to dimension the real energy storage capacity of the supercapacitor, i.e., the capacitance and its dynamical behaviour. The energy consumption pattern is a variable that depends on the application and the amount of available harvested energy, and it can be estimated statistically (windmills, solar panels indoors, etc.) [242]. This information and an accurate enough supercapacitor model will allow determining the required capacitance value for different conditions.

Electrochemical models can be found on [243][244], these studies and models use complex equations and relay on electrochemical theory based on physical principles show in Figure 1. Moreover, the parameters used in these equations are difficult to obtain because require complex, expensive measurement equipment and long measurement time. Despite this complexity, up to date, these models provide the best accuracy. Models based on equivalent circuits and mathematical equations are less complex and could provide enough accuracy. The present work uses the later techniques to characterize supercapacitors. The data required to parameterize the mathematical model is obtained through tests that provide the capacitors charge and discharge profiles under different conditions. The parameters identified are life cycle, voltage, time, temperature, moisture, Equivalent Series Resistance (ESR) and leakage resistance.

10.2 Experimental test

The mathematical model is verified through several experimental tests. The obtained results are used later for the training and verification processes of the machine learning algorithms of chapter 14. The tests also provide the charge current profile for the mathematical model.

As described in previous sections the behaviour of a supercapacitor is quite sensitive to several parameters. Therefore, to certify and guarantee that the measurements are valid the tests are defined as follows:

1- Define the number of tests, the test conditions, and measurement procedure.
2- Design and build an evaluation fixture for testing different supercapacitors simultaneously.
3- Implement the tests and obtain results.

10.2.1 Test definition

The number and type of test conditions are applied to variables or parameters are shown in table 10-1.

Table 10-1: List of variables and test conditions.

Variable	Temperature (°C)	Charge voltage (V)	Charge time (sec.)	Supercapacitor values (F)	Discharge time (sec.)
Test conditions	10, 25, 40, 60	2.5, 5	60, 600, 3600	1 F, 5 F	Infinity load, fixed value load, variable load steps

With this set of variables, it has been implemented, for each supercapacitor, 15 charge tests and 21 discharge tests, as shown in table 10-2:

Table 10-2: List of each test with each ambient condition.

Test number	Cap.	Operating conditions			Test number	Cap.	Operating conditions		
		Temp.	Volt.	Charge Time (sec)			Temp.	Volt.	Charge Time (sec)
Test1	1F	10	2.5	60	**Test2**	5F	10	2.5	60
Test3	1F	10	2.5	600	**Test4**	5F	10	2.5	600
Test5	1F	10	2.5	3600	**Test6**	5F	10	2.5	3600
Test7	1F	10	5	60	**Test8**	5F	10	5	60
Test9	1F	10	5	600	**Test10**	5F	10	5	600
Test11	1F	10	5	3600	**Test12**	5F	10	5	3600
Test13	1F	25	2.5	60	**Test14**	5F	25	2.5	60
Test15	1F	25	2.5	600	**Test16**	5F	25	2.5	600
Test17	1F	25	2.5	3600	**Test18**	5F	25	2.5	3600
Test19	1F	25	5	60	**Test20**	5F	25	5	60
Test21	1F	25	5	600	**Test22**	5F	25	5	600
Test23	1F	25	5	3600	**Test24**	5F	25	5	3600
Test25	1F	40	2.5	60	**Test26**	5F	40	2.5	60
Test27	1F	40	2.5	600	**Test28**	5F	40	2.5	600
Test29	1F	40	2.5	3600	**Test30**	5F	40	2.5	3600
Test31	1F	40	5	60	**Test32**	5F	40	5	60
Test33	1F	40	5	600	**Test34**	5F	40	5	600
Test35	1F	40	5	3600	**Test36**	5F	40	5	3600

Each test condition is reproduced in a climatic chamber. The test starts when the conditions are stabilized, and the power supply is turn on. Once the power supply is turned on the supercapacitor starts its charge. The charge process is isolated from the load to prevent energy losses. When the charge finishes, the power supply is disconnected from the supercapacitor. At this point, if there is no load, the self-discharge through the supercapacitor internal resistance starts. Different discharge profile are obtained connecting an electronic load to the capacitor. The load discharges profiles chosen goes range from a single constant discharge step up to five different constant discharge steps. This number is considered necessary to verify the mathematical and machine learning model, which may be of n stages.

10.2.2 Evaluation-board design and build

Figure 10-1b shows the evaluation board which is made of four test fixtures. The schematic of each text fixture is the same. The test circuit of Figure 10-1a has two switches and uses the following three states:

- Charging: first switch on and second off.
- Self-discharge process: with the capacitor in the charge state, the first switch is turned off.
- Load-dependent discharge process: with the capacitor in the charge state, the first switch is turned off and the second on.

This switched architecture emulates an energy-harvesting environment and prevents an instantaneous charge of the supercapacitor. The circuit has a current limiter resistor of 100 Ω at the input that limits the maximum charging current to 50 mA. The load is modelled with a variable resistance, and the voltage is regulated with a low dropout voltage regulator of 2V minimum input operation voltage (TPS79730-EP).

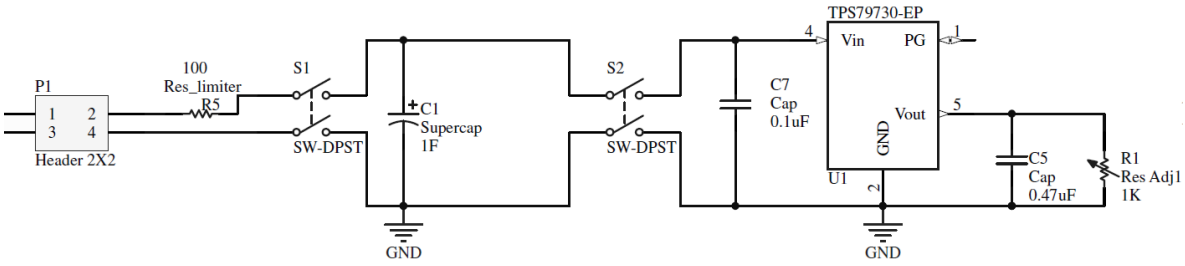

a) Schematic of a single capacitor test fixture.

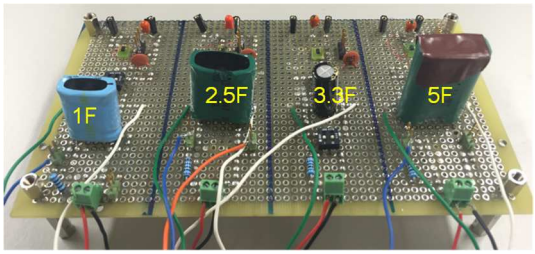

b) Complete test evaluation board.

Figure 10-1: Evaluation board set-up.

Unless the evaluation board has four capacitors, the measurement data obtained with two capacitors is enough to build, verify and validate the mathematical and machine learning model, the remain two are used to verify the test further. Therefore, the data present in this work comes from the models PM-5R0H105-R of 1F and PHV-5R4H505-R of 5F.

10.2.3 Tests results

The measurements of the charge current, charge and discharge voltage are obtained with a data logger switch unit, model 34970A and data acquisition periods of 1 second. The test set-ups results are summarized in the figures 10-2 and 10-3.

Traces of figure 10-2 show the charge and discharge profiles of the two aforementioned supercapacitors under test for a fix charging time of 600 seconds and voltage of 5 Volts, at four operation temperatures of 10, 25, 40 and 60 ºC.

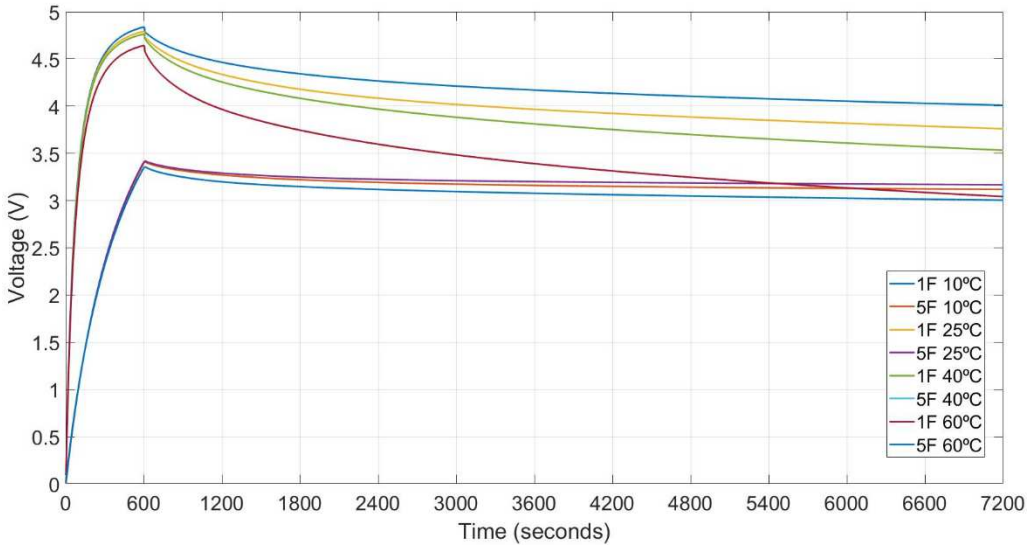

Figure 10-2: 1 F and 5 F supercapacitors charge and discharge curves at 10, 25, 40 and 60 ºC temperature.

The results show that the temperature impact on the supercapacitor charge and discharge profiles increases as its capacitance value decreases. Electrons movement is slower as the temperature decreases, which reduces the discharge rate. As the temperature builds up, the movement of internal electrons are faster. Thus, the number of the electrochemical reactions is higher, and therefore the discharge rate increases. Moreover, the temperature has a higher influence on the supercapacitor charge and discharge profile as its capacitance value decreases.

In figure 10-3, charge and discharge profiles of 1 and 5 F supercapacitor under different test conditions:

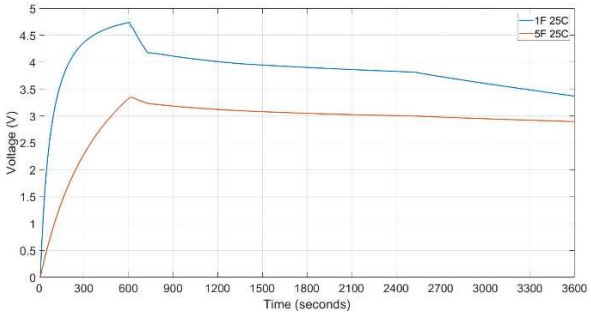

a) T=25 ºC, t_{charge}=600 sec, V_{charge}=5V, discharge profile (5 steps of I_{leak} 30sec, 3mA 90 sec, 0.058mA 600sec, I_{leak} 1200sec and 0.3mA until discharge).

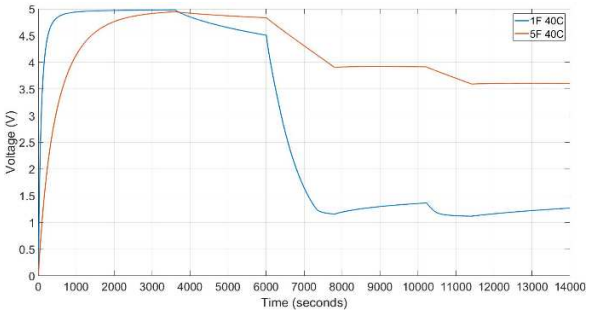

b) T=40 ºC, t_{charge} =3600 sec, V_{charge}=5 V, discharge profile (5 steps: I_{leak} 2400 sec, 3 mA 1800 sec, 0.025 mA 2400 sec, 1.5 mA 1200 sec, I_{leak} until discharge).

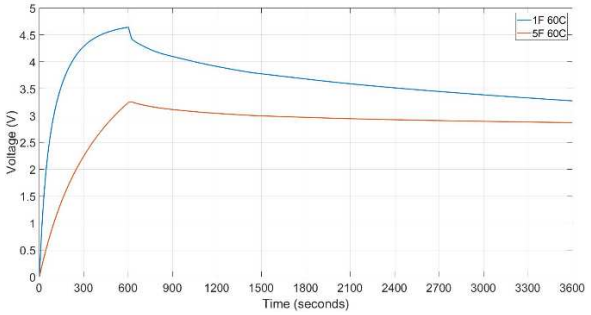

c) T=60 ºC, t_{charge} =600 sec, V_{charge}=5 V, discharge profile (3 steps: 0.3 mA 180 sec, 0.1 mA 600 sec, 0.058 mA until discharge).

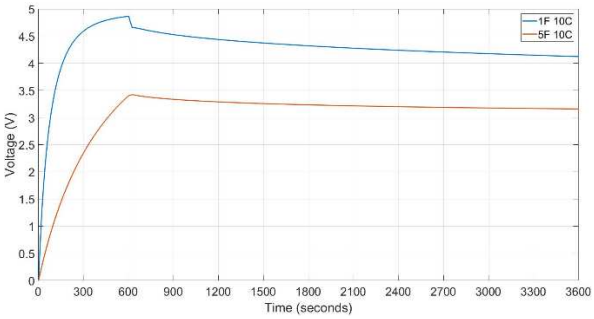

d) T=10 ºC, t_{charge} =600 sec, V_{charge}=5 V, discharge profile (single step: 0.02 mA until discharge).

Figure 10-3: Some of several experimental tests realized for future model verification.

Another test results are completed with the traces of figure 10-4 that provide the charge and discharge profiles of the two supercapacitors tested when the temperature conditions, the charging time, the load and the discharge pattern change. The profiles selected are quite different from validating the mathematical model for different ambient conditions and ranges. The results show that:

- The supercapacitor discharge curves are a function of the load and the discharge time.
- Changes in the ambient conditions and load produce a significant deviation of the discharge characteristic.
- The accuracy of the machine learning model is a direct function of the amount data.

Very different profiles have been chosen to validate the mathematical model in different ambient conditions and ranges. In addition, all realized tests are shown in appendix 16.4.2

10.3 Electro-mathematical model

The physical structure, chemical reactions and current distribution inside the capacitor could be modelled through mathematic expressions. These models characterise the non-linear behaviour of the leakage current, which is a function of the dynamic discharge pattern and the internal chemistry of the device.

Mathematical models take several critical parameters and give how this concrete parameter affect the operation way of the device. Models of these type are less complex to implement than models based on electrochemical equations. E.g., at [245] the state of charge estimation is realized considering charge redistribution in real-time systems as EHWSN. Implementation of such model without complex electrochemical equations provides good accuracy because requires low memory usage and has low computational cost.

The mathematical model selected is based on integro-differential equations. The electro-mathematical model presented combines the equations of [246]-[252]. As has aforementioned in section II, the existing electro-mathematical models [246]-[252] implements only one or two parameters, which produces a limited model. The present work increases the number of parameters, (capacitance life cycle, voltage, time, temperature, moisture, ESR, and leakage resistance), to characterize the supercapacitor behaviour and integrates them in a single model. Combining different parameters at the same time may produce unexpected or unwanted effects with the unknown root cause; therefore, the parameters are inserted and analysed one at a time to isolate and determine the origin of these issues whenever occurs.

10.3.1 Equations

Electro-mathematical model employs two equations [246], one for the charge (Eq. 10-1) and one for discharge (Eq. 10-2). These equations create an exponential increase/decrease curve for each case, which are principles of the operation mode.

$$V_{charge} = I_{charge} * R_{esr} + I_{charge} * R_{leak} * \left(1 - e^{\left(\frac{-t}{R_{leak} * C_{complet}}\right)}\right) \quad (10\text{-}1)$$

$$V_{discharge} = V_{charge} - I_{discharge} * R_{esr} - (V_{discharge-1} + I_{discharge} * R_{leak}) * \left(1 - e^{\left(\frac{-t}{R_{leak} * C_{complet}}\right)}\right) \quad (10\text{-}2)$$

, where V_{charge}/$V_{discharge}$ is the charge/discharge value of the supercapacitor in Volts, I_{charge}/$I_{discharge}$ is the profile of charge/discharge current in Amperes, R_{esr} is the equivalent series resistance in ohms, R_{leak} is the high internal resistance (leakage resistance) in ohms, $C_{complet}$ de capacitance of the supercapacitor in Farads and T the time in seconds. $C_{complet}$, R_{esr}, and R_{leak} values are a function of the ambient conditions, lifetime, applied voltage, moisture, etc.

Values as $C_{complet}$, R_{esr}, and R_{leak} are a function of the ambient conditions, lifetime, applied voltage, moisture, etc. These parameters are obtained with another set of equations, which model the operation basics of supercapacitors.

1) Capacity

Supercapacitor full capacity is obtained by multiplying the percent of change that life cycle introduces in theoretical nominal capacitance,

$$C_{complet} = C_0\ (F) * C_{cycle-life}(\%) \quad (10\text{-}3)$$

Capacitor lifetime decreases with increasing temperature, applied voltage, humidity, current and backup time requirements [247][248]. Therefore, operating at high temperature reduces the life of a device. According to "10-degrees-rule" lifetime of supercapacitor will be double for each 10-degree Celsius reduction in operating temperature. This rule employs the Arrhenius equation, a formula for the temperature dependence of reaction rates. Likewise, lifetime diminishes as operation time increases. In a supercapacitor, the internal capacity decreases by the root of cycles [249]. Moreover, this type of devices have a single voltage range, if this level is exceeded life-cycle is decreased, and eventually, the device may break. Finally, the last parameter includes in our life-cycle equation is moisture. Unless this ambient condition has less impinged than the other parameters, nonetheless, it is inserted in the equation to make the algorithm closer to a real application of EHWSN. Thus, the capacitor lifetime is:

$$C_{cycle-life}(\%) = 100 - \alpha^{\left(\frac{T-T_{ref}}{10}\right)} * \sqrt{N} * \left(\frac{V - Vc}{V}\right) * H \quad (10\text{-}4)$$

, where, α is acceleration factor. Usually, α equal 2 for this kind of applications, T actual operation temperature in Kelvin degrees, T_{ref} reference operation temperature (usually 298 K), N is the number of cycles used, V range voltage, V_c applied voltage both in Volts and H the ambient moisture.

2) Equivalent Series Resistance

Equivalent Series Resistance (ESR) of supercapacitor depends on temperature and device size [250]. When the temperature becomes low, ESR becomes high. Consequently, when supercapacitor is operating at low temperature, discharge efficiency becomes lower,

$$R_{esr} = b_1 * R_{esr0} * \left(1 + \gamma * \left(T - T_{ref}\right)\right) + b_2 * R_{esr0} * e^{\left(\left(\frac{-K_t}{2}\right)*\left(T - T_{ref}\right)\right)} \quad (10\text{-}5)$$

, where T_0 = 293 K, γ=0.007 (K^{-1}) the temperature coefficient of the aggregated aluminium and carbon constituents and kT=0.045 (K^{-1}) the aggregate ionic activation energy constituent. The electronic (b_1) and ionic (b_2) weight factors are dependent on supercapacitor cell size. Smaller cells have a greater imbalance in the electronic to ionic ratio, with b1, in this case, being a larger fraction of b_1+ b_2=1 [251]. R_{esr0} is the theoretical series resistance and must be measured if the manufacturer does not provide the value.

3) Leakage resistance

Supercapacitor usually has a high internal resistance, which implies a low leakage current, i.e., the current needed to keep the capacitor charged is low. When the capacitor is disconnected from the source, it begins to lose charge through the internal or leakage resistance. Manufacturers do not usually provide internal resistance information. Moreover, it is parameter hard to measure. This work uses equation 10-6 [252], to obtain the instantaneous theoretical or approximate leakage resistance value, R_{leak}.

$$R_{leak} = \frac{\tau_{leak}}{C_{complet} + k * u(t)} = \frac{\tau_{leak}}{C_{complet} + \left(\frac{2\left(I\Delta t_t - C_{complet}\Delta U_t\right)}{\Delta U_t^2}\right) * U_0 e^{\left(-\frac{t}{\tau_{leak}}\right)}} \quad (10\text{-}6)$$

, where τ_{leak} is the time constant of leakage current, k is the linear voltage-dependent capacitance, and u(t) is the voltage across the capacitor over time and is an exponential function where U_0 is the initial voltage. The evolution of voltage ΔU_t defines the slope k with time and the stored charge on the supercapacitor.

10.3.2 Model architecture and development

The aforementioned equations 1 and 2 require post-processing, figure 10-4, to obtain their coefficients and define the capacitor equivalent curves. To simulate the desired operating conditions the variables and the charge current profile, i.e., a data file must be introduced manually in the equations.

The first step defines the capacitor charging process. Temperature, moisture, lifecycle state, ESR theoretical resistance are introduced and the configuration charge voltage and time are inserted on equation (1), and the program provides the charge curve.

To end with this first configuration charge voltage and time must be inserted. After entering this data, resulting the program provides charge curve.

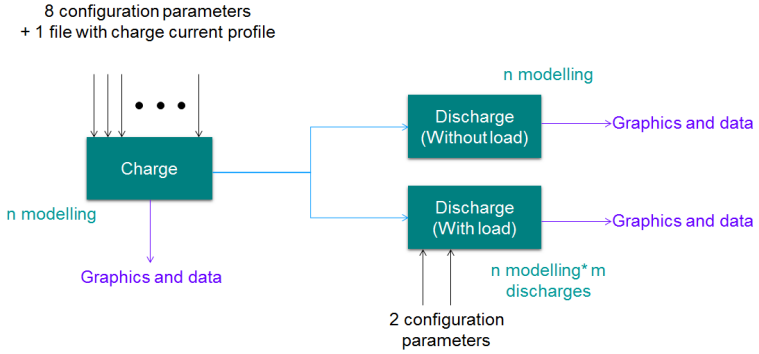

Figure 10-4: Architecture, input, and output of the program that runs the mathematical model.

The second step defines the discharge profile. There are two alternatives to define the discharge profile. The self-discharge one only uses the internal losses of supercapacitors. It describes how long does self-discharge discharge process takes, (usually a large period), and which is the amount of energy lost under different ambient conditions, thus, it does not require additional configuration parameters. The second option employs different loads to create discharge profiles, (those found in EHWSN applications), therefore, for each discharge profile test performed, load and time step must be defined.

The complete mathematical model was implemented in MATLAB®. It has a different algorithm for each case based on the aforementioned principles. All these algorithms have been integrated on a single program where the user can select the desired test set-up. The developed code could be seen in appendix 16.4.3.

10.3.3 Results

This electro-mathematical model is post-processed at different conditions of voltage, current, power, and energy levels to analyse its performance and verify its accuracy.

Three types of modelling and corresponding results are shown in next lines, which are based in following situations:

1- Charge
2- Charge and self-discharge
3- Charge and discharge with different electric loads.

Figure 10-5 represents the charge results of the model with 1 F and 5 F supercapacitors, 600 seconds charge with 5 V at 10 and 60 ºC temperatures. It could be seen how temperature difference influence more to less capacitance supercapacitor. Furthermore, current and power are the parameters where more difference could be appreciated, being voltage less affected.

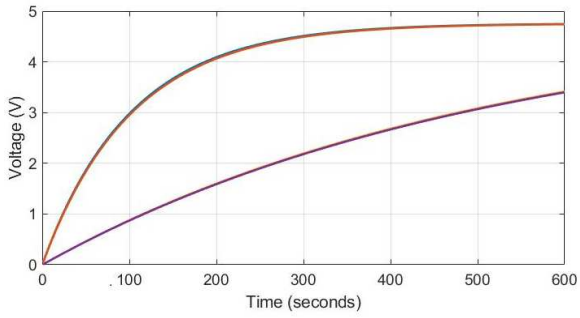

a) Voltage.

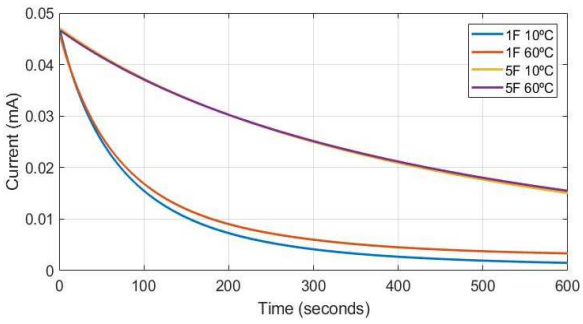

b) Current.

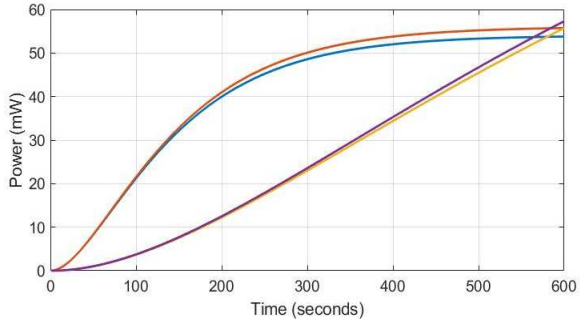

c) Power.

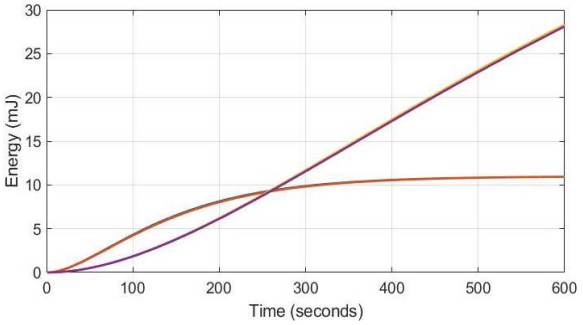

d) Energy.

Figure 10-5: Mathematical model results with 1 F and 5 F supercapacitors, 600 seconds charge with 5 V at 10 ºC and 60 ºC temperature.

Figure 10-6 analysed the effects of the charge situation. Using 1 F and 5 F supercapacitors, 600 seconds charge with 2.5 V and 5 V at 25 ºC temperature and different profiles of discharge. The difference in voltage at the end of the charge is considerably different based on the voltage applied and the capacitance value. In addition, supercapacitors are discharged with self-discharge condition.

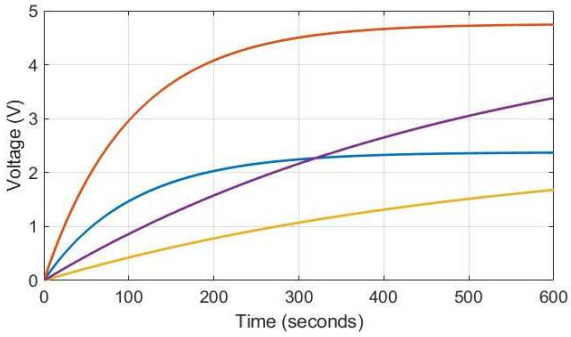

a) Voltage.

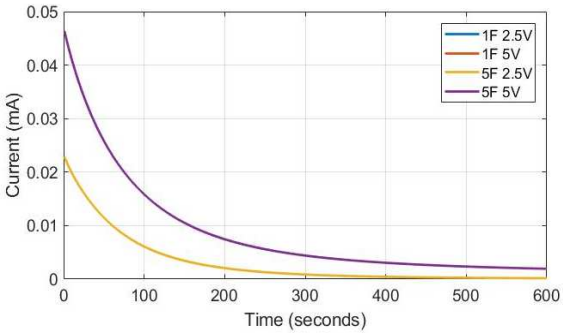

b) Current.

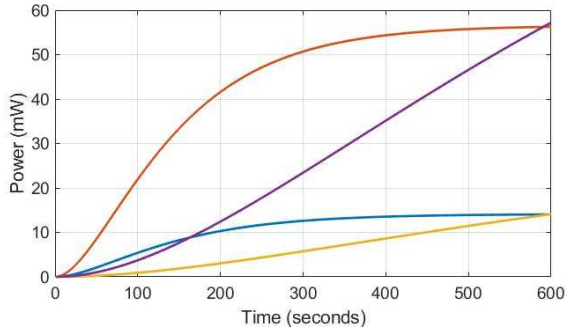

c) Power.

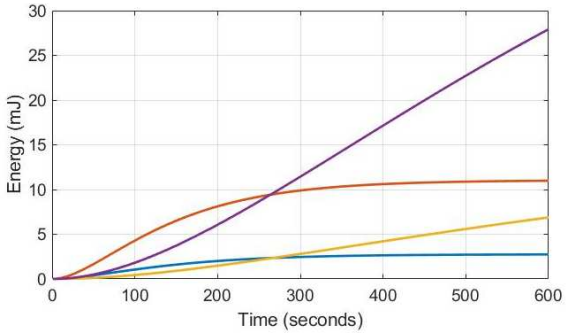

d) Energy.

Figure 10-6: Mathematical model results with 1 F and 5 F supercapacitors, 600 seconds charge with 2.5V and 5 V at 25 ºC temperature.

Figure 10-7 represents the results of the model with 1 F and 5 F supercapacitors, 3600 seconds charge with 5 V at 10 and 25 ºC temperature and self-discharge profiles. Being the self-discharge bigger when supercapacitor has less capacitance and/or with higher ambient temperature.

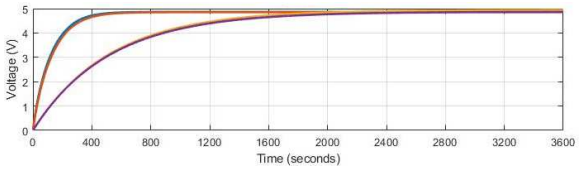

a) Charge voltage.

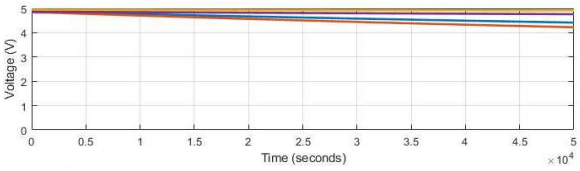

b) Discharge voltage.

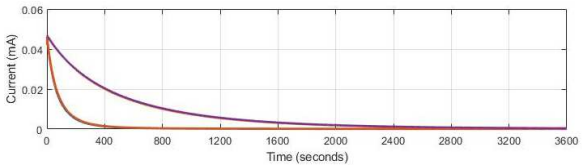

c) Charge current.

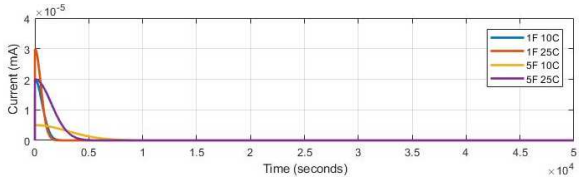

d) Discharge current.

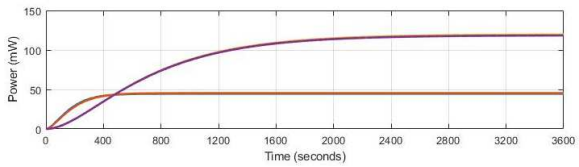

e) Charge power.

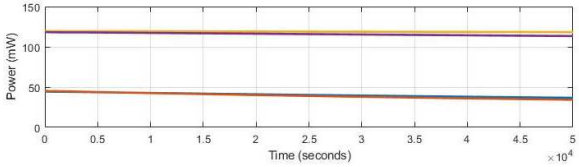

f) Discharge power.

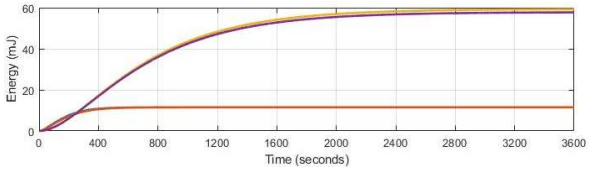

g) Charge energy.

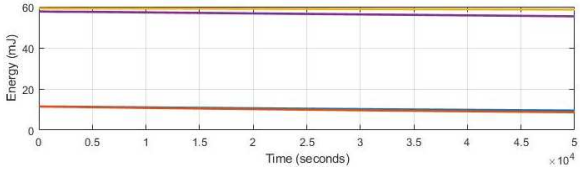

h) Discharge energy.

Figure 10-7: Mathematical model results with 1 F and 5 F supercapacitors, 3600 seconds charge with 5V at 10 °C and 25 °C temperature and self-discharge.

Figure 10-8 represents the results of the model also with 1 F and 5 F supercapacitors, 3600 seconds charge with 5 V at 10 and 25 °C temperature, different life status of supercapacitors and self-discharge profiles. Happening the same effects of temperature and capacitance described in before case and adding the effect of life cycles. It could be appreciated, that higher utilization of the devices, faster is the discharge.

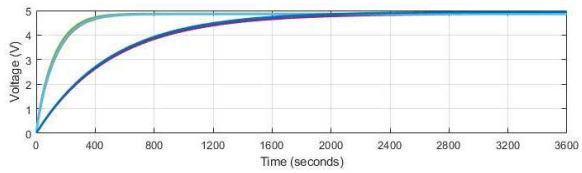

a) Charge voltage.

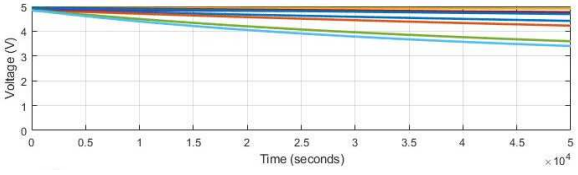

b) Discharge voltage.

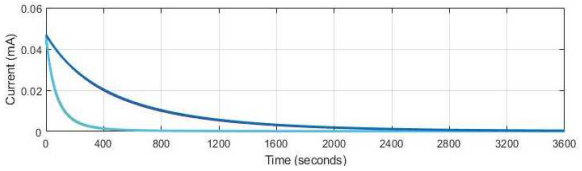

c) Charge current.

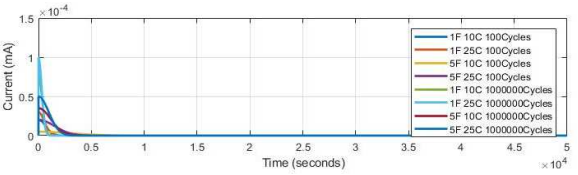

d) Discharge current.

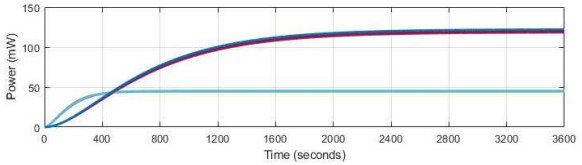

e) Charge power.

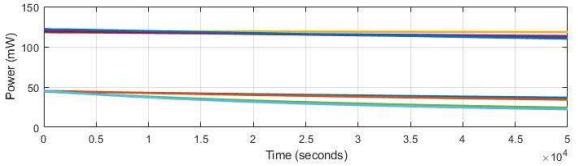

f) Discharge power.

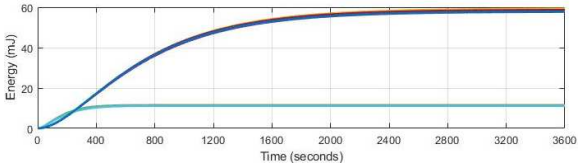

g) Charge energy.

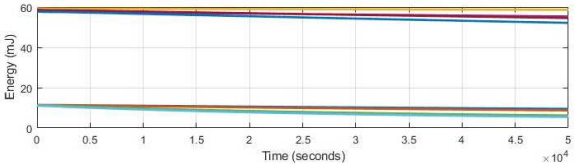

h) Discharge energy.

Figure 10-8: Mathematical model results with 1 F and 5 F supercapacitors, 3600 seconds charge with 5V at 10 °C and 25 °C temperature and self-discharge with 100 and 1e6 cycles of use.

Figure 10-9 provides the effects for different load consumption discharge profiles on the behaviour of the same and different supercapacitor at the same temperature. This case is represented with 1 F and 5 F supercapacitors, 600 seconds charge with 5 V at 40 °C temperature and different profiles of discharge. Yellow discharge profile has 5 steps all with 200 seconds of duration; First 1 mA, second self-discharge, third 0.5 mA, fourth 7 mA and fifth self-discharge. Purple discharge profile also has 5 steps; First 1.5 mA for 250 seconds, second self-discharge for 75 seconds, third 6 mA for 50 seconds, fourth 3.5 mA for 325 seconds and fifth self-discharge for 300 seconds.

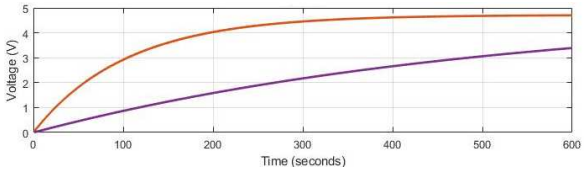

a) Charge voltage.

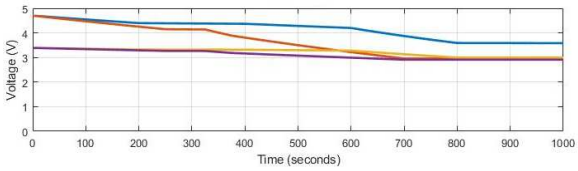

b) Discharge voltage.

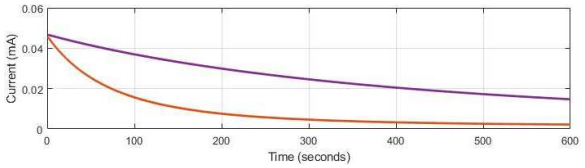

c) Charge current.

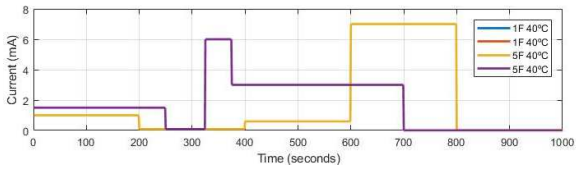

d) Discharge current.

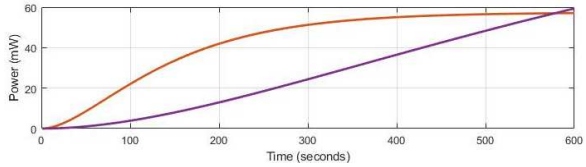

e) Charge power.

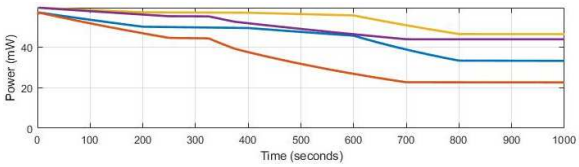

f) Discharge power.

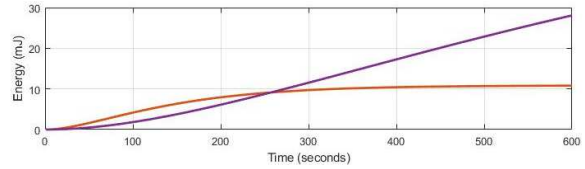

g) Charge energy.

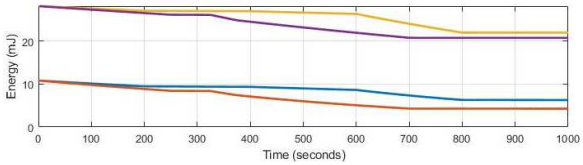

h) Discharge energy.

Figure 10-9: Mathematical model results with 1 F and 5 F supercapacitors, 600 seconds charge with 5V at 40 ºC temperature and different profiles of discharge.

Figure 10-10 presents how the changing of the temperature affects the supercapacitor's storage capacity having the same load consumption discharge profile and shows in which supercapacitor value goes into a critical working level. This case is presented using 1F and 5F capacitance at different temperatures (10, 25, 40 and 60 ºC), 600 seconds charge with 5V and same outer profile consumption composed by three steps; First step 0.5 mA for 2000 seconds, second step 1 mA during also 2000 seconds and third step as first one.

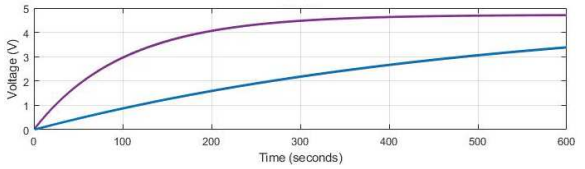

a) Charge voltage.

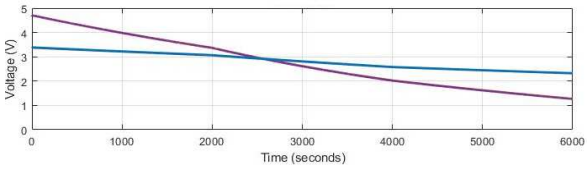

b) Discharge voltage.

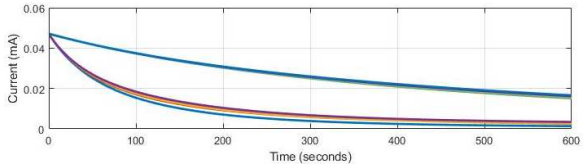

c) Charge current.

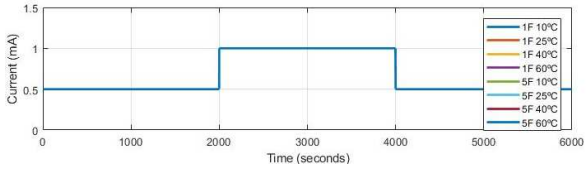

d) Discharge current.

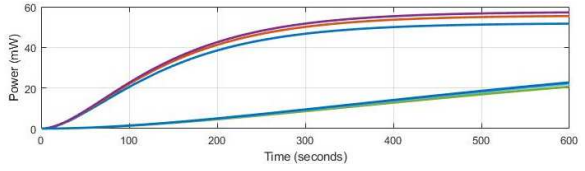

e) Charge power.

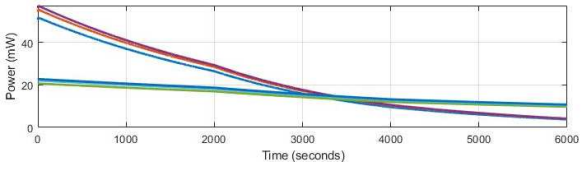

f) Discharge power.

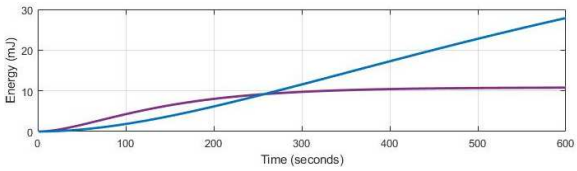

g) Charge energy.

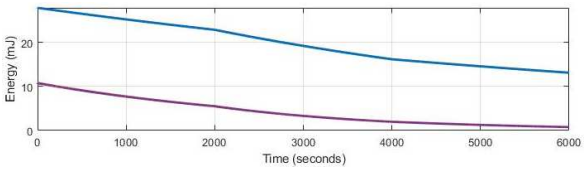

h) Discharge energy.

Figure 10-10: Mathematical model results with 1 F and 5 F supercapacitors, 600 seconds charge with 5V at 10 ºC, 25 ºC, 40 ºC and 60 ºC temperature and same profile of discharge.

10.4 Results of supercapacitor models

After realizing several simulations, the model is verified and validated with several statistical techniques:

- Root mean square error (RMSE) is a quadratic scoring rule that also measures the average magnitude of the error. It is the square root of the average of squared differences between prediction and actual observation.

$$RMSE = \sqrt{\frac{1}{n}\sum_{j=1}^{n}(y_j - \hat{y}_j)^2} \tag{10-7}$$

, where $\hat{y}$ is the vector of n predictions and y is the vector of observed values of the variable to be predicted.

- Mean absolute error (MAE) is the average over the test sample of the absolute differences between prediction and actual observation, where all individual differences have equal weight.

$$MAE = \frac{1}{n}\sum_{j}^{n} |\, y_j - \hat{y}_j| \tag{10-8}$$

, where $\hat{y}$ is the vector of n predictions and y is the vector of observed values of the variable to be predicted.

- Mean square error (MSE) measures the average of the squares of the errors or deviations; that is, the difference between the estimator and what is estimated.

$$MSE = \frac{1}{n}\sum_{j=1}^{n} (\, y_j - \hat{y}_j)^2 \tag{10-9}$$

, where $\hat{y}$ is the vector of n predictions and y is the vector of observed values of the variable to be predicted.

- Mean absolute percentage error (MAPE) expresses accuracy as a percentage and is defined by the formula:

$$MAPE = \frac{100}{n}\sum_{j}^{n} \left|\frac{At - Ft}{At}\right| \tag{10-10}$$

, where A_t is the actual value and F_t is the forecast value.

The Actual value divides the difference between A_t and F_t A_t again. The absolute value in this calculation is summed for every forecasted point in time and divided by the number of fitted points n. Multiplying by 100 makes it a percentage error.

Results of statistical validation with RMSE, MAE, MSE and MAPE techniques are shown in table 10-3. The last column contains statistical average results of all test performed during this work. This is the key column to observe the goodness of each model and the differences between them.

Table 10-3: Statistical results of comparison between test and model data.

State	Stat-tech	Test A	Test B	Test C	Test D	Test E	Test F	Test G	Test H	Test I	Test J	Aver.
Charge	RMSE	0.177	0.182	0.204	0.113	0.175	0.188	0.145	0.204	0.175	0.108	0.167
	MSE	0.031	0.033	0.041	0.012	0.03	0.035	0.021	0.041	0.03	0.011	0.029
	MAE	0.125	0.109	0.125	0.079	0.073	0.6	0.114	0.125	0.073	0.7	0.096
	MAPE	8.225	4.789	5.354	3.539	2.056	1.967	4.387	5.354	2.056	1.883	3.961
Discharge	RMSE	0.145	0.137	0.178	0.104	0.092	0.087	0.134	0.178	0.092	0.093	0.124
	MSE	0.021	0.018	0.031	0.01	0.0083	0.0074	0.017	0.031	0.008	0.0086	0.016
	MAE	0.141	0.123	0.167	0.091	0.057	0.055	0.118	0.167	0.057	0.081	0.1
	MAPE	15.677	8.692	11.642	7.548	2.632	2.555	8.607	11.642	2.632	3.007	7.463

Four figures comparing results achieved with experimental tests and electro-mathematical model are shown in figure 10-11, 10-12, 10-13 and 10-14. It must be mentioned that these examples have a 50 % value of ambient moisture.

Figure 10-11 represents a charge through 1 hour with 5 Volt of input at 10 ºC in 1 and 5 Farad supercapacitors. Then, single consumption profile of 1 mA is applied for the discharge. As is shown in this example, discharge curve descends quickly because of reproduced a constant consumption of an EHWSN.

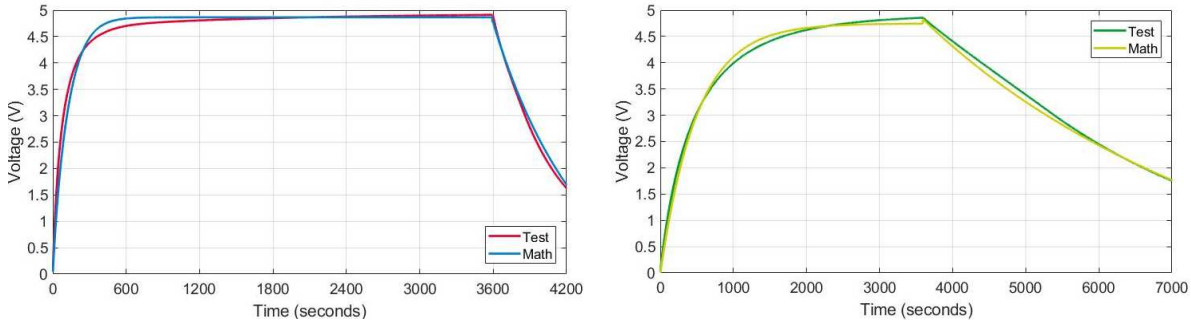

a) 1 Farad. b) 5 Farad.

Figure 10-11: Supercapacitors with 10 min charge at 5 V and 10 ºC temperature; discharge consumption is a single constant profile of 1 mA.

Figure 10-12 represents a 2.5 V of charge for 10 minutes at 25 ºC in 1 and 5 Farad supercapacitors. After charge time, represented profile belongs to the self-discharge curve.

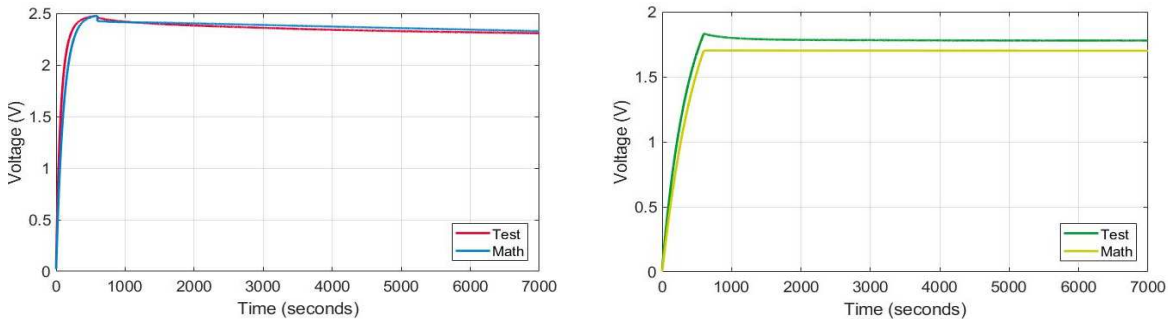

a) 1 Farad. b) 5 Farad.

Figure 10-12: Supercapacitors with 60 min charge at 2.5 V and 25 ºC temperature and self-discharge.

Then, Figure 10-13 represents a 40 ºC temperature, 1 and 5 Farad supercapacitors charge during 1 hour with 5 Volt of input. In this case discharge procedure also is based on self-discharge technique.

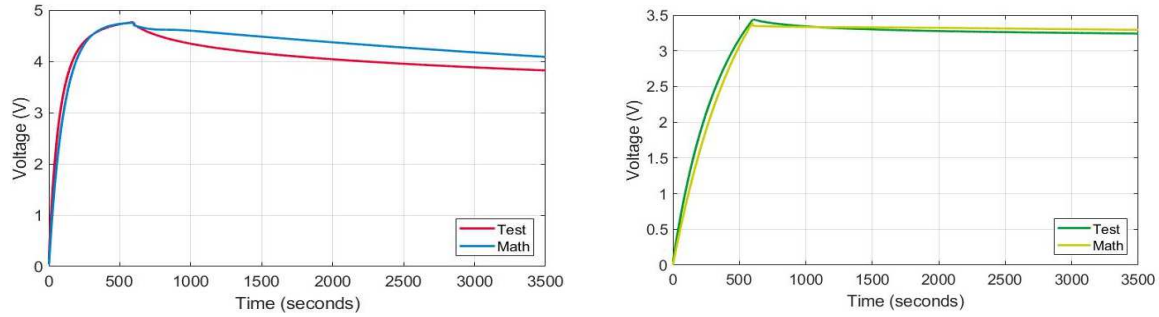

a) 1 Farad. b) 5 Farad.

Figure 10-13: Supercapacitors with 10 min charge at 5 V and 40 ºC temperature and self-discharge.

In last displayed test, Figure 10-14 represents 1, and 5 Farad supercapacitors charge with 5 V at 40 ºC temperature and for 10 minutes. Discharge has three different steps. The first one has 0.3 mA consumption profile through 3 minutes, and second one is self-discharge through 30 minutes and 0.1 mA consumption profile until measurement end.

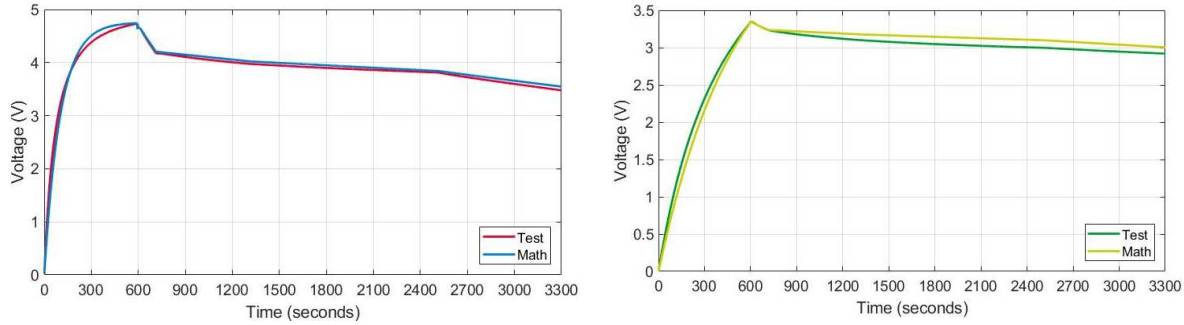

a) 1 Farad. b) 5 Farad.

Figure 10-14: Supercapacitors with 10 min charge at 5 V and 60 ºC temperature; 0.3 mA composes discharge consumption during 3 min, self-discharge for 30 min and 0.1 mA until the end.

It could be seen that an accurate supercapacitor model has been achieved. Thanks to this model, the energy storage by both input system of double power manager could be simulated for future design or study activities.

10.5 Application example of supercapacitor model

An example of an application for developing supercapacitor model is presented in this section. The idea is to create real consumption profiles based on data-sheets of common elements in sensor networks.

The tool has different fields some to be to be used/filled/modified by the user. Others give to the user different types of information in active and sleep, such as Total time of use, current, consumption, the percentage of consumption, the percentage of use and percentage of consumption per element. Besides, the user must fill the next fields:

In this work and theoretical scenario has been created to show the behaviour of the tool. Furthermore, in table 10-4, selected elements to make the modelling of profile consumption are shown:

Table 10-4: Selected elements to complete simulation table.

Device	Reference	Manufacturer
NFC device	PN512	NXP semiconductors
NH3 sensor	SGX-4NH3	SGX Sensortech
CO2 sensor	CDM7160	Figaro Engineering inc
Ambient light sensor	OPT3001	Texas Instruments
Detection sensor (PIR)	IRS-B210ST1-R1	Murata
Temperature and humidity sensor	HDC1080	Texas Instruments
Power manager	BQ25507	Texas Instruments
Microcontroller	STM32L162xE	ST electronics
Wi-Fi	AMW006	Silicon Labs

In table 10-5 described activity and selected electronic devices are inserted in the developed tool.

In addition, figure 10-15 is shows each element percent consumption in one hour:

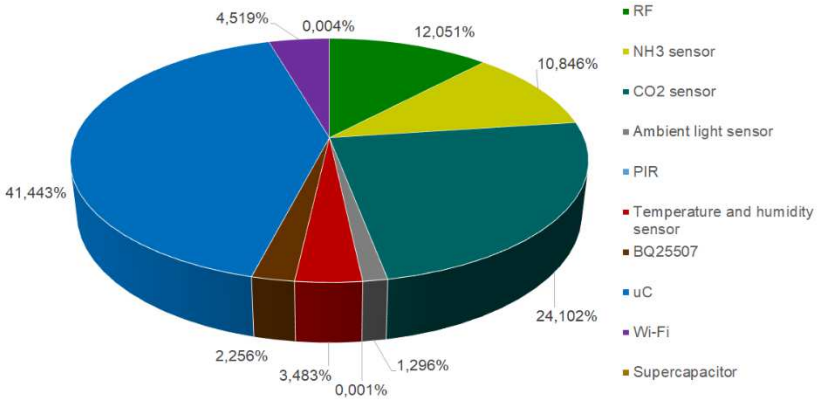

Figure 10-15: System devices consumption percentage in the designed scenario.

Now after creating time dependable profiles with calculated consumptions, the idea is to use supercapacitor electro-mathematical model supercapacitor discharge behaviour and make after-information processing.

Sometimes the consumption would be higher than available power amount, other times lower or enough. This activity would be iterative until reach to the ideal or necessary behaviour of the storage system.

Table 10-5: System devices consumption values at example scenario.

Number of act/h	Data send (Mbit)	Data receive (Mbit)	Mbit/s
2	4,00E-05	0,00E+00	1,00E+00

Consumption															
		Active Time (s)	Total Time (s)	Active Consumption (mA)	Active Consumption (mAh)	Sleep Time (s)	Sleep Consumption (mA)	Sleep Consumption (mAh)	Total (mAh)	Active consumption (%)	Active Time (%)	Sleep consumption (%)	Sleep Time (%)	Consumption per device (%)
RF	Ipd, hard power-down; pin NRSTPD set LOW					0	5,00E-03	0,00E+00	0,00E+00			0,000%	0,000%	12,051%
	Ipd, soft power-down; RF level detector on					0	1,00E-02	0,00E+00	0,00E+00			0,000%	0,000%	
	IDDD, digital supply current	0	0	6,500	0,00E+00				0,00E+00	0,000%	0,000%			
	IDDA, analog supply current, CommandReg register's RcvOff bit = 0	0,2	0,4	7,000	7,78E-04				7,78E-04	3,918%	0,111%			
	IDDA, analog supply current, receiver switched off, CommandReg register's RcvOff bit = 1	0	0	3,000	0,00E+00				0,00E+00	0,000%	0,000%			
	IDD(PVDD), PVDD supply current	0	0	40,000	0,00E+00				0,00E+00	0,000%	0,000%			
	IDD(TVDD), TVDD supply current	0,06	0,12	60,000	2,00E-03				2,00E-03	10,075%	0,003%			
NH3 sensor	Operation current	30	30	0,300	2,50E-03				2,50E-03	12,594%	0,833%			10,846%
CO2 sensor	Operation current	2	2	10,000	5,56E-03				5,56E-03	29,129%	0,056%			24,102%
Ambient ligth sensor	Dark, active	5	5	0,0018	2,50E-06				2,50E-06	0,013%	0,139%			1,296%
	Dark, shutdown					3555	0,0003	2,96E-04	2,96E-04			4,780%	98,750%	
	Full-scale lux, active	0	0	0,0037	0,00E+00				0,00E+00					
	Full-scale lux, shutdown					0	0,0004	0,00E+00	0,00E+00	0,000%	0,000%	0,000%	0,000%	
PIR	Stanby	3000				0	1,60E-06	0,00E+00				0,000%	0,000%	0,0005%
	Detector on	600	200	0,000	1,20E-07				1,20E-07	0,001%	5,556%			
Pressure and temperature	Sleep					3598	3,00E-03	3,00E-03				48,374%	99,944%	3,483%
	Stanby					0	5,00E-03	0,00E+00				0,000%	0,000%	
	Pressure measurament	1	2	1,120	6,22E-04				6,22E-04	3,135%	0,056%			
	Temperature measurament	1	2	0,325	1,81E-04				1,81E-04	0,910%	0,056%			
BQ25507	Start	0,05	0,1	0,050	1,39E-06				1,39E-06	0,007%	0,003%			2,256%
	Full operating mode	3	6,00	0,001	1,17E-06				1,17E-06	0,006%	0,167%			
	Partial standby mode	3000	3000	0,001	5,13E-04				5,13E-04	2,582%	83,333%			
	Ship mode					594	3,00E-05	4,95E-06	4,95E-06			0,080%	16,497%	
uC	USART	1	2	0,086	4,80E-05				4,80E-05	0,242%	0,056%			41,443%
	Flash	2	4	0,256	2,84E-04				2,84E-04	1,433%	0,111%			
	RTC	3600	3600	0,000	4,00E-04				4,00E-04	2,015%	100,000%			
	GPIOA	1	2	0,066	3,64E-05				3,64E-05	0,184%	0,056%			
	GPIOB	1	2	0,066	3,64E-05				3,64E-05	0,184%	0,056%			
	SPI2	2	4	0,056	6,22E-05				6,22E-05	0,313%	0,111%			
	SPI3	0,258	0,516	0,059	8,49E-06				8,49E-06	0,043%	0,014%			
	Run fhclk=16 MHz	2	4	5,200	5,78E-03				5,78E-03	29,107%	0,111%			
	Sleep with flash, fhclk=16 MHz					7	1,25E+00	2,50E-03	2,50E-03			40,334%	0,200%	
	Stop					3589	4,00E-04	3,99E-04	3,99E-04			6,433%	99,689%	
Wi-Fi	Active Receive (Mbit/s)	0	0	5,700	0,00E+00				0,00E+00	0,000%	0,000%			4,519%
	Active Transmit (Mbit/s)	0,00008	0	11,400	0,00E+00				0,00E+00	0,000%	0,000%			
	Wakeup and connect	0,25	0,25	15,000	1,04E-03				1,04E-03	5,248%	0,007%			
Supercapacitor	Losses	3600	3600	0,000	9,00E-07				9,00E-07	0,005%	100,000%			0,004%
									2,31E-02					100,000%

V.
Machine learning techniques for energy harvesting systems

Data mining and artificial intelligence techniques are being use in the management of the energy generation and distribution of electric lines. Harvesting systems are energy sources, thus, the aforementioned techniques could be applied on them with the proper sealing. The application of machine learning in energy harvesting has two main goal; to learn how to efficiently adapt its behaviour according to its environment and manage when and how to optimally the system could launch tasks.

This chapter includes the implementation of data mining and the machine learning techniques applied to the field of energy harvesting. It is divided into three sub-chapters:

- Chapter 11 Photovoltaic cell selection by data analysis
- Chapter 12 Supercapacitor model accuracy improvement with machine learning techniques
- Chapter 13 Power management strategy

Chapter 11 is focused on the selection of the harvester using data mining techniques. Sometimes the information to make a correct selection of the harvester is not available in the harvester data-sheet. To solve this problem, avoiding an incorrect selection of the harvester, a methodology using data science is implemented in this section.

Chapter 12 complements the work defined in chapter 10. This section evaluates the accuracy of several machine learning algorithms applied supercapacitors charge and discharge curves to improve their accuracy.

Chapter 13 defines the use case to predict income power and improve the power management. DC system of chapter 8 and AC system of chapter 9 are the references to developing the main task of this chapter. Both systems are implemented with different algorithms at different ambient conditions and with different noise levels. Finally obtained experimental results are presented and discussed.

11. Photovoltaic cell selection by data analysis

This section describes the methodology to make the right selection of a harvester using data mining techniques. The use case, power generated, size and technology of the harvester have been considered. In this work, this methodology has been proved with photovoltaic harvesters.

The photovoltaic harvesters selected were measured and tested under different conditions. Subsequently, the data mining techniques were applied to the collected data to determine which is the best harvester.

11.1 Measurement process

Measurement process consists of three steps:

1. Selection of photovoltaic cells to be analysed.
2. Prepare and define tests set-up.
3. Realize n test quantity and collect results.

11.1.1 Solar cell selection

The solar modules selection was based on a state of art search in solar cell manufacturers and distributors. Secondly, it is based on selecting three different cells for possible use and making the final selection.

The AM1816 is a cell that has been utilized in the European project TIBUCON [253]. Unless, the cell is obsolete, it could be used to compare the efficiency improvements in relation to actual solar cells. The requirements for selected photovoltaic cells has been their suitability for "interior" usual lights. However, dual cells (good response to sun and artificial light) have been found, which have better properties and efficiencies. These new cells are the IXYS08 and IXYS10, manufactured with "monocrystalline silicon" technology and shown in figure 11-1:

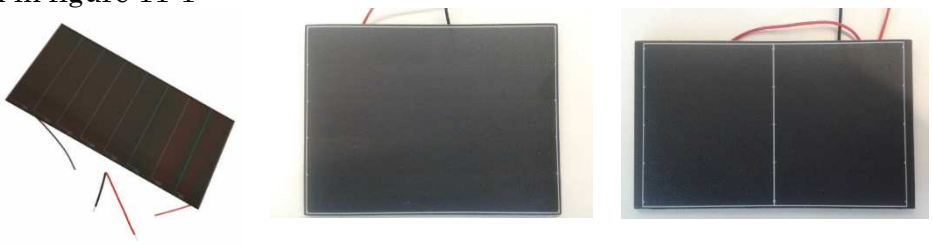

a) AM1816 b) IXYS08 c) IXYS10

Figure 11-1: Selected solar cells.

Size is another crucial factor in the EHWSN field, so the idea is to have cells as small as possible and with the highest energy harvesting efficiency.

Physical and electrical characteristics of selected solar cells are shown in table 11-1:

Table 11-1: Selected solar cells physical-electric characteristics.

Solar cell	AM1816	IXYS08	IXYS10
Material	Amorphous Silicon	Monocrystalline Silicon	Monocrystalline Silicon
Size (mm^2)	5482,89	4857,36	5960,64

V_{oc} (V)	4.9	5.04	6.30
I_{sc} (mA)	0.094	200	200
V_{mpp} (V)	3	4	5
I_{mpp} (mA)	0.084	178	178
P_{mpp} (mW)	0.252	714	892

11.1.2 Test description

The target information is how much energy can be harvest with each solar cell. The set-up has been implemented to measure solar module current generation in short circuit condition and under different ambient conditions. It has the following elements:

- Three solar modules (AM1816, IXYS08, IXYS10)
- Lux-meter
- Data logger
- PC
- Solar and fluorescent light

Devices previously appointed are shown in figure 11-2 as a block diagram:

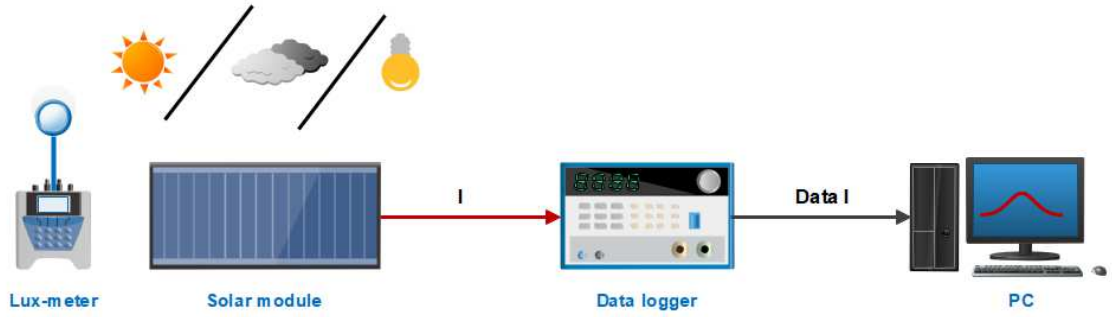

Figure 11-2: Test set-up block diagram for photovoltaic cell selection.

For short-circuit condition continuous measurement, the three solar cells have been connected to the data logger. The period set for current data measurement and saving has been 1 minute. Finally, current data has been visualized in the screen for real-time verification and saved in the database for future processing. Test duration has been set in 2/3/4 days of measurements to avoid any strange situation and observe changes of light quantity into solar cells.

Seven tests have been realized in different locations with different levels of lux and income light profiles. Six tests were made with the usual light of an industrial environment, i.e., cool light. And one test with winter sunlight coming in through the windows. So, the difference between tests is the location where has been made. Table 11-2 shows realized test conditions and each power quantity.

Table 11-2: Realized tests description and light power quantity.

Test number	Location	Light type	Lux	W/m2
Test 1	In Ph.D. student work side	Cool white fluorescent	545	1.597
Test 2	Near window in work side	Cool white fluorescent/ Sunlight	1540	6.191
Test 3	IK4-TEKNIKER 3th floor corridor	Cool white fluorescent/ Sunlight	860	3.457

Test 4	Electronic and Communication laboratory	Cool white fluorescent	438	1.283
Test 5	ETSIB Ph.D. director office	Cool white fluorescent/ Sunlight	770	2.256
Test 6	IK4-TEKNIKER set up workshop, downside	Incandescent tungsten halogen/ Sunlight	684	2.004
Test 7	0 floor IK4-TEKNIKER corridor	Sunlight	27900	81.747

11.1.3 Measurement results

Figure 13-1 provides the current profiles of current generation measurements.

Test 1 was realized in the IK4-TEKNIKER work zone, were principal light source is cool white fluorescent. People interfere with partial or entirely the light path to the solar cell.

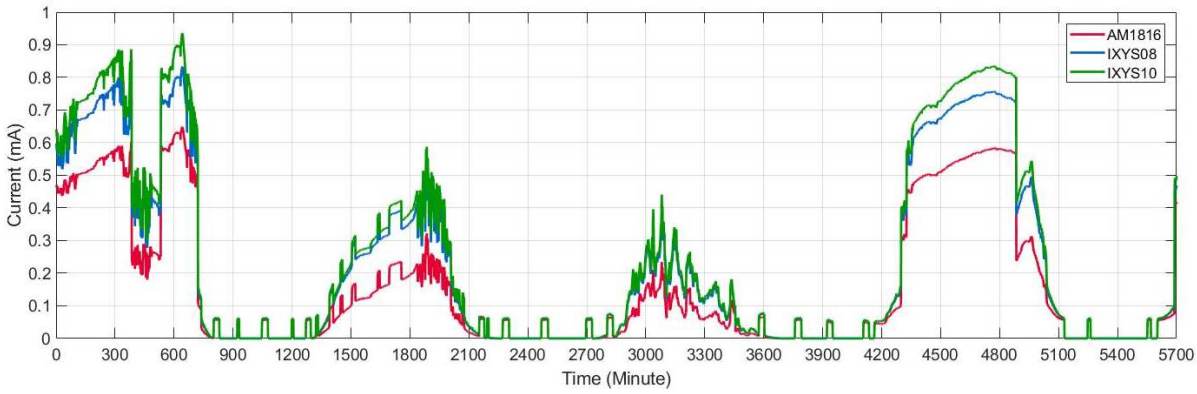

a) Test 1 profiles.

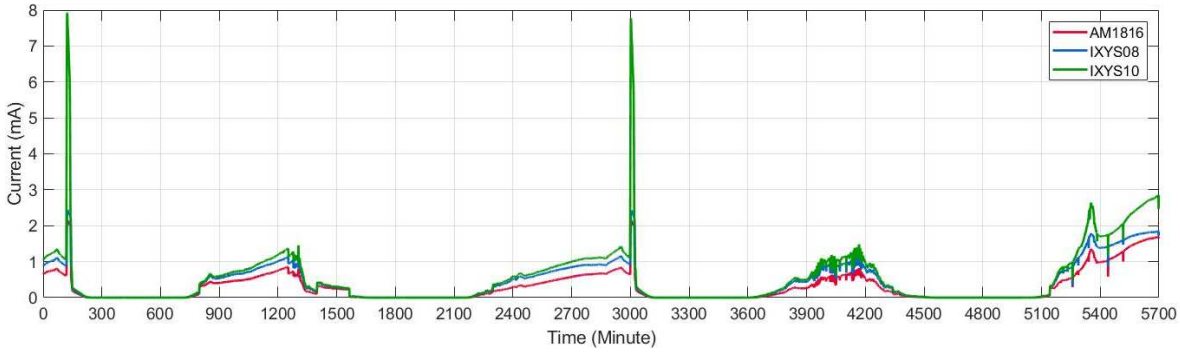

b) Test 2 profiles.

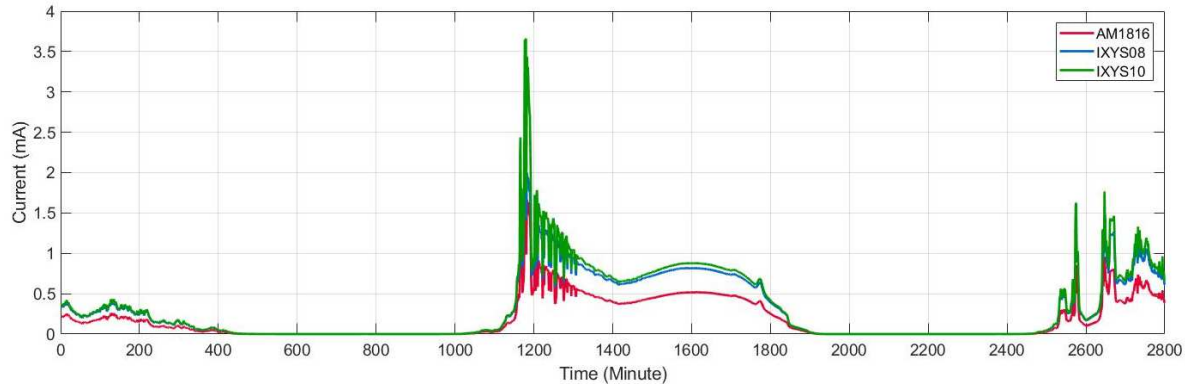

c) Test 3 profiles.

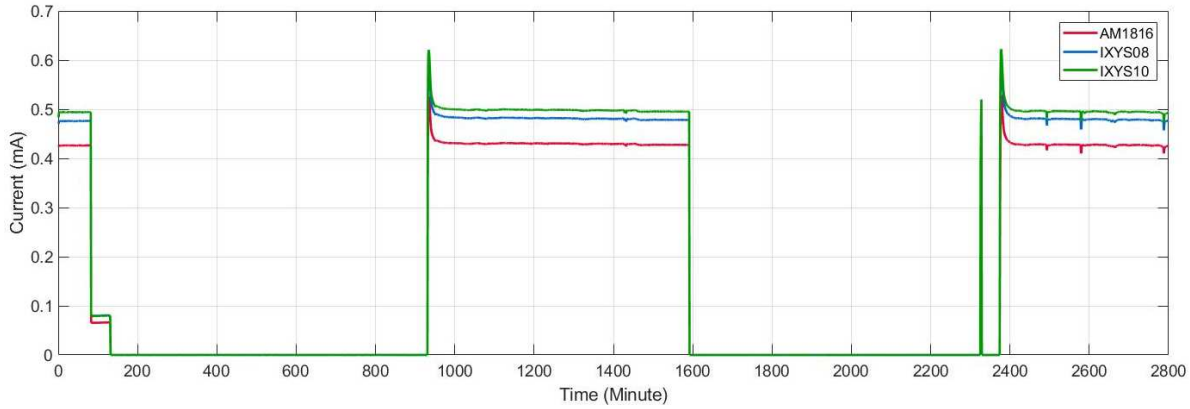

d) Test 4 profiles.

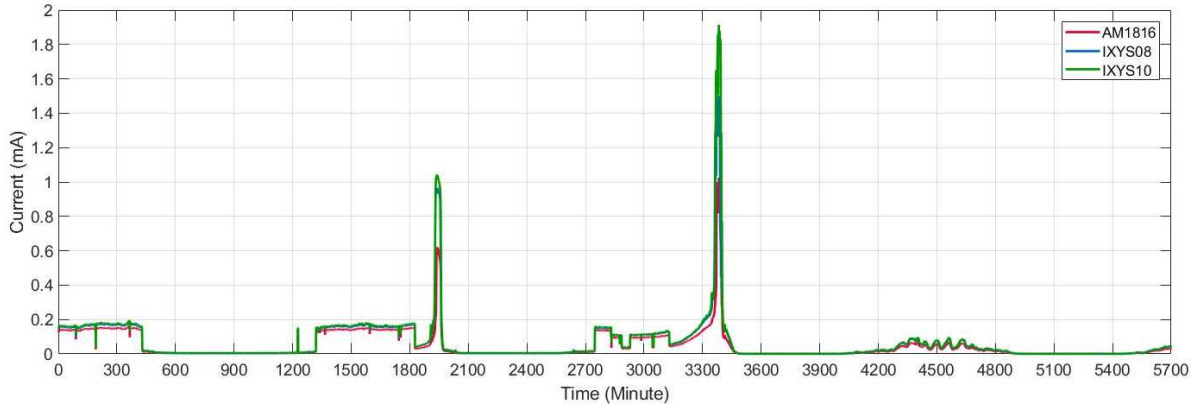

e) Test 5 profiles.

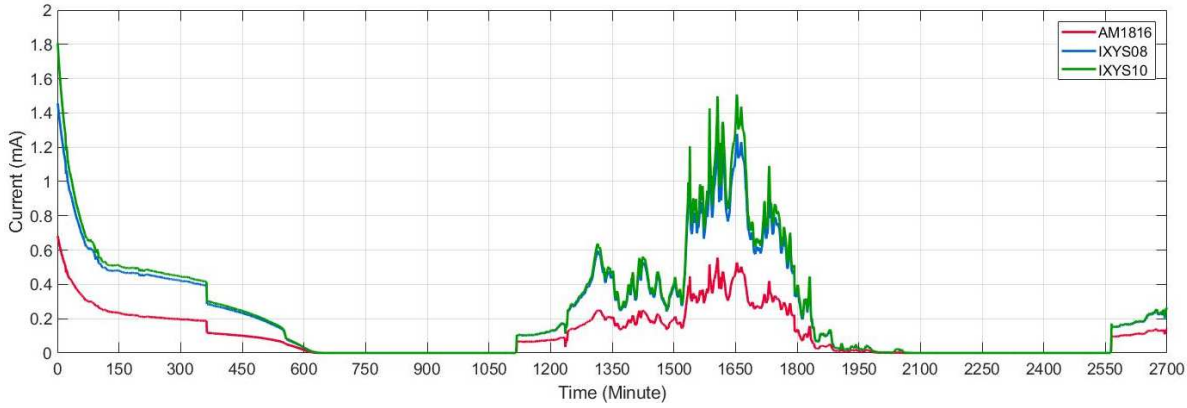

f) Test 6 profiles.

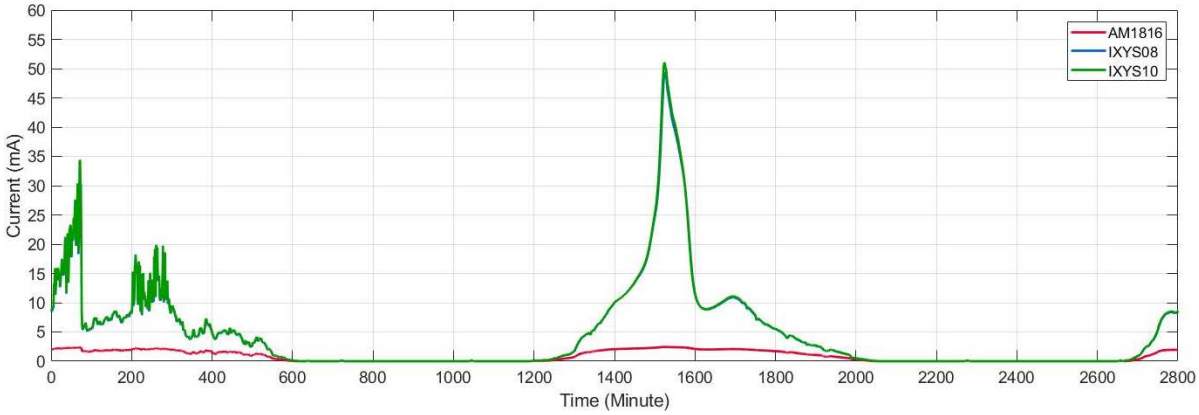

g) Test 7 profiles.

Figure 11-3: Obtained current profile at tests.

Four tests are explained as example of realized experiments:

Test 1 measures acceptable energy levels, but while the cell is illuminated there are significant changes of light intensity (sun, lights that turn off and on). The night sections only measure light periods from the lights switched on.

Test 4 was realized in the IK4-TEKNIKER laboratory. The main energy source is also a constant cool white fluorescent. In test 4 a periodicity is observed, this is because the light of the laboratory stays on during working hours and the rest of the time the light is switched off. The level of energy harvested is lower because the cell only received fluorescent light.

Test 5 was realized in University of Basque Country office. The main energy source is a regular cool white fluorescent but lower than used in test 4. In test 5 two periodicities are observed, first during the work period (fluorescent) and second when sunlight is down and enter into the office. Last period of measurement is a cloudy weekend because any of previously described periodicities appear.

Test 7 was realized in the corridor of IK4-TEKNIKER. The main energy source is the winter sunlight. In test 7 the difference between cloudy and sunny day is observed. However, on a cloudy day, more quantity is generated in comparison with any artificial light.

Maximum, average and values of 7 tests and the average of all are shown in table 11-3:

Table 11-3: Obtained results with different photovoltaic cells at several tests.

	Maximum	Average	mA/mm2	Maximum	Average	mA/mm2
	Test 1			Test 5		
AM1816	0.649	0.163	2.98E-05	1.025	0.050	9.04E-06
IXYS08	0.833	0.229	4.71E-05	1.503	0.063	1.29E-05
IXYS10	0.936	0.248	4.17E-05	1.914	0.067	1.12E-05
	Test 2			Test 6		
AM1816	2.144	0.323	5.89E-05	0.682	0.108	1.98E-05
IXYS08	2.440	0.438	9.03E-05	1.456	0.234	4.82E-05
IXYS10	7.922	0.567	9.51E-05	1.808	0.252	4.23E-05
	Test 3			Test 7		
AM1816	1.707	0.193	3.52E-05	2.438	0.883	1.61E-04
IXYS08	2.074	0.303	6.24E-05	49.392	4.832	9.95E-04
IXYS10	3.662	0.334	5.60E-05	51.065	4.911	8.24E-04
	Test 4			Average		
AM1816	0.529	0.187	3.42E-05	1.147	0.238	4.35E-05
IXYS08	0.599	0.210	4.33E-05	7.287	0.789	1.62E-04
IXYS10	0.622	0.217	3.65E-05	8.491	0.825	1.38E-04

The average level obtained in table 11-3 are low. The main reasons are night duration and the low power of light produced by artificial sources. Table 11-4 compares size and efficiency of the photovoltaic cells measured:

Table 11-4: Size and efficiency comparisons between different photovoltaic cells.

	Size bigger %	Efficiency average %
IXYS10 vs. IXYS08	18.509	12.817
IXYS10 vs. AM1816	8.015	46.078
AM1816 vs. IXYS08	11.409	38.156

There is a significant difference between IXYS modules, and AM1816 is dramatically high. Even though AM1816 it is 11% larger than the IXYS08, the efficiency of this second cell is 38% higher. In addition, AM1816 is not able to work with sunlight, no like other two cells, consequently means that it is not possible to generate energy when the system cell would receive sunlight sporadically. The difference between the IXYS08 and IXYS10 solar cells is quite similar maintaining the production-size ratio.

IXYS10 cell harvests more energy, however, if size and efficiency average are compared between IXYS10 and IXYS08 (first-row table 11-4), IXYS10 is 18.5 % bigger but only 12.8 % more efficient. Therefore, IXYS08 seems to be more efficient. Due to the number of banks that make up each cell. It is worth noting the significant difference in efficiency between these two cells concerning the AM1816, but it had already been mentioned that it was old technology.

After the experimental results, IXYS10 might be the best candidate to be selected. However, statistical testing has been carried out to identify if there is a significant statistical difference between the behaviour of each cell or they could be caused merely by randomness effects.

11.2 Cell selection with data analysis algorithms

ANOVA and Tukey's HSD (Honestly Significant Difference) test has been carried out to:

1. To select the solar cell for highest efficiency.
2. To evaluate the usefulness of this type of statistical techniques for the selection of the most appropriate system among a group of systems with different characteristics and benefits.

11.2.1 ANOVA

Analysis of variance (ANOVA) is a statistical model to analyse the differences among the group of measurements. It is useful for comparing three or more groups of variables for statistical significance.

ANOVA assumes the independence, normality, and homogeneity of the variances of the residuals. The presence of outliers can also cause problems, and it is necessary to ensure that the F statistics is well behaved. In particular, the F statistic is relatively robust to violations of normality but not so robust to violations of homogeneity of variances. If the sample sizes are unequal, then smaller differences in variances can invalidate the F-test. Much more attention needs to be paid to unequal variances than to non-normality of data.

F statistics compare the variation among sample means to the variation within groups.

$$\text{F statistics} = \frac{Variation\ among\ sample\ means}{variation\ within\ groups} \tag{11-1}$$

Through the F statistics, we can see if the variation among sample means dominates over the variation within groups, or not. In the first case, we will have strong evidence against the null hypothesis (means are all equals), while in the second case we would have little evidence against the null hypothesis.

- Null Hypothesis:
  H_0: $\mu_1 = \mu_2 = \mu_3 \ldots = \mu_k$

- Alternative Hypothesis:
  H_1: Means are not all equal.

  , where k is the number of independent groups comparison.

11.2.2 Tukey's HSD test

The Tukey's test has been used to compare means of different experimental tests and then, be able to study and verify the behaviour of each photovoltaic cell.

Tukey's test assumes that the observations being tested are independent within and among the groups, the groups associated with each mean in the test are normally distributed, and there is equal within-group variance across the groups associated with each means in the test (homogeneity of variance). It is a t-test, but it corrects for family-wise error rate. It means that when there are multiple comparisons to be made, as in our case, the probability of making a Type I error within at least one of the comparisons increases. Moreover, for that reason, it is more suitable for multiple comparisons than t-tests. The formula to be applied is:

$$q_s = \frac{Y_A - Y_B}{SE} \tag{11-2}$$

, where Y_A is the larger of the two means being compared, Y_B is the smaller of the two means being compared, and SE is the standard error of the sum of the means. This q_s value can then be compared to a q value from the studentized range distribution. If the q_s value is larger than the critical value q_α obtained from the distribution, the two means are said to be significantly different at level α, $0 \leq \alpha \leq 1$.
Since the Null Hypothesis for Tukey's test states that all means being compared are from the same population, the means should typically be distributed (according to the central limit theorem), rising the normality assumption of Tukey's test.

- Null Hypothesis:
  H0: $\mu 1 - \mu 2 = 0$ - or - H0: $\mu 1 = \mu 2$

- Alternative Hypothesis
  H1: $\mu 1 - \mu 2 \neq 0$ H1: $\mu 1 \neq \mu 2$

HSD = $q_{k,df,\alpha} \times \sqrt{\frac{MSerror}{n}}$, where HSD is Tukey's Honestly Significant Difference qk, df, α is the critical value of q with k levels, $within-groups$ degrees of freedom and α = 0.05

MSerror is Mean Square within-groups (error variance) from the ANOVA summary table, and n is the number of participants in a given condition.

If $|\ X1 - X2\ | \geq$ HSD, then reject H0; otherwise, fail to reject H0.

11.2.3 Results

The dataset contains the average of the energy stored in an electric field for the three solar cells (AM1816, IXYS08 and IXY10) for each test.

Firstly, the mean and distribution of each cell have been calculated and plotted in figure 11-4:

- The first graph (Means between cells) shows how the energy stored means change between cells. It seems that means differ among cells, with the AM1816 cell presenting the lowest value and IXYS10 the highest in all tests. However, it is enough to provide evidence and assume that IXYS10 cell is the best?
- The box plot (Distribution between cells) shows that the medians are quite similar. However, it also shows that each cell presents a different amount of variation or spread in the energy stored. Also, it can be observed many suspected outliers especially in some of the tests.

Hence, differences in means could have come about by chance. Initially, it is not possible to ensure that these differences are relevant and due to real differences about the means or just due to sampling variability. It is necessary to apply ANOVA test to check it.

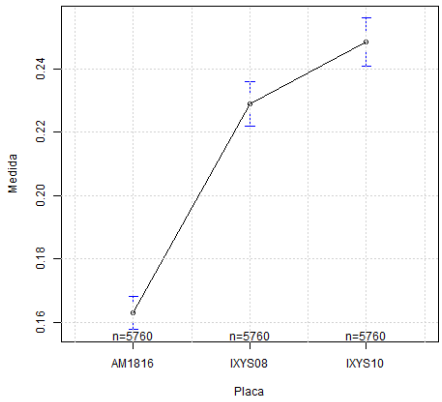

a) Means between cells at test 1

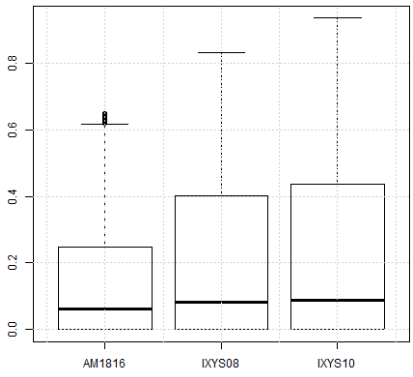

b) Distribution between cells at test 1

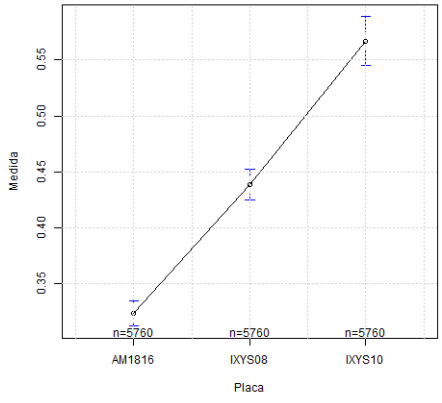

c) Means between cells at test 2

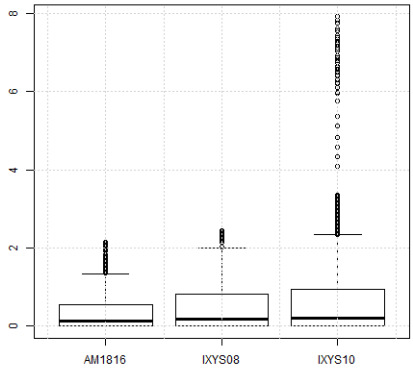

d) Distribution between cells at test 2

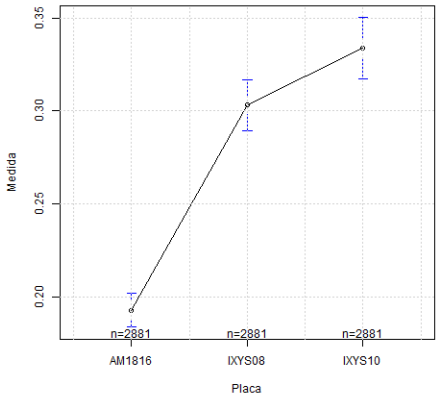

e) Means between cells at test 3

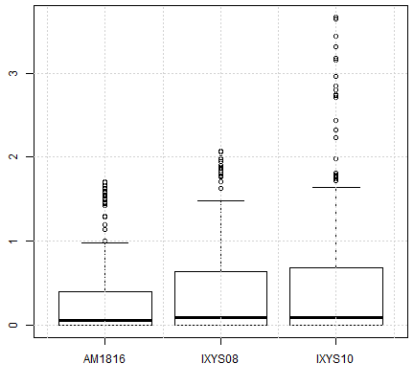

f) Distribution between cells at test 3

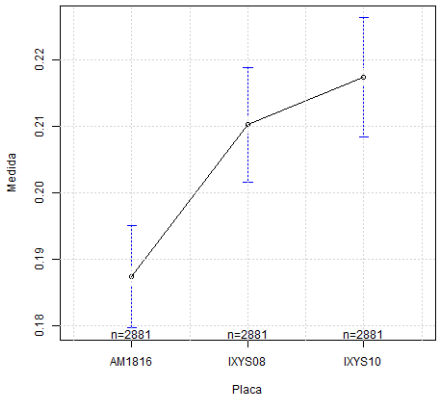

g) Means between cells at test 4

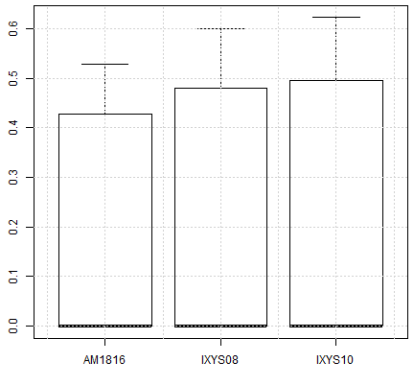

h) Distribution between cells at test 4

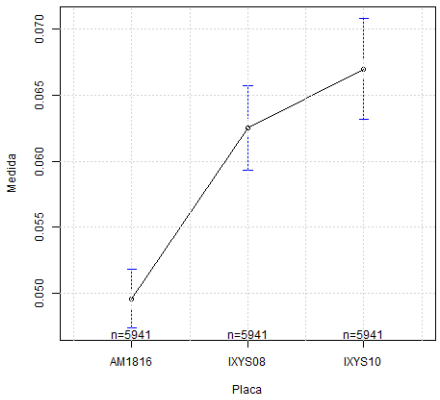

i) Means between cells at test 5

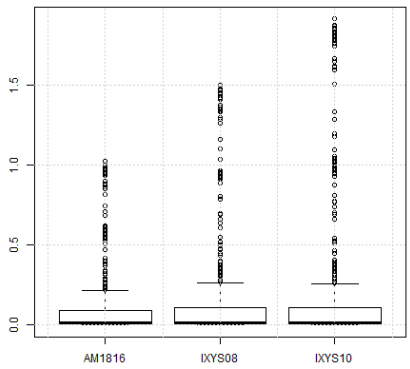

j) Distribution between cells at test 5

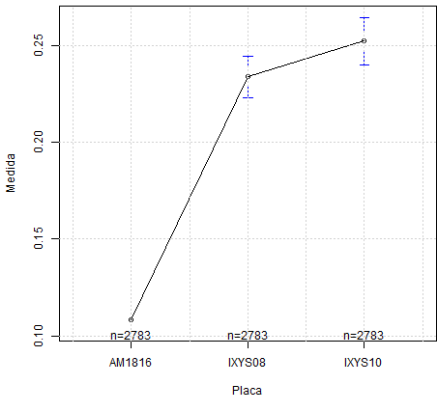

k) Means between cells at test 6

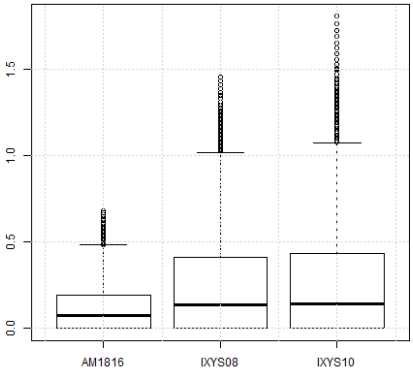

l) Distribution between cells at test 6

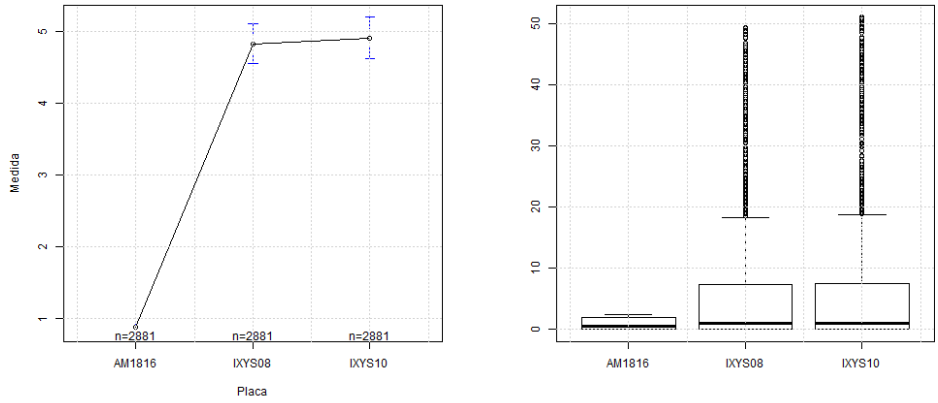

m) Means between cells at test 7 n) Distribution between cells at test 7

Figure 11-4: Mean and distribution for each cell.

Applying ANOVA to compare the variation among the different solar cells to the variation within groups we can see through the F statistics if the variation among sample means dominates over the variation within groups, or not. In the first case, we will have substantial evidence against the null hypothesis (means are all equals), while in the second case we would have little evidence against the null hypothesis.

F values are high, and p-values are very low in all the cases (tests). In other words, it means that the variation of the quantity of stored energy among different solar cells is much more significant than the variation of the quantity of that energy within the solar cells, and our p-values are less than 0.05. Therefore, it concludes that for the confidence interval the H1 hypothesis is accepted and there is a significant relationship between solar cells and the quantity of stored energy: not all the means are equal. There are significant differences between solar cells in all the cases (tests).

Table 11-5: ANOVA analysis of Variance results.

Test number	Analysis of Variance					
		Df	Sum Sq	Mean Sq	F value	Pr (>F)
Test 1	Cells	2	22.98	11.4908	172.13 <	2.2e-16 ***
	Residual	17277	1153.38	0.0668		
Test 2	Cells	2	171.7	85.853	216.2 <	2.2e-16 ***
	Residual	17277	6860.7	0.397		
Test 3	Cells	2	31.63	15.8167	117.4 <	2.2e-16 ***
	Residual	8640	1163.98	0.1347		
Test 4	Cells	2	1.41	0.70677	13.122 <	2.041e-6 ***
	Residual	8640	465.37	0.05386		
Test 5	Cells	2	0.971	0.48557	31.614 <	1.971e-14 ***
	Residual	17820	273.710	0.01536		
Test 6	Cells	2	34.09	17.0437	250.01 <	2.2e-16 ***
	Residual	8346	568.96	0.0682		
Test 7	Cells	2	30558	15278.9	373.15 <	2.2e-16 ***
	Residual	8640	353775	40.9		
Signif. codes: 0 '*' 0.001 '**' 0.01 '*' 0.05 '.' 0.1 ' ' 1**						

However, there are more than two solar cells (there are three systems), and it looks like one of the solar cells is not equal to the others. However, ANOVA test does not tell which groups (solar cells) are different from the others. So, in this sense, it is necessary to

compare each pair of solar cells to appreciate significant differences. To determine which cells are different from the others a Tukey's HSD test has been performed. Achieved results are shown in table 11-6 to analyse significant differences by plotting.

Table 11-6: Tukey's HSD test results.

Test number	Pair compared	diff	lwr	upr	p adj
Test1	IXYS08-AM1816	0.06575288	0.054468054	0.07703771	0.0000000
	IXYS10-AM1816	0.08524240	0.073957568	0.09652722	0.0000000
	IXYS10-IXYS08	0.01948951	0.008204686	0.03077434	0.0001534
Test2	IXYS08-AM1816	0.1155702	0.08804747	0.1430930	0. 0000000
	IXYS10-AM1816	0.2440590	0.21653620	0.2715817	0.0000000
	IXYS10-IXYS08	0.1284887	0.10096596	0.1560115	0.0000000
Test3	IXYS08-AM1816	0.11024490	0.087575692	0.13291410	0.0000000
	IXYS10-AM1816	0.14088115	0.118211941	0.16355035	0.0000000
	IXYS10-IXYS08	0.03063625	0.007967044	0.05330545	0.0043937
Test4	IXYS08-AM1816	0.022850191	0.008516294	0.03718409	0.0005498
	IXYS10-AM1816	0.029982298	0.015648401	0.04431619	0.0000029
	IXYS10-IXYS08	0.007132107	-0.007201790	0.02146600	**0.4733906**
Test5	IXYS08-AM1816	0.012941987	0.007612135	0.018271839	0.0000001
	IXYS10-AM1816	0.017406136	0.012076284	0.022735988	0.0000000
	IXYS10-IXYS08	0.004464149	-0.000865703	0.009794001	**0.1214593**
Test6	IXYS08-AM1816	0.12540525	0.108997874	0.14181262	0.0000000
	IXYS10-AM1816	0.14380632	0.127398952	0.16021370	0.0000000
	IXYS10-IXYS08	0.01840108	0.001993706	0.03480845	0.0233279
Test7	IXYS08-AM1816	3.94855970	3.5533504	4.3437690	0.0000000
	IXYS10-AM1816	4.02773662	3.6325273	4.4229459	0.0000000
	IXYS10-IXYS08	0.07917692	-0.3160324	0.4743862	**0.8855604**

Table 11-6 shows that:

- **There are no significant differences** in the storage capacity between cells IXYS10 and IXYS08 in Test4 (p= 0.473 >0.05), Test5 (p= 0.121>0.05) and Test8 (p=0.855 >0.05).
- **There is a significant difference** in the storage capacity of cells in the rest of the cases, where p is always less than 0.05.

Graphically, the visualization of pairs of solar cells (figure 11-5) shows the same results by plotting: significant differences are the ones which not cross the zero value.

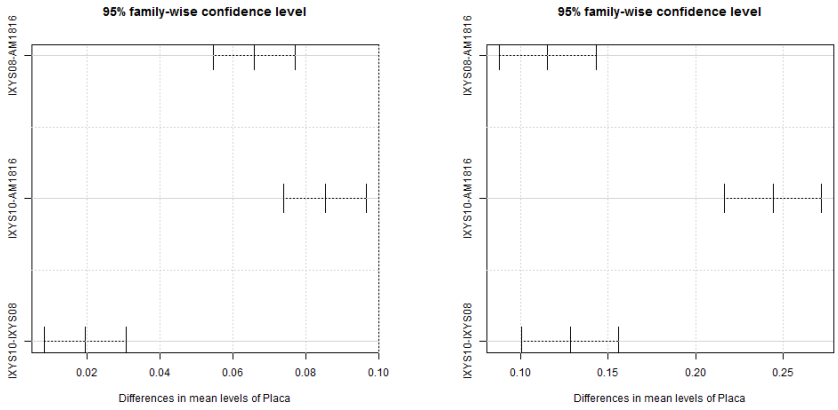

a) Test 1. b) Test 2.

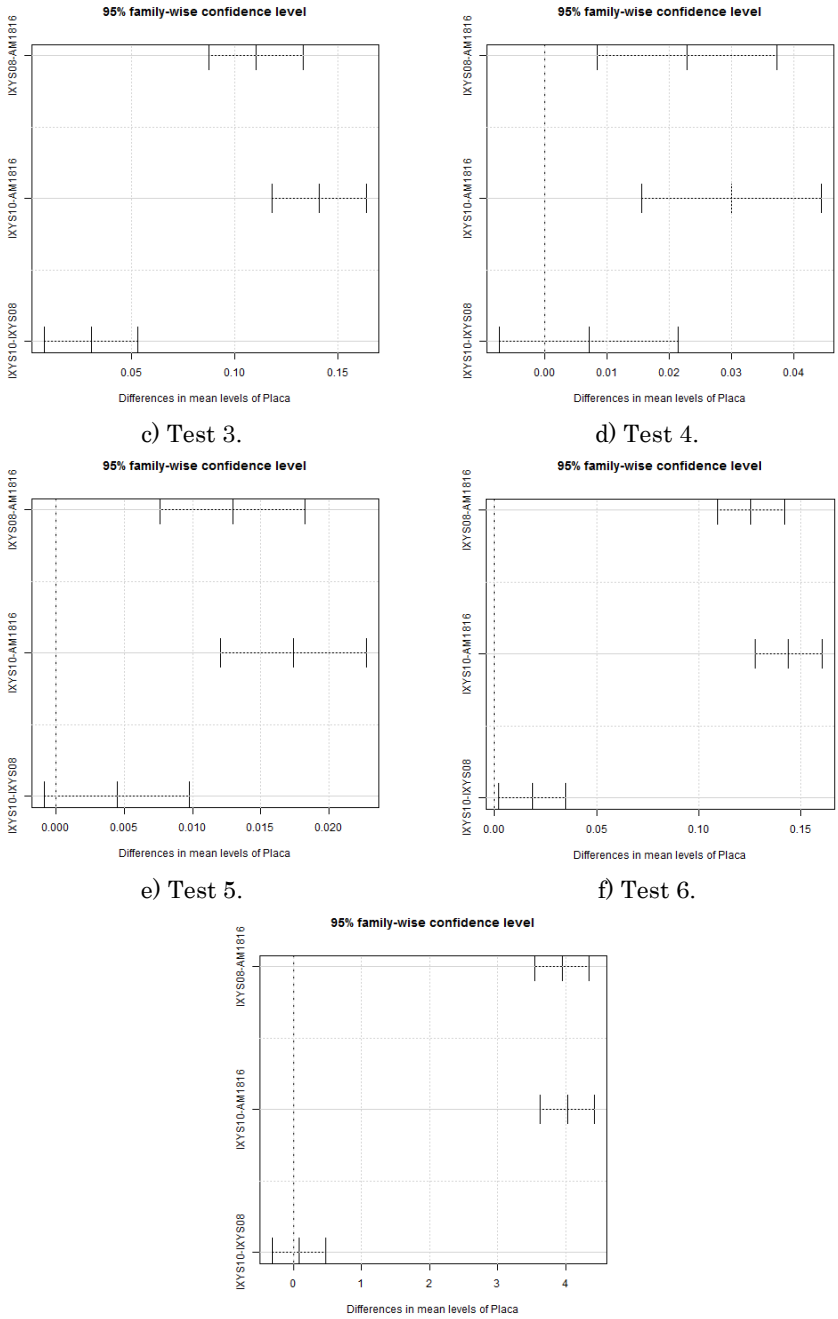

c) Test 3. d) Test 4.

e) Test 5. f) Test 6.

g) Test 7.

Figure 11-5: Realized Tukey's tests results.

The results after applying ANOVA and Tukey's HSD test, show that there are significant differences between the values obtained from the three solar cells. IXYS08 and IXYS10 have a higher capacity to store energy under the same working conditions than the AM1816 solar cell. Moreover, between IXYS08 and IXYS10, except for the Test4, Test5, and Test7, IXYS10 provides better performance and capability for the storage of energy than IXYS08. Based on the statistical testing, IXYS10 will be the best candidate to be used. However, contrasting these results with experts' criteria, it seems that the capacity to store energy for the IXYS10 solar cell is higher because it has more number of banks. Thus, taking into account this premise, IXS08 would be better regarding efficiency.

12. Supercapacitor model accuracy improvement with machine learning techniques

Machine learning techniques have been applied to assess the accuracy and stability of this type of algorithms to predict the curves and compare the results from both types of modelling: mathematical/theoretical modelling (chapter 10) and machine learning modelling.

12.1 Objective and Experimental setup

As mentioned in chapter 10, to model charge and discharge curves for supercapacitors, the analysis has been performed from a set of tests, carried out under different operating conditions which are described in table 12-1.

Table 12-1: Variables used for the development of the prediction models.

Variable	Data type	Values
Time	Integer	
Temperature (ºC)	Integer	10, 25, 40, 60
Voltage (V)	Integer	2.5, 5
Charge Time (sec)	Integer	60, 600, 3600
Capacitance	Integer	1F, 5 F
Current	Real	[0,45] mA

For each test, this set of variables has been gathered and used as predictors; while the variable to be predicted is VDC- real, the voltage. The design of experiments that have been designed is presented in table 12-2, being equal to table 10-2 of section 10.

Table 12-2: List of each test with each ambient condition.

Test number	Cap.	Operating conditions			Test number	Cap.	Operating conditions		
		Temp.	Volt.	Charge Time (sec)			Temp.	Volt.	Charge Time (sec)
Test1	1F	10	2.5	60	**Test2**	5F	10	2.5	60
Test3	1F	10	2.5	600	**Test4**	5F	10	2.5	600
Test5	1F	10	2.5	3600	**Test6**	5F	10	2.5	3600
Test7	1F	10	5	60	**Test8**	5F	10	5	60
Test9	1F	10	5	600	**Test10**	5F	10	5	600
Test11	1F	10	5	3600	**Test12**	5F	10	5	3600
Test13	1F	25	2.5	60	**Test14**	5F	25	2.5	60
Test15	1F	25	2.5	600	**Test16**	5F	25	2.5	600
Test17	1F	25	2.5	3600	**Test18**	5F	25	2.5	3600
Test19	1F	25	5	60	**Test20**	5F	25	5	60
Test21	1F	25	5	600	**Test22**	5F	25	5	600
Test23	1F	25	5	3600	**Test24**	5F	25	5	3600
Test25	1F	40	2.5	60	**Test26**	5F	40	2.5	60
Test27	1F	40	2.5	600	**Test28**	5F	40	2.5	600
Test29	1F	40	2.5	3600	**Test30**	5F	40	2.5	3600
Test31	1F	40	5	60	**Test32**	5F	40	5	60
Test33	1F	40	5	600	**Test34**	5F	40	5	600
Test35	1F	40	5	3600	**Test36**	5F	40	5	3600

Each test of table 12-2 has his own current profile, which has been measured during the charge procedure of each test. The current profile is another parameter which affects to the charge and discharge behaviour and is dependent of other parameters presented in the before table.

The outcome is a dataset of 36 tests plus the VDC value to be predicted.

12.2 Machine learning algorithms

Several algorithms from machine learning have been applied, such as regression trees, neural networks or support vector machines. The algorithms selection criteria is based on previous experiences with these types of algorithms. Many algorithms can be used for the prediction; however, as the final aim of this work is to prove the validity of these techniques in the field of energy harvesting applications, this set of algorithms suffices for the present work.

These algorithms have been used from Rapid Miner software [254], which is a code-free data science platform with a collection of machine learning algorithms, and they are listed and explained in more detail in the following lines:

- W-M5P

It performs the Weka learning algorithm of the same name. It implements base routines for generating M5 Model trees and rules. Also, it generates a decision list for regression problems using separate-and-conquer rules. In each iteration, it builds a model tree using M5 and makes the "best" leaf into a rule.

- NeuralNet

This operator learns a model employing a feed-forward neural network. The learning is done via back-propagation. The user can define the structure of the neural network with the parameter list "hidden layer types". Each list entry describes a new hidden layer. The key of each entry must correspond to the layer type, which must be either linear, sigmoid (default), tanh, sine, logarithmic or Gaussian. The key of each entry must be a number defining the size of the hidden layer. A size value of -1 or 0 indicates that the layer size should be calculated from the number of attributes of the input example set. In this case, the layer size will be set to (number of attributes + number of classes) / 2 + 1. The type of the input nodes is sigmoid. The type of the output node is sigmoid if the learning data describes a classification task, and linear for numerical regression tasks.

- W-MultilayerPerceptron

It performs the Weka learning scheme of the same name that uses back-propagation to predict instances. This network can be built by hand, created by an algorithm or both. The network can also be monitored and modified during training time. The nodes in this network are all sigmoid (except for when the class is numeric, in which case the output nodes become un-threshold linear units).

- SVM Linear

Support vector machines (SVMs) are a set of related supervised learning algorithms developed by Vladimir Vapnik in the mid 90's for classification and regression. They are new generation learning algorithms based on recent advances in statistical learning theory. The elegance and the rigorous mathematical foundations from

optimization and statistical learning theory have propelled SVMs to the very forefront of the machine learning field within the last decade.

12.3 Evaluation method

The objectives of the evaluation model are the following:

1. Estimate and compare the goodness of the model regarding future outcomes predictions.
2. Select the model amongst two or more models.

10-fold cross-validation model technique has been used for calculating RMSE measure to estimate the goodness of the model based on the difference between real and predicted values. Then, the best model (a ranking of models has been selected) is established based on the estimation of how accurately the predictive model will perform in practice. Also, the standard deviation is an important measure to be considered to quantify the variability of the accuracy provided by the algorithms: high variability implies dispersive and inaccurate results.

12.4 Experimental Results

Initially, two approaches have been taken into account considering the nature of the curves: charging or discharging. These approximations and their results are explained in the following items.

12.4.1 First approach: Charging curve modelling

Charging data is analysed in this approach. Before applying machine learning algorithms, a previous task has been performed to pre-process the data and to ensure that it is clean and prepared for the analysis. In this way, some tests move into discharge phase before reaching the charge time established. Moreover, it has been decided to ensure the same number of samples regardless of the charging time for all the algorithms which are going be applied. For these cases, VDC value has been set to -1 (VDC=-1). It means that VCD has been set to -1 when moving to discharge phase before reaching the set charge time, or in those samples with a Charge Time less than 3600; in the case of Charge Time equal to 60, the VCD has been set to -1 from sample number 61, and in the case of Charge Time equal to 600 it has been set to -1 from the sample number 601. In addition, the values begin to be collected as early as ADC parameter is positive. A visual example is shown in the figure 12-1:

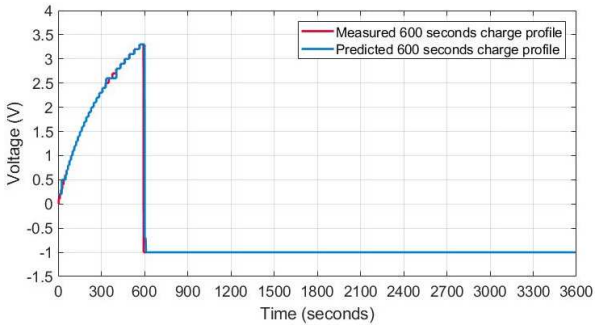

a) M5P, 5 F supercapacitor, 600 seconds charge, 25 ºC temperature and 5 V charge.

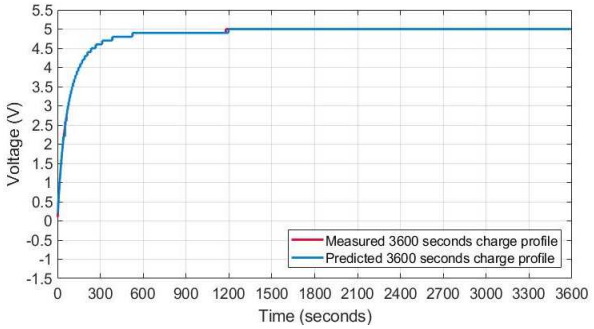

a) M5P, 1 F supercapacitor, 3600 seconds charge, 40 ºC temperature and 5 V charge.

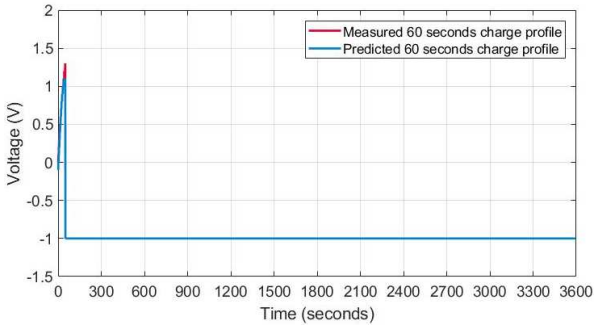

c) NeuralNet, 1F supercapacitor, 60 seconds charge, 10 ºC temperature and 2.5 V charge.

Figure 12-1: Charge curve modelling with -1 values.

Table 12-3 shows the results obtained by some of the machine learning algorithms for the charge curve prediction task. W-Multilayer Perceptron algorithm provides higher error value (RMSE) than the rest of the algorithms, and even its deviation measure is one of the biggest. Also, SVM Linear has one of the worst results obtained regarding accuracy, and although it presents the smallest deviation measure, it remains higher. Regarding the accuracy and deviation of the model, from this initial assessment, it can be considered that Neural Net and W-M5P can be the best options. The mainly Neural Net algorithm, whose accuracy is the biggest and one of the algorithms with the lowest degree of deviation. Also, W-M5P has not been discarded from our selection because its accuracy remains higher than the rest algorithms despite its deviation value.

Table 12-3: Charge curve prediction results in the first approach with the VDC=-1 condition.

Conditions	Algorithm	RMSE	Sd
VDC=-1	W-M5P	0.241	0.519
	NeuralNet	0.160	0.081
	W-MultilayerPerceptron	2.566	0.179
	SVM Linear	1.079	0.010

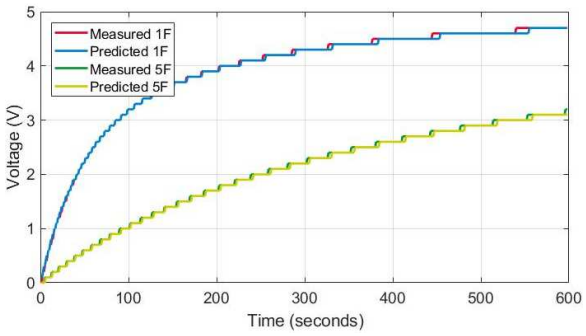

a) M5P.

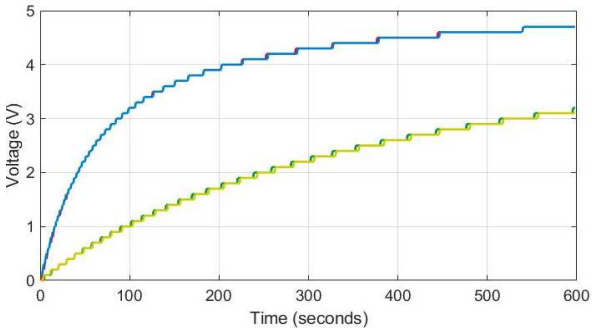

b) NeuralNet.

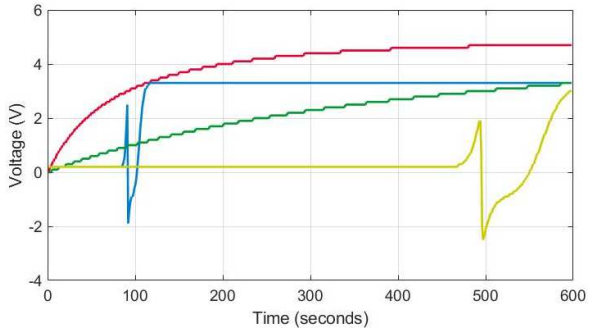

c) W-MultilayerPerceptron.

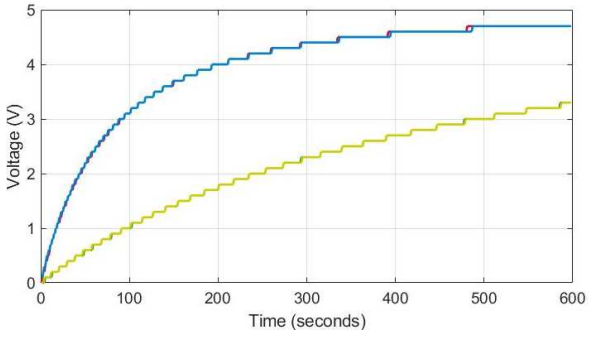

d) SVM Linear.

Figure 12-2: Charge curve prediction results with different algorithms when charge time 600, voltage 5 V, temperature 40 ºC.

Having a more in-depth look at the results for the selected algorithms (W-M5P and Neural Net), it seems that setting the VDC samples to -1 in a previous step of pre-processing the data may not have been accurate because it makes learning difficult for these algorithms. For this reason, the algorithms have been computed again, and the results have been improved in both cases regarding the error generated and deviation. Both provide similar results and present errors and low deviations.

Table 12-4: Charge curve prediction results in the first approach without VDC=-1 condition

Conditions	Algorithm	RMSE	Sd
not VDC=-1	W-M5P	0.008	0.004
	NeuralNet	0.007	0.005

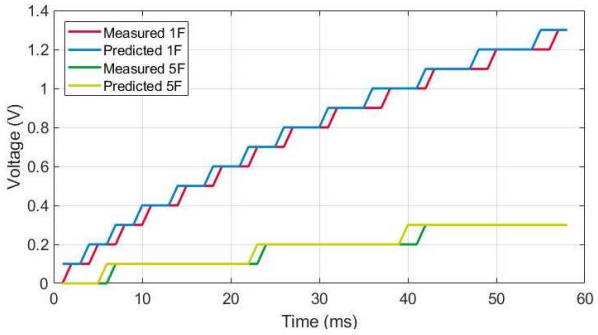

a) M5P algorithm, charge time 60 sec, voltage 2.5 V, temperature 60 ºC.

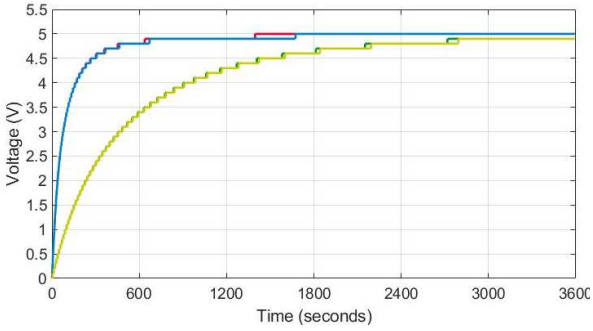

b) M5P algorithm, charge time 3600 sec, voltage 5 V, temperature 25 ºC.

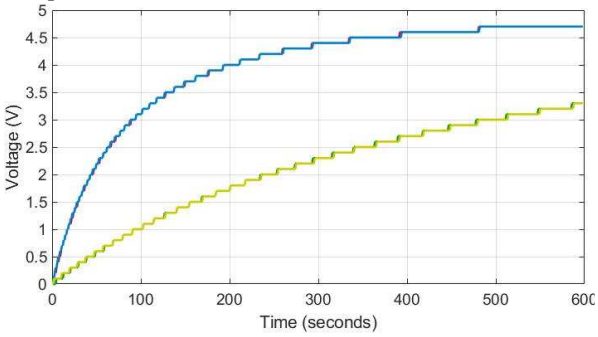

c) NeuralNet algorithm, charge time 600 sec, voltage 5 V, temperature 10 ºC.

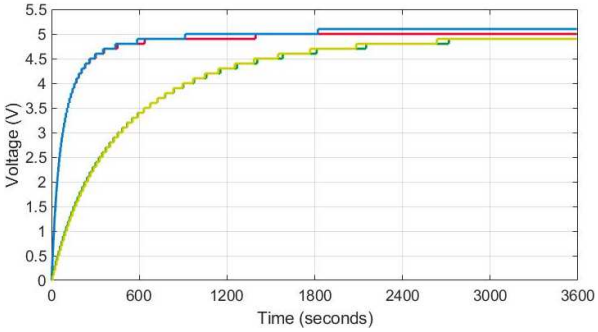

d) NeuralNet algorithm, charge time 3600 sec, voltage 5 V, temperature 25 ºC.

Figure 12-3: Charge curve prediction results in the first approach with the VDC=-1 condition.

12.4.2 Second approach: Discharge curve modelling

For the charging data case, the W-M5P and the NeuralNet algorithms provide the best performance. The same algorithms were applied to the discharge data to minimize the number of analyses.

Table 12-5: Prediction results in the second approach.

Conditions	Algorithm	RMSE	Sd
	W-M5P	0.034	0.001
	NeuralNet	0.222	0.035

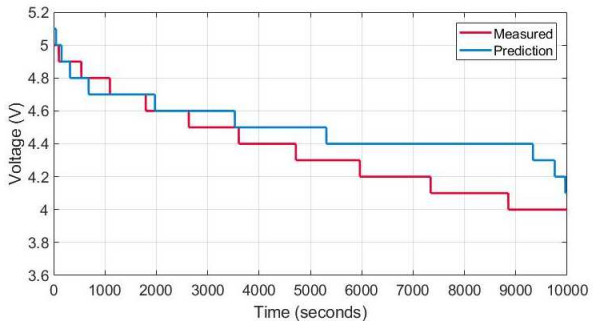

a) NeuralNet algorithm, 5 F, charge time 3600 sec, voltage 5 V, temperature 25 ºC and discharge 25 mA profile.

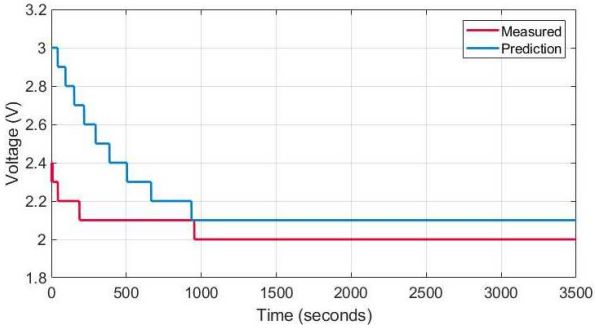

b) NeuralNet algorithm, 1 F, charge time 60 sec, voltage 5 V, temperature 40 ºC and self-discharge.

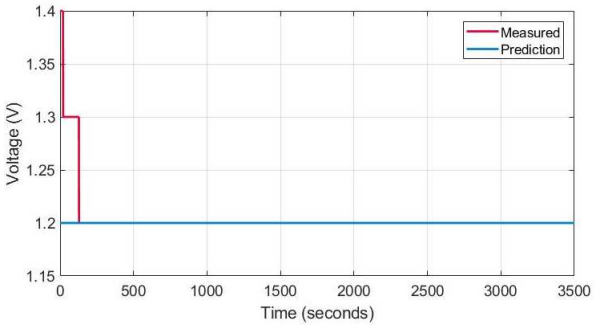

c) M5P algorithm, 1 F, charge time 60 sec, voltage 2.5 V, temperature 10 ºC and self-discharge.

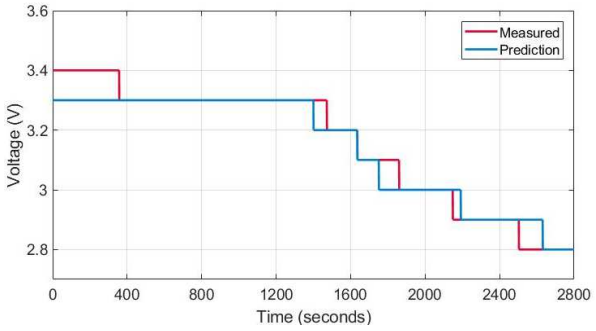

d) NeuralNet algorithm, 5 F, charge time 600 sec, voltage 5 V, temperature 40 ºC and self-discharge.

Figure 12-4: Discharge curve modelling results.

In this case, the W-M5P algorithm strengthens its use to predict the discharging curve, while Neural Net gets worse. Attempting to improve the model accuracy, a second analysis has been performed; three different models for the discharge curve have been developed, separating the dataset of the discharge curve according to the charge time used during the charge phase. The result for Charge Time equal to 60 has been improved, while for CT=600 and CT=3600 it remains similar.

Table 12-6: Prediction results in the second approach with Neural Net after charge time division.

Conditions	Algorithm	RMSE	Sd
ChargeTime (60)	NeuralNet	0.021	0.002
ChargeTime (600)	NeuralNet	0.213	0.071
ChargeTime (3600)	NeuralNet	0.244	0.098

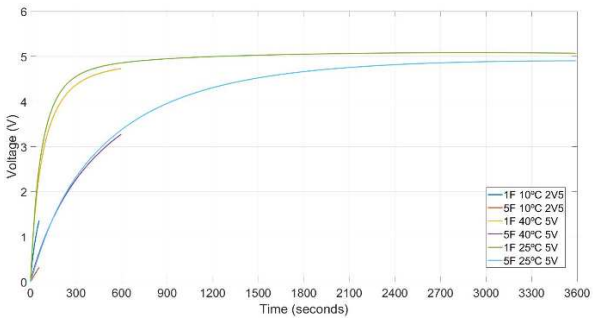

a) Charge curves at different conditions.

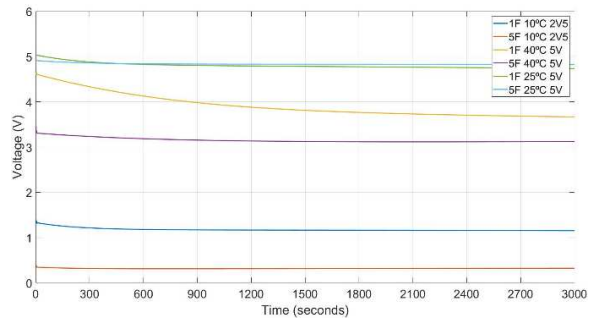

b) Self-discharge profiles.

Figure 12-5: Obtained results with time division approach at NeuralNet.

12.4.3 Approaches conclusions

Once the analysis is performed, it can be concluded that some of the machine learning algorithms provide us with the ability to predict charge and discharge curves as well as the mathematical model.

In the next section, validation of these two models is presented, and their results have been compared against those obtained from the mathematical modelling in a previous section.

12.5 Validation of machine learning and mathematical modelling

The last task is to compare and validate both types of models, the mathematical and the machine learning models (W-M5P and Neural Net), with measures from four tests.

Visual check is enough to certify the result and final approval between machine learning algorithms and mathematic model results (chapter 10). Therefore, the results are complemented with statistical techniques.

The algorithms accuracy verified and validated with several statistical techniques, such as root mean square deviation (RMSE), Mean Absolute Error (MAE), Mean Square error (MSE) and Mean Absolute Percentage Error (MAPE).

Figure 12-6 compares the experimental testing, electro-mathematical model, and machine learning models. The four new experiments performed for the validation task have been carried out inside a climatic chamber where 50% moisture has been established.

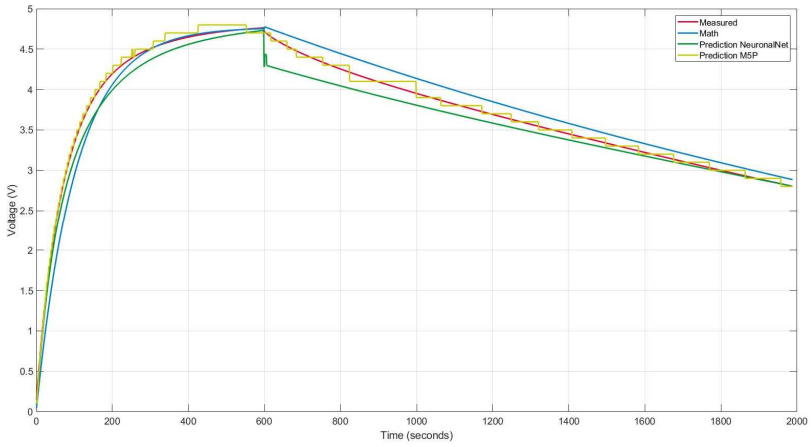

a) 1 Farad supercapacitor, charged for 10 minutes (Charge Time = 600 sec), setting the voltage to 5 V and the temperature to 40ºC. After the charging phase, unique consumption profile of 1 mA is applied for discharging phase.

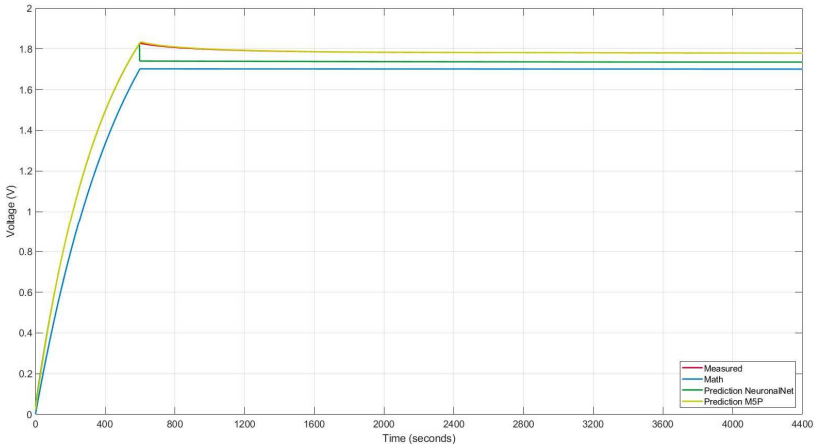

b) 5 Farad supercapacitor charged for 10 minutes (Charge Time = 600 sec) and setting the voltage to 2.5 V and the temperature to 25 ºC. After charge profile, the self-discharge curve is plotted.

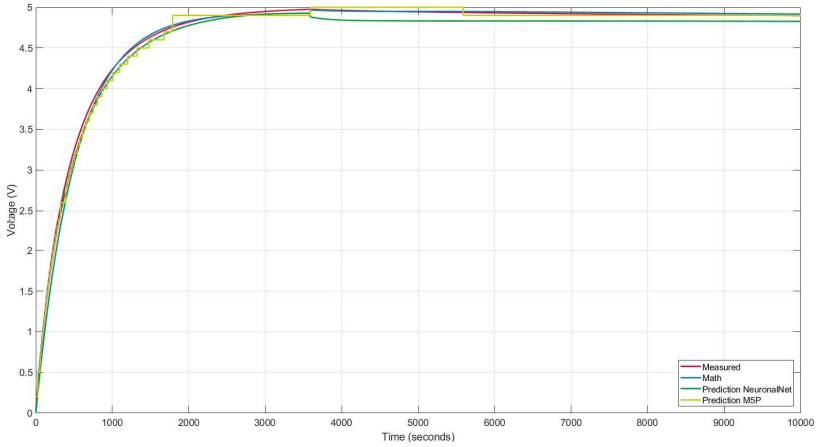

c) 1 Farad supercapacitor charged for one hour (Charge Time = 3600 sec) and setting the voltage to 5 V and the temperature to 10 ºC. In this case, discharge procedure also is based on self-discharge technique.

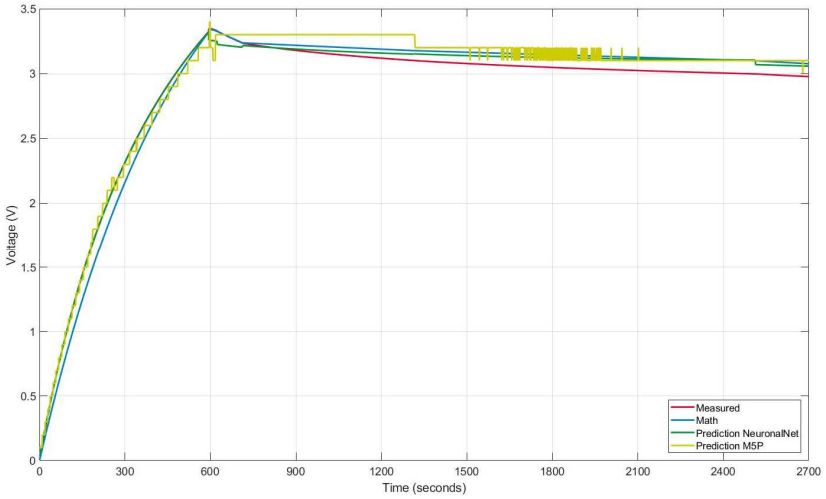

d) 5 Farad supercapacitor charged for 10 minutes (Charge Time = 600 sec) and setting the voltage to 5 V and the temperature to 40 ºC. In this case, the discharge phase has three different steps; the first one has 0.3 mA consumption profile through 3 minutes, while the second one has 0.1 mA consumption profile through 10 minutes and the last one represents the self-discharge process to the end.

Figure 12-6: Graphic results and comparisons of described four different tests.

Tables 12-7 and 12-8 shows the statistical validation results obtained with RMSE, MAE, MSE and MAPE techniques at a), b), c) and d) examples.

Table 12-7: Obtained statistical errors from NeuralNet prediction and electro-mathematical models on described four tests.

State	Metric	a) example		b) example		c) example		d) example	
		Pred.	Math	Pred.	Math	Pred.	Math	Pred.	Math
Charge	RMSE	0.137	0.204	0.113	0.178	0.007	0.145	0.005	0.134
	MSE	0.019	0.042	0.013	0.032	1e-4	0.021	2e-4	0.018
	MAE	0.123	0.125	0.103	0.167	0.006	0.114	0.004	0.118
	MAPE	3.606	5.354	4.689	11.64	0.655	4.387	1.514	8.607
Discharge	RMSE	0.119	0.123	0.071	0.083	0.157	0.048	0.074	0.086
	MSE	0.014	0.015	0.005	0.007	0.025	0.002	0.005	0.007
	MAE	0.079	0.111	0.064	0.078	0.143	0.047	0.069	0.081
	MAPE	2.013	3.210	2.211	2.653	3.659	1.230	2.272	2.685

Table 12-8: Statistical errors obtained from W-M5P prediction and electro-mathematical models on the described four tests.

State	Metric	a) example		b) example		c) example		d) example	
		Pred.	Math	Pred.	Math	Pred.	Math	Pred.	Math
Charge	RMSE	0.063	0.204	4.47	0.178	0.077	0.145	0.063	0.134
	MSE	0.004	0.042	1.998	0.032	0.006	0.021	0.004	0.018
	MAE	0.005	0.125	1.828	0.167	0.06	0.114	0.053	0.118
	MAPE	1.642	5.354	9.997	11.64	2.322	4.387	6.087	8.607
Discharge	RMSE	0.041	0.123	0.001	0.083	0.031	0.048	0.118	0.086
	MSE	0.001	0.015	1.261	0.007	9.975	0.002	0.014	0.007
	MAE	0.032	0.111	4.932	0.078	0.025	0.047	0.111	0.081
	MAPE	0.91	3.210	0.027	2.653	0.512	1.230	3.629	2.685

These tables show that machine learning models usually have a better performance than the mathematical models. Thus, machine learning algorithms improve the model accuracy. It means that in those cases in which data can be experimentally obtained, from real or simulated working conditions, the modelling based on machine learning algorithms will provide a better picture of the behaviour of the system than theoretical mathematical modelling.

13. Predictive power management strategy

Energy harvesting is a promising technology to ensure unlimited energy for wireless sensor networks (WSNs). However, environmentally-powered systems must deal with variable conditions related to the ambient energy sources, which implies variable ratios of available energy over the time. This is the reason why energy harvesting systems should be able to foresee energy availability to effectively use the harvested energy need capability of prediction. This means that based on a reliable estimation about the future quantity of harvested energy, the system will be able to make decisions about the utilization of this energy efficiently, meeting the specific needs of each system within the WSN over the time.

13.1 Use case definition

The present section describes two different uses cases to work on, the solar cell (AC) and the mini-turbine (DC). The following sections show the theoretical basis and formulation of the algorithms that have been used to predict future harvested energy. Unless, some of them have been utilized before in previous works, the objective of this work is to evaluate their accuracy and extend this assessment with few more algorithms from the field of machine learning to compare them. Finally, this section presents the two use cases from the data acquisition and experimentation steps until the achieved experimental results. To conclude, a theoretical strategy has been described to manage the harvested energy, taking into account the predictions obtained from machine learning algorithms.

13.2 Research and development of the algorithms

Several time series algorithms have been searched with the objective of predicting harvested energy form DC and AC systems:

- exponential smoothing,
- exponentially weighted moving average (EWMA),
- linear regression,
- support vector regression (SVR), and
- auto-regressive integrated moving average (ARIMA).

A. Exponential smoothing

Exponential smoothing (ETS) is one of the most used time series analysis methods. It takes into account not only current observations but also past observations. The weight of past observations gradually decreases exponentially. Mathematically, in simple exponential smoothing the following interpolation is calculated:

$$\hat{x}_t = \alpha x_t + (1-\alpha)\hat{x}_{t-1} \tag{13-1}$$

, where α weighs the contribution of current versus past information. By unfolding the recursion in the equation, it is possible to see that past observations are considered with a weighting factor gradually decreasing.

Simple exponential smoothing can be directly applied to the time series of energy production data.

B. Exponentially weighted moving average (EWMA)

An alternative application of this concept to energy production prediction is called EWMA). In this case, the days are divided into slots of predetermined duration. Thus, the prediction takes into account the current observation as well as those of previous days. The formulation is shown in equation 13-2:

$$\hat{x}_i = \alpha x_i + (1-\alpha)\hat{x}_{i-1} \tag{13-2}$$

, where i refers to the slots.

C. Linear Regression

In linear regression (LR) the general formulation of the relationship to be calculated is:

$$y = a\,x + b \tag{13-3}$$

, where y and x are the independent and dependent variables and a and b are coefficients to be estimated. In time series analysis linear regression can be applied to the prediction of the variable in time.

D. Support vector regression (SVR)

Other regression techniques are plausible for time series analysis. However, support vector regression (SVR) is based on the framework of support vector machines (SVM). The basic idea in SVM classification is to find a hyperplane separating two classes with the maximum margin between the classes. Samples on the margin are called support vectors. The formulation corresponds to a linear classifier. Nonetheless, a transformation via kernel functions can be used for classifying non-linearly separable classes. This formulation has been adapted for regression tasks (SVR), and the relationship expression is:

$$y = \sum_{i=1}^{l} (\alpha_i - \alpha_i^*) K(x_i, x) + b \tag{13-4}$$

, where i refers to the support vectors, K is a kernel function, and α and b are coefficients to be estimated.

E. ARIMA

Auto-regressive integrated moving average (ARIMA) models consist of an auto-regressive part (AR), a moving average part (MA), and an integral part (I). The AR part models the time series concerning its previous values. The MA part is a linear combination of the current and past errors. The I part is a differencing step for removing the non-stationarity, where their difference with the previous values replaces the values, and this differencing step may be applied more than once. This formulation has the following form:

$$x_t^{'} = \phi_1\, x_{t-1}^{'} + \cdots + \phi_p\, x_{t-p}^{'} + c + e_t + \theta_1\, e_{t-1} + \cdots + \theta_q\, e_{t-q} \tag{13-5}$$

, where x' are differenced time series values, e are the error terms, and ϕ, θ, and c are the coefficients and constant to be estimated. The order of the model is indicated as ARIMA(p,d,q), where p is the order of the AR part, d is the order of the I part (i.e., the number of differencing steps), and q is the order of the MA part.

ARIMA models bear a relation to exponential smoothing. In fact, a model ARIMA (0,1,1) without constant is of the order of simple exponential smoothing. However, these two families of models overlap and are complementary.

13.3 DC system

13.3.1 Data acquisition and consumption profile definition

DC system output (solar cell and DC/DC converter) from the laboratory simulation of an industrial plant provides the data to complete this task. This environment has artificial light and sampling rate is set in 1 minute.

The following table 13-1 represents the output values provided by the DC system.

Table 13-1: Irradiance and temperature dependable values to construct learning profiles.

Ambiental conditions		DC/DC operation conditions			Output values				
G (suns)	T (ºC)	f_{sw} (kHz)	R_{load} (Ω)	D	V_{in} (V)	V_{out} (V)	P_{in} (mW)	P_{out} (mW)	η (%)
0.1	5	150	500	0.2	2.707	3.216	22.246	20.695	93.03
	10				2.736	3.252	22.729	21.151	93.06
	15				2.764	3.286	23.206	21.603	93.09
	20				2.792	3.32	23.678	22.049	93.12
	25				2.818	3.353	24.143	22.49	93.15
	30				2.845	3.385	24.602	22.925	93.18
0.25	5	86	400	0.3	2.942	4.789	60.751	57.348	94.40
	10				2.97	4.839	61.976	58.551	94.47
	15				3	4.887	63.197	59.727	94.51
	20				3.029	4.935	64.394	60.89	94.56
	25				3.057	4.981	65.569	62.031	94.60
	30				3.085	5.025	66.722	63.145	94.64
0.5	5	66	150	0.3	3.135	4.281	130.007	122.206	94.00
	10				3.164	4.322	132.464	124.573	94.04
	15				3.192	4.362	134.874	126.901	94.09
	20				3.22	4.402	137.239	129.186	94.13
	25				3.246	4.44	139.559	131.43	94.18
	30				3.272	4.477	141.834	133.634	94.22

Different profiles of energy production have been simulated under three different lighting conditions: constant luminance, varying luminance, and varying luminance and temperature. Each of these lighting conditions has different levels depending on the values assigned to the 'luminance' and 'temperature' parameters. Table 13-2 summarises the characteristics and levels of the ten profiles generated. Each profile simulates energy production for a three-day period, and for two of them, test 6 and test 10, one and two non-productive days have also been inserted respectively.

Table 13-2: profiles construction parameters and conditions.

Profile number	Lighting conditions	Level	
		Irradiance	Temperature
1	constant irradiance and temperature	0-0.1	20
2		0-0.25	
3		0-0.5	
4		0-0.1-0.25-0.5	20

5	varying irradiance and constant temperature		
6			
7	varying irradiance and temperature	0-0.1-0.25-0.5	5-10-15-20-25
8			20-25-30-35
9			10-15-20
10			15-20-25

The figures 13-1 – 13-3 show simulation/test for each lighting conditions:

1- Figure 13-1 shows for constant light and temperature:

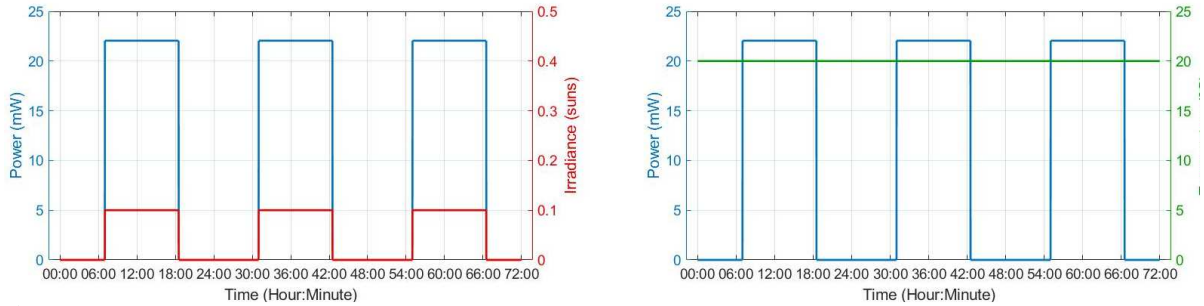

a) Constant irradiance and temperature case 1.

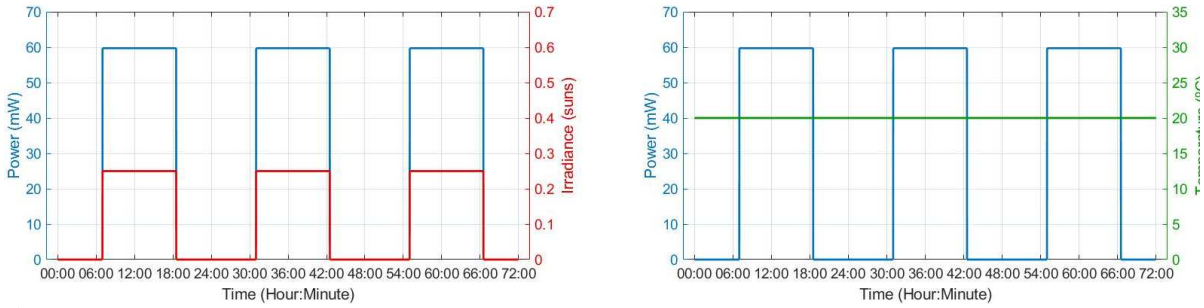

b) Constant irradiance and temperature case 2.

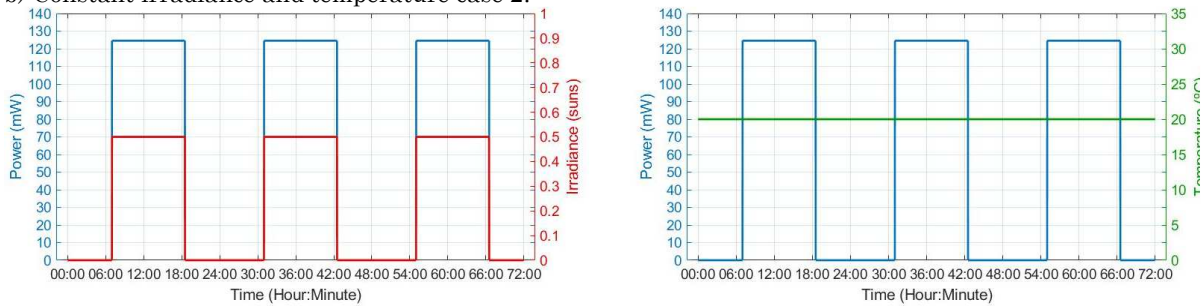

c) Constant irradiance and temperature case 3.

Figure 13-1: Constant light and temperature profiles.

2- Figure 13-2 shows for inconstant light and constant temperature:

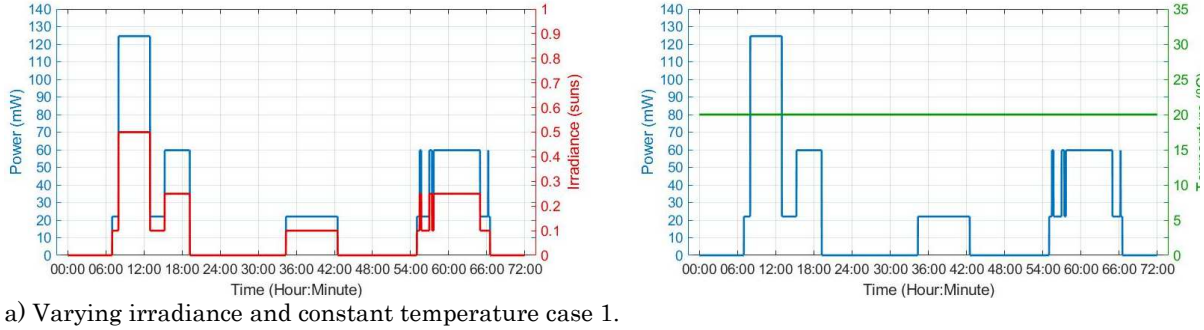

a) Varying irradiance and constant temperature case 1.

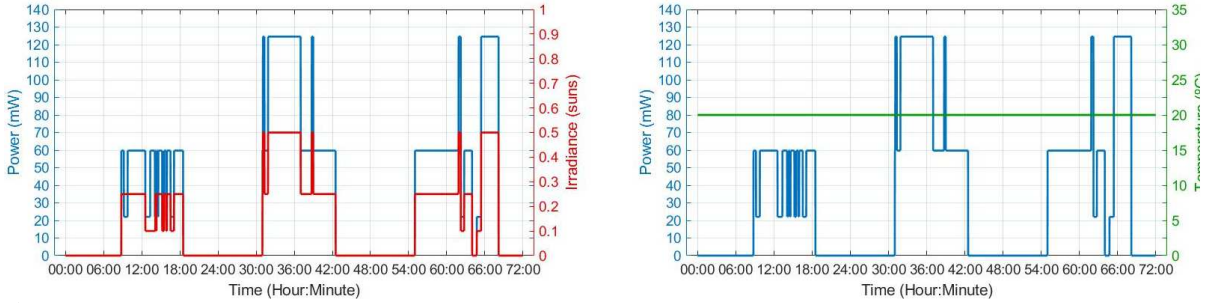

b) Varying irradiance and constant temperature case 2.

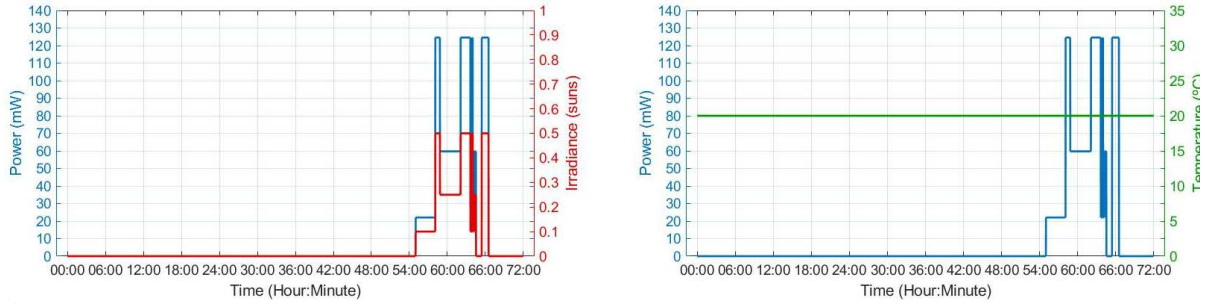

c) Varying irradiance and constant temperature case 3.

Figure 13-2: Inconstant light and constant temperature profiles.

3- Figure 13-3 for inconstant light and temperature:

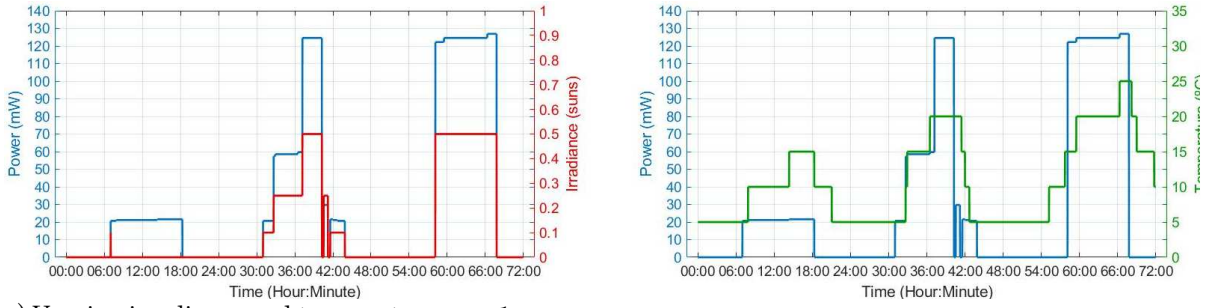

a) Varying irradiance and temperature case 1.

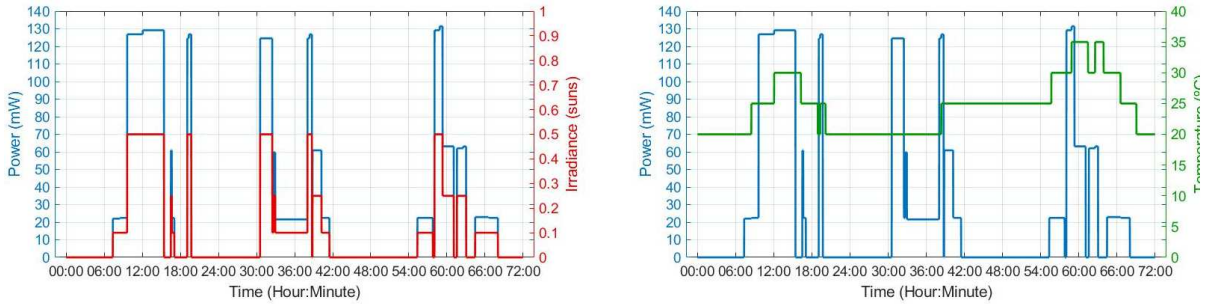

b) Varying irradiance and temperature case 2.

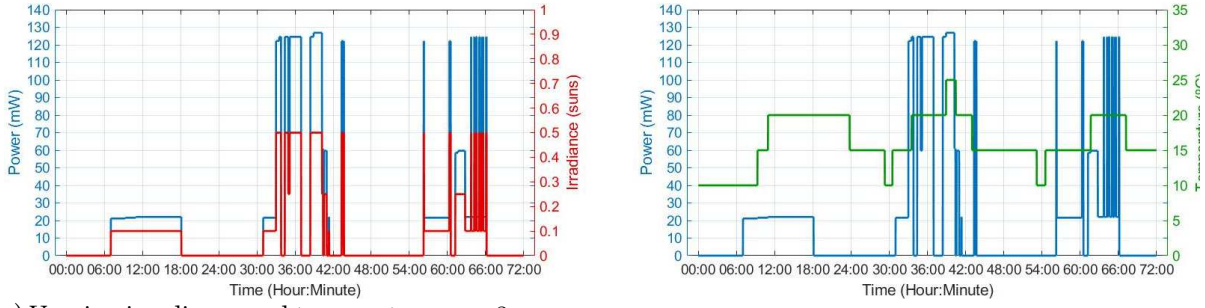

c) Varying irradiance and temperature case 3.

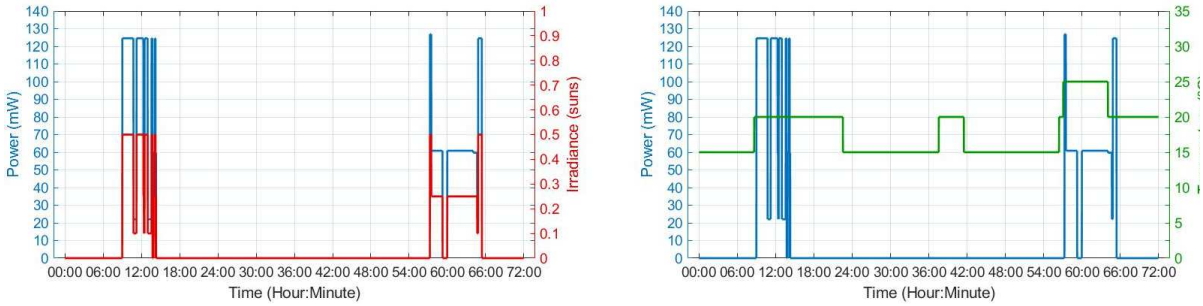

d) Varying irradiance and temperature case 4.

Figure 13-3: Inconstant light and temperature profiles.

13.3.2 Evaluation procedure

Evaluation is an important task to bear in mind after the learning process of the algorithms because their validity depends on the quality of this evaluation. The objective of this task is to estimate the real error rate of the prediction (with new samples) to validate the model. This error rate must be calculated using data sets that have not been previously used for learning the model because the error rate calculated from training samples underestimates the error rate predicted for new samples. The following procedure has been carried out for a good estimation of the error rate:

For the experiments, two-time series were built with the energy profiles (lab constant light → lcl, lab inconstant light → licl, lab inconstant light and temperature → lilat). One for training the algorithms and one for testing them.

- The training set includes following profiles: lilat1, lil3, lil1, lilat3, lcl3, lcl1.
- The test set includes following profiles: lilat2, lilat4, lil2, lcl2.

To build the training and test time series, their respective profiles were concatenated in random order. In total, the training time series consists of simulated energy production for 18 days, while the test set consists of simulated energy production for 12 days.

- The training set was used for estimating coefficients in LR, SVR, and ARIMA. For SVR and ARIMA, the training set was used as well for adjusting their hyper-parameters. For ETS, the training set was used for selecting a value for the alpha coefficient. For EWMA, the training set was used for initialization. One of the days in the training set, which was in the same group of luminance and temperature conditions as the first day in the test set, was used for initialization of EWMA.

- Finally, the test set was used for obtaining the final results with all algorithms. The mean absolute error (MAE) was calculated from the test set in order to assess and compare the goodness of the algorithms.

Besides this, random noise from a uniform distribution was added to the data. Noise is used to simulate small variations in energy harvesting conditions. The level of noise was ±10 mW or about ±8% of the maximum value in the series. Care was taken that there were no negative values of energy produced. Any negative value that could appear was replaced by positive random noise within a level of 0-10 mW. In this way, the experiments have been carried out also with a certain level of noise, adding complexity to the prediction task. And finally, the following groups of experiments have been conducted:

- Clean data: Clean training data and Clean test data (“clean data” condition)

- Noisy training data: Noisy training data and Clean data ("noisy training data" condition)
- Noisy data: Noisy training data and Noisy test data ("noisy data" condition)

In all cases, five algorithms (ETS, EWMA, LR, SVR, and ARIMA) have been used to predict the next value (1 minute later) of harvested energy.

13.3.3 Experimental results

Table 13-3 provides the MAE of the experiment data set-up for different prediction algorithms used.

Table 13-3: Obtained results for the various experiments and algorithms tested.

	Clean data	Noisy training data	Noisy data
ETS	**0.34**	0.81	4.40
EWMA	17.49	18.06	18.33
LR	0.56	0.92	4.92
SVR	0.41	3.83	**3.84**
ARIMA	**0.34**	**0.54**	4.42

The ETS algorithm obtains the best results with an alpha coefficient of 1.0 when it is executed on the clean dataset. Therefore, since the alpha coefficient is 1.0, it corresponds to the naïve method, which establishes the prediction based on the value of the last observation. Under noise conditions, the best alpha coefficient in the training set was 0.4, and therefore for this case, the ETS algorithm uses the current and historical values.

Applied on the clean data set, the obtained ARIMA model is of order (0,1,1), which corresponds to a simple exponential smoothing algorithm. Training with the noisy data set shows that the result obtained when applied to the clean data set is less affected compared to that obtained by the other algorithms.

Both simple LR and SVR obtain, in general, a little higher MAE. In this case, SVR achieves better performance with a linear kernel on a training set without added noise, and with a radial basis function kernel on a training set with added noise. With a noisy training set, performance on a clean test set would have been better using a linear kernel (MAE=0.68) than the radial basis function kernel (MAE=3.83). SVR has the added difficulty of tuning hyper-parameters. Note that SVR is typically computationally costlier since the number of support vectors can be quite high.

The following figures show the results obtained with the different algorithms on an excerpt of the time series. Figure 13-4 shows the clean data condition results:

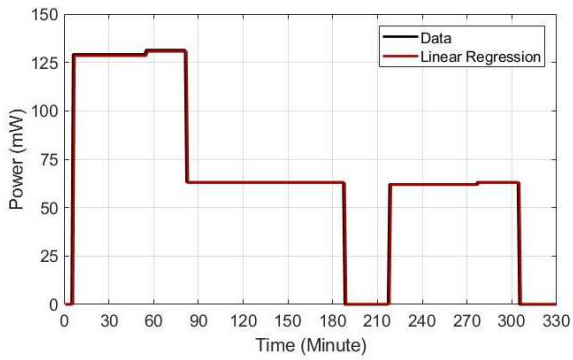

a) Linear regression algorithm vs. data.

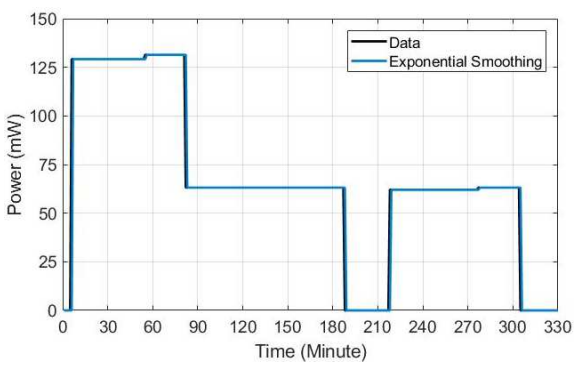

b) Exponential smoothing algorithm vs. data.

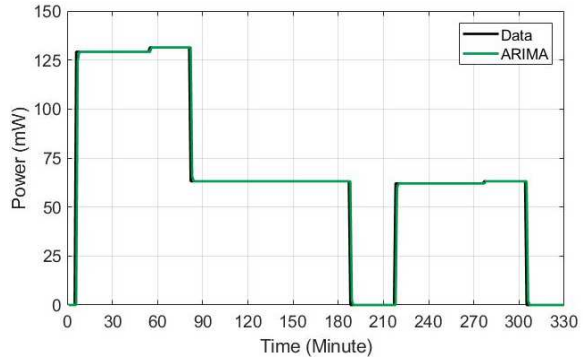

c) Arima algorithm vs. data.

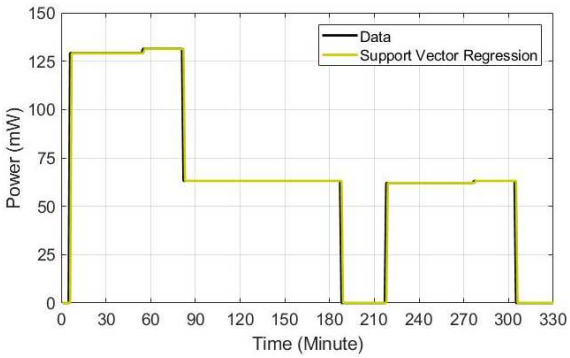

d) Support vector regression algorithm vs. data.

Figure 13-4: Obtained prediction profiles for solar power input with clean data condition.

Figure 13-5 shows the noisy training data condition results:

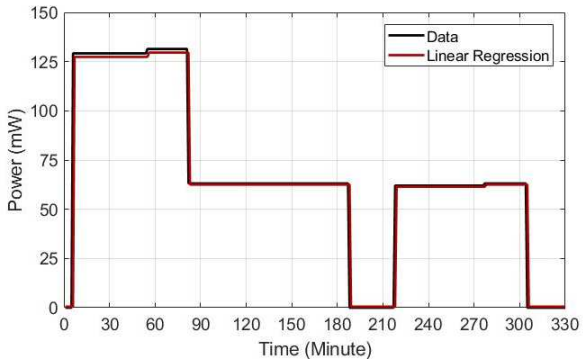

a) Linear regression algorithm vs. data.

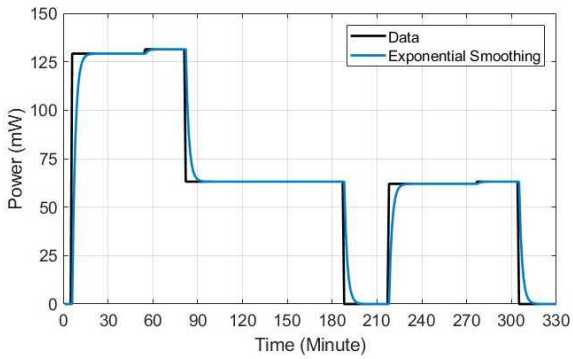

b) Exponential smoothing algorithm vs. data.

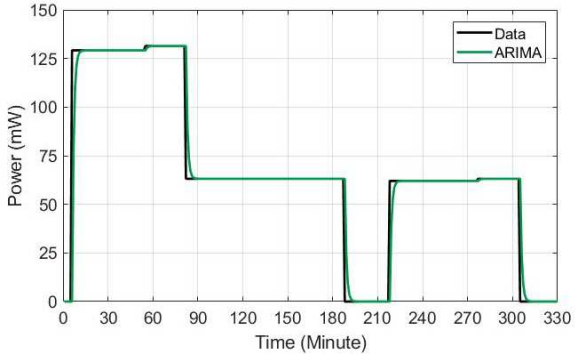

c) Arima algorithm vs. data.

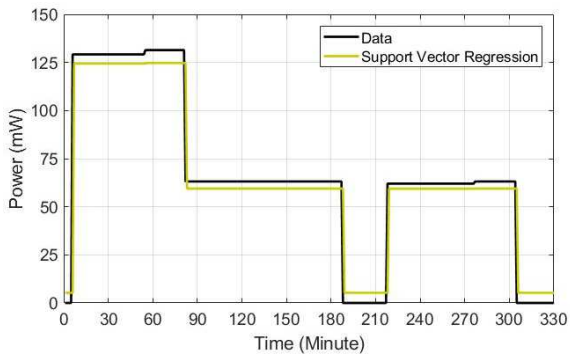

d) Support vector regression algorithm vs. data.

Figure 13-5: Obtained prediction profiles for solar power input with noisy training data condition.

Figure 13-6 shows the noisy data condition results:

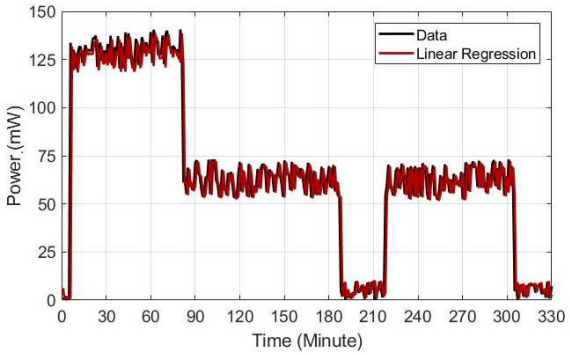

a) Linear regression algorithm vs. data.

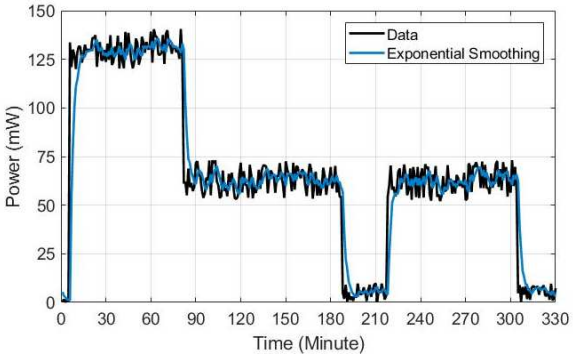

b) Exponential smoothing algorithm vs. data.

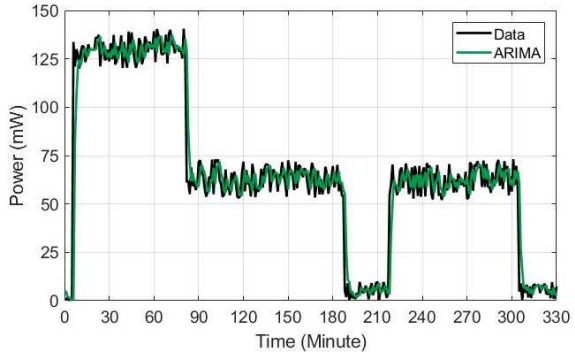

c) Arima algorithm vs. data.

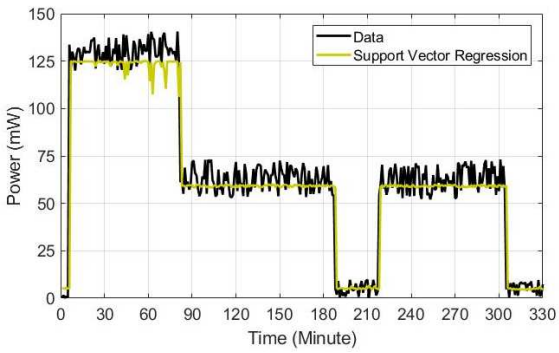

d) Support vector regression algorithm vs. data.

Figure 13-6: Obtained prediction profiles for solar power input with noisy data condition.

In all conditions, error with EWMA algorithm is higher than for the other algorithms. The main reason is due to EWMA prediction is based on previous days, and used daily energy profile changes often, consequently, the data performance suffers. An example of this behaviour is a sporadic day with no energy production, as can be seen in the figure below for the clean data condition:

Figure 13-7 shows EWMA results for the clean data condition, the noisy training data condition and the noisy data condition:

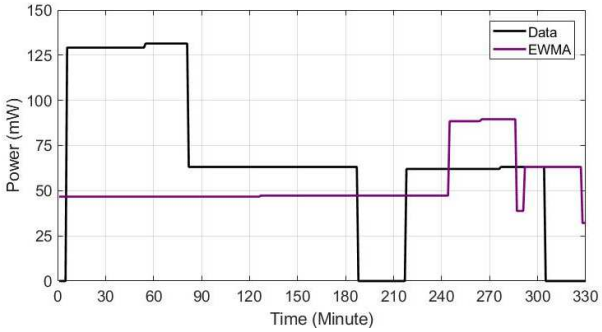

a) EWMA vs. data at clean data condition

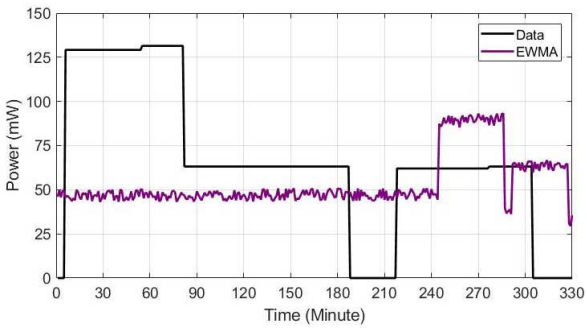

b) EWMA vs. data at noisy training condition

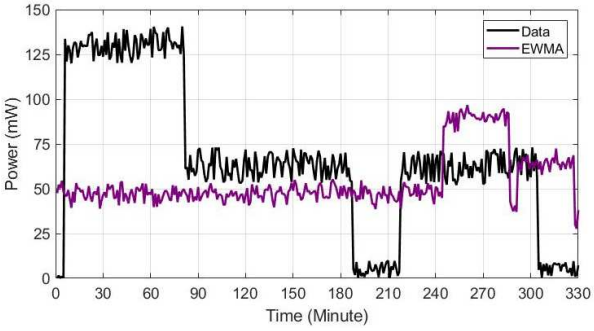

c) EWMA vs. data at noisy data condition

Figure 13-7: Obtained prediction profiles with EWMA algorithm for solar power input; a) clean data condition, b) noisy training data condition, c) noisy data condition.

Figure 13-8 shows data and all algorithms profiles at all range:

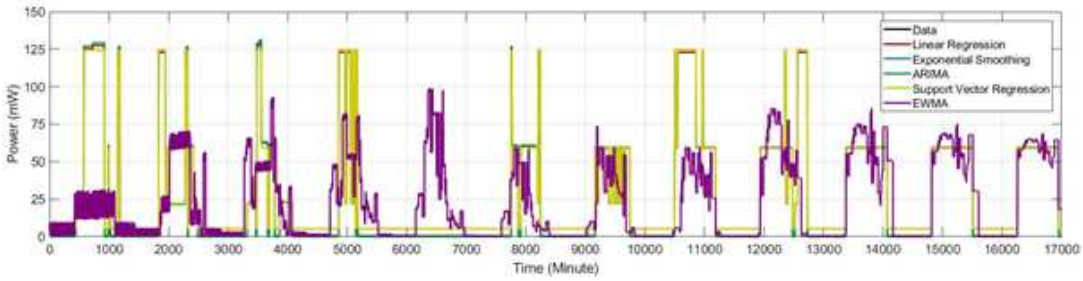

Figure 13-8: Obtained prediction profiles with all algorithm for solar power input overall range.

Overall, a methodology has been investigated for developing algorithms for energy harvesting prediction. Several algorithms have been tested on simulated data and a number of their characteristics and particularities discussed. Some of the algorithms showed potential on the data tested. Nonetheless, the choice might be dependent as well on how well parts of the profile should be modelled, with some models looking better at abrupt changes and others better at steady states; and also taking the complexity of the algorithm into account.

Considering this and as conclusions, it seems that LR and ARIMA can be an enough choice. Even though they have similar results to ETS or SVM, these algorithms have some disadvantages. SVM is a complex model because its computational load requirements and implementation; besides, it will be necessary to use different kernels depending on the condition of the data (whether it is clean). Moreover, in the case of ETS, it is observed that this algorithm detects worse sudden drops and rises. Nevertheless, the final choice between LR and ARIMA is not obvious. There are no differences between them regarding complexity (computational requirements and implementation) and regarding the adjustment provided against changes. Figures 13-5-6-7 shows that LR is the algorithm which best adapts to these changes, nevertheless this difference is not statistically confirmed.

13.4 AC system

13.4.1 Data acquisition and consumption profile definition

Data from AC system have been simulated and stored in a controlled environment with a sampling rate of 10 seconds. The experiments have been carried out according to experimental conditions and are shown in table 13-4. In this regard, different profiles of energy production have been simulated under three different conditions. These simulations are part of the group of experimental testing performed for the experimentation.

Table 13-4: Acquired data for profile construction.

Ambiental conditions		Output values (mW)	
Velocity (m/s)	Pressure (mbar)	P_{in} (mW)	P_{out} (mW)
3	20	15.28	9.168
4	36	31.16	18.69
5	52	55.49	38.84
6	91	111.02	77.71
7	112	160.72	112.50
8	142	239.69	191.75
9	144	272.54	218.03
10	163	333.15	266.52

Other values with 0.2 m/s difference have been obtained through interpolation, which are shown in table 13-5.

Table 13-5: Interpolation results for input and output power of converter with 0.2 m/s velocity change condition used for profile construction.

Ambiental conditions	Power (mW)		Ambiental conditions	Power (mW)	
Velocity (m/s)	P_{in}	P_{out}	Velocity (m/s)	P_{in}	P_{out}
3	15.28	9.16	6.6	140.84	98.58
3.2	18.45	11.07	6.8	150.78	105.54
3.4	21.63	12.97	7	160.72	112.50
3.6	24.80	14.88	7.2	176.51	127.09
3.8	27.98	16.79	7.4	192.30	142.30
4	31.16	18.69	7.6	208.10	158.15
4.2	36.02	21.61	7.8	223.89	174.63
4.4	40.89	24.53	8	239.69	191.75
4.6	45.75	27.45	8.2	246.25	197.00
4.8	50.62	30.37	8.4	252.81	202.25
5	55.49	38.84	8.6	259.38	207.50
5.2	66.59	46.617	8.8	265.94	212.75
5.4	77.70	54.39	9	272.54	218.03
5.6	88.80	62.16	9.2	284.66	227.72
5.8	99.91	69.93	9.4	296.78	237.42
6	111.02	77.71	9.6	308.90	247.12
6.2	120.96	84.67	9.8	321.02	256.82
6.4	130.9	91.63	10	333.15	266.52

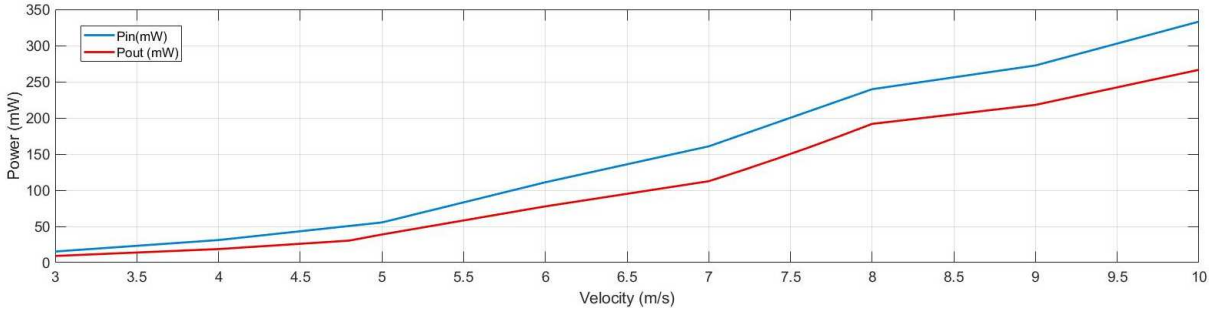

Figure 13-9: Interpolation results for input and output power of converter with 0.2 m/s velocity change condition used for profile construction.

Different profiles of energy production have been simulated under three different ambient conditions: Indistinct, winter, and summer. In one hand, indistinct ambient conditions have 1 m/s wind velocity steps change, and profiles have a duration of 1 hour. On the other hand, winter, and summer ambient conditions change with 0.2 m/s velocity steps, and profiles have a duration of 12 hours. Table 13-6 summarises the profiles and their levels. In total, nine different profiles have been generated.

Table 13-6: AC system profiles construction parameters and conditions.

Profile number	Conditions	Explanation	Hours
1	"Indistinct"	Short periods – introducing 'big' changes of speed in the wind (1 m/s)	1 hour
2			
3			
4	"Winter"		

5		Simulation of winter situations, more gas consumption and therefore more power collected – introducing 'small' changes of speed in the wind (0.2 m/s)	12 hours
6			
7	"Summer"	Simulation of summer situations, less gas consumption and therefore less power collected – introducing 'small' changes of speed in the wind (0.2 m/s)	12 hours
8			
9			

Figures 13-10, 13-11 and 13-12 show simulation/test for each one of the conditions:

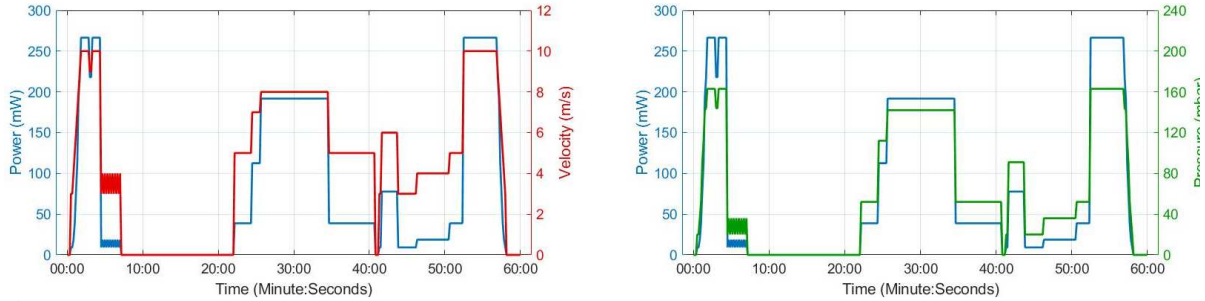

a) Indistinct case 1.

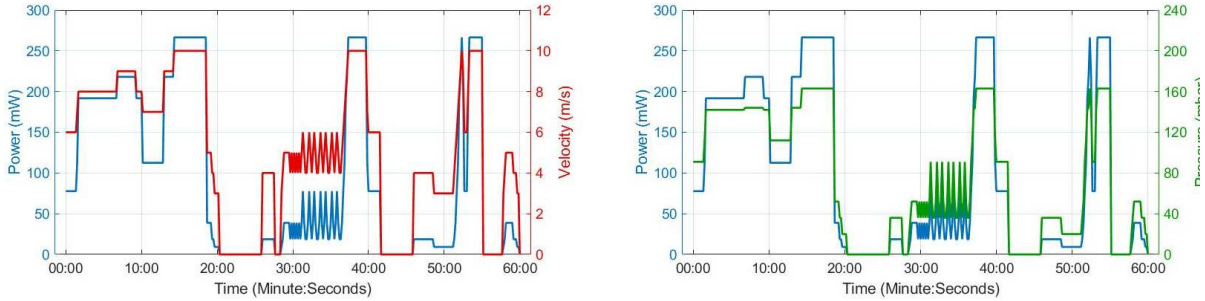

b) Indistinct case 2.

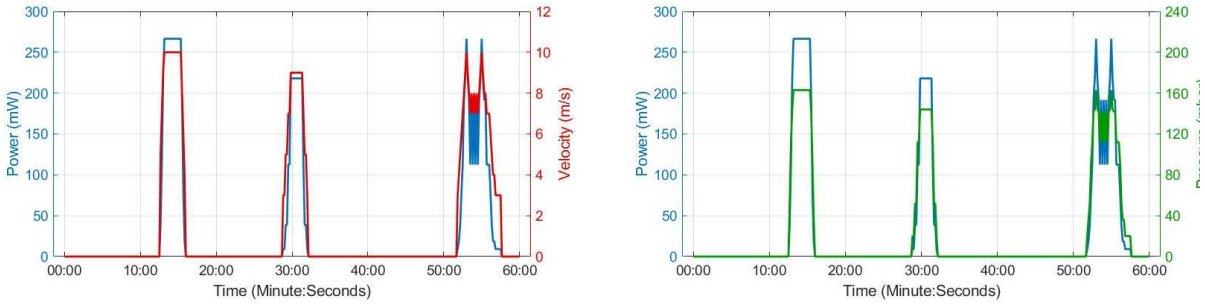

c) Indistinct case 3.

Figure 13-10: Profile for training with 1 m/s step change at wind velocity.

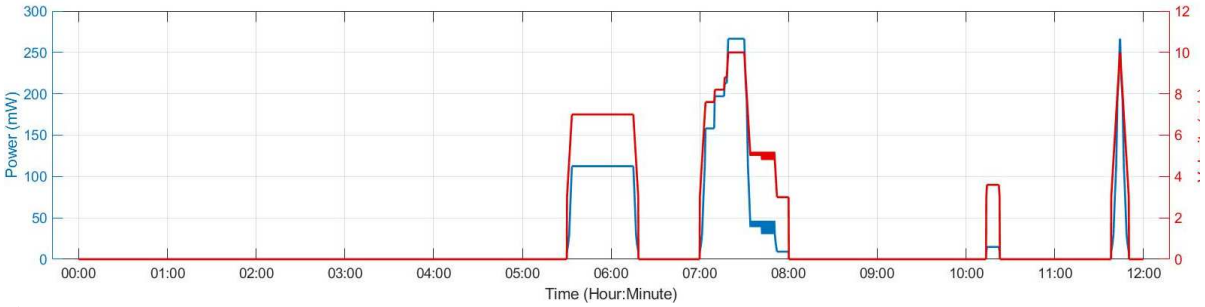

a) Winter case 1.

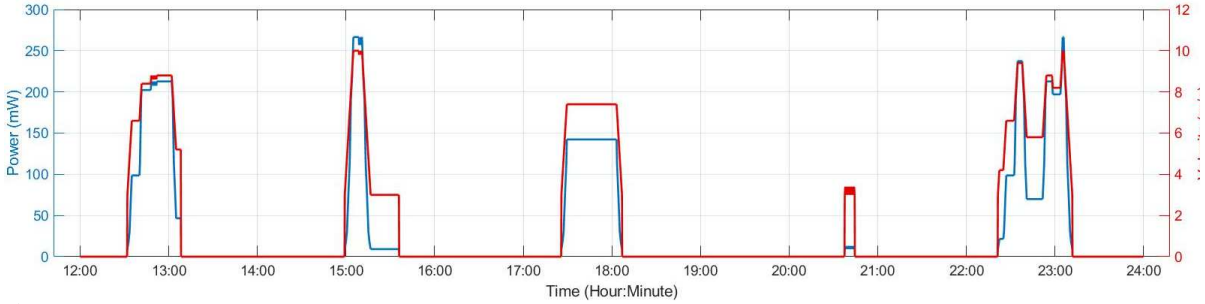

b) Winter case 2.

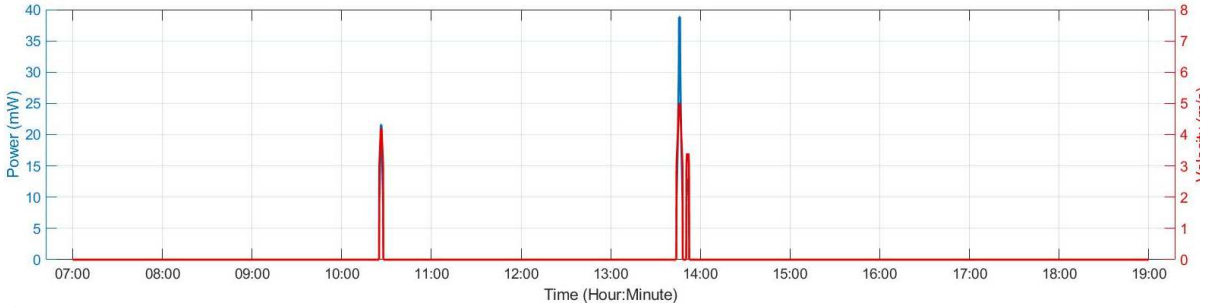

c) Winter case 3.

Figure 13-11: Profile for training with 0.2 m/s step change at wind velocity and in winter condition.

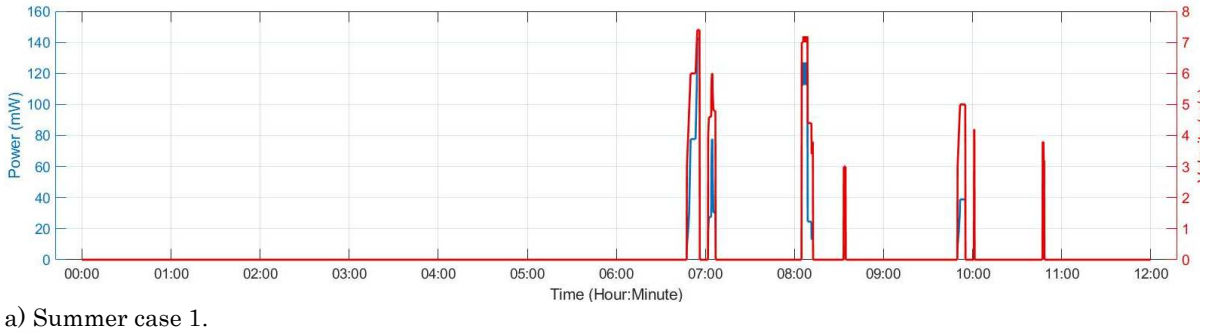

a) Summer case 1.

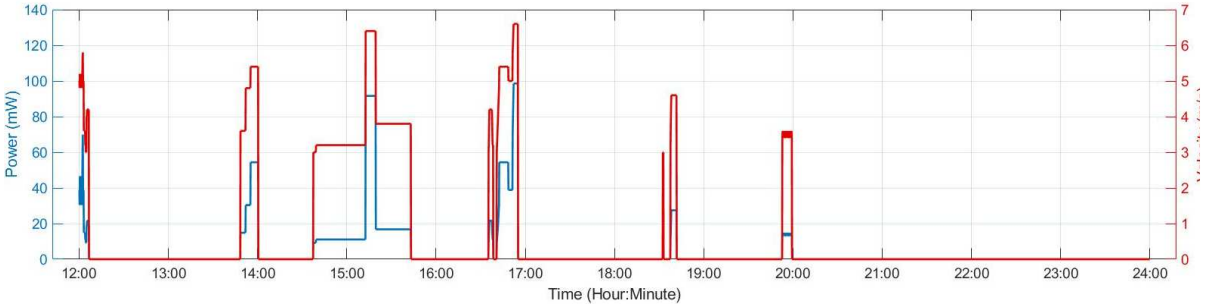

b) Summer case 2.

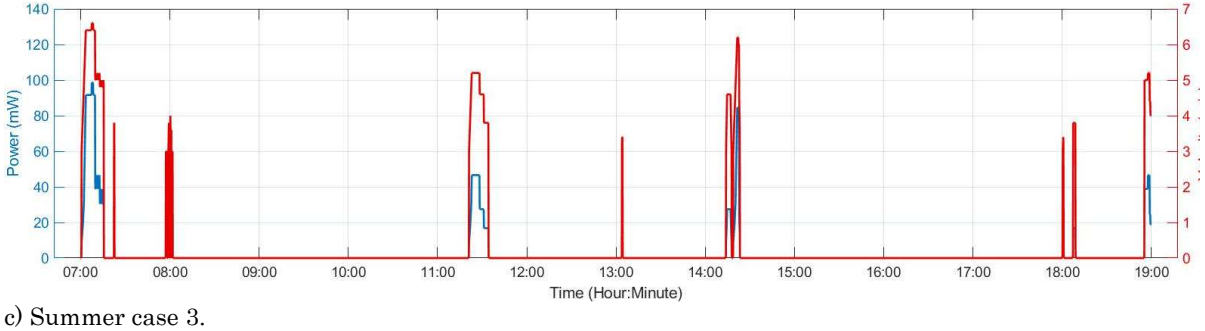

c) Summer case 3.

Figure 13-12: Profile for training with 0.2 m/s step change at wind velocity and in summer condition

13.4.2 Evaluation procedure

The methodology followed for the experimental results ate short periods 1h with constant changes → spcc, winter → w and summer → s.

- The training set includes s2, w3, w2, s3, spcc3, spcc2.
- The test set includes the other profile from each wind condition: s1, w1, spcc1.

For building the training and test time series, their respective profiles were concatenated in random order. In total, the training time series consists of simulated energy production for 50 hours, while the test time series consists of simulated energy production for 25 hours.

The following experiments were conducted as well:

- Clean data: Clean training data and clean test data ("clean data" condition)
- Noisy training data: Noisy training data and clean data ("noisy training data" condition)
- Noisy data: Noisy training data and noisy test data ("noisy data" condition)

As in the previous case, a level of noise has been added. In these experiments, the level of noise used was ±20 mW, again about ±8% of the maximum value in the series.

In all experiments, four algorithms (ETS, LR, SVR, and ARIMA) were investigated in the task of predicting the next value of harvested energy. EWMA was not tested because wind energy daily profile changes quite often in our data.

13.4.3 Experimental results

Table 13-7 provides the MAE of the experiment data set-up for different prediction algorithms used.

Table 13-7: Obtained results for the various experiments and algorithms tested.

	Clean data	Noisy training data	Noisy data
ETS	**0.56**	1.12	6.71
LR	0.72	1.56	7.67
SVR	0.66	10.73	**6.38**
ARIMA	0.57	**0.76**	6.84

The overall profile of results is similar to that obtained in the previous solar energy harvesting case.

As in the previous case, the ETS algorithm obtains the best results with an alpha coefficient of 1.0 when it is executed on the clean dataset. Therefore, since the alpha coefficient is 1.0, it corresponds to the naïve method. Under noise conditions, the best alpha coefficient in the training set was 0.4.

ARIMA on clean data is of the order of simple ETS, this is to say (0,1,1). However, in this case, higher order models obtain better results in the noisy conditions. Still, training on noisy data affects less the results of ARIMA on clean test data than for the other algorithms.

Applied on the clean data set, the obtained ARIMA model is of order (0,1,1). However, in this case, higher order models obtain better results in the noisy conditions. Still, training on noisy data affects less the results of ARIMA on clean test data than for the other algorithms.

Also, both simple LR and SVR obtain, in general, a little higher MAE. And with a noisy training set, SVR performance suffers on the clean test set.

The following figures show the results obtained with the different algorithms on an exception of the time series. Figure13-13 shows the results with clean data condition and medium wind variability:

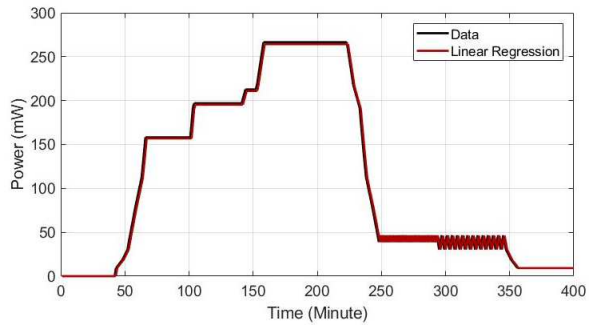

a) Linear regression algorithm vs. data.

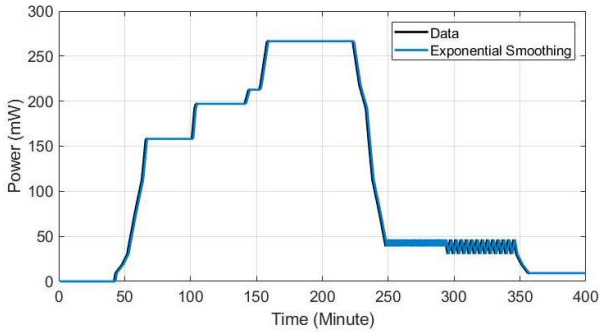

b) Exponential smoothing algorithm vs. data.

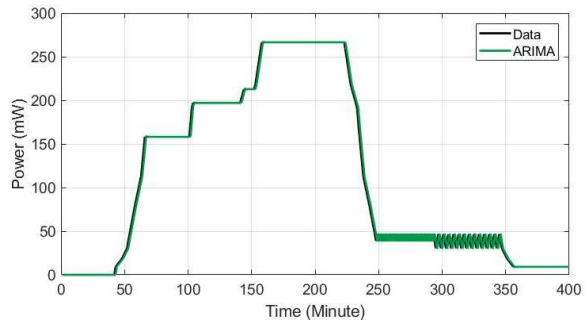

c) Arima algorithm vs. data.

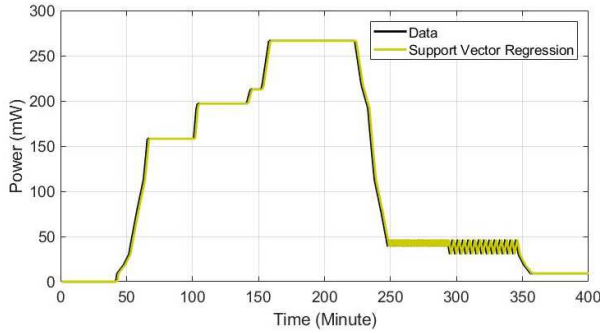

d) Support vector regression algorithm vs. data.

Figure 13-13: Obtained prediction profiles with clean data condition and medium wind variability.

Figure 13-14 shows the results with noisy training data condition and medium wind variability:

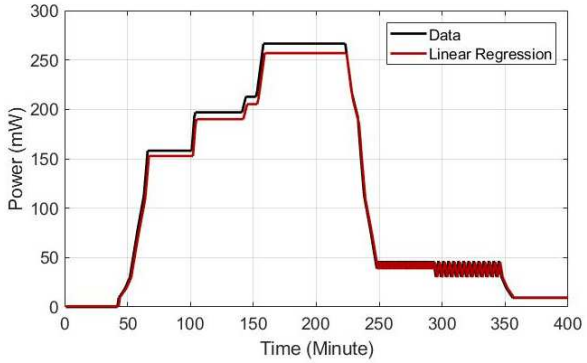

a) Linear regression algorithm vs. data.

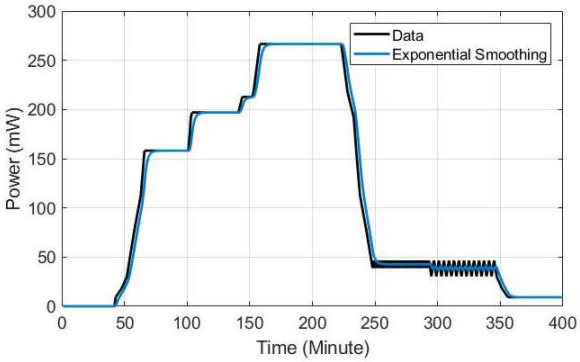

b) Exponential smoothing algorithm vs. data.

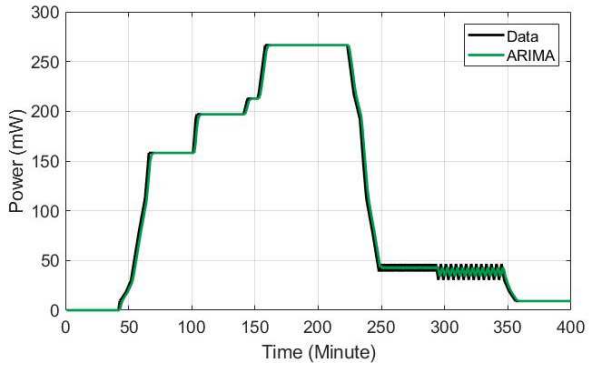

c) Arima algorithm vs. data.

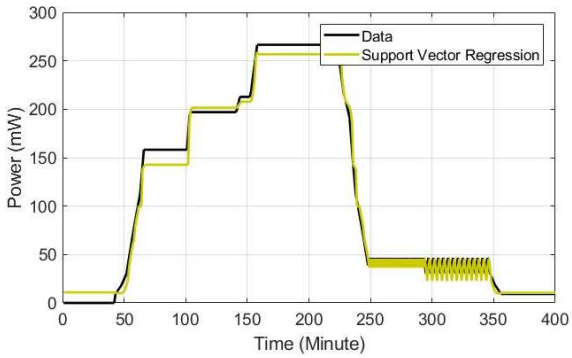

d) Support vector regression algorithm vs. data.

Figure 13-14: Obtained prediction profiles at noisy training condition and medium wind variability.

Figure 13-15 shows results with noisy data condition and medium wind variability:

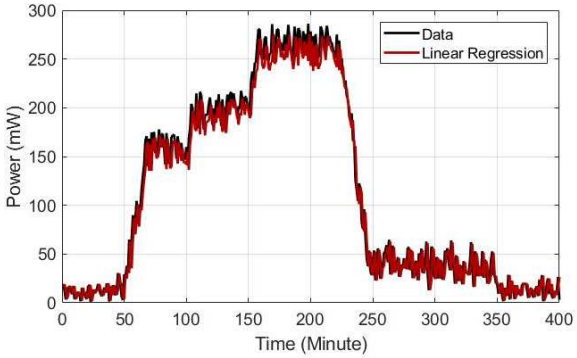

a) Linear regression algorithm vs. data.

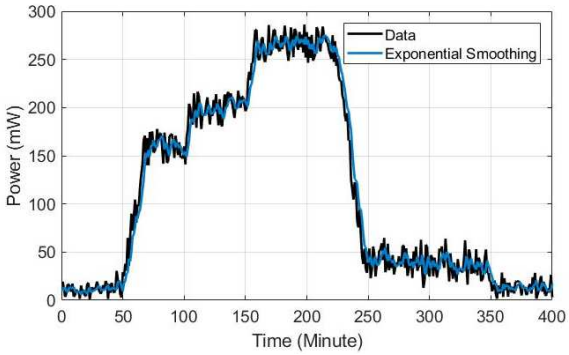

b) Exponential smoothing algorithm vs. data.

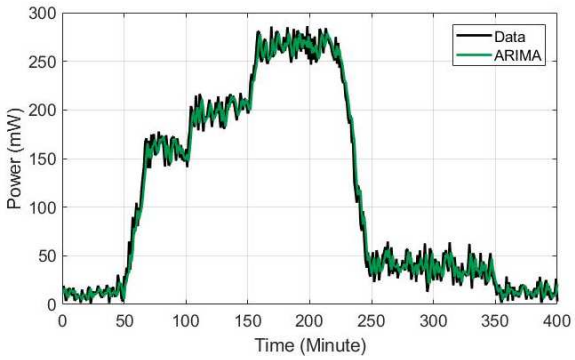

c) Arima algorithm vs. data.

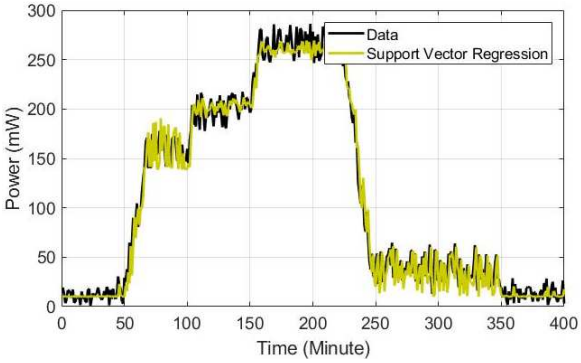

d) Support vector regression algorithm vs. data.

Figure 13-15: Obtained prediction profiles with noisy data condition and medium wind variability.

For the analysis, results on the test data have been further decomposed per wind variability condition {small, medium and large}:

Table 13-8: Obtained results with different algorithms and wind variability.

	Wind variability	Clean data	Noisy training data	Noisy data
ETS	small	0.26	0.51	5.87
	medium	0.49	0.87	6.60
	large	5.10	11.40	17.96
LR	small	0.36	1.03	6.99
	medium	0.68	1.60	7.73
	large	5.66	7.53	15.08
SVR	small	0.35	10.86	5.42
	medium	0.57	10.56	6.65

	large	5.17	11.22	14.62
ARIMA	small	0.27	0.34	6.14
	medium	0.47	0.62	6.82
	large	5.34	7.42	15.45

It can be seen that wind variability has a notable effect on the performance of the models, with large wind variability condition achieving an error about 2 to 10 times higher than for the small and medium wind variability conditions. Overall, the table 13-8 shows a pattern of results among algorithms and clean/noisy conditions similar to that on the general table 13-5 where, besides, results are most similar to those for the medium wind variability condition here.

The following figures illustrate the results obtained for the large wind variability condition. Figure 13-16 shows results with clean data:

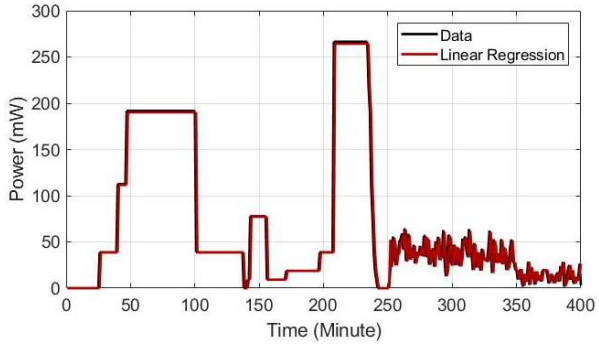

a) Linear regression algorithm vs. data.

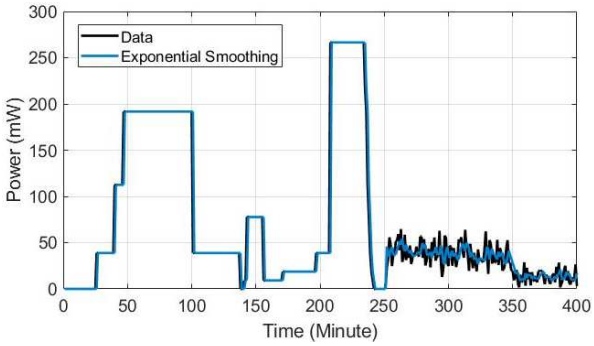

b) Exponential smoothing algorithm vs. data.

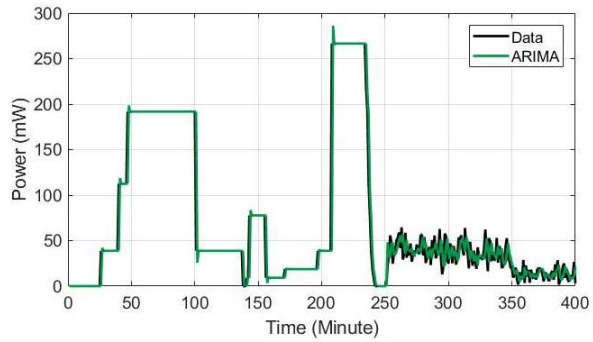

c) Arima algorithm vs. data.

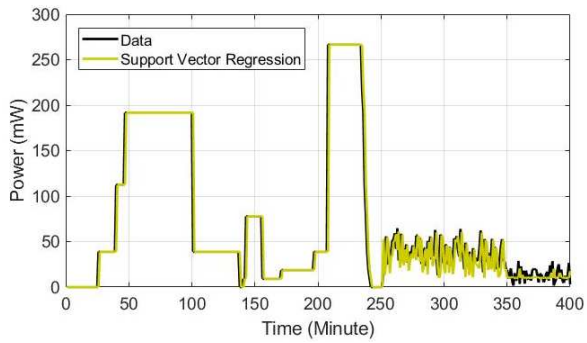

d) Support vector regression algorithm vs. data.

Figure 13-16: Obtained prediction profiles with clean data condition and large wind variability.

Figure 13-17 shows results with noisy training data:

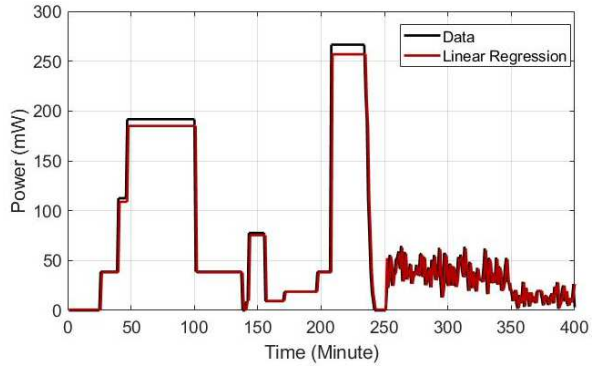

a) Linear regression algorithm vs. data.

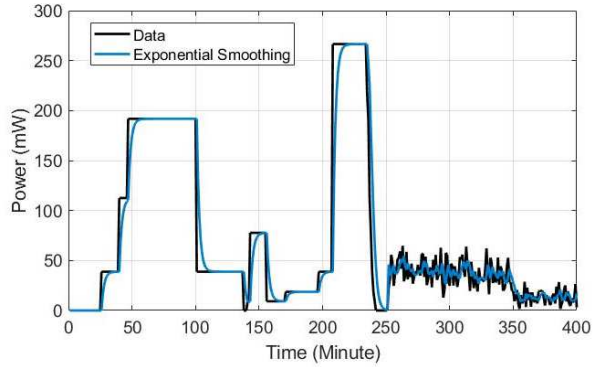

b) Exponential smoothing algorithm vs. data.

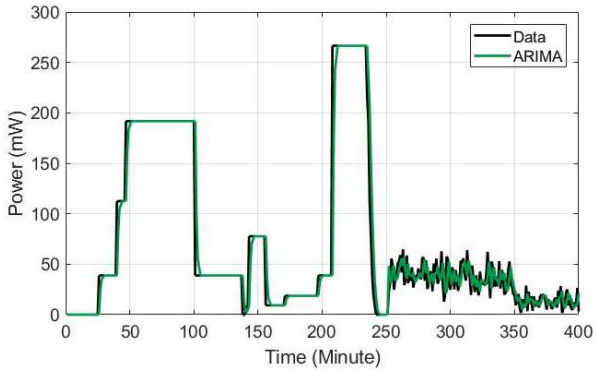

c) Arima algorithm vs. data.

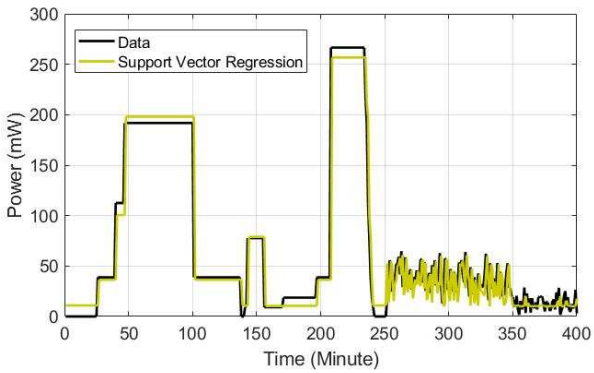

d) Support vector regression algorithm vs. data.

Figure 13-17: Obtained prediction profiles with noisy training data condition and large wind variability.

Figure 13-18 shows results with noisy data:

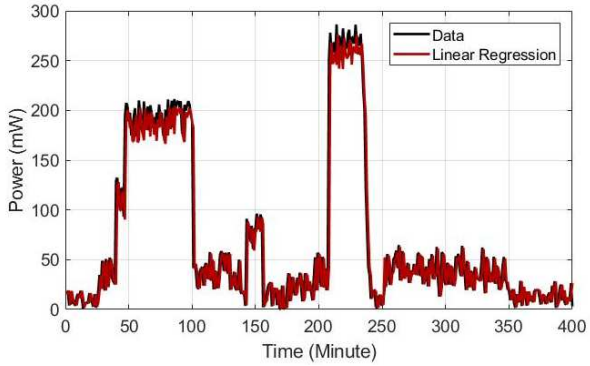

a) Linear regression algorithm vs. data.

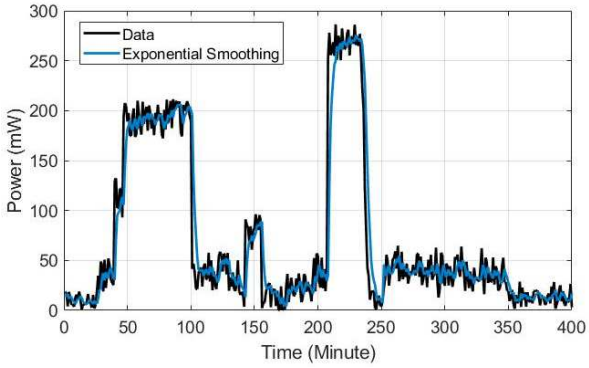

b) Exponential smoothing algorithm vs. data.

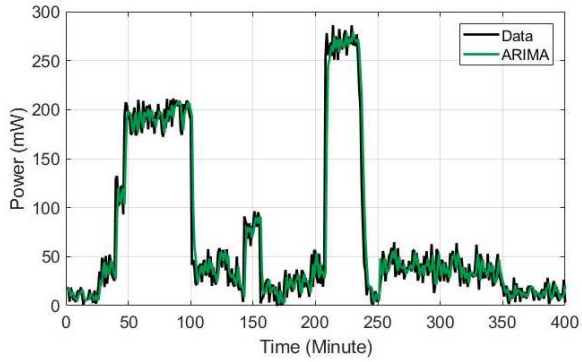

c) Arima algorithm vs. data.

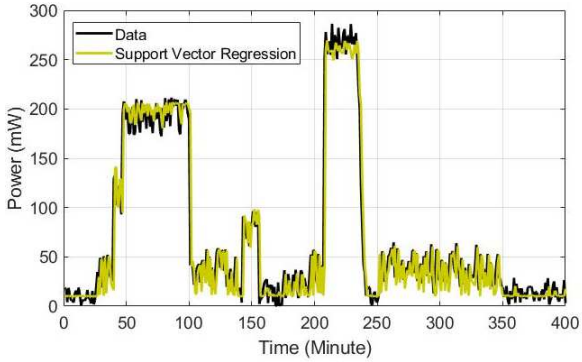

d) Support vector regression algorithm vs. data.

Figure 13-18: Obtained prediction profiles with noisy data condition and large wind variability.

To sum up, following the methodology utilized for solar energy harvesting prediction, the case of wind energy prediction has been researched. Three wind conditions were simulated and tested: small, medium and large wind variability. Several algorithms have been tested and discussed. Considering the results overall and also taking complexity into account, simple LR and ARIMA seem like a reasonable choice of the data tested.

Considering that results are assessed as good, future work ideas may include the investigation of separate models for different degrees of wind variability, and, more generally, the prediction of energy production for longer time horizons.

13.5 Energy management strategy

AI technologies related to advanced data analytics enables the system demand management to mimic the behaviour which appears in complex and continuously varying environments. The concept of the energy management strategy is postulated to advance a future power generation and consumption to maintain a balance between the distributed energy resources and demand requirements in a WSN, warranting the need of a self-adaptive and fully optimized energy management system.

When energy generation and use is being monitored and predicted, energy management strategy can actively manage real-time energy generation and use thanks to the ability of computer algorithms to intelligently learn and predict the quantity of energy harvested and/or consumed. Proactive, real-time data management can expose a wide range of unknown challenges. Real-time data allows identifying potential issues instantaneously, to implement corrective actions to prevent critical shutdowns. And consequently, to manage varying loads before they affected the system.

Data monitoring and prediction allow dynamic management of the energy consumption and permits to build a strategy that manages consumption on a daily, weekly, monthly or annual basis. It could help to identify many system parameters, e.g., peak demand reduction strategies or implement limit customer loads during peak moments.

VI.
Conclusions and future work

The present chapter discuss the most significant results presented in this thesis together with the concluding remarks. It also identifies future works and opened research lines.

This chapter is divided into two sub-chapters:

- Chapter 14 Conclusions
- Chapter 15 Future works and opened research line

Chapter 14 starts with the general conclusions section, remarking the four contributions of this work. Then, each contribution conclusions are presented.

Chapter 15 has two sections. Future works which describes the research activities to be completed in the near future. And the open research lines section enumerates the open research lines for future work.

14. Conclusions

14.1 General conclusions

The purpose of this work has been researching energy harvesting technology in the field of Industrial Internet of Things (IIoT).

The researchers presented demonstrates that energy harvesting systems are a feasible alternative to reduce or eliminate the dependence on batteries of IIoT devices, therefore contributing to the Industry 4.0 paradigm and its deployment.

As result of the above-mentioned research work, the following four contributions have been complete:

1. Development of a new type of harvester, mini-reactor harvester.
2. Proof the idea of a multi-harvester system in a single power management.
3. Modelling of a low power storage device.
4. Utilization of machine learning techniques on low power energy harvesting field to select the harvester correctly, improve supercapacitor models' accuracy and predict input energy to the system.

14.2 Mini-reactor conclusions

The validation of the harvester technology has been proved.

The harvester devised was functional and has a 32 mm diameter, which represents the technology edge.

The test and measurements performed unveiled that the harvester was best described and mathematically characterised as a reactor.

During modelling and test process, theoretical calculus and measured data do not match. Depending on the application field, the harvester behaves differently. If it is placed or installed in open space, the harvester works like a turbine, if it is placed in a pipe as a reactor. The aforementioned behaviour was not expected at the beginning of this work.

Realized tests show that the harvester, acting as a mini-reactor, has an efficiency of 20 % and delivers to the load around 15 to 333 mW of power for air pressure in pipes of 20 to 163 mbar (3 -10 m/s), respectively.

Simulation results show that in an environment with constant flow, an IIoT could be powered, and thus, it could remain measuring or communicating continuously. Nevertheless, the amount of energy available for this type of application is not always constant and could, eventually, become very low, thus reducing the available energy for the application.

Realized tests show that the harvester acting as a mini-turbine has an efficiency of 0.35 % and deliver to the load around 0.037 to 0.14 mW of power for air velocity in open spaces of 3-4 m/s, respectively.

Unless the aforementioned operation model is not efficient in the open air, it could be employed as main or power back-up for ultra-low power electronic system.

The harvester could work as two types of generator, monophasic or three-phase.

The main objective to develop a monophasic generator has been to study the viability of the system and with a triphasic generator achieve the results of how much energy could get.

14.3 Double low power management conclusions

This research introduces a structural and electrical model of a solar cell and a new electro-mechanical model of mini-reactor.

To analyse the feasibility of dual power management in harvester systems, two reference types of harvests have been used, a DC (solar panel) and an AC one, the mini-reactor.

The test results performed show that the DC system based on solar cell provides more energy for extended periods, due to the periodic availability of the light. On the other hand, the mini-reactor and its AC converter deliver more energy to the load but for shorter periods.

Harvesters complete modelling (physical/mechanical + electrical) gives higher accuracy to simulated systems if compared with systems which only use voltage, current or signals generators to implement the harvester model as harvester representation.

The process to obtain data results to design and scale the power and efficiency of the AC/DC and DC/DC converters required modelling both harvesters and their power supply.

Harvesters representation with generation sources only provides the electrical value of the complete system. However, full modelling of the harvesters, which includes mechanical or physical effects to the whole system, gave more accuracy and precision to the simulation results.

A multi-harvester system will give more energy, lifetime, functionalities and would extend the range of applications fields.

The research realized provides evidence of the feasibility to devise a future multi-harvester system with single power management. Table 14-1 shows power input and output efficiencies of DC/DC and AC/DC converters.

Table 14-1: Differences between DC/DC and AC/DC converters

Parameter	DC/DC	AC/DC
Converter efficiency average	91-93 %	45-52 %
Control type	MPPT	PWM
Output power range	21.24-285.31 mW	8.95-187.8 mW

DC/DC converter works in boost mode, obtaining an efficiency around the 92 %.

The DC/DC converter is composed of a standard boost topology. This DC input it is selected for its reduced complexity and shared with AC system. Helping in the validation of the double low power management and low power storage hypothesis.

Selected architecture for AC/DC converter is Split NP, obtaining an efficiency between 45 and 52 % when harvester gives 15-333 mW at two extreme ambient conditions.

In the simulations results at sections 8.2 and 9.2, when the harvester under test gives 15 mW and 333 mW, the power storage is 8.95 mW and 187.8 mW respectively.

Side-diode and Split N have less efficiency and output power than selected Split NP. Diode bridge and voltage doubler do not have the required voltage level at the output point for low wind flow conditions.

Table 14-2: AC/DC converters simulation results.

	Wind velocity 3 m/s					Wind velocity 10 m/s				
Architec.	V_{out} (V)	P_{out} (mW)	$\eta_{generator}$ (%)	$\eta_{converter}$ (%)	$\eta_{general}$ (%)	V_{out} (V)	P_{out} (mW)	$\eta_{generator}$ (%)	$\eta_{converter}$ (%)	$\eta_{general}$ (%)
Harvester	0.54	15.25	24.37	100	24.37	2.44	332.9	19.55	100	19.55
D-bridge	0.57	3.26	12.35	35.02	4.32	3.1	93.7	9.72	42.64	4.15
Volt. dou.	0.51	2.66	7.61	41.84	3.18	3.01	69.8	6.38	53.68	3.42
Side-diod.	3.08	6.32	13.6	74.32	10.11	4.19	176.0	13.01	80.04	10.46
Split N	3.20	7.88	15.37	75	11.53	4.26	181.7	13.97	76.20	10.65
Split NP	3.41	8.95	17.61	81.52	14.36	4.33	187.8	14.8	74.33	11.00

Output efficiency and power level of AC system have a direct dependence on the impedance matching between generator and rest of the system (converter + load).

Impedance matching between generator and converter is required to achieve efficient operation of the AC system.

Unless there are control architectures more adequate (suitable) for high power AC/DC converters, the selected control type provides good results in low power operating conditions.

Usually, these types of converters are employed in big wind turbines, but they apply a different type of control [255]. However, the small size of the harvester makes the use of encoders impossible (section 9-2).

Standard converters control has not been applied due to next two reasons:

- Amount of energy required to power measuring elements.
- Size of measuring elements.

Nevertheless, the control at AC/DC converter has the following issue:

- The control inserts harmonics, thus, decreasing system efficiency. Ideally, voltage and current must be of the same type, e.g., both sinusoidal. In this case, the voltage signal is sinusoidal and the current triangular (trapezoidal). These harmonics occurs only in the aforementioned cases.

14.4 Supercapacitor modelling with mathematical and machine learning techniques

The electro-mathematical model and machine-learning algorithm developed in the present work is devoted to low power Energy Harvesting Wireless Sensor Networks applications.

It constitutes an improvement of state of the art in supercapacitor electro-mathematical models for low power applications because uses more characteristic parameters.

The simulation and tests results show that machine learning model provides higher accuracy than the state of the art models and the electro-mathematical model.

The improvement of the electro-mechanical model with machine-learning algorithms needs less experimental data than electrochemical models to achieve the same accuracy. Besides, the machine-learning algorithm does not require any electrochemical parameter to implement the model, and the aforementioned parameters, if compared with the electromechanical ones, are not hard to obtain empirically.

Table 14-3: Comparison between this work and another model.

Model Type	Ref. Numb.	Statistical Error	Ref. Result	This Work Result
Electro-mathematical	[12]	Deviation	3–7%	2.35%
Electro-mathematical	[34]	Deviation	2.56%	2.35%
Electro-mathematical	[35]	RMSE	0.65	0.071–0.204
M.L. → ANN	[23]	MSE	0.089	0.005–0.017
M.L. → Kalman Filtering	[36]	MAE	0.50	0.047–0.090
		RMSE	0.63	0.052–0.099

The experimental tests show that the algorithms presented are able to model all types of supercapacitors for low power applications and any conditions.

Unless the model of machine learning increases the accuracy of the electro-mathematical model, it is less generic as it depends on predefined test conditions and it requires more processing resources, i.e., time.

14.5 Data mining and machine learning techniques for energy harvesting systems conclusions

Data mining analysis, machine learning, and predictive techniques have been validated or proved feasible for their application in energy harvesting systems.

There were defined the following three different ways to use the aforementioned machine learning techniques.:

1. Data analysis techniques for correct harvester selection of the same family.
2. Machine learning techniques, such as artificial neuronal networks and M5P algorithms to improve mathematical models for low power storage devices (conclusions at section 14.4).
3. Predictive power management strategy with data analysis and machine learning algorithms to study the availability of improvement in the management of the harvested energy.

This work demonstrates that data mining techniques are adequate to be applied in energy harvesting systems. The selection of the optimal solar cell for this application work was made with these techniques.

The insertion of data mining techniques to make a correct selection of commercial harvesters depending on the use case. Data mining uses data-sheet parameters or/and tests measurements data.

The present work evaluates if predictive methods and algorithms, borrowed from the field of artificial intelligence and advanced analytics, constitute the solution to overcome the technical challenges of the power management.

The recent research efforts in new technologies and techniques show that the harvesting of energy is a viable technology to improve the energy footprint of electronic devices. However, environmental energy systems such as solar cells and wind flow pipe systems depend on fluctuations in the amount of energy received, and in environmental and external factors. Thus, the harvested energy is neither constant nor continuous.

The developed work demonstrates that is possible to predict the availability of energy and the power consumption requirements. Making possible that the power management system could take decisions in critical situations and address tasks concerning how to use and distribute available energy in a network of IIoT systems.

The results obtained in this work shows that not all the algorithms tested are adequate for IIoT systems. Thus, further research is required in algorithms, harvesters, and energy harvesting applications.

15. Future works and opened research lines

15.1 Future works

Future works proposed are focused on test other AC/DC converter architecture and the implementation of research, developed ideas and techniques in a prototype to corroborate this work. Thus, it remains the following three tasks to be completed:

1. PCB design, manufacture and implementation
2. Control implementation
3. Extend the development and application of predictive algorithms
4. Extend mini-reactor operation to liquid fluids

15.1.1 PCB development

This task will be based on the design and manufacture of the PCB to make flexible the implementation of converters control and predictive algorithms in a real situation. The PCB general requirements are those of an energy harvesting system, such as low size, short traces (to avoid losses) and low power devices.

Figure 15-1 shows future PCB block diagram. It must include the minimum required devices to be used in the PCB, due to consumption of each any extra device.

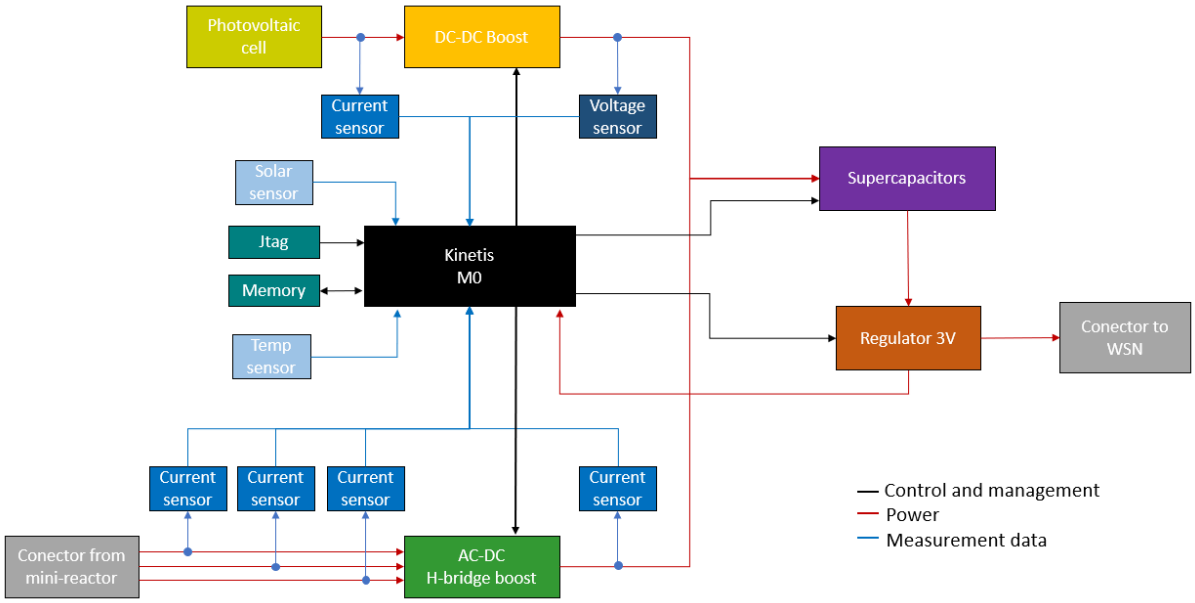

Figure 15-1: Future PCB block diagram.

Converters require voltage/current sensors to make the control operation possible. DC/DC boost has a current sensor in the entrance and a voltage sensor in the output to implement control designed in section 8.3. AC/DC converter requires three current sensors for each input phase and another at the output side enable the control process described in section 9.4.

Storage element selected is a supercapacitor. However, the consumption profiles of the load, the harvested energy average and peaks should be analysed to determine the needed capacitance by the system.

Then, a regulator or step-down must be installed to drive the stored energy at the supercapacitor to the microcontroller and the load.

The selected microcontroller, a Kinetics M0, is a low power consumption embedded system, which would be used to implement converters control and smart energy management. An external memory is required to act as a database for predictive algorithms, e.g., light and temperature sensors to provide information to DC system predictive algorithms and are stored in the database. However, AC system will not have any additional sensor. The available energy, in this case, would be calculated with a mathematical algorithm which will converse input signals frequency to air flow quantity.

Finally, the mini-reactor would supply a consumption load, e.g., WSN shown in figure 15-2.

Figure 15-2: Wireless sensor network device which will be powered by future energy harvester system developed in this work.

15.1.2 Controls implementation in the microcontroller

As has been exposed in state of the art section (chapter 2), the increasing market for low power microcontrollers will help in the execution of this task. Furthermore, the future improvements in this field will reduce more the consumption of these elements. For this reason, the control of the AC/DC converter, as well as the control of the DC/DC converter, would be implemented in the microcontroller firmware. Is expected that these devices will give more capabilities than current control architectures.

Nevertheless, measure converters input and output points will be necessary by the microcontroller to complete the control tasks. Sensors will measure these current/voltage levels. Then, measured values will be processed by the microcontroller, and the correct PWM will be produced to achieve efficient operation of the converter in each operation case.

The main challenge are to implement complex algorithms of control with low energy consumption and the conversion of code Simulink to C language.

15.1.3 Extend the application of predictive algorithms

A new method of energy management will be developed using predictive algorithms. When these algorithms are applied at the input/output of the supercapacitor and on the consumption load, the available energy management could be improved. E.g., decide between power the sensor network or maintain essential operating functions.

This activity is the continuation of AI algorithms applications for smart power management. The algorithms must have capabilities of duty cycle smart management of WSN nodes, as well as the energy stored. In figure 15-3, the future application of AI algorithms in the system is presented.

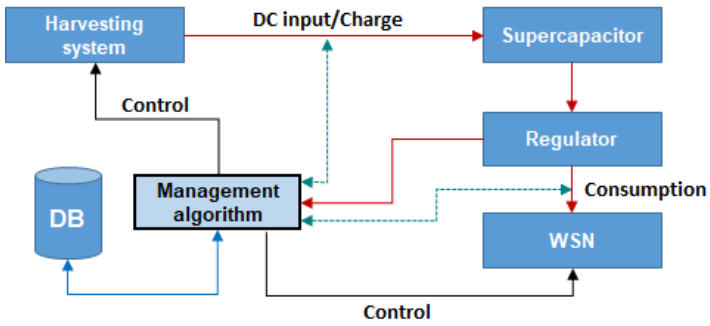

Figure 15-3: Block diagram of a future application of predictive algorithms in the system.

The task should be focused on:

- Define the information required as input for the algorithms
- Determine the information that the algorithms should deliver
- Data clean: misses, anomalous values

After the data preparation and pre-processing, the training and test of the algorithms should be started. In this process, different types of algorithms would be employed, tested and compared regarding accuracy for selecting the best option as the same way as realized through chapter 13. It is possible that different algorithms would be better than the one used.

Finally, implementation of developed algorithms in a low power embedded system should be realized. This task would consist of programming and test the algorithm(s) in a low power microcontroller. Then, implemented work operation may be tested in different use cases, for example, in different environments, ambient conditions, and load consumptions.

15.1.4 Mini-reactor application and extend to fluid ambient fields

Water quality monitoring in cities/towns/rivers is a goal due to the challenges of constantly verifying the water quality which is used by humans/animals. For it, zero power WSN will be necessary, and energy harvesting is identified as a viable solution. Specifically, an autonomous zero-power wireless sensor network device to meter water resources.

The aim will be to design, manufacture and validate an improved version of the mini-reactor for water flow environments, devoted to IoT applications in the water quality monitoring.

The operation will be based on next steps: First, the mini-reactor harvest energy from the water flows from the environment. Then, power management with the same operation described in this work, but with different levels of energy (probably with more power since the water flow contains more energy than the flow of gas). Finally, storage the harvested energy at a supercapacitor.

With this operation, the new mini-reactor will give to the wireless sensor network the capability to acquire, monitoring, analyse the water and communicate their data through a low power radio their measured values. Moreover, even, work cooperatively with other zero power sensors.

Thus, the main challenge will be the development of the harvesting system. Furthermore, obtaining maximum efficiency in conversion from hydraulic energy to electrical energy. Moreover, studying the risk of mechanics blocking by particles in the liquid.

The tasks identified to be performed are:

1. Mechanical design, according to the field of application, to obtain the maximum possible hydraulic energy and guarantee the correct operation of the system always.
2. Electromagnetic simulations to study the transmission of energy between magnets and harvester's coils. Possible changes to the current design should be considered for improvement and adaptation to the environment.
3. Manufacture, verification, and validation of the new mini-reactor design in water flow environments.

15.2 Opened research lines

Without further research into energy harvesting systems, it will not be possible to improve their global efficiency, increase the amount of energy harvested, decrease storage losses, give more functionalities and/or prolong their lifetime.

Future research into energy harvesting technology should be focused on improving actual harvesters or creating new ones, improving multi-source power managers/devices

and introducing artificial intelligence techniques in low power systems as in the same way of high power systems.

Two research lines are left open in this work for future researchers:

1. Development of a single power manager with n inputs. Thus, a "universal" system.
2. Implementation of predictive algorithms in energy harvesting systems

15.2.1 Multi-harvester universal power manager at energy harvesting systems

Nowadays, a significant number of Industrial Internet of Things (IIoT) are being deployed in several application areas of Industry 4.0. As has been remarked through this work, nowadays these applications are powered by primary or secondary batteries. The high cost of replacement when they are empty or to recharge the batteries, even when they are installed in difficult access locations, is a problem which must be solved.

Energy harvesting is becoming a real alternative. Nevertheless, it has, in most of the cases, depends of a single energy source, which cannot always guarantee or supply enough energy to maintain necessary functionalities.

Multisource energy harvesting will provide more energy from the environment, granting more functionalities to the powered application, extending its useful life or unlimiting operation times of measurement, communication, etc.

Figure 15-4 shows the block diagram of a multi-harvester system with universal integrated power management.

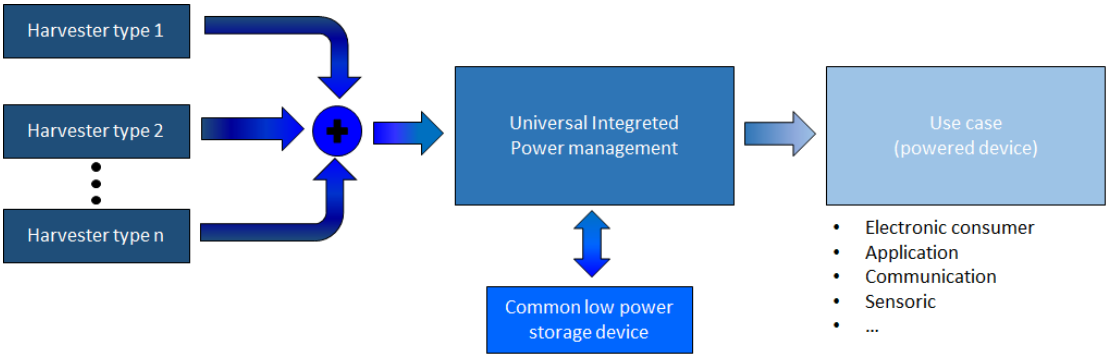

Figure 15-4: Multi-harvester block diagram with a universal integrated power management energy harvesting system.

In addition, increasing the energy available, smaller or fewer storage elements will be necessary, decreasing the use of batteries. So consequently, being more environmentally friendly and helping the circular economy concept.

Following this line of research, this thesis has used two harvesters to demonstrate that is possible use more than one harvester in a unique power manager. Moreover, the implementation should not be limited by the number of harvesters, but the application environment and the energy sources available in the field.

15.2.2 Machine learning and data mining in energy harvesting systems

The use of data mining could help in the implementation of big data techniques in future energy harvesting systems, providing more information for managing the small

amount of energy available. Consequently, helping to make the best decisions in each application case.

The machine learning application is substantiated on arbitrary phenomenon caused by the energetic environment, ambient conditions or wireless communication canal quality variations. These behaviours produce an increase in the consumption, needing an extra quantity of energy, contributing a possible system failure. Due to the complexity to model their environment, machine learning seems to be a more appropriate solution to make an efficient decision on tasks execution.

Consequently, the lifetime of IIoT will be theoretically unlimited. In this context where power is limited, it is the mean power consumption which drives the correct behaviour of the application.

VII. References

[1] S. P. Beeby, M. J. Tudor, and N. M. White, “Energy harvesting vibration sources for microsystems applications,” Meas. Sci. Technol., vol. 17, no. 12, 2006.
[2] V. Roblek, M. Meško, and A. Krapež, “A Complex View of Industry 4.0,” SAGE Open, vol. 6, no. 2, p. 215824401665398, 2016.
[3] K. Zhou, T. Liu, and L. Zhou, “Industry 4.0: Towards future industrial opportunities and challenges,” 2015 12th Int. Conf. Fuzzy Syst. Knowl. Discov. FSKD 2015, pp. 2147–2152, 2016.
[4] J. Barbosa, P. Leitão, D. Trentesaux, A. W. Colombo, and S. Karnouskos, “Cross Benefits from Cyber-Physical Systems and Intelligent Products for Future Smart Industries Cross Benefits from Cyber-Physical Systems and Intelligent Products for Future Smart Industries,” Ieee, no. July, pp. 504–509, 2016.
[5] A. Morkevicius, L. Bisikirskiene, and G. Bleakley, “Using a Systems of Systems modeling approach for developing Industrial Internet of Things applications.”
[6] F. Shrouf, J. Ordieres, and G. Miragliotta, “Smart factories in Industry 4.0: A review of the concept and of energy management approached in production based on the Internet of Things paradigm,” IEEE Int. Conf. Ind. Eng. Eng. Manag., vol. 2015-January, pp. 697–701, 2014.
[7] P. Lade, R. Ghosh, and S. Srinivasan, “Manufacturing analytics and industrial Internet of Things,” IEEE Intell. Syst., vol. 32, no. 3, pp. 74–79, 2017.
[8] X. Li, D. Li, J. Wan, A. V. Vasilakos, C. F. Lai, and S. Wang, “A review of industrial wireless networks in the context of Industry 4.0,” Wirel. Networks, vol. 23, no. 1, pp. 23–41, 2017.
[9] M. Rouse and I. Wigmore, “Internet of Things (IoT),” http://internetofthingsagenda.techtarget.com/definition/Internet-of-Things-IoT, no. step 4, pp. 1–8, 2016.
[10] “The Internet of Things Smart solutions to global problems,” Washington Post, pp. 3–4, 2017.
[11] A. Zanella, N. Bui, a Castellani, L. Vangelista, and M. Zorzi, “Internet of Things for Smart Cities,” IEEE Internet Things J., vol. 1, no. 1, pp. 22–32, 2014.
[12] IoF2020, Introducing Internet of Food & Farm 2020, European project part of Horizon 2020 Industrial Leadership, 2017-2020.
[13] S. Karnouskos, “The cooperative internet of things enabled smart grid,” Proc. 14th IEEE Int. …, pp. 1–6, 2010.
[14] J. Wan, S. Tang, Q. Hua, D. Li, C. Liu, and J. Lloret, “Context-Aware Cloud Robotics for Material Handling in Cognitive Industrial Internet of Things,” IEEE Internet Things J., vol. 4662, no. c, pp. 1–1, 2017.
[15] B. Lydon, “Industry 4.0 for Process Automation – Process Sensors 4.0 Roadmap,” Automation.com, 2016.
[16] C. Paper, P. Priller, A. V. L. List, A. Berger, M. Gmbh, and M. Gmbh, “Sustainable Energy Harvesting for Robust Wireless Sensor Networks in Industrial Applications,” IEEE Instrum. Meas. Soc., no. APRIL 2016.D. Tsai, H. Wu, and C. Wei, “A Low-Power-Consumption Boost Converter with Maximum Power Tracking Algorithm for Indoor Photovoltaic Energy Harvesting.”
[17] S. F. Ul Haq Gilani, R. Ibrahim, and M. H. M. Khir, “A case study for industrial centrifugal pump as a vibration source for macro-scale electromagnetic energy harvesting,” Int. Conf. Intell. Adv. Syst. ICIAS 2016, pp. 2–7, 2017.
[18] L. Columbus, “Roundup Of Internet Of Things Forecasts And Market Estimates, 2016,” Forbes, 2016.
[19] J. Greenough, “How the ‘Internet of Things’ will impact consumers, businesses, and governments in 2016 and beyond,” Business Insider, 2016.
[20] “The Internet of Things, Smart solutions to global problem,” The Washington Post, 2016.
[21] C. Perera, C. H. Liu, S. Jayawardena, and M. Chen, “A Survey on Internet of Things from Industrial Market Perspective,” IEEE Access, vol. 2, pp. 1660–1679, 2015.
[22] B. R. Haverkort and A. Zimmermann, “Smart Industry: How ICT Will Change the Game!”, IEEE Internet Comput., vol. 21, no. 1, pp. 8–10, 2017.

[23] Chiarotti, Ugo; Moroli, Valerio; Menchetti, Fernando; Piancaldini, Roberto; Bianco, Loris; Viotto, Alberto; Baracchini, Giulia; Gaspardo, Daniele; Nazzi, Fabio; Curti, Maurizio; Gabriele, Massimiliano, "Development of a Small Thermoelectric Generators Prototype for Energy Harvesting from Low Temperature Waste Heat at Industrial Plant" Journal of Nanoscience and Nanotechnology, Volume 17, Number 3, March 2017, pp. 1586-159.
[24] P. Amad, A. Shah, M. Habib, and T. Sajjad, "Future Intelligent Vehicular Technologies," vol. 185, pp. 182–188, 2017.
[25] J. Gubbi, R. Buyya, S. Marusic, and M. Palaniswami, "Internet of Things (IoT): A vision, architectural elements, and future directions," Futur. Gener. Comput. Syst., vol. 29, no. 7, pp. 1645–1660, 2013.
[26] L. Ruiz, J. M. Nogueira, and A. A. F. Loureiro, "MANNA: a management architecture for wireless sensor networks," IEEE Commun. Mag., vol. 41, no. 2, pp. 116–125, 2003.
[27] M. Aazam, I. Khan, A. A. Alsaffar, and E. N. Huh, "Cloud of Things: Integrating Internet of Things and cloud computing and the issues involved," Proc. 2014 11th Int. Bhurban Conf. Appl. Sci. Technol. IBCAST 2014, pp. 414–419, 2014.
[28] E. Morin, M. Maman, R. Guizzetti, and A. Duda, "Comparison of the Device Lifetime in Wireless Networks for the Internet of Things," IEEE Access, vol. 5, no. c, pp. 7097–7114, 2017.
[29] K. E. Nolan, W. Guibene, and M. Y. Kelly, "An evaluation of low power wide area network technologies for the Internet of Things," 2016 Int. Wirel. Commun. Mob. Comput. Conf., pp. 439–444, 2016.
[30] R. Sanchez-Iborra and M. D. Cano, "State of the art in LP-WAN solutions for industrial IoT services," Sensors (Switzerland), vol. 16, no. 5, 2016.
[31] Texas Instruments, "MSP Low-Power," 2015.
[32] NXP, "Freescale Energy- Efficient Solutions: Kinetis L Series MCUs."
[33] Silicon Labs, "8-bit ultra-low power microcontrollers."
[34] A. Gomez, A. Bartolini, D. Rossi, B. Can Kara, H. Fatemi, J. P. de Gyvez, and L. Benini, "Increasing the Energy Efficiency of Microcontroller Platforms with Low-Design Margin Co-Processors," Microprocess. Microsyst., vol. 53, pp. 213–228, 2017.
[35] J. Tollefson, "Understanding & Managing the Plethora of MCU Low-Power Modes," 2017.
[36] CNBC, "China will help drive 33% increase in global copper prices by 2020," 2017.
[37] https://www.lme.com/Metals/Non-ferrous/Copper#tabIndex=2
[38] P. Woias, "Energy Harvesting, Courses in Microtec and Nanotec, fsrm.", Zurich, 2016.
[39] C. Walker, "Surpassing The Limits Of Battery Technology," Chemical Manufacturing Excellence, Elsevier, 2016.
[40] The Guardian, "The rise of electric cars could leave us with a big battery waste problem," pp. 3–5, 2017.
[41] M. Zorzi, A. Gluhak, S. Lange, and A. Bassi, "From today's INTRAnet of things to a future INTERnet of things: A wireless- and mobility-related view," IEEE Wirel. Commun., vol. 17, no. 6, pp. 44–51, 2010.
[42] A. Jabil, "Energy Harvesting: How We'll Build the Internet of Perpetual Things."
[43] V. C. Gungor and G. P. Hancke, "Industrial Wireless Sensor Networks: Challenges, Design Principles, and Technical Approaches," IEEE Trans. Ind. Electron., vol. 56, no. 10, pp. 4258–4265, 2009.
[44] R. Vullers, R. Schaijk, H. Visser, J. Penders, and C. Hoof, "Energy harvesting for autonomous wireless sensor networks," IEEE Solid-State Circuits Mag., vol. 2, no. 2, pp. 29–38, 2010.
[45] A. S. Weddell, N. J. Grabham, N. R. Harris, N. M. White, and E. M. Force, "Energy-Harvesting Sensor Nodes," p. 17, 2007.
[46] Enocean, "Solar cells ECS 300 and ECS 310," p. 310, 2010.
[47] P. N. Key, "Series: Cp85 | Description: Peltier Module Cp85," pp. 1–11, 2016.
[48] P. E. Harvesters, "Piezoelectric Energy Harvesters," pp. 1–24, 2010.

[49] E. Bouendeu, A. Greiner, P. J. Smith, and J. G. Korvink, “An Efficient Low Cost Electromagnetic Vibration Harvester of Harvesters” pp. 320–323, 2009.
[50] E. Sordiashie, “Electromagnetic Harvesting to Power Energy Management Sensors,” 2012.
[51] TDK, “WRM483245-15F5-5V-G,” 2013.
[52] S. Boisseau, G. Despesse, and B. A. Seddik, “Electrostatic Conversion for Vibration Energy Harvesting,” pp. 1–39, 2012.
[53] D. a Howey, a Bansal, and a S. Holmes, “Design and performance of a centimetre-scale shrouded wind turbine for energy harvesting,” Smart Mater. Struct., vol. 20, no. 8, p. 085021, Aug. 2011.
[54] J. a. R. Azevedo and F. E. S. Santos, “Energy harvesting from wind and water for autonomous wireless sensor nodes,” IET Circuits, Devices Syst., vol. 6, no. 6, pp. 413–420, Nov. 2012.
[55] M. Kroener and P. Woias, “A Standalone Pyroelectric Harvester for Thermal Energy Laboratory” for Design of Microsystems, Department of Microsystems Engineering – IMTEK, Components, no. 1, pp. 5–8, 2012.
[56] F. U. Khan and I. Izhar, “Acoustic-Based Electrodynamic Energy Harvester for Wireless Sensor Nodes Application,” Int. J. Mater. Sci. Eng., vol. 1, no. 2, pp. 72–78, 2013.
[57] Enocean, “Solar cells ECS 300 and ECS 310,” p. 310, 2010.
[58] P. N. Key, “Series: Cp85 | Description: Peltier Module Cp85,” pp. 1–11, 2016.
[59] P. E. Harvesters, “Piezoelectric Energy Harvesters,” pp. 1–24, 2010.
[60] TDK, “WRM483245-15F5-5V-G,” 2013.
[61] M. Beidaghi and Y. Gogotsi, “Capacitive energy storage in micro-scale devices: recent advances in design and fabrication of micro-supercapacitors,” Energy Environ. Sci., vol. 7, no. 3, p. 867, 2014.
[62] L. Grande, V. T. Chundi, D. Wei, C. Bower, P. Andrew, and T. Ryhänen, “Graphene for energy harvesting/storage devices and printed electronics,” Particuology, vol. 10, no. 1, pp. 1–8, Feb. 2012.
[63] A. Othman, “Energy storage system options in Intelligent Wireless Sensor Network,” 2017 Int. Conf. Mil. Technol., pp. 772–778, 2017.
[64] B. Charger et al., “Ultra Low Power Boost Charger with Battery Management and Autonomous Power Multiplexor for Primary Battery in Energy Harvester Applications,” no. January 2014.
[65] Würth Elektronik, “Energy Harvesting Solution to Go,” pp. 1–2.
[66] V. Roblek, M. Meško, and A. Krapež, “A Complex View of Industry 4.0,” SAGE Open, vol. 6, no. 2, p. 215824401665398, 2016.
[67] Energy Harvesting Market By Technology (Light Energy Harvesting, Vibration Energy Harvesting, Electromagnetic/Radio Frequency (RF) Energy Harvesting, Thermal Energy Harvesting, Thermopile, Thermo Harvester), By System (Electrodynamic, Photovoltaic, Thermoelectric, Piezoelectric, Radio Frequency (RF) Transducers, Electromagnetic Transducers), By Application (Building And Home Automation, Consumer Electronics, Industrial, Transportation, Security), Industry Size, Growth, Share And Forecast To 2022. Brisk Insights, Jul 27, 2016.
[68] Linear Technology Corporation, “Practical Ambient Energy Harvesting for WSNs.”
[69] C. Paper, P. Priller, A. V. L. List, A. Berger, M. Gmbh, and M. Gmbh, “Sustainable Energy Harvesting for Robust Wireless Sensor Networks in Industrial Applications,” IEEE Instrum. Meas. Soc., no. APRIL 2016.D. Tsai, H. Wu, and C. Wei, “A Low-Power-Consumption Boost Converter with Maximum Power Tracking Algorithm for Indoor Photovoltaic Energy Harvesting.”
[70] S. F. Ul Haq Gilani, R. Ibrahim, and M. H. M. Khir, “A case study for industrial centrifugal pump as a vibration source for macro-scale electromagnetic energy harvesting,” Int. Conf. Intell. Adv. Syst. ICIAS 2016, pp. 2–7, 2017.
[71] Chiarotti, Ugo; Moroli, Valerio; Menchetti, Fernando; Piancaldini, Roberto; Bianco, Loris; Viotto, Alberto; Baracchini, Giulia; Gaspardo, Daniele; Nazzi, Fabio; Curti,

Maurizio; Gabriele, Massimiliano, “Development of a Small Thermoelectric Generators Prototype for Energy Harvesting from Low Temperature Waste Heat at Industrial Plant” Journal of Nanoscience and Nanotechnology, Volume 17, Number 3, March 2017, pp. 1586-159.

[72] A. Bertacchini, G. Napoletano, S. Scorcioni, L. Larcher, and P. Pavan, “System with RF power delivery capabilities for active safety enhancement in industrial vehicles using interchangeable implements,” IEEE Trans. Intell. Transp. Syst., vol. 17, no. 12, pp. 3471–3483, 2016.

[73] M. Alhawari, T. Tekeste, B. Mohammad, H. Saleh, and M. Ismail, “Power Management Unit for Multi-Source Energy Harvesting in Wearable Electronics,” no. October, pp. 16–19, 2016.

[74] M. Magno, D. Boyle, D. Brunelli, B. O. Flynn, E. Popovici, S. Member, and L. Benini, “Hybrid Energy Supply,” vol. 61, no. 4, pp. 1871–1881, 2014.

[75] A. S. Weddell, M. Magno, G. V Merrett, D. Brunelli, B. M. Al-Hashimi, and L. Benini, “A Survey of Multi-Source Energy Harvesting Systems,” DATE_IEEE Conf. Des. Autom. Test Eur., p. 4, 2013.

[76] H. Yang and Y. Zhang, “Analysis of Supercapacitor Energy Loss for Power Management in Environmentally Powered,” vol. 28, no. 11, pp. 5391–5403, 2013.

[77] A. S. Weddell, G. V Merrett, T. J. Kazmierski, S. Member, and B. M. Al-hashimi, “Accurate Supercapacitor Modeling for Energy-Harvesting Wireless Sensor Nodes,” vol. X, no. X, 2011.

[78] M. Kaus, J. Kowal, and D. U. Sauer, “Modelling the effects of charge redistribution during self-discharge of supercapacitors,” Electrochim. Acta, vol. 55, no. 25, pp. 7516–7523, 2010.

[79] D. Torregrossa, M. Bahramipanah, R. Cherkaoui, and M. Paolone, “Experimental evidences of redistribution phenomenon in supercapacitors and consequent improvement of their dynamic model,” 2013 IEEE Grenoble Conf., pp. 1–7, Jun. 2013.

[80] D. Torregrossa, “Improvement of Dynamic Modeling of Supercapacitor by Residual Charge Effect Estimation,” Ind. Electron. …, vol. 61, no. 3, pp. 1345–1354, 2014.

[81] J. E. Zuliani, M. Zereen, C. Q. Jia, and D. W. Kirk, “Effects of Temperature on Electrochemical Double Layer Capacitor Performance using Activated Carbon Electrodes,” J. Chem. Inf. Model., vol. 53, no. 9, pp. 1689–1699, 2013.

[82] T. N. Le, O. Sentieys, O. Berder, A. Pegatoquet, and C. Belleudy, “Adaptive Filter for Energy Predictor in Energy Harvesting Wireless Sensor Networks,” vol. 9, pp. 1–4, 2013.

[83] D. Porcarelli, D. Spenza, D. Brunelli, A. Cammarano, C. Petrioli, and L. Benini, “Adaptive rectifier driven by power intake predictors for wind energy harvesting sensor networks,” IEEE J. Emerg. Sel. Top. Power Electron., vol. 3, no. 2, pp. 471–482, 2015.

[84] K. Tutuncuoglu, A. Yener, and S. Ulukus, “Optimum Policies for an Energy Harvesting Transmitter under Energy Storage Losses,” IEEE J. Sel. Areas Commun., vol. 33, no. 3, pp. 467–481, 2015.

[85] J. a. Stankovic, “Wireless Sensor Networks,” Computer (Long. Beach. Calif)., vol. 41, no. 10, pp. 6793–6804, 2008.

[86] C. Yang and K.-W. Chin, “Novel Algorithms for Complete Targets Coverage in Energy Harvesting Wireless Sensor Networks,” IEEE Commun. Lett., vol. 18, no. 1, pp. 118–121, Jan. 2014.

[87] S. Priya, D. J. Inman, “Energy Harvesting Technologies”, 2009.

[88] S. B. Tom J. Kazmierski, “Energy Harvesting Systems”, 2011.

[89] A. E. Niell Elvin, “Advances in Energy Harvesting Methods”, 2013.

[90] P. Spies, M. Pollak, L. Mateu, "Handbook of Energy Harvesting Power Supplies and Applications, 2013.

[91] Akbari, S., “Energy Harvesting for Wireless Sensor Networks Review,” 987–992 (2014).

[92] Seah, W. K. G., Eu, Z. A. and Tan, H.-P., “Wireless sensor networks powered by ambient energy harvesting (WSN-HEAP) - Survey and challenges,” 2009 1st Int. Conf. Wirel. Commun. Veh. Technol. Inf. Theory Aerosp. Electron. Syst. Technol., 1–5 (2009).

[93] G. Zhou, L. Huang, W. Li, and Z. Zhu, “Harvesting ambient environmental energy for wireless sensor networks: A survey,” J. Sensors, vol. 2014.

[94] R. Moghe, Y. Yang, S. Member, F. Lambert, and G. T. Neetrac, “A Scoping Study of Electric and Magnetic Field Energy Harvesting for Wireless Sensor Networks in Power System Applications Deepak Divan,” pp. 3550–3557, 2009.
[95] J. M. Gilbert and F. Balouchi, “Comparison of energy harvesting systems for wireless sensor networks,” Int. J. Autom. Comput., vol. 5, no. 4, pp. 334–347, 2008.
[96] P. D. Mitcheson, E. M. Yeatman, G. K. Rao, A. S. Holmes, and T. C. Green, “Energy harvesting from human and machine motion for wireless electronic devices,” Proc. IEEE, vol. 96, no. 9, pp. 1457–1486, 2008.
[97] J. Randall, N. B. Bharatula, N. Perera, T. Von Büren, S. Ossevoort, and G. Tröster, “Indoor Tracking using Solar Cell Powered System: Interpolation of Irradiance,” pp. 0-1.
[98] I. Mathews, G. Kelly, P. J. King, and R. Frizzell, “GaAs solar cells for Indoor Light Harvesting,” 2014 IEEE 40th Photovolt. Spec. Conf., pp. 0510–0513, Jun. 2014.
[99] A. Nasiri, S. Member, S. A. Zabalawi, S. Member, and G. Mandic, “Indoor Power Harvesting Using Photovoltaic Cells for Low-Power Applications,” vol. 56, no. 11, pp. 4502–4509, 2009.
[100] Solar Energy Technologies Office, 2014.
[101] A. Chirap, V. Popa, E. Coca, and D. A. Potorac, “A study on light energy harvesting from indoor environment: The autonomous sensor nodes,” 2014 Int. Conf. Dev. Appl. Syst., pp. 127–131, May 2014.
[102] S. Boisseau, G. Despesse, and B. A. Seddik, “Electrostatic Conversion for Vibration Energy Harvesting,” pp. 1–39, 2012.
[103] Y. C. Shu and I. C. Lien, “Analysis of power output for piezoelectric energy harvesting systems,” Smart Mater. Struct., vol. 15, no. 6, pp. 1499–1512, Dec. 2006.
[104] R. L. Harne and K. W. Wang, “A review of the recent research on vibration energy harvesting via bistable systems,” Smart Mater. Struct., vol. 22, no. 2, p. 23001, Feb. 2013.
[105] A. Khaligh, S. Member, P. Zeng, S. Member, and C. Zheng, “Kinetic Energy Harvesting Using Piezoelectric and Electromagnetic Technologies — State of the Art,” vol. 57, no. 3, pp. 850–860, 2010.
[106] A. Cadei, A. Dionisi, E. Sardini, and M. Serpelloni, “Kinetic and thermal energy harvesters for implantable medical devices and biomedical autonomous sensors,” Meas. Sci. Technol., vol. 25, no. 1, 2014.
[107] D. Marioli, E. Sardini, and M. Serpelloni, “Electromagnetic Generators Employing Planar Inductors for Autonomous Sensor Applications,” Procedia Chem., vol. 1, no. 1, pp. 469–472, Sep. 2009.
[108] S. P. Beeby et al., “A micro electromagnetic generator for vibration energy harvesting,” J. Micromechanics Microengineering, vol. 17, no. 7, pp. 1257–1265, Jul. 2007.
[109] C. P. Le, E. Halvorsen, O. Søråsen, and E. M. Yeatman, “Wideband excitation of an electrostatic vibration energy harvester with power-extracting end-stops,” Smart Mater. Struct., vol. 22, no. 7, p. 75020, Jul. 2013.
[110] M. Deterre, S. Risquez, B. Bouthaud, R. D. Molin, M. Woytasik, and E. Lefeuvre, “Multilayer out-of-plane overlap electrostatic energy harvesting structure actuated by blood pressure for powering intra-cardiac implants,” J. Phys. Conf. Ser., vol. 476, p. 12039, Dec. 2013.
[111] Y. Naruse, N. Matsubara, K. Mabuchi, M. Izumi, and S. Suzuki, “Electrostatic micro power generation from low-frequency vibration such as human motion,” J. Micromechanics Microengineering, vol. 19, no. 9, p. 94002, Sep. 2009.
[112] A. Cuadras, M. Gasulla, and V. Ferrari, “Thermal energy harvesting through pyroelectricity,” Sensors Actuators A Phys., vol. 158, no. 1, pp. 132–139, Mar. 2010.
[113] F. Y. Lee, A. Navid, and L. Pilon, “Pyroelectric waste heat energy harvesting using heat conduction,” Appl. Therm. Eng., vol. 37, pp. 30–37, May 2012.
[114] M. Kroener and P. Woias, “A STANDALONE PYROELECTRIC HARVESTER FOR THERMAL ENERGY Laboratory for Design of Microsystems, Department of Microsystems Engineering – IMTEK, ε,” Components, no. 1, pp. 5–8, 2012.
[115] V. Leonov, “Thermoelectric energy harvester on the heated human machine,” J. Micromechanics Microengineering, vol. 21, no. 12, p. 125013, 2011.
[116] S. Li, X. Yao, and J. Fu, “Research on a power management system for thermoelectric generators to drive wireless sensors on a spindle unit,” Sensors (Switzerland), vol. 14, no. 7, pp. 12701–12714, 2014.
[117] M. E. Kiziroglou et al., “Design and Fabrication of Heat Storage Thermoelectric Harvesting Devices,” vol. 61, no. 1, pp. 302–309, 2014.
[118] R. Moghe, D. Divan, and F. Lambert, “Powering Low-Cost Utility Sensors using Energy Harvesting Keywords Energy harvesting for powering smart sensors.”

[119] N. M. Roscoe, M. D. Judd, and S. Member, “Harvesting Energy from Magnetic Fields to Power Condition Monitoring Sensors,” vol. 13, no. 6, pp. 2263–2270, 2013.
[120] T. Taithongchai and E. Leelarasmee, “Adaptive electromagnetic energy harvesting circuit for wireless sensor application,” 2009 6th Int. Conf. Electr. Eng. Comput. Telecommun. Inf. Technol., no. 1, pp. 278–281, May 2009.
[121] X. Lu, P. Wang, D. Niyato, D. I. Kim, and Z. Han, “Wireless Networks with RF Energy Harvesting: A Contemporary Survey,” pp. 1–34, Jun. 2014.
[122] V. Talla, S. Pellerano, H. Xu, A. Ravi, and Y. Palaskas, “Wi-Fi RF energy harvesting for battery-free wearable radio platforms,” 2015 IEEE Int. Conf. RFID, pp. 47–54, 2015.
[123] Z. W. Sim, “Radio Frequency Energy Harvesting for Embedded Sensor Networks in the Natural Environment,” 2011.
[124] D. a Howey, a Bansal, and a S. Holmes, “Design and performance of a centimetre-scale shrouded wind turbine for energy harvesting,” Smart Mater. Struct., vol. 20, no. 8, p. 85021, Aug. 2011.
[125] X. Wu and D.-W. Lee, “An electromagnetic energy harvesting device based on high efficiency windmill structure for wireless forest fire monitoring application,” Sensors Actuators A Phys., vol. 219, pp. 73–79, Nov. 2014.
[126] D. Ramasur and G. P. Hancke, “A wind energy harvester for low power wireless sensor networks,” 2012 IEEE Int. Instrum. Meas. Technol. Conf. Proc., pp. 2623–2627, May 2012.
[127] J. a. R. Azevedo and F. E. S. Santos, “Energy harvesting from wind and water for autonomous wireless sensor nodes,” IET Circuits, Devices Syst., vol. 6, no. 6, pp. 413–420, Nov. 2012.
[128] D. Hoffmann, a Willmann, R. Göpfert, P. Becker, B. Folkmer, and Y. Manoli, “Energy Harvesting from Fluid Flow in Water Pipelines for Smart Metering Applications,” J. Phys. Conf. Ser., vol. 476, p. 12104, Dec. 2013.
[129] P. Hardik and D. Sanat, “Performance Prediction of Horizontal Axis Wind Turbine,” Int. J. Innov. Res. Sci. Eng. Technol., vol. 2, no. 5, pp. 1401–1406, 2013.
[130] Ibrahim, 1999.
[131] Heier, 1998.
[132] Calderaro et al, 2008.
[133] Sengupta and Verma, 1992.
[134] Slootweg et al., 2003.
[135] Borowy and Salameh, 1997.
[136] Salameh, 1986.
[137] R. Abdulmunam, “Modeling of Low Power Electrostatic Wind EnergyHarvester for Macro-Scale Applications,” Int. J. Inf. Electron. Eng., vol. 2, no. 6, 2012.
[138] R. Bhat, “Acoustic Energy Harvesting,” vol. 3, no. 5, pp. 1354–1359, 2014.
[139] F. U. Khan and I. Izhar, “Acoustic-Based Electrodynamic Energy Harvester for Wireless Sensor Nodes Application,” Int. J. Mater. Sci. Eng., vol. 1, no. 2, pp. 72–78, 2013.
[140] C. M. Park and S. H. Lee, “Propagation of acoustic waves in a metamaterial with a refractive index of near zero,” Appl. Phys. Lett., vol. 102, no. 24, p. 241906, Jun. 2013.
[141] E. Macii, Ultra Low-Power Electronics and Design. Springer Science + Business Media, Inc. 2004, 2004.
[142] S. Adami, V. Marian, N. Degrenne, C. Vollaire, and B. Allard, “energy harvesting Self-Powered Ultra-Low Power DC-DC Converter for RF Energy Harvesting,” 2012.
[143] B. H. Calhoun and A. P. Chandrakasan, DESIGN FOR ULTRA LOW-POWER. 2006.
[144] Google, Glucose monitoring smart contact lens for diabetics, 2014.
[145] C. Dagdeviren et al., “Conformal piezoelectric energy harvesting and storage from motions of the heart, lung, and diaphragm,” Proc. Natl. Acad. Sci., vol. 111, no. 5, pp. 1927–1932, 2014.
[146] N. Symonds, I. Corni, R. J. K. Wood, A. Wasenczuk, and D. Vincent, “Observing early stage rail axle bearing damage,” Eng. Fail. Anal., vol. 56, pp. 216–232, 2015.
[147] Allianz, Industry 4.0: A new definition of manufacturing?; Global Risk Dialogue Issue 1/2016.
[148] J. Zhou, J. Wang, and H. Chen, “Mode-decomposing Analysis of the Extreme Load in Hybrid Electric Vehicles Using Extreme Value Theory,” Open Mech. Eng. J., vol. 10, no. 1, pp. 136–147, 2016.
[149] M. L. Seol, J. W. Han, D. Il Moon, and M. Meyyappan, “Triboelectric nanogenerator for Mars environment,” Nano Energy, vol. 39, no. July, pp. 238–244, 2017.
[150] E. E. Aktakka and K. Najafi, “A Micro Inertial Energy Harvesting Platform With Self-Supplied Power Management Circuit for Autonomous Wireless Sensor Nodes,” IEEE J. Solid-State Circuits, vol. 49, no. 9, pp. 2017–2029, Sep. 2014.

[151] A E. J. Carlson, K. Strunz, and B. P. Otis, “A 20 mV input boost converter with efficient digital control for thermoelectric energy harvesting,” IEEE J. Solid-State Circuits, vol. 45, no. 4, pp. 741–750, 2010.
[152] J. K. Ward and S. Behrens, “Adaptive learning algorithms for vibration energy harvesting,” Smart Mater. Struct., vol. 17, no. 3, p. 035025, 2008.
[153] M. Stühlmeyer, A. Goehlich, and M. Figge, “Post-CMOS integration of miniaturized solar cells for energy harvesting of autonomous sensor nodes,” pp. 151–155, 2016.
[154] Muhammad H. Rashid, Power Electronics Handbook. 2011.
[155] J. D. Irwin, The Handbook of Power Electronics. 2002.
[156] J. I. Garate, T. Doctoral, “Aportaciones a los Sistemas de Alimentación con Cargas Discontinuas,” 2010.
[157] C. Park and P. H. Chou, “AmbiMax: Autonomous Energy Harvesting Platform for Multi-Supply Wireless Sensor Nodes AmbiMax : Autonomous Energy Harvesting Platform for Multi-Supply Wireless Sensor Nodes,” vol. 0, no. December, pp. 168–177, 2016.
[158] A. S. Weddell, N. R. Harris, and N. M. White, “AN EFFICIENT INDOOR PHOTOVOLTAIC POWER HARVESTING SYSTEM FOR ENERGY-AWARE WIRELESS SENSOR NODES,” vol. 44, no. 0.
[159] X. Wang and L. Lin, “Dimensionless optimization of piezoelectric vibration energy harvesters with different interface circuits,” Smart Mater. Struct., vol. 22, no. 8, p. 85011, Aug. 2013.
[160] H. Liu, Z. Ji, T. Chen, L. Sun, S. C. Menon, and C. Lee, “An Intermittent Self-Powered Energy Harvesting System from Low-Frequency Hand Shaking,” IEEE Sens. J., vol. 15, no. 9, pp. 4782–4790, 2015.
[161] S. R. Hunter, N. V. Lavrik, T. Bannuru, S. Mostafa, S. Rajic, and P. G. Datskos, “Development of MEMS based pyroelectric thermal energy harvesters,” vol. 8035, no. May, p. 80350V–80350V–12, May 2011.
[162] S. Li, X. Yao, and J. Fu, “Research on a power management system for thermoelectric generators to drive wireless sensors on a spindle unit,” Sensors (Switzerland), vol. 14, no. 7, pp. 12701–12714, 2014.
[163] S. Members, F. Lambert, and G. T. Neetrac, “Design of a Low-Cost Self Powered ‘Stick-on’ Current and Temperature Wireless Sensor for Utility Assets Rohit Moghe and Yi Yang Deepak Divan,” pp. 4453–4460, 2010.
[164] S. Adami and C. Vollaire, “Ultra-low Power Autonomous Power Management System with Effective Impedance Matching for RF Energy Harvesting,” pp. 25–27, 2014.
[165] Y. Wu, W. Liu, and Y. Zhu, “Design of a wind energy harvesting wireless sensor node,” 2013 IEEE Third Int. Conf. Inf. Sci. Technol., pp. 1494–1497, Mar. 2013
[166] A. Phipps, F. Liu, L. Cattafesta, M. Sheplak, and T. Nishida, “Demonstration of a wireless, self-powered, electroacoustic liner system.,” J. Acoust. Soc. Am., vol. 125, no. 2, pp. 873–81, Feb. 2009.
[167] Y. K. Tan, S. Member, S. K. Panda, and S. Member, “Light and Thermal Energy Sources for Enhanced Performance of Wireless Sensor Nodes,” vol. 58, no. 9, pp. 4424–4435, 2011.
[168] F. Frequencies et al., “MSP430FR59xx Mixed-Signal Microcontrollers,” 2017.
[169] P. Reset and B. Detector, “Efm32gg990 datasheet.”
[170] M. C. U. Arm, K. B. Flash, K. B. Sram, and K. B. Eeprom, “STM32L051x6 STM32L051x8,” no. June, pp. 1–28, 2014.
[171] T. Instruments, “bq25504 Ultra Low - Power Boost Converter with Battery Management for Energy Harvester Applications,” 2015.
[172] Analog Devices, “ADP5090 Datasheet,” 2015.
[173] P. Sharma and T. S. Bhatti, “A review on electrochemical double-layer capacitors,” Energy Convers. Manag., vol. 51, no. 12, pp. 2901–2912, Dec. 2010.
[174] M. R. Palacín, “Recent advances in rechargeable battery materials: a chemist’s perspective,” Chem. Soc. Rev., vol. 38, no. 9, p. 2565, 2009.
[175] D. Park, Batteries, Supercapacitors, Alternative Storage for Portable Devices. 2009-2019.
[176] S. B. and D. B. Schougaard, “Electrochemical energy storage systems.”
[177] Wang, W.; Wang, N.; Vinco, A.; Siddique, R.; Hayes, M.; O’Flynn, B.; O’Mathuna, C. Super-capacitor and Thin Film Battery Hybrid Energy Storage for Energy Harvesting Applications. J. Phys. Conf. Ser. 2013, 476, 12105.
[178] Sudevalayam, S.; Kulkarni, P. Energy harvesting sensor nodes: Survey and implications. IEEE Commun. Surv. Tutor. 2011, 13, 443–461.
[179] Kumar, K.; Pahariya, Y. “Analysis of Battery Lifetime Extension in a Small-Scale Wind-Energy System Using Supercapacitors”. IEEE Trans. Energy Convers. 2012, 28, 24–33.

[180] L. Yu and G. Z. Chen, “Redox electrode materials for supercapatteries,” J. Power Sources, vol. 326, pp. 604–612, 2016.
[181] H. Shen et al., “A novel activated carbon for supercapacitors,” Mater. Res. Bull., vol. 47, no. 3, pp. 662–666, 2012.
[182] G. Wu et al., “High-performance Supercapacitors Based on Electrochemical-induced Vertical-aligned Carbon Nanotubes and Polyaniline Nanocomposite Electrodes,” Sci. Rep., vol. 7, no. December 2016, pp. 1–8, 2017.
[183] G. R. Li, Z. P. Feng, Y. N. Ou, D. Wu, R. Fu, and Y. X. Tong, “Mesoporous MnO2/Carbon aerogel composites as promising electrode materials for high-performance supercapacitors,” Langmuir, vol. 26, no. 4, pp. 2209–2213, 2010.
[184] J. Cao, Y. Wang, Y. Zhou, J. H. Ouyang, D. Jia, and L. Guo, “High voltage asymmetric supercapacitor based on MnO2and graphene electrodes,” J. Electroanal. Chem., vol. 689, pp. 201–206, 2013.
[185] M. Kaus, J. Kowal, and D. U. Sauer, “Modelling the effects of charge redistribution during self-discharge of supercapacitors,” Electrochim. Acta, vol. 55, no. 25, pp. 7516–7523, 2010.
[186] Cahela, D.; Tatarchuk, B. Overview of electrochemical double layer capacitors. In Proceedings of the IECON 97 23rd International Conference on Industrial Electronics, Control and Instrumentation, New Orleans, LA, USA, 14 November 1997; Volume 3, pp. 1068–1073.
[187] Saha, P. Equivalent Circuit Model of Supercapacitor for Self- Discharge Analysis—A Comparative Study. In Proceedings of the 2016 International Conference on Signal Processing, Communication, Power and Embedded System (SCOPES), Paralakhemundi, India, 3–5 October 2016; pp. 5–10.
[188] Amaral, A.M.R.; Cardoso, A.J.M. Simple experimental techniques to characterize capacitors in a wide range of frequencies and temperatures. IEEE Trans. Instrum. Meas. 2010, 59, 1258–1267.
[189] Zubieta, L.; Bonert, R. Characterization of double-layer capacitors for power electronics applications. IEEE Trans. Ind. Appl. 2000, 36, 199–205.
[190] Torregrossa, D. Improvement of Dynamic Modeling of Supercapacitor by Residual Charge Effect Estimation. Ind. Electron. 2014, 61, 1345–1354.
[191] G. P. Hammond and T. Hazeldine, “Indicative energy technology assessment of advanced rechargeable batteries,” Appl. Energy, vol. 138, pp. 559–571, 2015.
[192] S. Editor and J. A. Milke, Lithium-Ion Batteries Hazard and Use Assessment. 2011.
[193] M. Park, X. Zhang, M. Chung, G. B. Less, and A. M. Sastry, “A review of conduction phenomena in Li-ion batteries,” J. Power Sources, vol. 195, no. 24, pp. 7904–7929, 2010.
[194] S. Priya, D. J. Inman, “Energy Harvesting Technologies”, p.358, Fig. 13.3, 2009.
[195] D. J. Hand, “Principles of data mining,” Drug Saf., vol. 30, no. 7, pp. 621–622, 2007.
[196] J. Han, M. Kamber, and J. Pei, Data Mining: Concepts and Techniques. 2012.
[197] T. M. Mitchell, “Machine learning in ecosystem informatics and sustainability”, McGraw-Hill Science/Engineering/Math, 1997.
[198] Eddahech, O. Briat, M. Ayadi, and J.-M. Vinassa, “Modeling and adaptive control for supercapacitor in automotive applications based on artificial neural networks,” Electr. Power Syst. Res., vol. 106, pp. 134–141, 2014.
[199] A Mitchell, T.M. Machine Learning in Ecosystem Informatics and Sustainability; McGraw-Hill Science/Engineering/Math: New York, NY, USA, 1997.
[200] A. Cammarano, C. Petrioli, and D. Spenza, “Pro-Energy: A novel energy prediction model for solar and wind energy-harvesting wireless sensor networks,” 2012 IEEE 9th Int. Conf. Mob. Ad-Hoc Sens. Syst. (MASS 2012), pp. 75–83, Oct. 2012.
[201] J. P. Yoon and J. Ortiz, “Data mining approach to situation-aware sensor actuation in wireless sensor networks,” 2015 4th Int. Conf. Futur. Gener. Commun. Technol. FGCT 2015, no. Fgct, pp. 149–154, 2015.
[202] S. K. Singh, R. Paulus, S. Veer, S. Rajput, and T. Kaur, “Analysis of energy model and QoS in wireless sensor network under different modulation schemes,” pp. 1–5, 2014.
[203] S. K. Singh, R. Paulus, S. Veer, S. Rajput, and T. Kaur, “Analysis of energy model and QoS in wireless sensor network under different modulation schemes,” pp. 1–5, 2014.
[204] R. Talmale, N. Ramaraj, and N. Thakare, “Analysis of energy efficient data mining techniques in wireless sensor networks: A review,” 2017 2nd Int. Conf. Converg. Technol., pp. 435–438, 2017.

[205] Eddahech, A.; Briat, O.; Ayadi, M.; Vinassa, J.-M. Modeling and adaptive control for supercapacitor in automotive applications based on artificial neural networks. Electr. Power Syst. Res. 2014, 106, 134–141.
[206] C. H. Wu, Y. H. Hung, and C. W. Hong, "On-line supercapacitor dynamic models for energy conversion and management", Energy Convers. Manag., vol. 53, no. 1, pp. 337–345, 2012.
[207] A Zhang, L.; Hu, X.; Wang, Z.; Sun, F.; Dorrell, D.G. Fractional-order modeling and State-of-Charge estimation for ultracapacitors. J. Power Sources 2016, 314, 28–34.
[208] H. Kodama, "Electrical Energy Storage Devices & Systems," Hitachi Chem., vol. 57, no. 57, pp. 6–15, 2014.
[209] S. Peng and C. P. Low, "Prediction free energy neutral power management for energy harvesting wireless sensor nodes," Ad Hoc Networks, vol. 13, pp. 351–367, Feb. 2014.
[210] R. C. Hsu, C.-T. Liu, and H.-L. Wang, "A Reinforcement Learning-Based ToD Provisioning Dynamic Power Management for Sustainable Operation of Energy Harvesting Wireless Sensor Node," IEEE Trans. Emerg. Top. Comput., vol. 2, no. 2, pp. 181–191, Jun. 2014.
[211] W. Dargie and C. Poellabauer, Fundamentals of Wireless Sensor Networks. 2010.
[212] S. Basagni, M. Y. Naderi, and C. Petrioli, "WIRELESS SENSOR NETWORKS WITH ENERGY HARVESTING," in Mobile Ad Hoc Networking: Cutting Edge Directions, Second Edition, vol. Chapter 20, 2013, pp. 1–36.
[213] K. Cho, G. Park, W. Cho, J. Seo, and K. Han, "Performance analysis of device discovery of Bluetooth Low Energy (BLE) networks," Comput. Commun., vol. 81, pp. 72–85, 2015.
[214] R. (Washington U. Jain, "Low Power WAN Protocols for IoT," Washingt. Univ. St. Louis Lect. Ser. LPWA, 2016.
[215] M. S. Levin, "Modular System Design and Evaluation," vol. 4, no. i, pp. 401–413, 2015.
[216] M. Luque, "Autor: Ramón Pérez Hernández Tutor: Germán Madinabeitia Luque," 2015.
[217] P. Neumann, J. Montavont, and T. Noel, "Indoor deployment of low-power wide area networks (LPWAN): A LoRaWAN case study," Int. Conf. Wirel. Mob. Comput. Netw. Commun., 2016.
[218] D. Thomas, E. Wilkie, and J. Irvine, "Comparison of Power Consumption of WiFi Inbuilt Internet of Things Device with Bluetooth Low Energy," vol. 10, no. 10, pp. 1693–1696, 2016.
[219] F. Touati, R. Tabish, and A. Ben Mnaouer, "A Real-time BLE Enabled ECG System for Remote Monitoring," APCBEE Procedia, vol. 7, pp. 124–131, 2013.
[220] M. Vergara-Gallego, O. Mokrenko, M. Louvel, S. Lesecq, and F. Pacull, "Implementation of an Energy Management Control Strategy for WSNs using the LINC Middleware Implementation of an Energy Management Control Strategy for WSNs using the LINC Mid," 2016.
[221] A. J. Wixted, P. Kinnaird, H. Larijani, A. Tait, A. Ahmadinia, and N. Strachan, "Evaluation of LoRa and LoRaWAN for wireless sensor networks," Proc. IEEE Sensors, vol. 0, pp. 5–7, 2017.
[222] D. Esign et al., ", Cfd S," no. January, pp. 568–571, 2004.
[223] A. S. Holmes, G. Hong, and K. R. Pullen, "Axial-flux permanent magnet machines for micropower generation," J. Microelectromechanical Syst., vol. 14, no. 1, pp. 54–62, 2005.
[224] D. a Howey, a Bansal, and a S. Holmes, "Design and performance of a centimetre-scale shrouded wind turbine for energy harvesting," Smart Mater. Struct., vol. 20, no. 8, p. 85021, Aug. 2011.
[225] L. Tang, L. Zhao, Y. Yang, and E. Lefeuvre, "Equivalent Circuit Representation and Analysis of Galloping-Based Wind Energy Harvesting," IEEE/ASME Trans. Mechatronics, vol. 20, no. 2, pp. 834–844, 2015.
[226] N. G. Elvin, "Equivalent electrical circuits for advanced energy harvesting," J. Intell. Mater. Syst. Struct., vol. 25, no. 14, pp. 1715–1726, 2014.
[227] C. P. Yue, C. Ryu, J. Lau, T. H. Lee, and S. S. Wong, "A physical model for planar spiral inductors on silicon," Int. Electron Devices Meet. Tech. Dig., pp. 155–158, 1996.
[228] J. Zhao, "A new calculation for designing multilayer planar spiral inductors," Edn, vol. 55, no. 14, pp. 37–40, 2010.
[229] G. Stojanovic, L. Zivanov, and M. Damjanovic, "Compact form of expressions for inductance calculation of meander inductors," Serbian J. Electr. Eng., vol. 1, no. 3, pp. 57–68, 2004.
[230] M. Pospisilik, L. Kouril, I. Motyl, and M. Adamek, "Single and Double Layer Spiral Planar Inductors Optimisation with the Aid of Self-Organising Migrating Algorithm," pp. 272–277.

[231] Alhawari, M., Tekeste, T., Mohammad, B., Saleh, H. and Ismail, M., "Power Management Unit for Multi-Source Energy Harvesting in Wearable Electronics," 16–19 (2016).
[232] C. Vimalarani and N. Kamaraj, "Modeling and performance analysis of the solar photovoltaic cell model using Embedded MATLAB," Simulation, vol. 91, no. 3, pp. 217–232, 2015.
[233] K. Ishaque, Z. Salam, H. Taheri, and Syafaruddin, "Modeling and simulation of photovoltaic (PV) system during partial shading based on a two-diode model," Simul. Model. Pract. Theory, vol. 19, no. 7, pp. 1613–1626, 2011.
[234] Vergura, S., "A complete and simplified datasheet-based model of pv cells in variable environmental conditions for circuit simulation," Energies 9(5) (2016).
[235] D. Sera, R. Teodorescu, and P. Rodriguez, "PV panel model based on datasheet values," IEEE Int. Symp. Ind. Electron., no. July 2007, pp. 2392–2396, 2007.
[236] C. V Long, J. a Flint, and P. a Lepper, "Wind Turbines," J. Acoust. Soc. Am., vol. 128, no. 4, pp. 2238–45, 2010.
[237] Alejandro Rivas; Gorka SánchezGoi, "Flujo de aire a través de tuberías y toberas," Campus Tecnológico la Univ. Navarra, 2007.
[238] S. Dwari, R. Dayal, L. Parsa, and K. N. Salama, "Efficient Direct AC-to-DC Converters for Vibration- Based Low Voltage Energy Harvesting," Ind. Electron. 2008. IECON 2008., pp. 2320–2325, 2008.
[239] S. Dwari, R. Dayal, L. Parsa, and K. N. Salama, "Efficient Direct AC-to-DC Converters for Vibration- Based Low Voltage Energy Harvesting," Ind. Electron. 2008. IECON 2008., pp. 2320–2325, 2008.
[240] R. Dayal, S. Dwari, and L. Parsa, "Design and implementation of a direct ACDC boost converter for low-voltage energy harvesting," IEEE Trans. Ind. Electron., vol. 58, no. 6, pp. 2387–2396, 2011.
[241] El Mejdoubi, A.; Chaoui, H.; Sabor, J.; Gualous, H. Remaining Useful Life Prognosis of Supercapacitors Under Temperature and Voltage Aging Conditions. IEEE Trans. Ind. Electron. 2018, 65, 4357–4367.
[242] Cammarano, A.; Petrioli, C.; Spenza, D. Pro-Energy: A novel energy prediction model for solar and wind energy-harvesting wireless sensor networks. In Proceedings of the 2012 IEEE 9th International Conference on Mobile Adhoc and Sensor Systems (MASS), Las Vegas, NV, USA, 8–11 October 2012; pp. 75–83.
[243] Park, S.W.; DeYoung, A.D.; Dhumal, N.R.; Shim, Y.; Kim, H.J.; Jung, Y.J. Computer Simulation Study of Graphene Oxide Supercapacitors: Charge Screening Mechanism. J. Phys. Chem. Lett. 2016, 7, 1180–1186.
[244] Merlet, C.; Péan, C.; Rotenberg, B.; Madden, P.A.; Simon, P.; Salanne, M. Simulating supercapacitors: Can we model electrodes as constant charge surfaces? J. Phys. Chem. Lett. 2013, 4, 264–268.
[245] Chai, R.Z.; Zhang, Y. A Practical Supercapacitor Model for Power Management in Wireless Sensor Nodes. IEEE Trans. Power Electron. 2015, 30, 6720–6730.
[246] Ban, S.; Zhang, J.; Zhang, L.; Tsay, K.; Song, D.; Zou, X. Charging and discharging electrochemical supercapacitors in the presence of both parallel leakage process and electrochemical decomposition of solvent. Electrochim. Acta 2013, 90, 542–549.
[247] Rajan, R.S.; Rahman, M.M. Lifetime Analysis of Super Capacitor for Many Power Electronics Applications. IOSR J. Electr. Electron. Eng. 2014, 9, 55–58.
[248] Kötz, R.; Hahn, M.; Gallay, R. Temperature behavior and impedance fundamentals of supercapacitors. J. Power Sources 2006, 154, 550–555.
[249] Murray, D.B.; Hayes, J.G. Cycle testing of supercapacitors for long-life robust applications. IEEE Trans. Power Electron. 2015, 30, 2505–2516.
[250] Liu, K.; Zhu, C.; Lu, R.; Chan, C.C. Improved study of temperature dependence equivalent circuit model for supercapacitors. IEEE Trans. Plasma Sci. 2013, 41, 1267–1271.
[251] Miller, J.M. Ultracapacitor Applications Ultracapacitor Applications; The Institution of Engineering and Technology: London, UK, 2011; pp. 37–91.
[252] Diab, Y.; Venet, P.; Gualous, H.; Rojat, G. Self-discharge characterization and modeling of electrochemical capacitor used for power electronics applications. IEEE Trans. Power Electron. 2009, 24, 510–517.
[253] TIBUCON, Self-Powered Wireless Sensor Network for HVAC System Energy Improvement. Seventh Framework Programme, FP7, EU.

[254] Hofmann, M.; Klinkenberg, R. RapidMiner: Data Mining Use Cases and Business Analytics Applications; CRC Press: Boca Raton, FL, USA, 2013.
[255] Y. J. L. Ali Emadi, Alireza Khaligh, Zhong Nie, Integrated Power Electronic Converters and Digital Control. 2009.

VIII.
Appendix

16. Appendix

16.1 Mini-reactor

16.1.1 Magnetic simulations

16.1.1.1 Teflon ™ rings

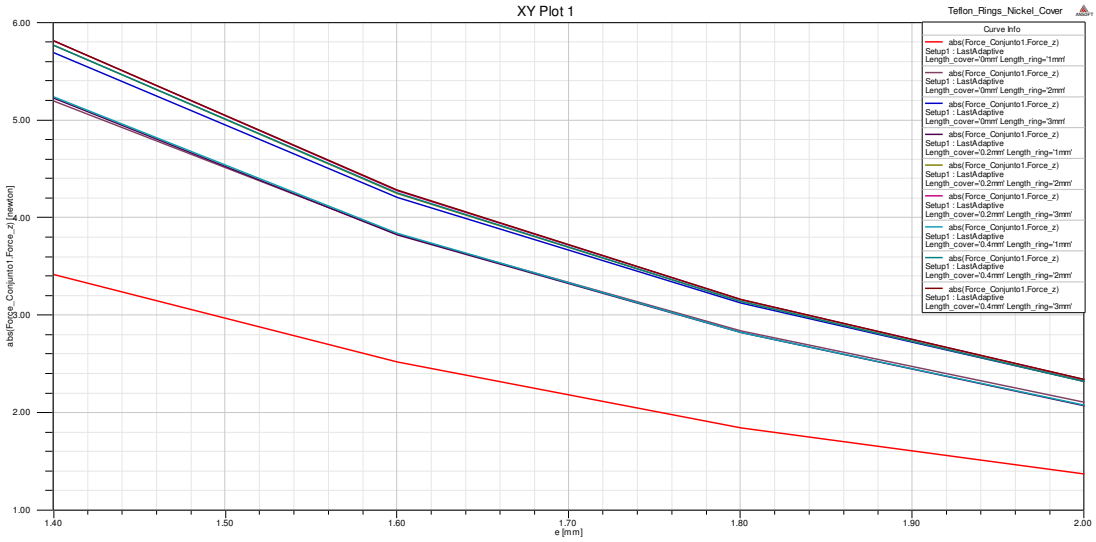

a) Absolute value of force on one ring according to distance between rings.

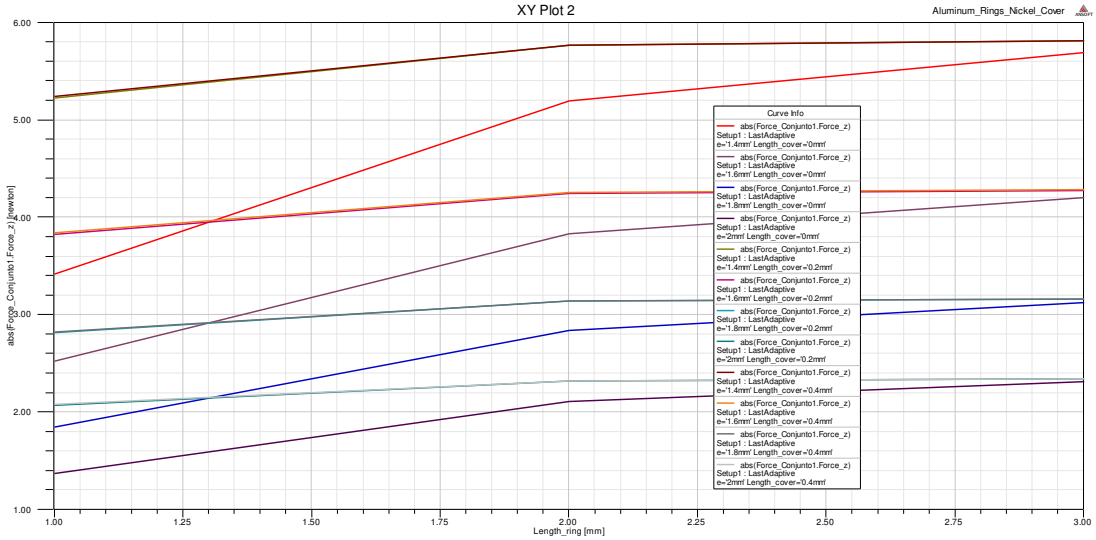

b) Absolute force on one of the rings as a function of the width of the rings.

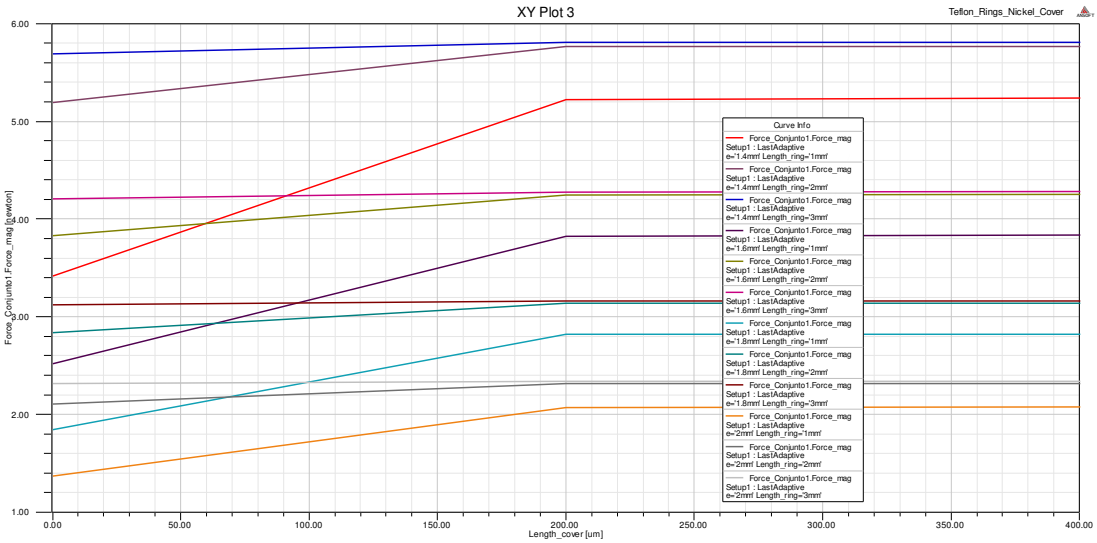

c) Absolute force on one of the rings depending on the width of the coating.

16.1.1.2 Aluminum rings

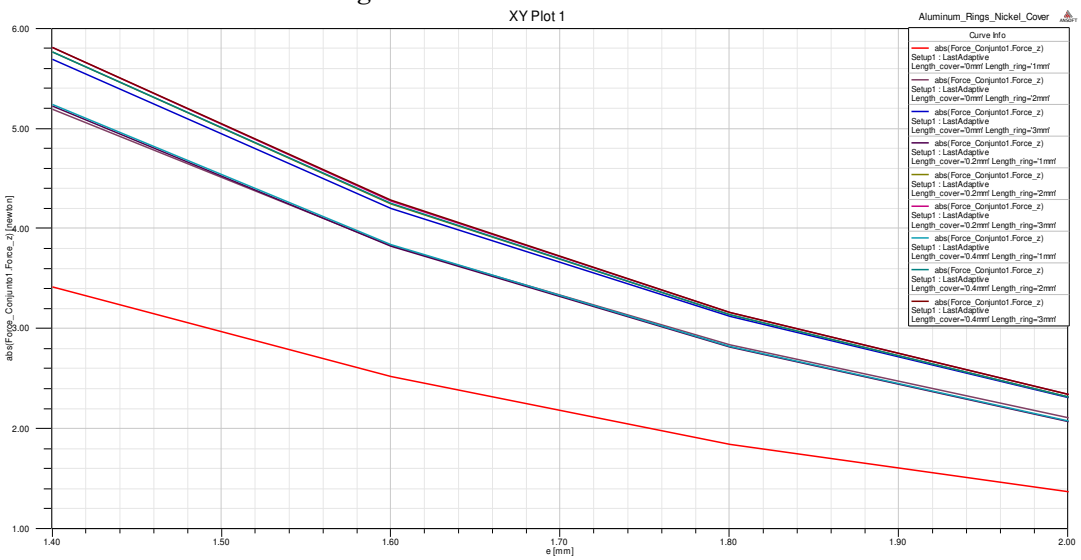

a) Absolute value of force on one ring according to distance between rings.

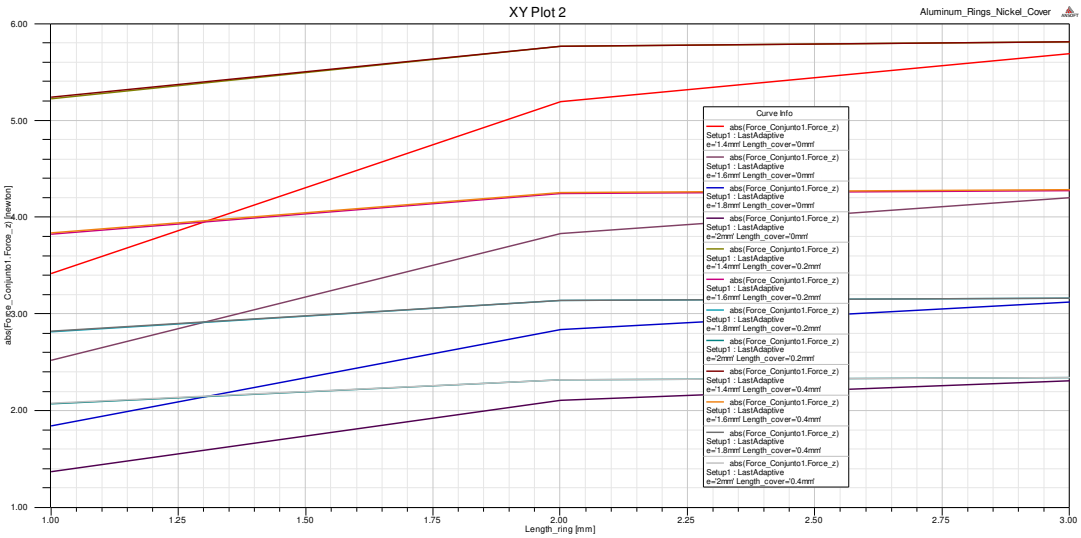

b) Absolute force on one of the rings as a function of the width of the rings.

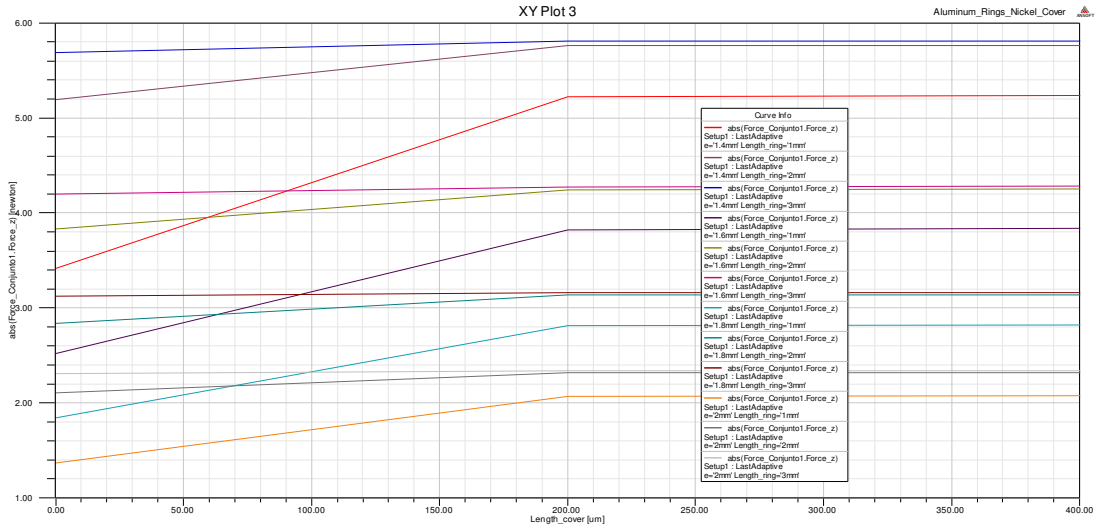

c) Absolute force on one of the rings depending on the width of the coating.

16.1.1.3 Nickel rings

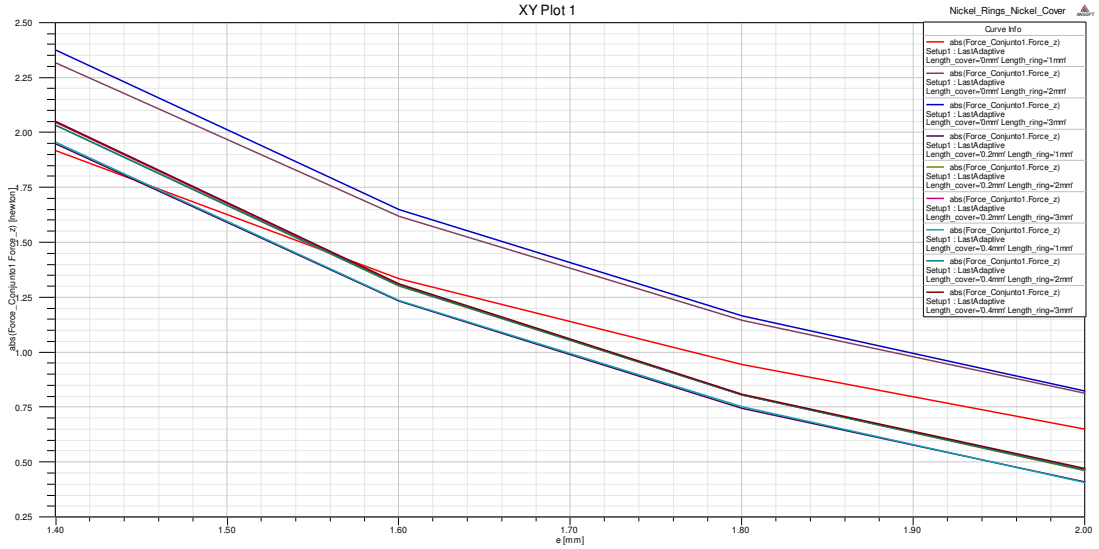

a) Absolute value of force on one ring according to distance between rings.

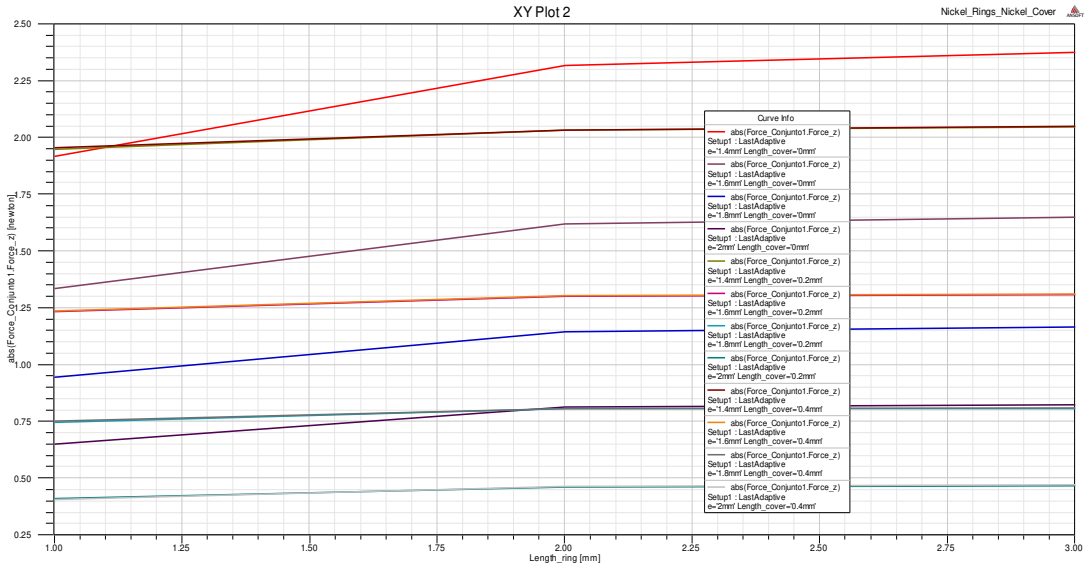

b) Absolute force on one of the rings as a function of the width of the rings.

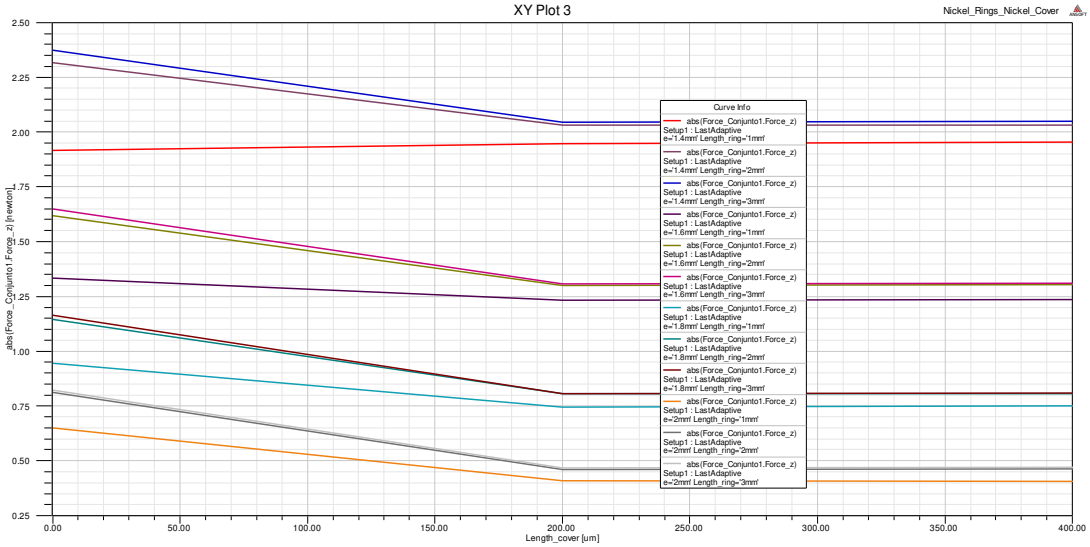

c) Absolute force on one of the rings depending on the width of the coating.

16.1.2 Electrical generators theoretical calculus

16.1.2.1 Resistance

$$R = \rho_c \cdot \frac{l_c}{w} \cdot \left[\frac{1}{\delta(1 - e^{-t_c/\delta})}\right] \tag{16-1}$$

16.1.2.1.1 Monophasic:

$$R_{(coil)} = \frac{1.68 \cdot 10^{-8} \cdot 22.661 \cdot 10^{-3}}{80 \cdot 10^{-6} \cdot 20 \cdot 10^{-6} \cdot \left(1 - e^{\frac{-80 \cdot 10^{-6}}{20 \cdot 10^{-6}}}\right)} = 0.2423\ \Omega$$

$$R_{(coil)} = 0.2423 \cdot 48 \cdot 2 = 23.268\ \Omega$$

$$R_{(track)} = \frac{1.68\cdot10^{-8}\cdot15.35\cdot10^{-3}}{80\cdot10^{-6}\cdot20\cdot10^{-6}\cdot\left(1-e^{\frac{-80\cdot10^{-6}}{20\cdot10^{-6}}}\right)} = 0.1641\ \Omega$$

$$R_{(track)} = 0.1641 \cdot 4 = 0.6567\ \Omega$$

$$R_{(pad)} = \frac{1.68\cdot10^{-8}\cdot1.65\cdot10^{-3}}{0.4\cdot10^{-3}\cdot20\cdot10^{-6}\cdot\left(1-e^{\frac{-80\cdot10^{-6}}{20\cdot10^{-6}}}\right)} = 3.46\cdot10^{-3}\ \Omega$$

$$R_{(pad)} = 3.46\cdot10^{-3}\cdot4 = 1.386\cdot10^{-2}\ \Omega$$

$$R_{(total)} = 23.268 + 0.6567\ + 1.386\cdot10^{-2} = 23.938\ \Omega$$

16.1.2.1.2 Triphasic:

$$R_{(coil)} = \frac{1.68\cdot10^{-8}\cdot21.625\cdot10^{-3}}{80\cdot10^{-6}\cdot20\cdot10^{-6}\cdot\left(1-e^{\frac{-80\cdot10^{-6}}{20\cdot10^{-6}}}\right)} = 0.454\ \Omega$$

$$R_{(coil)} = 0.454\cdot16 = 7.269\ \Omega$$

$$R_{(track)} = \frac{1.68\cdot10^{-8}\cdot15.35\cdot10^{-3}}{80\cdot10^{-6}\cdot20\cdot10^{-6}\cdot\left(1-e^{\frac{-80\cdot10^{-6}}{20\cdot10^{-6}}}\right)} = 0.1641\ \Omega$$

$$R_{(track)} = 0.1641\cdot4 = 0.6567\ \Omega$$

$$R_{(pad)} = \frac{1.68\cdot10^{-8}\cdot1.65\cdot10^{-3}}{0.4\cdot10^{-3}\cdot20\cdot10^{-6}\cdot\left(1-e^{\frac{-80\cdot10^{-6}}{20\cdot10^{-6}}}\right)} = 3.46\cdot10^{-3}\ \Omega$$

$$R_{(pad)} = 3.46\cdot10^{-3}\cdot4 = 1.386\cdot10^{-2}\ \Omega$$

$$R_{(total)} = 23.268 + 0.6567\ + 1.386\cdot10^{-2} = 23.938\ \Omega$$

16.1.2.2 Capacitor

$$C_p = (\alpha\varepsilon_{rc} + \beta\varepsilon_{rs})\cdot\varepsilon_0\cdot\frac{t_c}{s}\cdot l_g \qquad (16\text{-}2)$$

16.1.2.2.1 Monophasic

$$C_{p(pad)} = 0.1\cdot4.5\cdot8.854\cdot10^{-12}\cdot\frac{20\cdot10^{-6}}{0.25\cdot10^{-3}}\cdot1.65\cdot10^{-3} = 5.2698\cdot10^{-16}F$$

$$C_{p(pad)} = 5.2698\cdot10^{-16}\cdot2 = 1.10518\cdot10^{-15}F$$

$$C_{p(coil)} = 0.1\cdot4.5\cdot8.854\cdot10^{-12}\cdot\frac{20\cdot10^{-6}}{50\cdot10^{-6}}\cdot20.57\cdot10^{-3} = 3.278\cdot10^{-14}F$$

$$C_{p(coil)} = 3.278\cdot10^{-14}\cdot48\cdot2 = 3.1471\cdot10^{-12}F$$

$$C_{p(track)} = 0.1\cdot4.5\cdot8.854\cdot10^{-12}\cdot\frac{20\cdot10^{-6}}{0.57\cdot10^{-3}}\cdot15.53\cdot10^{-3} = 2.145\cdot10^{-15}F$$

$$C_{p(track)} = 2.145\cdot10^{-15}\cdot2 = 4.291\cdot10^{-14}F$$

$C_{p(total)} = 1.10518 \cdot 10^{-15} + 3.1471 \cdot 10^{-12} + 4.291 \cdot 10^{-14} = 3.191 \cdot 10^{-12} F$

16.1.2.2.2 Triphasic:

$C_{p(pad)} = 0.1 \cdot 4.5 \cdot 8.854 \cdot 10^{-12} \cdot \frac{20 \cdot 10^{-6}}{0.25 \cdot 10^{-3}} \cdot 3.556 \cdot 10^{-3} = 1.2154 \cdot 10^{-15} F$

$C_{p(pad)} = 1.2154 \cdot 10^{-15} \cdot 10 = 1.10518 \cdot 10^{-14} F$

$C_{p(coil)} = 0.1 \cdot 4.5 \cdot 8.854 \cdot 10^{-12} \cdot \frac{20 \cdot 10^{-6}}{50 \cdot 10^{-6}} \cdot 21.625 \cdot 10^{-3} = 3.446 \cdot 10^{-14} F$

$C_{p(coil)} = 3.446 \cdot 10^{-14} \cdot 2 \cdot 16 = 1.1028 \cdot 10^{-12} F$

$C_{p(track)} = 0.1 \cdot 4.5 \cdot 8.854 \cdot 10^{-12} \cdot \frac{20 \cdot 10^{-6}}{0.57 \cdot 10^{-3}} \cdot 17.724 \cdot 10^{-3} = 2.8247 \cdot 10^{-15} F$

$C_{p(track)} = 2.145 \cdot 10^{-15} \cdot 10 = 2.8247 \cdot 10^{-14} F$

$C_{p(total)} = 1.10518 \cdot 10^{-14} + 1.1028 \cdot 10^{-12} + 2.8247 \cdot 10^{-14} = 1.1432 \cdot 10^{-12} F$

16.1.2.3 Coil

16.1.2.3.1 Monophasic

$$L_{tot} = L_{selftot} + M_{tot} \tag{16-3}$$

$$L_{selftot} = N \cdot L_h + (N+1) \cdot L_d \tag{16-4}$$

$$L = 0.002 \cdot l \cdot \left\{ ln\left[\frac{2l}{(w+t)}\right] - 1.25 + \left[\frac{(w+t)}{3l}\right] + \left(\frac{\mu}{4}\right) T \right\} \tag{16-5}$$

$$L = 0.002 \cdot l \cdot \left\{ ln\left[\frac{2l}{(w+t)}\right] + 0.50049 + \left[\frac{(w+t)}{3l}\right] \right\} \tag{16-6}$$

$$M_{tot} = M_2 + M_5 \tag{16-7}$$

$$M_2 = \sum_{i=1}^{(N-1)/2} (2N + 2 - 4i) \cdot M_b(d, d, (2i-1)d) \tag{16-8}$$

$$M_5 = \sum_{i=1}^{N-1} (-1)^i \cdot 2(N-1) \cdot M_c(h, id) \tag{16-9}$$

$$\begin{aligned} M_b(l_1, l_2, s) = {} & \frac{\mu_0}{4\pi} \\ & \cdot [(l_1 + l_2 + s)\, ln(l_1 + l_2 + s) \\ & - (l_1 + s)\, ln(l_1 + s) - (l_2 + s)\, ln(l_2 + s) + s\, ln\, s] \end{aligned} \tag{16-10}$$

$$M_c(l, r) = \frac{\mu_0}{2\pi} \cdot l \cdot \left[ln\left(\frac{l}{r} + \sqrt{1 + \left(\frac{l}{r}\right)^2} \right) - \sqrt{1 + \left(\frac{r}{l}\right)^2} + \frac{r}{l} \right] \tag{16-11}$$

$M_b = \frac{4\pi\cdot10^{-7}}{4\pi} \cdot [(130 \cdot 10^{-6} + 130 \cdot 10^{-6} + 50 \cdot 10^{-6})\, ln(130 \cdot 10^{-6} + 130 \cdot 10^{-6} + 50 \cdot 10^{-6}) - (130 \cdot 10^{-6} + 50 \cdot 10^{-6})\, ln(130 \cdot 10^{-6} + 50 \cdot 10^{-6}) - (130 \cdot 10^{-6} + 50 \cdot 10^{-6})\, ln(130 \cdot 10^{-6} + 50 \cdot 10^{-6}) + 50 \cdot 10^{-6}\, ln\, 50 \cdot 10^{-6}] = 1.0447 \cdot 10^{-11}$

$M_c = \frac{4\pi\cdot10^{-7}}{2\pi} \cdot 1.25 \cdot 10^{-3} \cdot \left[ln\left(\frac{1.25\cdot10^{-3}}{50\cdot10^{-6}} + \sqrt{1 + \left(\frac{1.25\cdot10^{-3}}{50\cdot10^{-6}}\right)^2}\right) - \sqrt{1 + \left(\frac{50\cdot10^{-6}}{1.25\cdot10^{-3}}\right)^2} + \frac{50\cdot10^{-6}}{1.25\cdot10^{-3}}\right] = 7.379 \cdot 10^{-10}$

$M_2 = \sum_{i=1}^{3}(2N + 2 - 4i) \cdot 1.0447 \cdot 10^{-11} = [16 + 12 + 8 + 4] \cdot 1.0447 \cdot 10^{-11} = 40 \cdot 1.0447 \cdot 10^{-11} = 4.178 \cdot 10^{-10}$

$M_5 = \sum_{i=1}^{6}(-1)^i \cdot 2(N-1) \cdot 7.379 \cdot 10^{-10} = [2 \cdot 7 - 2 \cdot 6 + 2 \cdot 5 - 2 \cdot 4 + 2 \cdot 3 - 2 \cdot 2 + 2 \cdot 1] \cdot 7.379 \cdot 10^{-10} = 8 \cdot 7.379 \cdot 10^{-10} = 5.903 \cdot 10^{-9}$

$M_{tot} = 4.178 \cdot 10^{-10} + 5.903 \cdot 10^{-9} = 6.321 \cdot 10^{-9}$

$L = 0.002 \cdot 1.25 \cdot 10^{-1} \cdot \left\{ln\left[\frac{2\cdot1.25\cdot10^{-1}}{(80\cdot10^{-4}+20\cdot10^{-4})}\right] + 0.50049 + \left[\frac{(80\cdot10^{-4}+20\cdot10^{-4})}{3\cdot1.25\cdot10^{-1}}\right]\right\} = 9.36 \cdot 10^{-4}\ \mu H$

$L = 0.002 \cdot 1.25 \cdot 10^{-1} \cdot \left\{ln\left[\frac{2\cdot0.13\cdot10^{-1}}{(80\cdot10^{-4}+20\cdot10^{-4})}\right] + 0.50049 + \left[\frac{(80\cdot10^{-4}+20\cdot10^{-4})}{3\cdot0.13\cdot10^{-1}}\right]\right\} = 4.452 \cdot 10^{-5}\ \mu H$

$L_{selftot} = 9.36 \cdot 10^{-4} + 4.452 \cdot 10^{-5} = 0.1466\ \mu H$

$L_{tot} = (0.1466 \cdot 10^{-6} + 6.321 \cdot 10^{-9}) \cdot 48 \cdot 2 = 2.01449\ \mu H$

16.1.2.3.2 Triphasic

$$L = L_1 + L_2 \pm 2M \tag{16-12}$$

$$M = k_c\sqrt{L_1 L_2} = \frac{n^2}{0.64 \cdot (Ax^3 + Bx^2 + Cx + D)(1.67n^2 - 5.84n + 65)} \tag{16-13}$$

$$L_1, L_2 = \frac{\mu \cdot n^2 \cdot D_{avg} \cdot C_1}{2} \cdot \left(ln\left(\frac{C_2}{\sigma}\right) + C_3 \cdot \sigma + C_4 \cdot \sigma^2\right) \tag{16-14}$$

$$\sigma = \frac{D_{out} - D_{in}}{D_{out} + D_{in}} = \frac{n \cdot (w + s) + w}{2 \cdot D_{out} - (n \cdot (w + s) + w)} \tag{16-15}$$

$$D_{avg} = \frac{D_{out} + D_{in}}{2} = D_{out} - \frac{w \cdot (n + 1) + n \cdot s}{2} \tag{16-16}$$

$$\begin{aligned} L = 2 \cdot \left(1 + \frac{n^2}{0.64 \cdot (Ax^3 + Bx^2 + Cx + D)(1.67n^2 - 5.84n + 65)}\right) \\ \cdot \frac{\mu \cdot n^2 \cdot \left(D_{out} - \frac{w \cdot (n + 1) + n \cdot s}{2}\right) \cdot C_1}{2} \\ \cdot \left[ln\left(\frac{C_2}{\frac{n \cdot (w + s) + w}{2 \cdot D_{out} - (n \cdot (w + s) + w)}}\right) + C_3 \cdot \left(\frac{n \cdot (w + s)}{2 \cdot D_{out} - (n \cdot (w + s) + w)}\right)\right. \\ \left. + C_4 \cdot \left(\frac{n \cdot (w + s)}{2 \cdot D_{out} - (n \cdot (w + s) + w)}\right)^2\right] \end{aligned} \tag{16-17}$$

$$L = 2 \cdot \left(1 + \frac{5^2}{0.64 \cdot (0.184 \cdot (0.8 \cdot 10^{-3})^3 - 0.525 \cdot (0.8 \cdot 10^{-3})^2 + 1.038 \cdot 0.8 \cdot 10^{-3} + 1.001)(1.67 \cdot 5^2 - 5.84 \cdot 5 + 65)}\right) \cdot \frac{4\pi \cdot 10^{-7} \cdot 5^2 \cdot \left(D_{out} - \frac{w \cdot (5+1) + 5 \cdot s}{2}\right) \cdot 1.27}{2} \cdot \left[ln\left(\frac{2.07}{\frac{5 \cdot (w+s) + w}{2 \cdot D_{out} - (5 \cdot (w+s) + w)}}\right) + 0.18 \cdot \left(\frac{5 \cdot (w+s)}{2 \cdot D_{out} - (5 \cdot (w+s) + w)}\right) + 0.13 \cdot \left(\frac{5 \cdot (w+s)}{2 \cdot D_{out} - (5 \cdot (w+s) + w)}\right)^2\right] = 2 \cdot 0.5026 \cdot 0.281 \cdot [2.1308 + 4.676 \cdot 10^{-2} \cdot 8.77 \cdot 10^{-3}] = 0.2468\, mH$$

$$L = 0.2468 \cdot 10^{-3} \cdot 16 = \ 3.949\, mH$$

16.1.3 Test-bench mechanical designs

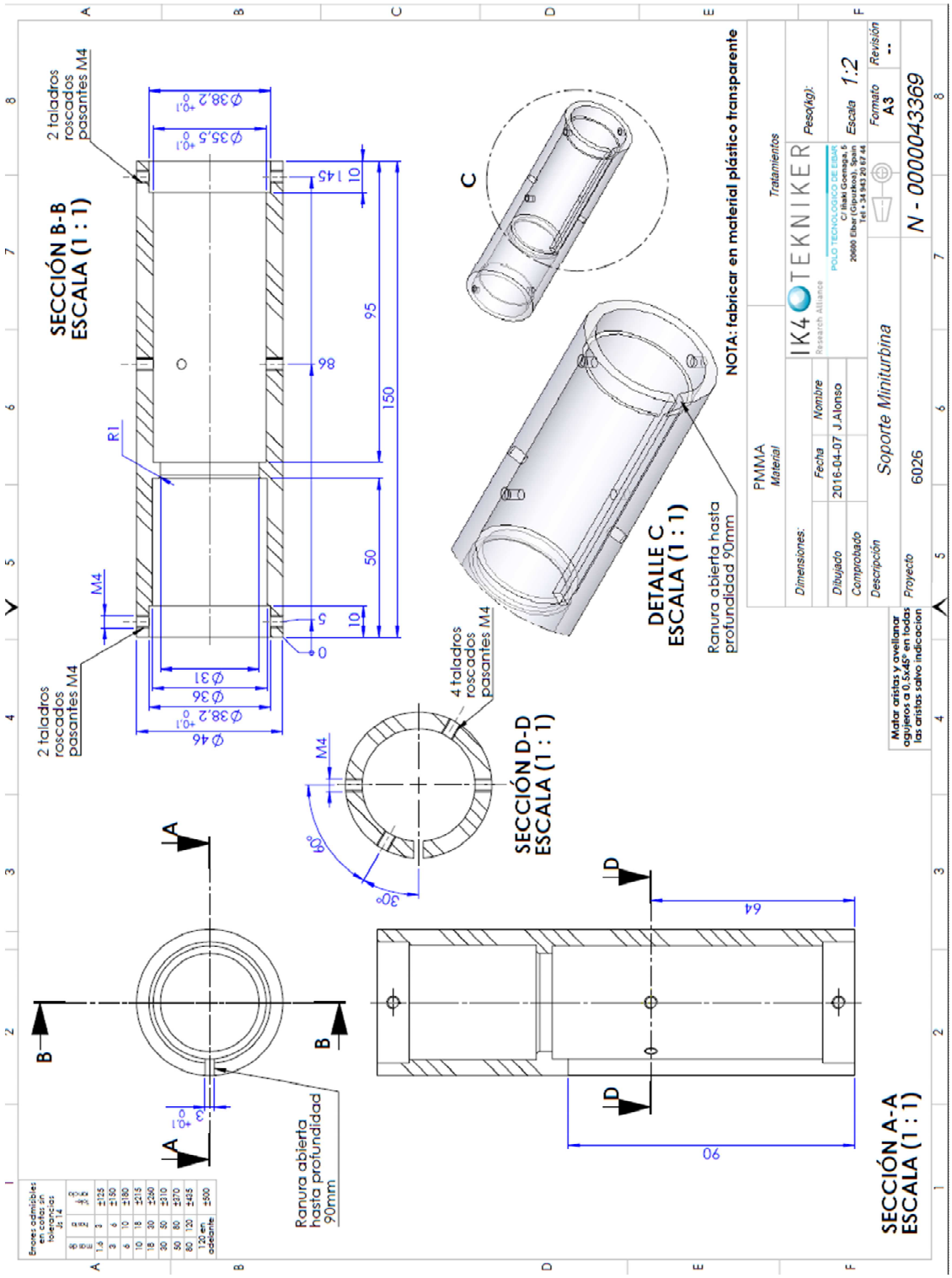

16.1.4 Results graphics

16.1.4.1 Monophasic

16.1.4.1.1 24 Ω load

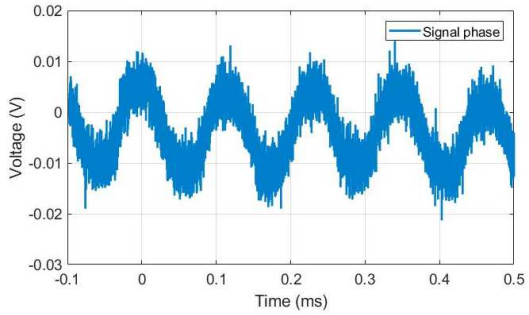

a) Wind velocity 3 m/s.

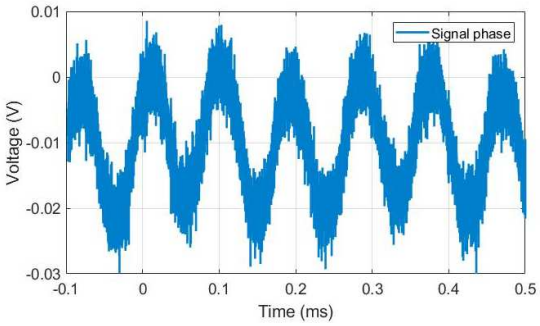

b) Wind velocity 4 m/s.

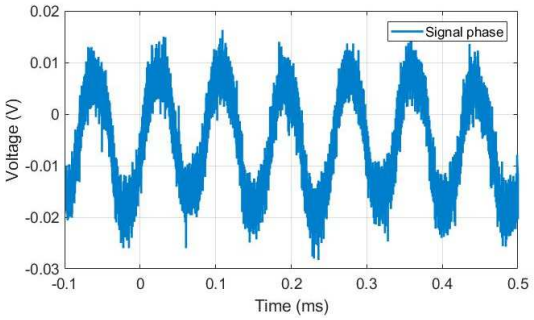

c) Wind velocity 5 m/s.

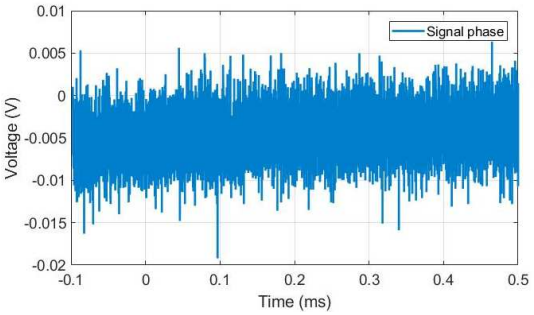

d) Wind velocity 6 m/s.

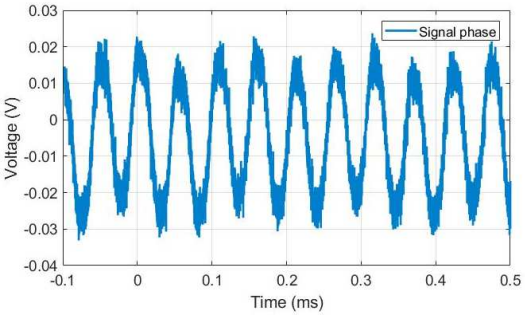

e) Wind velocity 7 m/s.

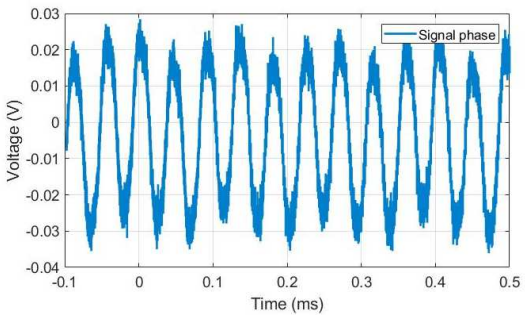

f) Wind velocity 8 m/s.

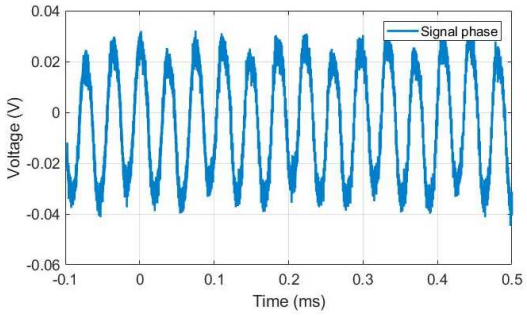

g) Wind velocity 9 m/s.

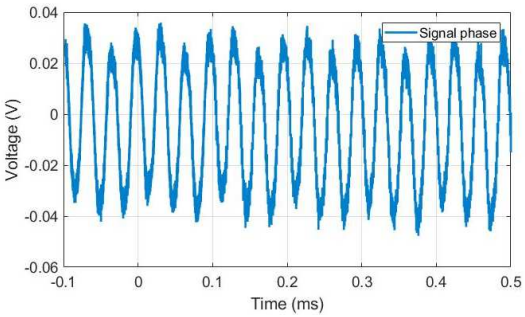

h) Wind velocity 10 m/s.

16.1.4.1.2 30 Ω load

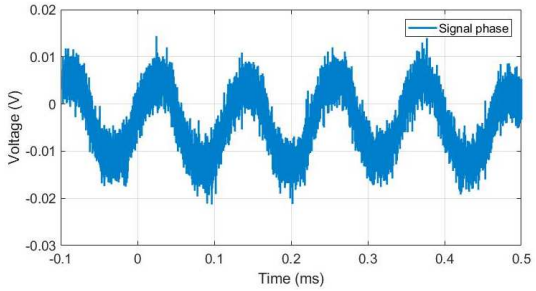

a) Wind velocity 3 m/s.

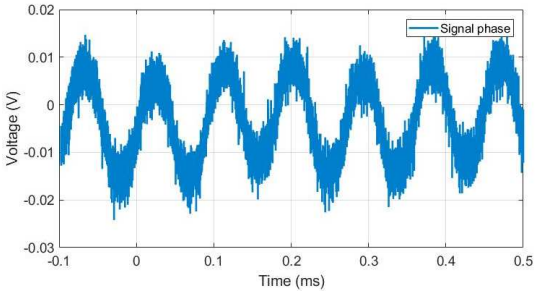

b) Wind velocity 4 m/s.

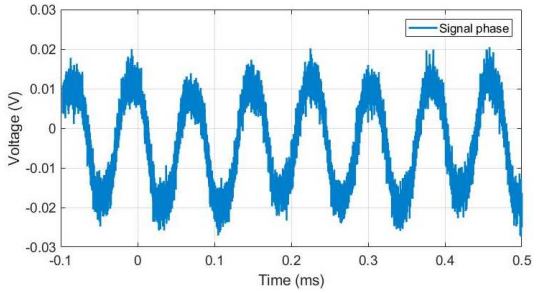

c) Wind velocity 5 m/s.

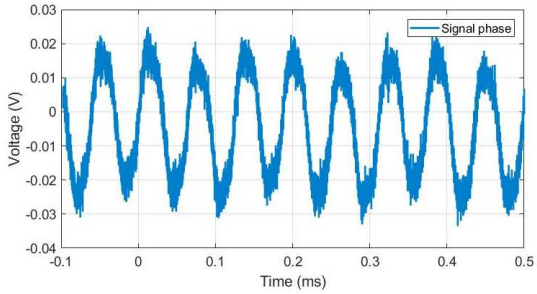

d) Wind velocity 6 m/s.

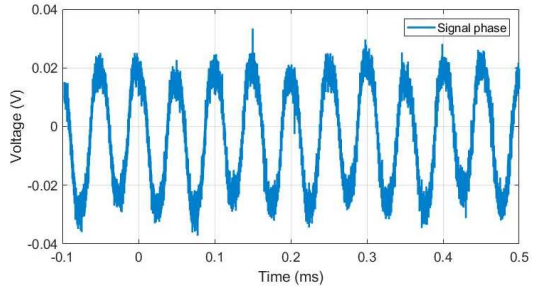

e) Wind velocity 7 m/s.

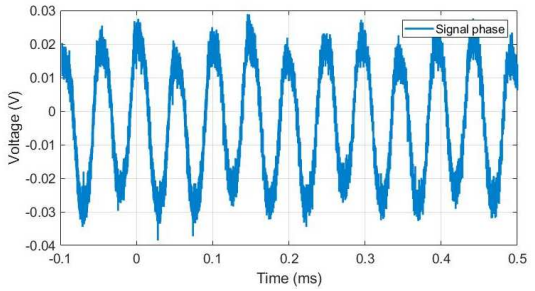

f) Wind velocity 8 m/s.

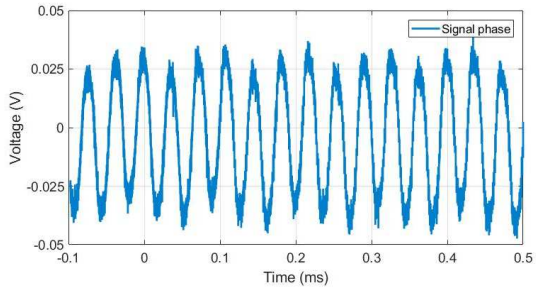

g) Wind velocity 9 m/s.

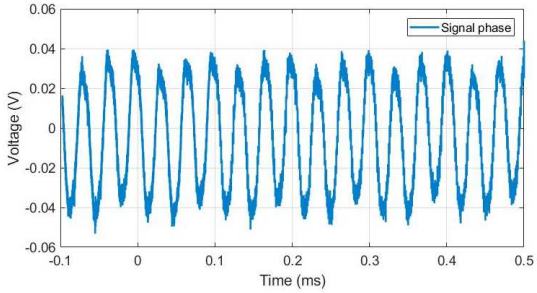

h) Wind velocity 10 m/s.

16.1.4.1.3 100 Ω load

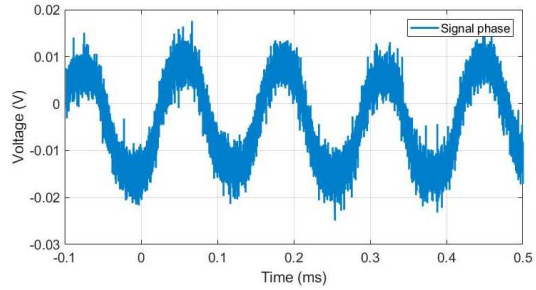

a) Wind velocity 3 m/s.

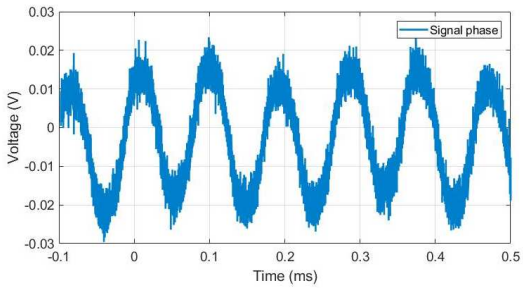

b) Wind velocity 4 m/s.

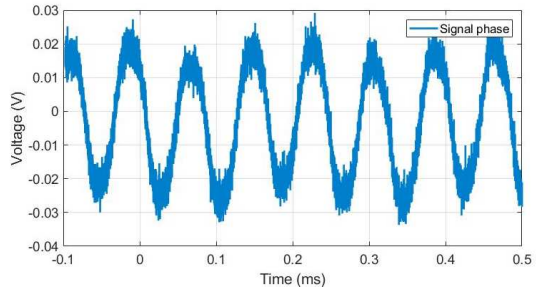

c) Wind velocity 5 m/s.

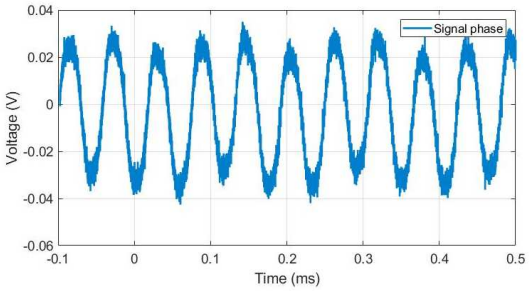

d) Wind velocity 6 m/s.

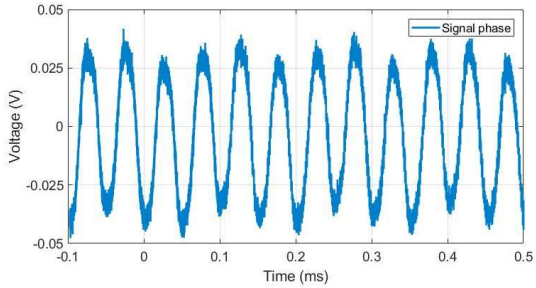

e) Wind velocity 7 m/s.

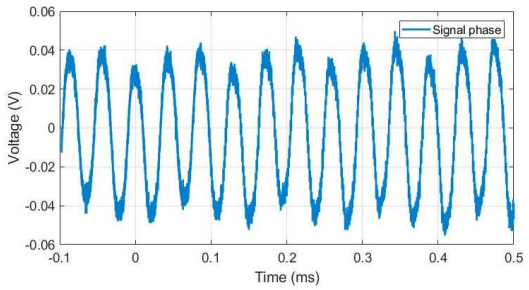

f) Wind velocity 8 m/s.

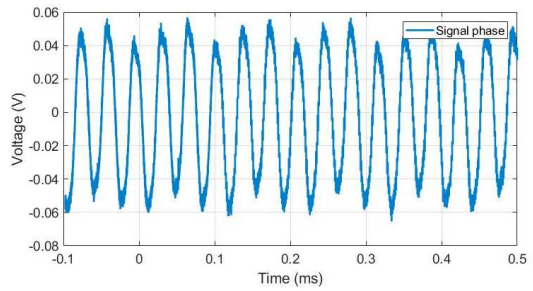

g) Wind velocity 9 m/s.

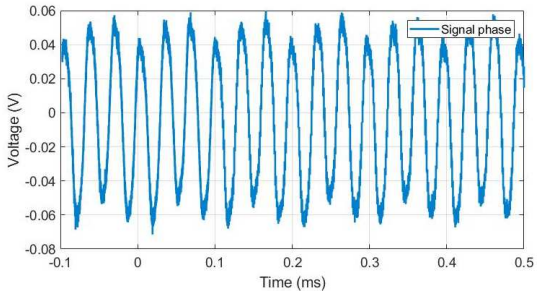

h) Wind velocity 10 m/s.

16.1.4.1.4 1 kΩ load

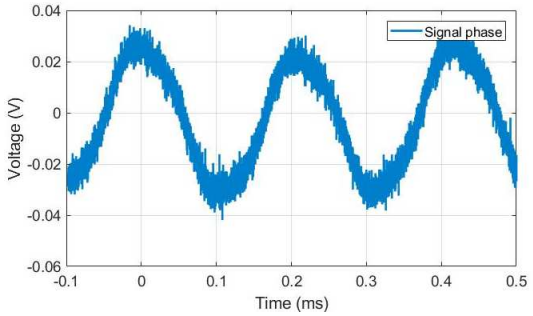

a) Wind velocity 3 m/s.

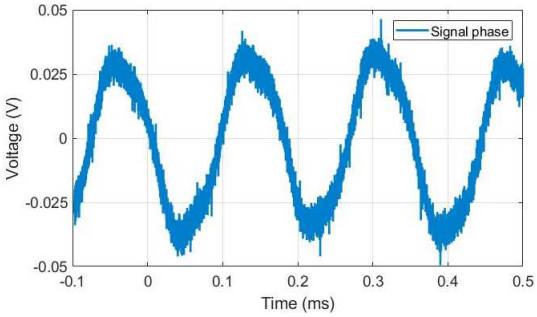

b) Wind velocity 4 m/s.

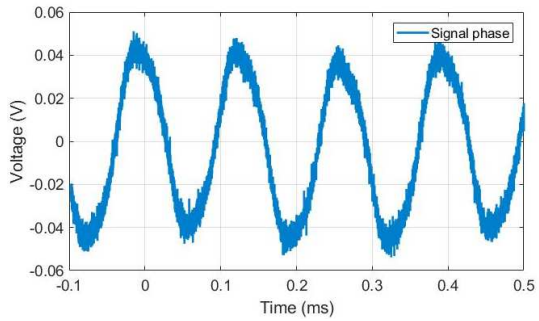

c) Wind velocity 5 m/s.

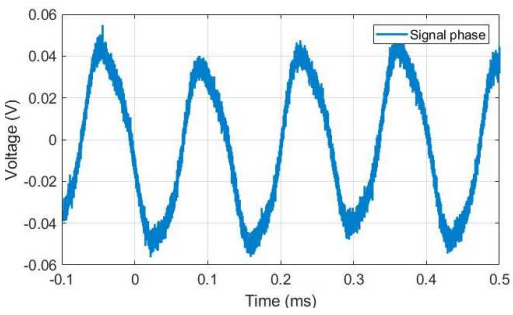

d) Wind velocity 6 m/s.

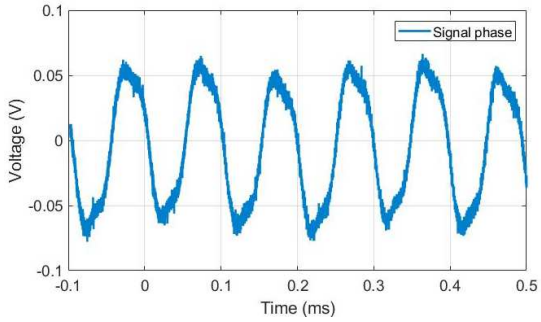

e) Wind velocity 7 m/s.

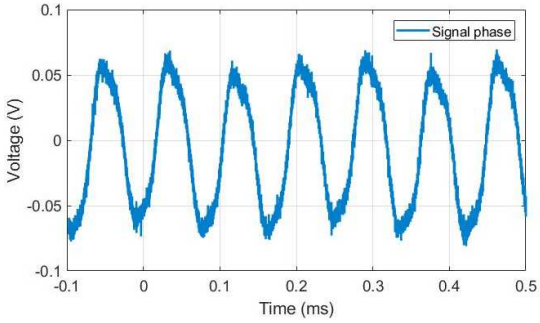

f) Wind velocity 8 m/s.

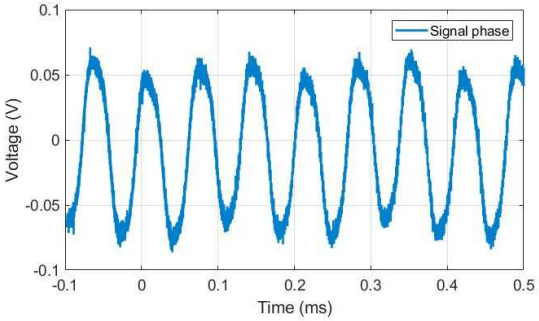

g) Wind velocity 9 m/s.

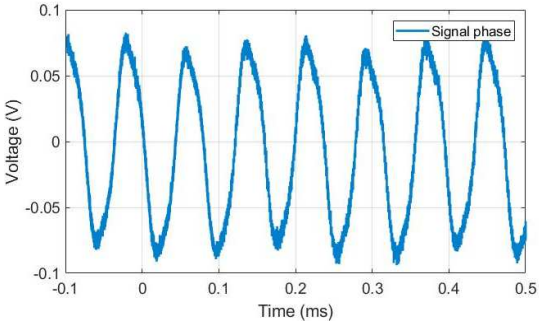

h) Wind velocity 10 m/s.

16.1.4.2 Three-phase

16.1.4.2.1 11 Ω load

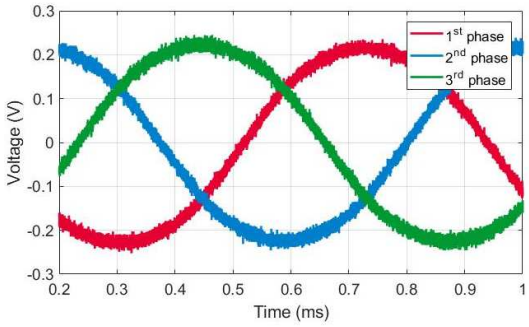

a) Wind velocity 3 m/s.

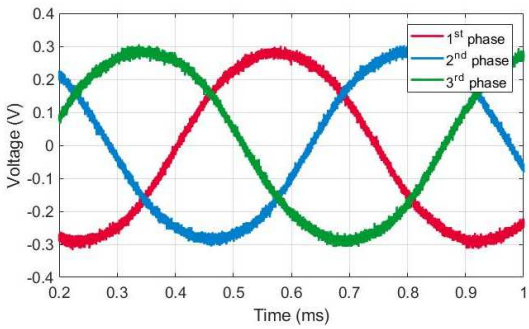

b) Wind velocity 4 m/s.

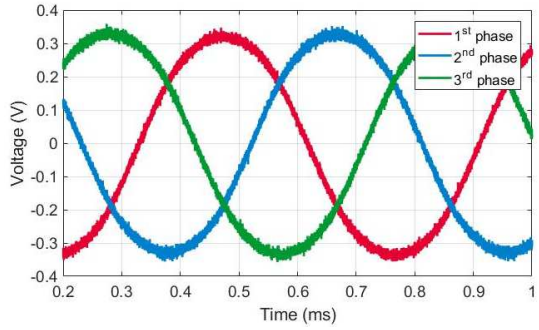

c) Wind velocity 5 m/s.

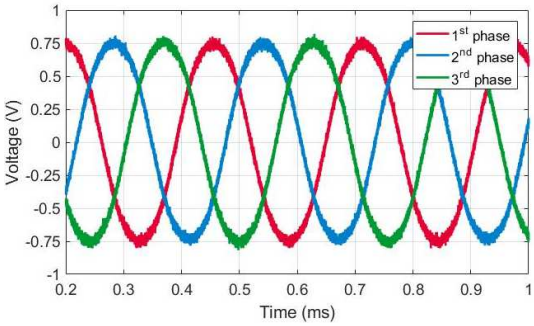

d) Wind velocity 6 m/s.

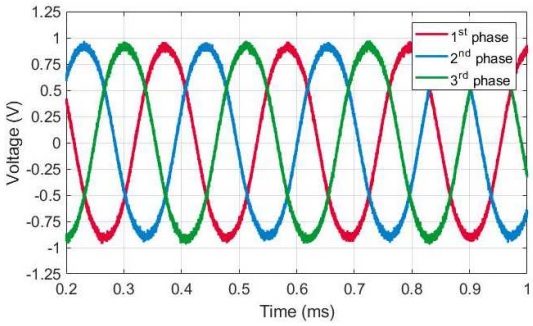

e) Wind velocity 7 m/s.

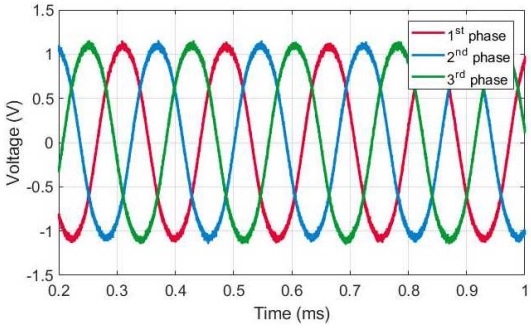

f) Wind velocity 8 m/s.

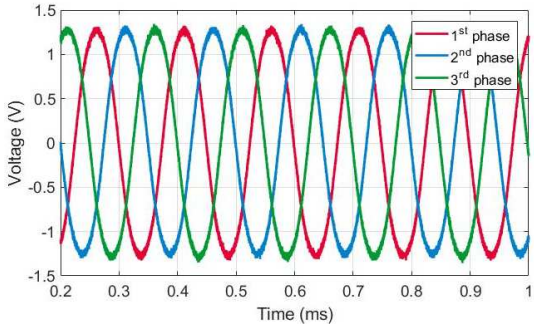

g) Wind velocity 9 m/s.

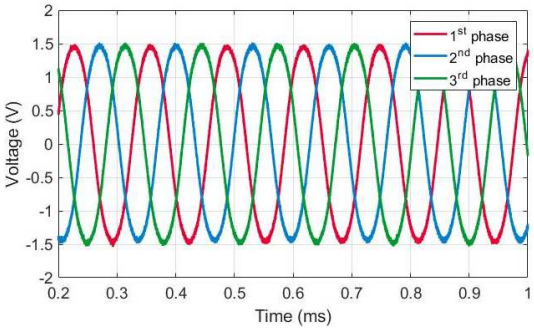

h) Wind velocity 10 m/s.

16.1.4.2.2 27 Ω load

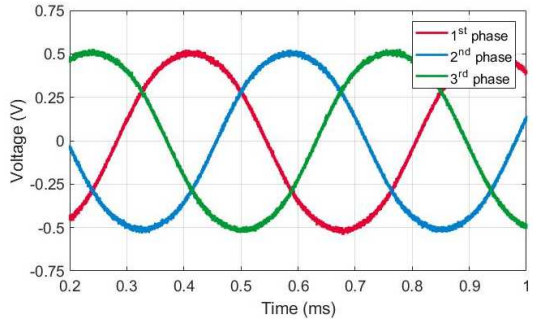

a) Wind velocity 3 m/s.

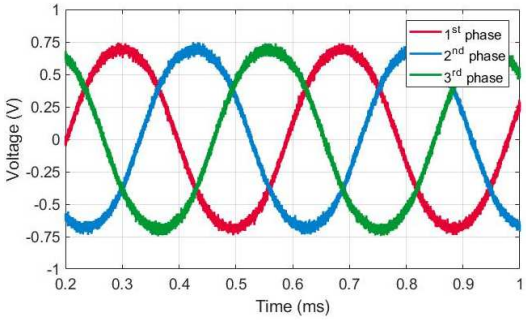

b) Wind velocity 4 m/s.

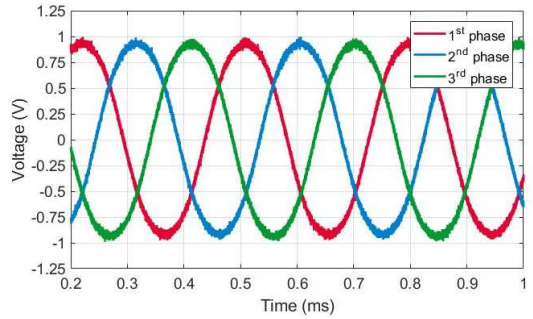

c) Wind velocity 5 m/s.

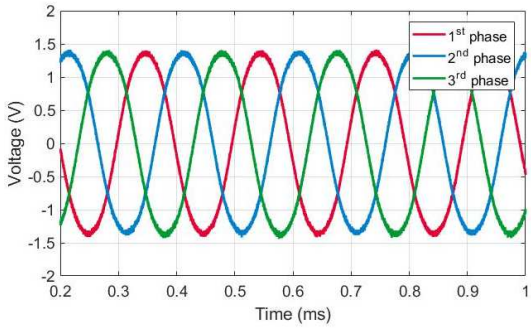

d) Wind velocity 6 m/s.

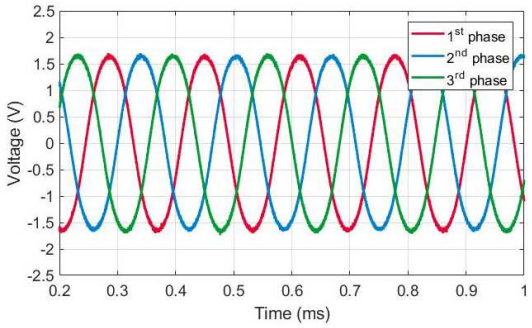

e) Wind velocity 7 m/s.

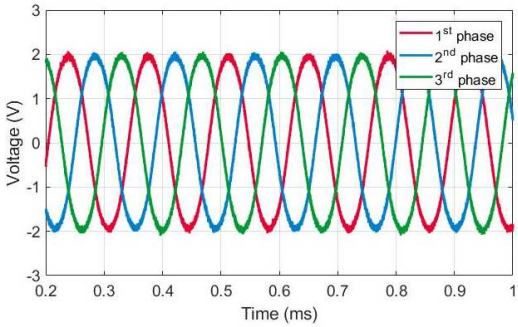

f) Wind velocity 8 m/s.

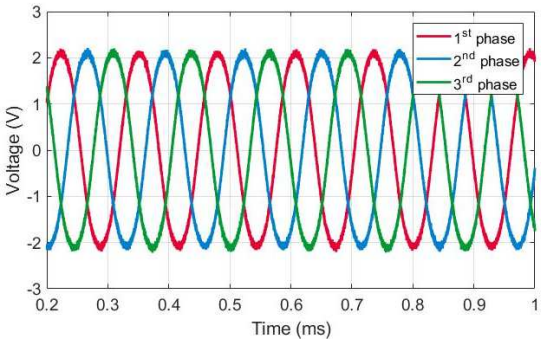

g) Wind velocity 9 m/s.

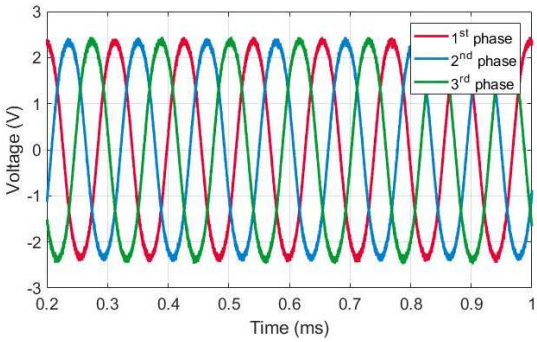

h) Wind velocity 10 m/s.

16.1.4.2.3 100 Ω load

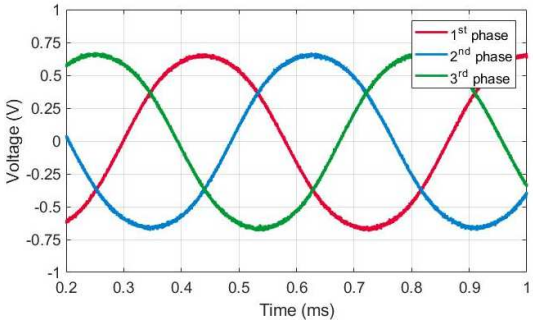

a) Wind velocity 3 m/s.

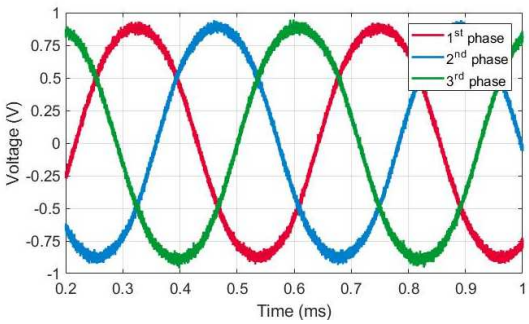

b) Wind velocity 4 m/s.

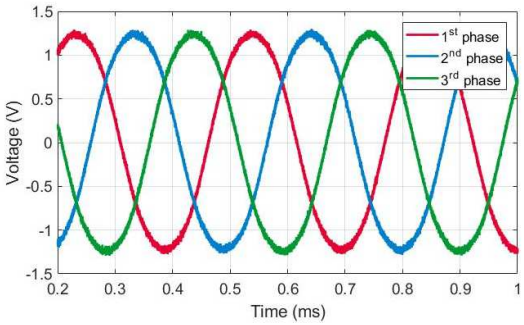

c) Wind velocity 5 m/s.

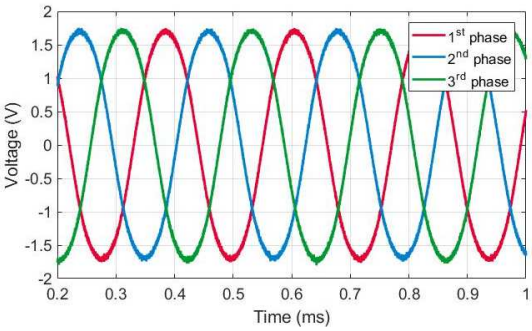

d) Wind velocity 6 m/s.

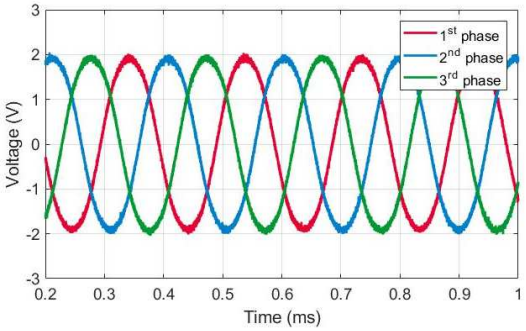

e) Wind velocity 7 m/s.

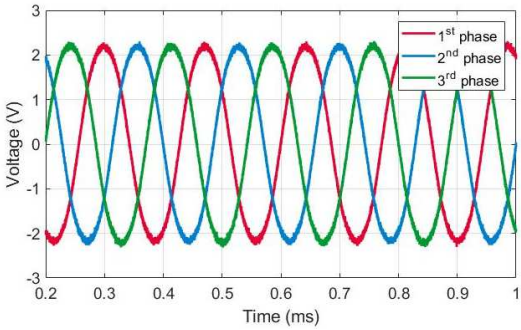

f) Wind velocity 8 m/s.

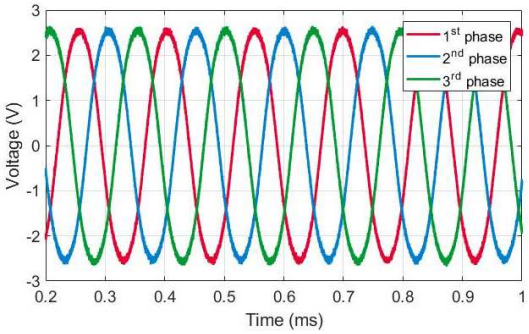

g) Wind velocity 9 m/s.

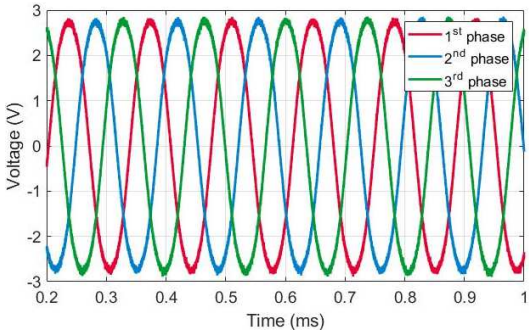

h) Wind velocity 10 m/s.

16.1.4.2.4 1 kΩ load

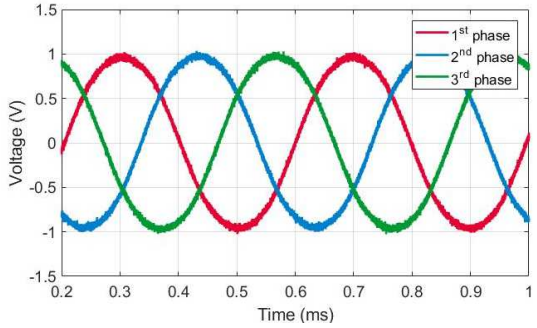

a) Wind velocity 3 m/s.

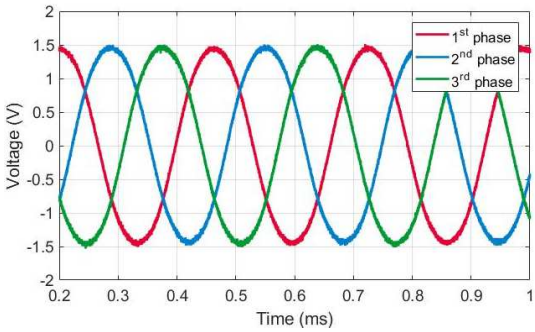

b) Wind velocity 4 m/s.

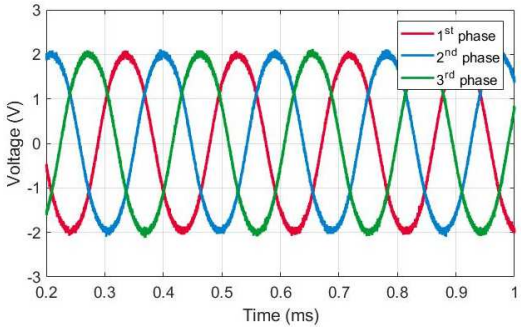

c) Wind velocity 5 m/s.

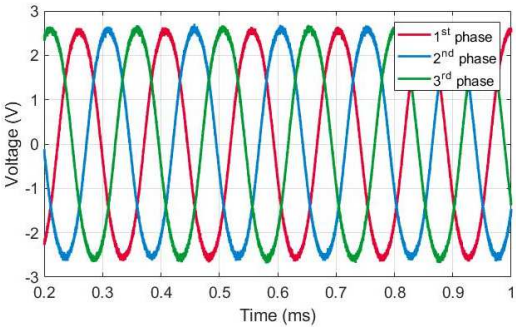

d) Wind velocity 6 m/s.

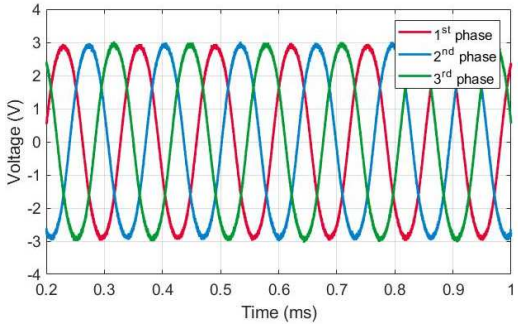

e) Wind velocity 7 m/s.

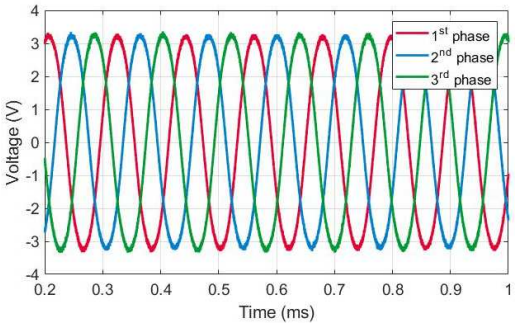

f) Wind velocity 8 m/s.

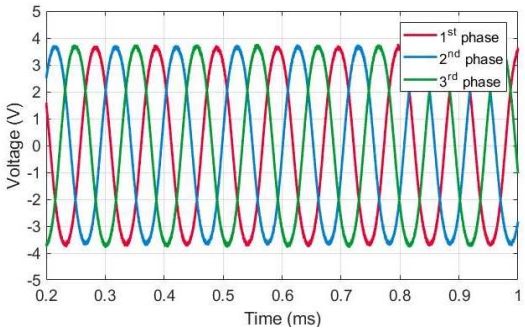

g) Wind velocity 9 m/s.

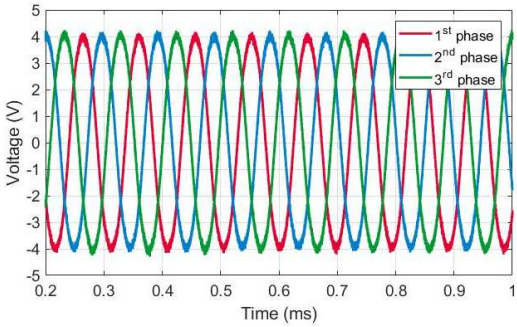

h) Wind velocity 10 m/s.

16.2 DC input system

16.2.1 Photovoltaic harvester model vs test result interpolation and plot functions

```
[V1,id1,~] = unique(V1);
I1 = I1(id1);
[V2,id2,~] = unique(V2);
I2 = I2(id2);

[V3,id3,~] = unique(V1);
P1 = P1(id3);
[V4,id4,~] = unique(V2);
P2 = P2(id4);

V = unique([V1' V2']);
I1_interp = interp1(V1,I1,V);
I2_interp = interp1(V2,I2,V);
P1_interp = interp1(V3,P1,V);
P2_interp = interp1(V4,P2,V);

I1_interp(isnan(I1_interp)) = 0;
I2_interp(isnan(I2_interp)) = 0;
P1_interp(isnan(P1_interp)) = 0;
P2_interp(isnan(P2_interp)) = 0;

for i=1:length(I1_interp)
   C(i)=abs(I1_interp(i)-I2_interp(i));
   D(i)=abs(P1_interp(i)-P2_interp(i));
end
for j=15:length(I1_interp)-30
   ErrorI(j)=100-((I2_interp(j)*100)/I1_interp(j));
   ErrorP(j)=100-((P2_interp(j)*100)/P1_interp(j));
end

D_I=mean(C)
D_P=mean(D)

E_I=median(ErrorI)
E_P=median(ErrorP)
```

```
subplot(4,1,1);
[hAx,hLine1,hLine2]=plotyy(V_sim,I_sim,V_test,I_test);
set(hLine1,'linewidth', 2);
set(hLine2,'linewidth', 2);
xlabel('Voltage, Volt');
ylabel(hAx(1),'Current-sim, mA');
ylabel(hAx(2),'Current-test, mA');
title('Solar module test results, G=0.5, temp=65');
grid on;
subplot(4,1,2);
[hAx,hLine1,hLine2]=plotyy(V_sim,P_sim,V_test,P_test);
set(hLine1,'linewidth', 2);
set(hLine2,'linewidth', 2);
xlabel('Voltage, Volt');
ylabel(hAx(1),'Power-sim, mW');
ylabel(hAx(2),'Power-test, mW');
grid on;
subplot(4,1,3);
[hAx,hLine1,hLine2]=plotyy(V_sim,I_sim,V_sim,P_sim);
set(hLine1,'linewidth', 2);
set(hLine2,'linewidth', 2);
xlabel('Voltage, Volt');
ylabel(hAx(1),'Current-sim, mA');
ylabel(hAx(2),'Power-sim, mW');
grid on;
subplot(4,1,4);
[hAx,hLine1,hLine2]=plotyy(V_test,I_test,V_test,P_test);
set(hLine1,'linewidth', 2);
set(hLine2,'linewidth', 2);
xlabel('Voltage, Volt');
ylabel(hAx(1),'Current-test, mA');
ylabel(hAx(2),'Power-test, mW');
grid on;
```

16.2.2 Photovoltaic module model + DC/DC converter schematic

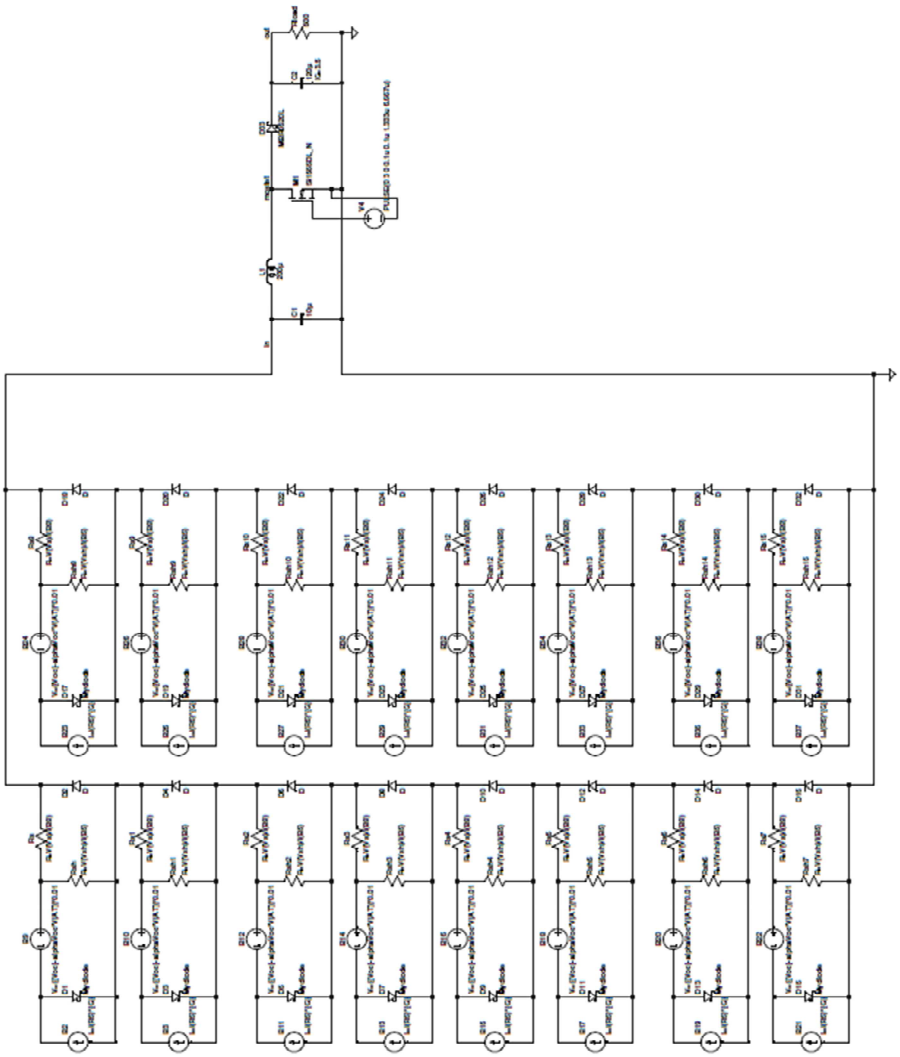

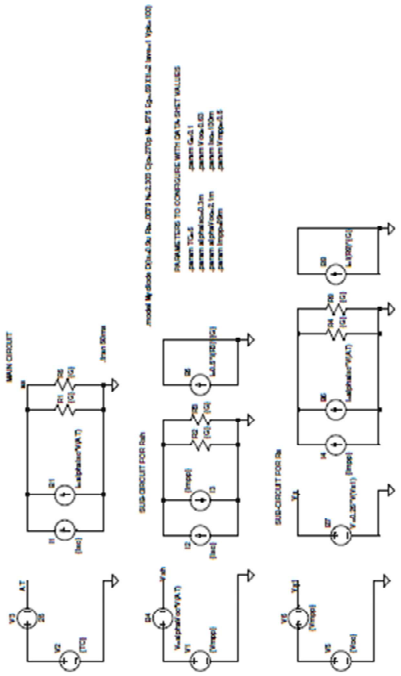

16.2.3 DC/DC converter behaviour signals

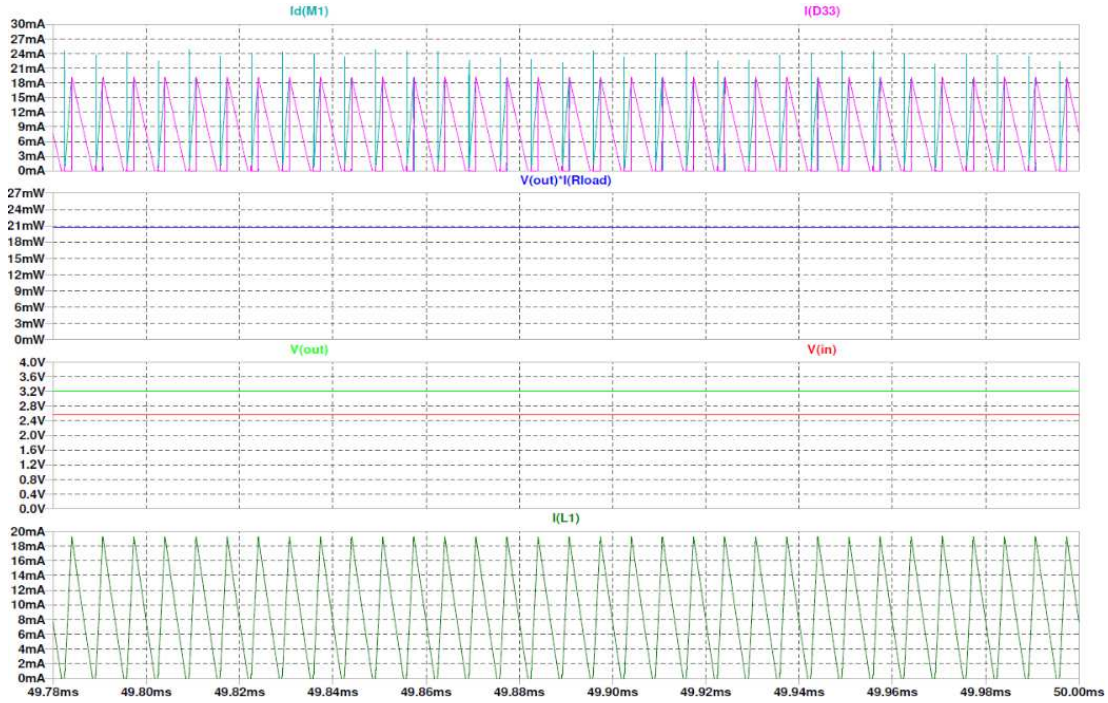

a) case is with 0.1 suns of irradiance and at 10 ºC temperature. Switching frequency of mosfet was set at 150 kHz with a duty-cycle of 0.2

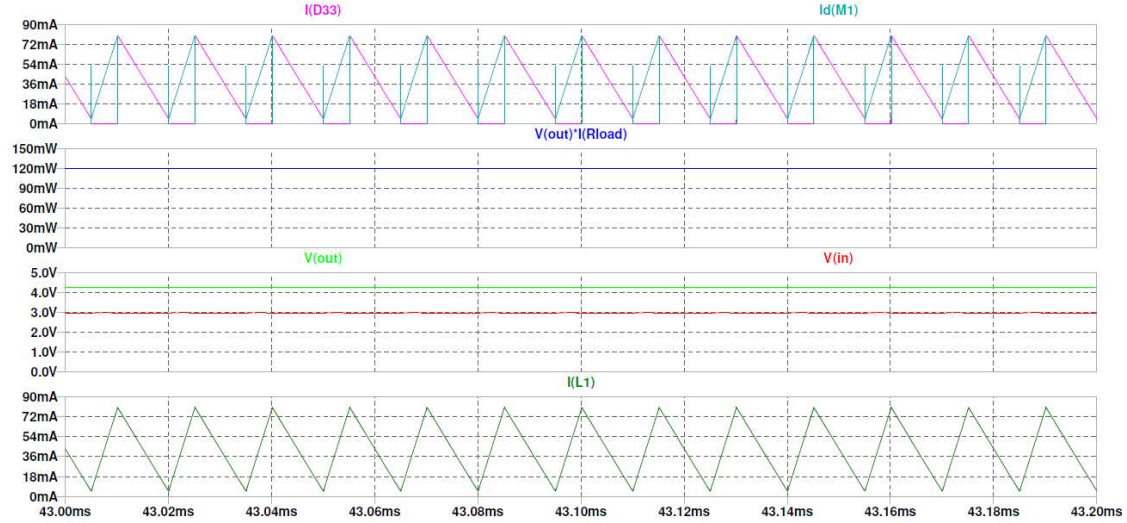

b) case is with 0.5 suns of irradiance and at 15 ºC temperature. Switching frequency of mosfet was set at 66 kHz with a duty-cycle of 0.3.

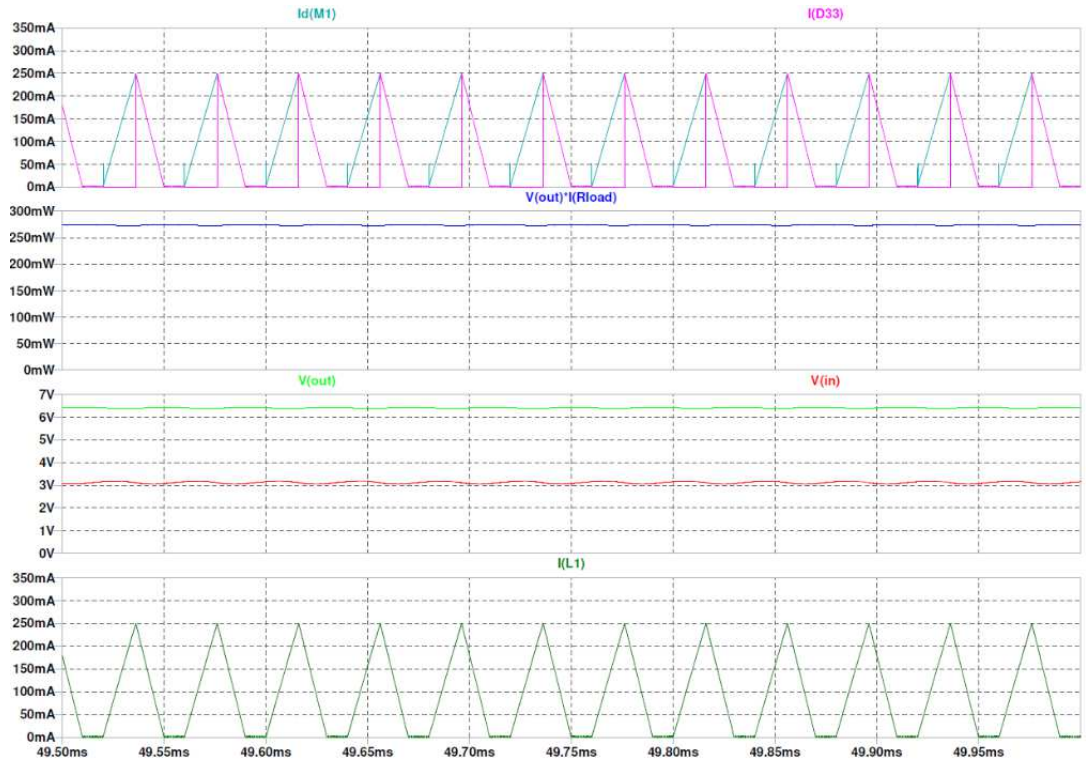

c) case is with 1 sun of irradiance and at 60 ºC temperature. Switching frequency of mosfet was set at 25 kHz with a duty-cycle of 0.4.

16.3 AC input system

16.3.1 Power coefficients comparison

Cp coefficient	c1	c2	c3	c4	c5	c6	c7	c8	c9
MHAWT	0.6	160	0.93	0	0	9.3	9.8	0.037	0
CSMWT	0.5	116	0.4	0	0	5	21	0.08	0.035

w (rpm)	w (rad/s)	Velocity (m/s)	Pwind (mW)	Paero (mW)	Cp (λ,θ)	λi	λ
MHAWT							
9495.263	997.003	3	13.719	3.622	0.2640	2.4544	1.1798
14271.563	1498.514	4	32.518	9.104	0.2800	2.6046	1.3299
19344.225	2031.144	5	63.513	18.147	0.2857	2.7168	1.4421
24057.113	2525.997	6	109.750	31.443	0.2865	2.7692	1.4945
26180.963	2749.001	7	174.279	49.484	0.2839	2.6688	1.3941
30666.525	3219.985	8	260.148	74.230	0.2853	2.7035	1.4289
35995.200	3779.496	9	370.405	106.114	0.2865	2.7655	1.4908
39616.688	4159.752	10	508.101	145.507	0.2864	2.7514	1.4767
CSMWT							
9495.263	997.003	3	13.719	0.353	0.0258	3.9358	1.1798
14271.563	1498.514	4	32.518	0.916	0.0282	4.0859	1.3299
19344.225	2031.144	5	63.513	1.890	0.0298	4.1981	1.4421
24057.113	2525.997	6	109.750	3.340	0.0304	4.2505	1.4945
26180.963	2749.001	7	174.279	5.071	0.0291	4.1501	1.3941
30666.525	3219.985	8	260.148	7.694	0.0296	4.1849	1.4289
35995.200	3779.496	9	370.405	11.254	0.0304	4.2468	1.4908
39616.688	4159.752	10	508.101	15.347	0.0302	4.2327	1.4767

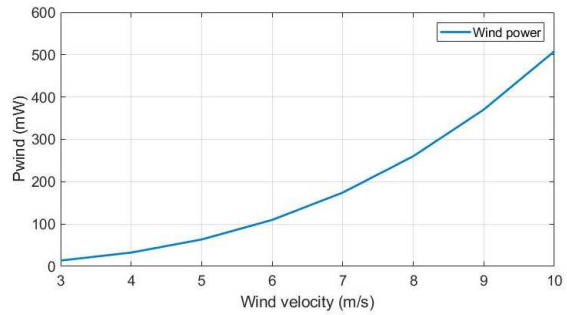

Wind power at different velocities

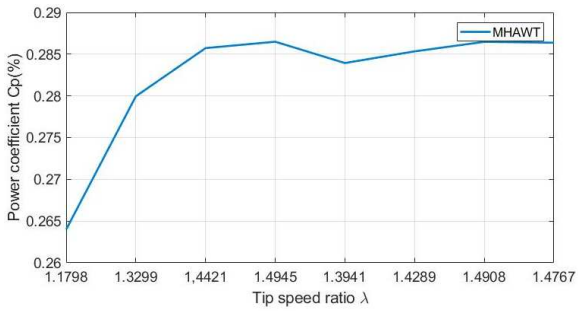

MHAWT power coefficient at different tip speed ratio

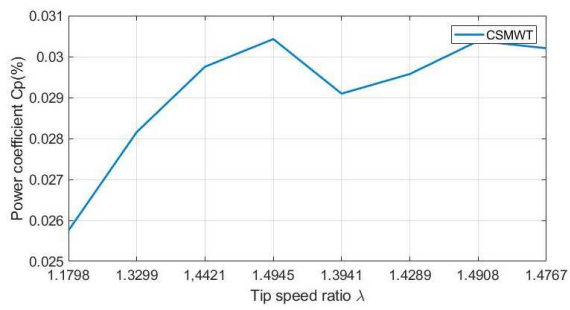

CSMWT power coefficient at different tip speed ratio

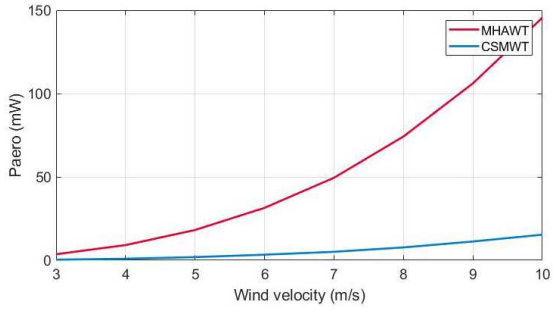

Harvested wind power

16.3.2 Micro-reactor model + AC/DC converter circuits

16.3.2.1 D-bridge

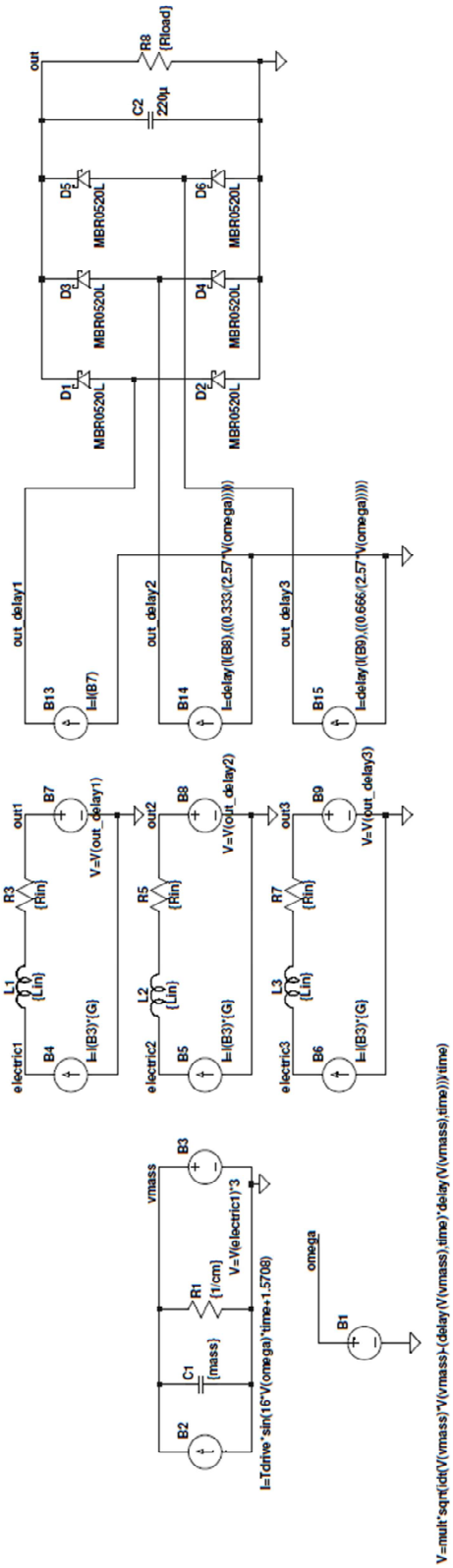

Schematic of mini-reactor model + diode bridge converter.

16.3.2.2 Voltage-doubler

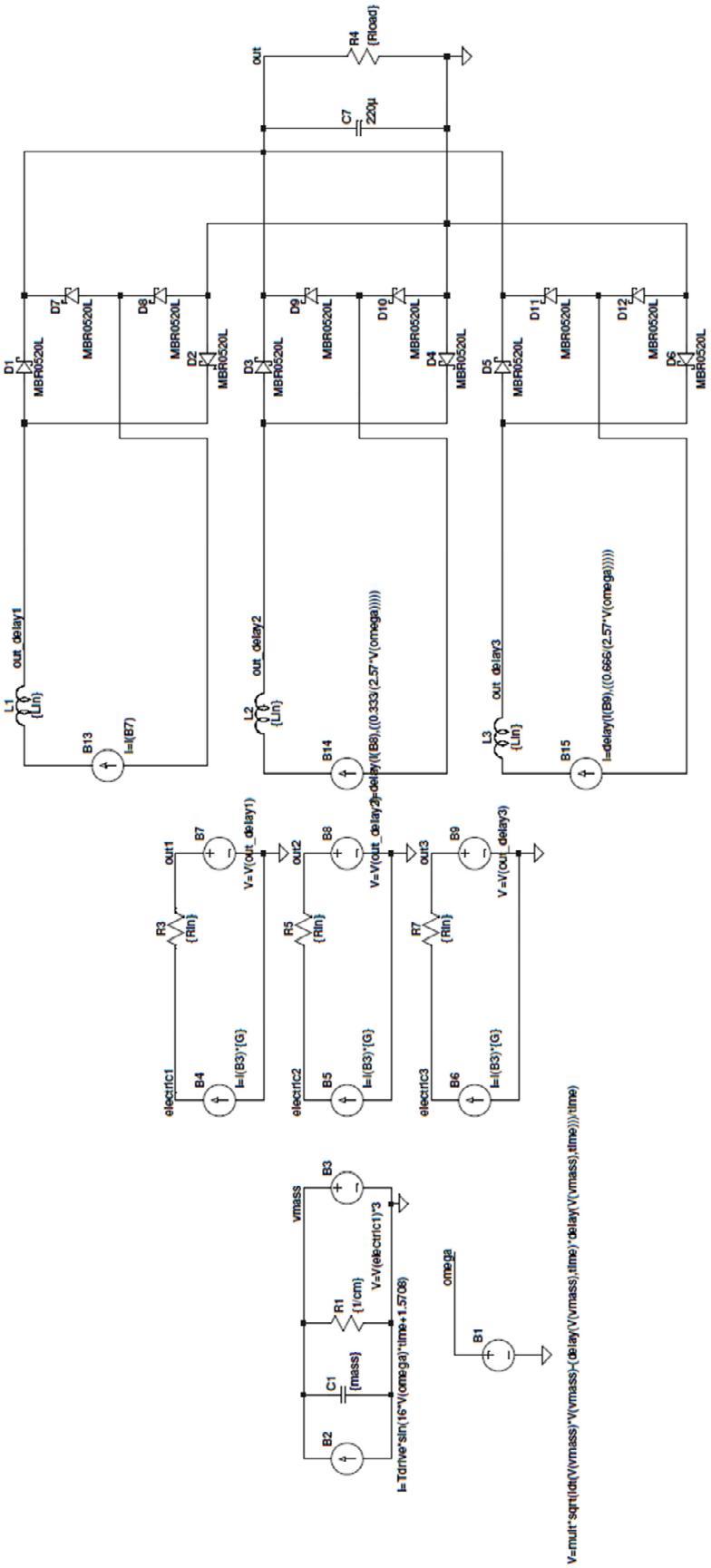

Schematic of mini-reactor model + voltage doubler converter.

16.3.2.3 Side-diode

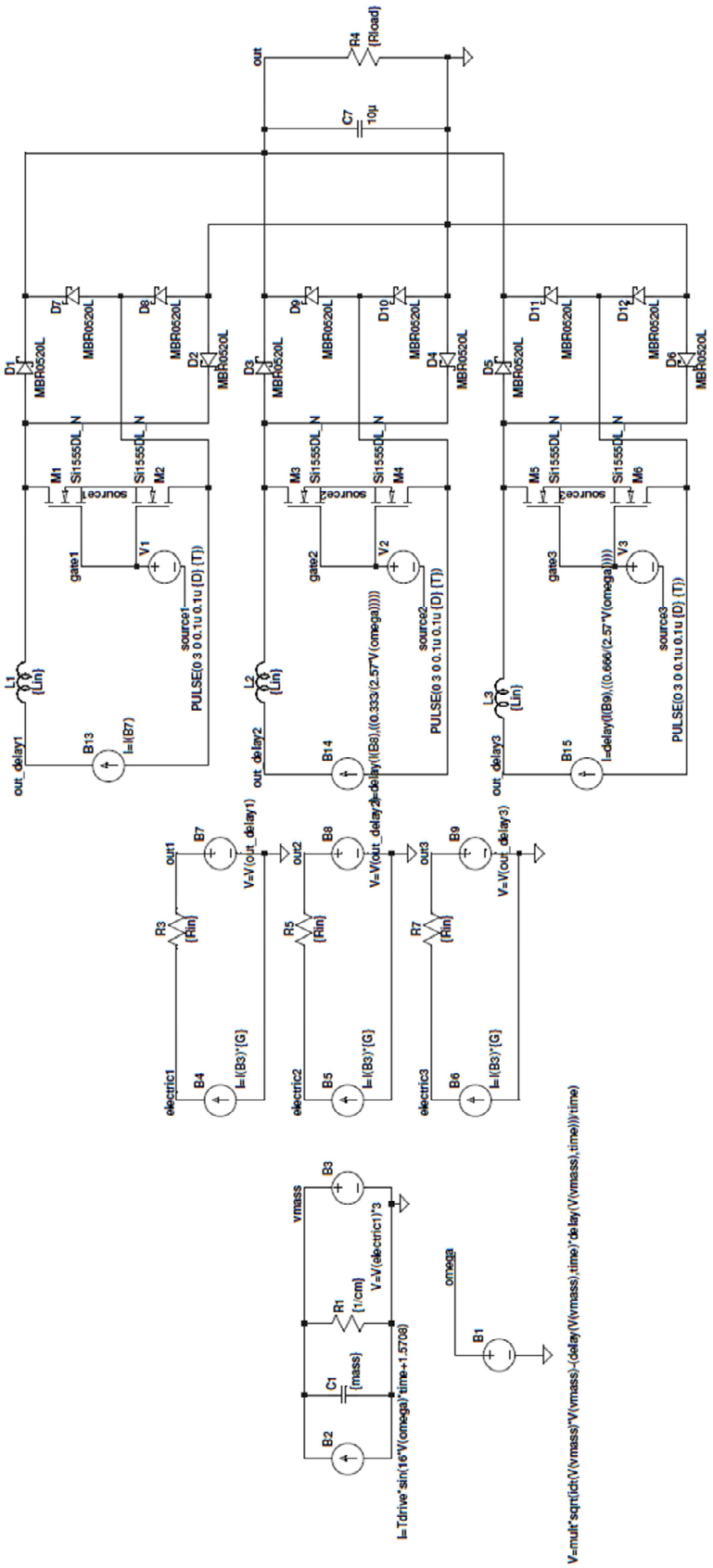

Schematic of mini-reactor model + side-diode converter.

16.3.2.4 Split N

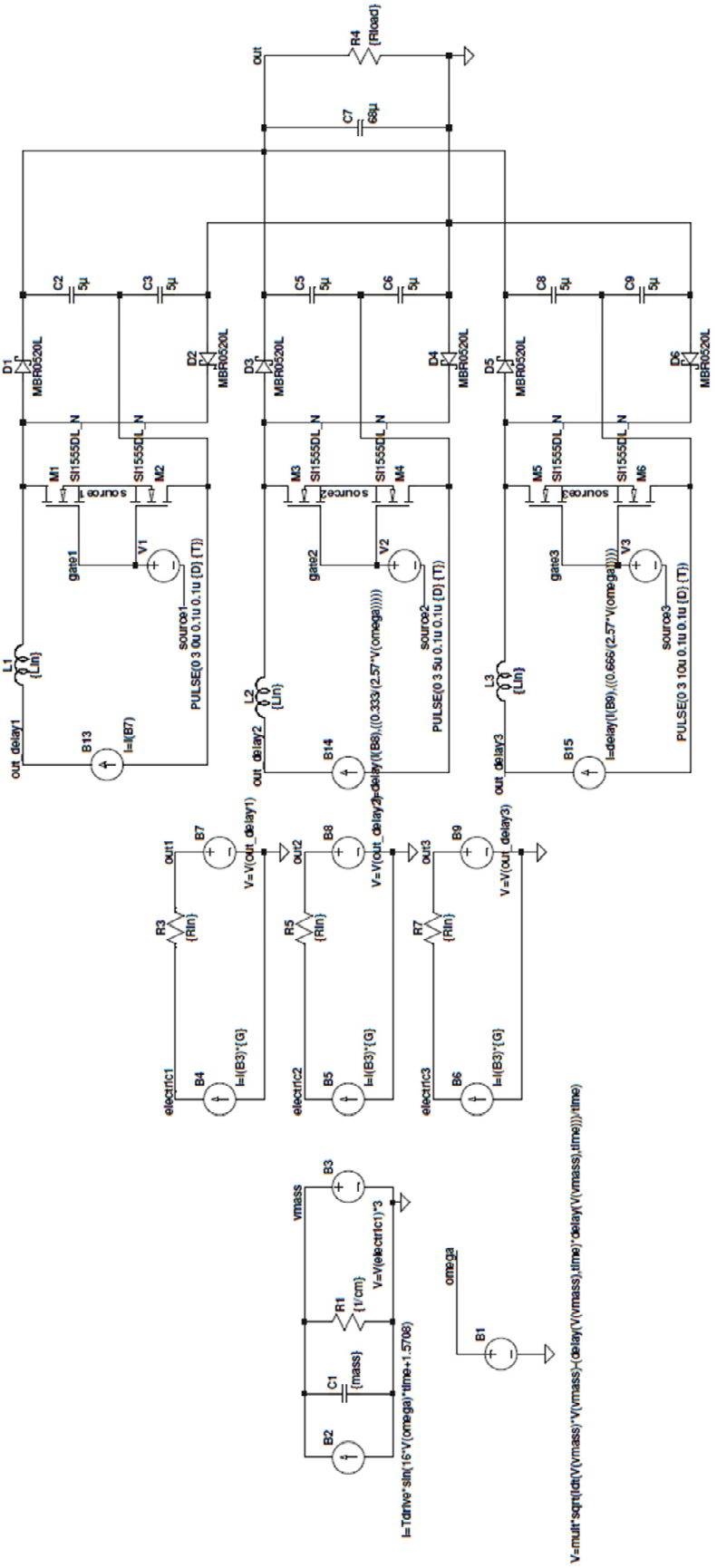

Schematic of mini-reactor model + Split N converter.

16.3.2.5 Split NP

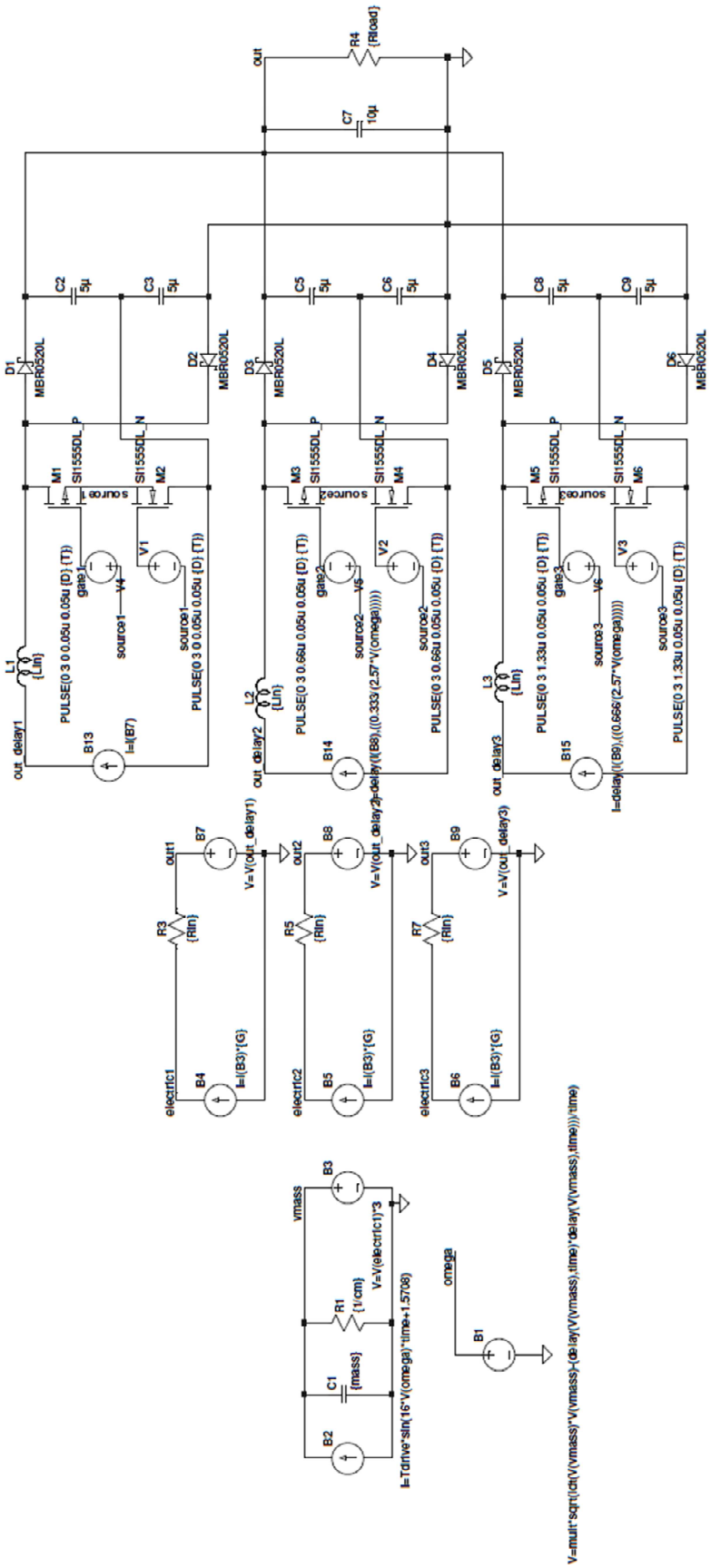

Schematic of mini-reactor model + Split NP converter.

16.3.3 AC/DC converters behaviour signals

16.3.3.1 Diode bridge

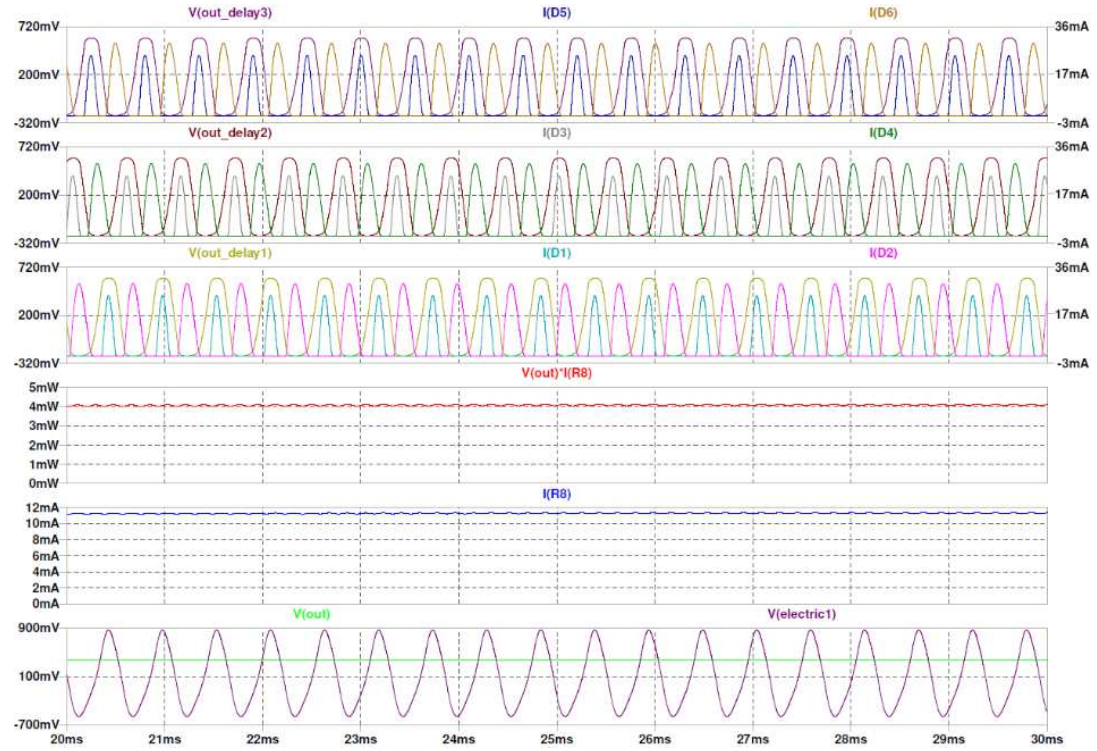

a) Diode bridge rectifier internal signals with 3 m/s wind velocity.

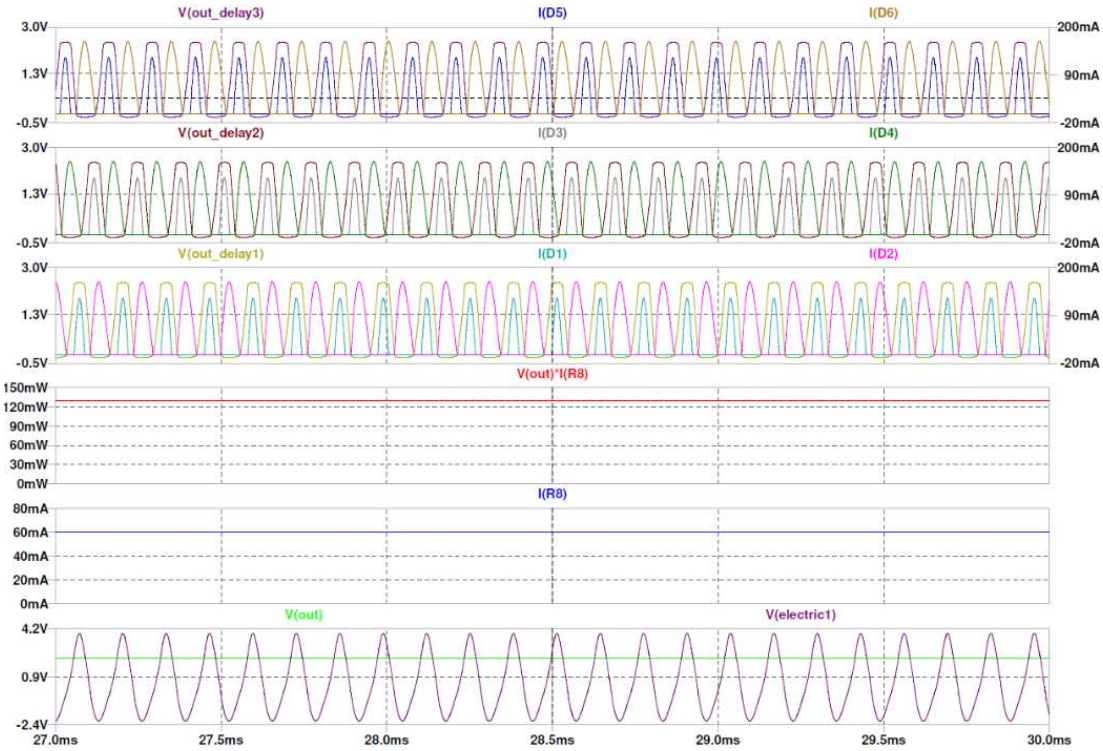

b) Diode bridge rectifier internal signals with 10 m/s wind velocity.

16.3.3.2 Voltage doubler

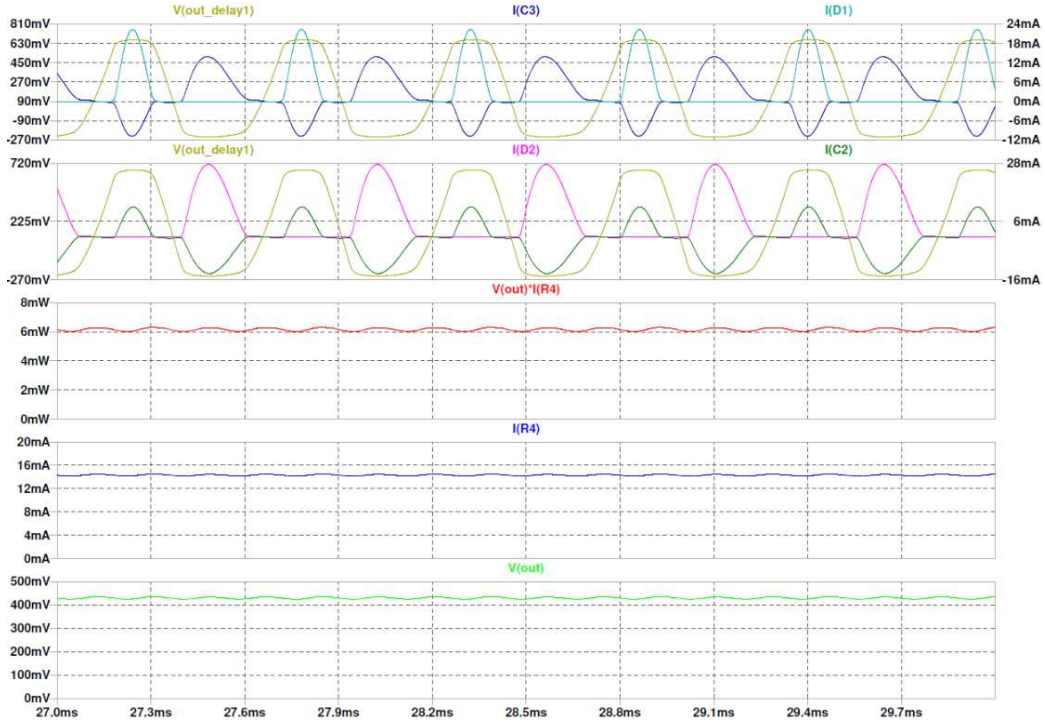

a) Voltage doubler internal signals with 3 m/s wind velocity.

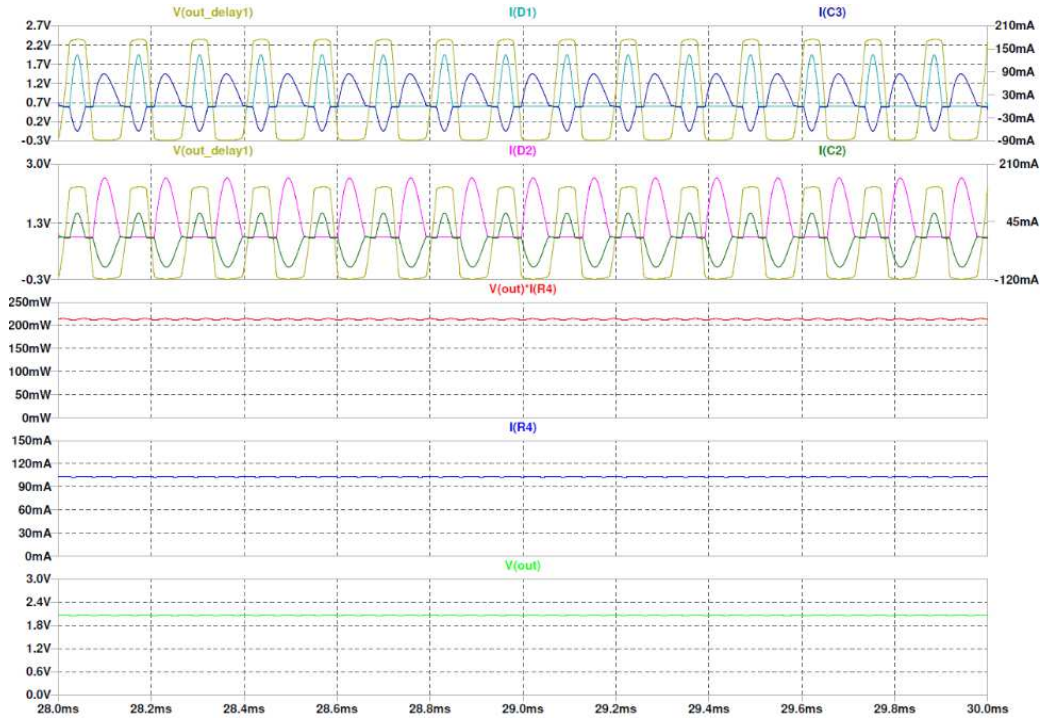

b) Voltage doubler internal signals with 10 m/s wind velocity.

16.3.3.3 Side-diode

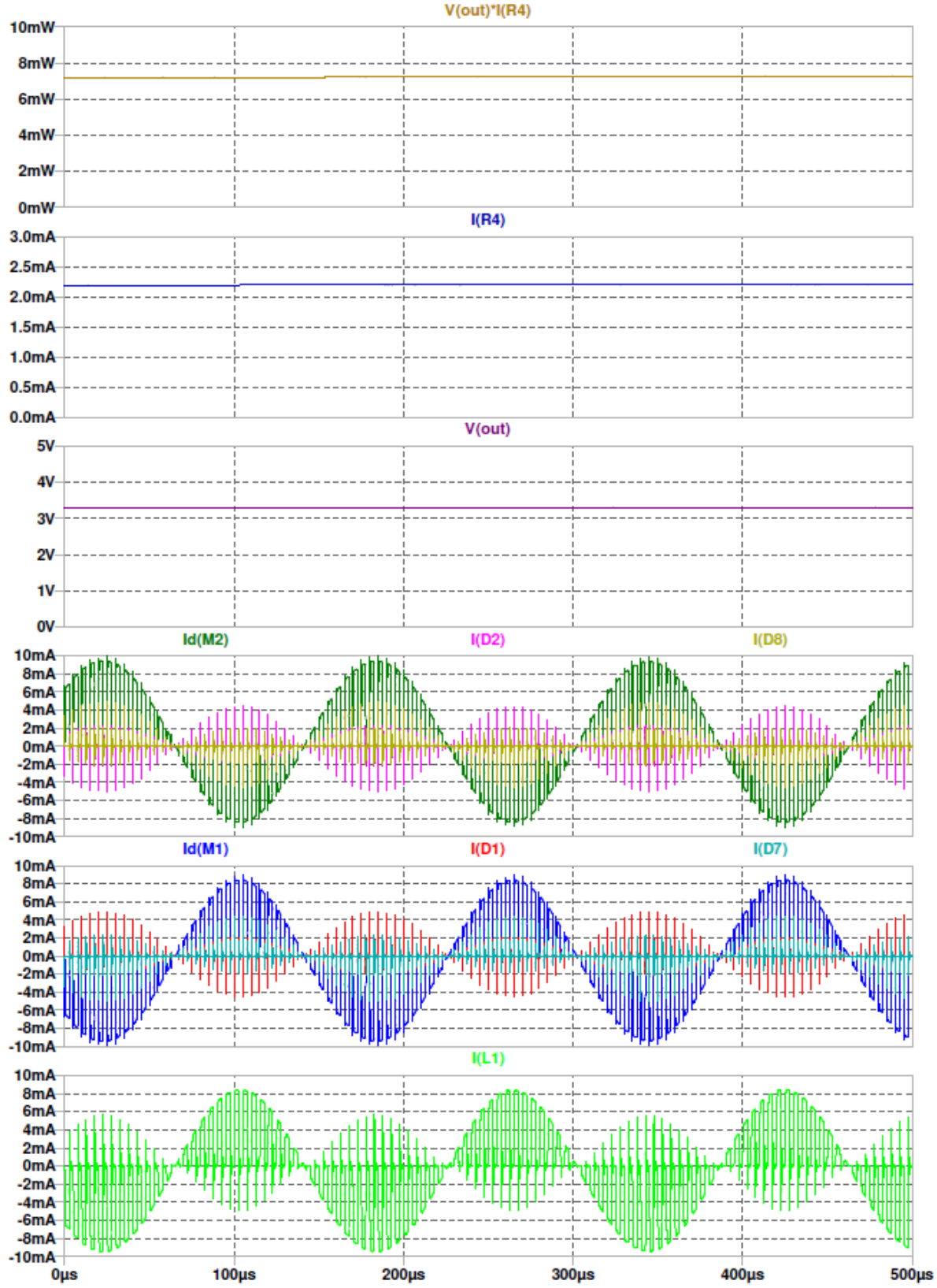

a) Side-diode converter internal signals with 3 m/s wind velocity.

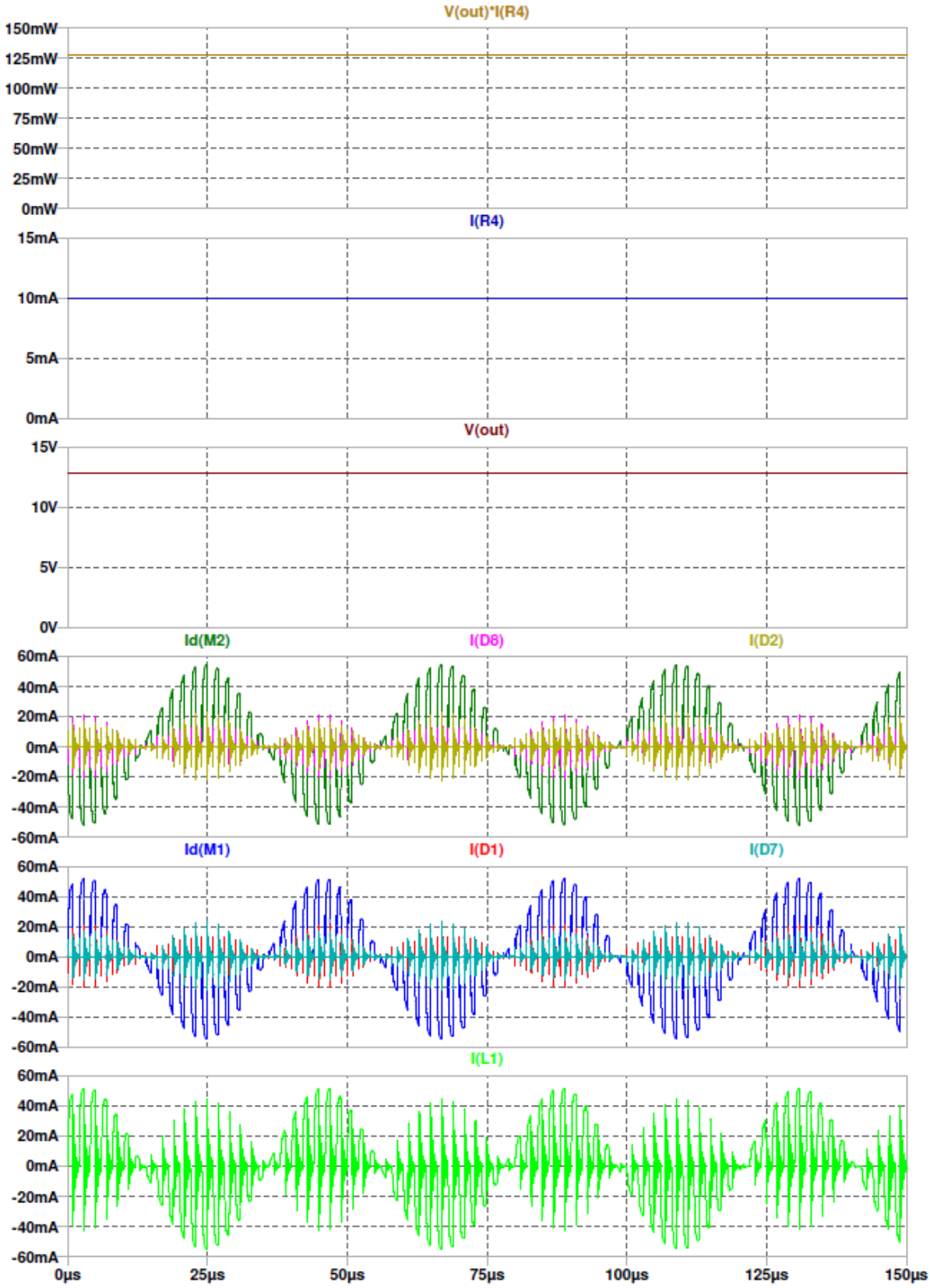

b) Side-diode converter internal signals with 10 m/s wind velocity.

16.3.3.4 Split N

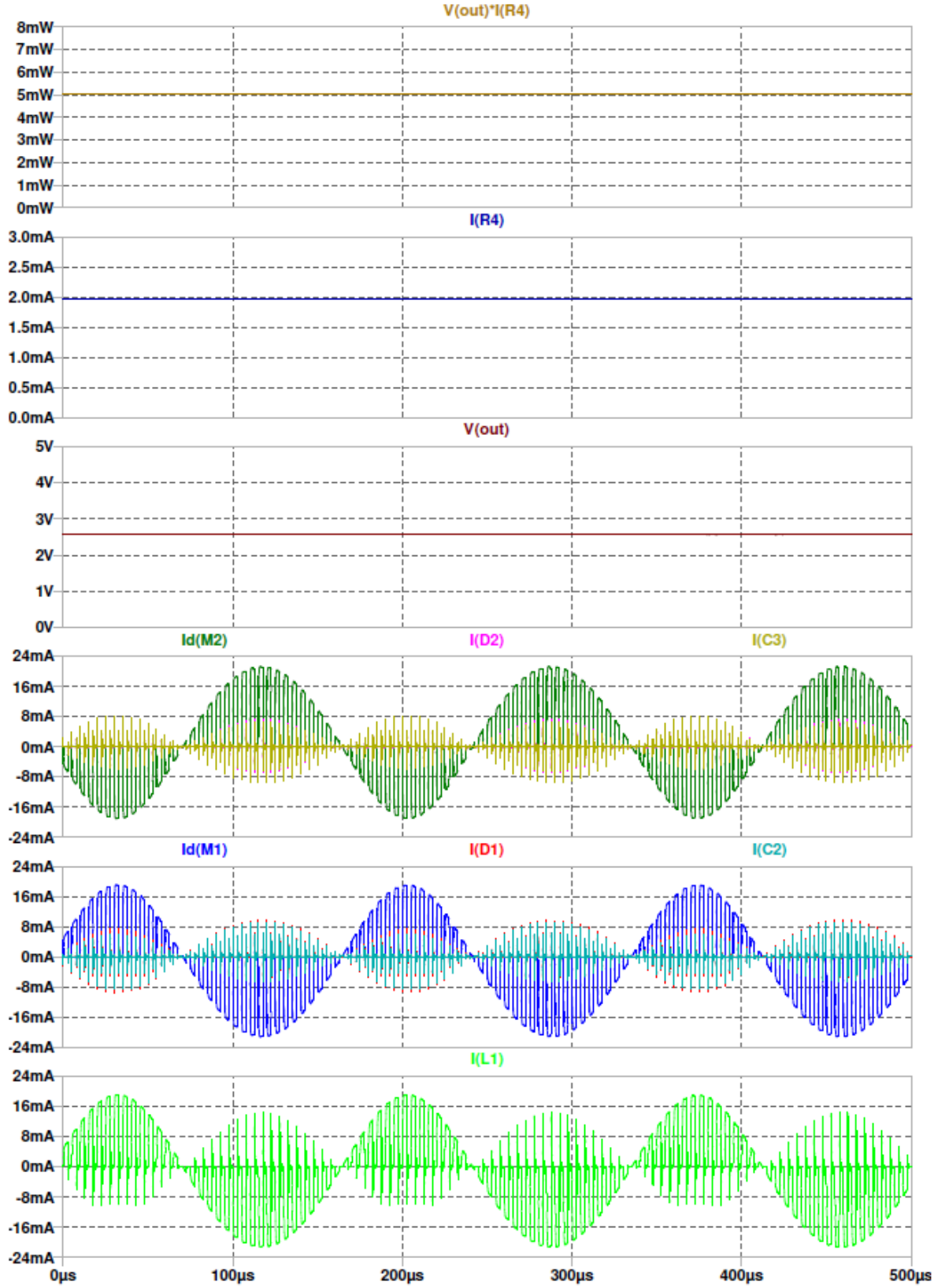

a) Split N converter internal signals with 3 m/s wind velocity.

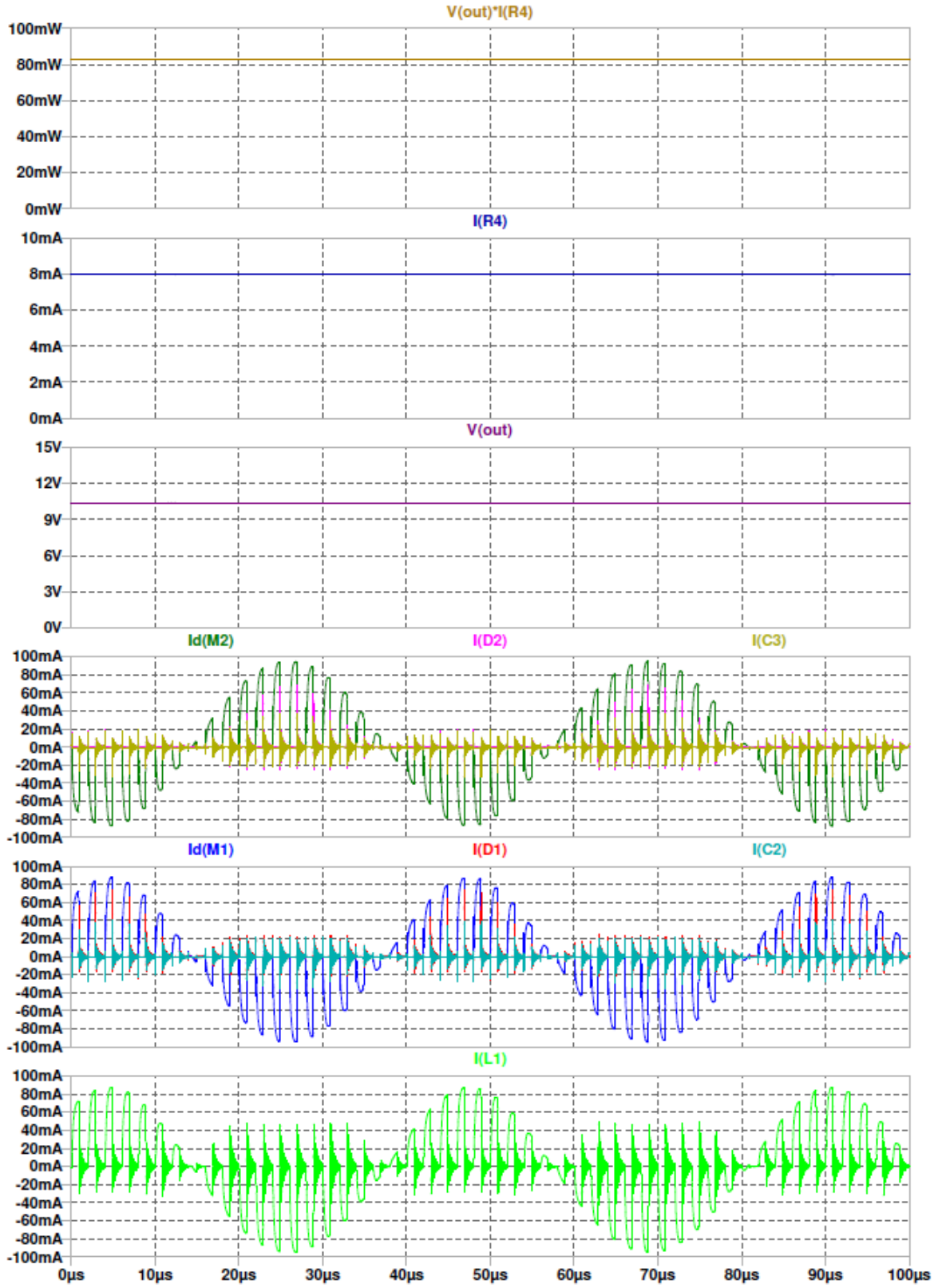

b) Split N converter internal signals with 10 m/s wind velocity.

16.3.3.5 Spilt NP

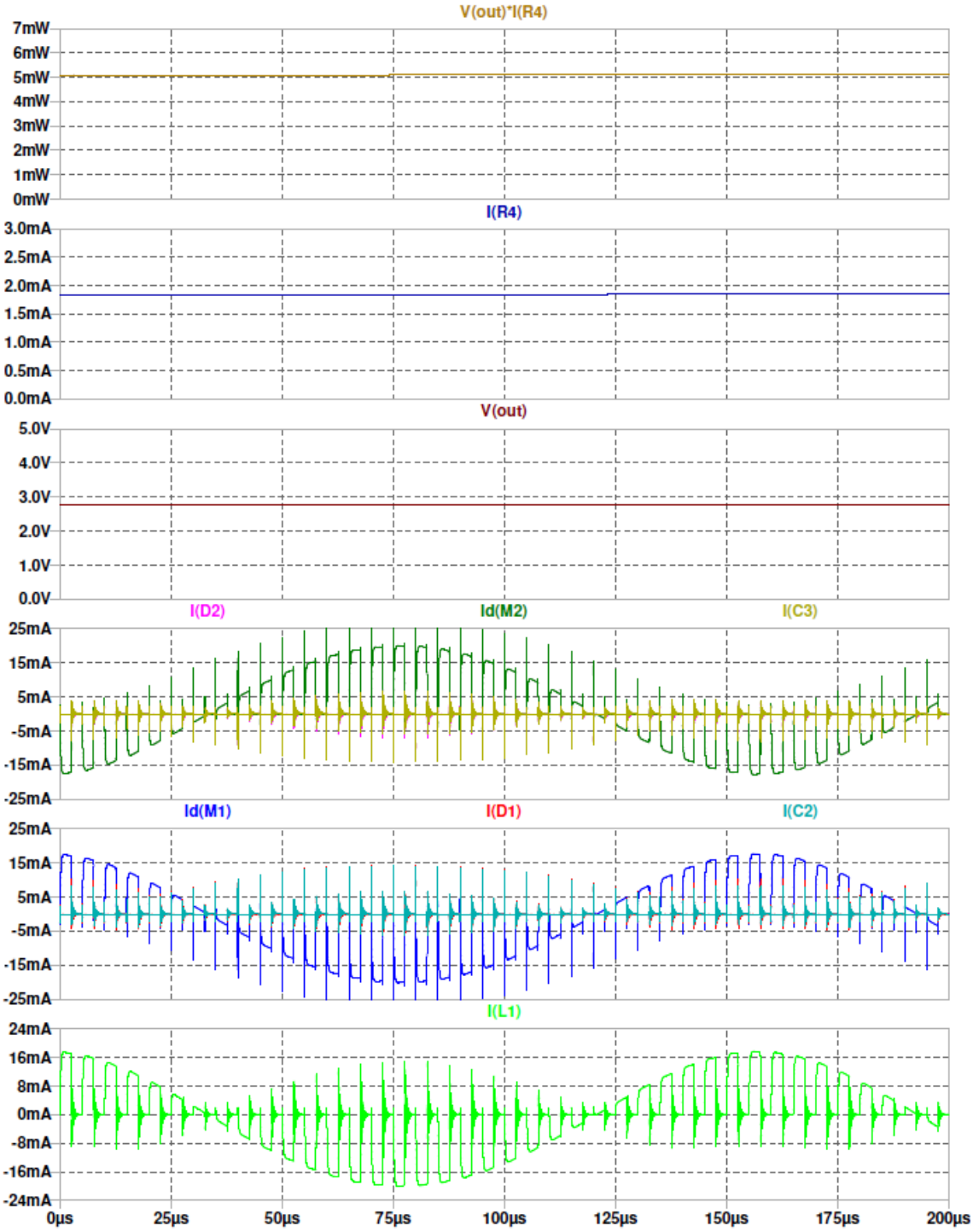

a) Split NP converter internal signals with 3 m/s wind velocity.

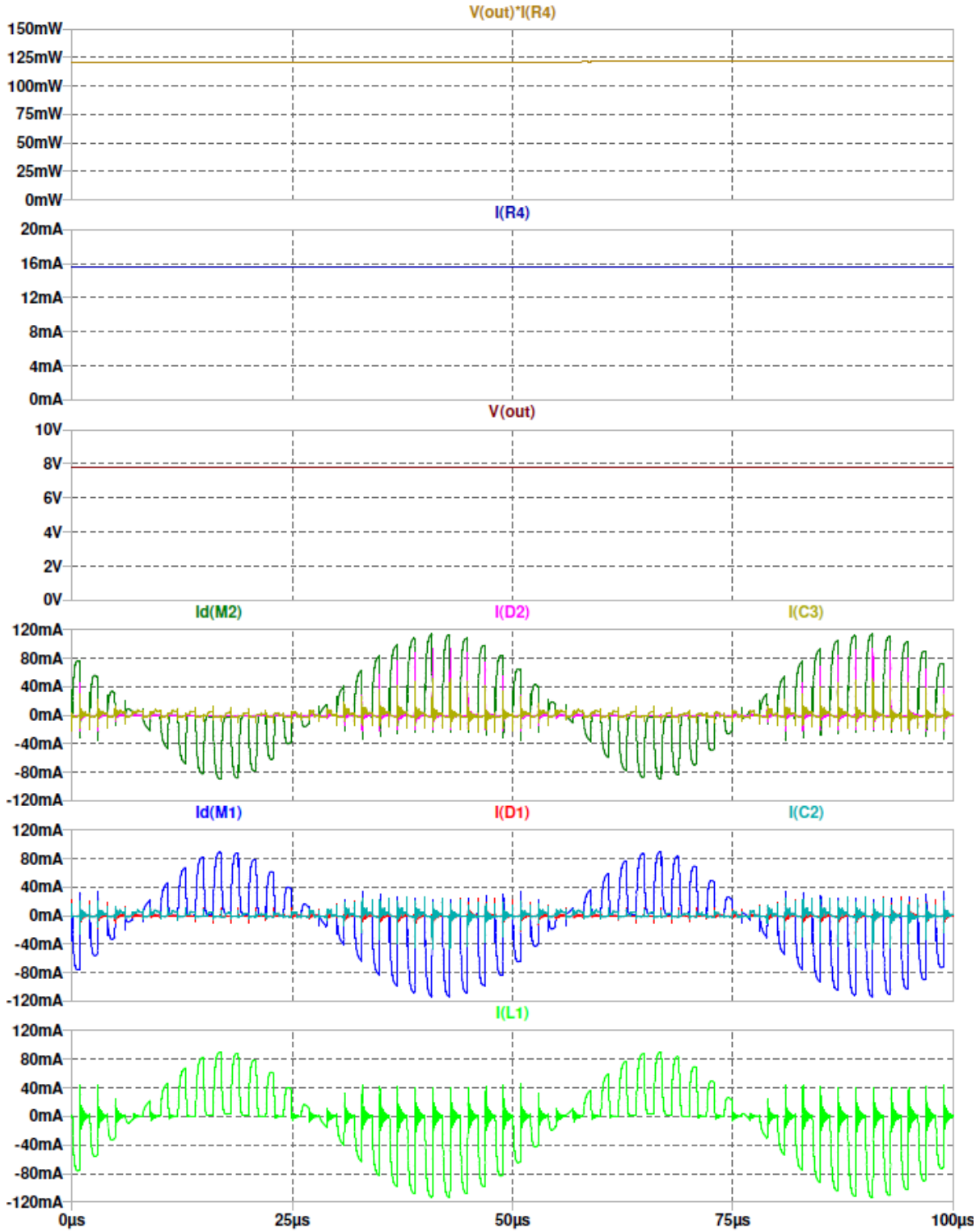

b) Split NP converter internal signals with 10 m/s wind velocity.

16.4 Supercapacitor

16.4.1 Schematic evaluation board

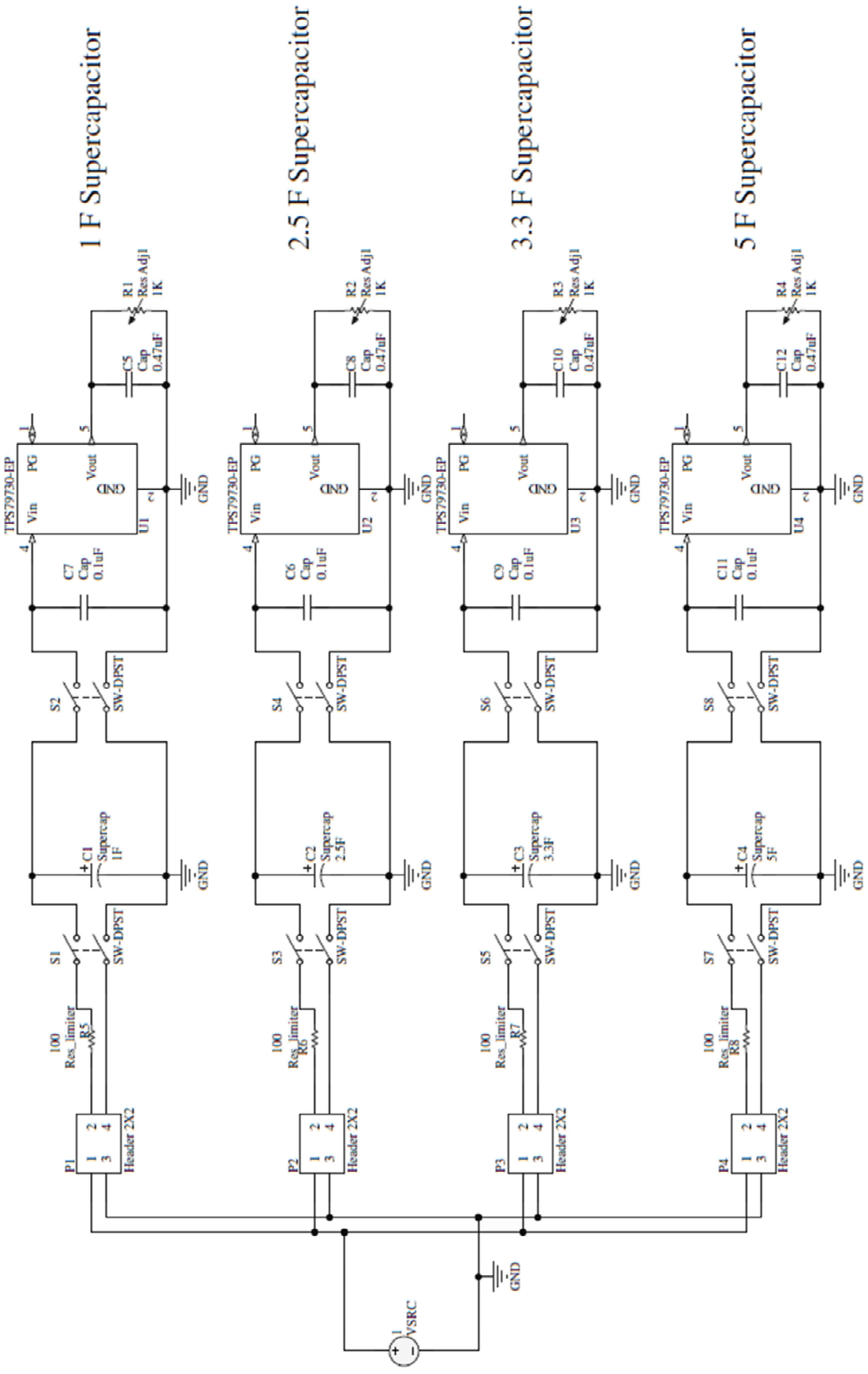

Supercapacitors evaluation board with space for four storage devices.

16.4.2 Test to validate supercapacitor models

Test	Cap. (F)	Temp. (ºC)	Charge (V)	Charge (seconds)	Discharge description
1	1 & 5	10	2.5	60	Self- discharge, 1 hour
2	1 & 5	25	2.5	600	Self- discharge, 2 hours
3	1 & 5	60	2.5	3600	Self- discharge, 3 hours
4	1 & 5	10	5	60	Self- discharge, 1 hour
5	1 & 5	25	5	60	Self- discharge, 1 hour
6	1 & 5	40	5	60	Self- discharge, 1 hour
7	1 & 5	60	5	60	Self- discharge, 1 hour
8	1 & 5	10	5	600	Self- discharge, 2 hours
9	1 & 5	25	5	600	Self- discharge, 2 hours
10	1 & 5	40	5	600	Self- discharge, 2 hours
11	1 & 5	60	5	600	Self- discharge, 2 hours
12	1 & 5	10	5	3600	Self- discharge, 3 hours
13	1 & 5	25	5	3600	Self- discharge, 3 hours
14	1 & 5	25	5	600	1. SW= Off, I= leak, t= 30 seg 2. V=3 V, R= 1 kΩ, I= 3 mA, t= 1:30 min 3. V=3 V, R= 51 kΩ, I= 0.058 mA, t= 10 min 4. SW= Off, I= leak, t= 20 min 5. V=3 V, R= 10k Ω, I= 0.3 mA, t= finish
15	1 & 5	60	5	600	1. V=3 V, R= 10 kΩ, I= 0.3 mA, t= 3 min 2. V=3 V, R= 30 kΩ, I= 0.1 mA, t= 10 min 3. V=3 V, R= 51 kΩ, I= 0.058 mA, t= finish
16	1 & 5	10	5	600	1. V=3 V, R= 150 kΩ, I= 0.02 mA, t= finish
17	1 & 5	40	5	600	1. V=3 V, R=3 kΩ, I= 1 mA, t= finish
18	1 & 5	10	5	3600	1. V=3 V, R= 100 kΩ, I= 0.03 mA, t= 70 min 2. V=3 V, R= 2 kΩ, I= 1.5 mA, t= 30 min 3. SW= Off, I= leak, t= finish
19	1 & 5	25	5	3600	1. V=3V, R= 120 kΩ, I= 0.025 mA, t= finish
20	1 & 5	60	5	3600	1. V=3V, R= 510 Ω, I= 5.88 mA, t= finish
21	1 & 5	40	5	3600	1. SW= Off, I= leak, t= 40 min 2. V=3V, R= 1 kΩ, I= 3 mA, t= 30 min 3. V=3V, R= 120 kΩ, I= 0.025 mA, t= 40 min 4. V=3V, R= 2 kΩ, I= 1.5 mA, t= 20 min 5. SW= Off, I= leak, t= finish

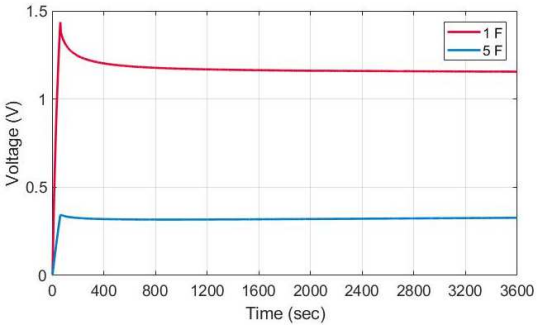

1) Temperature 10 ºC, charge voltage 2.5 V, charge time 60 seconds; self-discharge.

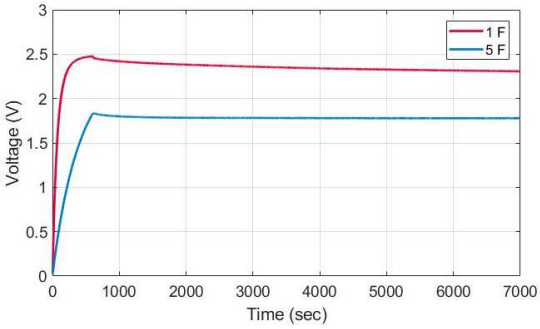

2) Temperature 25 ºC, charge voltage 2.5 V, charge time 600 seconds; self-discharge.

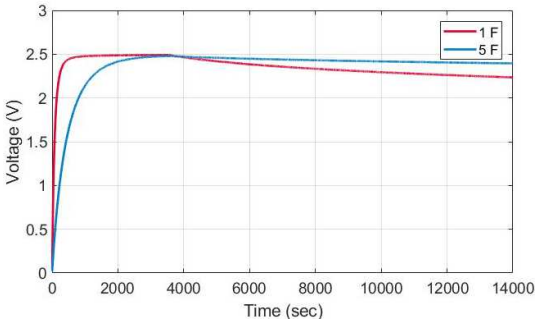

3) Temperature 40 ºC, charge voltage 2.5 V, charge time 3600 seconds; self-discharge.

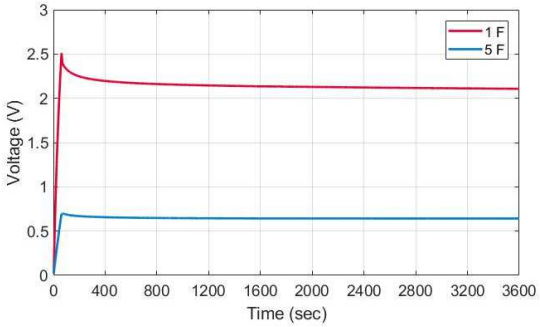

4) Temperature 10 ºC, charge voltage 5 V, charge time 60 seconds; self-discharge.

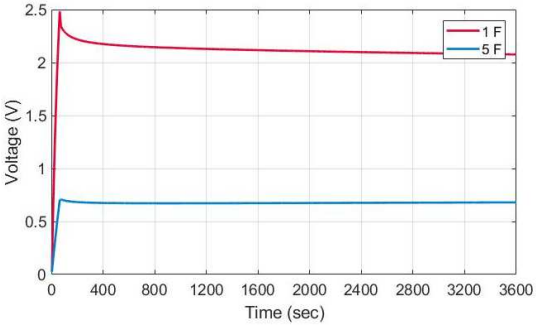

5) Temperature 25 ºC, charge voltage 5 V, charge time 60 seconds; self-discharge.

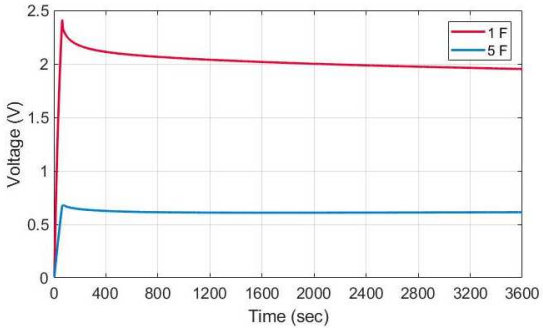

6) Temperature 40 ºC, charge voltage 5 V, charge time 60 seconds; self-discharge.

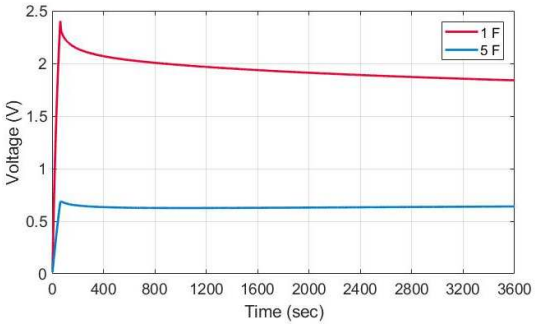

7) Temperature 60 ºC, charge voltage 5 V, charge time 60 seconds; self-discharge.

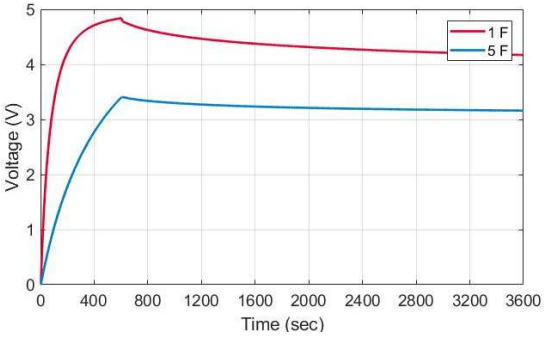

8) Temperature 10 ºC, charge voltage 5 V, charge time 600 seconds; self-discharge.

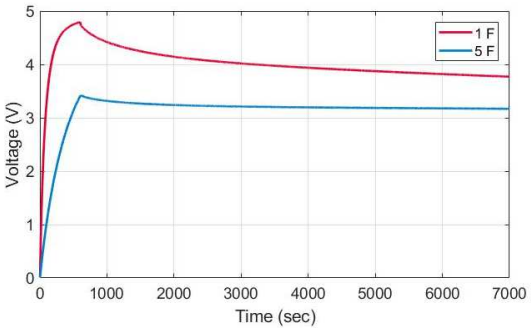

9) Temperature 25 ºC, charge voltage 5 V, charge time 600 seconds; self-discharge.

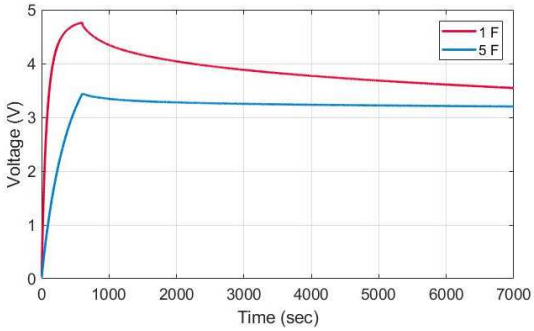

10) Temperature 40 ºC, charge voltage 5 V, charge time 600 seconds; self-discharge.

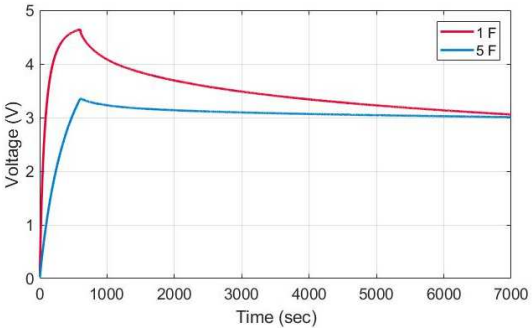

11) Temperature 60 ºC, charge voltage 5 V, charge time 600 seconds; self-discharge.

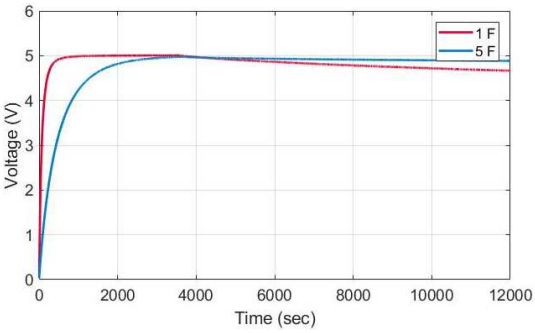

12) Temperature 10 ºC, charge voltage 5 V, charge time 3600 seconds; self-discharge.

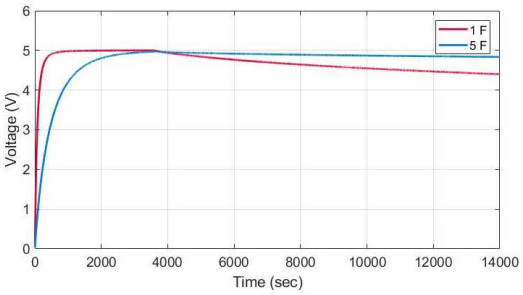

13) Temperature 25 ºC, charge voltage 5 V, charge time 3600 seconds; self-discharge.

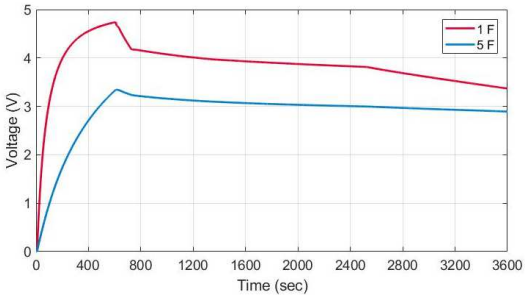

14) Temperature 25 ºC, charge voltage 5 V, charge time 600 seconds; 4 discharge steps.

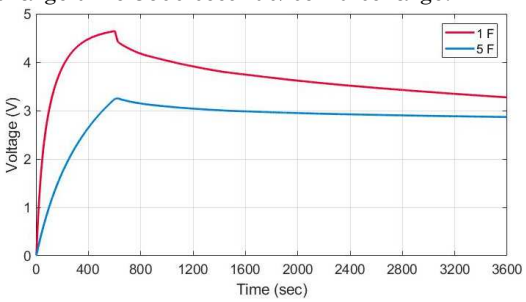

15) Temperature 60 ºC, charge voltage 5 V, charge time 600 seconds; 4 discharge steps.

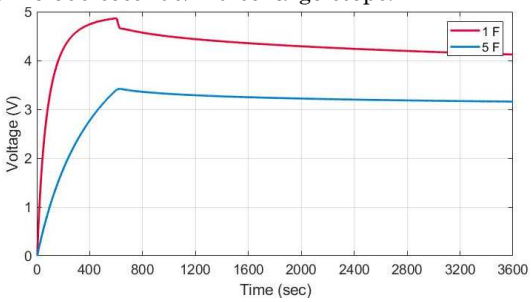

16) Temperature 10 ºC, charge voltage 5 V, charge time 600 seconds; 1 discharge step.

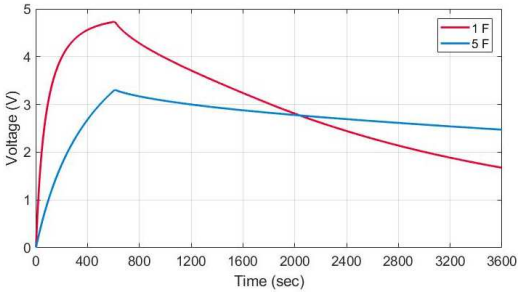

17) Temperature 40 ºC, charge voltage 5 V, charge time 600 seconds; 1 discharge step.

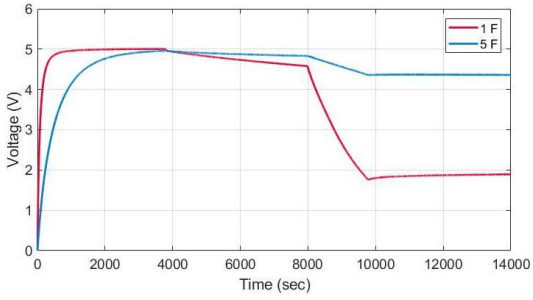

18) Temperature 10 ºC, charge voltage 5 V, charge time 3600 seconds; 4 discharge steps.

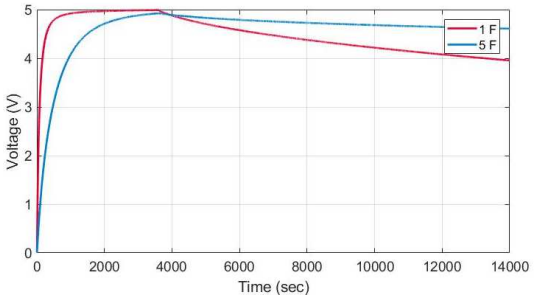

19) Temperature 25 ºC, charge voltage 5 V, charge time 3600 seconds; 1 discharge step.

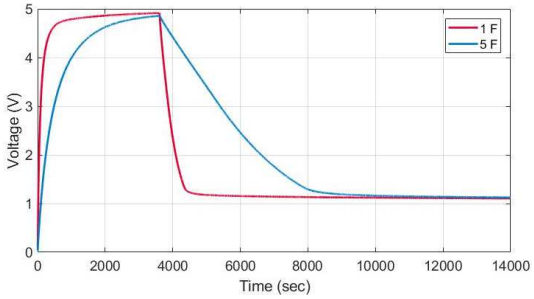

20) Temperature 40 ºC, charge voltage 5 V, charge time 3600 seconds; 1 discharge step.

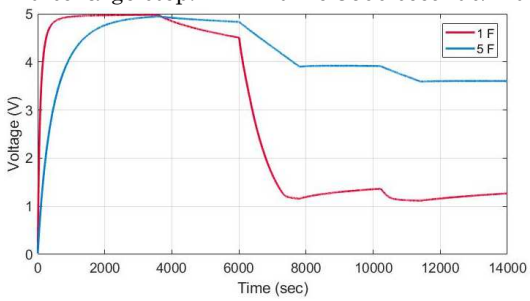

21) Temperature 60ºC, charge voltage 5 V, charge time 3600 seconds; 4 discharge steps.

16.4.3 Electro-mathematical model code

```
%Charge and Rleak

   for i=1:quan
     for z=1:at(i)
        for j=1: at(i)
           if j==1
             u_ch{i,z}(j)=0;
           else
             u_ch{i,z}(j)=Vcell_charge{i,z}(1)*exp(-tch{i,z}(j)/tlk{i}(z));
           end

           k_ch{i,z}(j)=2*(Icell_charge{i}(z)* at(i)-Cdl(i)*(Av(i)))./((Av(i))^2);

           C1_ch{i,z}(j)=Cdl(i)+k_ch{i,z}(j)*u_ch{i,z}(j);
           Rlk_ch{i,z}(j)=(tlk{i}(z))./C1_ch{i,z}(j);

           Vcell_charge{i,z}(j)=-Icell_charge{i}(z)*Resr(i)+Icell_charge{i}(z)*Rlk_ch{i,z}(j).*(1-exp(-
tch{i,z}(j)/(Rlk_ch{i,z}(j).*Cdl(i))));
           time_start{i,z+1}=j;
        end
     end
  end

%Union of charge profiles
  for i=1:quan
    Vcell_charge{i,at(i)+1} = Vcell_charge{i,1}(1:time_start{i,2}-1);
    for z=2:at(i)
      Vcell_charge{i,z} = Vcell_charge{i,z}-Vcell_charge{i,z}(time_start{i,z})+Vcell_charge{i,z-1}(time_start{i,z});
      Vcell_charge{i,at(i)+1} = [Vcell_charge{i,at(i)+1} Vcell_charge{i,z}(time_start{i,z}:time_start{i,z+1}-1)];
    end
    leyenda{i} = [num2str(C0(i)) 'F'];
    Vcell_charge{i,at(i)+1} = [Vcell_charge{i,at(i)+1} Vcell_charge{i,at(i)}(time_start{i,at(i)+1}:end)];

%Discharge without load

    for i=1:quan
          Icell_discharge_load{i}(1)=10e-6;
          tlk_dis{i}=-log(0.7/Vcell_charge{i,at(i)+1}(at(i)))*((Vcell_charge{i,at(i)+1}(at(i))/ Icell_discharge_load{i}(1))*Cdl(i));
          tdis{i}=1:1:tlk_dis{i};
  end
  for i=1:quan
```

```
    for j=1:50000
      if j==1
        Vcell_discharge{i}(j)=-Icell_discharge_load{i}(1)*Resr(i)+Vcell_charge{i,at(i)}(at(i))-
(Vcell_charge{i,at(i)+1}(at(i))+Icell_discharge_load{i}(1)*Rlk_ch{i,at(i)}(at(i))).*(1-exp(-
tdis{i}(j)/(Rlk_ch{i,at(i)}(at(i)).*Cdl(i))));
        Rlk_dis{i}(1)=Rlk_ch{i,at(i)}(at(i));
      else
        Icell_discharge_load{i}(j)= Icell_discharge_load{i}(j-1)*(exp(-tdis{i}(j-1)/(Rlk_dis{i}(j-1).*Cdl(i))));
        u_dis{i}(j)=Vcell_charge{i,at(i)+1}(1)*exp(-tdis{i}(j)/tlk_dis{i});
        k_dis{i}(j)=2*( Icell_discharge_load{i}(j)*tlk_dis{i}-
Cdl(i)*(Vcell_charge{i,at(i)}(at(i))))./((Vcell_charge{i,at(i)+1}(at(i)))^2);

        C1_dis{i}(j)=Cdl(i)+k_dis{i}(j)*u_dis{i}(j);
        Rlk_dis{i}(j)=(tlk_dis{i})./C1_dis{i}(j);

        Vcell_discharge{i}(j)=- Icell_discharge_load{i}(j)*Resr(i)+Vcell_charge{i,at(i)+1}(at(i))-(Vcell_discharge{i}(j-1)+
Icell_discharge_load{i}(j)*Rlk_dis{i}(j)).*(1-exp(-tdis{i}(j)/(Rlk_dis{i}(j).*Cdl(i))));

       Icell_discharge_plot{i}(j)=Icell_discharge_load{i}(j-1);
      end
    end
  end


%Discharge with load

   for i=1:quan
     for z=1:quan_load
       tlk_dis_load{i}(z)=-log(0.7/Vcell_charge{i}(at(i)))*((Vcell_charge{i}(at(i))/Icell_discharge_load{i}(z))*Cdl(i));
       tdis_load{i,z}=1:1:tlk_dis_load{i}(z);
     end
   end
  for i=1:quan
    for z=1:quan_load(i)
      for j=1: tlk_dis_load{i}(z)
        if j==1
         Vcell_discharge_load{i,z}(j)=-Icell_discharge_load{i}(z)*Resr(i)+Vcell_charge{i}(at(i))-(Vcell_charge{i}(at(i))+
         Icell_discharge_load{i}(z)*Rlk_ch{i}(at(i))).*(1-exp(-tdis_load{i,z}(j)/(Rlk_ch{i}(at(i)).*Cdl(i))));
        else
          u_dis_load{i,z}(j)=Vcell_charge{i}(1)*exp(-tdis_load{i,z}(j)/ tlk_dis_load{i}(z));
         k_dis_load{i,z}(j)=2*(Icell_discharge_load{i}(z)* tlk_dis_load{i}(z) Cdl(i)*(Vcell_charge{i}(at(i)))./
         ((Vcell_charge{i}(at(i)))^2);

         C1_dis_load{i,z}(j)=Cdl(i)+k_dis_load{i,z}(j)*u_dis_load{i,z}(j);
         Rlk_dis_load{i,z}(j)=(tlk_dis_load{i}(z))./C1_dis_load{i,z}(j);

         Vcell_discharge_load{i,z}(j)=-Icell_discharge_load{i}(z)*Resr(i)+Vcell_charge{i}(at(i))-(Vcell_discharge_load{i,z}(j-
         1)+Icell_discharge_load{i}(z)*Rlk_dis_load{i,z}(j)).*(1-exp(-tdis_load{i,z}(j)/(Rlk_dis_load{i,z}(j).*Cdl(i))));
        end
      end
       Icell_discharge_load_plot{i,z}=Icell_discharge_load{i}(z)*ones(1,j);
    end
  end

%Union of discharge curves

  for i=1:quan
   Vcell_discharge_load{i,quan_load(i)+1} = Vcell_discharge_load{i,1}(1:time_start_dis{i,2}-1);
     Icell_discharge_load_plot{i,quan_load(i)+1} = Icell_discharge_load_plot{i,1}(1:time_start_dis{i,2}-1);

   for z=2:quan_load(i)
         Vcell_discharge_load{i,z} = Vcell_discharge_load{i,z}- Vcell_discharge_load{i,z}(time_start_dis{i,z})
         +Vcell_discharge_load{i,z-1}(time_start_dis{i,z});
         Vcell_discharge_load{i,quan_load(i)+1} = [Vcell_discharge_load{i,quan_load(i)+1}
         Vcell_discharge_load{i,z}(time_start_dis{i,z}:time_start_dis{i,z+1}-1)];
         Icell_discharge_load_plot{i,quan_load(i)+1} = [Icell_discharge_load_plot{i,quan_load(i)+1}
         Icell_discharge_load_plot{i,z}(time_start_dis{i,z}:time_start_dis{i,z+1}-1)];
     end
    Vcell_discharge_load{i,quan_load(i)+1} = [Vcell_discharge_load{i,quan_load(i)+1}   Vcell_discharge_load{i,quan_load(i)}
(time_start_dis{i,quan_load(i)+1}:end)];

   Icell_discharge_load_plot{i,quan_load(i)+1} = [Icell_discharge_load_plot{i,quan_load(i)+1}
Icell_discharge_load_plot{i,quan_load(i)}(time_start_dis{i,quan_load(i)+1}:end)];
```